

**Assessing the Tissue-Level Response and the Risk of Neck Pain in Rotary-Wing Aircrew using a
Finite Element Model of the Neck**

by

Prasannaah Hadagali

A thesis

presented to the University of Waterloo

in fulfilment of the

thesis requirement for the degree of

Doctor of Philosophy

in

Mechanical and Mechatronics Engineering

Waterloo, Ontario, Canada, 2024

© Prasannaah Hadagali 2024

Examining Committee Membership

The following served on the Examining Committee for this thesis. The decision of the Examining Committee is by majority vote.

External Examiner	ROBERT THOMSON Professor, Mechanics and Maritime Sciences Chalmers University of Technology
Supervisor	DUANE S. CRONIN Professor, Mechanical and Mechatronics Engineering University of Waterloo
Internal Member	NAVEEN CHANDRASHEKAR Associate Professor, Mechanical and Mechatronics Engineering University of Waterloo
Internal Member	ARASH ARAMI Assistant Professor, Mechanical and Mechatronics Engineering University of Waterloo
Internal-External Member	JACK P. CALLAGHAN Professor, Kinesiology and Health Sciences University of Waterloo

Author's Declaration

This thesis consists of material all of which I authored or co-authored: see Statement of Contributions included in the thesis. This is a true copy of the thesis, including any required final revisions, as accepted by my examiners.

I understand that my thesis may be made electronically available to the public.

Statement of Contributions

Prasannaah Hadagali (PH) developed all presented methods in this thesis including: (1) assessments, enhancements/modifications, verification and validation of an existing finite element head-neck model with experimental data, (2) muscle-based repositioning, (3) numerical implementation of the head-supported mass with its properties and (4) kinematic, kinetic and tissue-level assessments. Duane S. Cronin (DSC), in collaboration with Steven L. Fischer (SLF) and Jack P. Callaghan (JPC), formulated a project proposal for assessing the risk of neck pain in the rotary-wing aircrew using an existing finite element head-neck model. The work related to upper cervical spine model enhancements, verification and validation, reported in Phase #1 of this research, was done with the support from GHBM and was outside the proposed rotary-wing aircrew neck pain project.

Some of the thesis content has been previously published in the following journal articles or conference proceedings:

Hadagali P, Cronin DS (2020), Quantification of Ligament Contribution for Physiologic Loading in the Upper Cervical Spine Using Detailed FE Model, 16th Annual Injury Biomechanics Symposium, May 17-19, 2020, Columbus, OH. (Phase #1)

PH identified the need to enhance the existing model, performed model simulations, post-processing, analysis and drafted the abstract (75%). DSC provided technical guidance and changes to improve the abstract (25%).

Hadagali P, Cronin DS (2020) Quantification of Upper Cervical Spine Motion Sensitivity to Ligament Laxity Using a Finite Element Human Body Model for Occupant Safety, Proceedings of the IRCOBI 2020, Munich, Germany, Sept, 8-10, pp. 229-230. (Phase #1)

PH identified the need to enhance the existing model, performed model simulations, post-processing, analysis and drafted the manuscript (75%). DSC provided technical guidance and changes to improve the manuscript (25%).

Hadagali P, Callaghan JP, Fischer SL, Cronin DS (2022) Importance of Muscle-Based Repositioning of a Detailed FE Neck Model in Flexion to Predict Kinematics and Tissue-Level Loading, 9th World Congress of Biomechanics, July 10-14, 2022, Taipei, Taiwan. (Phase #2)

PH identified the research gap, performed model simulations, post-processing, model assessments and drafted the abstract (55%). SLF (10%) and JPC (10%) provided data for model input and assessments. DSC provided technical guidance and changes to improve the abstract (25%).

Hadagali P, Cronin DS (2022) Anatomical Enhancements to the Upper Cervical Spine FE Model Improved the Intervertebral Response Required for Injury Assessments in Non-neutral Neck Postures, Proceedings of the IRCOBI 2022, Porto, Portugal, Sept, 14-16, pp. 890-891. (Phase #1)

PH identified the need to enhance the existing model, performed model simulations, post-processing, analysis and drafted the manuscript (75%). DSC provided technical guidance and changes to improve the manuscript (25%).

Hadagali P, Cronin DS (2023) Enhancing the Biofidelity of an Upper Cervical Spine Finite Element Model Within the Physiologic Range of Motion and its Effect on the Full Ligamentous Neck Model Response, J Biomech. Eng., 145(1), p. 011007. DOI: 10.1115/1.4055037. (Phase #1)

PH identified the need to enhance the existing model, performed model simulations, post-processing, analysis, model verification & validation and drafted the manuscript (75%). DSC provided technical guidance and changes to improve the manuscript (25%).

Hadagali P, Callaghan JP, Fischer SL, Cronin DS (2023) Effect of Rotary-Wing Aircrew Head-Supported Mass in Flexion Position on the Tissue-Level Response of the Neck: A Finite Element Study, Ontario Biomechanics Conference, May 09-11, 2023, Waterloo, Ontario. (Phase #3)

PH performed model simulations, post-processing, model assessments and drafted the abstract (55%). SLF (10%) and JPC (10%) provided data for model input and assessments. DSC provided technical guidance and changes to improve the abstract (25%).

Hadagali P, Fischer SL, Callaghan JP, Cronin DS (2024) Quantifying the Importance of Active Muscle Repositioning a Finite Element Neck Model in Flexion Using Kinematic, Kinetic and Tissue-Level Responses, Ann Biomed Eng. 52, 510-525 DOI: 10.1007/s10439-023-03396-7. (Phase #2)

PH identified the research gap, performed model simulations, post-processing, model validation, assessments and drafted the manuscript (55%). SLF (10%) and JPC (10%) provided data for model input and assessments. DSC provided technical guidance and changes to improve the manuscript (25%).

Co-authors agree with the evaluation of the roles and contributions:

(Steven L. Fischer)

(Jack P. Callaghan)

(Duane S. Cronin)

Abstract

Epidemiological studies report a prevalence of neck pain among rotary-wing aircrew (RWA) potentially associated with head-supported mass (HSM), frequent physiologic motions of head-neck, aircraft vibration, and prolonged time in non-neutral head-neck positions. Experimental studies with human volunteers and computational studies using head-neck models have suggested potential causal pathways for neck pain in RWA, including increased activity in muscles and increased forces in the spinal column. However, additional insight is required to understand the interactions of HSM, which comprises a helmet with optional mounted devices, and non-neutral head-neck positions. The present study aimed to simulate RWA non-neutral head-neck positions with the HSM using a detailed finite element (FE) head-neck model to assess the tissue-level biomechanical response and potential sources for neck pain in RWA.

A detailed FE head-neck model (NM_{M50}) was extracted from a full human body model of a 50th percentile male. The NM_{M50} model was enhanced, verified and validated starting sequentially from the ligamentous upper cervical spine (UCS), full cervical spine, and full head-neck with active musculature for physiologic loading conditions ($NM_{M50-Hill-E}$). The $NM_{M50-Hill-E}$ model was simulated for non-neutral head-neck positions (flexion and axial rotation) using a conventional boundary condition and a novel active muscle repositioning approach, demonstrating the importance of active muscle repositioning on tissue-level response. Finally, the $NM_{M50-Hill-E}$ model with active muscle repositioning was simulated for non-neutral head and neck positions with HSM.

The present study demonstrated that the muscle-based method of repositioning the FE head-neck model improved the head and neck kinematic response by capturing the in vivo flexion and axial rotation positions better than the conventional boundary condition method. In the simulated RWA head-neck positions, tissue-level investigations demonstrated an increase in the muscle force, intervertebral disc (IVD) force, endplate stress and annulus fibrosus (AF) collagen fiber strain with an increase in the HSM in flexion. Similarly, an increase in the magnitude of non-neutral position from flexion to a combined position was shown to increase the ligament distraction along with an increase in muscle force, IVD force, endplate stress and AF collagen fiber strain. The detailed FE head-neck model provided valuable insight by predicting tissue-level biomechanical responses in the RWA neck while providing guidance on factors that may contribute to neck pain risk in the RWA.

Acknowledgements

I want to take this opportunity to thank my advisor, Prof. Duane Cronin, for accepting me into his research group and providing me with a fantastic opportunity to pursue research on an exciting and less-explored topic. Duane, thank you for offering me support and guidance in every aspect during my journey as a doctoral trainee. I appreciate your time and dedication to mentoring me amidst your busy (sleepless) schedule.

I want to express my appreciation to the Natural Sciences and Engineering Research Council of Canada DND/NSERC program, the Canada Research Chairs program and the University of Waterloo for their financial support. I am thankful to the Digital Research Alliance of Canada for the computing resources and the Global Human Body Model Consortium (GHBMC) for the use of the computational human model. I am thankful to Gentex Corp., Thumbprint Solutions Inc., Profs. Steven Fischer and Jack Callaghan for the collaboration and for providing the necessary support that helped me progress in my research.

I want to express my sincerest gratitude to my committee members, Profs. Robert Thomson, Jack Callaghan, Naveen Chandrashekar and Arash Arami for the thought-provoking questions and for imparting knowledge that helped improve the quality of my work.

I am grateful to all my colleagues in the Impact Mechanics and Material Characterization (IMMC) group (both past and present) for making my journey as a doctoral student memorable. Specifically, I would like to acknowledge Jeff Barker for helping me understand the ‘nuts and bolts’ of the GHBMC neck model and always being available to provide any clarifications and timely feedback to help me move forward in my research. To Matheus C and Mike, for all the wonderful conversations we have had so far on various topics. Also, I would like to thank all my fellow students in EC4-Solid Mechanics for their friendship. The immigration consulting office at the University of Waterloo, especially Louann and Shannon, deserves acknowledgement for their time reviewing my documents and ensuring I don’t miss anything important that would crazily affect the processing times. I am grateful to the Constituency Assistant at Waterloo (Alison Brown) for all the timely help.

I am thankful to Jeff Barrett for sharing insights on the musculoskeletal neck model that was used as a reference throughout this research. I miss the ‘*Bagel with Barrett*’ sessions at *Balzac's* and *Matter of Taste* during my initial days in Waterloo. All the knowledge imparted by Jeff during our hangouts

bettered my thought process and how I look at research problems. I would also like to thank Sayed Naseel for offering a listening ear and some words of wisdom whenever I felt discouraged.

Thanks to all my buddies (especially Raghav Kulkarni, Kiran Koya) and colleagues in different parts of the USA, with whom I have shared numerous wonderful occasions. Most importantly, I thank all of them for being with me during one of the most challenging phases of my life. I cannot imagine coping with the situation without their support, for which I am forever grateful. I would also like to thank all my friends in Waterloo for all the beautiful experiences since my arrival to Canada, and I look forward to more fun in the future.

To all my relatives in India and across the globe for constantly keeping me in their prayers. Especially Thimmu *Anna* and Suma *Vaini* for their unconditional love and moral support and for ensuring that I have never missed home from the time since I moved to North America to pursue grad school. I feel blessed to have wonderful parents-in-law (Rajendra Joshi and Shashikala Joshi) and thank them for being very supportive.

I want to thank Pramodh for being such a nice brother and taking care of many responsibilities on my behalf. I could not have pursued a PhD without the blessings from my parents, the late Vijaykumar and Shailaja. Words do not do justice in describing the sacrifices they made to ensure a good life for me and my brother despite all the challenges that life threw on them. Lastly, thanks to my dear wife, Priyanka, for being very understanding and patient and unconditionally supporting me in all possible ways. There are no words to describe all her sacrifices for me, and I sincerely pray that all her wishes are fulfilled!

To the Almighty, for granting me everything!

Dedication

In loving memory of my late *Appa* (Dad)

Mr. Vijaykumar Hadagali

Appa, I cannot imagine achieving anything without your blessings and guidance. You will be missed in every aspect of my life!

Table of Contents

Examining Committee Membership	ii
Author’s Declaration	iii
Statement of Contributions	iv
Abstract	vi
Acknowledgements	vii
Dedication	ix
List of Figures	xvii
List of Tables	xxxii
List of Nomenclature	xxxiii
List of Symbols	xxxv
Chapter 1 Introduction	1
1.1 Motivation	1
1.2 Research objectives	5
1.2.1 Objective #1.....	5
1.2.2 Objective #2.....	6
1.2.3 Objective #3.....	7
1.3 Thesis outline	7
Chapter 2 Background and literature review	10
2.1 Anatomical terms	10
2.2 Anatomy of the human neck.....	11
2.2.1 Cervical spine	11
2.2.2 Articulations in the cervical spine	24
2.2.3 Neck muscles.....	26

2.3 Physiologic kinematics of the head and neck	28
2.3.1 In vitro ROM of the neck	28
2.3.2 In vivo ROM of the neck.....	32
2.3.3 Differences between in vitro and in vivo head and neck ROM.....	33
2.3.4 In vivo ROM of the neck when head is subjected to an external moment with a passive (relaxed) neck	34
2.3.5 In vivo flexion of the passive (relaxed) neck under gravity	35
2.4 Neck pain.....	37
2.4.1 Pain physiology	38
2.4.2 Potential pain sources in the neck.....	41
2.5 Neck pain risk factors in the rotary-wing aircrew	45
2.5.1 Head-supported mass (HSM)	47
2.5.2 Non-neutral head-neck positions	47
2.5.3 Time spent in non-neutral head-neck positions during different tasks.....	52
2.5.4 Workspace and organization factors.....	55
2.5.5 Human-related factors	55
2.6 Computational head-neck models	56
2.6.1 Computational head-neck models for biomechanical assessments	56
2.6.2 Existing computational head-neck models applied to assess risk of neck pain in RWA	58
2.7 Representation of muscles in existing computational head-neck models.....	61
2.7.1 Hill-type muscle material model	61
2.7.2 Simplified externally applied loads to simulate muscles.....	64
2.7.3 Passive muscle property in existing computational head-neck models.....	67
2.8 Methods to achieve non-neutral positions in computational head-neck models	70

2.8.1 Computational approaches	70
2.8.2 Methodologies to reposition computational head-neck models	71
2.8.3 Research gap in computational head-neck model repositioning methodologies	75
2.9 GHBMC human body FE model	76
2.9.1 GHBMC M50-O neck model	77
2.9.2 GHBMC M50-O neck model validation	84
Chapter 3 Methods	85
3.1 Methodology overview	85
3.2 Phase #1: Enhancement, verification, and validation of the cervical spine model	85
3.2.1 Preliminary assessment of the UCS _{M50} model	86
3.2.2 Anatomical enhancements to the UCS _{M50} model	91
3.2.3 Ligament Laxity Identification in the UCS _{M50-G} model using optimization	92
3.2.4 Verification and validation of the UCS _{M50-Opt} model	94
3.2.5 Validation of the full ligamentous cervical spine model	95
3.3 Phase #2a: Simulating non-neutral head-neck positions using muscle activation	98
3.3.1 Head-neck model updated with enhanced UCS and simplified head	98
3.3.2 Passive neck stiffness assessment of the NM _{M50} model	100
3.3.3 Active neck stiffness assessment of the NM _{M50} model	102
3.3.4 Exclusion of skin and adipose tissue and modification of passive muscles in the NM _{M50} model	102
3.3.5 Passive neck stiffness assessment and improvement of the NM _{M50-Hill} model	103
3.3.6 Simulating head-neck flexion in the NM _{M50-Hill-E} model using active muscles	105
3.3.7 Simulating head-neck axial rotation in the NM _{M50-Hill-E} model using active muscles	107

3.4 Phase #2b: Quantifying the importance of active muscle repositioning using kinematic, kinetic and tissue-level responses.....	110
3.4.1 Global kinematics of the head-neck	112
3.4.2 Intervertebral kinematics	114
3.4.3 Ligament distractions	114
3.4.4 Muscle force	115
3.4.5 IVD deformation	115
3.4.6 IVD force.....	117
3.4.7 Collagen fiber strains in the AF.....	117
3.5 Phase #3: Neck pain risk in rotary-wing aircrew (RWA).....	119
3.5.1 Simulating the HSM relevant to RWA.....	119
3.5.2 Identifying the target non-neutral head-neck positions from the literature	120
3.5.3 Methodology to measure the RWA head-neck angles	121
3.5.4 Simulating a flexion position with and without the HSM	122
3.5.5 Simulating a combined position with the HSM (HHNC configuration)	123
3.5.6 Neck pain assessments using tissue-level responses	125
Chapter 4 Results	129
4.1 Phase #1: Enhancement, verification, and validation of the cervical spine model.....	129
4.1.1 Preliminary assessment of the UCS _{M50} model	129
4.1.2 Anatomical enhancements to the UCS _{M50} model.....	132
4.1.3 Ligament laxity identification in the UCS _{M50-G}	133
4.1.4 Verification and Validation of UCS _{M50-Opt} model.....	134
4.1.5 Validation of the full ligamentous cervical spine model	136
4.2 Phase #2a: Simulating non-neutral head-neck positions using muscle activation.....	142

4.2.1	Passive neck stiffness assessment of the NM_{M50} model	142
4.2.2	Active neck stiffness assessment of the NM_{M50} model	144
4.2.3	Passive neck stiffness assessment and improvement of the $NM_{M50-Hill}$ model	145
4.2.4	Simulating head-neck flexion in the $NM_{M50-Hill-E}$ model using active muscles.....	146
4.2.5	Simulating head-neck axial rotation in the $NM_{M50-Hill-E}$ model using active muscles.....	147
4.3	Phase #2b: Quantifying the importance of active muscle repositioning using kinematic, kinetic and tissue-level responses.....	149
4.3.1	Comparing a conventional external BC- and muscle-based approaches of repositioning the $NM_{M50-Hill-E}$ model in flexion	149
4.3.2	Comparing a conventional external BC- and muscle-based approaches of repositioning the $NM_{M50-Hill-E}$ model in axial rotation	156
4.4	Phase #3: Neck pain risk in rotary-wing aircrew (RWA).....	163
4.4.1	Effect of HSM configuration in 25° head-neck flexion.....	163
4.4.2	Effect of non-neutral head-neck position magnitude with the HSM (HHNC configuration)	175
Chapter 5 Discussion.....		188
5.1	Phase #1: Enhancement, verification, and validation of the cervical spine model.....	188
5.1.1	Benefits of the LHS-based DOE method	189
5.1.2	Importance of intervertebral kinematics as the target response in the optimization process	190
5.1.3	Verification of the computed ligament laxities with previous studies	191
5.1.4	Effect of facet-cartilage on the ROM response	194
5.1.5	Summary of Phase #1	194
5.2	Phase #2a: Simulating non-neutral head-neck positions using muscle activation.....	196
5.2.1	Basis for simulating non-neutral head-neck positions using muscle activation	196

5.2.2	Passive and active neck stiffness assessment of the NM_{M50} model.....	197
5.2.3	Passive neck stiffness assessment of the $NM_{M50-Hill}$ model	199
5.2.4	Simulating non-neutral head-neck positions in the $NM_{M50-Hill-E}$ model using active muscles	200
5.2.5	Summary of Phase #2a	201
5.3	Phase #2b: Quantifying the importance of active muscle repositioning using kinematic, kinetic and tissue-level responses.....	203
5.3.1	Comparing a conventional external BC- and muscle-based approaches of repositioning the $NM_{M50-Hill-E}$ model in flexion	204
5.3.2	Comparing a conventional external BC- and muscle-based approaches of repositioning the $NM_{M50-Hill-E}$ model in axial rotation	206
5.3.3	Demonstrating the importance of muscle-based repositioning method.....	208
5.3.4	Importance of muscle-based repositioning method in the RWA context.....	210
5.3.5	Summary of Phase #2b.....	211
5.4	Phase #3: Risk of neck pain in rotary-wing aircrew (RWA).....	212
5.4.1	Muscle force response	213
5.4.2	IVD force response.....	214
5.4.3	Collagen fiber strain response in the AF	215
5.4.4	Endplate stress response	217
5.4.5	Ligament distraction response	220
5.4.6	Tissue-level neck pain pathway.....	221
5.4.7	Cumulative trauma	222
5.4.8	Clinical relevance of the model outcome	223
5.4.9	Other mechanisms that may lead to neck pain	224
5.4.10	Summary of Phase #3.....	224

Chapter 6 Limitations and future work	225
6.1 Limitations.....	225
6.2 Future work	226
Chapter 7 Conclusions	228
Letters of copyright permission	229
Bibliography.....	250
Appendices	297
Appendix A Supplementary materials for Phase #1	297
Appendix B Supplementary materials for Phase #2a.....	319
Appendix C Supplementary materials for Phase #2b	322
Appendix D Supplementary materials for Phase #3	340

List of Figures

Figure 1: The rotary-wing aircrew (RWA) operating the CH-146 rotary-wing aircraft during a mission. The figure shows three types of RWA including flying pilots, non-flying pilots and flight engineers.....	2
Figure 2: An overview of the work-flow undertaken to assess the risk of neck pain in RWA using an FE head-neck model. The list of tasks i.e. ligamentous spine model enhancements, verification and validation required to meet Objective #1 were performed in Phase #1. The list of tasks required to reposition the neck model in physiologic range using active muscles to meet Objective #2 was included in Phase #2. The tissue-level assessments with the HSM and non-neutral head-neck positions, as stated in Objective #3, were done in Phase #3.....	9
Figure 3: Anatomical planes and directions.	10
Figure 4: Primary motions of the head and neck in different anatomical planes.	11
Figure 5: A) Illustration of the structure of human spine. The region enclosed within the solid black line is called the cervical spine and B) A sagittal view of the cervical spine illustrating the upper cervical and lower cervical spine enclosed within the solid orange and blue lines, respectively.....	12
Figure 6: Illustration of the thin cortical bone tissue surrounding the porous trabecular bone tissue in an exemplar human vertebra (Gray, 1918).....	13
Figure 7: Typical structure of a cervical vertebra in the LCS (superior view).....	14
Figure 8: Illustrating the orientation of the facet articular processes in 45 with respect to the horizontal in the C4 vertebra.	16
Figure 9: Superior view of the first cervical vertebra (atlas).....	17
Figure 10: Anterior and posterior views of the second cervical vertebra (axis).....	17
Figure 11: Illustration of a sectioned IVD with the AF, NP and vertebral endplate.	18
Figure 12: Illustration of the AF structure with the lamellar layers and the orientation of collagen fibers in a lamella.	19
Figure 13: Schematic representation of the tension response in the AF when exposed to a compressive loading, as described in the literature (Levangie and Norkin, 2005).....	20
Figure 14: Sagittal view of the upper cervical spine ligaments.....	21
Figure 15: Posterior view of the upper cervical spine ligaments.....	22
Figure 16: Sagittal view of the lower cervical spine ligaments.....	23
Figure 17: Illustration of the saddle/interbody joint and facet/zygapophyseal joint in an FSU.	25

Figure 18: A) Illustrating the flexion and extension motion in the UCS that demonstrates the dominance of atlanto-occipital joint in sagittal plane and B) Illustrating the axial rotation of C1 around dens to show that dominance of atlanto-axial joint in the transverse plane. 25

Figure 19: Hierarchical structure of the skeletal muscle. 26

Figure 20: Illustration of the actin and myosin filaments within a sarcomere in a relaxed and contracted state. 27

Figure 21: Illustrating the effect of cross-bridge in generation of active muscle force using the length-tension relationship. 28

Figure 22: Illustrating the constraint of the inferior end and application of an external moment to the superior end of the cadaveric cervical spine specimens as described in the experimental procedures. 29

Figure 23: A summary of the experimental intervertebral ROM when a moment of 1.0 Nm is applied to the ligamentous cervical spine specimen in flexion, extension and axial rotation loading modes. The experimental summary highlights the dominance of UCS when the ligamentous cervical spine is subjected to all the three modes of physiologic loading. 31

Figure 24: A summary of the mean in vivo intervertebral ROM reported at the end-range of voluntary flexion, extension and axial rotation. The experimental summary highlights the dominance of LCS during voluntary flexion and dominance of UCS during a voluntary axial rotation of the head and neck. 33

Figure 25: A comparative figure illustrating the similarities in the mean global head rotation (C0-C7) and differences in the mean intervertebral rotations (C0-C1 to C6-C7) in physiologic flexion and extension in cadaveric specimens (in vitro) and live humans (in vivo). 34

Figure 26: The mean rotation of the head relative to the torso plotted against the applied moment to the head (in flexion and extension) from the experimental study by McGill et al. (1994). 35

Figure 27: The experimental setup used to assess the response of head flexion under gravity and passive neck muscles. 36

Figure 28: An illustration of nociceptive pain pathway ascending and descending pain pathways in response to external noxious stimulus. 39

Figure 29: A flowchart summarizing the pathophysiology of acute and chronic pain based on the literature (Dureja et al., 2017; Solomonow, 2004; Treede et al., 2015). The potential neck pain path (chronic pain) in the RWA is highlighted in the flowchart. 40

Figure 30: Illustrating the innervation and the presence of pain receptors in the peripheral aspects of the IVD (A). Also, the growth of the nerve endings into the NP as the IVD degenerates is illustrated (B).....	42
Figure 31: Location of the referred pain regions in the neck corresponding to different stimulated facet levels.....	43
Figure 32: Head-neck angle measurement in the three anatomical planes in the RWA as reported in the literature (Tack et al., 2014).	48
Figure 33: Quantification of the head-neck angle in the RWA flying pilot while performing the ‘outside scan chin bubble’ task during a night mission i.e. with the NVG. The figure demonstrates the combined motion of the head and neck in the RWA during a given scanning task (Tack et al., 2014).	49
Figure 34: The calculated mean and ± 1 SD from the reported mean head-neck angles in flexion-extension, axial rotation and lateral bending across all the tasks in flying pilots (A), non-flying pilots (B) and flight engineers (C) in the literature (Tack et al., 2014). F: Flexion, E: Extension, L. AR: Left axial rotation, R. AR: Right axial rotation, L. LB: Left lateral bending and R. LB: Right lateral bending	50
Figure 35: Illustrating the reduction in FOV in the RWA with the addition of NVG during night missions.....	51
Figure 36: Mean head-neck angle in left and right axial rotation in the flying pilots during day and night missions as reported in the literature (Tack et al., 2014). The literature indicates an increase in the head-neck angle in most of the tasks as a result of NVG.	52
Figure 37: Mean percentage time spent by RWA in different head-neck positions as observed in different planes.....	53
Figure 38: Mean time spent by the flying pilots in each of the 12 tasks as reported in the literature (Tack et al., 2014).....	54
Figure 39: Mean time spent by the non-flying pilots in each of the 12 tasks as reported in the literature (Tack et al., 2014).....	54
Figure 40: Mean time spent by the flight engineers in each of the 22 tasks as reported in the literature (Tack et al., 2014).....	55
Figure 41: MB model of the head-neck used to study the effect of HSM in RWA.	58
Figure 42: MB model of the head-neck to investigate the neck pain countermeasures in RWA.	59

Figure 43: EMG-driven MSK model of the head-neck to provide insight on the effect of HSM and non-neutral positions on the risk of neck pain in the RWA. 60

Figure 44: MSK model of the head-neck to study the interaction of HSM with the neck in a neutral posture. 60

Figure 45: Detailed FE head-neck model developed at the Royal Military College, Canada, to assess the risk of neck pain in the RWA due to HSM and non-neutral positions. 61

Figure 46: Illustration of the Hill-type muscle model showing the active contractile element (CE), passive elastic element (PEE) and an optional parallel damping element (PDE). 62

Figure 47: Illustration of the force vs. length ($fL(L)$), force vs. velocity ($fV(V)$) and activation levels ($a(t)$) properties of the contractile element (CE) in the Hill-type muscle model. An exemplar activation vs. time curve from one of the existing computational neck models (Barker and Cronin, 2021; Cronin, 2014; Fice et al., 2011; Panzer, 2006; Panzer et al., 2011; Shateri and Cronin, 2015) is shown for illustrative purpose. 63

Figure 48: (A) Illustrating the simplification of in vivo muscle forces in the in vitro experimental studies on cadaveric cervical spine specimens by applying an (i) axial load or a (ii) follower load (Patwardhan et al., 2000). (B) Illustration of an experimental set-up used to apply (i) axial load and (ii) follower load on cadaveric cervical spine specimens (Wawrose et al., 2021). 65

Figure 49: Illustrating the simplification of muscle action in the existing cervical spine FE models by applying an axial load or a follower load. The axial load or follower load, although represents the in vivo muscles, cannot reposition the model. A non-exhaustive list of cervical spine FE models that incorporated muscles in the form of axial load and follower load is shown in this figure. 66

Figure 50: Illustrating the combined approach where MSK human body model with HSM is simulated for gait (A) and neck muscle forces are estimated (B). Estimated muscle forces from the MSK model are applied to a ligamentous cervical spine FE model as force vectors. 67

Figure 51: Summarizing a non-exhaustive list of passive muscle tensile properties of the whole muscle-tendon units obtained from experimental studies in the literature that could potentially be used in the computational head-neck models. 68

Figure 52: The tensile material property of the passive muscle in the Hill-type model is expressed as a product of peak isometric stress (σ_{max}) and the dimensionless stress vs. stretch relationship. In the existing computational neck models, the σ_{max} is assumed to be 500 kPa and the dimensionless stress vs. stretch relationship ($h(\lambda)$) is obtained from Winters (1995). 69

Figure 53: Summary of a non-exhaustive list of material properties that have been used to define the tensile properties of passive muscles in existing head-neck models. 70

Figure 54: An illustration of the input head angular displacement as a function of time (external BC) to reposition an MB head-neck model from neutral posture to forward flexion position. 72

Figure 55: Illustrating the repositioning of (A) a forward- and (B) an inverse-dynamic MSK head-neck model from a neutral to a non-neutral position using an external BC such as moment or a kinematic data from experimental trials. 73

Figure 56: The figures illustrate the application of an external BC (moment or displacement) to the superior aspects of the model to simulate non-neutral positions along with an axial load or a follower load that simulate cervical spinal muscles. 74

Figure 57: Detailed FE head-neck model with the musculature developed at the University of Waterloo (Shateri, 2012; Shateri and Cronin, 2015). The figure illustrates the application of an external BC (rotational displacement) to simulate a non-neutral head-neck position in the FE model. The muscles were not activated during the application of rotational displacement. 75

Figure 58: Illustration of the GHBMC M50-O neck model showing the bottom-up build of the model starting from FSU to ligamentous cervical spine and the detailed muscles and soft tissues surrounding the cervical spine. 77

Figure 59: Illustrating the hard tissues in the GHBMC M50-O neck model. The cortical, trabecular and vertebral endplates of C4 vertebra is shown for illustrative purposes. 78

Figure 60: Illustrating an IVD in the GHBMC M50-O neck model with details including nucleus pulposus, annular ground substance and annular collagen fibers. The black and grey diagonal lines within the lamellar shell elements indicates the orientation of the collagen fibers. The dotted lines illustrate the common nodes between the corners of the lamellar shell elements. 79

Figure 61: Illustration of the collagen fiber orientation in the lamellae of the IVD AF in GHBMC M50-O neck model. The fiber orientation angle progressively reduced from inner to outer concentric layers. 80

Figure 62: Representation of the active component (contractile element, CE) and passive muscles (solid element) in the GHBMC M50-O neck model. An example of the sternocleidomastoid muscle is shown for illustrative purposes. 82

Figure 63: Illustration of 1D muscle elements (CE) with the series of supporting (truss) elements to maintain line of action of muscle force and mimic the in vivo force generating capacity in the muscles

(A). Illustration of the spring elements connecting the hyoid bone to skull and C4-C6 vertebrae (B). 3D passive muscle elements are masked for illustrative purposes.....	83
Figure 64: The muscle activation as a function of time for the flexors (contraction) and extensors (co-contraction) in the GHBMC M50-O neck model (Correia et al., 2020).....	83
Figure 65: Preliminary assessment of UCS _{M50} model starting from model extraction, applying BCs, model verification with literature (Lasswell et al. 2017), assessment of the intervertebral response and identifying the areas for model enhancements.	87
Figure 66: Schematic showing ligament laxity (dashed blue line) calculated using optimization methods, the typical force-displacement response of a ligament (red dashed line) and the post-ultimate load response (dashed grey line). Ligament laxity was defined as the ligament’s elongation amount without substantial applied force. In the model, the difference between ‘Actual length’ and ‘Length with laxity’ was calculated as ligament laxity using optimization methods.	88
Figure 67: Flow chart elaborating the preliminary DOE process that identified the need for UCS _{M50} model enhancements.	90
Figure 68: Anatomical enhancements to the UCS _{M50} model a) decreased C1 cartilage thickness, b) corrected alar ligament insertion location. Flow-chart describing the update of the UCS model from UCS _{M50} to UCS _{M50-G}	92
Figure 69: Steps involved in identifying the ligament laxity values in the UCS _{M50-G} model. Flowchart showing the update of the model from UCS _{M50-G} to UCS _{M50-Opt}	93
Figure 70: The figure shows the original and enhanced models that are color coded black and blue, respectively. A) The biofidelity of the original UCS (UCS _{M50} , color coded black) and the enhanced UCS (UCS _{M50-Opt} , color coded blue) models were assessed with experimental data B) To the original LS model (LS _{M50}), the enhanced UCS model (UCS _{M50-Opt} , color coded blue) was included while retaining the original LCS and named LS _{M50-Opt} . Next, the original LS model was replaced with enhanced UCS (UCS _{M50-Opt}) and LCS (LCS _{M50-FC}) and named LS _{M50-FC-Opt}	96
Figure 71: The GHBMC M50 v5.1 head-neck model updated with the UCS _{M50-Opt} with the detailed head (A) and simplified head, NM _{M50} (B).	99
Figure 72: The effect of the skin, adipose tissue and passive muscles in the NMM50 model are assessed under gravity loading. In the NM _{M50} model (A), skin (SK) was excluded (B), skin (SK) and adipose tissue (AT) were excluded (C), and SK, AT and passive muscle (PM) were removed, retaining the inactive 1D contractile element ($a(t)=0$) from the Hill-type muscle model (D).	101

Figure 73: The effect of the skin, adipose tissue and passive muscles in the NM_{M50} model are assessed for an externally applied moment. (A) The NM_{M50} model, (B) Skin (SK) was excluded, (C) Skin (SK) and adipose tissue (AT) were excluded, (D) The SK, AT and passive muscle (PM) were removed, retaining the inactive 1D contractile element ($a(t)=0$) from the Hill-type muscle..... 101

Figure 74: Assessment of the NM_{M50} model response to flexor muscle activation under gravity. 102

Figure 75: Illustrating the substitution of 3D passive muscle elements in the NM_{M50} with the passive elastic element (PEE), parallel to the contractile element (CE) within the Hill-type muscle material ($NM_{M50-Hill}$). Parallel damping element (PDE) was not included in the current study. 103

Figure 76: Illustrating the application of gravity loading (A), flexion moment (B) and extension moment (C) to the $NM_{M50-Hill}$ model with relaxed muscles ($a(t)=0$) in the CE of Hill-type muscle model..... 104

Figure 77: Enhancing the $NM_{M50-Hill}$ model by replacing the low strain rate ($0.01s^{-1}$) passive muscle property proposed by Gierczycka et al. (2021) with the in vivo physiologic property of human gracilis muscle reported by Persad et al. (2021). 105

Figure 78: Repositioning the $NM_{M50-Hill-E}$ model by activating the flexors and co-activating the extensors under gravity. The activation levels resulted in the head flexing forward by approximately 30° 106

Figure 79: Muscle activation levels, $a(t)$, in the $NM_{M50-Hill-E}$ model corresponding to the %MVC levels for physiologic flexion from experimental data in the literature. The illustrated activation levels repositioned the $NM_{M50-Hill-E}$ model in 30° head flexion. 107

Figure 80: Muscle activation levels, $a(t)$, to reposition the $NM_{M50-Hill-E}$ model in 30° axial rotation position within the physiologic ROM, identified in this study based on multiple iterations. 109

Figure 81: Repositioning the $NM_{M50-Hill-E}$ model in 30° flexion using two approaches. A) An external BC (moment) is applied to the head of the passive $NM_{M50-Hill-E}$ model, and B) as described in Phase #2a, flexors and extensors are activated at 0.1 and 0.012 activation levels, respectively, under gravity. 111

Figure 82: Repositioning the $NM_{M50-Hill-E}$ model in 30° axial rotation using two approaches. A) An external BC (moment) is applied to the head of the passive $NM_{M50-Hill-E}$ model, and B) as described in Phase #2a, different muscle groups are activated under gravity. 111

Figure 83: Illustration of the head and neck kinematic measurement methods in the $NM_{M50-Hill-E}$ model as described in the literature (Tapanya et al., 2021). 113

Figure 84: Illustrating the method to measure the ligament distractions in the NM _{M50-Hill-E} model....	115
Figure 85: An illustration of the IVD global deformation measurement procedure as described in the literature (Ito et al. 2005).....	116
Figure 86: Illustrates the IVD force measurement using section plane in LS-Prepost when the NM _{M50-Hill-E} model was repositioned in a non-neutral position. The compressive forces were measured in the direction normal to the section plane. During measurement, all other components except the IVDs were masked.	117
Figure 87: Illustration of the fiber orientation in the AF collagen fibers, along which the strains were measured and compared with the experimental data that reported strains along the fiber orientation on isolated fiber specimens.	118
Figure 88: Illustrating the mass properties of the head and the HGU/56P RWA HSM that include the helmet, NVG, BP and CW.	119
Figure 89: Illustrating the CoG locations for the helmet (A) and helmet with NVG (BP inclusive) and CW (B) relative to the CoG of the head as reported by Forde et al. (2011). The image of the RWA helmet in the inset is adapted from Forde et al. (2011).	120
Figure 90: Reported head-neck angles in non-neutral positions adapted by the flying pilots (a sub-category of the RWA) that were investigated in this research. F: Flexion, E: Extension, AR: Axial rotation, LB: Lateral bending, L: Left and R: Right.....	121
Figure 91: An illustration of the head-neck angle (θ_f) measurement in the sagittal plane (flexion), as described in the literature (Tack et al., 2014). This method of measurement was also applicable to measure the head-neck angle (θ_{lb}) in the coronal plane (lateral bending).	122
Figure 92: Illustration of the muscle-based methodology to reposition the validated NM _{M50 Hill-E} model without (a) and with the HSM (b and c) in 25°±5% head-neck flexion to assess the effect of HSM on the tissue-level response and associate the risk of neck pain in RWA.	123
Figure 93: Muscle activation strategy describing the activation levels applied to different muscles to reposition the NM _{M50-Hill-E} model with the helmet, NVG and CW in a combined flexion, lateral bending and axial rotation position to mimic the RWA task (HHNC _{25F 10LB 25AR}).	124
Figure 94: Pictorial representation of the four simulated cases relevant to the RWA and the comparisons made to understand the effect of added HSM and magnitude of head-neck positions on the risk of neck pain in the RWA.	125

Figure 95: An exemplar Force vs. Displacement curve assigned to ligaments in the model is shown to illustrate the distinct phases in the mechanical response of ligament. 128

Figure 96: Response of the UCS_{M50} model (blue bars) compared with the experimental data (horizontal lines) during the preliminary assessment in flexion and extension. Horizontal black lines and the shaded grey region are experimental mean and ± 1 SD, respectively, from Panjabi et al. (1991b). The horizontal red lines and shaded red region are the experimental mean and ± 1 SD, respectively, from Oda et al. (1992). 130

Figure 97: Response of the UCS_{M50} model (blue bars) compared with the experimental data (horizontal lines) during the preliminary assessment in axial rotation. Horizontal black lines and the shaded grey region are experimental mean and ± 1 SD, respectively, from Panjabi et al. (1991a). The horizontal red lines and shaded red region are the experimental mean and ± 1 SD, respectively from Oda et al. (1992). 131

Figure 98: Effect of geometrical enhancements on the UCS model ROM in flexion and extension. 133

Figure 99: Verification of the optimized UCS_{M50-Opt} model with the target experimental data (Panjabi et al., 1991a, 1991b) used for optimization. Loading conditions for the models are shown in Figure 65. 135

Figure 100: Validation of the optimized UCS_{M50-Opt} model with another experimental data (Oda et al., 1992). Loading conditions are shown in Figure 65. 136

Figure 101: Comparison of the UCS_{M50} and UCS_{M50-Opt} intervertebral rotations within the full ligamentous spine LS_{M50-FC-Opt} model to experimental data reported by Panjabi et al. (1991a,b)..... 137

Figure 102: Comparison of the UCS_{M50} and UCS_{M50-Opt} intervertebral rotations within the full ligamentous spine LS_{M50-FC-Opt} model to experimental data reported by Oda et al. (1991). 138

Figure 103: Left: Assessment of the UCS_{M50} in LS_{M50} and UCS_{M50-Opt} in LS_{M50-FC-Opt} for intervertebral rotations of the LS_{M50} and LS_{M50-FC-Opt} models. Models are assessed with experimental data reported by Panjabi et al. (1998) and Panjabi et al. (2001). Right: A single mean of the percentage error was calculated for UCS and LCS in flexion and extension. 139

Figure 104: Preliminary assessments on the passive NM_{M50} model under gravitational loading indicated that the passive tissue components contributed to the stiff response. 143

Figure 105: Preliminary assessments on the passive NM_{M50} model with the experimental data from McGill et al. (1994) also confirms the contribution of passive tissues to the stiff response. 143

Figure 106: Response of the NM _{M50} model when the flexor muscles were fully activated under gravity.....	144
Figure 107: Comparing the response of the passive NM _{M50-Hill} (A) and the passive NM _{M50-Hill-E} (B) models under gravitational loading. The head in the NM _{M50-Hill} and NM _{M50-Hill-E} models with relaxed muscles rotated 17° and 33°, respectively.....	145
Figure 108: Comparing the head rotation in the NM _{M50-Hill} and the NM _{M50-Hill-E} models simulated for McGill et al. (1994) experiment on relaxed neck in flexion (A) and extension (B). The results indicate that the biofidelic passive muscle property improved the response of the model in physiologic conditions.	146
Figure 109: FBD of the NM _{M50-Hill-E} model, demonstrating equilibrium in the 30° flexed position. FBD in the sagittal plane where the red and blue lines indicated flexor and extensor group of muscles, respectively.....	147
Figure 110: FBD of the NM _{M50-Hill-E} model, demonstrating equilibrium in the 30° axially rotated position. FBD in the sagittal plane where the red and blue lines indicated flexor and extensor group of muscles, respectively.	148
Figure 111: Intervertebral rotation response of the NM _{M50-Hill-E} model repositioned using external BC (blue bars) and active muscle (orange bars) methods for 30° head flexion, compared with average (solid black) and ±1 SD values (dashed black) from the CSP (Reed and Jones, 2017). The CSP did not report the SD for C7-T1.	150
Figure 112: Capsular ligament (CL) distraction response for 30° head flexion. The distractions of the CL were measured in the anterior (A) and posterior (P) aspects of the ligaments.	152
Figure 113: The mean difference in ligament distraction across C2-C3 to C7-T1 levels when the NM _{M50-Hill-E} model was repositioned in 30° flexion using external BC- and muscle-based methods. The results show that the differences were highest in the ISL compared to other ligaments.	152
Figure 114: Muscle force at different vertebral levels when NM _{M50-Hill-E} model was repositioned using different methods. The findings show that the muscles forces as a result of activation were not uniform through the length of the spinal column, in contrast with the existing assumptions from the literature.....	153
Figure 115: IVD global deformation angles in 30° head flexion simulated using external BC and muscle-based methods, compared to the experimental data reported for physiologic flexion (Ito et al., 2005).....	154

Figure 116: IVD compressive forces (a) and AP shear forces (b) in 30° head flexion simulated using an external BC- and muscle-based methods, compared to an MSK neck model (Barrett et al., 2020).	155
Figure 117: Collagen fiber strains along the fiber orientation in AF when 30° head flexion was simulated using external BC- and muscle-based methods.	156
Figure 118: Axial rotation response of C0-C2 and C2-T1 in the model when the head was repositioned in 30° axial rotation using external BC (blue bar) and active muscle (orange bar) is compared with the experimental data (Guo et al., 2021). The experimental average (solid black) and ±1 SD values (dashed black) correspond to 30° head axial rotation.	157
Figure 119: Coupled lateral bending response of C2-T1 in the model when the head was repositioned in 30° axial rotation using external BC (blue bar) and active muscle (orange bar) is compared with the experimental data (Guo et al., 2021). The experimental average (solid black) and ±1 SD values (dashed black) correspond to 30° head axial rotation.	157
Figure 120: Capsular ligament distraction response in 30° head axial rotation simulated using different repositioning methods. The distractions in the CL were measured in the anterior and posterior aspects on the left (L) and right (R) sides of the spine.	158
Figure 121: The mean difference in ligament distraction across C2-C3 to C7-T1 levels when the NM _{M50-Hill-E} model was repositioned in 30° axial rotation using external BC- and muscle-based methods. The results show that the differences were highest in the ipsilateral CL compared to other ligaments.	159
Figure 122: Muscle force at different vertebral levels when NM _{M50-Hill-E} model was repositioned using different methods. The findings show that the muscles forces as a result of activation were not uniform through the length of the spinal column, in contrast with the existing assumptions from the literature.....	160
Figure 123: IVD compressive forces (a) and AP shear forces (b) in 30° head axial rotation simulated using an external BC- and muscle-based methods.	161
Figure 124: Collagen fiber strains along the fiber orientation in AF when 30° head axial rotation was simulated using external BC- and muscle-based methods.	162
Figure 125: Intervertebral flexion response of the NM _{M50-Hill-E} model with and without the HSM in 25° head-neck flexion. The assessment shows similarities in the intervertebral response in the C2-T1 levels ensuring consistency in the non-neutral head-neck position.....	163

Figure 126: FBDs of the $NM_{M50-Hill-E}$ model in 25° head-neck flexion with and without the HSM....	164
Figure 127: Summary of the overall muscle forces in H_{25F} , HH_{25F} and $HHNC_{25F}$ cases across C2 to C7 vertebral levels, indicating an increase in muscular demand with the addition of HSM.	165
Figure 128: Summary of the flexor and extensor muscle forces in H_{25F} , HH_{25F} and $HHNC_{25F}$ cases across C2 to C7 vertebral levels, specifically indicating an increase in the extensor muscle demand with the addition of HSM.	165
Figure 129: (a) Summary of the compressive forces in C2-C3 to C7-T1 IVDs in H_{25F} , HH_{25F} and $HHNC_{25F}$ cases. (b) Percent change showing increase in compression in C2-C3 to C7-T1 IVDs due to the added HSM.	166
Figure 130: (a) Summary of the AP shear forces in C2-C3 to C6-C7 IVDs in H_{25F} , HH_{25F} and $HHNC_{25F}$. (b) Percent change showing increase in AP shear in C2-C3 to C6-C7 IVDs due to the added HSM.	167
Figure 131: Peak endplate effective stresses across C2 to C7 vertebrae increased with the addition of HSM.	168
Figure 132: Effective stress contours in the C2 inferior endplate demonstrating an increase in stress as a result of added HSM.	169
Figure 133: Collagen fiber peak strains along the fiber orientation in AF in 25° head-neck flexion with and without the HSM.	170
Figure 134: Illustrating the collagen fiber strain contours in the C5-C6 AF in 25° head-neck flexion with and without the HSM in different perspectives, namely superior-inferior, inferior-posterior and posterior-lateral. In the posterior-lateral view, the outer four layers of lamellae are made transparent for visual purposes.	171
Figure 135: Quantifying the strain based on area fractions in the innermost collagen fiber layer of the AF that experienced relatively higher strains than the other layers. The results showed an increase in the area experiencing higher strains with the addition of HSM.	172
Figure 136: The mean difference in ligament distraction across C2-C3 to C7-T1 levels with and without the HSM in 25° head-neck flexion. The increase and decrease in distractions are denoted in positive and negative, respectively. There were minor differences in the ligament distractions due to HSM.	173

Figure 137: Ligament injury risk summary during the 25° head-neck flexion with and without the HSM. The results confirm that the ligaments elongated within the physiologic limits (toe and linear regions).....	174
Figure 138: Intervertebral flexion response of the NM _{M50-Hill-E} model inclusive of HSM in flexion (HHNC _{25F}) and a combined position (HHNC _{25F 10LB 25AR}). The assessment showed differences in the intervertebral response in the C6-T1 levels in the combined position relative to a flexion-only position.	176
Figure 139: FBD of the NM _{M50-Hill-E} model in head-neck flexion and combined positions with the HSM (HHNC).	177
Figure 140: Summary of the overall muscle forces in HHNC _{25F} and HHNC _{25F 10LB 25AR} cases across C2 to C7 vertebral levels, indicating an increase in muscular demand in the C2 vertebral level due to axial rotation.....	178
Figure 141: Summary of the flexor and extensor muscle forces in HHNC _{25F} and HHNC _{25F 10LB 25AR} cases across C2 to C7 vertebral levels, specifically indicating an increase in the extensor muscle demand at the C2 vertebral level due to axial rotation.	178
Figure 142: (a) Summary of the compressive forces in C2-C3 to C7-T1 IVDs in HHNC _{25F} and HHNC _{25F 10LB 25AR} cases, (b) Percent change showing an increase in compression in C2-C3 and C3-C4 IVDs due to axial rotation.	179
Figure 143: (a) Summary of the AP shear forces in C2-C3 to C6-C7 IVDs in HHNC _{25F} and HHNC _{25F 10LB 25AR} cases, (b) Percent change showing increase in AP shear in C2-C3, C3-C4 and C6-C7 IVDs due to axial rotation.....	180
Figure 144: Peak endplate effective stresses across C2 to C7 vertebrae increased slightly when the head-neck deviated from a flexion-only to a combined position with the HSM (HHNC).....	181
Figure 145: Effective stress contours in the C4 superior endplate demonstrating an increase in stress as a result of increase in magnitude of non-neutral position from a flexion-only to a combined position with the HSM (HHNC).....	182
Figure 146: Collagen fiber peak strains along the fiber orientation in AF in head-neck flexion and combined positions with the HSM (HHNC).	183
Figure 147: Illustrating the collagen fiber strain contours in the C2-C3 AF in head-neck flexion and combined positions with the HSM (HHNC) in different perspectives, namely superior-inferior,	

inferior-posterior and posterior-lateral. In the posterior-lateral view, the outer four layers of AF are made transparent for visual purposes to highlight the innermost layer. 184

Figure 148: Quantifying the strains based on area fractions in the innermost collagen fiber layer of the AF that experienced relatively higher strains than the other layers. The results showed a modest increase in the area experiencing higher strains with the increase in magnitude of non-neutral position with the HSM (HHNC). 185

Figure 149: The mean difference in ligament distraction across C2-C3 to C7-T1 levels in head-neck flexion and combined positions with the HSM (HHNC). The increase and decrease in distractions are denoted in positive and negative, respectively. The differences were higher in the contralateral CL. 186

Figure 150: Ligament injury risk summary in head-neck flexion and combined positions with the HSM (HHNC). The results confirm that the ligaments elongated within the physiologic limits (toe and linear regions) with exception in the posterior ISL. 187

Figure 151: Intervertebral responses of the original (blue), geometrically enhanced (orange) and optimized (grey) UCS models verified with the target experimental mean response (black lines) from (Panjabi et al., 1991b) used for laxity optimization. 193

Figure 152: Demonstrating the effect of alar ligament laxity on the C0-C1 axial rotation response. The intermittent rapid increase in angular displacement in the UCS_{M50} and UCS_{M50-G} models were eliminated in the enhanced UCS_{M50-Opt} model owing to the inclusion of alar ligament laxity. 194

Figure 153: Illustration of reaction compressive force and moment in the spinal column due to activation and co-activation of muscles and head force during physiologic flexion in vivo..... 197

Figure 154: Anterior translations at the intervertebral levels when the NM_{M50-Hill-E} model was repositioned using different methods in flexion. The increase in the anterior translation of the superior vertebra relative to the inferior vertebra in the model repositioned using the muscle-based method could be attributed to the differences in the line of muscle force..... 205

Figure 155: Illustrating the repositioning of the NM_{M50-Hill-E} model in 30° flexion using an external BC (moment). An axial load of 43 N is also applied to simulate the weight of the head (Left side). The applied moment and axial load to the model were consistent with the literature (del Palomar et al., 2008). IVD compressive force comparison (Right side). 209

Figure 156: Illustrating the potential pathways to neck pain as reported in the literature. Annulus-driven IVD degeneration (Adams and Dolan, 2012; Carragee et al., 2009), a potential pathway to neck pain in the RWA, is highlighted in yellow..... 215

Figure 157: Illustrating the potential pathways to neck pain as reported in the literature. Endplate-driven IVD degeneration (Adams and Dolan, 2012), a potential pathway to neck pain in the RWA, is highlighted in yellow..... 218

Figure 158: Flowchart illustrating the potential neck pain pathway at the tissue-level due to HSM and non-neutral position magnitudes in the RWA. 222

Figure 159: A) An illustration of an acute injury that is caused from a single loading event where the load exceeds the tolerance level of the tissue. B) An illustration of a chronic injury that is caused from reduced tissue tolerance due to multiple loading events within the physiological limits (Barrett, 2022).
..... 223

List of Tables

Table 1: Maximum applied moments on ligamentous cervical spine specimens for different experimental studies.	30
Table 2: Classification of the head-neck angles in the RWA in the literature.	49
Table 3: Hard tissue material property in GHBMCM50-O neck model.	78
Table 4: Passive muscle strain rate material constants.	81
Table 5: Summary of the ligaments in the UCS _{M50} model, the laxities of which were varied during the DOEs (F: Flexion, E: Extension and AR: Axial rotation)	90
Table 6: Experimental data used for verification and validation of the UCS _{M50-Opt} model. Grey areas indicate the kinematics was not available in the particular experimental study.	94
Table 7: Experimental data used to assess the ligamentous cervical spine models. Grey areas indicate the kinematics was not available in the particular experimental study.	97
Table 8: The location of the head CoG in the NMM50 model was compared to the experimental data from the literature.	99
Table 9: Range of laxity for the highly contributing ligaments determined from DOE studies, and final ligament laxity values from the optimization study.	134
Table 10: The experimental mean and the model response in flexion with the head rotated 30°. CV- Craniovertebral, FHD-Forward head distance, GMA-Gravitational moment arm.	149
Table 11: The intervertebral rotation response (mean) predicted by the CSP (Reed and Jones, 2017) and the repositioned models in flexion with the head rotated 30°.	151
Table 12: The experimental mean (Guo et al., 2021) and the model response in axial rotation with the head rotated 30°. AR-Axial rotation, CLB-Coupled lateral bending.	157
Table 13: Comparing the contribution levels of intervertebral UCS in extension in the UCS models with the experimental mean response. The results highlight the importance of assessing intervertebral response during UCS model validation to avoid disproportionate intervertebral rotations during non-neutral position simulations. NZ = Neutral Zone.	191
Table 14: A comparison chart of laxity values (mm) in different UCS models indicating that the computed laxities vary when the model is validated at the full UCS level or intervertebral UCS levels.	192

List of Nomenclature

AF	Annulus fibrosus
AP	Anterior-posterior
BC	Boundary condition
BP	Battery pack
CSP	Cervical spine predictor
CE	Contractile element
CII	Crash-induced injury
CoG	Center of gravity
CT	Computed tomography
CV	Craniovertebral
CW	Counterweight
DOE	Design of experiments
EMG	Electromyography
FBD	Free-body diagram
FE	Finite element
FHD	Forward head distance
FOV	Field-of-vision
FSU	Functional spinal unit
GMA	Gravitational moment arm
GHBMC	Global Human Body Model Consortium
H	NM _{M50-Hill-E} model without an HSM
HH	NM _{M50-Hill-E} model with helmet
HHNC	NM _{M50-Hill-E} model with helmet, NVG and CW
HSM	Head-supported mass
IVD	Intervertebral disc
LCS	Lower cervical spine
LHS	Latin Hypercube Sampling
LS	Full ligamentous cervical spine
MB	Multibody
MFR	Muscle force replication
MRI	Magnetic resonance imaging
MSK	Musculoskeletal
NATO	North Atlantic Treaty Organization
NP	Nucleus pulposus
NVG	Night vision goggles
OFAT	One-factor-at-a-time
PCSA	Physiologic cross-section area

PDE	Parallel damping element
PEE	Passive elastic element
RCAF	Royal Canadian Air Force
ROM	Range of motion
RWA	Rotary-wing aircrew
SD	Standard deviation
UCS	Upper cervical spine
25F	25° head-neck flexion as measured in RWA
10LB	10° head-neck lateral bending as measured in RWA
25AR	25° head-neck axial rotation as measured in RWA

Cervical spine ligaments:

AA-AM	Anterior atlanto-axial membrane
AA-OM	Anterior atlanto-occipital membrane
AL	Alar ligament
AL-AT	Alar ligament (Atlanto-Axial branch)
ApL	Apical ligament
ALL	Anterior longitudinal ligament
CL	Capsular ligament
Cx	Cruciate ligament
ISL	Interspinous ligament
LF	Ligamentum flavum
PA-AM	Posterior atlanto-axial membrane
PA-OM	Posterior atlanto-occipital membrane
PLL	Posterior longitudinal ligament
SSL	Supraspinous ligament
TL	Transverse ligament
TM	Tectorial membrane

List of Symbols

σ^F	Total stress in the muscle
σ^{CE}	Stress in the contractile element (CE)
σ^{PEE}	Stress in the passive elastic element (PEE)
σ_{max}	Peak isometric stress
$a(t)$	Muscle activation level as a function of time
$f_L(L)$	Force-length relationship of the muscle
$f_V(V)$	Force-velocity relationship of the muscle
$h(\lambda)$	Dimensionless stress as a function of stretch
θ_f	RWA head-neck angle in flexion
θ_{lb}	RWA head-neck angle in lateral bending
θ_{ar}	RWA head-neck angle in axial rotation

Chapter 1 Introduction

1.1 Motivation

The Royal Canadian Air Force (RCAF) comprises various categories of aircrafts for multitude roles including air-demonstration, fighting, maritime aviation, search & rescue, tactical aviation, training and transport. The aircrafts are of two types: 1) fixed-wing (fighter jets) and 2) rotary-wing (helicopter) and operated by highly trained military personnel, also known as aircrew or pilots (Figure 1). Neck pain in the RCAF aircrew, including fixed- and rotary-wing, has been recognized as a significant concern that required the North Atlantic Treaty Organization (NATO) to convene a research task group (HFM 252) to make efforts to address the problem (Derouin, 2020; McKinnon et al., 2016). The term ‘neck pain’ or ‘neck trouble’ in the context of RCAF aircrew has no clear definition. The term ‘neck trouble’ can include any combination of acute or chronic neck pain and neck discomfort (De Loose et al., 2009; Derouin, 2020). The type of neck pain experienced by the RCAF aircrew while flying aircraft and performing occupational demands over the career duration can be acute, episodic or chronic in nature (Farrell et al., 2018). The fixed-wing aircrew likely experience an acute neck pain or injury owing to the $+G_z$ environments while operating a fighter jet. The symbol G_z represents the gravitational forces acting along mid-body axis and parallel to the spinal column. The positive notation (+) describes the direction of the gravitational force in the cranial-caudal direction as the aircraft engages in steep climb or high-speed turns (O’Conor et al., 2020; Warm et al., 2006). The rotary-wing aircrew (RWA) likely experience chronic neck pain or overuse injury owing to the nature of the occupational demands that involve search & rescue, surveillance and other tasks that classify under tactical aviation (Farrell et al., 2020).

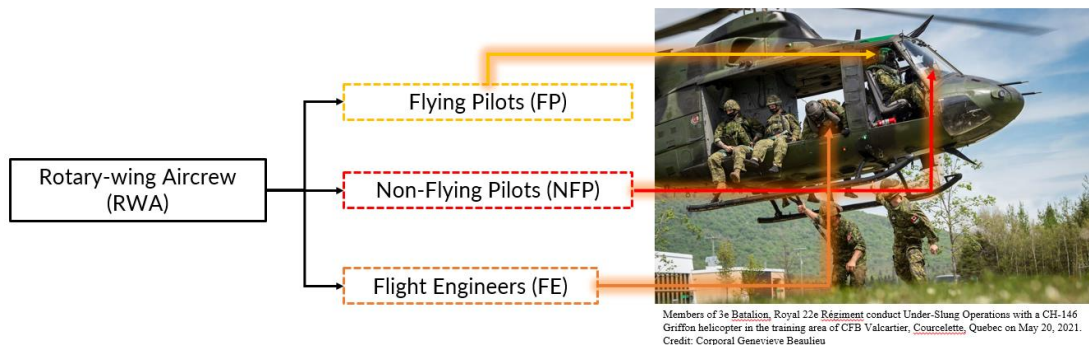


Figure 1: The rotary-wing aircrew (RWA) operating the CH-146 rotary-wing aircraft during a mission. The figure shows three types of RWA including flying pilots, non-flying pilots and flight engineers.

[Image credits: Corporal Genevieve Beaulieu and Royal Canadian Air Force]

In recent times, RWA including flying pilots, non-flying pilots and flight engineers have reported neck pain (Adam, 2004; Bridger et al., 2002; Chafé and Farrell, 2016; Madison et al., 2023). Two large-scale surveys were conducted on the RCAF RWA in 2004 and 2014 to document the prevalence of neck pain in the flying pilots, non-flying pilots and flight engineers of the RWA (Adam, 2004; Chafé and Farrell, 2016). The 2004 survey was conducted on CH-146 Griffon RWA and CH-124 Sea King RWA. The 2014 survey was conducted on the CH-146 Griffon RWA. From the survey conducted in 2004 and 2014, 80% (n=281) and 75% (n=215) of the responded RWA reported neck pain, respectively. In the 2004 survey, 81.2% of CH-146 Griffon RWA reported flight-related neck pain (Adam, 2004). Within the RCAF, 90% of the RWA that accumulated over 150 hours of night vision goggles (NVG) experience were reported to have neck pain (Adam, 2004). In Canada, 15% of the RWA pilots have been grounded at least once during their career due to flight-related neck pain (Adam, 2004). From another survey, 53% (n=40) of the RCAF RWA including flying pilots, non-flying pilots and flight engineers reported neck pain (Harrison et al., 2011).

Several studies have explored the potential causal pathways for neck pain in RWA. Typically, an inflammatory response occurs in any innervated tissue resulting from damage induced by external loads. The tissues could undergo macro-level damage and failure due to loads beyond physiologic limits or micro-level damage due to repeated loads within physiologic limits. The tissue in the neck experience a micro-damage due to repetitive head-neck motions within the physiologic full range of motion (ROM)

or maintenance of a non-neutral position over a prolonged duration (Karakolis et al., 2015; Solomonow, 2004; Solomonow et al., 2003; Steilen et al., 2014; Ulrich et al., 2007). When the micro-damage, which may go unnoticed, is not allowed to heal and is further exposed to repeated motions and non-neutral positions, chronic inflammation develops. Chronic inflammation in innervated neck tissues can then lead to neck pain (Barr and Barbe, 2002; Solomonow, 2004). As a part of their tasks, RWA scan the internal (aircraft) and external environments, which requires rapid movement of the head-neck within physiologic full ROM and maintaining static non-neutral positions (Adam, 2004; Chafé and Farrell, 2016). Such tasks result in the neck tissues in RWA being subjected to static, repetitive loads over an extended period. Repeated loading on the neck may increase the risk of micro-damage on one or more innervated tissues, which may develop into a chronic inflammation (Adam, 2004; Harrison et al., 2007; Healey, 2019; Karakolis et al., 2015; Posch et al., 2019; Pousette et al., 2016; Solomonow, 2004; Van den Oord et al., 2012). Performing the scanning tasks and maintaining non-neutral head-neck positions while wearing the head-supported mass (HSM) further exacerbates the risk of micro-damage and, eventually, the risk of a chronic inflammatory response in the innervated neck tissues (Karakolis et al., 2015). The HSM in the RWA context primarily comprises a helmet with an option to mount the NVG, counterweight (CW) and other devices such as heads-up display on the helmet. The identified causal pathways of neck pain in RWA were based on questionnaires and experimental measurements from live humans (Adam, 2004; Callaghan, 2014; Chafé and Farrell, 2016; Healey, 2019; Healey et al., 2021; Posch et al., 2019). Most of the RWA responses to the questionnaire indicated the mounting of NVG and CW to the helmet during night missions, non-neutral head-neck positions and duration of mission as factors that may contribute to neck pain. The findings from questionnaire-based studies were supported by experiments on live human volunteers, which reported increased electromyographic (EMG) activities in neck muscles with the inclusion of HSM and increasing magnitude of non-neutral positions with the inclusion of NVG. Persistent neck pain among RWA impacts the health and performance of trained personnel. It leads to enormous financial cost (Salmon et al., 2011), driving the need to further understand and mitigate this issue.

Additional insight regarding the loads and distractions of individual tissues is still needed to better understand the potential for injury and pain response at the tissue-level, which may be addressed, in part, through advanced computational models. Multibody (MB) models of the head-neck has been previously used to investigate the risk of neck pain in RWA and test potential solutions to reduce the risk of neck pain in RWA (Fathollahi, 2012; Hetzler, 2021). MB neck models typically comprise hard

tissues modelled as rigid bodies, intervertebral discs (IVDs) modelled using kinematic joints and ligaments modelled as beam elements. Such models are exercised for physiologic ROMs using an externally applied load or displacement until the desired non-neutral position is achieved. Musculoskeletal (MSK) models are an evolution of MB models as it includes representation of in vivo musculature. Non-neutral positions in MSK models are simulated using externally applied displacement (experimental kinematic data) from which active muscle forces and joint forces are computed using inverse-dynamic approach (Alizadeh et al., 2020b; Barrett et al., 2021). Presence of active musculature make MSK models more suitable to mimic in vivo physiologic ROMs and non-neutral positions as observed in live humans. The high computational efficiency of the MB and MSK models is due to the assumption of rigid hard tissues and treating the intervertebral discs as kinematic joints. In particular, MSK models are often preferred to investigate the injury risk associated with an occupational environment, such as rotary-wing aircraft, due to the ability to simulate in vivo head-neck motions in a computationally efficient manner (Alizadeh et al., 2020b; Barrett et al., 2022a, 2022b; Moore et al., 2021). The MSK model muscles are treated as 1-dimensional (1D) elements with a Hill-type formulation, including active and passive properties (Barrett et al., 2021; Mortensen et al., 2018; Vasavada et al., 2002). The active properties of the muscles in the MSK model that are challenging to obtain from live humans are identified using optimization algorithms. Specifically, in a head-neck MSK model, the activation levels of deep neck muscles are optimized until the head trajectory of the model matches with the trajectory obtained from human volunteers in experiments (Barrett, 2016; Barrett et al., 2020; Dibb et al., 2013; Mortensen et al., 2018; Vasavada et al., 2002). In both MB and MSK models, the tissue-level responses are then inferred from vertebral kinematics and joint-reaction forces.

Finite Element (FE) head-neck models include a detailed representation of the structural tissues in the neck. To date, only one FE head-neck model has been applied to assess neck pain in HSM conditions (Mesfar and Moglo, 2013, 2012). However, one limitation of Mesfar and Moglo FE head-neck model includes non-neutral position simulation by applying external loads and moments rather than activating the muscles as in live humans. Comparison of experimental ROM studies on isolated cervical spine specimens (in vitro) and live humans (in vivo) have shown differences in intervertebral kinematics. The difference in intervertebral kinematic response might affect the tissue-level response (Ordway et al., 1999; Panjabi et al., 2001b, 1998; Sato et al., 2015). Hence, there is a need to mimic the voluntary head-neck motions and non-neutral positions by activating the muscles to predict the tissue-level response in a detailed FE head-neck model accurately.

A clear understanding of the interaction of HSM and non-neutral head-neck positions on tissue-level response is an essential step towards understanding and mitigating the potential for neck pain in RWA. This research aims to simulate the range of neck motions and non-neutral positions in RWA across various HSM configurations using a contemporary FE head-neck model by activating the muscles and assess the effects of HSM and non-neutral head-neck positions on tissue-level distractions. Existing studies have associated the increased forces in the IVDs, increased distraction in ligaments and increased EMG activity in muscles with increased risk of pain (Cronin, 2014; Fice et al., 2011; Healey, 2019; Shateri and Cronin, 2015; Shen, 2020; Tampier et al., 2007). Ultimately, it is hoped that this research will lead to a quantitative approach to evaluate the impact of HSM and non-neutral head-neck positions on neck tissues and guide future optimization of HSM design to reduce the risk of neck pain in RWA.

1.2 Research objectives

The overarching goal of this research is to assess potential sources of neck pain in RWA. Potential for pain will be based on predicted tissue response from a detailed FE head-neck model, which will be simulated for non-neutral head-neck positions with the HSM as observed in RWA during a mission. A novel methodology to simulate in vivo non-neutral head-neck positions in a contemporary FE head-neck model by activating the muscles is proposed to achieve this goal. It is assumed that increased tissue-level strains may correlate with the potential for long-term neck pain in RWA. The proposed research will quantify the effect of HSM and non-neutral positions on tissue-level response and can inform future studies to optimize HSM integration to reduce the risk of neck pain. The objectives towards achieving the goal are as follows.

1.2.1 Objective #1

Validate and enhance the ligamentous spine FE model (C0-T1) for physiologic ROM using experimental data.

A contemporary FE head-neck model of a 50th percentile male occupant from Global Human Body Model Consortium (GHBMC M50-O), used to predict crash-induced injuries (CIIs), will be explored to predict the tissue-level responses during simulated non-neutral positions with the HSM. As the GHBMC M50-O head-neck model (referred to as NM_{M50} in this thesis) has been used to predict CIIs, there is a necessity to evaluate the model in physiologic conditions at different levels of complexity,

starting from motion segments to the full cervical spine with passive and active musculature. Previously, the GHBMC M50-O ligamentous cervical spine model (C0-T1), referred to as LS_{M50} in this thesis, has been assessed at the individual functional spinal unit (FSU) levels (C2-C3 to C7-T1), and the UCS has been evaluated as one FSU (C0-C2) for physiologic ROMs. The LS_{M50} model, C0-C1 FSU and C1-C2 FSU have not been assessed for physiologic responses. As part of the current study involves simulating the physiologic ROMs to reposition the head-neck, it is required to evaluate the LS_{M50} against experimental data. Due to the dominance of UCS at the ligamentous level in physiologic ROMs, their response needs to be evaluated against experimental data at the C0-C1 and C1-C2 FSU levels individually. Therefore, the first objective is to assess the physiologic response of the ligamentous cervical spine model at the C0-C1, C1-C2 and C0-T1 levels, identify scope for enhancements to the model, and improve the model biofidelity.

1.2.2 Objective #2

Develop a methodology to simulate non-neutral head-neck positions using muscle activation in the FE head-neck model, validate with human volunteer data, and assess tissue-level response in the repositioned head-neck model.

In humans, the neck muscles activate to enable physiologic ROM of the head-neck and maintain the non-neutral position at the desired line of sight. Maintaining non-neutral head-neck positions over a prolonged duration while flying on a mission has been associated with the risk of neck pain in RWA. Hence, it is required to gain insight into the tissue-level responses in different head-neck positions using a detailed FE head-neck model. Conventionally, FE head-neck models are simulated for non-neutral positions by applying external loads, moments or prescribed motion to the head or superior vertebra while constraining the inferior vertebra until the desired posture is achieved. However, with this methodology, there are chances that the intervertebral kinematic trends would be different than a live human (based on the literature). The difference in kinematic response could result in an unrealistic prediction of stress and strain patterns in the tissues, leading to an inaccurate conclusion on the site of neck injuries in RWA. Hence, the objective is to simulate the non-neutral positions of the head-neck by activating the muscles. Specifically, the objective is to simulate non-neutral positions of the head-neck in flexion and axial rotation within the physiologic ROM. Further, the Objective #2 in this research is to quantify the importance of active muscle-based approach for simulating non-neutral head-neck positions by assessing the kinematic, kinetic and tissue-level responses.

1.2.3 Objective #3

Evaluate the effect of HSM configurations and different non-neutral positions simulated using active musculature on predicted tissue-level strains.

During the missions, RWA wear a helmet to be protected against impacts and mount devices like NVG during night missions to the helmet for visibility. The mass, inertia and CoG location of the NVG induces a flexion moment in the head-neck as NVG are mounted and to counteract the increasing moment, CW is added to the back of the helmet. The inclusion of NVG and CW to the helmet would add up to 3 kg of mass for the neck to support and cause an anterior shift in the head's and HSM's combined CoG. The added mass, inertia and anterior shift in CoG have been shown to increase the extensor muscle activity, thereby causing an increase in compressive force in the spinal column. The increasing forces in the neck due to increased muscle activity have been associated with the cause of neck pain in RWA, for which there has been no evidence-based data at the tissue-level to date. The mounting of NVG also causes a reduction of field-of-vision (FOV) from 140° to 40°, thereby increasing the magnitude of non-neutral head-neck positions required for environment scanning. The increase in the non-neutral head-neck position magnitude due to NVG has been shown to increase muscle activity which has been associated with the cause of neck pain in RWA. Hence, the objective is to simulate the RWA non-neutral head-neck positions under varying HSM configurations (only helmet and helmet with NVG and CW) and correlate the same with the potential for neck pain in RWA using the FE head-neck model. The non-neutral head-neck flexion and combined (flexion, lateral bending and axial rotation) positions frequently assumed by the RWA will be simulated using active musculature in the FE head-neck model, as mentioned in the 2nd objective.

1.3 Thesis outline

This research comprises three different phases corresponding to each objective. Phase #1 includes enhancements, verification and validation of the ligamentous cervical spine in the GHBMC M50-O head-neck model. Phase #2a includes preliminary assessment on the GHBMC M50-O head-neck model for physiologic conditions leading to modifications, enhancements and validation of the model and describes the strategy to reposition the model using active muscles. Phase #2b includes kinematic, kinetic and tissue-level comparison between the model repositioned using active muscle method and a conventional method. In Phase #3, the modified, enhanced and validated model is simulated for

different HSM configurations and repositioned in flexion and combined positions as observed in the RWA using the active muscle method described in Phase #2 (Figure 2).

Chapter one introduces the readers to the existing research problem, explains the motive to pursue this research, details the research objectives and outlines the thesis organization. *Chapter two* first provides a brief overview of the anatomy and physiologic motions of the human neck. Next, a background on neck pain and the contributing factors in the RWA is provided, followed by a review of the computational head-neck models in simulating occupational tasks. Finally, the detailed FE head-neck model (GHBMC M50-O), used in this research, is reviewed. *Chapter three* elaborates on the methodology used for assessing the detailed FE head-neck model for physiologic conditions, enhancing the model, repositioning the model using active muscles and assessing the risk of neck pain in a simulated RWA non-neutral position. *Chapters four and five* summarize and discuss the results obtained from the three phases of this research work. *Chapter six* discusses the limitations of the current research and potential work for the future. *Chapter seven* highlights the findings from this research and provides conclusions.

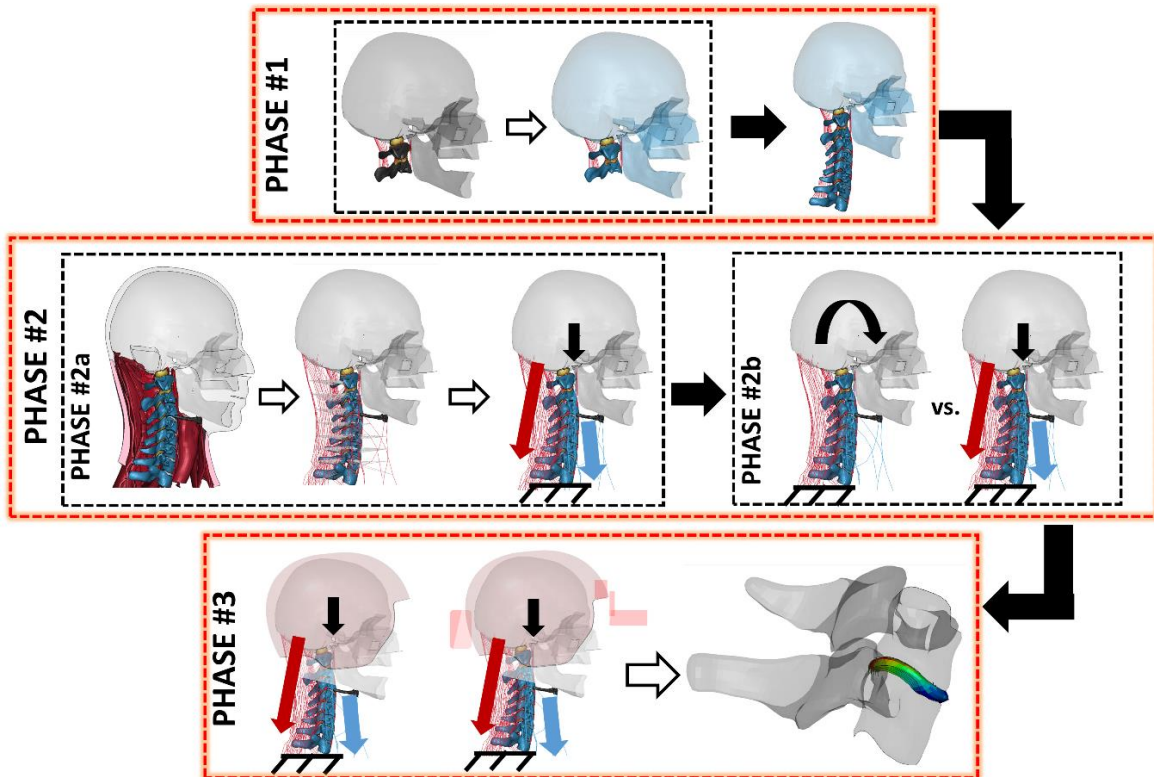


Figure 2: An overview of the work-flow undertaken to assess the risk of neck pain in RWA using an FE head-neck model. The list of tasks i.e. ligamentous spine model enhancements, verification and validation required to meet Objective #1 were performed in Phase #1. The list of tasks required to reposition the neck model in physiologic range using active muscles to meet Objective #2 was included in Phase #2. The tissue-level assessments with the HSM and non-neutral head-neck positions, as stated in Objective #3, were done in Phase #3.

Chapter 2 Background and literature review

2.1 Anatomical terms

The study of anatomy focuses on the physical makeup of living things. The body is divided into sections using anatomical planes and directions, which are also used to define common nomenclature for anatomical features (Figure 3). The coronal, transverse, and sagittal planes make up the anatomical planes. The body is divided into front and back parts by the coronal plane, top and bottom parts by the transverse plane, and right and left sides by the sagittal plane. The superior and inferior directions, which are in opposition to one another, are created at the point where the sagittal and coronal planes intersect. The sagittal and transverse planes meet at their intersection to form the anterior and posterior directions. The perpendicular directions towards and away from the median are referred to as the medial and lateral directions, respectively. These directions are formed by the intersection of the transverse and coronal planes (Kh et al., 2021).

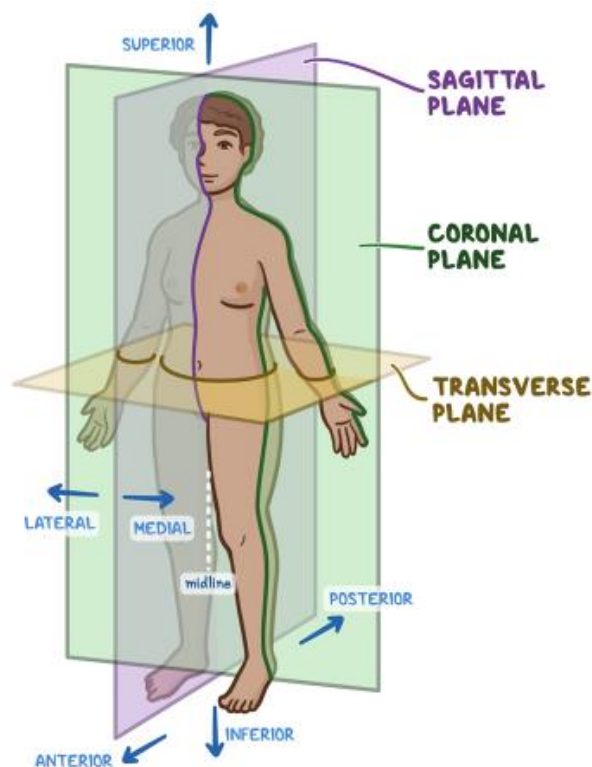


Figure 3: Anatomical planes and directions.

[Taken from <https://www.osmosis.org/answers/anatomical-position>]

The rotation of the head and neck comprises flexion, extension, lateral bending and axial rotation (Figure 4) (Standing and Borley, 2008). During flexion, the head and neck bends in the anterior direction looking towards the ground. During extension, the head and neck bends in the posterior direction looking up the sky. The rotation of the head and neck in flexion and extension occurs in the sagittal plane and around the medial-lateral direction. During lateral bending, the head and neck tilts towards either side of the shoulder in the coronal plane and around the anterior-posterior (AP) direction. During axial rotation, the head and neck looks left and right over the shoulder in the transverse plane and around the superior-inferior direction (Figure 4).

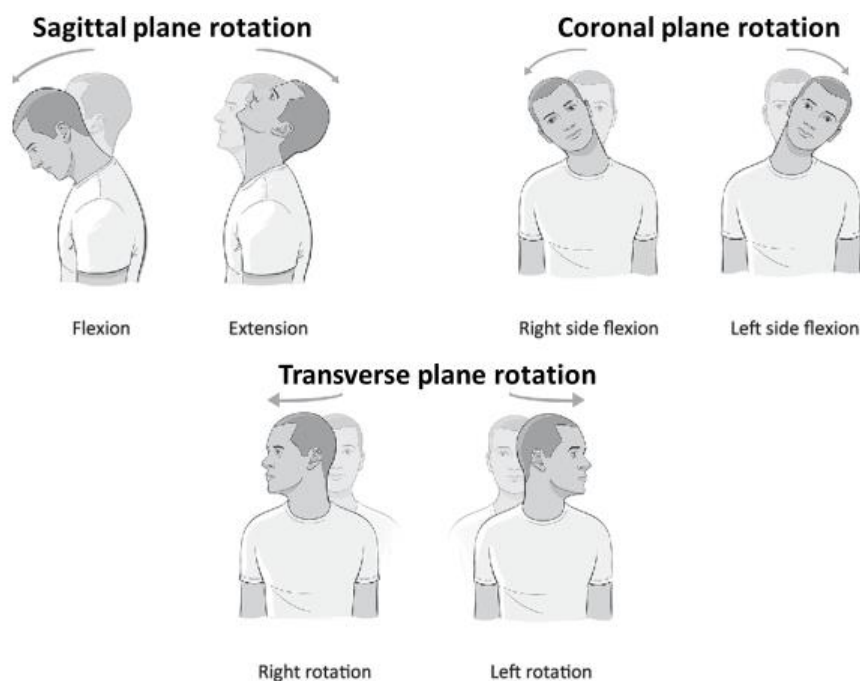


Figure 4: Primary motions of the head and neck in different anatomical planes.

[Adapted from Lascurain-Aguirrebena et al. (2018)]

2.2 Anatomy of the human neck

2.2.1 Cervical spine

A group of thirty-three bones called vertebrae and the tissues connecting the adjacent vertebrae make up the human spinal column. The tissues connecting the adjacent vertebrae include intervertebral discs

(IVDs), facets, and ligaments. The human spine is divided into five separate regions based on their structure, function, and location: the cervical, thoracic, lumbar, sacral, and coccyx. The cervical region of the spine, which is the focus of this thesis, is made up of the first seven vertebrae (C1 to C7) along with the IVDs, facets, and ligaments connecting these vertebrae (Figure 5). The cervical spine is further divided in two distinctive regions based on their structure and functions: Upper cervical spine (UCS) and Lower cervical spine (LCS) (Figure 5). The cervical spine is naturally curved (cervical lordosis) and forms a posterior concavity of the cervical spine from T1 to the base of the skull. The cervical lordosis is essential to maintain an upright position of the head and a forward gaze (Been et al., 2017).

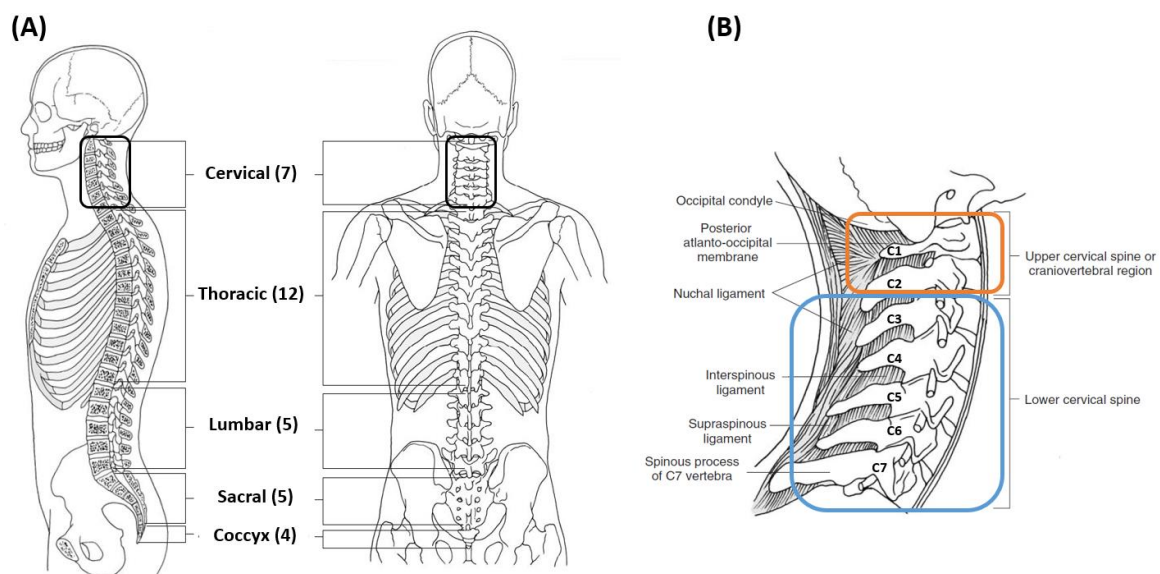


Figure 5: A) Illustration of the structure of human spine. The region enclosed within the solid black line is called the cervical spine and B) A sagittal view of the cervical spine illustrating the upper cervical and lower cervical spine enclosed within the solid orange and blue lines, respectively.

[Adapted from Levangie and Norkin (2005)]

The cervical spine comprises seven vertebrae and is typically considered in two sections: the upper cervical spine (C1 and C2) and the lower cervical spine (C3-C7) (Cusick and Yoganandan, 2002; Levangie and Norkin, 2005; Mattucci et al., 2012). The UCS vertebrae are differently structured while the LCS vertebrae have similar anatomical structures. The bony vertebrae comprise complex materials

possessing anisotropic, asymmetric, viscoelastic and strain-rate dependent material properties and is composed of two types of tissues: 1) cortical or compact bone and 2) trabecular or spongy bone.

The cortical bone tissue covers the exterior aspects of the vertebra and characterized to withstand large compressive forces. The cortical bone that surrounds the vertebral body of the vertebra is thin, measuring only 0.4 to 0.7 millimeters thick (Panjabi et al., 2001a). The cortical bone surrounding the posterior vertebral components, however, are substantially thicker (Gray, 1918; Standring and Borley, 2008). The trabecular bone tissue, which makes up the interior of the cervical vertebrae, is porous. According to the literature, the trabecular bone has an anisotropic lattice structure called trabeculae which are oriented along the principal axis of stress to provide strength to the vertebra (Kopperdahl and Keaveny, 1998) (Figure 6). The cortical and trabecular bones, together, contribute to the lightweight structure of the vertebra that can endure the forces experienced by the neck during regular life activities.

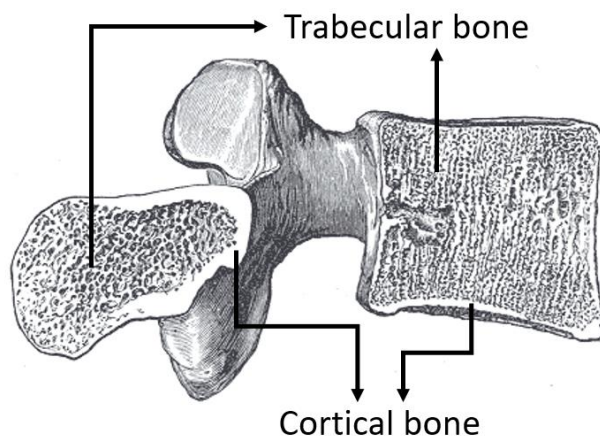


Figure 6: Illustration of the thin cortical bone tissue surrounding the porous trabecular bone tissue in an exemplar human vertebra (Gray, 1918).

[Adapted from Gray (1918)]

The LCS consists of five vertebrae, C3 to C7, all of which share comparable morphological traits. The vertebral body, vertebral processes and two articular pillars are the four primary structural components of the cervical vertebrae, particularly in the LCS (Gray, 1918; Standring and Borley, 2008). The vertebral processes (a total of 7) include two transverse processes, four articular facet processes and one spinous process, each of which contain a bony protrusion called tubercle. The tubercle serves as an attachment point for the muscles and ligaments (Yoganandan et al., 2005). The neural arch

comprises the lamina and pedicle and connect the four primary structural components of the vertebra. The vertebral foramen (spinal canal), a triangular opening in the middle of the vertebra through which the spinal cord travels, is formed by the vertebral body, pedicle, and lamina (Figure 7).

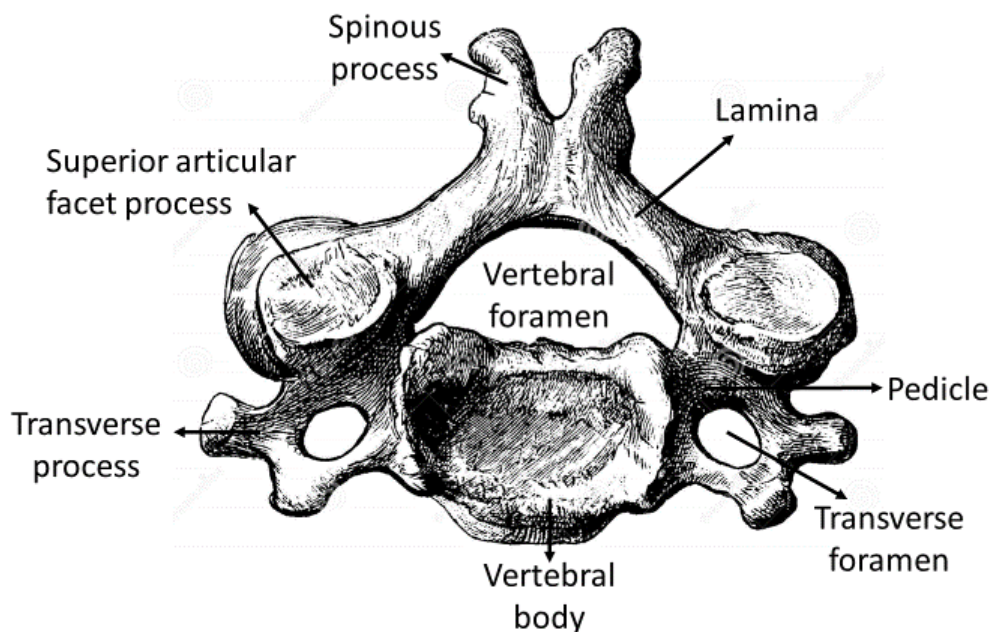


Figure 7: Typical structure of a cervical vertebra in the LCS (superior view).

[Adapted from <https://www.dreamstime.com/illustration/vertebra-drawing.html>]

The cylindrical vertebral body in the LCS is designed to withstand compressive loads exerted on the spinal column. Particularly in the cervical spine, the transverse diameter of the vertebral body is larger than the AP diameter (Cramer, 2014). The anterior aspect of the vertebral body is convex, while the posterior aspect is flat. The C3 through C7 vertebral bodies have uncinate processes on the posterior-lateral aspects of the superior surfaces. The superior surface of the vertebral body has a saddle-like structure to accommodate the uncinate processes (Levangie and Norkin, 2005; Nikita, 2017).

Typically, the pedicles lie anterior to the articular processes and posterior to the vertebral body on either side. The pedicles transmit the tensile forces and bending forces from the posterior elements to the vertebral bodies. In the cervical vertebrae, the pedicles project postero-laterally and increase in size from the cervical to lumbar regions (Yow et al., 2020). The transverse process protrudes from either side of the cervical vertebral body laterally and travels postero-medially to connect with the pedicle. The transverse process and the pedicle together form the transverse foramen, through which the

vertebral arteries pass through and spinal nerve root exits the spinal cord. The transverse processes also serve as a site for muscle attachments (Levangie and Norkin, 2005; Yoganandan et al., 2005).

The laminae serve as an origin for the articular processes and spinous process (Yow et al., 2020). Laminae in the cervical vertebrae are thin (relative to thoracic and lumbar), vertically oriented and projected postero-medially. They serve as the ‘roof’ to the neural arch that protects the spinal cord. Pars interarticularis is a portion of the laminae that is present in between the superior and inferior articular processes. Laminae serve to transmit the forces from the posterior elements to the pedicles. The spinous process projects posteriorly from the region where the two laminae fuse together. Like the transverse process, the spinous process too serves as a site for muscle and ligament attachments. The presence of a bifurcation in the spinous process of the cervical vertebrae is a distinguishable feature from the spinous process of other spinal regions. The length of the spinous process is similar in C2 to C5 levels and increases significantly in C7 (Levangie and Norkin, 2005; Nikita, 2017).

The superior and inferior articular facet processes in the vertebrae connect to form a supportive column, referred to as the articular pillar. The superior and inferior articular facet processes are oriented in the posterior-superior and antero-inferior directions, respectively. The superior and inferior articular facet processes form the facet joint with the inferior and superior articular processes of the adjacent vertebrae, respectively (Levangie and Norkin, 2005). The facet joint typically makes an angle of 45° with respect to the transverse plane owing to the orientation of the articular facet processes (Shah, 2014) (Figure 8). The facet joints which provide stability to the spine and are important sources of neck pain (Jaumard et al., 2011).

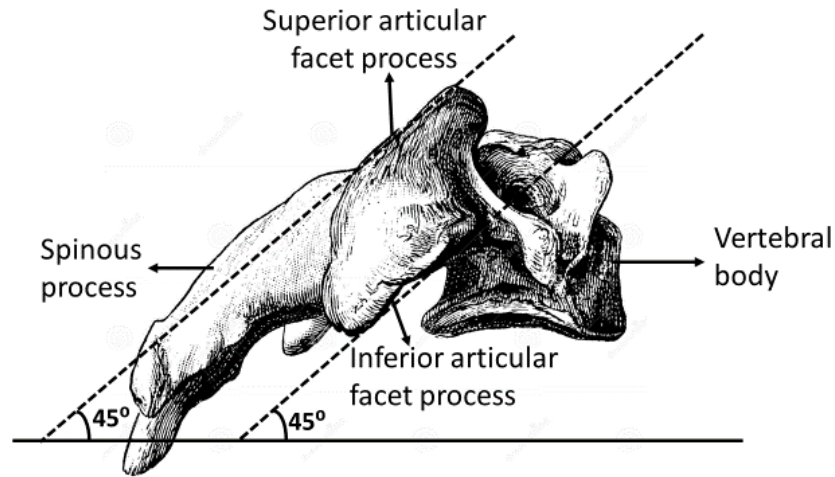


Figure 8: Illustrating the orientation of the facet articular processes in 45 with respect to the horizontal in the C4 vertebra.

[Adapted from <https://www.dreamstime.com/illustration/vertebra-drawing.html>]

The structure of the vertebrae in the UCS (C1 and C2) are unique compared to the vertebrae in the rest of the cervical spine. The C1, also called atlas, is a ring-shaped structure and responsible for supporting the base of the skull (occipital condyles or C0). The two articular pillars (lateral mass) that make up the primary structure of the atlas are joined by the anterior arch and posterior arch. The superior aspect of the articular pillars consists of large concave facets while the inferior aspect consists of convex facets. The occipital condyles of the skull (C0) rest on the large concave facets of the superior aspects of articular pillars forming the atlanto-occipital joint. The convex facets of the inferior aspects of the articular pillars rests on the superior facets of the C2 vertebra (axis) (Figure 9). While there is a lack of vertebral body and the spinous process, the atlas consists of transverse process and a transverse foramen (Levangie and Norkin, 2005; Yow et al., 2020).

Although the C2 vertebra is structured similar to the rest of the vertebrae from C3 to C7, the vertebral body extends further vertically forming a process called the odontoid process or dens. In the anterior region of the dens, a facet is present for articulating with the anterior arch of the atlas. Posteriorly, the dens comprise of a groove for the transverse ligament to articulate (Figure 10). Relative to the LCS, the pedicles, laminae, and spinous process of the axis are larger (Gray, 1918; Levangie and Norkin, 2005; Yow et al., 2020).

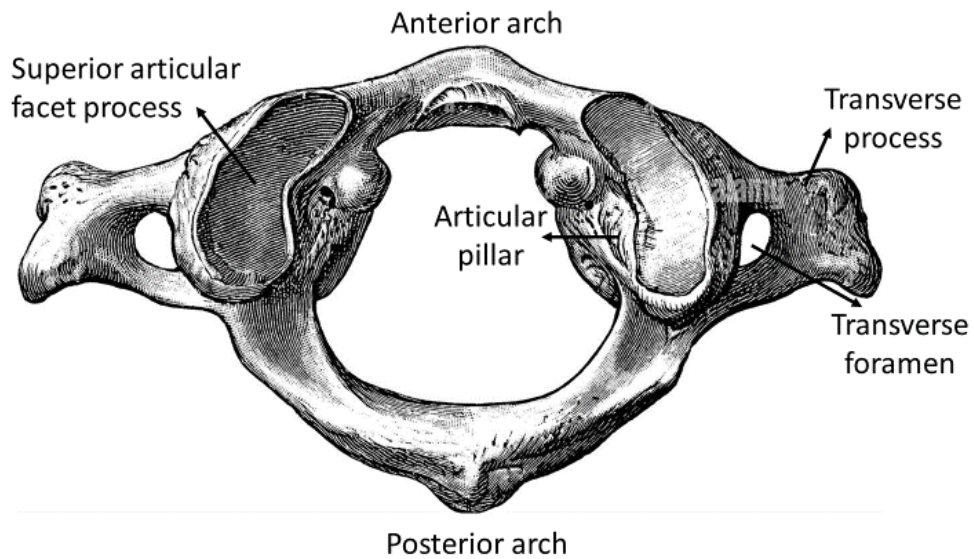


Figure 9: Superior view of the first cervical vertebra (atlas).

[Adapted from: <https://www.alamy.com/stock-photo/atlas-vertebra-and-human.html?sortBy=relevant>]

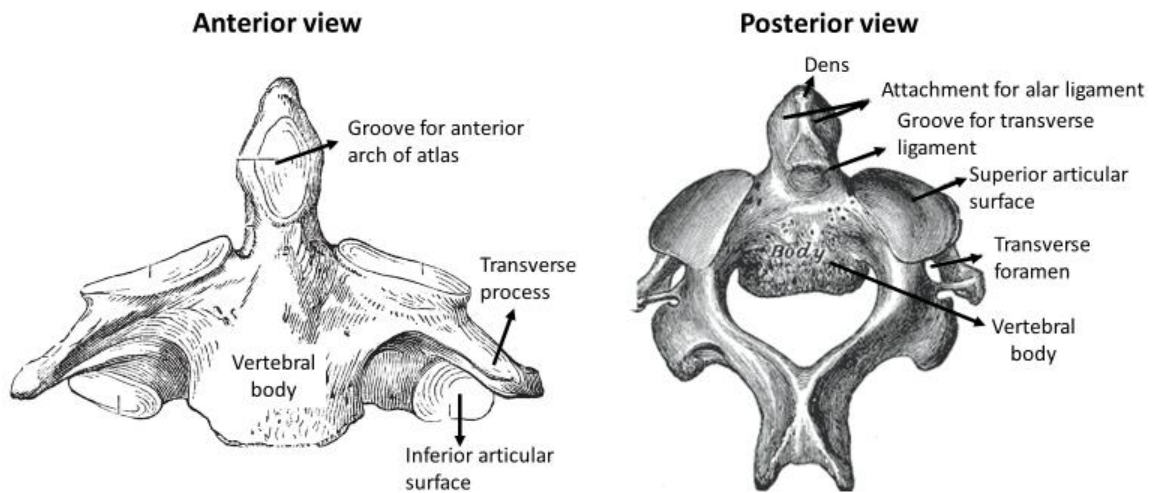


Figure 10: Anterior and posterior views of the second cervical vertebra (axis).

[Adapted from <https://www.alamy.com/stock-photo/atlas-vertebra-and-human.html?sortBy=relevant> and <https://boneandspine.com/anatomy-cervical-spine/>]

The intervertebral discs (IVDs) are fibrocartilaginous, composite soft-tissue structures that account for 20% to 33% of the vertebral column length (Kapandji, 1974). The IVDs primarily connect the two

adjacent vertebrae starting from C2-C3 in the cervical spine up to L5-S1 in the lumbar spine and allow the intervertebral motion. The only spinal segment in the neck that lacks an IVD is the UCS, which is held together exclusively by a convoluted network of ligaments and two facet joints.

The IVDs are approximately 3 mm thick in the cervical region, also act as shock-absorbing structures, and are typically composed of the annulus fibrosus (AF), nucleus pulposus (NP) and cartilaginous/vertebral endplate (Levangie and Norkin, 2005; Yoganandan et al., 2005) (Figure 11). The AF is a composite structure composed of 60% to 70% water and 50% to 60% collagen fibers encircling the NP (Levangie and Norkin, 2005). The collagen fibers in the AF are concentrically arranged in the form of layers called lamella (Gruber and Hanley, 2002). Each lamellar layer has collagen fibers oriented parallelly to each other, making $\pm 25^\circ$ to $\pm 45^\circ$ from the transverse plane and sustaining the tensile, shear and torsional loads in the cervical spine (Martin, 2015; Yoganandan et al., 2001) (Figure 12). The orientation of the collagen fibers in the lamellae varies from $\pm 45^\circ$ in innermost layers to $\pm 25^\circ$ in the outermost (Pezowicz, 2010). The lamellae are embedded in the annular ground substance which is composed of water and proteoglycans (Cassidy et al., 1989).

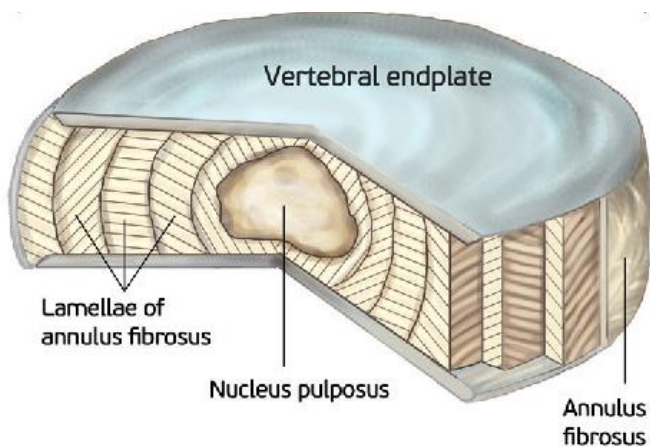


Figure 11: Illustration of a sectioned IVD with the AF, NP and vertebral endplate.

[Taken from Tomaszewski et al. (2015)]

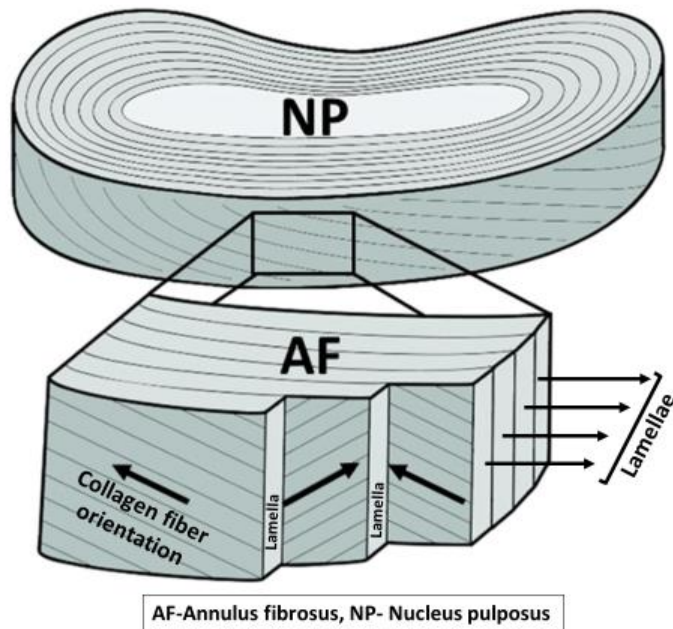


Figure 12: Illustration of the AF structure with the lamellar layers and the orientation of collagen fibers in a lamella.

[Adapted from Martin (2015)]

The NP is an incompressible fluid-like gelatinous material comprising 70% to 90% water and encapsulated by the AF and the vertebral endplates. The proteoglycans and collagen fibers make up $\approx 65\%$ and $\approx 20\%$ of the dry weight, respectively, in the NP. The NP is responsible for sustaining and distributing the compressive loads to the vertebral endplates (Cassidy et al., 1989). The ability to resist compressive loads is attributed to the dominance of type-2 collagen in the NP (Levangie and Norkin, 2005). During compression, the NP expands and causes bulging of the AF thereby loading the collagen fibers in tension (Levangie and Norkin, 2005) (Figure 13). During anterior bending, the posterior aspect of the IVD experiences tension while the anterior aspect experiences compression. Vertebral endplates are a layer of cartilage (0.6 mm to 1.0 mm thick) found at the superior and inferior surfaces of the vertebral body to which the superior and inferior ends of the IVDs adhere. The vertebral endplates comprise proteoglycans, collagen and water in addition to cartilage cells that are aligned along the collagen (Levangie and Norkin, 2005). Overall, the composition of the IVDs permit the intervertebral flexibility while providing shock absorption by deforming as a result of neck motion.

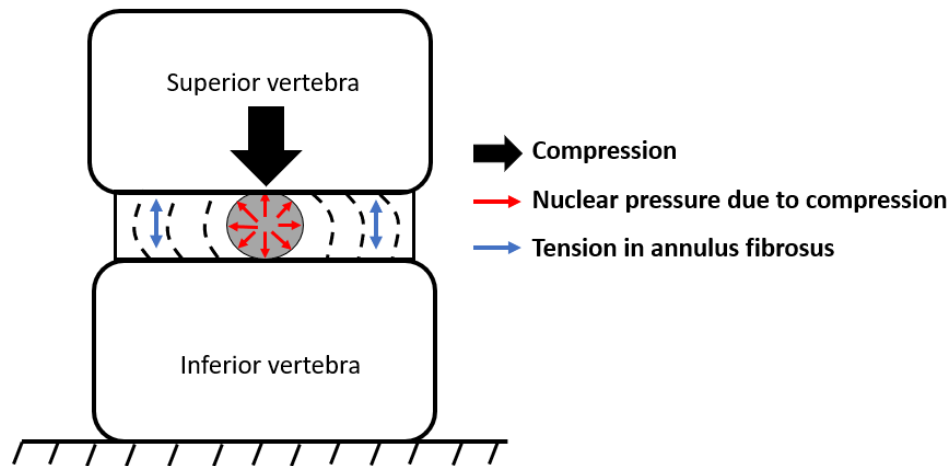


Figure 13: Schematic representation of the tension response in the AF when exposed to a compressive loading, as described in the literature (Levangie and Norkin, 2005).

The ligaments are fibrous connective tissues primarily composed of Type-1 collagen and elastin proteins and connect the adjacent vertebrae to provide stability to the spinal system (Standring and Borley, 2008). The presence of collagen and elastin provide tensile strength to the ligaments to limit neck motions within the physiologic range (Yoganandan et al., 2005, 2001). While there are ligaments that are common to the UCS and LCS, there are ligaments that are unique to the UCS. The structure of ligament interconnectivity between the UCS vertebrae vary from the LCS. The passive stability in the UCS is primarily provided by the ligaments in the absence of IVDs (Gray, 1918; Mattucci et al., 2013).

The ligaments of the UCS comprise anterior atlanto-occipital membrane (AA-OM) that connect the superior surface of anterior arch of atlas to the anterior aspect of foramen magnum (Standring and Borley, 2008). The AA-OM continues in the inferior direction as anterior atlanto-axial membrane (AA-AM) and connect the anterior arch of atlas (C1) to the anterior surface of C2 vertebral body. The posterior atlanto-occipital membrane (PA-OM) connects the posterior arch of atlas to the posterior aspect of foramen magnum. The posterior atlanto-axial membrane (PA-AM), located directly below the PA-OM, connect the posterior arch of atlas (C1) to the posterior arch of axis (C2) (Figure 14). The tectorial membrane (TM) runs from posterior surface of the C2 vertebral body and attaches to the basilar occipital bone. The transverse ligament (TL) runs laterally connecting the left and right lateral mass (articular pillar) of the C1 via the posterior aspect of dens. While some ligaments directly connect C0

to C1 and C1 to C2, other ligaments connect C0 to C2, bypassing the C1. From the medial aspects of the TL, the ligament fibers extend longitudinally to connect with the TM and connect to posterior aspect of C2 vertebral body (inferior cruciate ligament) and the occipital bone (superior cruciate ligament). The TL, superior and inferior cruciate ligaments together is called the cruciate ligament of the atlas (C_x). The alar ligament (AL) comprises two bands of tissues that bilaterally extend from the dens and connect to the medial aspects of the occipital condyle. The apical ligament (ApL) is located anterior to the superior C_x ligament and connects the dens with the anterior margin of the foramen magnum (Akçali et al., 2020; Mattucci et al., 2013; Oda et al., 1992) (Figure 15).

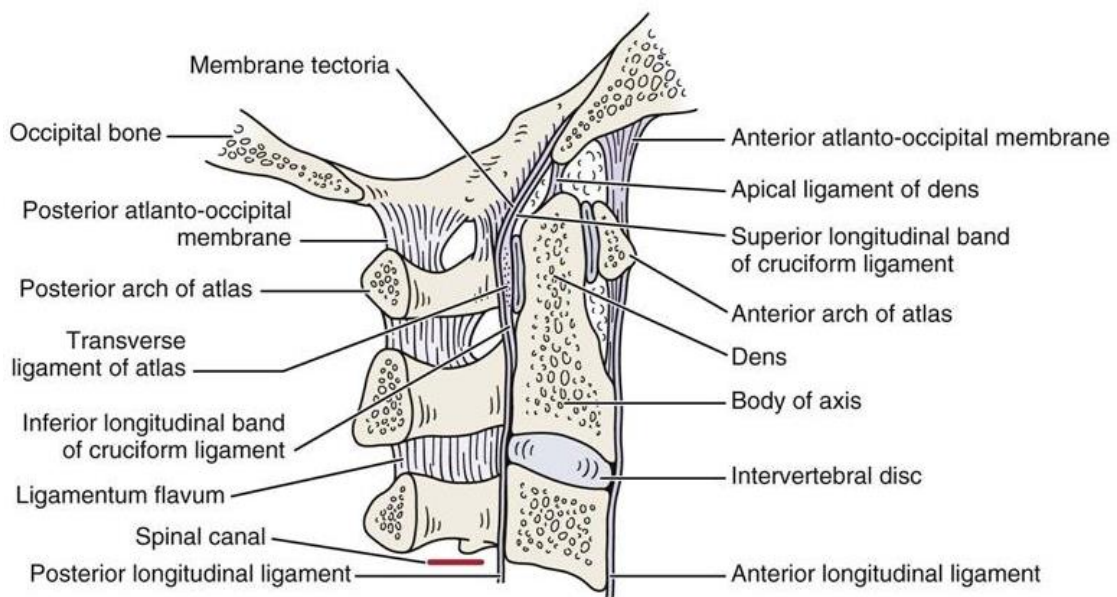


Figure 14: Sagittal view of the upper cervical spine ligaments.

[Taken from <https://musculoskeletalkey.com/cervical-spine-5/>]

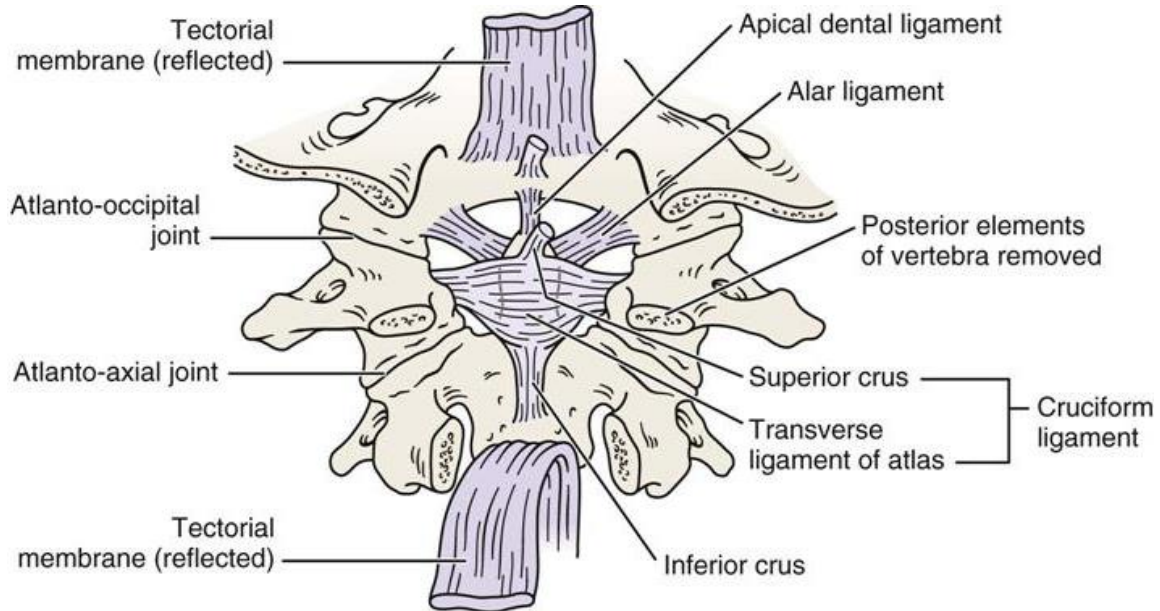


Figure 15: Posterior view of the upper cervical spine ligaments.

[Taken from <https://musculoskeletalkey.com/cervical-spine-5/>]

The AA-OM and AA-AM continues in the LCS as the anterior longitudinal ligament (ALL). The PA-OM and PA-AM extends further into the LCS as ligamentum flavum (LF). The TM continues in the LCS in the form of posterior longitudinal ligament (PLL) (Figures 15 and 16). The ALL and PLL run through the anterior and posterior surfaces of the vertebral body, respectively. The LF runs from C2 to C7 and connects the laminae of adjacent vertebrae. The supraspinal ligaments (SSL) run from C2 to C7 connecting the posterior tip of the spinous processes of adjacent vertebrae. The interspinous ligament (ISL) is common to UCS and LCS and run vertically connecting the spinous processes of adjacent vertebrae through the entire length of the cervical spine (Figure 16). Similarly, the capsular ligament (CL) is found in UCS and LCS connecting the inferior articular process of the superior vertebra and the superior articular process of the inferior vertebra and enclosing the facet joint.

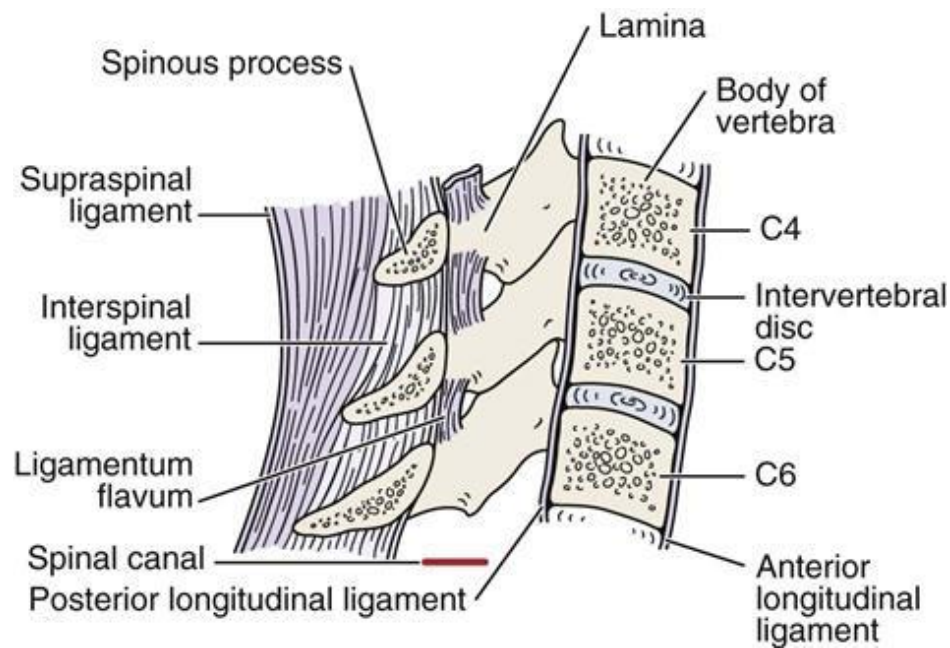


Figure 16: Sagittal view of the lower cervical spine ligaments.

[Taken from <https://musculoskeletalkey.com/cervical-spine-5/>]

The ligaments running posterior to the vertebral body primarily act to limit the cervical spine from hyperflexion (all the ligaments excluding ALL). The ligaments running anterior to the vertebral body (ALL) primarily act to limit the cervical spine from hyperextension. Ligaments exhibit non-linear viscoelastic properties and are strain-rate dependent. The tensile property of the ligament exhibit are four distinct regions: toe, linear, traumatic (sub-failure) and post-traumatic (failure) regions before completely rupturing (Mattucci and Cronin, 2015). During the initial stage of distraction, the collagen fibers in the ligaments begin to straighten from a relaxed crimped state, resulting in a non-linear ‘toe’ region. Further distraction causes the straightened fibers in the ligaments to transition from ‘toe’ to the ‘linear’ region where the ligament exhibits a constant stiffness. Continued distraction beyond the ‘linear’ region may cause microlesions and reduce the stiffness in the ligament leading into the ‘traumatic’ region (Mattucci et al., 2013, 2012; Mattucci and Cronin, 2015; Yoganandan et al., 2001, 1988). In the ‘traumatic’ region, despite microlesions, the ligaments are intact, and the damages cannot be observed macroscopically (Nordin and Frankel, 2001). As the microlesions increase due to continued distraction, the stiffness decreases and causes macroscopic failure. The amount of force required to produce a macroscopic failure is called an ultimate load. The post-traumatic region begins

at the point of ultimate load, from where the force response continues to drop as collagen fibers in the ligaments progressively fail until full rupture (DeWit and Cronin, 2012).

2.2.2 Articulations in the cervical spine

The smallest physiologic motion unit in the spine that exhibit the characteristics of the entire spine is termed as FSU. Typically, an FSU comprises a superior and an inferior vertebra with all the tissues and joints that interconnect them. In an FSU, specifically the C2-C3 to C6-C7, there are two primary types of articulations: 1) Symphysis joint and 2) Diarthrodial or Synovial joint. The symphysis type of joint comprises interaction between the two adjacent vertebral bodies through a fibrocartilaginous tissue (IVD) between them and referred to as saddle joint or interbody joint (Bogduk and Mercer, 2000; Levangie and Norkin, 2005). The synovial type of joint is formed between the bilateral facet articular processes of two adjacent vertebrae and called facet/zygapophyseal joint (Levangie and Norkin, 2005). The facet joints are usually enclosed within the capsular ligament (CL) (Figure 17). The structure of the FSUs in the LCS allows for motions in flexion and limited axial rotation while resisting lateral bending. Lateral bending may possibly occur as a coupled-motion in the cervical spine during the head axial rotation (Swartz et al., 2005).

The articulation of the UCS is unique to the cervical spine. In the atlanto-occipital joint (C0-C1 FSU), the occipital condyle (C0) rests on the horizontally oriented superior facet (articular surface) of C1 via the occipital condyle, forming a facet/zygapophyseal joint (Bogduk and Mercer, 2000; Steilen et al., 2014). The convex shape of the occipital condyle enables it to fit into the concave surface of the superior articular surface of C1. The atlanto-axial joint (C1-C2 FSU) comprises three synovial type joints. A synovial trochoid (pivot) joint between the anterior aspect of dens and the anterior arch of C1. Two synovial joints in the bilateral aspects of C2 in the facet articular processes. The odontoid process (dens) in the C2 vertebral body acts as a pivot for C1 to rotate around its axis (Bogduk and Mercer, 2000; Levangie and Norkin, 2005; Steilen et al., 2014) (Figure 18). The unique structure in the UCS causes the C0-C1 to be dominant in sagittal plane motions (flexion-extension) and C1-C2 motions to be dominant in transverse plane motions (left-right axial rotation) (Bogduk and Mercer, 2000; Heller et al., 2005; Steilen et al., 2014; Swartz et al., 2005).

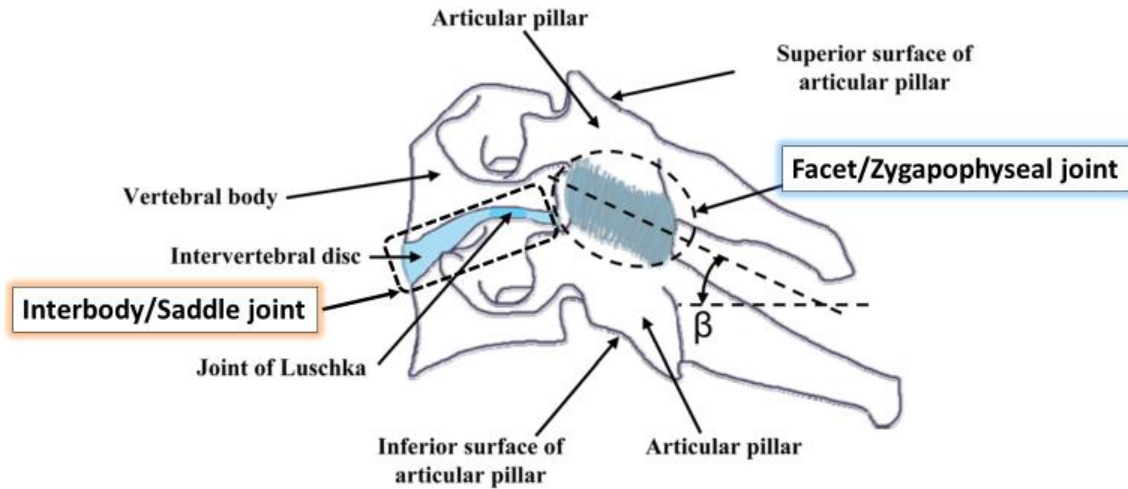


Figure 17: Illustration of the saddle/interbody joint and facet/zygapophyseal joint in an FSU.

[Adapted from Jaumard et al. (2011)]

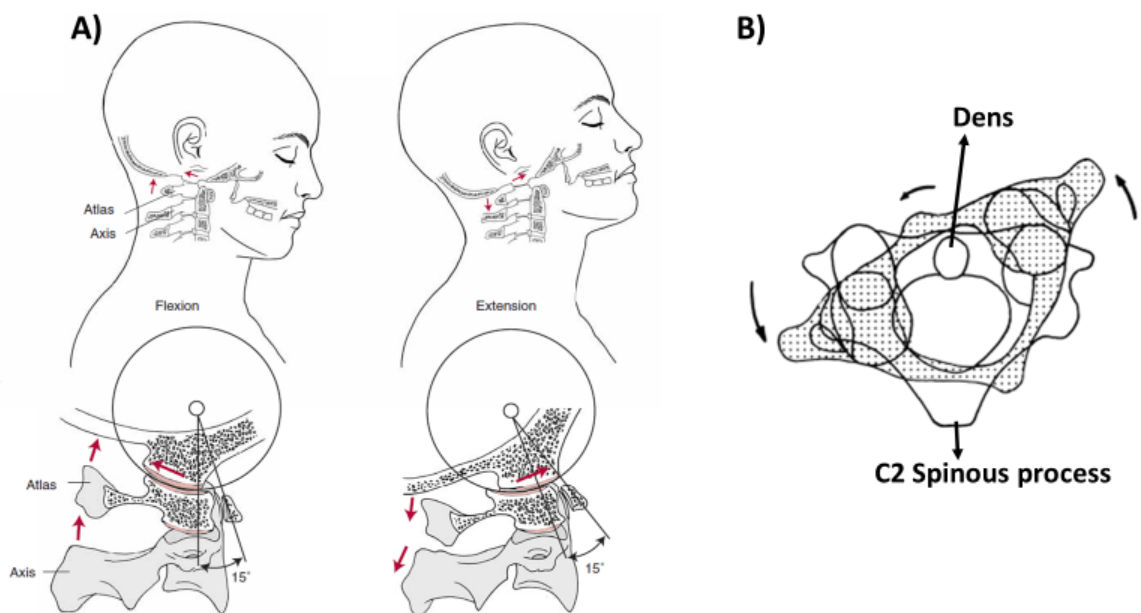


Figure 18: A) Illustrating the flexion and extension motion in the UCS that demonstrates the dominance of atlanto-occipital joint in sagittal plane and B) Illustrating the axial rotation of C1 around dens to show that dominance of atlanto-axial joint in the transverse plane.

[Taken from Levangie and Norkin (2005) and Bogduk and Mercer (2000)]

2.2.3 Neck muscles

Skeletal muscles surrounding the ligamentous cervical spine provide further stability in addition to the ligaments and facilitate head and neck physiologic motion. These muscles are attached to the hard tissues by tendons and transmit the tensile forces produced during muscle contractions. There are over 26 symmetric pairs of skeletal muscles in the neck region, each facilitating either flexion, extension, lateral bending or axial rotation of the head and neck (Bogduk and Mercer, 2000; Panjabi et al., 1991b, 2001b; Shen, 2020).

A skeletal muscle is hierarchical in structure and is composed of bundles of fascicles. Each fascicle contains bundles of muscle fibers. Each muscle fiber is composed of parallel bundles of myofibrils that contain a series of contractile units called sarcomeres (Figure 19). Every hierarchical structure in the muscle is enclosed by collagenous sheaths called epimysium (whole muscle), perimysium (fascicles) and endomysium (muscle fibers) (Standring and Borley, 2008). When the skeletal muscle is in a resting state, the length of each sarcomere unit is approximately $2.6 \mu\text{m}$ (Kamibayashi and Richmond, 1998). The sarcomere is composed of thin and thick filaments namely actin and myosin, respectively, that slide over each other.

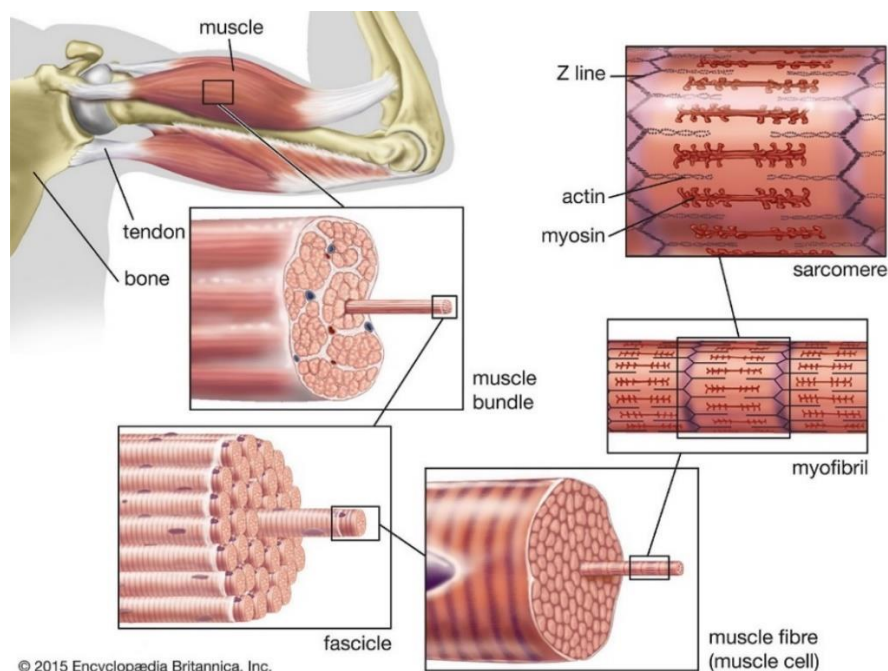


Figure 19: Hierarchical structure of the skeletal muscle.

[Taken from <https://www.britannica.com/science/muscle/Vertebrate-muscle-systems>]

In the contractile unit, the portion between the two Z-disc is the sarcomere. The Z-disc is located at regular intervals across the myofibril. The portion between the Z-discs comprises different bands and zones. The area that include only the actin filament is called I-band. The area that majorly comprises myosin and a small portion of actin is called A-band. The area in which there is no overlap of actin or myosin filaments is called H-zone (Figure 20) (Levangie and Norkin, 2005; Richfield, 2014). Interaction of the actin and myosin filaments indicate muscle contractions which are controlled by neural impulses that originate from the central nervous system and transmitted through the motor neurons to the actuating cells. The neural impulse evokes an action potential across the muscle fiber which initiates the release of calcium ions. The calcium ions set the receptor sites on the actin free and ready to bind with myosin. The actin and myosin binding/overlap results in the formation of a cross-bridge. Tensile force is generated in the active muscles from the myosin head with the hydrolysis of adenosine triphosphate (ATP) and release of adenosine diphosphate (ADP) (Levangie and Norkin, 2005). However, stretching the muscle beyond a limit can lead to separation of actin and myosin where there is no formation of cross-bridge causing the active muscles to stop generating force (Figure 21).

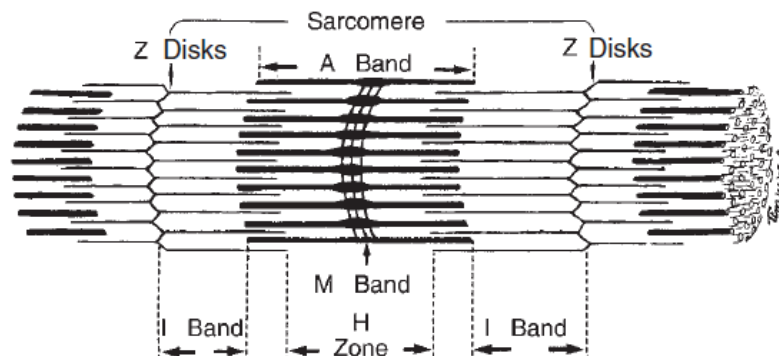


Figure 20: Illustration of the actin and myosin filaments within a sarcomere in a relaxed and contracted state.

[Taken from Levangie and Norkin (2005)]

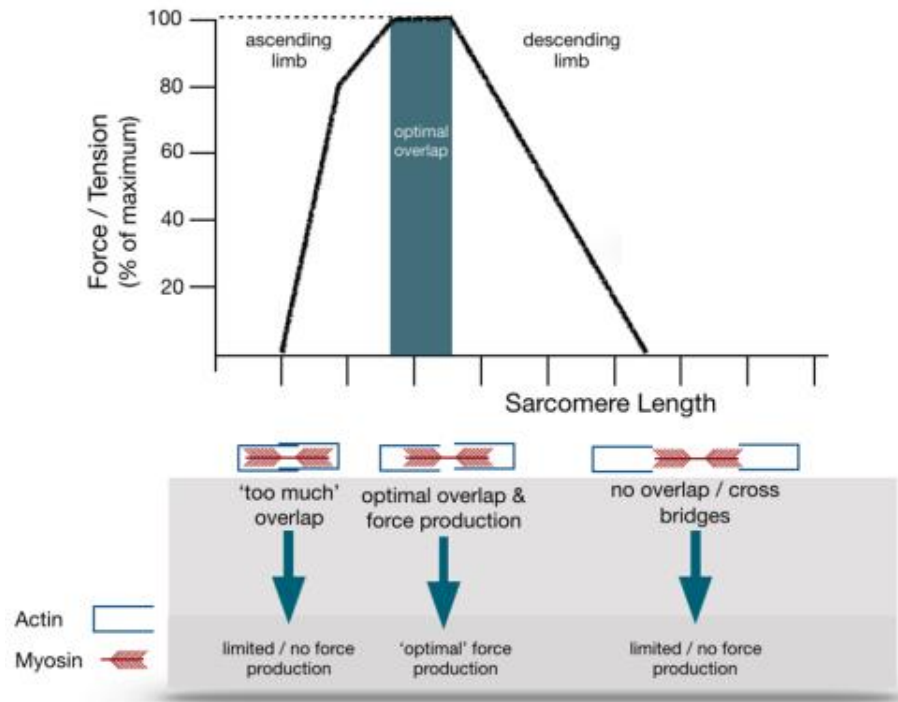


Figure 21: Illustrating the effect of cross-bridge in generation of active muscle force using the length-tension relationship.

[Taken from <https://getbacktosport.com/latest-news/length-tension-relationship/>]

2.3 Physiologic kinematics of the head and neck

2.3.1 In vitro ROM of the neck

Several experimental investigations on the physiologic kinematics of the UCS (C0-C2), LCS (C2-C7) and full cervical spine (C0-C7) have been conducted on isolated cadaveric ligamentous cervical spines. Experiments on the cadaveric ligamentous spine specimens involve constraining one end (mostly inferior end) and applying a moment on the free end (Figure 22). The degree of rotation of the entire specimen or at each FSU level is recorded for different modes of loading including flexion, extension and axial rotation across the ROM spectrum starting from 0 Nm to the maximum applied moment. Some experimental studies reported the intervertebral (C0-C1 and C1-C2) kinematic response (Ivancic, 2013; Oda et al., 1992; Panjabi et al., 1991b, 1991a, 2001b, 1998) and global (C0-C2) kinematic response (Nightingale et al., 2007, 2002) of the UCS specimens in flexion, extension and axial rotation at regular intervals of applied incremental moments (Figure 22a) (Table 1). Some experimental studies

reported the kinematic response in flexion and extension for the individual FSUs of the LCS (C2-C3 to C6-C7) at different points in applied moments (Camacho et al., 1997; Nightingale et al., 2007, 2002; Wheeldon et al., 2006) (Figure 22b) (Table 1). Some experimental studies reported the intervertebral kinematic response for the whole cervical spine (C0-C7) (Ivancic, 2013; Panjabi et al., 2001b, 1998) when subjected to externally applied moments in flexion, extension and axial rotation loading modes (Figure 22c) (Table 1).

The maximum applied moment to the superior aspects of the cadaveric ligamentous spine varies (1.0 Nm to 3.5 Nm) with different studies (Table 1). From the experimental findings, UCS contribute to 50% of the cervical spine flexion, 46% of extension and 73% of axial rotation while the remaining contribution comes from the LCS (C2-C7) (Ivancic, 2013; Panjabi et al., 2001b, 1998). The rotation of the UCS was found to be dominant from the in vitro experimental studies in all the three modes of loading (Figure 23). The in vitro experimental data are considered valuable and have been widely used for ligamentous cervical spine model validations (Barker et al., 2017; Cronin et al., 2012; Hadagali and Cronin, 2023; Lasswell et al., 2017; Shateri and Cronin, 2015).

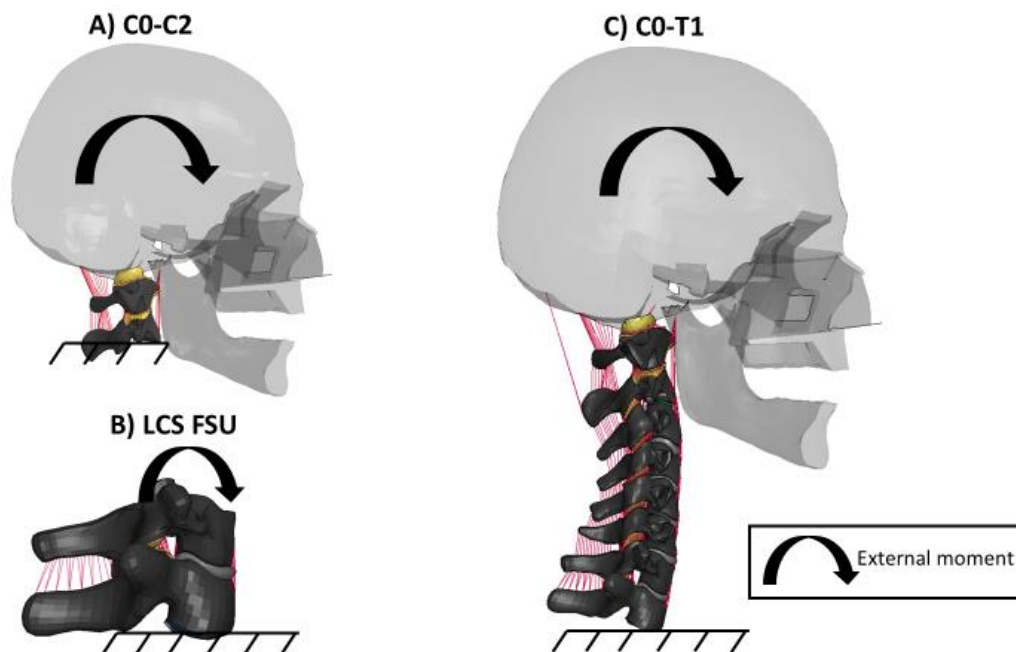


Figure 22: Illustrating the constraint of the inferior end and application of an external moment to the superior end of the cadaveric cervical spine specimens as described in the experimental procedures.

Table 1: Maximum applied moments on ligamentous cervical spine specimens for different experimental studies.

Literature			Maximum moment applied	Kinematic output levels
Author and Year	Tested segment	Loading mode		
Panjabi et al 1991a	C0-C2	Flexion	1.5 Nm	Intervertebral level
		Extension		
Panjabi et al 1991b		Axial Rotation	1.5 Nm R 1.5 Nm L	
Oda et al 1992	C0-C2	Flexion	1.5 Nm	Intervertebral level
		Extension		
		Axial Rotation	1.5 Nm R 1.5 Nm L 1.5 Nm L + 1.5 Nm R	
Panjabi et al 1998	C0-C7	Flexion + Extension	1.0 Nm F + 1.0 Nm E	Intervertebral level
		Flexion	1.0 Nm	
		Extension		
Panjabi et al 2001	C0-C7	Flexion	1.0 Nm	Intervertebral level
		Extension		
		Axial Rotation	1.0 Nm L + 1.0 Nm R	
Ivancic 2013	C0-T1	Flexion	1.5 Nm	Intervertebral level
		Extension		
		Axial Rotation	3.0 Nm R 3.0 Nm L 3.0 Nm L + 3.0 Nm R	
Camacho 1997	C2-C3 to C6-C7	Flexion	1.5 Nm	
		Extension		
Wheeldon 2006	C2-C3 to C6-C7	Flexion	2.0 Nm	
		Extension		
Nightingale 2002, 2007	C3-C4 to C6-C7	Flexion	3.5 Nm	
		Extension		
	C0-C2	Flexion	3.5 Nm	Global level
		Extension		

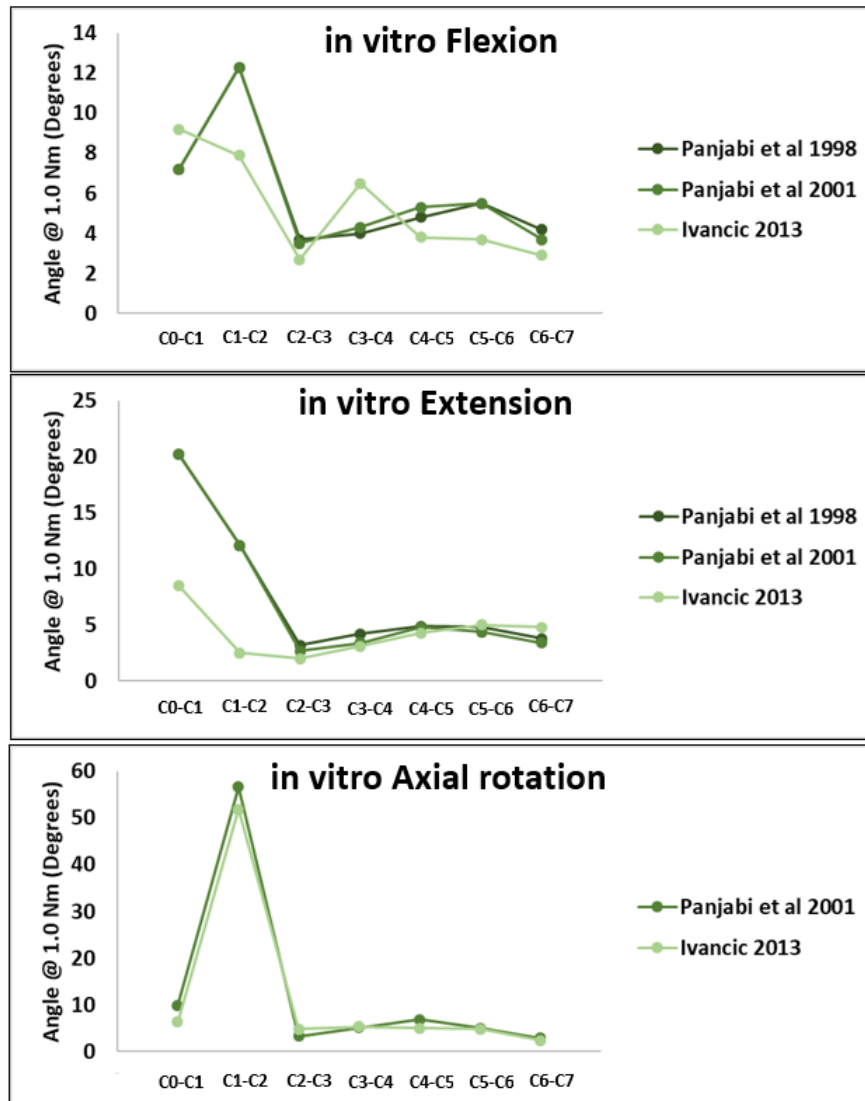


Figure 23: A summary of the experimental intervertebral ROM when a moment of 1.0 Nm is applied to the ligamentous cervical spine specimen in flexion, extension and axial rotation loading modes. The experimental summary highlights the dominance of UCS when the ligamentous cervical spine is subjected to all the three modes of physiologic loading.

2.3.2 In vivo ROM of the neck

In vivo, the muscles surrounding the ligamentous cervical spine, under the influence of gravity, activate (contract) to move the head and neck to a desired position. During in vivo experiments, volunteers were instructed to perform maximum bending (full) motions of the head and neck in different anatomical planes (flexion, extension, axial rotation and lateral bending) (Lascurain-Aguirrebeña et al., 2018). The kinematics of the cervical spine were recorded at the global and intervertebral levels (Anderst et al., 2015; Dvorak et al., 1991; Liu et al., 2015; Ordway et al., 1999; Salem et al., 2013; Sato et al., 2015; Takatori et al., 2008; Wu et al., 2010). The volunteers were instrumented with kinematic reflective markers and the voluntary head and neck motions were captured using radiographic instruments (Lascurain-Aguirrebeña et al., 2018; Zheng et al., 2012). Few studies also instrumented EMG electrodes on the volunteers to capture the neck muscle activities during in vivo head and neck motions (Cheng et al., 2008; Healey et al., 2021; Mousavi-khatir et al., 2015). A majority of the in vivo experiments reported the ROM of the cervical spine at the end-range of the head and neck motions. Only few studies have reported the in vivo ROM of the cervical spine across the spectrum of ROM starting from a neutral posture to the end-range, non-neutral position (Guo et al., 2021; Wu et al., 2010). From the in vivo experimental findings, UCS contribute to 7%-22% of the C0-C7 end-range flexion, 20%-25% of C0-C7 end-range extension and 66%-78% of C0-C7 end-range axial rotation (Figure 24). Some in vivo experiments also identified coupled motions (lateral bending and extension) in the cervical spine during a voluntary axial rotation motion (Anderst et al., 2015; Guo et al., 2021; Kang et al., 2019; Senouci et al., 2007).

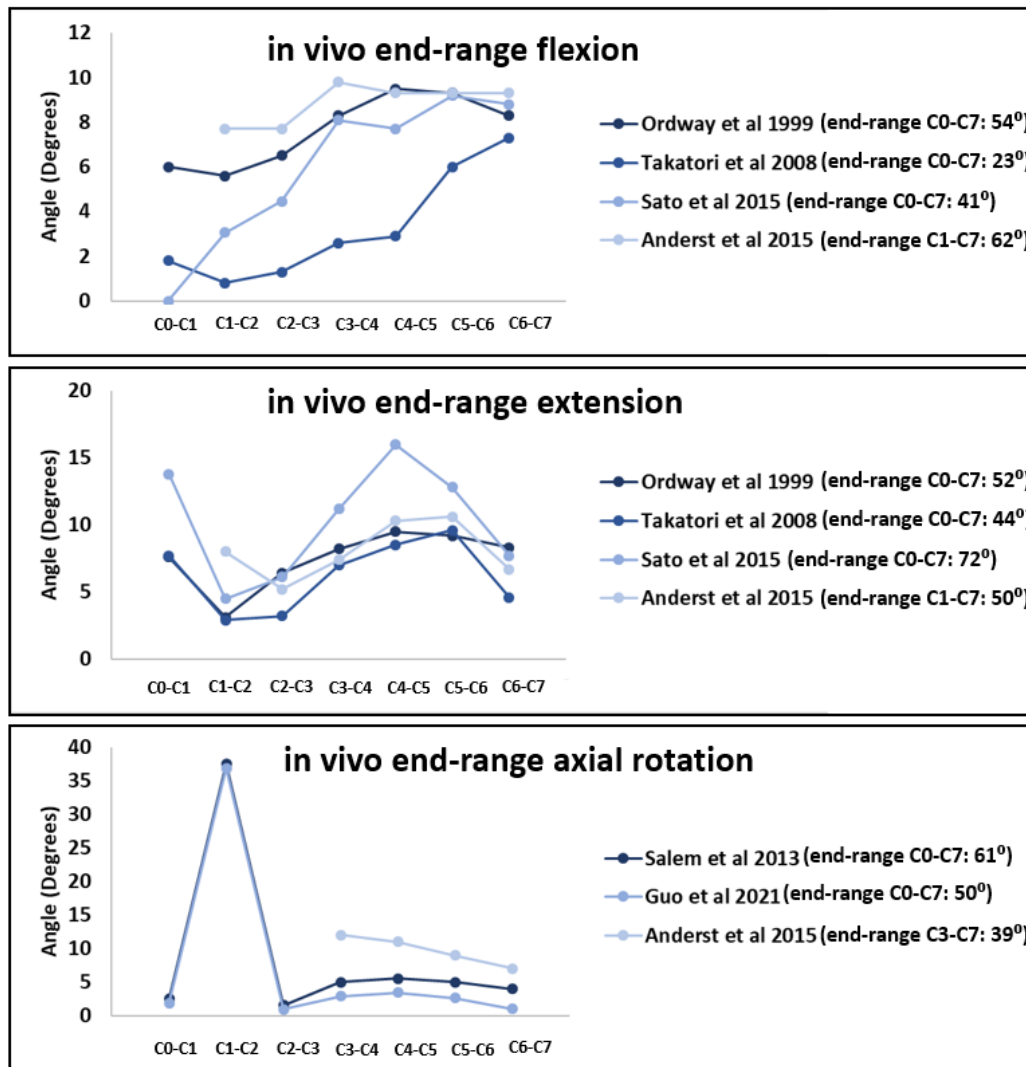


Figure 24: A summary of the mean in vivo intervertebral ROM reported at the end-range of voluntary flexion, extension and axial rotation. The experimental summary highlights the dominance of LCS during voluntary flexion and dominance of UCS during a voluntary axial rotation of the head and neck.

2.3.3 Differences between in vitro and in vivo head and neck ROM

Differences were observed between the reported ROMs obtained from cadaveric cervical spine specimens (in vitro) and live humans during voluntary physiologic motions (in vivo). The contribution of the UCS in flexion and extension was >50% and <25% in the cadaveric spine specimens and live humans, respectively. Trends in axial rotation were similar in both the type of experiments, where

C1-C2 recorded the maximum rotation. The differences in kinematic trend between in vitro and in vivo conditions can be attributed to the effects of muscles and other pharyngeal tissues that act as a boundary condition (BC) for the jaw and the UCS. Although global head rotation can be similar between the in vitro and in vivo studies, there could be variations in the intervertebral rotations, as demonstrated in the experimental studies (Figure 25).

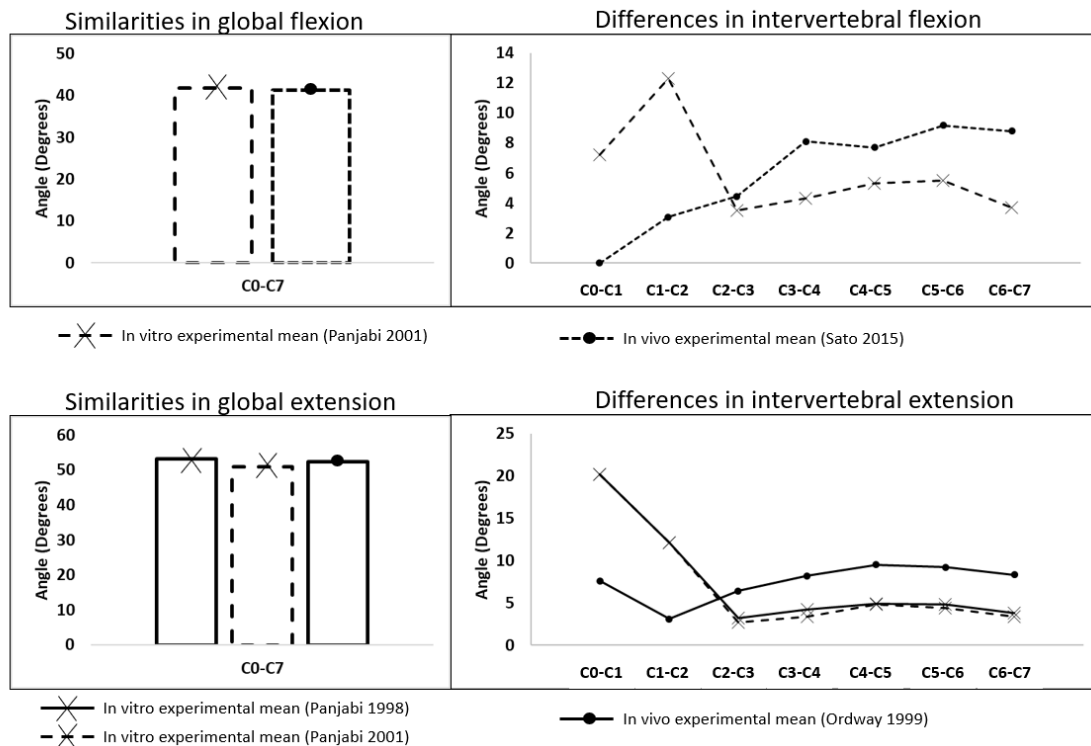


Figure 25: A comparative figure illustrating the similarities in the mean global head rotation (C0-C7) and differences in the mean intervertebral rotations (C0-C1 to C6-C7) in physiologic flexion and extension in cadaveric specimens (in vitro) and live humans (in vivo).

2.3.4 In vivo ROM of the neck when head is subjected to an external moment with a passive (relaxed) neck

An external load was applied to the head with torso fixed and head rotations were recorded on live subjects (in vivo) in flexion, extension and lateral bending modes by McGill et al. (1994). This experiment involved testing 40 male and 19 female volunteers who had no history of neck pain. The volunteers were made to lie down on their sides on a custom-made jig while their head was attached to a movable cradle to allow flexion, extension and lateral bend. The head attached to the cradle also

started moving, thereby inducing a bending moment in the neck. It was ensured that the subjects maintained relaxed musculature throughout the bending procedure. The mean head flexion relative to the torso in males at 7 Nm was 54° while the mean male head extension at 6 Nm was 60° (Figure 26a). The mean female head flexion relative to the torso at 7 Nm was 60° while the mean female head extension at 5 Nm was 65° (Figure 26b). The variability in the experimental data could not be calculated owing to the practical difficulties in digitizing each curve from the published literature.

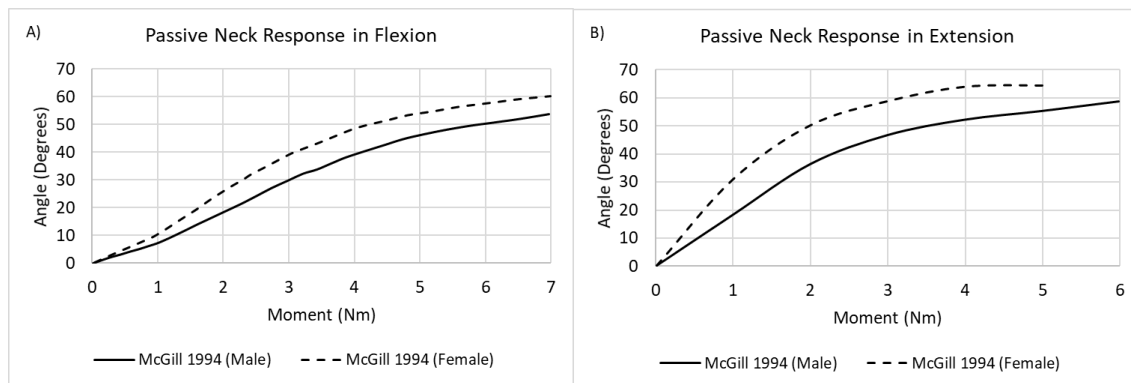


Figure 26: The mean rotation of the head relative to the torso plotted against the applied moment to the head (in flexion and extension) from the experimental study by McGill et al. (1994).

2.3.5 In vivo flexion of the passive (relaxed) neck under gravity

To date, there was only one study that investigated the behavior of passive neck under gravity loading and negligible muscle activation (Seacrist et al., 2012). The experimental study involved testing male and female volunteers aged between 6-12 years (pediatric) and 20-40 years (adult). The volunteers were seated on test apparatus that comprised a rotatable rigid seat with four-point belt system and adjustable lower extremity restraints. The volunteers were instructed to relax their neck muscles to allow the head to flex forward under the influence of gravity using phrases “relax your neck muscles, as if you were asleep” and “allow your head to fall forward”. To ensure that muscles were relaxed during experimentation, a passive-to-active transition threshold (PATT) was established prior. To establish PATT, the volunteers were instructed to forward fall their heads and then raise their heads slowly. The maximum voltage from any of the muscles when the head began to raise was recorded as PATT. In the head forward fall relaxed state, it was ensured that the muscles did not exceed PATT. The head flexion test was conducted with different seat angles (Figure 27). The experimental study measured the head

rotation relative to the motion of the upper thoracic spine angles with respect to the horizontal (Figure 27a). The study demonstrated that under gravity, the passive head and neck (relaxed musculature) flexed forward owing to the anteriorly placed center of gravity (CoG) of the head relative to the spinal column. The study reported that the maximum rotation of the head owing to inactive muscles and under gravity was similar to the head rotation in a voluntary full flexion ($\approx 60^\circ$) that involved muscle contractions (Seacrist et al., 2012). The study also reported that there was flexion in the upper thoracic spine (T1-T4) by approximately 25° with respect to the vertical indicating the influence of upper thoracic spine in sagittal plane head and neck motions. The intervertebral ROM of the neck was not reported in this study.

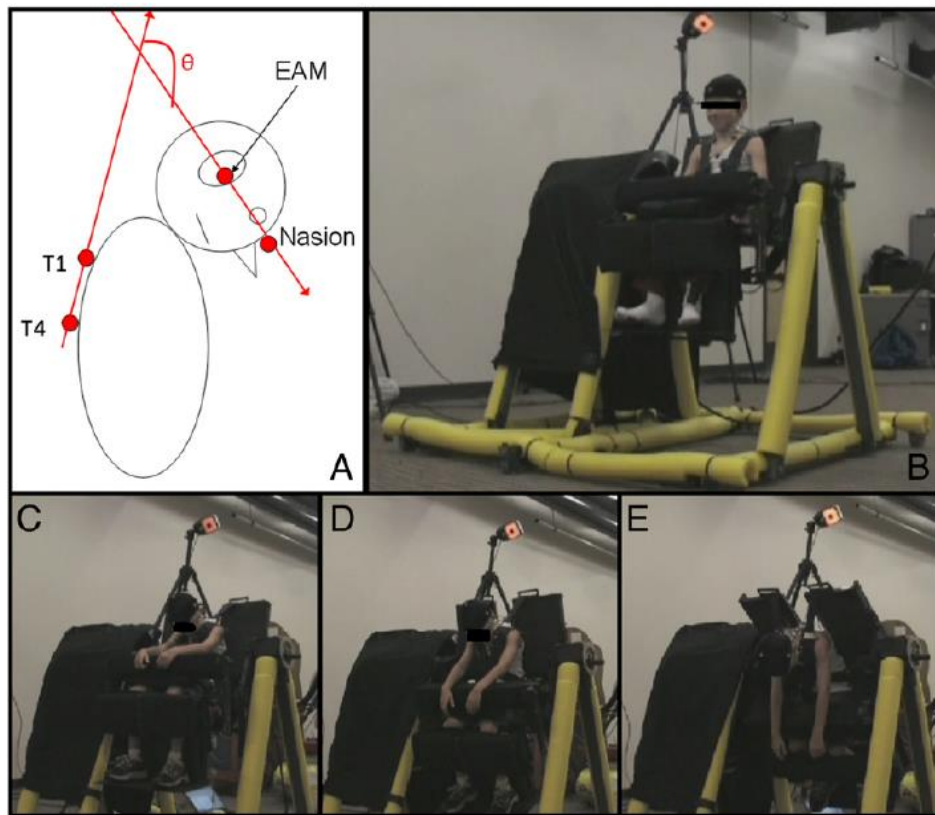


Figure 27: The experimental setup used to assess the response of head flexion under gravity and passive neck muscles.

[Taken from Seacrist et al. (2012)]

2.4 Neck pain

To date, the definition of ‘neck pain’ and the underlying mechanism of neck pain in the RWA population has not been well understood (Farrell et al., 2020; Healey, 2019). As quoted by the International Association for the Study of Pain (IASP), pain is defined as “an unpleasant sensory and emotional experience associated with actual or potential tissue damage, or described in terms of such damage. Pain is always subjective”. As quoted by the World Health Organization (WHO) pain is defined as “an unpleasant sensory or emotional experience associated with actual or potential tissue damage, or described in terms of such damage.” (Farrell et al., 2020). In a generalized context, a pain that is experienced between the superior nuchal line and imaginary transverse line on T1 and between the lateral margins of the neck can be defined as neck pain (Bogduk, 2003).

In general, pain can be classified based on the underlying pathophysiology, duration, etiology and location. Based on the underlying pathophysiology, pain can be classified as 1) nociceptive, 2) neuropathic and 3) mixed. Nociceptive pain occurs as a response to a noxious stimulus resulting in sharp, burning pain or dull aching pain. Examples of nociceptive pain include back pain, headaches, neck pain, shoulder pain, pain due to burns and injuries. Neuropathic pain occurs as a result of neuronal damage resulting in numbing, burning and increased sensitivity to stimuli. Examples of neuropathic pain include diabetic neuropathy, peripheral neuropathy, trigeminal neuralgia and other neuropathic pains due to spinal injury. Mixed pain is defined as a combination of nociceptive and neuropathic pains. Lower back pain radiculopathy is a common example for mixed pain (Dureja et al., 2017). Based on the duration, pain can be classified as 1) acute, 2) chronic and 3) breakthrough. While the duration of acute pain lasts from few seconds to ≤ 6 months, the duration of chronic pain lasts beyond 6 months. A breakthrough pain is episodic and lasts from few seconds to hours as a result of incidental movement in a well-treated patient that wean off the effect of applied drugs. For example, a breakthrough pain can be experienced in the interim between two doses of administered drug (Dureja et al., 2017). Based on the etiology, pain can be classified as 1) cancerous and 2) chronic non-cancerous pain (CNCP). Pain due to osteoarthritis, rheumatoid arthritis, etc. can be considered examples of CNCP. Based on the location, pain can be anatomically classified regardless of the region from where the pain originates (Dureja et al., 2017).

2.4.1 Pain physiology

The general physiology of nociceptive pain remains common for all the anatomical regions. There are two types of neural pathways involved in pain physiology: 1) ascending pathway and 2) descending pathway. While the ascending pathway is responsible for transmitting the pain from the location of injury to the brain, the descending pathway is responsible for controlling and inhibiting the ascending pathway through neuronal inhibition (Figure 28). Anatomical regions comprise sensory nerve fibers (nociceptors) that respond to noxious stimuli. There are two types of nociceptors to sense pain: 1) A δ fibers and 2) C fibers. The A δ fibers are small, myelinated and responsible for perception of fast, localized and sharp pains. The C fibers are smaller and unmyelinated and responsible for perception of slow, and burning pains. The nociceptors are also referred to as the afferent nerve fibers as they are bringing the information in to the spinal cord and to the brain (Christiansen and Cohen, 2018; Cross, 1994; Dureja et al., 2017; Katz and Rothenberg, 2005; Schug et al., 2011; Steeds, 2009). During an injurious event, damaged cells release cytokines (e.g. prostaglandins) as a response to inflammation. The nociceptors respond to the cytokines released by the cells. When the nociceptors are stimulated, the signals are propagated to the dorsal side of the spinal cord via the dorsal horn. The nociceptors then release chemicals called pain neurotransmitters (e.g. Substance P) in the dorsal side of the spinal cord. A second-order neuron in the spinal cord receives the pain signals from the neurotransmitters and transmit the information to the third-order neuron in the thalamus ('relay station' in the brain) via the spinothalamic pathway. In the thalamus, the third-order neuron receives the pain signal via the neurotransmitters from the second-order neuron and transmits the information to somatosensory cortex region of the brain where the pain and the location of pain is perceived. The noxious stimuli in the right side of the body is perceived as pain in the left side of the brain and vice versa (Christiansen and Cohen, 2018; Cross, 1994; Dureja et al., 2017; Katz and Rothenberg, 2005; Schaible and Richter, 2004; Schug et al., 2011; Steeds, 2009) (Figure 28). The response of the human body to noxious stimuli and the perception of pain in the brain is an important process to prevent further damage to the already injured tissues (Costigan et al., 2009).

The general physiology of neuropathic pain is similar to nociceptive pain as it involves the ascending and descending pathways. In this type of pain, the nerves are directly affected by nerve trapping or a physical pressure from conditions such as IVD herniation, causing radiculopathy (radiating pain) (Bogduk, 2003; Song et al., 2017). Some conditions like diabetes and vitamin-B deficiencies directly affect the nerves and cause peripheral neuropathy (Dureja et al., 2017).

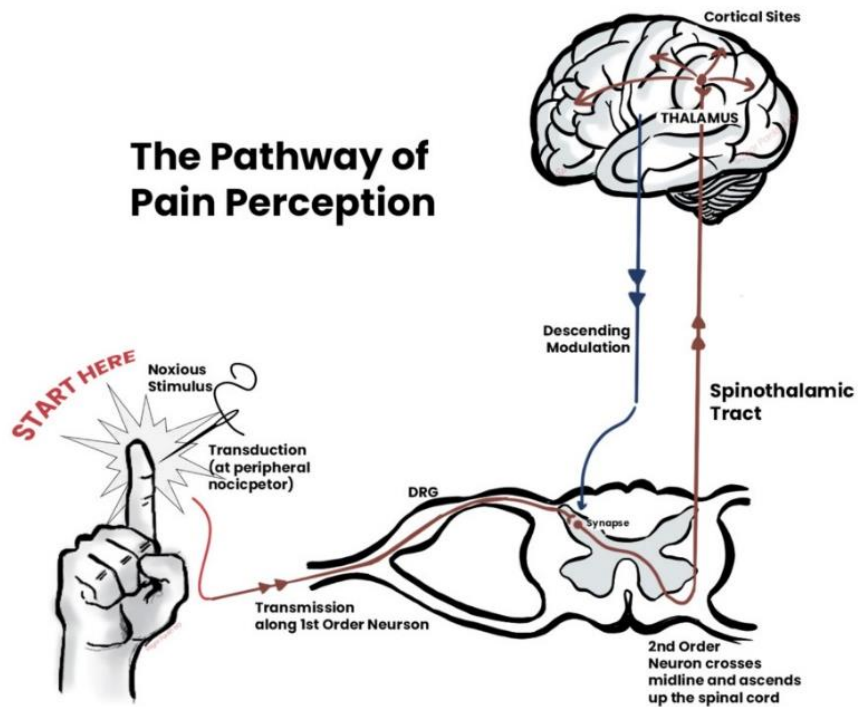


Figure 28: An illustration of nociceptive pain pathway ascending and descending pain pathways in response to external noxious stimulus.

[Image taken from <https://now.aapmr.org/pain-and-placebo-physiology/#references>]

In both acute and chronic type of pains, an inflammatory response occurs within hours post-injury and is characterized by a burning sensation, pain, numbing or tingling at the site of injury (Omoigui, 2007). In cases where tissue is abruptly over-loaded (e.g. car crash, fall, collisions), the acute inflammation is triggered within several hours and may last for many weeks and sometimes up to a year. The inflammatory response in this case is symptomatic, as a result, allowed to heal. In such a case, there is limited tissue healing post-injury, although the affected tissue is allowed to rest (Woo and Buckwalter, 1988). Pain that persists past normal healing time for tissues and recurs for more than 3 to 6 months is defined as chronic pain (Katz and Rothenberg, 2005; Treede et al., 2015). Inflammatory responses in the tissues are triggered when they are abruptly loaded beyond the physiologic limits or subjected to static loading within its physiologic limits over an extended period (Barr and Barbe, 2004; Frank et al., 1985; Solomonow, 2004) (Figure 29).

Sometimes, the acute inflammatory response in the tissue is triggered due to micro-damage caused by static/repeated loading. In such cases, the micro-damage is often left unnoticed, and the tissue is further exposed to repetitive loads without allowing it to recover. Thus, the acute inflammation extends to become chronic inflammation (Barbe and Barr, 2006; Ulrich et al., 2007). The chronic inflammation builds over a prolonged duration (months or years) without showing any symptoms before causing permanent disability (Safran, 1995) (Figure 29).

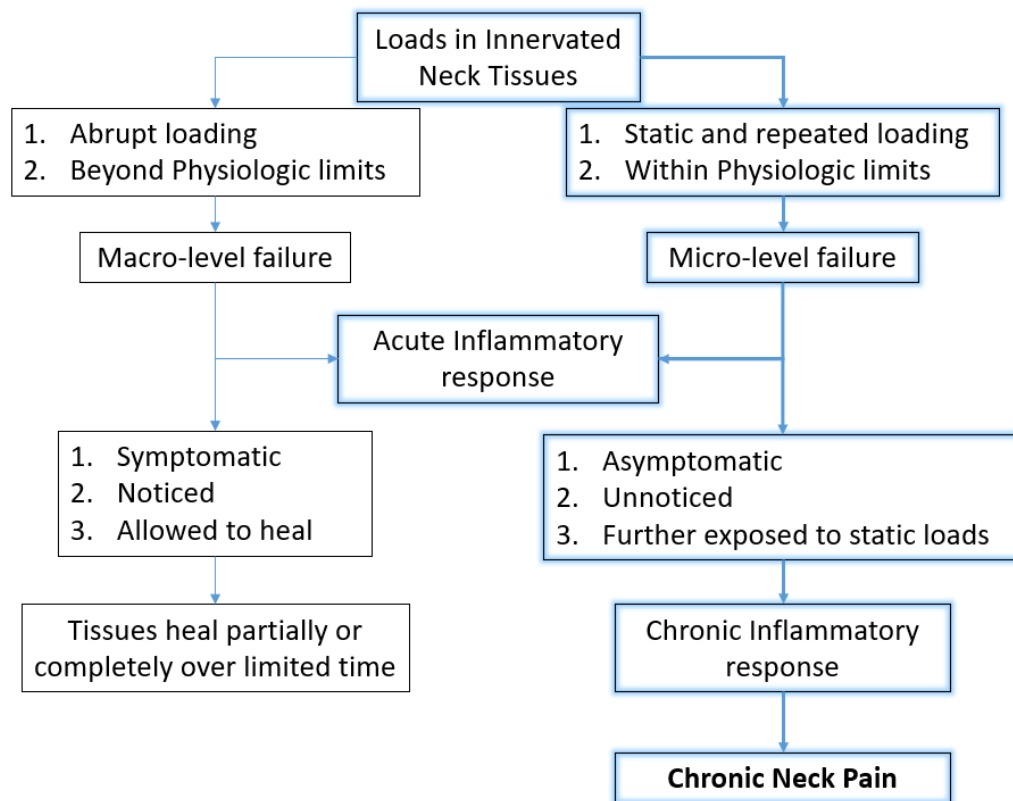


Figure 29: A flowchart summarizing the pathophysiology of acute and chronic pain based on the literature (Dureja et al., 2017; Solomonow, 2004; Treede et al., 2015). The potential neck pain path (chronic pain) in the RWA is highlighted in the flowchart.

Based on location, pain can be further classified as 1) somatic and 2) visceral. Somatic pain originates from the musculoskeletal system such as joints, bones, muscles, ligaments and associated tissues, for example neck. Visceral pain originates from the visceral organs such as blood vessels, heart, lungs, liver, stomach, intestines, etc. Somatic pain is sharp, well-localized and easy to locate while visceral

pain is vague, poorly-localized and challenging to identify the exact source. Somatic pain follows specific nerve pathways that are mapped to specific areas of the body unlike the visceral pain that involves broader network of nerve pathways (Boezaart et al., 2021; Dureja et al., 2017).

2.4.2 Potential pain sources in the neck

Cervical IVDs are endowed with appropriate factors for nociception, hence a potential source of neck pain. Nerve fibers innervating the IVDs are primarily found in the peripheries of the IVDs (Edgar, 2007; Raj, 2008; Sayson and Hargens, 2008). In the cervical IVDs, the posterior parts are innervated by sinuvertebral nerves, lateral parts by the vertebral nerves, and anterior parts by the branches of cervical sympathetic trunks (Bogduk, 1985; Peng and Bogduk, 2019). These nerves feed the entire anterior and posterior plexus (network of nerves) that cover the anterior and lateral parts of the vertebral column and the entire length of posterior longitudinal ligament (PLL). From the anterior plexus, nerve fibers enter the cervical IVDs and terminate with free endings in the outer layers of AF (Dowdell et al., 2017). These nerve endings are nociceptors (pain receptors) as indicated by the presence of nerve growth factors and neurotransmitters called substance P (Dowdell et al., 2017; Peng and Bogduk, 2019) (Figure 30). Several studies on the etiology of lower back pain have been associated with IVD degeneration and herniation that compresses the nerve root, causing pain (Dowdell et al., 2017; Molinos et al., 2015; Ulrich et al., 2007). An experimental study showed that stimulating the anterior and posterior surfaces of cervical IVDs evoked neck pain, indicating that cervical IVDs are sources of neck pain (CLOWARD, 1960). In degenerated IVDs, the nociceptive nerve endings further grow into the NP and potentially increase the risk of pain (Adams and Dolan, 2012; García-Cosamalón et al., 2010; LIANG et al., 2013; Peng and Bogduk, 2019; Tomaszewski et al., 2015) (Figure 30). Clinical findings have reported that the number of nerve fibers increases as the IVDs starts to degenerate and the reasons for this phenomenon are several (Binch et al., 2021; LIANG et al., 2013). As the IVD degeneration progresses, there would be a reduction in joint space and osteophyte formation. The osteophytes are also enriched with nociceptive nerve fibers that can potentially cause pain (Inoue and Espinoza Orías, 2011; Menkes and Lane, 2004; Roelofs et al., 2020; Rustenburg et al., 2018; van der Kraan and van den Berg, 2007). A chronic inflammatory response has been observed post injury in peripheral annular regions in experimental animal models. The experimental observations on the chronic inflammatory response location agree with the clinical observations in lower back pain patients (Barr and Barbe, 2002; Callaghan and McGill, 2001; Wang et al., 2006). Damage to the collagen fibers within the

annulus can also be perceived as pain provided the innervated portion of the fibers are involved in any lesion (BOGDUK et al., 1988).

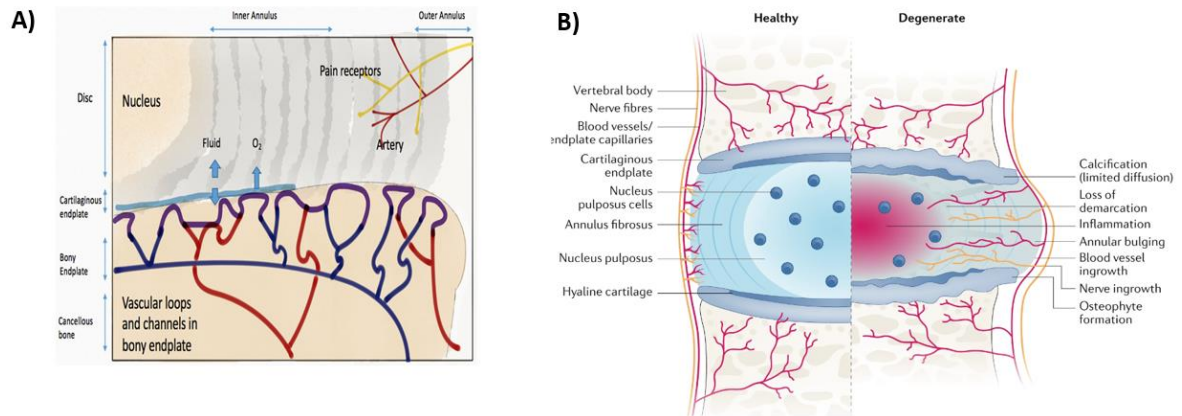


Figure 30: Illustrating the innervation and the presence of pain receptors in the peripheral aspects of the IVD (A). Also, the growth of the nerve endings into the NP as the IVD degenerates is illustrated (B).

[Taken from Binch et al. (2021) and Dowdell et al. (2017)]

The facet joints, composed of capsular ligaments encompassing the synovial fluid and facet cartilage, are often reported to be a contributor to chronic neck pain (Jaumard et al., 2011; Panjabi, 2006; Siegmund et al., 2009). Facet joints in the LCS are innervated by cervical dorsal rami (Manchikanti et al., 2004). In the UCS, the lateral part of the atlanto-axial facet joint is innervated by the C2 ventral ramus. The medial atlanto-axial facet joint is innervated by sinuvertebral nerves of C1, C2 and C3. The atlanto-occipital facet joint is innervated by C1 ventral ramus (Bogduk, 2003; Shih et al., 2019). Histological evidence shows the presence of mechanoreceptors (motion sensing nerve endings) and nociceptors in the synovial fold of the facet joint, which can cause inflammation and pain (Inami et al., 2001; Jaumard et al., 2011; Kallakuri et al., 2004). Experimental and computational studies have implied facet joint distraction/stretching as a potential cause for chronic neck pain in car occupants who experienced rear-end impact (Bogduk, 2011; Fice et al., 2011; Pearson et al., 2004; Shateri and Cronin, 2015; Shen, 2020; Siegmund et al., 2008). Stretching of the facet joints also causes the embedded afferent nerve endings (nociceptors) to stretch. Studies have shown that the stretching of the nerve endings can be noxious and can trigger inflammatory response that transmit pain (Dong and Winkelstein, 2010; Lee et al., 2004; Lu et al., 2005a, 2005b, 2005c). Noxious stimulation of the facet

joints in the cervical spine can also cause referred pain in different neck regions (Bogduk, 2003). Experimental studies reported the locations of referred pain corresponding different facet joint levels by stimulating the joints using mechanical and electrical impulses (Aprill et al., 1990; Dwyer et al., 1990; Fukui et al., 1996) (Figure 31). The distraction of the facet joints can potentially tear the capsular ligaments which can lead to loss in the mechanical integrity of the spinal structures. A loss in mechanical integrity even due to a micro-damage to the facet capsular ligament can induce pathophysiological response including nociception and pain (Dong and Winkelstein, 2010; Lee et al., 2004). Micro-damage to the facet capsular ligaments have also shown to cause ligament laxity leading to chronic cervical spine instability if left untreated (Quinn et al., 2010, 2007; Siegmund et al., 2001; Tominaga et al., 2006; Winkelstein et al., 2000). Facet joint compression beyond physiologic limits can potentially damage the articular cartilage and alter the mechanical properties of the facet joint. The risk of neck pain as a consequence of articular cartilage damage has not been reported (Liu et al., 1985; Pearson et al., 2004).

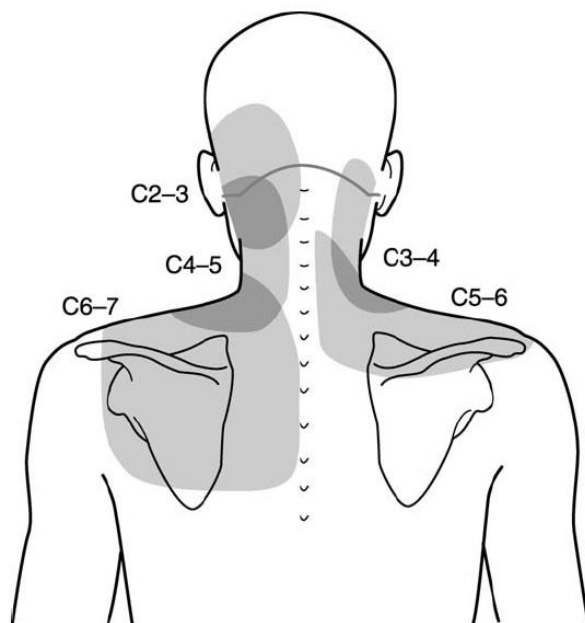


Figure 31: Location of the referred pain regions in the neck corresponding to different stimulated facet levels.

[Taken from Bogduk (2003)]

The cervical spine ligaments have also been identified as potential sources of neck pain resulting from low severity impact, leading to whiplash-associated disorders (Cronin, 2014; Siegmund et al., 2009). Ligaments have also been considered a source of work-related disorders as they undergo creep due to repeated loading within physiologic limits (Solomonow, 2004). While the ligaments in the atlanto-occipital and lateral atlanto-axial joints are innervated by C1 and C2 ventral rami, the ligaments in atlanto-axial region are innervated by C1 and C3 sinuvertebral nerves. In the LCS, the PLL are also innervated by the sinuvertebral nerves. The ligaments along the vertebral column are innervated by the recurrent meningeal branches of the spinal nerves (Frick et al., 1990). Other than providing joint stability, the ligaments also act as sensory organs in the joints. Ligaments in the spinal regions are embedded with mechanoreceptors consisting of Pacinian, Golgi, Ruffini and bare nerve endings and may contribute to kinesthesia (sense of perception of position and movement including maintaining balance). Other sensory functions include reflex activation/inhibition of muscles. Damage or rupture to ligaments by means of any kind of loading could not only lead to loss of mechanical stability in joints, but also sensory loss of kinesthesia and decreased reflex function to activate or inhibit the muscles (Panjabi, 2006; Solomonow, 2004). Mechanical conditions, including joint laxity, joint instability, sprain, rupture, etc., originate from the ligament's inflammatory response. Neuromusculoskeletal disorders such as muscle activation changes also occur from the ligament's inflammatory response (Panjabi, 2006; Solomonow, 2004). Ligament laxity can cause excessive motion in the cervical spine, which can irritate the nerves and cause vertigo, dizziness, facial pain, arm pain, painful muscle spasms and paresthesia (Steilen et al., 2014).

Another component that could potentially cause neck pain is the neck muscles. The lateral branches of the dorsal rami innervate the superior posterior muscles. Medial branches of the cervical dorsal rami supply the deeper and medial muscles of the neck. The ventral rami of C1 innervate the longus cervicis and longus capitis muscles to C6 vertebral nerves (Bogduk, 1985). Sternocleidomastoid (SCM), scalenus and trapezius muscles are innervated by the central ventral rami. Muscle strains have potentially exceeded the muscle injury thresholds in rear impact cases and may be associated with acute neck pain (Brault et al., 2000; Vasavada et al., 2007). However, muscle pain resulting from physiologic tasks has been associated with reflex activation of muscles as a consequence of load applied to ligaments, discs or facet joints over a prolonged period (Solomonow et al., 2003, 1998). Several live human studies have reported increase in extensor muscle activity due to prolonged flexion posture while using hand-held devices and have implicated it with increased risk of chronic neck pain (Namwongsa

et al., 2019; Ning et al., 2015). Some experimental studies have also found variations in muscle activity patterns in human volunteers with and without chronic neck pain (Christensen et al., 2017; Falla et al., 2004; Juul-Kristensen et al., 2013). Tendons, which are the fibrous structures that join muscles to bones can also be considered important sources of pain. Tendonitis, i.e. inflammation in the tendons is one of the most prevalent work-related musculoskeletal disorders and often associated with repetitive activities (Harniman et al., 2004). Human tendons are shown to be scantily innervated. Examination of painful tendons revealed pathological features such as disoriented collagens, collagen fiber disorientation and fiber separation (Bjur et al., 2005; Rio et al., 2014). In the neck, there are several clinical case studies that have documented tendonitis in the longus colli muscle in patients with neck pain (Artenian et al., 1989; Kim et al., 2017; Wu et al., 2023).

2.5 Neck pain risk factors in the rotary-wing aircrew

From the literature survey, it was concluded that the RWA across the globe experience neck pain while flying the rotary-wing aircraft during a mission over the duration of their career (Ang and Harms-Ringdahl, 2006; Farrell et al., 2020; Fraser et al., 2015; Orsello et al., 2013; Salmon et al., 2011; Sharma and Agarwal, 2008; Thomae et al., 1998). The alarmingly high rates of neck pain in the RWA substantially reduces the operational effectiveness in the RWA, jeopardizes the mission safety and results in loss of working days for the highly trained RWA (Derouin, 2020). Persistent neck pain among RWA impacts the health and performance of the highly trained personnel and lead to loss of manpower along with enormous financial cost (Salmon et al., 2011), driving the need to understand further and mitigate this issue.

Evidence-based radiographic studies have shown that RWA are more susceptible to spinal degeneration relative to civilian population (Aydoğ et al., 2004; Byeon et al., 2013; Landau et al., 2006). One of the studies reported IVD degeneration in 50% of the RWA (Landau et al., 2006). Another radiographic study conducted for one year reported that 19% of RWA had IVD changes over the year, with 13.84% having osteoarthritis, 3.14% with decreased lordosis, and 1.25% with an avulsion fracture and 1.25% with ligament calcification (Aydoğ et al., 2004). Another study conducted radiographic examinations on 186 RWA and 94 military clerical workers and concluded that cervical spine degeneration was significantly more prevalent in RWA than in military clerical workers (Byeon et al., 2013). A relatively recent study reported that the incidences of ambulatory visits due to neck pain and IVD degeneration in RWA aged 20-24 occurred at a rate of 31.23 per 1000 persons per year. The rate

of ambulatory visits due to neck pain and IVD degeneration increased with the age of the RWA (Madison et al., 2023).

The origin and the precise pathophysiology of neck pain in the RWA remains obscure to date (Neary et al., 2010). The RWA in service, including flying pilots, non-flying pilots and flight engineers, were surveyed for flight-related neck pain. HSM related factors like the type of helmet, the mass of helmet, usage of NVGs, duration of wear, frequency of usage, etc. Human-related factors including age, gender, anthropometric details, exercise habits, social habits and total flight hours were surveyed. The survey also included questions regarding neck pain episodes, the intensity of pain, number of times treated, anatomical areas of pain, tasks, postures, aircraft workspace, etc. (Adam, 2004; Chafé and Farrell, 2016; Posch et al., 2019). Survey-based studies intended towards understanding the interaction of various factors with the RWA neck to provide recommendations to mitigate the risk of neck pain. Responses from RWA indicated that the HSM with a combined usage of NVGs and CW while assuming non-neutral positions to scan/inspect the environment inside and outside the aircraft for long durations in the presence of aircraft vibrations caused neck pain (Adam, 2004; Chafé and Farrell, 2016; Farrell et al., 2020; Posch et al., 2019). Addition of NVG has been identified to be a major cause for neck pain in the RWA, in agreement with the findings from Adam (2004) survey that reported neck pain in 90% of RWA with more than 150 hours of NVG experience. Exposing the neck tissues to additional loads in subsequent missions without allowing it to rest sufficiently after a mission can increase the risk of a chronic inflammatory response in any of the innervated neck tissues and thereby chronic neck pain (Karakolis et al., 2015). Statistical studies have shown that a group with reported neck pain had total flying hours of 2203+/-2015 hours. The group without neck pain had 1915+/-1857 total hours, and increasing cumulative flying hours directly increased the risk of neck trouble in RWA (Karakolis et al., 2015). The workspace organization in the rotary-wing aircraft and human-related factors have been identified as potential risk factors for neck pain causation in RWA.

In general, other non-RWA occupations involving HSM and non-neutral head-neck positions have also reported neck pain. For example, increased usage of hand-held devices is shown to cause 'text neck' in general population (Ariëns et al., 2001; Fiebert et al., 2021). Medical practitioners performing microsurgies with HSM (loupes and head lamps) in a combined flexion and rotated head-neck positions are at an increased risk of neck musculoskeletal disorder (Nimbarte et al., 2013). Similarly, fire-fighters, who are exposed to HSM during occupation, are also at an increased risk of neck

musculoskeletal disorders (Park et al., 2014; Wang et al., 2021). Poor workspace organization factors such as chair design and display screen position have shown to cause neck discomfort in desk workers (Arndt, 1983). Human-related factors such as gender differences were also observed in ‘text neck’ cases, where, postural differences were observed between men and women. The study also observed that women perceived greater musculoskeletal pain in the neck and upper extremities compared to men (Fiebert et al., 2021).

2.5.1 Head-supported mass (HSM)

During a mission, the RWA neck is subjected to additional loads in the form of HSM. The HSM primarily comprises the helmet that weigh approximately 1.5 kgs. The helmet serves as a mounting platform for essential devices such as NVG that weigh approximately 0.6 kgs, battery pack (BP) that power the NVG and weigh approximately 0.2 kgs and an optional CW that weigh approximately 0.6 kgs. The NVG is an essential device when the RWA undertake a night mission.

Studies on RWA and neck pain had the participants wear HSM (helmet with or without NVG and CW) during the physiologic head-neck motion. (Äng, 2008; Fischer et al., 2014; Healey, 2019; Thuresson et al., 2003). The addition of a helmet (≈ 1.5 kg) has shown to affect the natural CoG of the head. The helmet’s mass combined with the shift in natural CoG and increase in moment of inertia affects the neutral position on the head, thereby inducing the head to flex more forward (Butler, 1992; Forde et al., 2011; Knight and Baber, 2004). In turn, the extensor group of muscles act to hold the neck in the neutral position (Harrison et al., 2015).

During a night mission, the RWA rely on the NVG (≈ 0.6 kg) to better view the region of inspection. The inclusion of NVG to the helmet further increases the mass, the moment of inertia and shifts the CoG further forward, thereby increasing the extensor muscle activity to balance the head (Sovelius et al., 2008). A CW (≈ 0.9 kg) is usually attached to the back of the helmet, although its counteractive effect is uncertain (Farrell et al., 2014; Harrison et al., 2009; Healey et al., 2021; McKinnon et al., 2016). The increasing muscle activities due to addition of HSM can potentially increase the loads in the cervical spine, which has been associated with increased risk of neck pain (Healey et al., 2021).

2.5.2 Non-neutral head-neck positions

Within the RWA, flying pilots, non-flying pilots and flight engineers are reportedly assigned different tasks during a mission. With the added HSM, RWA are obliged to perform tasks that involve

repeated head-neck motions and adaptation to non-neutral head-neck positions while scanning the environment inside and outside the aircraft. The flying and non-flying pilots perform 12 different tasks while flight engineers perform 22 different tasks. Each task demands different motions of the head and neck within a certain physiologic limit. A large-scale study on the RWA quantified the head-neck angles separately in flexion-extension, lateral bend and axial rotation during each task in flying pilots, non-flying pilots and flight engineers (Tack et al., 2014). In the large-scale study, the head-neck angle was measured using a rigid link connecting the base of the neck to the head (Tack et al., 2014) (Figure 32). The magnitude of head-neck angles assumed by the RWA were classified into three zones, namely ‘neutral’, ‘mild’ and ‘severe’ for flexion-extension, axial rotation and lateral bending (Forde et al., 2011; Tack et al., 2014) (Table 2). As per this classification, the head-neck angle assumed by the RWA was mostly in ‘mild’ flexion and axial rotation while ‘neutral’ in lateral bending (Tack et al., 2014). Further, the head-neck motions performed by the RWA during each task over a certain period of time was identified to be a combination of flexion, extension, right and left axial rotation, right and left lateral bending rather than motion in a single anatomical plane (Figure 33). The peak and the mean value in flexion-extension, left-right axial rotation and left-right lateral bending over the time period in each specific task for day and night missions was reported in this study (Tack et al., 2014). In the present study, a mean value and ± 1 standard deviation (SD) was calculated from the reported mean head-neck angles for all the tasks specific to flying pilots, non-flying pilots and flight engineers (Figure 34).

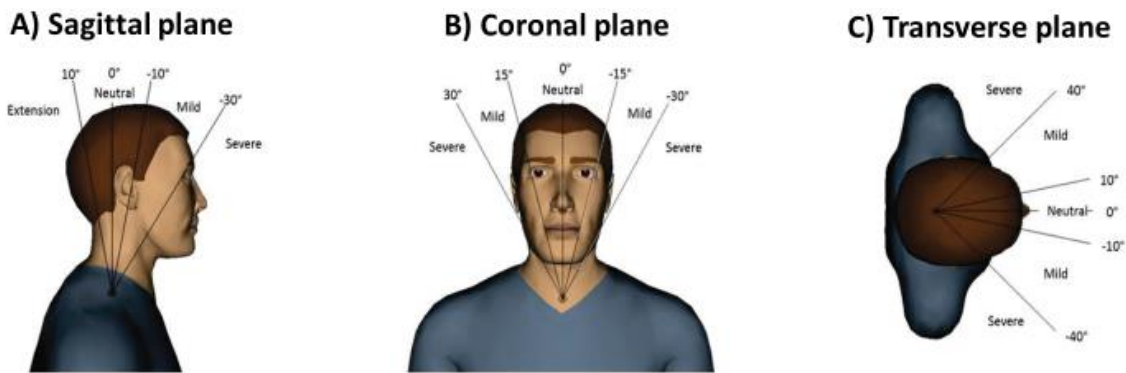


Figure 32: Head-neck angle measurement in the three anatomical planes in the RWA as reported in the literature (Tack et al., 2014).

[Adapted from Tack et al. (2014)]

Table 2: Classification of the head-neck angles in the RWA in the literature.

Plane	Motion	Head-neck angle (degrees)		
		Neutral	Mild	Severe
Sagittal	Extension	< -10		
	Flexion	-10 to 10	10 to 30	30 <
Coronal	Lateral Bending	-15 to 15	15 to 30	30 <
Transverse	Axial Rotation	-10 to 10	10 to 40	40 <

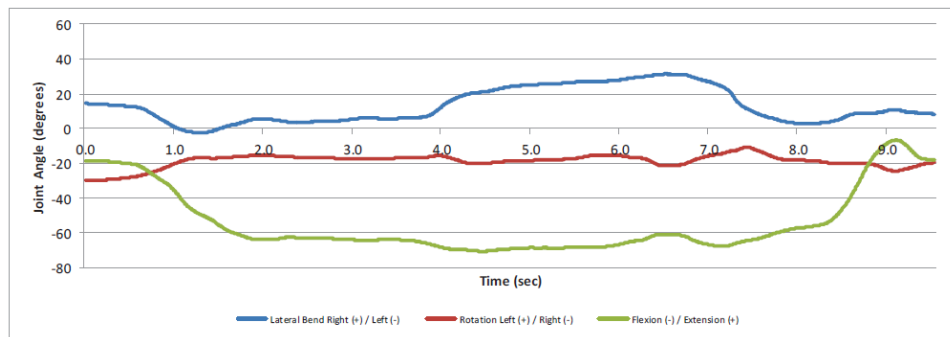


Figure 33: Quantification of the head-neck angle in the RWA flying pilot while performing the ‘outside scan chin bubble’ task during a night mission i.e. with the NVG. The figure demonstrates the combined motion of the head and neck in the RWA during a given scanning task (Tack et al., 2014).

[Adapted from Tack et al. (2014)]

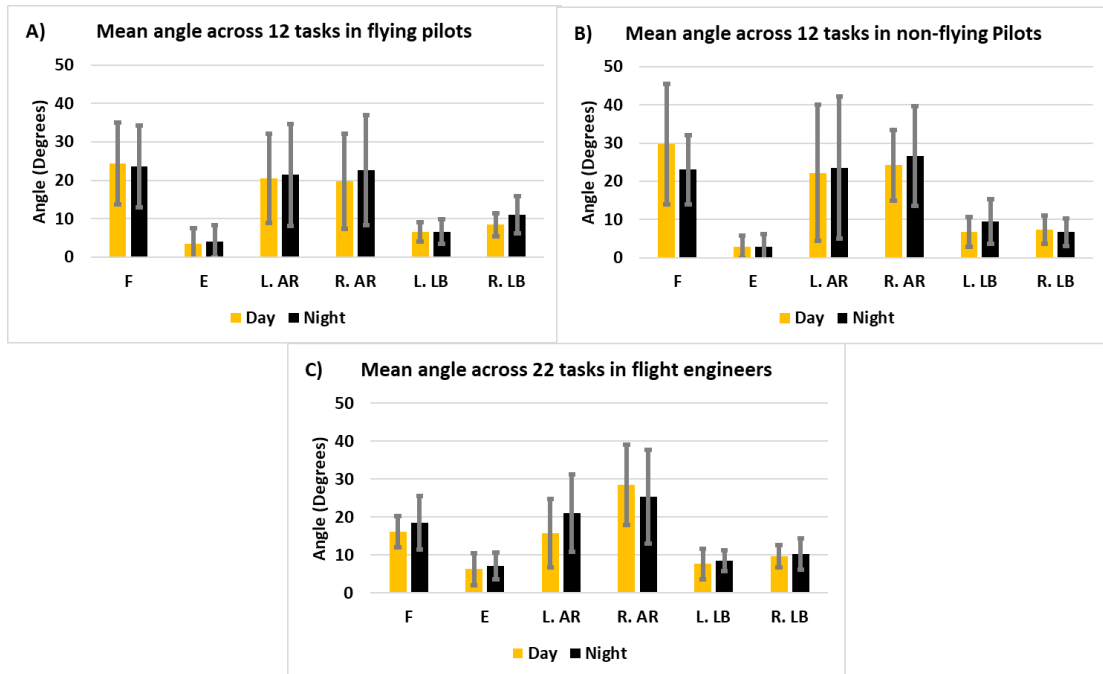


Figure 34: The calculated mean and ± 1 SD from the reported mean head-neck angles in flexion-extension, axial rotation and lateral bending across all the tasks in flying pilots (A), non-flying pilots (B) and flight engineers (C) in the literature (Tack et al., 2014). F: Flexion, E: Extension, L. AR: Left axial rotation, R. AR: Right axial rotation, L. LB: Left lateral bending and R. LB: Right lateral bending.

Literature indicates that the RWA cervical spine is constantly exposed to a combined compression and bending owing to HSM and physiologic non-neutral positions, respectively. The FOV in a healthy human is approximately 140-degrees in the horizontal and vertical directions. During a night mission, inclusion of NVG reduces the FOV from 140 degrees to 40 degrees in both horizontal and vertical directions (Harrison et al., 2015) (Figure 35). A reduction in the FOV has shown to increase the magnitude of non-neutral head-neck positions (Forde et al., 2011; Tack et al., 2014). For instance, in flying pilots, there was an increase in left axial rotation by a mean of 41.3% in 6 out of 12 tasks in the night mission compared to day mission. Similarly, there was an increase in right axial rotation by a mean of 75.4% in 6 out of 12 tasks in the night mission compared to day mission (Figure 36). Increase in magnitude of non-neutral positions indicate an increase in bending or twisting of cervical spine. From laboratory-based studies, FSUs subjected to a combined compression and physiologic bending

have demonstrated damages to the IVD tissues, which are considered to be one of the potential sources of pain (Desmoulin et al., 2020; Gooyers et al., 2015; Gooyers and Callaghan, 2015; Rajasekaran et al., 2013).

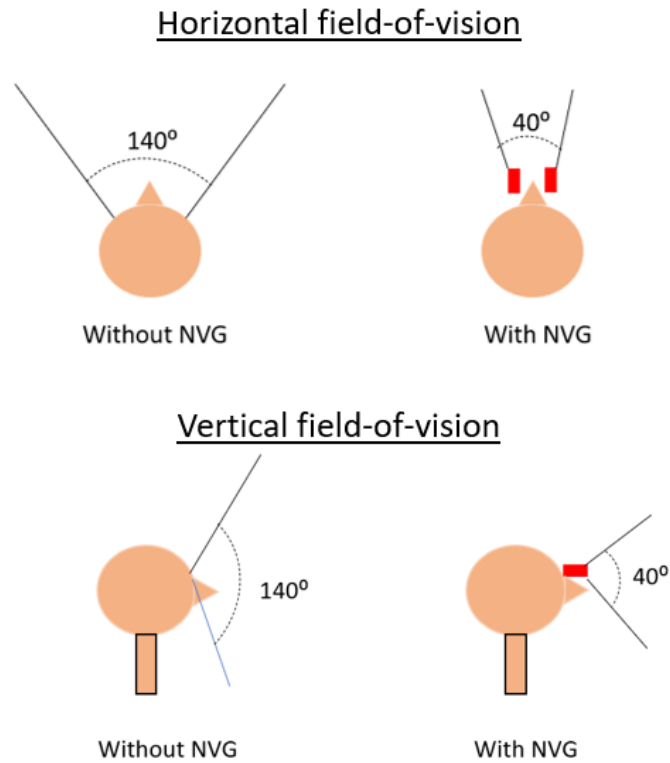


Figure 35: Illustrating the reduction in FOV in the RWA with the addition of NVG during night missions.

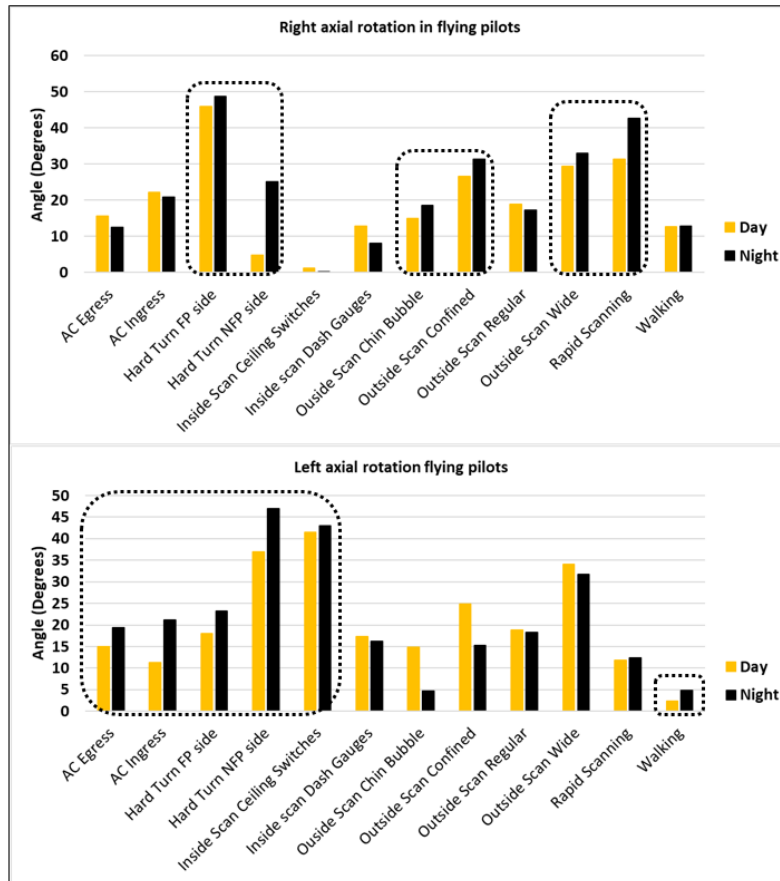


Figure 36: Mean head-neck angle in left and right axial rotation in the flying pilots during day and night missions as reported in the literature (Tack et al., 2014). The literature indicates an increase in the head-neck angle in most of the tasks as a result of NVG.

2.5.3 Time spent in non-neutral head-neck positions during different tasks

Forde and Tack quantified the amount of time spent in different non-neutral positions in individual anatomical planes (coronal, sagittal and transverse). RWA spent most of the time in 10° to 30° (‘mild’) flexion in the sagittal plane, 0° to 15° (‘neutral’) left- or right-lateral bent position in the coronal plane and 10° to 40° (‘mild’) in left- or right-axially rotated position in the transverse plane (Forde et al., 2011; Tack et al., 2014) (Figure 37). Compared to day missions, the time spent in non-neutral head-neck positions during night missions increases during some of the tasks (Tack et al., 2014). In flying pilots, the mean time spent across all the 12 tasks was 17.5±14.3 seconds and 19.5±20.9 seconds in day and night, respectively. The maximum time was spent in ‘AC ingress’ task which

increased from 57.1 seconds in day to 82.2 seconds in night with NVG (Figure 38). In non-flying pilots, the mean time spent across all the 12 tasks was 18.0 ± 13.4 seconds and 24.9 ± 20.9 seconds in day and night, respectively. The maximum time was spent in ‘AC ingress’ task which increased from 53.3 seconds in day to 78.9 seconds in night with NVG (Figure 39). In flight engineers, the mean time spent across all the 22 tasks was 15.1 ± 19.7 seconds and 15.6 ± 20.7 seconds in day and night, respectively. The maximum time was spent in ‘Start-up last chance inspection’ task where, the time spent in day and night were similar (66.8 seconds and 68.5 seconds, respectively) (Figure 40). The increase in time spent during night time, specifically in tasks such as AC ingress, was attributed to the mounting of NVG to enable enhanced vision. From literature, the RWA spend most of the time within the physiologic limits. Exposure of spinal tissues to prolonged loading within physiologic limits can greatly increase the risk of IVD and ligament injury (Desmoulin et al., 2020; Solomonow, 2004).

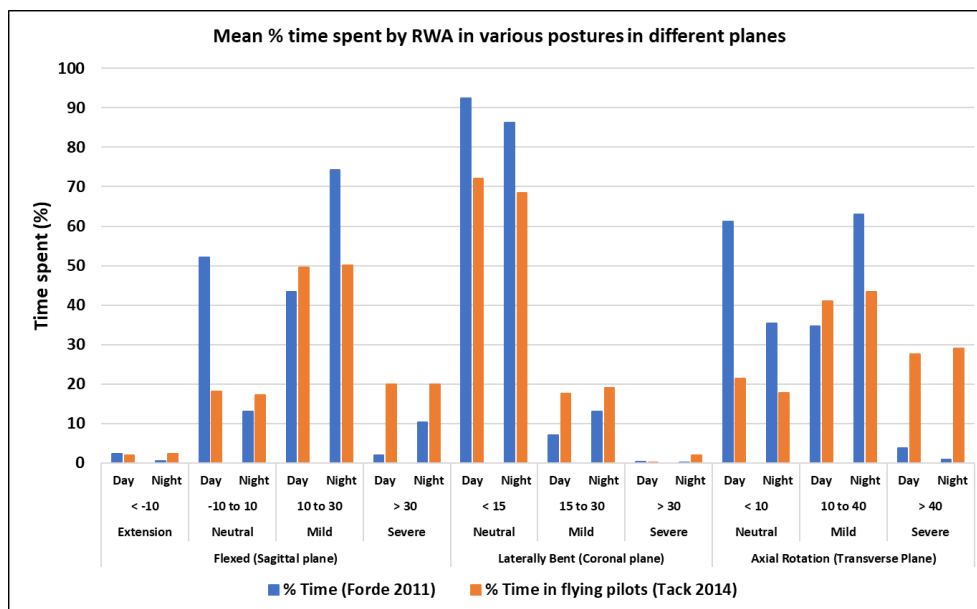


Figure 37: Mean percentage time spent by RWA in different head-neck positions as observed in different planes.

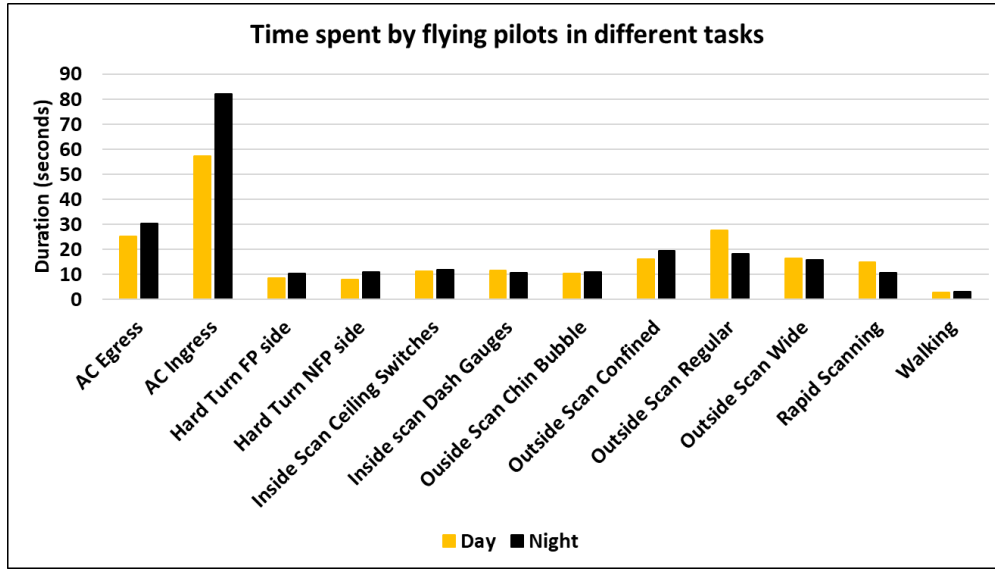


Figure 38: Mean time spent by the flying pilots in each of the 12 tasks as reported in the literature (Tack et al., 2014).

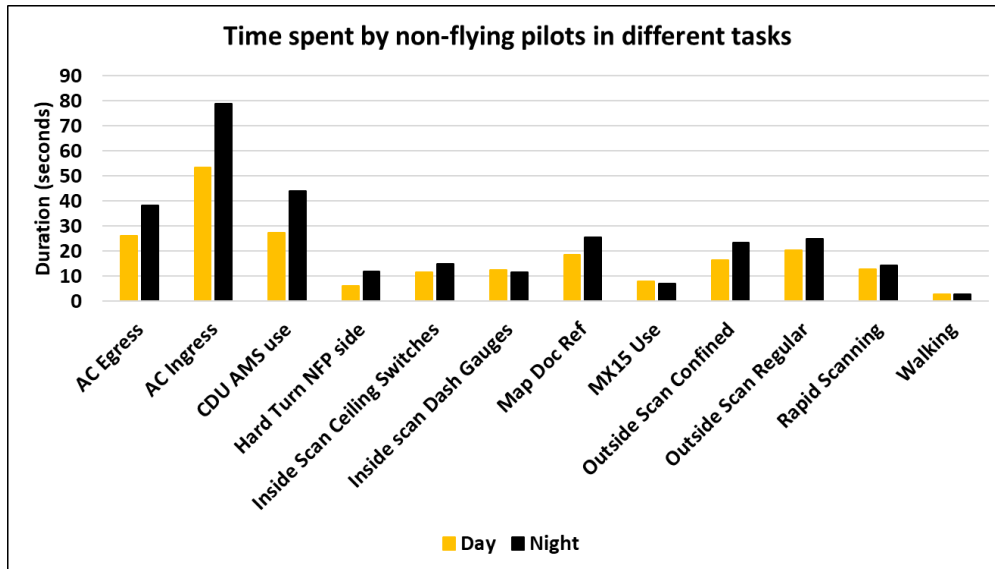


Figure 39: Mean time spent by the non-flying pilots in each of the 12 tasks as reported in the literature (Tack et al., 2014).

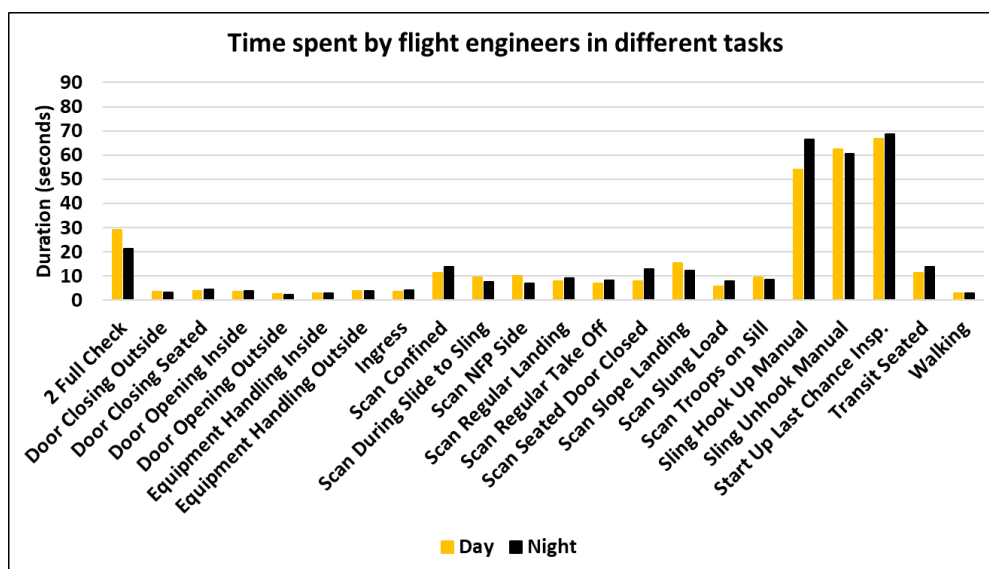


Figure 40: Mean time spent by the flight engineers in each of the 22 tasks as reported in the literature (Tack et al., 2014).

2.5.4 Workspace and organization factors

The RWA experiences vibration, and altered gravitational vectors within the aircraft workspace (O’Conor et al., 2020). Interaction with the controls and display, aviation life support equipment and other cabin devices in a small workspace in the rotary-wing aircraft compels the RWA head-neck to be often flexed and slightly rotated (Chafé and Farrell, 2016; Lopez-Lopez et al., 2001; Tack et al., 2014). Organizing the mission aspects may also aggravate the risk of neck pain. For example, a 2-hour training mission might be risky for student flight engineers while extremely risky for trainer flight engineers who need to adopt ‘severe’ head-neck non-neutral positions to ensure safe operation (Chafé and Farrell, 2016). The RWA cervical spine is constantly exposed to a cyclic loading while experiencing a combined compression and bending, all of which can potentially injure the spinal tissues.

2.5.5 Human-related factors

Demographics of an individual RWA such as age, gender, anthropometry, fitness levels, neck pain history, total number of flying hours, performance of preventive exercises, performance of strength training, work-rest cycle, sleep and nutrition may also contribute to the risk of neck pain. However, from surveys, the CH-146 aircrew demographics were relatively similar with no obvious relationship to neck pain (Chafé and Farrell, 2016; Farrell et al., 2020).

2.6 Computational head-neck models

2.6.1 Computational head-neck models for biomechanical assessments

The use of computational models as an alternative to experimental methods is advantageous as they provide insight into some of the internal tissue-level biomechanical responses that cannot be measured directly from cadavers or live humans in a laboratory setting (Alizadeh et al., 2020b; Arun et al., 2018; Yang et al., 2006). Computational head-neck models can be broadly classified based on several factors including the intended purpose of the model and levels of complexity (Alizadeh et al., 2020b).

Computational models of the human head-neck are developed with an intent to assess the risk of traumatic injuries, chronic pain, efficacy of spinal implants, interventions, etc. A wide array of computational models of different complexity exists for the human head-neck for various purposes including assessing the risk of acute neck injuries during short-duration (<200 ms) impact scenarios such as motor vehicle collision (e.g. car crash), collision in sports (e.g. football, rugby) and military (e.g. aircraft mishaps) (Barker and Cronin, 2021; Brodin et al., 2008, 2005; Cazzola et al., 2017; Dibb et al., 2014; Fice et al., 2011; Lasswell et al., 2017; Li et al., 2021, 2023; Liu et al., 2023; Mathys and Ferguson, 2012; Meyer et al., 2004; Nasim and Galvanetto, 2023; Panzer et al., 2011; Pramudita et al., 2017; Putra et al., 2021; Shateri and Cronin, 2015; Stemper et al., 2006; Storvik and Stemper, 2011; White et al., 2016; Yang et al., 2006). A plethora of computational head-neck models also exists for assessing the risk of neck injuries in occupational or long-duration scenarios (>1000 ms) such as text-neck due to overuse of hand-held devices and chronic neck pain in military personnel with HSM (Barrett et al., 2022a, 2020; Diao et al., 2018; Fathollahi, 2012; Hetzler, 2021; Mesfar and Moglo, 2012; Moore et al., 2021; Motiwale et al., 2018; Subramani et al., 2020; Zhou et al., 2019). Similarly, a number of computational head-neck models exists for biomedical and clinical applications to assess the biomechanical outcome of spinal implants, surgical/non-surgical interventions and degenerated spinal diseases on the cervical spine instability (X.-Y. Cai et al., 2020a; X. Cai et al., 2020; Chang et al., 2022; Cheng et al., 2023; Erbulut et al., 2014; Kwon et al., 2017; Lee et al., 2011; Lin et al., 2023; Manickam et al., 2023; Nikkhoo et al., 2021, 2019; Pengrong et al., 2019; Rahman et al., 2023; Sun et al., 2023; Wang et al., 2017; Zhang et al., 2023).

Computational models of the human head-neck, based on the complexity, can be classified as MB models, MSK models and FE models (Alizadeh et al., 2020b). The MB head-neck models typically comprise bony vertebrae represented as rigid bodies, IVDs represented using kinematic joints with

prescribed stiffness and ligaments (optionally) represented using beam elements with stiffness properties (Fathollahi, 2012; Hetzler, 2021; Lopik and Acar, 2007; RattanaGraikanakorn et al., 2022; Stemper et al., 2004; Tierney and Simms, 2017). The MB head-neck models with the inclusion of muscle components are regarded as MSK head-neck models (Alizadeh et al., 2020a; Arshad et al., 2022; Barrett et al., 2021, 2020; Cazzola et al., 2017; de Bruijn et al., 2016; Diao et al., 2017; Dibb et al., 2014, 2013; Mathys and Ferguson, 2012; Mortensen et al., 2018; Motiwale et al., 2018; Roos et al., 2020; Storvik and Stemper, 2011; van Lopik and Acar, 2007). The muscles in the MSK models are represented using truss elements with a Hill-type active muscle formulation (Hallquist, 2017; Millard et al., 2013). In both MB and MSK head-neck models, the potential for injury is inferred from vertebral kinematics and joint forces. FE head-neck models, unlike MB and MSK models, treat hard and soft tissues as deformable materials enabling prediction of tissue-level deformations, stresses and strains in physiologic and traumatic loading conditions. Depending on the scope of the biomechanical problem, several FE models have been developed at various levels of complexity starting from a single FSU (Barker et al., 2017; Brodin and Halldin, 2004; DeWit and Cronin, 2012; Mustafy et al., 2016; Panzer and Cronin, 2009; Silva et al., 2022; Wang et al., 2019; Ye et al., 2022), ligamentous cervical spine (Beauséjour et al., 2020; Chang et al., 2022; Erbulut et al., 2014; Herron et al., 2020; Lin et al., 2023; Mesfar and Moglo, 2012; Subramani et al., 2020; Sun et al., 2022; Tongprapai et al., 2021; Zhang et al., 2005) to full neck with detailed neck structures (Barker and Cronin, 2022, 2021; Brodin et al., 2005; Cronin, 2014; Fice and Cronin, 2012; John et al., 2019a; Li et al., 2021, 2023; Meyer et al., 2004; Putra et al., 2021; Shateri and Cronin, 2015). In FSU and ligamentous head-neck models, the in vivo force from the head and neck muscles are simplified using an externally applied compressive load or a follower load (X.-Y. Cai et al., 2020b; Manickam and Roy, 2021; Mesfar and Moglo, 2012; Palepu, 2013; Srinivasan et al., 2021; Sun et al., 2022). The muscles in few of the existing FE head-neck models are detailed and represented using truss elements with a Hill-type active muscle formulation (Cronin, 2014; Fice et al., 2011; John et al., 2019a; Li et al., 2023; Nasim and Galvanetto, 2023; Panzer, 2006; Panzer et al., 2011; Pramudita et al., 2017; Shateri and Cronin, 2015). Some FE head-neck models allow for the representation of muscles tissues with anatomical details using volumetric continuum elements to enable localized tissue-level injury predictions (Barker and Cronin, 2022, 2021; Gierczycka et al., 2021; Li et al., 2021).

2.6.2 Existing computational head-neck models applied to assess risk of neck pain in RWA

The focus of this research is on the occupational neck injuries, specifically neck pain in the RWA which is attributed to factors like HSM, non-neutral positions, etc. Different head-neck models have been developed particularly to investigate the risk of neck pain in the RWA (Barrett et al., 2022a, 2022b; Fathollahi, 2012; Hetzler, 2021; Mesfar and Moglo, 2012; Moore et al., 2021).

To date, two MB head-neck models have been developed to investigate the risk of occupational neck injury in the RWA (Fathollahi, 2012; Hetzler, 2021). Fathollahi (2012) developed an MB model of the ligamentous cervical spine using MSC-ADAMS (MSC Software Corporation, CA). The HSM was simulated by assuming the helmet to be a 95 mm sphere covering the head with the CoG location coinciding with the CoG of the head. Non-neutral positions in flexion, extension and axial rotation were simulated by prescribing a displacement to the head CoG (Figure 41). The model computed higher loads in the C2-C3, C4-C5 and C7-T1 intervertebral levels with the addition of HSM (Fathollahi, 2012). Similarly, in the MB head-neck model developed by Hetzler (2021) using Altair Motion View (Altair Engineering Inc, MI), angular displacements were prescribed to the head to simulate the non-neutral positions adapted by the RWA. The HSM system inclusive of the helmet, NVG and CW was simulated using point-mass at relevant locations based on the literature (Figure 42). The model developed by Hetzler (2021) was used to investigate the effect of a prototype neck pain countermeasure device for the RWA helmets (Hetzler, 2021).

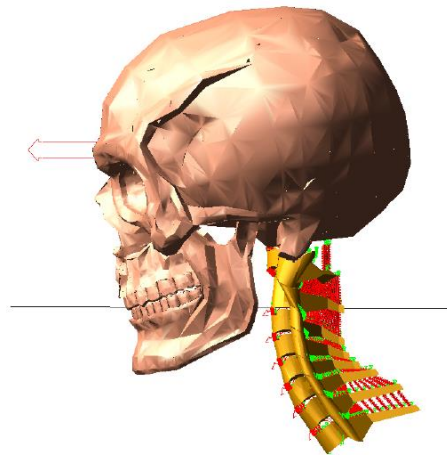


Figure 41: MB model of the head-neck used to study the effect of HSM in RWA.

[Taken from Fathollahi (2012)]

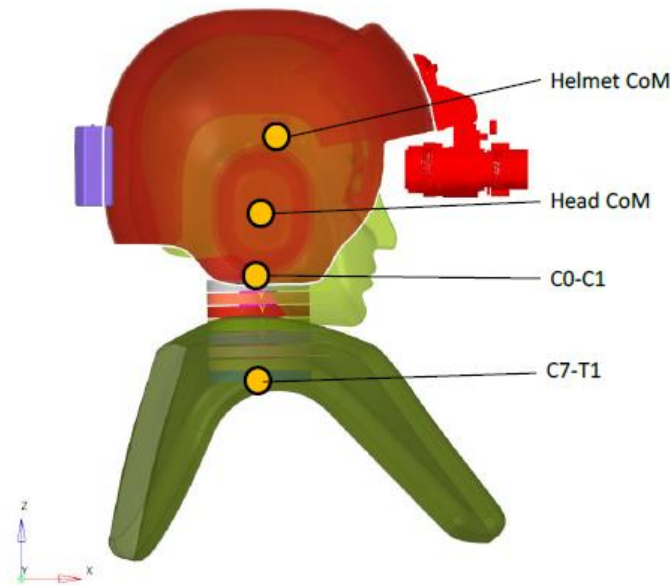


Figure 42: MB model of the head-neck to investigate the neck pain countermeasures in RWA.

[Taken from Hetzler (2021)]

An MSK model of the head-neck was developed at the University of Waterloo, Canada, to assess the risk of neck pain during occupational activities such as hand-held device interactions in civilian population (Barrett, 2016; Barrett et al., 2021, 2020). The application of the model was further extended toward assessing the risk of neck pain in the RWA (Barrett et al., 2022a, 2022b; Moore et al., 2021). The MSK model demonstrated an increase in compressive and shear forces at the C5-C6 joint with the addition of HSM, thereby confirming that the increased muscle activity due to increased mass and inertia (with HSM condition) increases the spinal loads and risk of pain (Barrett et al., 2022a, 2022b; Moore et al., 2021) (Figure 43). Another MSK head-neck model was developed at the Royal Military College, Canada, to gain insight into the interaction of HSM with the neck in a neutral posture (Arshad et al., 2022) (Figure 44).

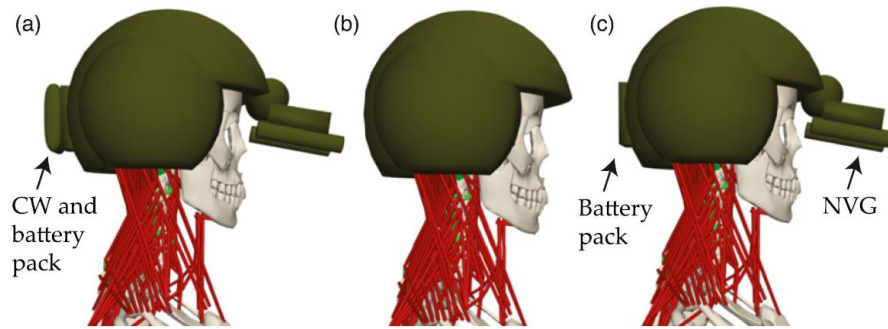


Figure 43: EMG-driven MSK model of the head-neck to provide insight on the effect of HSM and non-neutral positions on the risk of neck pain in the RWA.

[Taken from Barrett et al. (2022a)]

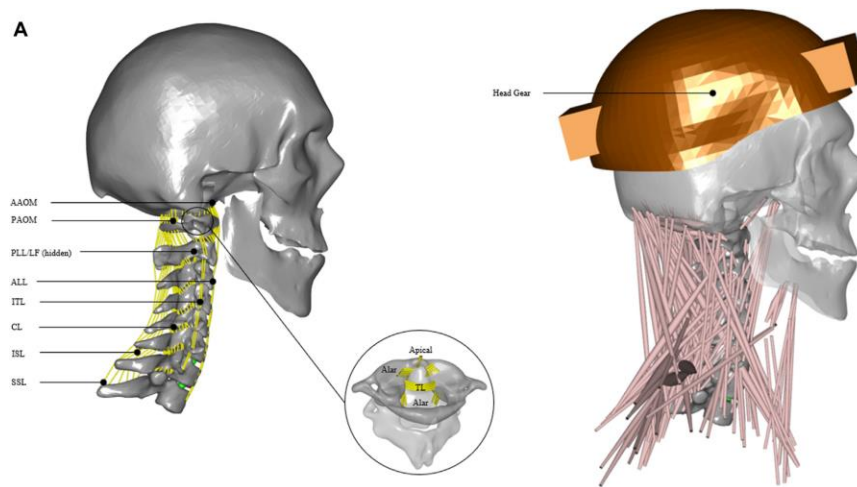


Figure 44: MSK model of the head-neck to study the interaction of HSM with the neck in a neutral posture.

[Taken from Arshad et al. (2022)]

The only FE head-neck model that was developed specifically to study the effects of HSM in the physiologic modes of loading was by Mesfar & Moglo (Mesfar and Moglo, 2013, 2012). The model included geometrically accurate structures consisting of bones, discs and ligaments, and was validated

against PMHS experimental data reported in the literature for physiologic ROMs. Mesfar and Moglo then explored the validated model to assess the effect of HSM on spinal forces (Mesfar and Moglo, 2012) (Figure 45). The effect of HSM in different flexion postures was simulated by initially applying a moment to the head until the desired angle was achieved and applying a compressive force incrementally. Despite detailed ligamentous structures, this model required simulating the muscle forces and non-neutral positions using simplified externally-applied axial loads owing to the lack of muscle representation. Hence, there was a need to explore the effects of HSM and non-neutral positions in RWA using an FE head-neck model with anatomical details. The risk of neck pain at the tissue-level was not explored using this model.

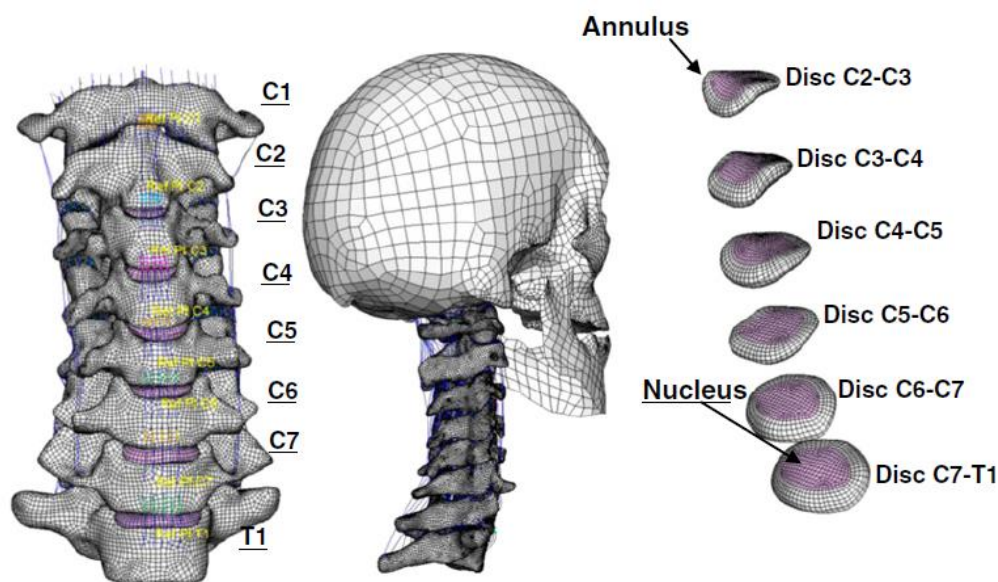


Figure 45: Detailed FE head-neck model developed at the Royal Military College, Canada, to assess the risk of neck pain in the RWA due to HSM and non-neutral positions.

[Image taken from Mesfar and Moglo (2013)]

2.7 Representation of muscles in existing computational head-neck models

2.7.1 Hill-type muscle material model

The Hill-type material model has been widely used in the MSK models and limitedly used in the FE models to simulate the effects of muscles in various biomechanical scenarios. The Hill-type material model of the muscle comprises two components: active and passive. The active component comprises

a contractile element (CE) while the passive component comprises a passive elastic element (PEE) in parallel to the CE. There is also an optional damping element (PDE) in parallel to the CE and PEE (Kleinbach et al., 2017) (Figure 46). In the Hill-type material model, the total force/stress generated from in vivo muscle contractions are considered to be a sum of forces/stresses from the active and passive components (Equation 2.1) (Hallquist, 2017).

$$\sigma^F = \sigma^{CE} + \sigma^{PEE} \quad (\text{Equation 2.1})$$

where, σ^F = Total stress in the muscle, σ^{CE} = Stress in the CE and σ^{PEE} = Stress in the PEE

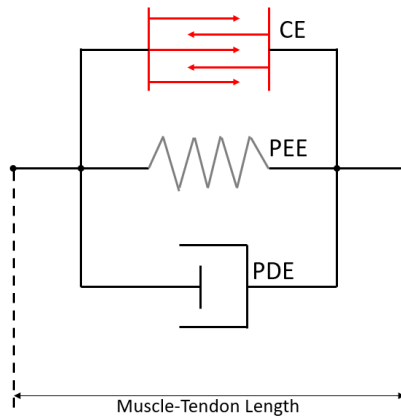


Figure 46: Illustration of the Hill-type muscle model showing the active contractile element (CE), passive elastic element (PEE) and an optional parallel damping element (PDE).

The stress generated in the active muscle contractile element (σ^{CE}) is a product of muscle activation level (ranges from 0 to 1), peak isometric stress (σ_{max}) and two functions: force vs. muscle length and force vs. velocity (rate of change in muscle length) (Hallquist, 2017; Millard et al., 2013; Panzer, 2006; Panzer et al., 2011) (Figure 47). From the literature, the σ_{max} varied between 0.2 MPa to 1.0 MPa (Maganaris et al., 2001; Panzer, 2006; Winters and Stark, 1988). The stress in the contractile element is represented by the equation 2.2 below.

$$\sigma^{CE} = a(t) \times \sigma_{max} \times f_L(L) \times f_V(V) \quad (\text{Equation 2.2})$$

where, $a(t)$ = Activation level of muscle, σ_{max} = Peak isometric stress, $f_L(L)$ = force-length and $f_V(V)$ = force-velocity function

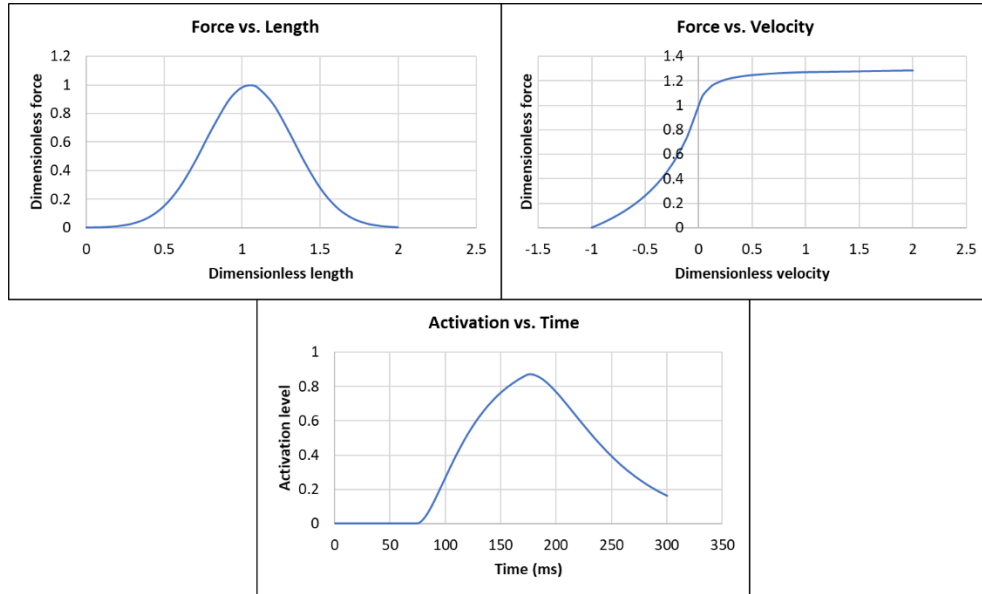


Figure 47: Illustration of the force vs. length ($fL(L)$), force vs. velocity ($fV(V)$) and activation levels ($a(t)$) properties of the contractile element (CE) in the Hill-type muscle model. An exemplar activation vs. time curve from one of the existing computational neck models (Barker and Cronin, 2021; Cronin, 2014; Fice et al., 2011; Panzer, 2006; Panzer et al., 2011; Shateri and Cronin, 2015) is shown for illustrative purpose.

The passive muscle component in the Hill-type material model is represented using an elastic element in parallel to the contractile element (Figure 46). The stress in the passive muscle (σ^{PEE}) in the Hill-type material model is expressed as a product of peak isometric stress (σ_{max}) and the dimensionless stress vs. stretch curve ($h(\lambda)$) as shown in equation 2.3. In the curve $h(\lambda)$, the dimensionless stress is the ratio of engineering stress (σ) in tension and peak isometric stress (σ_{max}), while stretch (λ) is the ratio of the final length of the muscle (L) at a given time and optimal length of the muscle (L_{orig}) (Equation 2.4). The dimensionless stress vs. stretch curve ($h(\lambda)$) in the passive component of the Hill-type material model is based on equation 2.4, proposed by Winters (1995) (Hallquist, 2017).

$$\sigma^{PEE} = \sigma_{max} \times h(\lambda) \quad (\text{Equation 2.3})$$

$$h(\lambda) = h\left(\frac{L}{L_{orig}}\right) = \frac{1}{e^{CER-1}} \left(e^{\left(\frac{CER}{SSM}\right)*\varepsilon} - 1\right) \quad (\text{Equation 2.4})$$

where, h = Dimensionless stress as a function of stretch (λ), $\lambda = L/L_{orig}$, CER = Constant, governing the exponential rise of λ and SSM = Strain when λ reaches its maximum stress value

2.7.2 Simplified externally applied loads to simulate muscles

The axial load and follower load represented in vivo musculature as it was challenging to recreate the active muscle contractions in an in vitro ligamentous cervical spine cadaveric study (Barrey et al., 2015; Patwardhan et al., 2000; Wawrose et al., 2021). In brief, implementing the in vivo musculature on the cadaveric spine specimens to replicate the in vivo kinetics and kinematics during in vitro biomechanical testing is challenging. As a result, different loading paradigms were implemented on the cadaveric spine specimens to mimic the in vivo musculature in an in vitro experiment under controlled laboratory environment. The loading paradigms that were used to simulate in vivo musculature on the cadaveric cervical spine specimens in different studies included axial loading and follower loading (Figure 48). The axial load is applied to the superior aspects of the specimen while the follower load is applied along the curvature of the spinal column (Figure 48) (Barrey et al., 2015; Patwardhan et al., 2000; Wawrose et al., 2021). The magnitude of the axial load and the follower load in the experiment studies ranges between 50 N to 150 N.

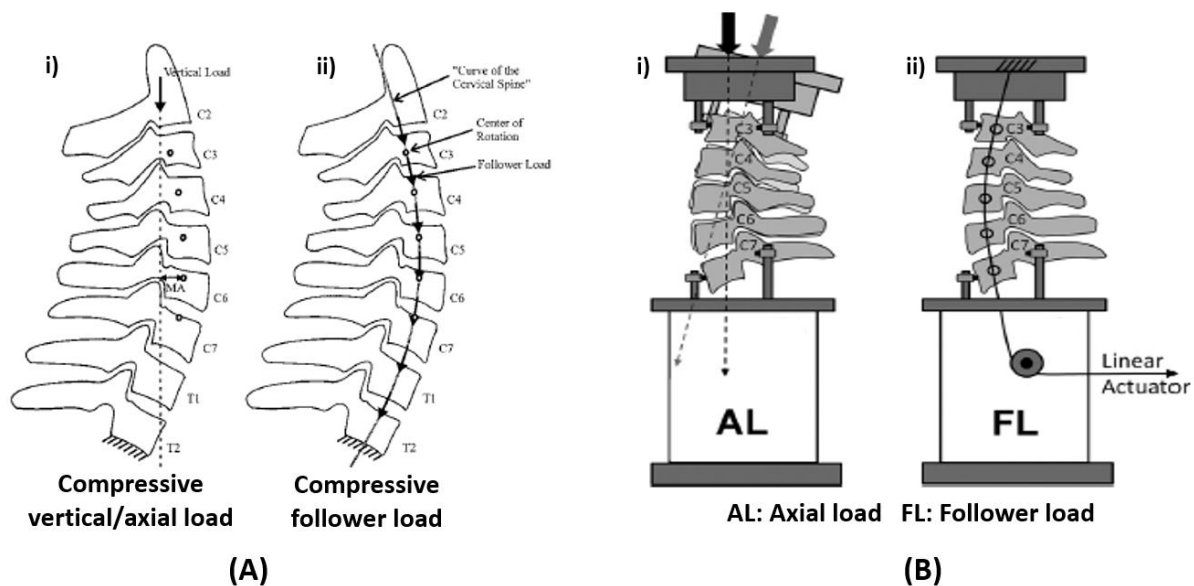


Figure 48: (A) Illustrating the simplification of in vivo muscle forces in the in vitro experimental studies on cadaveric cervical spine specimens by applying an (i) axial load or a (ii) follower load (Patwardhan et al., 2000). (B) Illustration of an experimental set-up used to apply (i) axial load and (ii) follower load on cadaveric cervical spine specimens (Wawrose et al., 2021).

[Adapted from Patwardhan et al. (2000) and Wawrose et al. (2021)]

The method of applying axial load or follower load to cadaveric spine specimens during in vitro experiments was eventually adopted by the FE modeling community that developed ligamentous cervical spine FE models. Ligamentous cervical spine FE models simulated muscles using either compressive axial load (del Palomar et al., 2008; Manickam et al., 2023; Manickam and Roy, 2021; Mesfar and Moglo, 2012; Sun et al., 2023; Xu et al., 2023; Yu et al., 2016) or compressive follower load (X.-Y. Cai et al., 2020b; Kwon et al., 2020, 2017; Lee et al., 2011; Liang et al., 2022; Palepu, 2013; Rahman et al., 2023; Shen et al., 2022; Sun et al., 2022) (Figure 49). Similar to experimental studies, the magnitude of the axial load and the follower load in the FE modeling studies ranged between 50 N to 150 N. The axial load and follower load were only meant to simulate the in vivo muscle forces but not to reposition the head-neck.

In a recent study, a combined approach was used to simulate the in vivo muscle forces in a ligamentous cervical spine FE model. The approach involved simulating a gait cycle with the HSM on an MSK human body model, measuring the neck muscle forces and joint forces during the simulated gait cycle and applying the measured forces in form of load vectors to the ligamentous cervical spine

FE model (Motiwale et al., 2018; Subramani et al., 2020) (Figure 50). Similar approach has been previously used to simulate in vivo muscle forces in ligamentous lumbar spine FE models (Liu et al., 2019; Naserkhaki et al., 2016).

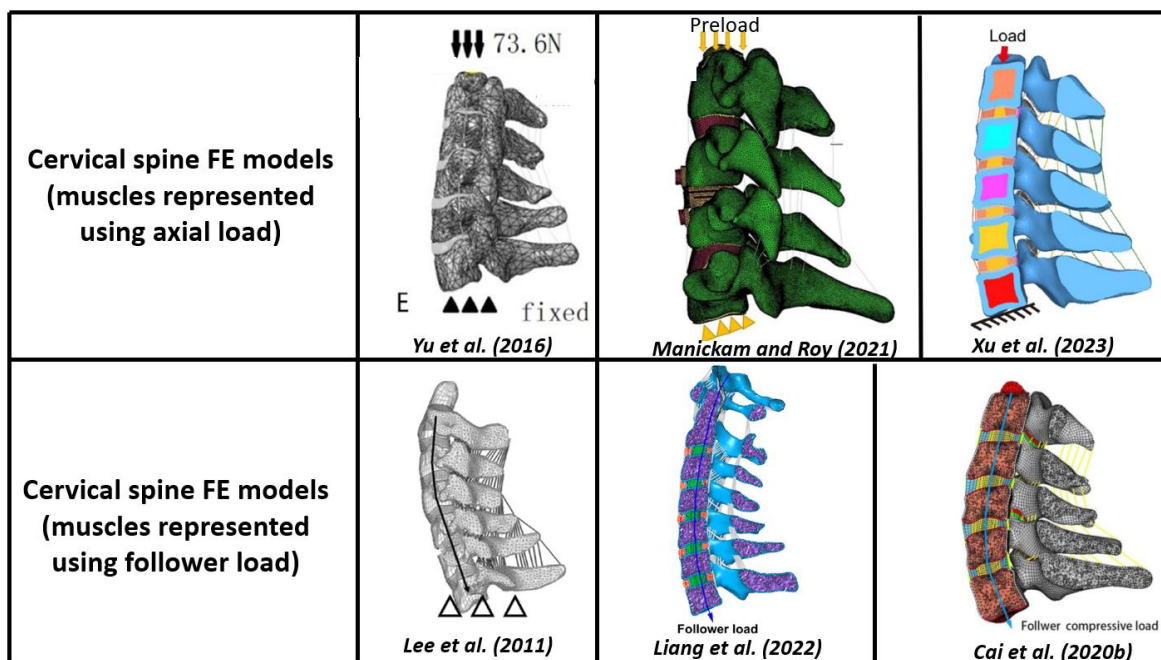


Figure 49: Illustrating the simplification of muscle action in the existing cervical spine FE models by applying an axial load or a follower load. The axial load or follower load, although represents the in vivo muscles, cannot reposition the model. A non-exhaustive list of cervical spine FE models that incorporated muscles in the form of axial load and follower load is shown in this figure.

[Images are adapted from the literature which is referred within the figure]

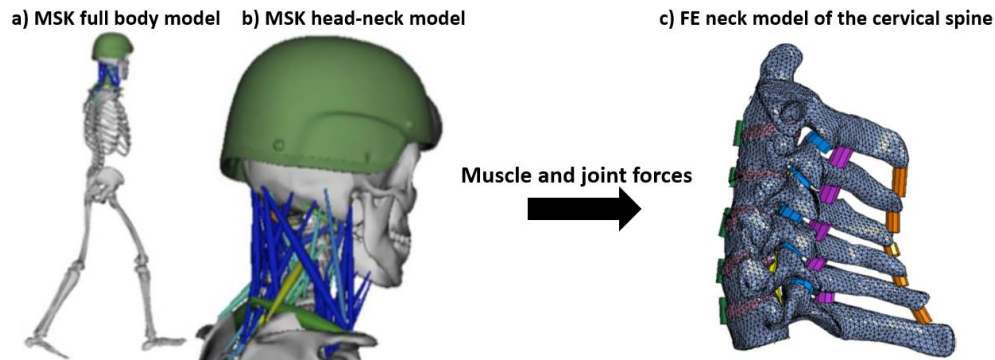


Figure 50: Illustrating the combined approach where MSK human body model with HSM is simulated for gait (A) and neck muscle forces are estimated (B). Estimated muscle forces from the MSK model are applied to a ligamentous cervical spine FE model as force vectors.

[Image adapted from Motiwale et al. (2018) and Subramani et al. (2021)]

2.7.3 Passive muscle property in existing computational head-neck models

Typically, computational human body models rely on experimental data to accurately represent the mechanical behavior of tissues (Barker and Cronin, 2021; Cronin et al., 2018; Gierczycka et al., 2021; Yang et al., 2006). A number of experimental studies have reported the passive tensile and compressive properties of excised muscle samples or whole muscle-tendon unit from non-humans such as rabbits, cats, pigs, rats, frogs, etc. (Calvo et al., 2010; Davis et al., 2003; Morrow et al., 2010; Myers et al., 1998; Nie et al., 2010; Ward et al., 2020). A limited number of studies reported the properties of whole muscle-tendon unit (Davis et al., 2003; Myers et al., 1998). Myers et al. (1998) and Davis et al. (2003) reported the passive muscle property of the whole muscle-tendon unit (tibialis anterior) in anesthetized live rabbits. The tibialis anterior muscle was exposed from the *in vivo* environment with the proximal end intact with the bone that was fixed and the distal end clamped to the test apparatus. Myers et al. (1998) reported the passive muscle property at varying strain rates while Davis et al. (2003) reported the passive muscle property for quasi-static loading (Figure 51). A limited number of studies reported the passive muscle properties of human muscles (Persad et al., 2021; Yamada, 1977). Both the studies (Persad et al., 2021; Yamada, 1977) reported the tensile properties of the human passive muscles. Yamada (1977) tested the excised human passive muscle samples in a post-rigor state while Persad et al. (2021) directly measured the properties of a whole muscle-tendon unit (gracilis muscle) from live humans *in vivo*. The study on the human gracilis muscle provided a direct measurement of the *in vivo*

passive property in the physiologic range of motion. The in vivo force vs. displacement was measured in the whole gracilis muscle starting from a neutral leg position to a fully extended leg position within the physiologic range of motion. The leg of the volunteer, who was relaxed, was passively extended with the help of manual intervention in an intraoperative environment while measuring the force and displacement (Persad et al., 2021) (Figure 51).

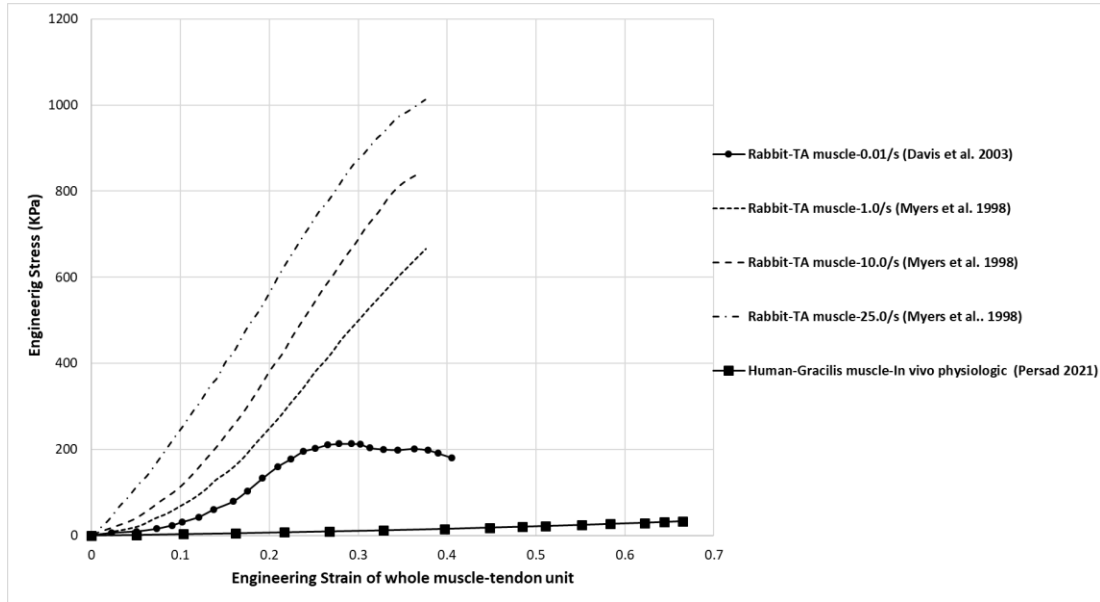


Figure 51: Summarizing a non-exhaustive list of passive muscle tensile properties of the whole muscle-tendon units obtained from experimental studies in the literature that could potentially be used in the computational head-neck models.

In the Hill-type muscle model, which is widely used to represent muscles in the existing computational head-neck models (MSK and FE), the property of the passive muscles are modeled to resist tensile loading (Hallquist, 2017; Kleinbach et al., 2017; Millard et al., 2013). Most of the MSK and FE head-neck models represented the passive muscle property using the exponential relationship developed by Winters (1995) in the Hill-type muscle, where CER was assumed to be 3.0 and SSM was assumed to be 0.6. A value of 500 KPa was assumed for σ_{max} in these MSK and FE head-neck models. Based on equation 2.3, the passive muscle property in the existing neck models was obtained by multiplying the dimensionless $h(\lambda)$ with 500 KPa (Barrett, 2016; Barrett et al., 2020; Cronin, 2014; Fice et al., 2011; Fice and Cronin, 2012; Nasim and Galvanetto, 2023; Panzer, 2006; Panzer et al., 2011;

Shateri and Cronin, 2015) (Figure 52). The passive muscle property of a relatively recent FE head-neck model also incorporated the passive muscle property using Winter (1995) relationship and assumed CER=6.0 and SSM=0.375 with an assumption of 500 KPa for the σ_{max} (John et al., 2022, 2019a) (Figure 53).

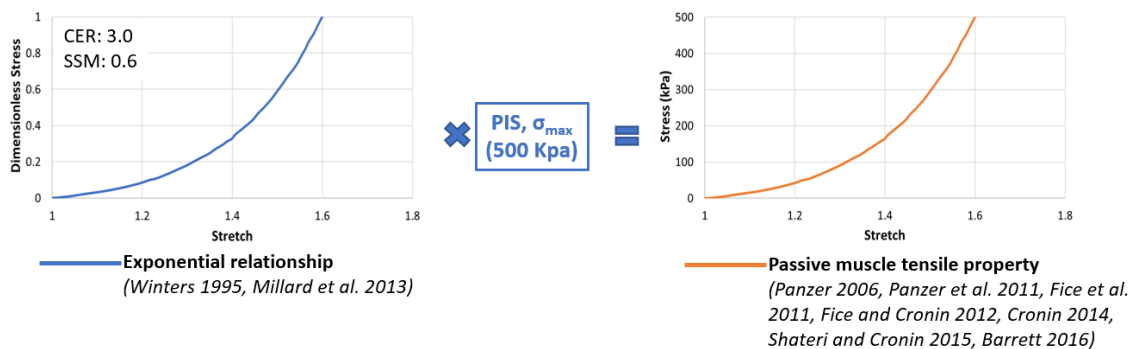


Figure 52: The tensile material property of the passive muscle in the Hill-type model is expressed as a product of peak isometric stress (σ_{max}) and the dimensionless stress vs. stretch relationship. In the existing computational neck models, the σ_{max} is assumed to be 500 kPa and the dimensionless stress vs. stretch relationship ($h(\lambda)$) is obtained from Winters (1995).

Recently, Gierczycka et al. (2021) proposed tensile properties for the passive muscles for a detailed FE head-neck model based on the experimental data from Myers et al. (1998). Myers et al. (1998) measured the tensile properties of rabbit tibialis anterior muscles at strain rates $1.0s^{-1}$, $10.0s^{-1}$ and $25.0s^{-1}$. Davis et al. (2003) measured the tensile properties of rabbit tibialis anterior muscles at quasi-static strain rate ($0.01s^{-1}$). The experimental data was interpolated to identify the passive muscle tensile property at other strain rates including $0.1s^{-1}$, $100.0s^{-1}$ and $1000.0s^{-1}$. The proposed passive muscle tensile properties for a spectrum of strain rates was incorporated in a detailed FE head-neck model (GHBMC M50-O) for further validation and biofidelity assessments (Gierczycka et al., 2021) (Figure 53).

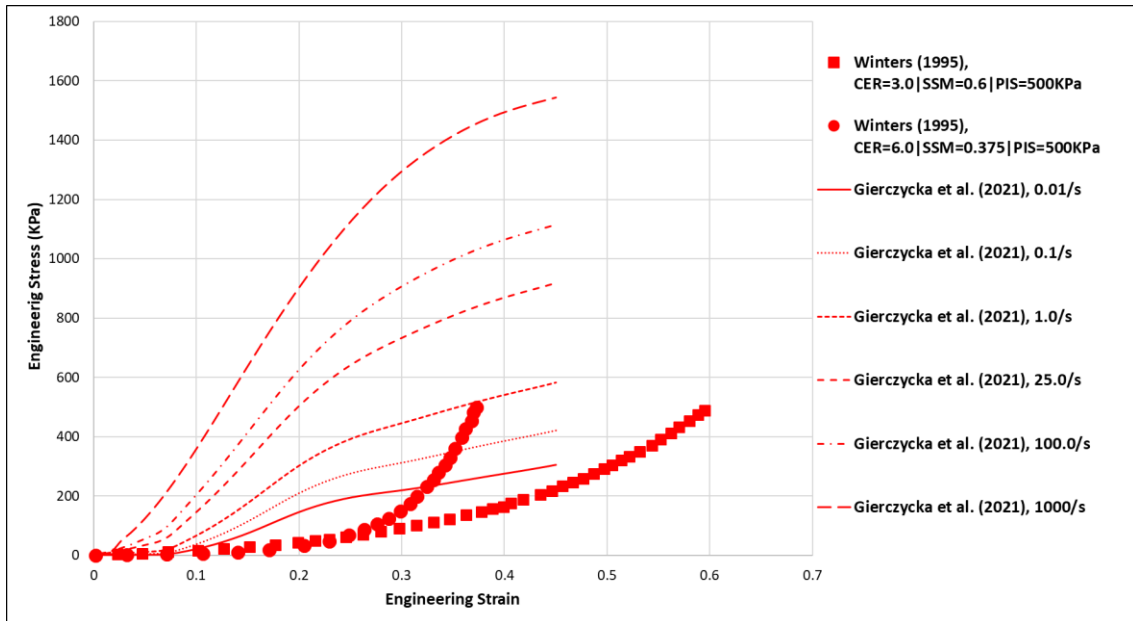


Figure 53: Summary of a non-exhaustive list of material properties that have been used to define the tensile properties of passive muscles in existing head-neck models.

2.8 Methods to achieve non-neutral positions in computational head-neck models

2.8.1 Computational approaches

It is essential to understand different computational approaches that actuate computational head-neck models towards mimicking a short- or a long-duration biomechanical event. Two approaches i.e. inverse-dynamic and forward-dynamic are used to drive the computational head-neck models. The usage of the approaches depends on several factors such as the type of biomechanical problem, complexity of the model, duration of the biomechanical event, availability of BCs, etc.

In the inverse-dynamic approach, the motion/kinematics of the bones in the musculoskeletal system that is captured experimentally is used as an input to the model to calculate net joint forces and moments at the joint centers of rotation, muscle activation levels and muscle forces (Barrett, 2016; Faber et al., 2018; Röhrle et al., 2017). Sometimes, experimentally captured EMG data are also used as input along with the captured motion from which the joint forces, moments, muscle activation and muscle forces

are computed (Alizadeh et al., 2020a; Barrett, 2016; Esrafilian et al., 2020; Mathys and Ferguson, 2012; Röhrle et al., 2017). A static optimization tool is used in the inverse-dynamic simulations to estimate the muscle activations required to balance the forces and moments in the system i.e. head-neck model (Cazzola et al., 2017; Mathys and Ferguson, 2012; Mortensen et al., 2018). Most of the MSK head-neck models are actuated using the inverse-dynamic approach (Arshad et al., 2022; Barrett, 2016; Cazzola et al., 2017; Mathys and Ferguson, 2012; Moore et al., 2021; Mortensen et al., 2018; Vasavada et al., 2002). The inverse-dynamic approach used in the MSK models can counter the challenges faced during in vivo experiments to obtain the in vivo biomechanical properties of muscles such as activation levels, muscle forces, joint forces and moments. Also, the representation of tissues as rigid bodies and kinematic joints make the MSK models computationally less expensive and more suitable to simulate long-duration scenarios using static optimization in the inverse-dynamic approach.

In the forward-dynamic approach, The process typically involves applying a pre-determined load (force or moment) or prescribed kinematics (acceleration, velocity or displacement) to the model to reproduce the motion as an output (Alizadeh et al., 2020b; Röhrle et al., 2017). If the model comprises muscle components, a pre-determined muscle activation is required as an input to simulate a desired motion using the forward-dynamics approach (Barker and Cronin, 2021; Correia et al., 2020; Röhrle et al., 2017). For example, in a detailed FE head-neck model, the measured T1 vertebral kinematics (from experiments) is applied to the T1 vertebra in the FE head-neck model and the kinematic response of the head is output and compared with experimental data (Barker and Cronin, 2021; Gierczycka et al., 2021). In another example, an external moment is applied to the superior ends of the ligamentous cervical spine FE models to simulate a physiologic motion through which the intervertebral kinematics is output and compared with experimental data (Barker et al., 2017; Hadagali and Cronin, 2023; Herron et al., 2020; Lasswell et al., 2017). The forward-dynamic approach can be used on MB (Fathollahi, 2012; Hetzler, 2021; Rattanaikorn et al., 2022; van Lopik and Acar, 2007), MSK (Nightingale et al., 2016; Stemper et al., 2006; Storvik and Stemper, 2011) and FE (Barker and Cronin, 2021; Beauséjour et al., 2021; Hadagali and Cronin, 2023; Mesfar and Moglo, 2013) head-neck models.

2.8.2 Methodologies to reposition computational head-neck models

Contemporary head-neck models have been developed for initially neutral postures. Achieving a non-neutral neck position requires a method of moving the head and neck to a new position. To simulate a non-neutral head-neck position, different computational methodologies are employed. The current

section in the literature review will specifically focus on the methodologies used in existing computational head-neck models to simulate non-neutral head-neck positions which is one of the risk factors for neck pain in the RWA.

The MB head-neck models are usually repositioned using a forward-dynamic approach. Existing MB head-neck models have been repositioned by applying an external BC i.e. prescribed moment or displacement to the head while constraining the inferior aspect of the model (Fathollahi, 2012; Hetzler, 2021) (Figure 54).

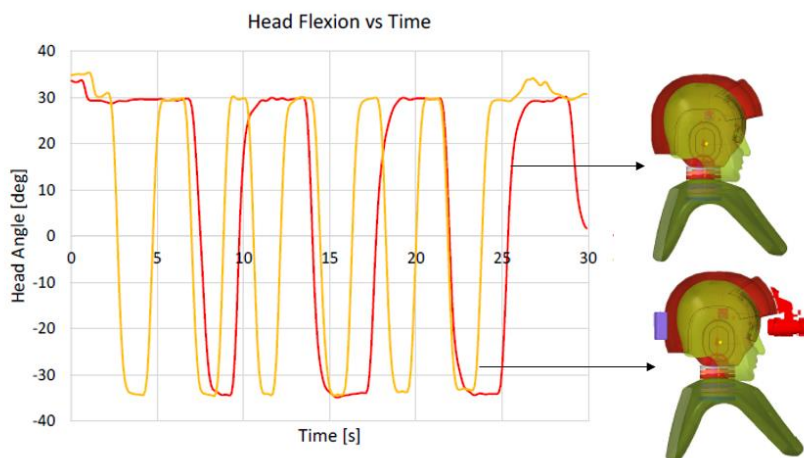
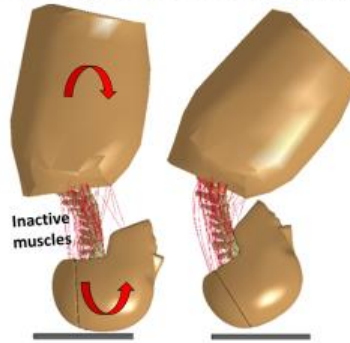


Figure 54: An illustration of the input head angular displacement as a function of time (external BC) to reposition an MB head-neck model from neutral posture to forward flexion position.

[Adapted from Hetzler (2021)]

Existing MSK head-neck models were also repositioned from a neutral to a non-neutral position by applying external BCs such as moment or displacement (measured from experiments) to the head while constraining the T1/torso (Barrett, 2016; Barrett et al., 2022a, 2020; Nightingale et al., 2016; Storvik and Stemper, 2011) (Figure 55). In the MSK head-neck models that were actuated using forward-dynamic approach, the muscles were optionally activated using pre-determined activation levels after repositioning using an external moment or displacement (Nightingale et al., 2016; Storvik and Stemper, 2011). In the MSK head-neck models that were actuated using inverse-dynamic approach, the muscle activation levels were computed using static optimization during the process of repositioning (Barnamehei et al., 2020; Barrett, 2016; Barrett et al., 2022b, 2022a, 2020).

A) Forward-dynamic MSK head-neck model (Nightingale et al. 2016)



B) Inverse-dynamic MSK head-neck model (Barrett et al. 2022)

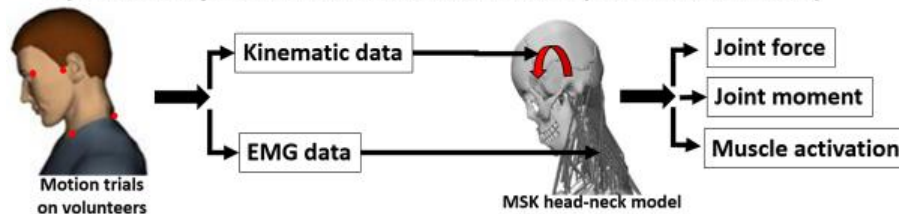


Figure 55: Illustrating the repositioning of (A) a forward- and (B) an inverse-dynamic MSK head-neck model from a neutral to a non-neutral position using an external BC such as moment or a kinematic data from experimental trials.

[Adapted from Nightingale et al. (2016), Callaghan (2014) and Barrett et al. (2022)]

An existing method to reposition FE head-neck models from a standard/neutral posture to a non-neutral position include applying external BCs such as a moment or displacement (Boakye-Yiadom and Cronin, 2018; Nightingale et al., 2016; Palepu, 2013; Shateri, 2012; Shateri and Cronin, 2015). Although morphing methods offer viable option, such methods have typically been used to investigate postural and geometrical effects on biomechanical outcomes (Corrales and Cronin, 2021a; Hadagali, 2014; Hadagali et al., 2018; Janak et al., 2018; Jani et al., 2012; John et al., 2019a; Vavalle et al., 2014), where, the repostured geometry does not include tissue-level stresses and strains. That is, the repostured model begins in a stress-free state, although it is no longer in a neutral position. External BC-based repositioning methods have the ability to generate and retain stresses and strains in the tissues (Boakye-Yiadom and Cronin, 2018). However, simple external BCs are often used and may not accurately represent the complex loading in the neck arising from active musculature.

Existing FE head-neck models, to date, have been repositioned using external BC-based methods using the forward-dynamic approach. Usually, an external moment or displacement is applied to the

superior aspects of the cervical spine model to reposition the cervical spine FE model with the simulated in vivo musculature (an axial load or a follower load) (X.-Y. Cai et al., 2020b; del Palomar et al., 2008; Kwon et al., 2020, 2017; Lee et al., 2011; Liang et al., 2022; Manickam et al., 2023; Manickam and Roy, 2021; Mesfar and Moglo, 2012; Palepu, 2013; Rahman et al., 2023; Shen et al., 2022; Sun et al., 2023, 2022; Xu et al., 2023; Yu et al., 2016; Zhang et al., 2023) (Figure 56). In another similar study, the T1 vertebra of a detailed FE neck model inclusive of detailed passive neck muscles (Hill-type model) was constrained, and a rotational displacement was applied to the head to simulate an axially rotated head-neck position (Shateri, 2012; Shateri and Cronin, 2015) (Figure 57). In a different study pertaining to RWA, the effect of HSM in different flexion postures was simulated using a forward-dynamic approach, by initially applying a moment to the head until the desired angle was achieved and applying a compressive force incrementally (Mesfar and Moglo, 2012). Some studies rely on the MSK head-neck models for the BCs (kinematics or moments) which can be applied to the FE head-neck model to reposition (Subramani et al., 2020) (Figure 50).

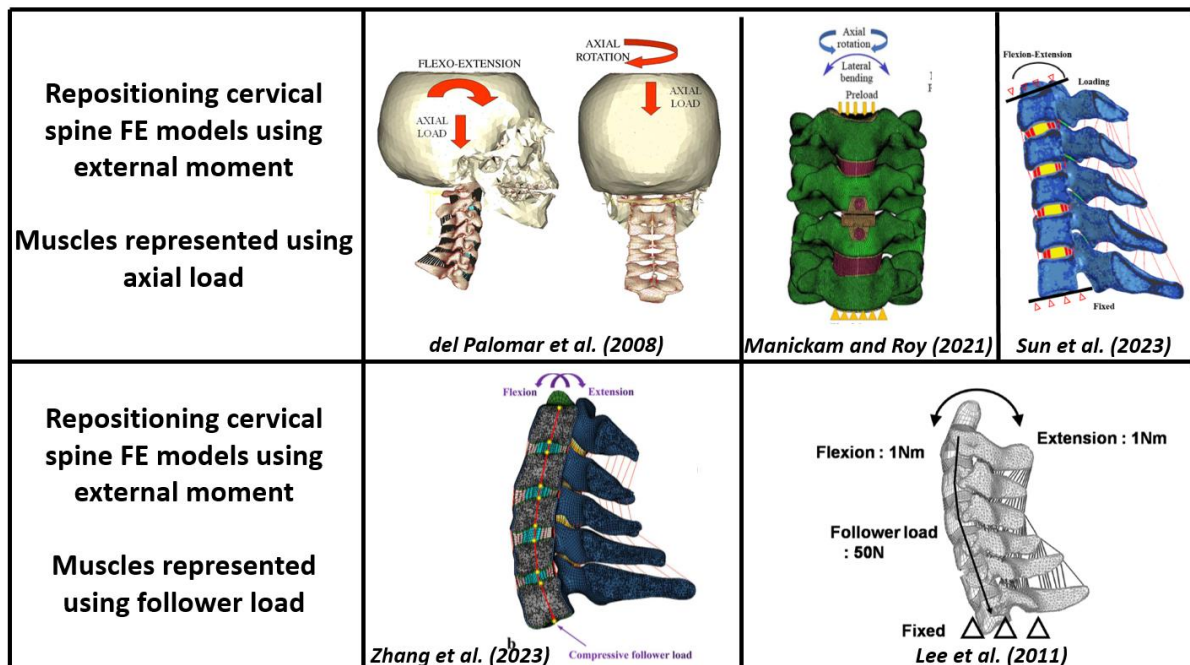


Figure 56: The figures illustrate the application of an external BC (moment or displacement) to the superior aspects of the model to simulate non-neutral positions along with an axial load or a follower load that simulate cervical spinal muscles.

[Images are taken from the literature which is referred within the figure]

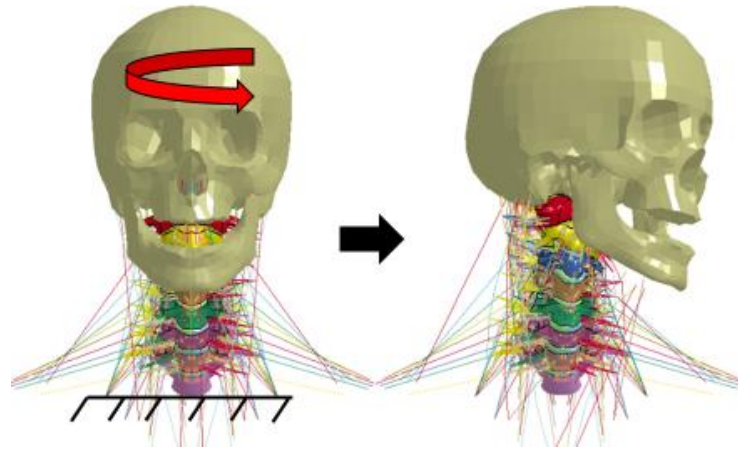


Figure 57: Detailed FE head-neck model with the musculature developed at the University of Waterloo (Shateri, 2012; Shateri and Cronin, 2015). The figure illustrates the application of an external BC (rotational displacement) to simulate a non-neutral head-neck position in the FE model. The muscles were not activated during the application of rotational displacement.

[Adapted from Shateri (2012)]

2.8.3 Research gap in computational head-neck model repositioning methodologies

During an in vivo physiologic head-neck repositioning, the muscles surrounding the ligamentous cervical spine are activated under gravity. In vivo, the active neck muscles perform two main functions: 1) reposition the head-neck to a desired non-neutral position and 2) stabilize and maintain the head-neck in a desired position or line of sight. Due to the active muscles, tensile force is produced in the muscles, as a result of which, reactive compressive forces and moments are generated in the spinal column (Barrett et al., 2020; Straker et al., 2009).

Despite the existence of detailed muscle components in forward-dynamic MSK head-neck models (Section 2.8.2), external moment or displacement has been applied to reposition the model (Nightingale et al., 2016) (Figure 55a). The process of repositioning inverse-dynamic MSK head-neck models also involve application of an external BC (rotational displacement) to the head as a first-step and later identification of the muscle activity via static optimization. Muscles are not activated to reposition the head-neck as observed in vivo (Barrett, 2016) (Figure 55b). From Section 2.3.3, the application of external BC may not accurately represent the in vivo kinematic conditions in the model, and might affect the predictive capability of the model, yet to be explored (Figure 25). However, the

inverse-dynamic MSK head-neck models are still considered better to mimic the in vivo repositioning owing to the muscle activation (Arshad et al., 2022; Barrett, 2016; Barrett et al., 2020; Dibb et al., 2013; Mortensen et al., 2018).

Similarly, from the literature review, it can be understood that the repositioning phenomena that occurs in vivo has not been accurately represented in the existing FE head-neck models as well. For instance, the axial load or follower load methodology (Section 2.7.2) that represent the in vivo muscles, cannot reposition the ligamentous cervical spine specimen (in a laboratory setting) or an FE head-neck model from a neutral to a non-neutral position. Thus, there is a requirement for another external BC (moment or displacement) to reposition (del Palomar et al., 2008; Palepu, 2013) (Figure 56). In another instance, despite the existence of detailed musculature in some FE head-neck models (Section 2.8.2), external applied BC (moment or displacement) is used for repositioning (Shateri, 2012; Shateri and Cronin, 2015) (Figure 57). The existing repositioning methodologies in FE head-neck models undermine the capability of in vivo muscles in repositioning which might affect the response outcomes, not explored in the literature. One of the objectives (Objective #2) in this research is to address the limitations in FE head-neck model repositioning methodologies.

2.9 GHBMC human body FE model

The Global Human Body Model Consortium (GHBMC, Elemance LLC, NC) developed a detailed FE model (GHBMC M50-O) of the full human body of a 26-year-old, 50th percentile male subject with a mass of 78.6 kg and body mass index of 25.7. The purpose of the GHBMC M50-O has been to assess the risk of crash-induced injuries from motor vehicle crashes (Arun et al., 2016; Gierczycka and Cronin, 2021, 2017; Hayes et al., 2014; Vavalle et al., 2015). The purpose of the GHBMC M50-O is currently being extended to assess the risk of injuries in other domains such as sports, military, aerospace, medicine, etc. as well (White et al., 2016, 2014). The geometry of the subject that was used to develop the GHBMC M50-O model was obtained using computed tomography (CT) and magnetic resonance imaging (MRI) techniques (Gayzik et al., 2011; Schwartz et al., 2015). The efforts to develop the GHBMC M50-O is collaborative between institutions across the globe, where different institutions (Center of Expertise, COE) contribute towards the development and validation of each body region in the model. The body regions comprise head, neck, upper extremities, thorax, abdomen and lower extremities. The validated body regions are then assembled into a full body model at the full body COE and further validated against full body post-mortem specimen and volunteer experimental data in

different impact directions including frontal, rear, side and oblique. The neck region in the GHBMC M50-O model was developed and validated at the University of Waterloo, Canada, the COE of neck model. The GHBMC M50-O was developed and validated against experimental data in LS-DYNA (Ansys, Canonsburg PA), a commercially available explicit FE solver. The GHBMC M50-O model is regularly updated by the COEs and a new version of the model is released after any update. The subsequent paragraphs in this section will provide a background on the GHBMC M50-O neck model.

2.9.1 GHBMC M50-O neck model

The GHBMC M50-O neck model comprises ligamentous cervical spine surrounded by muscles and passive soft tissues. The neck model is made of key anatomical components including bony vertebrae (cortical and trabecular bones), IVDs, endplate, facet cartilage, ligaments, muscles (active and passive components), adipose tissue and skin (Figure 58).

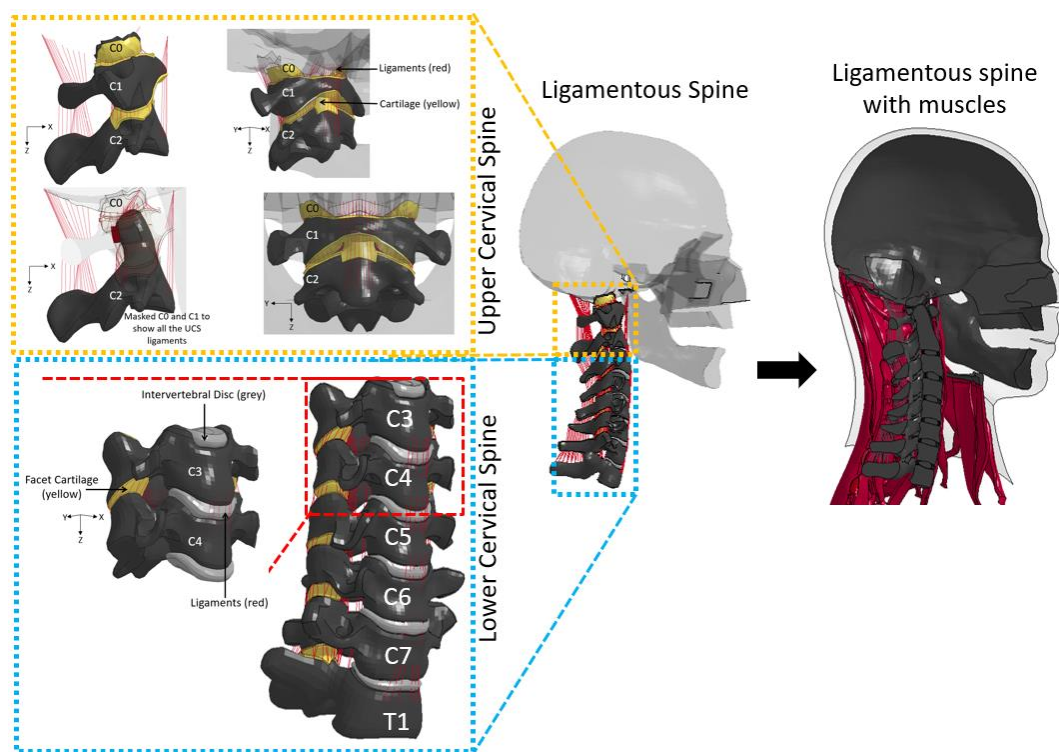


Figure 58: Illustration of the GHBMC M50-O neck model showing the bottom-up build of the model starting from FSU to ligamentous cervical spine and the detailed muscles and soft tissues surrounding the cervical spine.

[Adapted from Hadagali and Cronin (2023)]

The trabecular bones were represented using 3D hexahedral solid elements. The cortical bones and vertebral endplates were represented using 2D quadrilateral shell elements that covered the trabecular bones in accordance with the anatomy (Figure 59). The material of the trabecular bone was represented using *MAT_ISOTROPIC_ELASTIC_PLASTIC property with a failure strain of 9.5%. The material of the cortical bone was represented using *MAT_PLASTIC_KINEMATIC property with a failure strain of 1.78%. The vertebral endplates were also modeled using *MAT_PLASTIC_KINEMATIC material property (Barker et al., 2017) (Table 3).

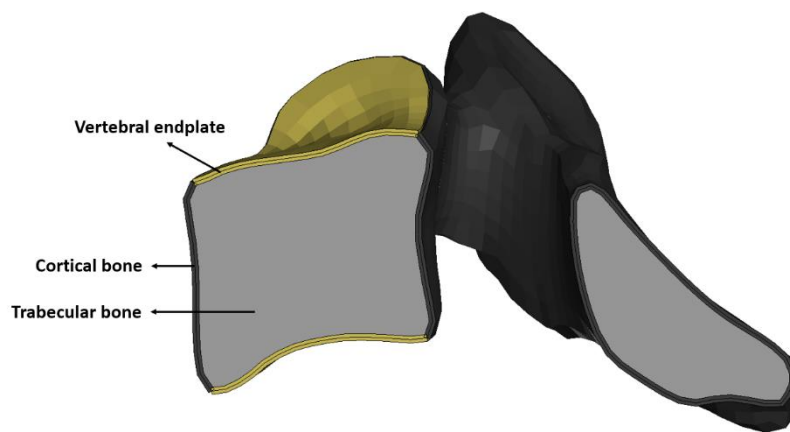


Figure 59: Illustrating the hard tissues in the GHBMC M50-O neck model. The cortical, trabecular and vertebral endplates of C4 vertebra is shown for illustrative purposes.

Table 3: Hard tissue material property in GHBMC M50-O neck model.

Property	Hard tissue		
	Cortical	Trabecular	Endplate
Density (kg/mm ³)	2.00E-06	1.10E-06	2.00E-06
Elastic modulus (Gpa)	18.439	0.442	5.6
Poisson's ratio	0.28	0.3	0.3
Yield stress (Gpa)	0.1898	0.00283	0.03673
Plastic modulus (Gpa)	1.2489	0.0301	0.2977
Failure strain	0.0178	0.095	0

The IVDs in the GHBMC M50-O include NP, annular ground substance and annular collagen fibers. The annular ground substance and annular collagen fibers collectively represent the AF in the model.

The NP and the annular ground substance were represented using 3D hexahedral solid elements. The model comprised five layers of annular collagen fibers, represented using 2D quadrilateral shell elements, concentrically around the NP and embedded within the 3D annular ground substance (Figure 60). Each layer in the annular collagen fibers comprised 2 layers of lamellae that was created by superimposing two 2D elements over each other (Figure 60). Overall, there were 10 layers of lamellae embedded within the annular ground substance in the model. The 3D elements of the annular ground substance and 2D elements of the collagen fibers shared common nodes.

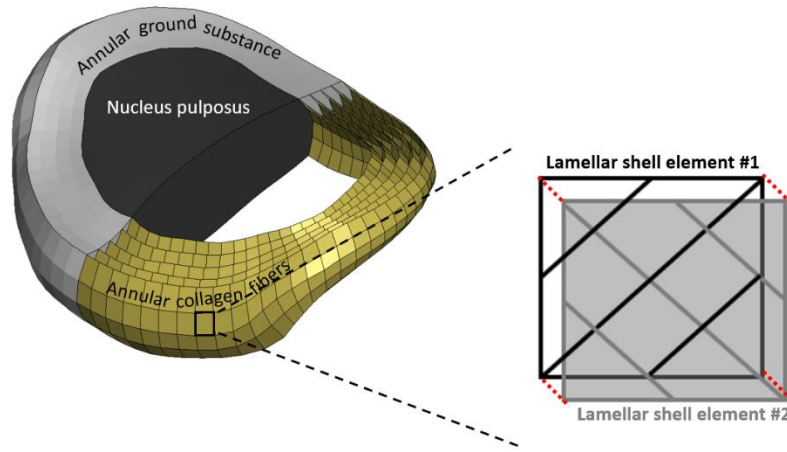


Figure 60: Illustrating an IVD in the GHBMCM50-O neck model with details including nucleus pulposus, annular ground substance and annular collagen fibers. The black and grey diagonal lines within the lamellar shell elements indicates the orientation of the collagen fibers. The dotted lines illustrate the common nodes between the corners of the lamellar shell elements.

[Adapted from Hadagali et al. (2024)]

The material of NP was represented using *MAT_ELASTIC_FLUID (elastic fluid model) with a bulk modulus of 1720 MPa (Barker et al., 2017; Von Forell et al., 2015; Yang and Kish, 1988). The annular ground substance material was represented using *MAT_HILL_FOAM (compressible foam material). The tensile and compressive behavior of the ground substance was obtained from the experimental data that tested the isolated annular specimens (Fujita et al., 1997; Iatridis et al., 1998). The experimental material response was fitted into an isotropic strain-energy function using the equation 2.5 below (Hill, 1979).

$$W = \sum_{j=1}^m \frac{c_j}{b_j} \left[\lambda 1^{b_j} + \lambda 2^{b_j} + \lambda 3^{b_j} - 3 + \frac{1}{n} (J^{-nb_j} - 1) \right]; \quad n = 2, m = 3 \quad (\text{Equation 2.5})$$

The collagen fibers were represented using *MAT_FABRIC which is a non-linear anisotropic elastic material model with tensile properties obtained from experimental data on collagen fiber tensile tests (Ebara et al., 1996; Holzapfel et al., 2005; Skaggs et al., 1994). The crisscross orientation of the collagen fiber layers was modeled by orienting the fiber material in '+' direction in one lamellar shell element and '-' direction in the other, as observed in the anatomical studies (Martin, 2015; Yoganandan et al., 2001). The orientation of the collagen fibers with respect to the transverse plane varied from $\pm 45^\circ$ (innermost layer) to $\pm 25^\circ$ (outermost layer) based on the literature (Figure 61).

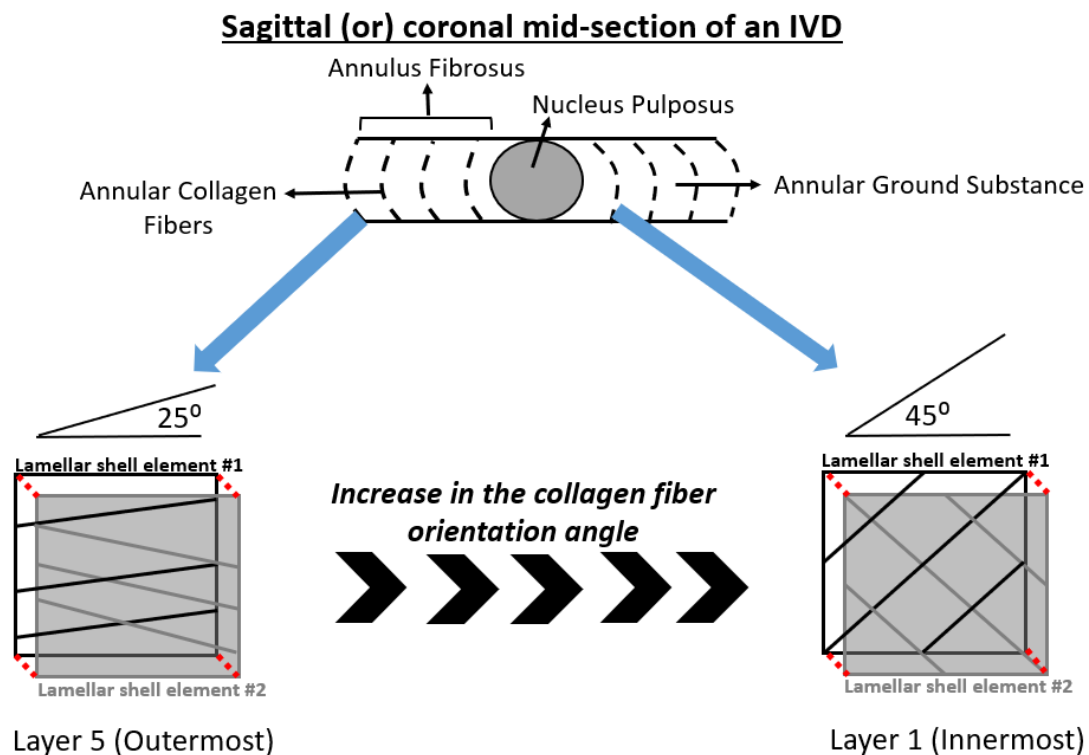


Figure 61: Illustration of the collagen fiber orientation in the lamellae of the IVD AF in GHBMC M50-O neck model. The fiber orientation angle progressively reduced from inner to outer concentric layers.

The superior and inferior surfaces of the IVDs were attached to the cartilaginous vertebral endplates through a tiebreak contact interface available in the LS-DYNA code (*CONTACT_AUTOMATIC_ONE_WAY_SURFACE_TO_SURFACE_TIEBREAK). A stress

failure criteria of 10 MPa was assigned to the tiebreak contact interface to model the IVD avulsion, an injury that is typically observed in the neck during impact (DeWit and Cronin, 2012).

The ligaments were represented using 2-noded 1D tension-only discrete beam elements with *MAT_ELASTIC_SPRING_DISCRETE BEAM material formulation in LS-DYNA code. The ligament material behavior was defined using a non-linear force vs. displacement response along with strain rate effects obtained from experimental data (Mattucci et al., 2013, 2012; Mattucci and Cronin, 2015). The 1D elements of the ligaments shared nodes with the hard tissue. A progressive failure of the ligaments was implemented to mimic the failure progression of collagen fiber bundles in the post-traumatic region of the force vs. displacement curve. A critical distraction values is assigned to simulate a progressive failure in the ligaments (DeWit and Cronin, 2012; Shen, 2020).

A total of 27 pairs of neck muscles were included in the GHBMCM50-O neck model. The muscles consisted of 3D hexahedral solid elements modelled using Ogden rubber material (*MAT_OGDEN_RUBBER) to represent the passive muscle based on the governing equation 2.6 below (Hedenstierna et al., 2008). Additional material constants were applied to account for strain rate effects (Table 4).

$$W = \sum_{i=1}^3 \sum_{j=1}^n \frac{\mu_j}{\alpha_j} (\lambda^{\alpha_j} - 1) + K (J - 1 - \ln J); j = 1, \mu = 1.33 \text{ kPa}, \alpha = 14.5 \quad (\text{Equation 2.6})$$

Table 4: Passive muscle strain rate material constants.

m	G	β
1	522 kPa	1.02 s ⁻¹
2	211 kPa	0.40 s ⁻¹
3	375 kPa	0.65 s ⁻¹
4	290 kPa	0.30 s ⁻¹
5	80 kPa	1.00 s ⁻¹

Embedded within the 3D passive muscle elements are the 2-noded 1D CE from the Hill-type muscle material model (*MAT_MUSCLE) that represent the active muscles (Figure 62). The PEE in the Hill-type material was turned off due to the presence of passive muscle that was represented using 3D elements (Figure 62). The model comprised a series of support (truss) elements (stiffness: 0.01 kN/mm) connecting the 1D CE with the vertebrae (muscle attachments) to maintain the line of action of muscles,

which were considered important to mimic the in vivo force and moment generating capacity in the muscles (Varghese et al., 2022) (Figure 63a). The model also included a series of 1D elastic spring discrete beam elements (stiffness: 0.001 kN/mm) that connected the hyoid bone with the skull and C4-C6 vertebrae (hyoid attachments) (Figure 63b). A σ_{max} value of 500 KPa was assumed for the 1D CE in the GHBMCM50-O neck model, based on the literature (Maganaris et al., 2001; Panzer, 2006; Winters and Stark, 1988). A physiologic cross-section area (PCSA) was assigned to each CE, based on the literature and as implemented in other existing neck models (Panzer, 2006; Van Ee et al., 2000). The normalized force-velocity and force-length curves for the CE were assigned from the literature (Millard et al., 2013; Panzer, 2006) (Figure 47). An activation level was assigned as a function of time to simulate muscle activation as proposed in the literature and implemented in other existing neck models (Fice and Cronin, 2012; Panzer, 2006; Winters and Stark, 1985). Specifically, the GHBMCM50-O v5.1 neck model had a unique co-contraction activation scheme where the flexors and extensors were activated at different levels based on recent studies (Correia et al., 2020; Shen, 2020) (Figure 64).

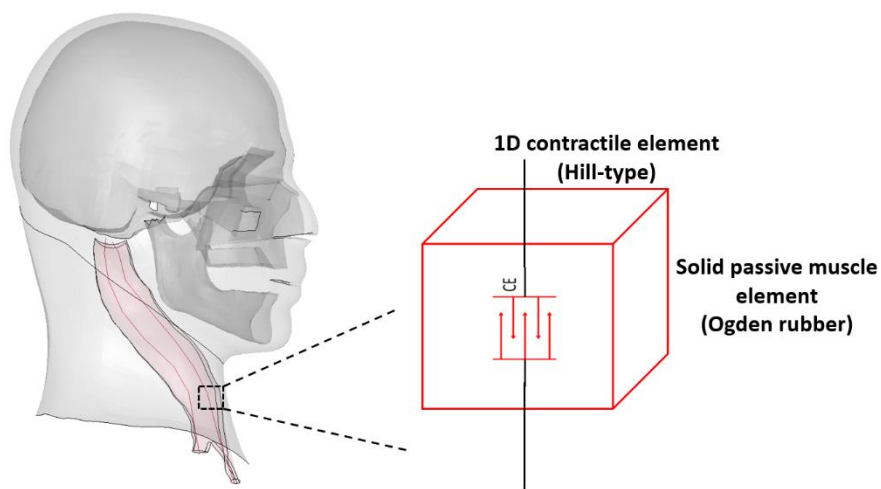


Figure 62: Representation of the active component (contractile element, CE) and passive muscles (solid element) in the GHBMCM50-O neck model. An example of the sternocleidomastoid muscle is shown for illustrative purposes.

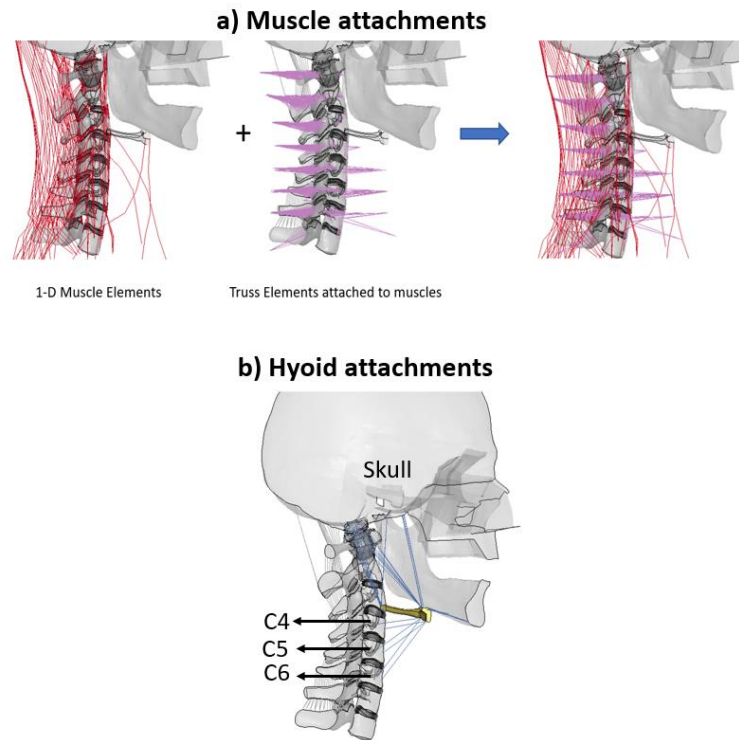


Figure 63: Illustration of 1D muscle elements (CE) with the series of supporting (truss) elements to maintain line of action of muscle force and mimic the in vivo force generating capacity in the muscles (A). Illustration of the spring elements connecting the hyoid bone to skull and C4-C6 vertebrae (B). 3D passive muscle elements are masked for illustrative purposes.

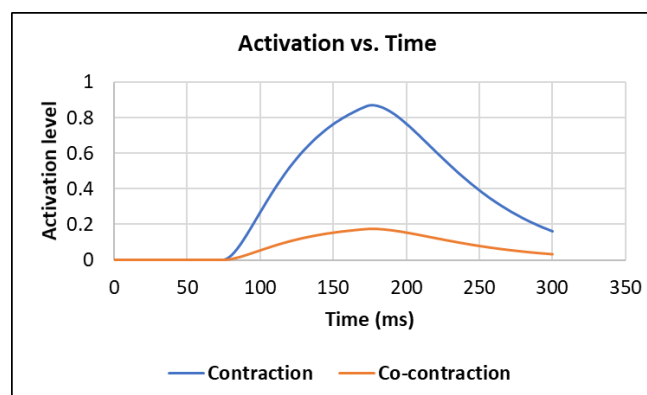


Figure 64: The muscle activation as a function of time for the flexors (contraction) and extensors (co-contraction) in the GHBMC M50-O neck model (Correia et al., 2020).

2.9.2 GHBMC M50-O neck model validation

The GHBMC M50-O neck model is validated against experimental data from the bottom-up starting from an FSU to the full neck. The neck model has been separately validated at the FSU level (C0-C2 and C2-C3 to C7-T1) for quasi-static and high-rate loading conditions against experimental data (Barker et al., 2017, 2014; Lasswell et al., 2017). For the applied moment on the superior FSU, the ROM of the FSU was assessed with the experimental data. The ligamentous cervical spine in the GHBMC M50-O neck model has been validated with the experimental data from the literature for ligament and IVD deformations in 8g frontal and rear impact conditions (Barker and Cronin, 2021). The experimental set-up in the literature included a muscle force replication (MFR) system to recreate the neck musculature in the laboratory setting (Ito et al., 2005; Panjabi et al., 2004). The information on the MFR in the literature was limited (Ito et al., 2005; Panjabi et al., 2004). Hence, Barker and Cronin (2021) modelled the MFR system using the passive component of the Hill-type muscle material from existing neck models (Cronin, 2014; Panzer, 2006; Panzer et al., 2011; Shateri and Cronin, 2015). The detailed GHBMC M50-O neck model has been verified and validated for various impact loading conditions such as frontal, rear, side and oblique across different speeds ranging from 2g to 15g (Barker and Cronin, 2022, 2021; Correia et al., 2020).

Chapter 3 Methods

3.1 Methodology overview

The head and neck were extracted from a contemporary FE human body model of a 26-year-old, 50th percentile male (GHBMC M50-O). The model was used to identify the potential sources of neck pain in the RWA by assessing the loads and distractions in the tissues. The methodology adopted in this research can be classified into three phases corresponding to each objective. Phase #1 comprised model enhancements, verification and validation of the ligamentous cervical spine model (Objective #1). Phase #2a included repositioning the head-neck model from a neutral posture to a non-neutral position using a novel muscle-based repositioning methodology that simulated the *in vivo* head-neck repositioning observed in live humans (Objective #2). Phase #2b of this research included a quantitative comparison between the head-neck model repositioned using conventional and novel muscle-based repositioning methodologies at the tissue-level (Objective #2). In the final phase (Phase #3), non-neutral head-neck positions pertaining to RWA with the HSM were simulated by repositioning the validated head-neck model using the novel muscle-based approach. The risk of neck pain in the RWA due to the HSM and head-neck positions was assessed at the tissue-level (Objective #3).

3.2 Phase #1: Enhancement, verification, and validation of the cervical spine model

The GHBMC M50-O head-neck model was developed and validated to predict CIIs (Barker and Cronin, 2021; Cronin et al., 2018). However, one of the objectives of this research was to assess the potential sources of neck pain in the RWA due to non-neutral head-neck positions, which can be considered to be within the physiologic ROM (Forde et al., 2011; Tack et al., 2014). Hence, there was a necessity to evaluate the head-neck model within the physiologic ROM at different levels of complexity, starting from motion segments to full head-neck. Phase #1 of this research assessed the motion segments and whole ligamentous cervical spine in the GHBMC M50-O head-neck model for three loading modes, including flexion, extension and axial rotation. The whole UCS (C0-C2) (Lasswell et al., 2017) and the motion segments of the LCS (C2-C3 to C6-C7) (Barker et al., 2017, 2014) in this model were previously validated for physiologic ROM and impact loading conditions. The full cervical spine model (C0-C7) was previously validated against impact conditions (8g frontal and rear impact experiments) (Barker and Cronin, 2021) but was not assessed for physiologic ROM at

the global and intervertebral levels (C0-C1 to C6-C7). Also, the physiologic ROM response of the UCS model at the intervertebral level (C0-C1 and C1-C2) has not been assessed to date.

As the ROM of the UCS at the intervertebral level is unique, with C0-C1 dominant in flexion-extension and C1-C2 in axial rotation, their response in the model needs to be assessed with the experimental data at the intervertebral (C0-C1 and C1-C2) levels, rather than at the global level (C0-C2) (Beyer et al., 2020; Bogduk and Mercer, 2000; Heller et al., 2005; Steilen et al., 2014; Swartz et al., 2005). Also, owing to the non-linear nature of the UCS response across the ROM, the model response across the ROM at regular intervals need to be evaluated.

In the Phase #1 of this research, the ROM response of the ligamentous cervical spine in flexion, extension and axial rotation loading modes was assessed with in vitro experimental ROM from the literature (Ivancic, 2013; Oda et al., 1992; Panjabi et al., 1991a). First, a preliminary study was conducted on the existing UCS model (Lasswell et al., 2017) to assess the intervertebral ROM response. Based on the preliminary assessment, enhancements to the model geometry, followed by optimization of ligament laxities, were made to enhance the biofidelity of the UCS model. Finally, the enhanced UCS was integrated with the ligamentous cervical spine (C0-C7) model and assessed for intervertebral ROM using an independent set of cervical spine in vitro experimental data.

3.2.1 Preliminary assessment of the UCS_{M50} model

The UCS (UCS_{M50}) model, previously validated by Lasswell et al. (2017) for global (C0-C2) ROMs, was extracted from the GHBMCM50 v4.5 detailed FE neck model (Figure 65). The extracted UCS_{M50} model consisted of laxities that were incorporated into selected ligaments, which enhanced the biofidelity of the model in C0-C2 flexion, extension, lateral bending and axial rotation (Lasswell et al., 2017). Ligament laxity was defined as the initial elongation of the ligament without substantial applied force and was incorporated into the ligaments using a displacement-offset method in the force-displacement material curve (Cronin et al., 2012; Lasswell et al., 2017; Shateri and Cronin, 2015) (Figure 66). To the extracted UCS_{M50} model, the C2 vertebra was constrained in all the degrees of freedom and a pure moment was applied to the skull (C0 vertebra) in the three loading modes: flexion, extension, and axial rotation, separately.

The global (C0-C2) ROM response of the extracted UCS_{M50} model and the UCS_{M50} model reported by Lasswell et al. (2017) were verified. Later, a preliminary assessment of the UCS_{M50} model was conducted and comprised an evaluation of the model response with the experimental data (Oda et al.,

1992; Panjabi et al., 1991b, 1991a) at the intervertebral levels (C0-C1 and C1-C2) (Figure 65). The assessments were made by calculating the percentage error (Equation 3.1) between the model response and the experimental mean reported by Panjabi et al. (1991a, 1991b), and Oda et al. (1992).

$$\% \text{ Error} = \frac{|\text{Experimental Mean} - \text{Model Response}|}{\text{Experimental Mean}} * 100 \quad (\text{Equation 3.1})$$

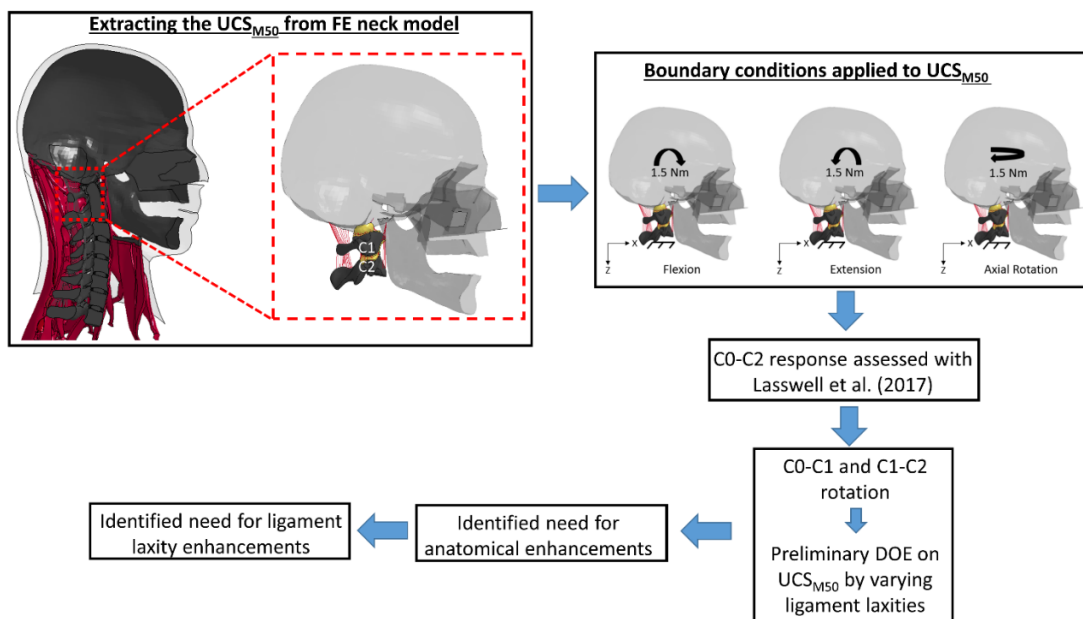


Figure 65: Preliminary assessment of UCS_{M50} model starting from model extraction, applying BCs, model verification with literature (Lasswell et al. 2017), assessment of the intervertebral response and identifying the areas for model enhancements.

[Adapted from Hadagali and Cronin (2023)]

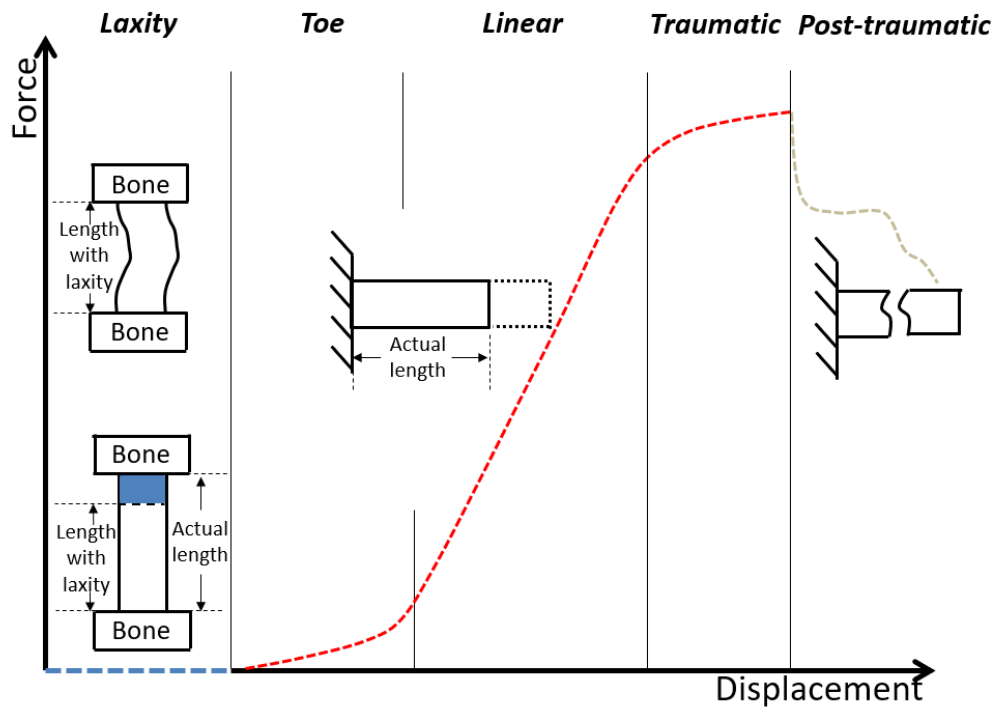


Figure 66: Schematic showing ligament laxity (dashed blue line) calculated using optimization methods, the typical force-displacement response of a ligament (red dashed line) and the post-ultimate load response (dashed grey line). Ligament laxity was defined as the ligament’s elongation amount without substantial applied force. In the model, the difference between ‘Actual length’ and ‘Length with laxity’ was calculated as ligament laxity using optimization methods.

[Taken from Hadagali and Cronin (2023)]

A preliminary design of experiments (DOE) was conducted to assess the behaviour of the UCS_{M50} model at the intervertebral level with varying ligament laxities. The preliminary DOE study was performed on the UCS_{M50} model separately in flexion, extension, and axial rotation. The Latin Hypercube Sampling (LHS)-based DOE method was used to vary the laxities of the UCS ligaments using a commercial optimization software package (LS-OPT v5.2). The LHS, similar to the full-factorial and one-factor-at-a-time (OFAT), is a design-space generating approach that was used to obtain several iterations/simulation cases with a range of variations in the laxity of UCS ligaments.

Unlike the full-factorial and OFAT approaches, the LHS approach helped reduce the design-space and obtain a uniform distribution of variables across the range of variations (John et al., 2019b; Yang et al., 2005). The LHS also captured the interactions between variables, which was not possible using the OFAT or full-factorial approaches, considering two or more ligaments resisting the UCS motion in one direction (Yang et al., 2005). Typically, to construct a design-space, a range of values for the variables need to be assigned so that the values are distributed for each variable and iterations/simulation cases are generated accordingly. Laxities of all the ligaments varied between 0.0 mm (no laxity) to 8.0 mm. Based on the stiff intervertebral response of the UCS_{M50} model incorporated with a maximum laxity of 5.8 mm (Lasswell et al., 2017), a relatively higher laxity value of 8.0 mm was selected to get a better understanding of the model behaviour with higher laxities, for preliminary assessments.

The laxities of 11 ligaments were varied for flexion, the laxities of 4 ligaments were varied for extension, and the laxities of 7 ligaments were varied for axial rotation (Table 5). The LHS-based DOE generated three sets of design-space, each for flexion, extension and axial rotation. Each design-space generated using the LHS approach comprised a set of iterations/simulation cases with varying ligament laxities (Tables A1-A3 in Appendix A). All the iterations/simulation cases in the three design spaces were solved using a commercial explicit FE solver (LS-DYNA R9.2) from which the intervertebral responses were extracted (Figure 67).

Preliminary assessments on the UCS_{M50} model at the intervertebral level along with the preliminary DOE study, identified the need for enhancements to the UCS_{M50} model (Figure 65). Consequently, the response from the anatomically enhanced UCS_{M50} model (UCS_{M50-G}) suggested a revision of the existing ligament laxity values. The existing ligament laxity values were revised using an optimization method to further enhance the biofidelity of the UCS model at the intervertebral levels in the flexion, extension and axial rotation loading modes (elaborated in the following sections).

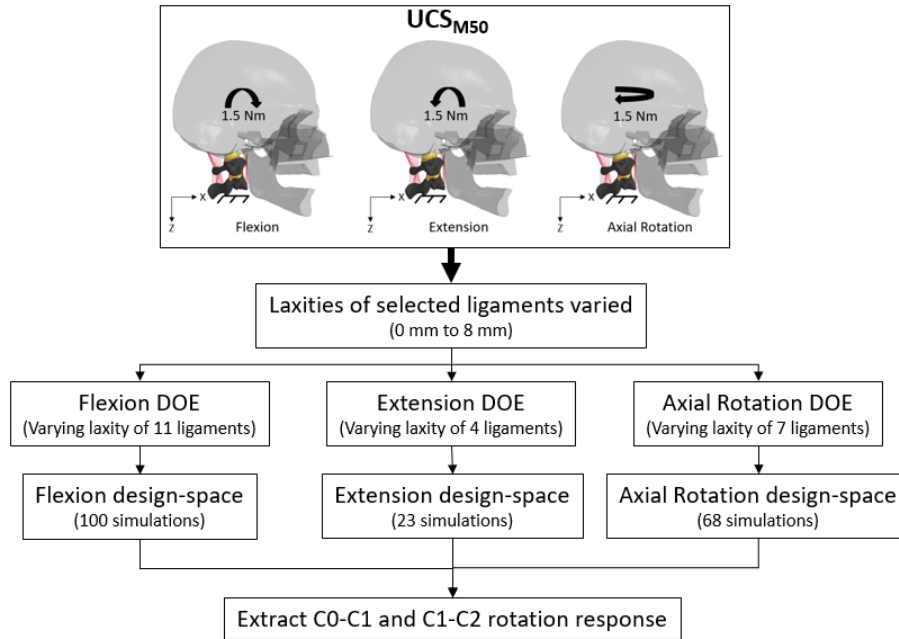


Figure 67: Flow chart elaborating the preliminary DOE process that identified the need for UCS_{M50} model enhancements.

[Adapted from Hadagali and Cronin (2023)]

Table 5: Summary of the ligaments in the UCS_{M50} model, the laxities of which were varied during the DOEs (F: Flexion, E: Extension and AR: Axial rotation)

Independent variables (Laxities of ligaments)	Abbreviation	Loading modes		
		F	E	AR
Anterior Atlanto-Occipital Membrane	AA-OM		•	
Posterior Atlanto-Occipital Membrane	PA-OM	•		
Anterior Atlanto-Axial Membrane	AA-AM		•	•
Posterior Atlanto-Axial Membrane	PA-AM	•		•
Interspinous ligament	ISL	•		
Capsular ligament C0-C1	CL01	•	•	•
Capsular ligament C1-C2	CL12	•	•	•
Tectorial Membrane	TM	•		•
Transverse ligament	TL	•		
Upper Cruciform ligament	UCrx	•		
Lower Cruciform ligament	LCrx	•		
Alar ligament	AL	•		•
Alar (Atlanto-Axial) ligament	AL-AT			•
Apical ligament	ApL	•		

3.2.2 Anatomical enhancements to the UCS_{M50} model

Two areas for anatomical enhancement in the UCS model were identified and improved to create the geometrically enhanced model, described as UCS_{M50-G} (Figure 68). The distances between the cartilage surfaces of occipital-condyle and C1 in the UCS_{M50} model (0 mm to 0.2 mm) combined with the global contact thickness parameter (0.2 mm) in the GHBM model led to interference between the surfaces. Intermittent rapid increases in the C0-C1 rotations were observed in the preliminary DOE simulations owing to the interference between the occipital-condyle and C1 cartilage surfaces. The described limitation was addressed by decreasing the thickness of the C1 superior cartilage by 0.3 mm while maintaining the joint space (Rojas et al., 2007) in the model. The model with the decreased C1 superior cartilage will henceforth be termed UCS_{M50-Cartilage} (Figure 68a). Second, the alar ligaments, having an insertion point on the skull in the UCS_{M50} model, were reoriented to have the insertion point located on the medial part of the occipital condyle, as reported in the literature (Panjabi et al., 1991a). The model with decreased C1 cartilage thickness and enhanced alar ligament orientation will subsequently be referenced as the UCS_{M50-G} (Figure 68b). The percentage change (Equation 3.2) and percentage difference (Equation 3.3) were calculated between the UCS_{M50} and UCS_{M50-Cartilage} models to assess the effect of reducing the C1 cartilage thickness on the ROM response. Similarly, the percentage change and percentage difference were calculated between the UCS_{M50-Cartilage} and UCS_{M50-G} models to assess the effect of alar ligament reorientation on the ROM response. The percentage change was calculated to assess if the ROM response increased or decreased relative to the model on which the geometrical enhancements were made.

$$\% \text{ Change} = \frac{\text{Enhanced Model Response} - \text{Model Response}}{\text{Model Response}} * 100 \quad (\text{Equation 3.2})$$

$$\% \text{ Difference} = \frac{|\text{Model Response} - \text{Enhanced Model Response}|}{(\text{Model Response} + \text{Enhanced Model Response})/2} * 100 \quad (\text{Equation 3.3})$$

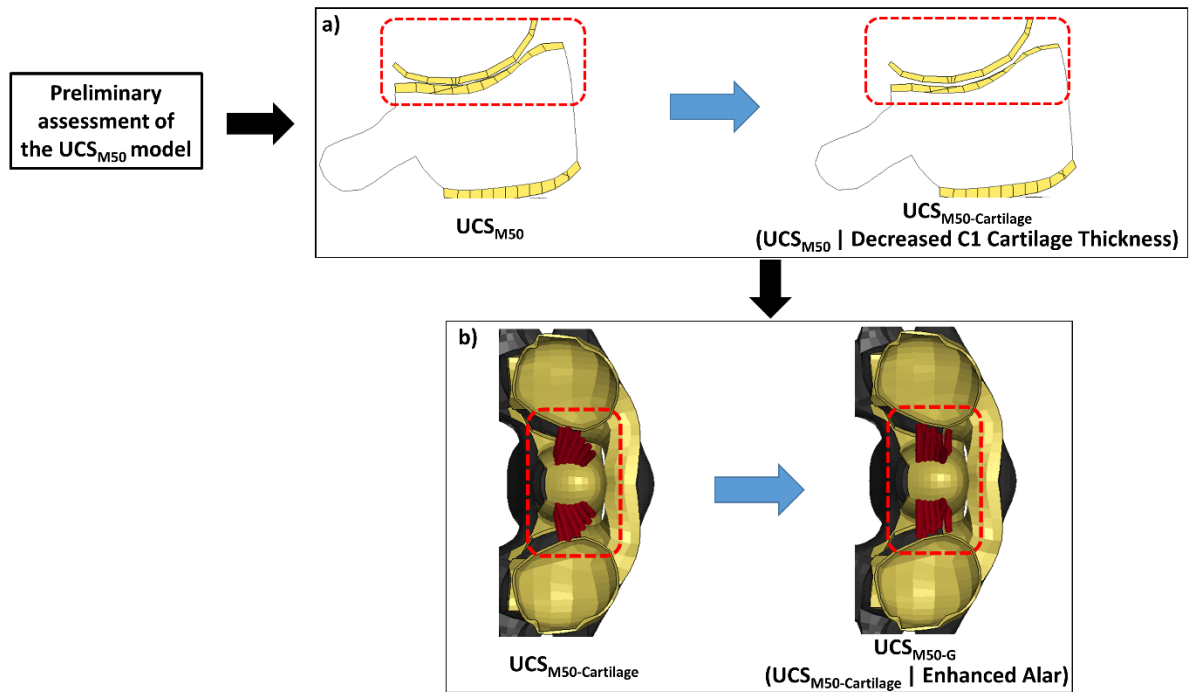


Figure 68: Anatomical enhancements to the UCS_{M50} model a) decreased C1 cartilage thickness, b) corrected alar ligament insertion location. Flow-chart describing the update of the UCS model from UCS_{M50} to UCS_{M50-G}.

[Adapted from Hadagali and Cronin (2023)]

3.2.3 Ligament Laxity Identification in the UCS_{M50-G} model using optimization

The UCS_{M50-G} model comprised ligament laxities identified from the previous study (Lasswell et al., 2017) and had to be revised to minimize the differences between the anatomically enhanced model and the experimental mean (Oda et al., 1992; Panjabi et al., 1991b, 1991a). In the first step, a DOE study was conducted on the UCS_{M50-G} model as described in the previous section (Figure 67 and Table 5). From the DOE, six metamodels were generated for C0-C1 and C1-C2 for the three modes of loading. The metamodels were validated for accuracy. A sensitivity study was undertaken on each metamodel to identify the ligaments that highly contributed to the intervertebral rotation response for a particular loading mode. The sensitivity analysis was pursued because optimizing the laxities for all 14 ligaments in the UCS for the three loading modes could potentially increase the number of iterations and compute time for the laxity values to converge. For context, the metamodel generation and sensitivity for 100 design points in a design space (11 variables) took approximately one week to run on Intel Core i7-

8700 3.7 GHz processor. Therefore, with the guidance of a sensitivity study, the highest contributing ligaments and a reduced range of laxity for each contributing ligament were determined to ensure a biofidelic kinematic response within a manageable compute time. Laxities from one or more ligaments that individually or combinedly contributed to 95% of the intervertebral motion in each loading mode were considered for the final ligament optimization study.

A metamodel-based optimization procedure was implemented on the UCS_{M50-G} model using LS-OPT v5.2 to identify the optimum ligament laxity values for the highest contributing ligaments within their reduced range of laxity identified from the sensitivity study. The process terminated with optimum results after the accuracy of the metamodels met the specified convergence criteria. The experimentally measured mean intervertebral ROM for the three loading modes was used as the target for the intervertebral response of the UCS_{M50-G} model to match (Panjabi et al., 1991a, 1991b). The laxity values converged at the fourth optimization iteration when the metamodel accuracy had a root mean square error of less than 3%. The UCS model with geometric enhancements and updated ligament laxity will subsequently be called UCS_{M50-Opt} (Figure 69).

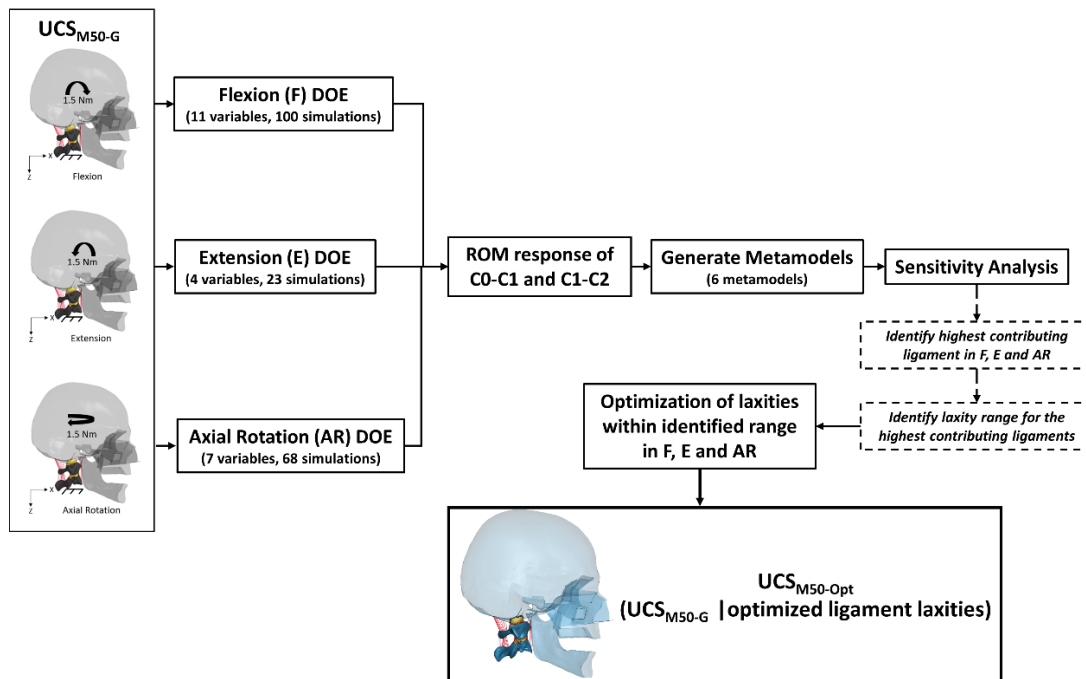


Figure 69: Steps involved in identifying the ligament laxity values in the UCS_{M50-G} model.
Flowchart showing the update of the model from UCS_{M50-G} to UCS_{M50-Opt}.

3.2.4 Verification and validation of the UCS_{M50-Opt} model

First, the intervertebral responses of the UCS_{M50-Opt} were verified with the target experimental data across the ROM in flexion, extension and axial rotation (Panjabi et al., 1991b, 1991a). The mean values from the experimental study (Panjabi et al., 1991b, 1991a) were used as the target response due to the detailed reporting of UCS intervertebral ROM from the neutral zone to 1.5 Nm in the three loading modes (Table 6). The UCS intervertebral ROM in the neutral zone was necessary to optimize the ligament laxities. The percentage error between the target and the UCS_{M50-Opt} model response was calculated for verification.

Next, the UCS_{M50-Opt} was validated with an independent set of existing experimental data (Oda et al., 1992) that reported the UCS intervertebral ROM in the three modes of loading. The model was validated at the intervertebral levels by assessing the percentage error between the experimental data (mean) and the ROM response in the original (UCS_{M50}) and the enhanced (UCS_{M50-Opt}) models.

Table 6: Experimental data used for verification and validation of the UCS_{M50-Opt} model. Grey areas indicate the kinematics was not available in the particular experimental study.

			Verification of UCS _{M50-Opt} model		Validation of UCS _{M50-Opt} model
			Panjabi et al. (1991b)	Panjabi et al. (1991a)	Oda et al. (1992)
C0-C1	Flexion	NZ	•	[Grey Area]	•
		0.5 Nm	•		•
		1.0 Nm	•		•
		1.5 Nm	•		•
	Extension	NZ	•	[Grey Area]	•
		0.5 Nm	•		•
		1.0 Nm	•		•
		1.5 Nm	•		•
	Axial Rotation	NZ	[Grey Area]	•	•
		0.5 Nm		•	•
		1.0 Nm		•	•
		1.5 Nm		•	•
C1-C2	Flexion	NZ	•	[Grey Area]	•
		0.5 Nm	•		•
		1.0 Nm	•		•
		1.5 Nm	•		•
	Extension	NZ	•	[Grey Area]	•
		0.5 Nm	•		•
		1.0 Nm	•		•
		1.5 Nm	•		•
	Axial Rotation	NZ	[Grey Area]	•	•
		0.5 Nm		•	•
		1.0 Nm		•	•
		1.5 Nm		•	•

3.2.5 Validation of the full ligamentous cervical spine model

The UCS_{M50} and UCS_{M50-Opt} (C0-C2) models were integrated with the lower cervical spine (LCS_{M50}) model (C3-T1) to assess the full ligamentous cervical spine (LS) model response. However, during the course of this research, an updated version of the GHBMCM50-O v4.5 model (GHBMCM50-O v5.1), which consisted of enhanced facet cartilages at the ligamentous C2-T1 intervertebral levels, was released (Corrales and Cronin, 2021b). It was beneficial to transition to an upgraded model at an earlier stage in the research to ensure an improved biofidelic response from the model. Before transitioning to the upgraded model, it was also necessary to assess the LS model that had the UCS_{M50-Opt} integrated with the upgraded LCS model with enhanced C2-T1 facet cartilages (LCS_{M50-FC}). The full ligamentous spine models: 1) UCS_{M50} integrated with LCS_{M50} (LS_{M50}), 2) UCS_{M50-Opt} integrated with LCS_{M50} (LS_{M50-Opt}) and 3) UCS_{M50-Opt} integrated with LCS_{M50-FC} (LS_{M50-FC-Opt}) were simulated for flexion, extension and axial rotation by constraining T1 and applying moment at C0, as described in the literature (Ivancic, 2013; Panjabi et al., 2001b, 1998) (Figure 70). The percentage change (increase or decrease) in ROM from the LS_{M50-Opt} to LS_{M50-FC-Opt} model was quantified to assess the effect of enhancements to the C2-T1 facet cartilages.

For validation, the intervertebral responses from the LS_{M50}, LS_{M50-Opt} and LS_{M50-FC-Opt} model simulations were assessed with experimental data (Camacho et al., 1997; Ivancic, 2013; Nightingale et al., 2007; Oda et al., 1992; Panjabi et al., 1991a, 1991b, 2001b, 1998; Wheeldon et al., 2006) across the ROM in the three loading modes (Table 7). The model response was assessed sequentially in the following order:

- 1) The percentage error between the experimental mean reported by independent studies (Table 7) and the LS models was calculated.
- 2) The percentage error between the experimental mean from studies that reported the UCS and the full cervical spine (Table 7) and the LS models was calculated.
- 3) A cumulative mean value for the experimental ROM response for each level from C0-C1 to C6-C7 was calculated from the mean values reported in all the experimental studies summarized in Table 7. The percentage error between the cumulative mean from experimental data and the LS model response was calculated for assessment.

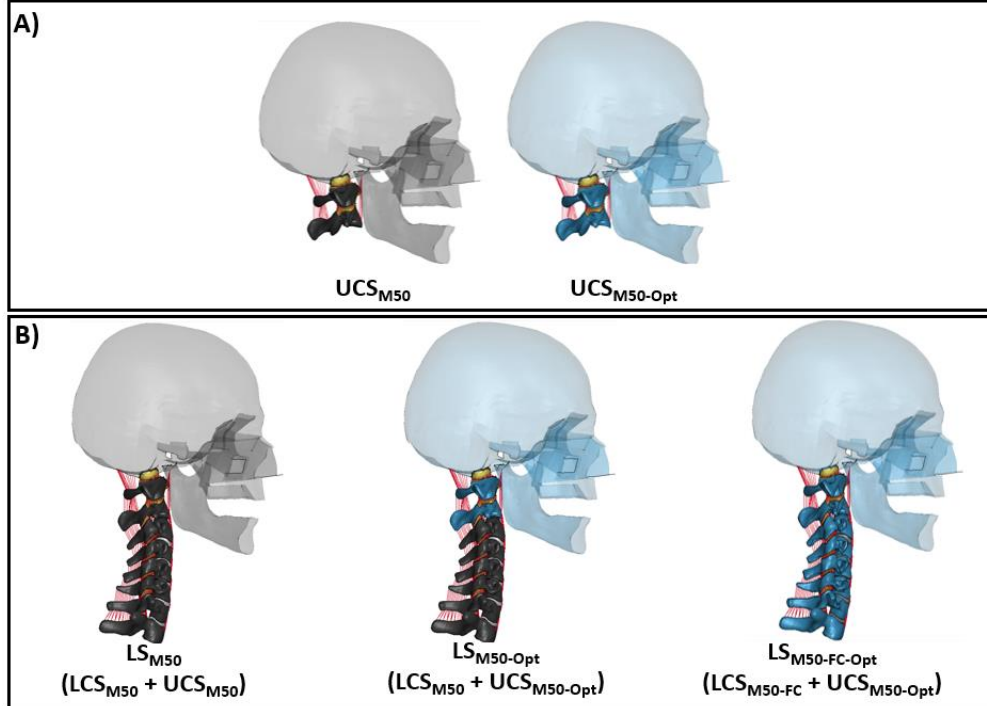


Figure 70: The figure shows the original and enhanced models that are color coded black and blue, respectively. A) The biofidelity of the original UCS (UCS_{M50} , color coded black) and the enhanced UCS ($UCS_{M50-Opt}$, color coded blue) models were assessed with experimental data B) To the original LS model (LS_{M50}), the enhanced UCS model ($UCS_{M50-Opt}$, color coded blue) was included while retaining the original LCS and named $LS_{M50-Opt}$. Next, the original LS model was replaced with enhanced UCS ($UCS_{M50-Opt}$) and LCS (LCS_{M50-FC}) and named $LS_{M50-FC-Opt}$.

[Adapted from Hadagali and Cronin (2023)]

Table 7: Experimental data used to assess the ligamentous cervical spine models. Grey areas indicate the kinematics was not available in the particular experimental study.

		Set of experimental data used to assess the LS models								
		Level	Panjabi et al. (1991a, b)	Oda et al. (1992)	Camacho et al. (1997)	Panjabi et al. (1998)	Panjabi et al. (2001)	Wheeldon et al. (2006)	Nightingale et al. (2007)	Ivancic (2013)
Flexion	0.5 Nm	C0-C1	*	*						*
		C1-C2	*	*						*
		C2-C3			*				*	
		C3-C4			*				*	*
		C4-C5			*				*	*
		C5-C6			*				*	*
	C6-C7			*				*	*	
	1.0 Nm	C0-C1	*	*		*	*			*
		C1-C2	*	*		*	*			*
		C2-C3			*	*	*	*		*
		C3-C4			*	*	*	*	*	*
		C4-C5			*	*	*	*	*	*
		C5-C6			*	*	*	*	*	*
	C6-C7			*	*	*	*	*	*	
	1.5 Nm	C0-C1	*	*						*
		C1-C2	*	*						*
		C2-C3			*				*	*
		C3-C4			*				*	*
C4-C5				*				*	*	
C5-C6				*				*	*	
C6-C7			*				*	*		
Extension	0.5 Nm	C0-C1	*	*						*
		C1-C2	*	*						*
		C2-C3			*				*	*
		C3-C4			*				*	*
		C4-C5			*				*	*
		C5-C6			*				*	*
	C6-C7			*				*	*	
	1.0 Nm	C0-C1	*	*		*	*			*
		C1-C2	*	*		*	*			*
		C2-C3			*	*	*	*		*
		C3-C4			*	*	*	*	*	*
		C4-C5			*	*	*	*	*	*
		C5-C6			*	*	*	*	*	*
	C6-C7			*	*	*	*	*	*	
	1.5 Nm	C0-C1	*	*						*
		C1-C2	*	*						*
		C2-C3			*				*	*
		C3-C4			*				*	*
C4-C5				*				*	*	
C5-C6				*				*	*	
C6-C7			*				*	*		
Axial Rotation	0.5 Nm	C0-C1	*	*						*
		C1-C2	*	*						*
		C2-C3								*
		C3-C4								*
		C4-C5								*
		C5-C6								*
	C6-C7								*	
	1.0 Nm	C0-C1	*	*						*
		C1-C2	*	*						*
		C2-C3								*
		C3-C4								*
		C4-C5								*
		C5-C6								*
	C6-C7								*	
	1.5 Nm	C0-C1	*	*						*
		C1-C2	*	*						*
		C2-C3								*
		C3-C4								*
C4-C5									*	
C5-C6									*	
C6-C7								*		

3.3 Phase #2a: Simulating non-neutral head-neck positions using muscle activation

Maintaining non-neutral head-neck positions over a prolonged duration while flying on a mission has been associated with the risk of neck pain in the RWA along with other factors such as HSM (Adam, 2004; Chafé and Farrell, 2016; Forde et al., 2011; Tack et al., 2014). In humans, the head-neck is constantly exposed to gravity and requires counteracting forces from the muscles to maintain a position, thereby preventing the head from losing balance (Seacrist et al., 2012). The neck muscles activate under the influence of gravity to enable the in vivo physiologic motion and maintain head-neck positions at the desired line of sight (Barrett et al., 2020; Straker et al., 2009). The specific objective in Phase #2a of this research was to develop a methodology to simulate non-neutral head-neck positions within the physiologic ROM by activating the neck muscles, as observed in vivo in live humans. Forward flexion and axial rotation of the head-neck, with the head rotated at 30° in both positions, were considered to be the target non-neutral position. The target non-neutral positions were consistent with the literature that quantified head rotation in the general population during hand-held device activities and the RWA during scanning tasks (Forde et al., 2011; Han et al., 2018; Lee et al., 2015; Tack et al., 2014). The FE neck model repositioned using both methods was solved using commercial FE software (LS-DYNA MPP 9.2, LSTC, Livermore, CA).

The GHBMC M50-O head-neck model comprising the active and passive muscle components has been verified and validated for various impact scenarios (Barker and Cronin, 2020; Bruneau and Cronin, 2019; Correia et al., 2021, 2020; Cronin et al., 2018). However, to date, there are a limited number of studies that explored the response of the model in physiologic conditions (Feller et al., 2016). Hence, it was necessary to sequentially analyze the model response under conditions like gravity and an externally applied moment. Identifying the limitations in the model enabled improving the model biofidelity to allow repositioning the model from a neutral to a non-neutral position using active muscles.

3.3.1 Head-neck model updated with enhanced UCS and simplified head

The GHBMC M50-O v5.1 FE head-neck model with the enhanced, validated and verified UCS (UCS_{M50-Opt} from Phase #1) (Hadagali and Cronin, 2023) and simplified rigid head (Barker and Cronin, 2021) was used in the current phase. The mass, moment of inertia and location of the CoG of the simplified head was calculated from the detailed head model (Barker and Cronin, 2021; Bruneau and

Cronin, 2019). The location of the head CoG calculated from the detailed head model were verified with the experimental data reported in the literature (Beier et al., 1980; Plaga et al., 2005; Walker et al., 1973) (Table 8). The GHBMC M50 v5.1 FE neck model with UCS_{M50-Opt} and simplified rigid head will subsequently be called NM_{M50} (Figure 71).

Table 8: The location of the head CoG in the NMM50 model was compared to the experimental data from the literature.

Study	Distance between CG and OC (mm)					
	X			Z		
	Mean (SD)	Minimum	Maximum	Mean (SD)	Minimum	Maximum
Walker et al. (1973)	17.8 (7.1)	4.3	34.5	53.1 (5.1)	42.9	60.5
Beier et al. (1980)	17.3 (2.5)	11.7	22.6	63.0 (5.6)	53.6	74.2
Plaga et al. (2005)	19.8 (5.8)	7.6	26.9	60.2 (3.8)	53.3	67.6
NM _{M50}	21.8			56.5		

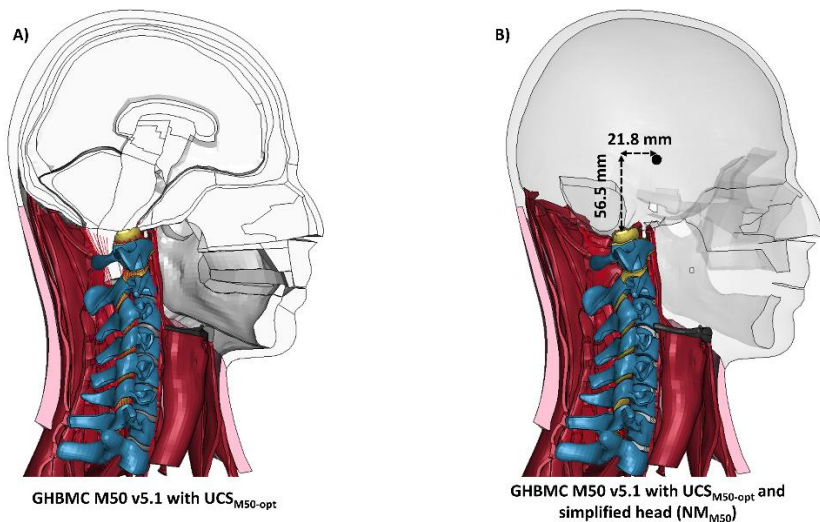


Figure 71: The GHBMC M50 v5.1 head-neck model updated with the UCS_{M50-Opt} with the detailed head (A) and simplified head, NM_{M50} (B).

3.3.2 Passive neck stiffness assessment of the NM_{M50} model

Under the action of gravity (acting in the craniocaudal direction), lack of muscle activation and the placement of the head CoG relatively anterior to the spinal column, the passive head-neck pitch forward to an almost fully flexed position (Seacrist et al., 2012). Several in vivo experimental studies have reported the contraction and co-contraction of the muscles when the head-neck reposition from a neutral posture to a desired non-neutral position. Experimental studies also suggested that the co-contractor muscles are recruited to restrict the head-neck from making a full ROM when the contractor muscles activate under gravity (Cheng et al., 2008; Mousavi-khatir et al., 2015). From the literature, all three factors, including gravity, muscle contraction and co-contraction were considered crucial for the head-neck to reposition from a neutral posture to a non-neutral position within the full physiologic ROM. Hence, it was necessary to assess the response of the NM_{M50} model for different factors as such an assessment could be necessary at a preliminary stage of this research to gain insight into the model capabilities and a potential opportunity for enhancements. Assessments were made by calculating the percentage error between the model response and the experimental data, as described in Section 3.2.1.

The in vivo experiment by Seacrist et al. (2012) was simulated on the NM_{M50} model to assess the response under only gravity with relaxed muscles i.e. passive neck. The relaxed muscles were simulated by turning off the activation parameter in the CE ($a(t) = 0$) of the Hill-type muscle model. The T1 vertebra, the caudal ends of the skin, adipose tissue and the muscles were constrained in all the degrees of freedom. Gravity was applied in the cranio-caudal direction to the NM_{M50} model with relaxed muscles and assessed for head rotation with the experimental data (Seacrist et al., 2012). Based on the response, the NM_{M50} model was further assessed under gravity by sequentially removing the skin, adipose tissue, and passive muscles to assess the contribution of each passive tissue to the head rotation response (Figure 72).

To further assess the capabilities of the NM_{M50} model with relaxed muscles, the head rotation response to an applied external moment was assessed with in vivo experimental data reported by McGill et al. (1994). In the model, to simulate the McGill et al. (1994) experiment, the T1 vertebra, the caudal ends of the skin, adipose tissue and the muscles were constrained in all the degrees of freedom. The CE was turned off to simulate the relaxed muscles, and a flexion moment of 7.0 Nm was applied to the rigid head at a rate of 1 Nm/s (Figure 73a). Based on the response in the NM_{M50} model, further assessments were made by sequentially removing the skin, adipose tissue, and passive muscles to assess the contribution of each passive component to the head rotation response (Figure 73).

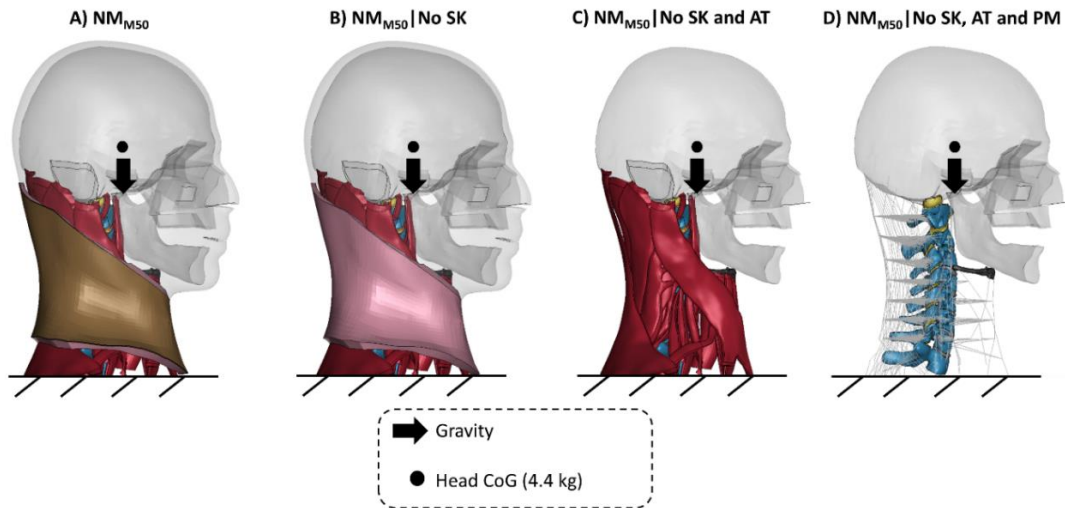


Figure 72: The effect of the skin, adipose tissue and passive muscles in the NM_{M50} model are assessed under gravity loading. In the NM_{M50} model (A), skin (SK) was excluded (B), skin (SK) and adipose tissue (AT) were excluded (C), and SK, AT and passive muscle (PM) were removed, retaining the inactive 1D contractile element ($a(t)=0$) from the Hill-type muscle model (D).

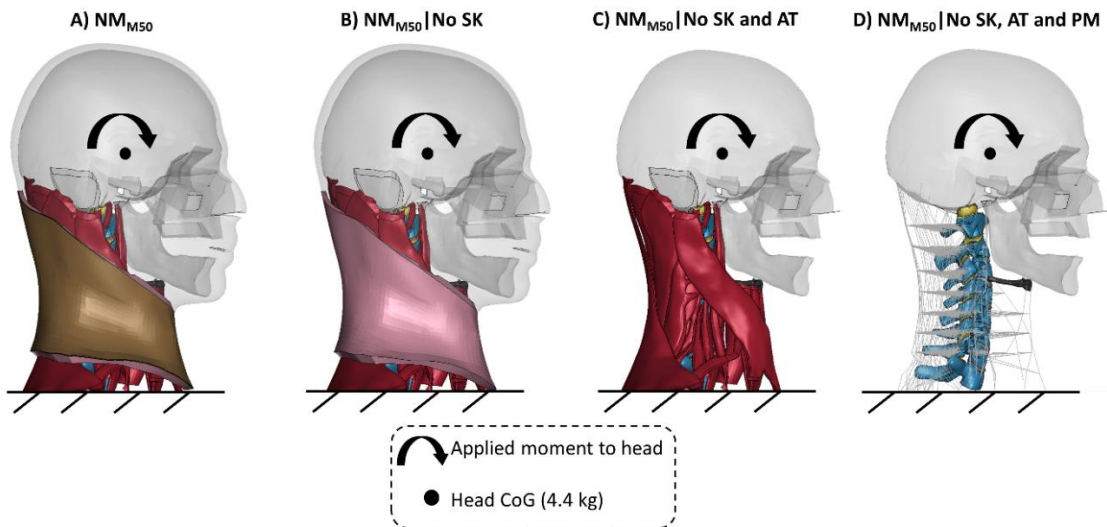


Figure 73: The effect of the skin, adipose tissue and passive muscles in the NM_{M50} model are assessed for an externally applied moment. (A) The NM_{M50} model, (B) Skin (SK) was excluded, (C) Skin (SK) and adipose tissue (AT) were excluded, (D) The SK, AT and passive muscle (PM) were removed, retaining the inactive 1D contractile element ($a(t)=0$) from the Hill-type muscle.

3.3.3 Active neck stiffness assessment of the NM_{M50} model

From the literature, muscle activation levels in the existing head-neck models during simulated non-neutral positions within the physiologic ROMs varied between 0 to 0.15 (Arshad et al., 2022; Barrett, 2016; Storvik and Stemper, 2011). To assess the effect of muscle activation on the model response during a simulated flexion, a preliminary study was conducted on the NM_{M50} model. To the NM_{M50} model, flexor muscles were fully activated ($a(t) = 1.0$) under gravity with the relaxed co-contractor muscles (extensors) (Figure 74). The head rotation and the IVD forces were extracted from the repositioned model for assessment.

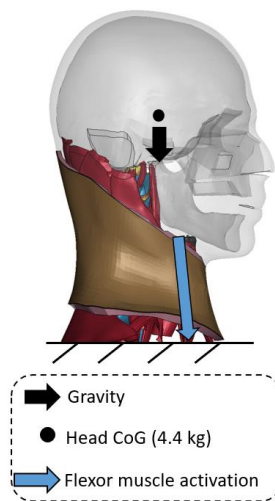


Figure 74: Assessment of the NM_{M50} model response to flexor muscle activation under gravity.

3.3.4 Exclusion of skin and adipose tissue and modification of passive muscles in the NM_{M50} model

Assessments from sections 3.3.2 and 3.3.3 suggested that the passive muscles (3D elements), adipose tissue (3D elements) and skin (2D elements) components contributed to the non-biofidelic response in the NM_{M50} model for physiologic reposition conditions. To enable further investigations in this research, the NM_{M50} model was simplified. The detailed passive tissues in the NM_{M50} model, including the adipose tissue (3D elements) and skin (2D elements), were removed from the model and represented with only muscles. The detailed passive muscles (3D elements) were replaced with the passive elastic element (PEE) within the 1D Hill-type muscles (Cronin, 2014; Kleinbach et al., 2017; Millard et al., 2013; Panzer, 2006; Shateri and Cronin, 2015; Winters, 1995) (Figure 75). The tensile material property of the passive muscle pertaining to low strain rate ($0.01s^{-1}$), previously proposed by Gierzycka et al.

(2021), was assigned to the PEE (Figure 53). The NM_{M50} model with the excluded skin and adipose tissue components and the replacement of the detailed passive muscle with the PEE within the 1D Hill-type muscles will subsequently be called $NM_{M50-Hill}$. The assumptions pertaining to contribution of skin and adipose tissues on the structural response and the replacement of 3D passive muscle element with PEE within the Hill-type muscle model to modify the NM_{M50} model agreed with the literature (Alizadeh et al., 2020b; Barrett et al., 2020; Moore et al., 2021). The 1D support elements connecting the vertebrae with the 1D CE elements (muscle attachments) were retained in the $NM_{M50-Hill}$ model. Similarly, the 1D support elements connecting the hyoid bone to skull and the anterior aspects of C4-C6 vertebrae (hyoid attachments) were retained in the $NM_{M50-Hill}$ model.

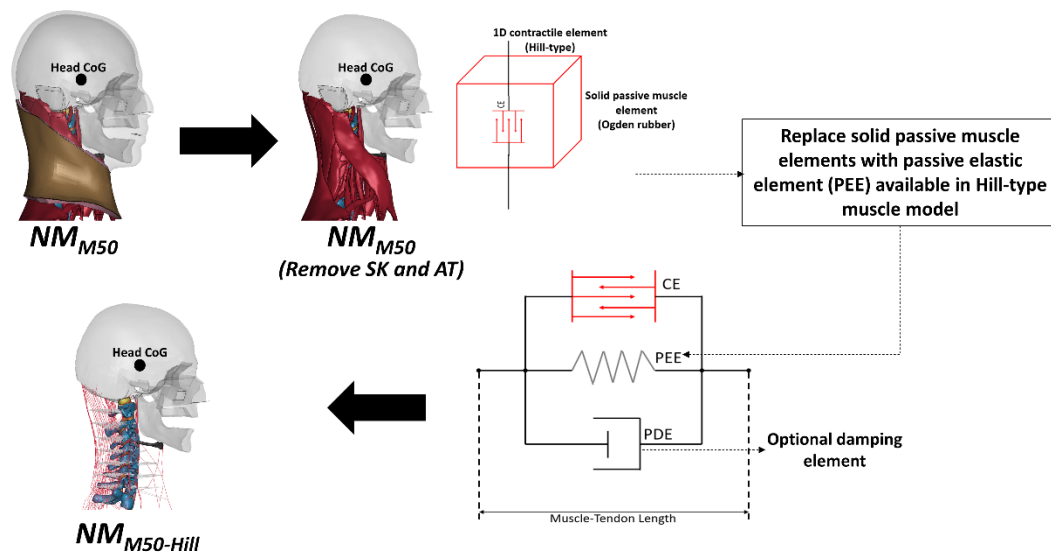


Figure 75: Illustrating the substitution of 3D passive muscle elements in the NM_{M50} with the passive elastic element (PEE), parallel to the contractile element (CE) within the Hill-type muscle material ($NM_{M50-Hill}$). Parallel damping element (PDE) was not included in the current study.

[Taken from Hadagali et al. (2024)]

3.3.5 Passive neck stiffness assessment and improvement of the $NM_{M50-Hill}$ model

The inferior ends of the muscle elements and the T1 vertebra were constrained in all degrees of freedom. The active muscle component (CE) in the Hill-type material was turned off to simulate the relaxed neck (Figure 76a). In the first condition, the $NM_{M50-Hill}$ model with the relaxed muscles was tested under

gravity loading in the craniocaudal direction. In the second condition, the in vivo flexion experiments from McGill et al. (1994) were simulated on the relaxed $NM_{M50-Hill}$ model by applying flexion and extension moments (7 Nm and 6 Nm, respectively) to the rigid skull and assessing the rotation response of the head with the experimental data (Figures 76b and 76c).

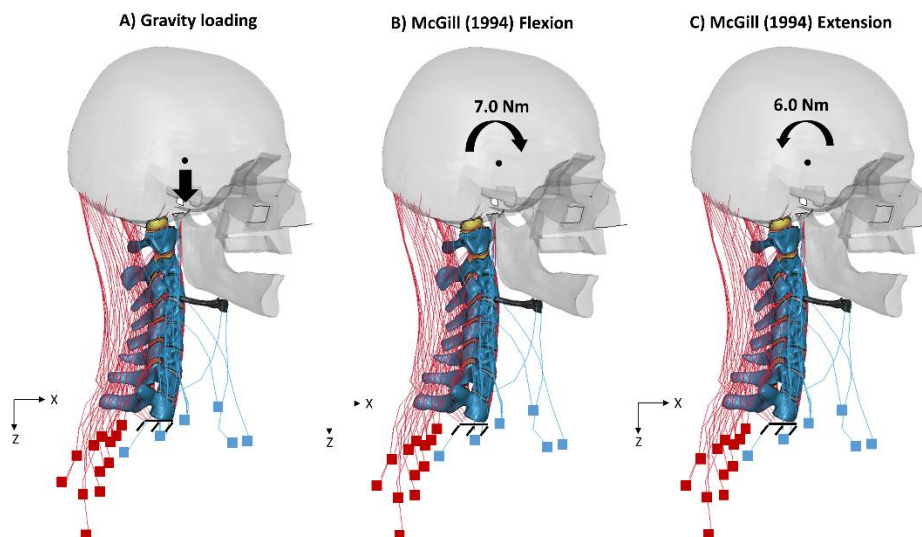


Figure 76: Illustrating the application of gravity loading (A), flexion moment (B) and extension moment (C) to the $NM_{M50-Hill}$ model with relaxed muscles ($a(t)=0$) in the CE of Hill-type muscle model.

Preliminary assessments on the passive $NM_{M50-Hill}$ model in physiologic conditions indicated a need for a biofidelic material property for the passive muscles (PEE). The property of the PEE in the $NM_{M50-Hill}$ model was updated with a recently reported material property from in vivo experiments on human gracilis muscles (Persad et al., 2021) (Figure 77). The improved model with the updated passive muscle property ($NM_{M50-Hill-E}$) was assessed for the conditions illustrated in Figure 76.

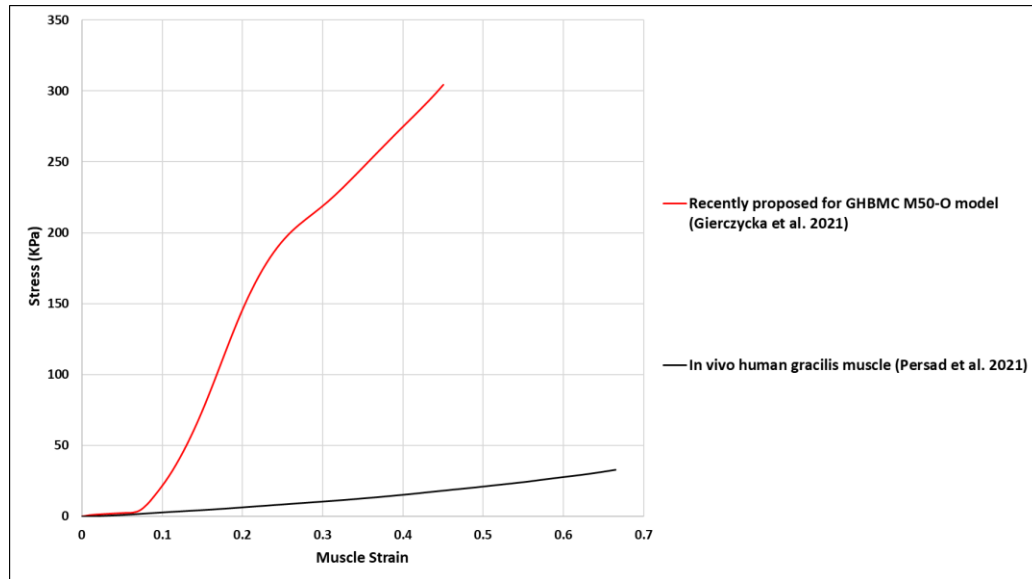


Figure 77: Enhancing the $NM_{M50-Hill}$ model by replacing the low strain rate ($0.01s^{-1}$) passive muscle property proposed by Gierczycka et al. (2021) with the in vivo physiologic property of human gracilis muscle reported by Persad et al. (2021).

3.3.6 Simulating head-neck flexion in the $NM_{M50-Hill-E}$ model using active muscles

To simulate the head-neck flexion using active muscles, the inferior ends of the muscles and the T1 vertebra were fully constrained, gravity was applied, and the CE (active muscle) was activated. The $NM_{M50-Hill-E}$, being a forward dynamic model, required pre-determined muscle activation levels for simulations. The muscles in the model were divided into two groups: flexors and extensors, which were activated and co-activated, respectively, using activation level parameters in the Hill-type muscle model (Millard et al., 2013; Panzer, 2006). The muscle activations, expressed as a percent of maximum voluntary contraction (% MVC), measured from in vivo experimental studies on voluntary physiologic head-neck flexion (Callaghan, 2014; Cazzola et al., 2017; Cheng et al., 2016; Kim and Jeong, 2020; Mahmood et al., 2021; Newell et al., 2018), were used to determine the activation levels for the flexors in the $NM_{M50-Hill-E}$ model. The mean value of the experimentally measured % MVC for flexor muscles from different studies in the literature (Callaghan, 2014; Cazzola et al., 2017; Cheng et al., 2016; Kim and Jeong, 2020; Mahmood et al., 2021; Newell et al., 2018) was calculated to be 10% of the MVC. The activation levels for simulating muscle contraction using the contractile elements in the Hill-type

muscle model were between 0 (no activation) to 1 (maximum activation), where one corresponded to 100% MVC (Arshad et al., 2022; Barrett et al., 2020; Cazzola et al., 2017; Storvik and Stemper, 2011). Hence, an activation level of 0.1, corresponding to 10% MVC, was applied to the flexor muscles.

Within the current study, the extensor co-contraction activation was iteratively determined to be 0.012, which resulted in the $NM_{M50-Hill-E}$ model repositioning in forward flexion with 30° head rotation (Figure 78). The identified muscle activation levels for the $NM_{M50-Hill-E}$ model were comparable to those in existing MSK neck models (0 to 0.15) that simulated physiologic conditions (Arshad et al., 2022; Barrett et al., 2020; Storvik and Stemper, 2011) (Figure 79).

The equilibrium of the model repositioned in 30° head flexion was verified using a free-body diagram (FBD). A section-plane was created that approximately sheered the mid-transverse section of the C7 vertebra. Other components that passed through that plane were also included in the plane. The resultant force and moment at the centroid of the C7 vertebra were calculated. In addition, angular velocities of the head and the cervical vertebrae were extracted to ensure equilibrium in the model.

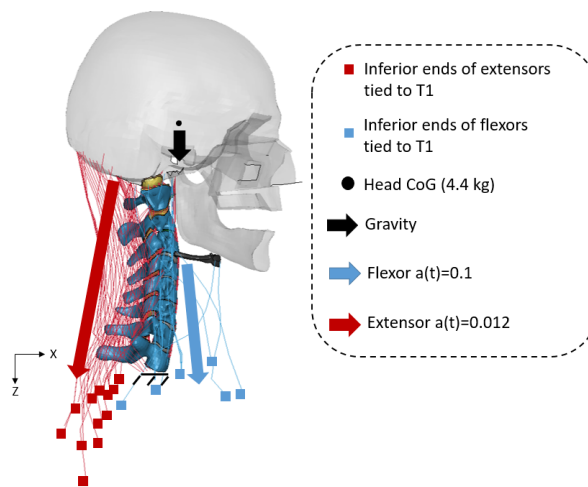


Figure 78: Repositioning the $NM_{M50-Hill-E}$ model by activating the flexors and co-activating the extensors under gravity. The activation levels resulted in the head flexing forward by approximately 30° .

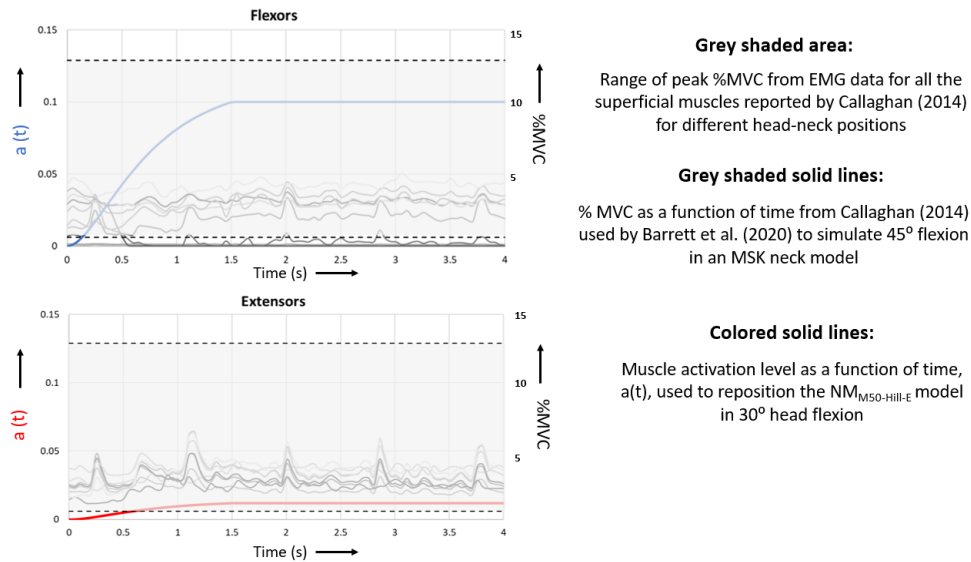


Figure 79: Muscle activation levels, $a(t)$, in the $NM_{M50-HIII-E}$ model corresponding to the %MVC levels for physiologic flexion from experimental data in the literature. The illustrated activation levels repositioned the $NM_{M50-HIII-E}$ model in 30° head flexion.

3.3.7 Simulating head-neck axial rotation in the $NM_{M50-HIII-E}$ model using active muscles

Next, a muscle-activation strategy was developed to reposition the model in axial rotation. The experimental measures of %MVC reported in the literature were referred to identify the muscle activation levels required to reposition the model in axial rotation. The literature comprised only a few experimental studies that reported the muscle activities during head and neck axial rotation without the HSM (Callaghan, 2014; Cazzola et al., 2017; Kim, 2015) and with the HSM (Callaghan, 2014; Healey, 2019; Netto and Burnett, 2006). The experimental studies reported the activities from a limited number of muscles which mostly included the superficial muscles such as SCM, levator scapulae and trapezius. Due to the limited information pertaining to the activities of deep muscles during axial rotation of the head and neck, an iterative study was performed to identify the effect of each muscle group on the behaviour of the head and neck.

To simulate a right-sided axial rotation in the $NM_{M50-HIII-E}$ model, the contralateral SCM, ipsilateral trapezius and ipsilateral levator scapulae were stimulated at an activation level of 0.2, an approximate value identified from the literature, under gravity loading (Cazzola et al., 2017; Kim, 2015). Activating these muscles in the model resulted in the sagittal and coronal motion of the head (combined extension

and lateral bend) and negligible axial rotation, attributed to the lack of rotation of the C1 vertebra relative to the C2 vertebra.

In vivo, head and neck axial rotation demonstrated that a majority of the rotation ($\approx 70\%$) occurred at the C1-C2 level along with some amount of coupled motion in flexion/extension ($\approx 10\%$) and lateral bending ($\approx 35\%$) (Anderst et al., 2016). Activating a limited group of superficial muscles did not allow the NM_{M50-Hill-E} model to reposition to the desired axially rotated position, per the literature.

A preliminary study on the NM_{M50-Hill-E} model identified that two of the four sub-occipital muscles (rectus capitis major and oblique capitis inferior), unilaterally activated together, majorly contributed to the axial rotation of C1 relative to C2. The point of attachments and the line of muscle action (mediolateral oblique direction) in the rectus capitis major, and the oblique capitis inferior muscles enabled the axial rotation in the upper cervical spine. Activation of the mentioned sub-occipital muscles unilaterally, i.e., contracting the right side while deactivating the left side or vice versa, enabled an ipsilateral rotation (side of the activated muscles) of the skull and C1 vertebra around the odontoid process of the C2 vertebra. Simultaneously, the extensor muscles were co-contracted to prevent the head and the lower cervical spine from flexing due to the presence of gravity loading. Based on multiple iterations, it was identified that co-contracting the superficial extensor muscles resulted in over-extension of the neck (due to higher moment-arm) instead of stabilizing the head and neck in a neutral position. In summary, the unilateral contraction of the upper neck muscles and co-contraction of the extensors resulted in the model repositioning in approximately 30° axial rotation, which was considered to be within the full ROM (Anderst et al., 2015; Guo et al., 2021).

The muscle activation levels and their relationship with respect to time had to be determined iteratively due to the lack of sufficient details in the literature pertaining to deep neck muscle activities during the in vivo head-neck axial rotation. Identifying the activation levels using an optimization algorithm could be technically robust compared to a manual iterative method. However, there were challenges, including the involvement of multiple muscles, lack of insight into the activation levels in relationship with time and lack of details on activities of deeper neck muscles in the axial rotation position. Due to these challenges, manual intervention was necessary to gain insight into the contribution of each group of muscles to pre-determine the muscle activation levels required to reposition the head-neck model in axial rotation.

The average activation level in all the muscles required to reposition the model was 0.3. An activation level of 1.0 for the ipsilateral rectus capitis major and oblique capitis inferior muscles along with an activation of 0.2 for the contralateral rectus capitis major and oblique capitis inferior muscles, enabled the head to rotate 30° axially. Unlike flexion, where a group of flexors activated along the line of gravity, axial rotation involved only two muscles, the activation of which produced force in a direction nearly perpendicular to the line of action of gravity to rotate the head and C1 relative to C2, resulting in an unrealistically high activation level. Also, due to a relatively lower moment arm for the rectus capitis superior and oblique capitis inferior muscles, a higher activation level was required to generate sufficient force in an oblique direction against the 43 N force generated by the head under gravity in the caudal direction, to prevent the downward displacement of the head. All the flexors, excluding the contralateral SCM, had zero activation to reduce the head from flexion under the gravitational load. Similarly, the multifidus muscle (a deep extensor) activated at 0.25 prevented the neck from flexing under gravity. The superficial extensor muscles and a couple of deep extensor muscles (Semi splenius cervicis and longissimus cervicis) were activated at 0.02 to avoid over-extension of the head (Figure 80). The equilibrium of the repositioned model was verified using an FBD and angular velocities, as described in the previous section (Section 3.3.6).

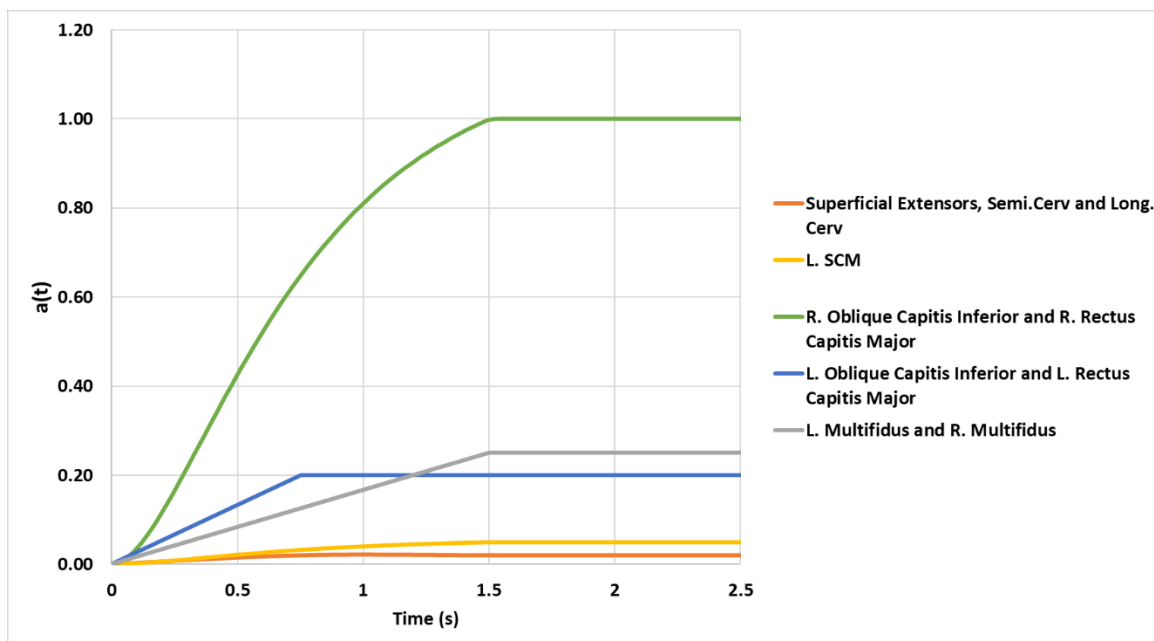


Figure 80: Muscle activation levels, $a(t)$, to reposition the $NM_{M50-HIII-E}$ model in 30° axial rotation position within the physiologic ROM, identified in this study based on multiple iterations.

3.4 Phase #2b: Quantifying the importance of active muscle repositioning using kinematic, kinetic and tissue-level responses

From Phase #2a, the novel muscle-based approach was adopted to reposition the FE head-neck model (NM_{M50-Hill-E}) to closely mimic the in vivo phenomena because conventional external BC approach resembled the in vitro experimental procedure to simulate physiologic ROMs. It was assumed that the repositioning approach could influence the model response based on the noted differences between in vitro and in vivo physiologic ROMs from the literature (Section 2.3). Hence, it was necessary to verify if the approaches adopted to reposition FE head-neck model had any effect on the biomechanical outcomes. Also, to date, there has been no formal study in the literature that investigated the influence of repositioning approaches on the model response outcome. Phase #2b included repositioning the NM_{M50-Hill-E} model from a neutral posture to 30° head flexion and 30° head axial rotation using a conventional external BC method. The results from the two repositioning approaches were compared based on head and neck kinematics, IVD forces and deformation, and ligament distractions. Lastly, the model results were quantitatively compared to an MSK model and experimental human volunteer data from the literature to assess the importance active muscle repositioning (Hadagali et al., 2024).

The NM_{M50-Hill-E} model was repositioned in flexion and axial rotation using a conventional external BC method as described in the literature (Shateri and Cronin, 2015). The external BC-based method of repositioning involved turning off the active component (CE) in the Hill-type model ($a(t) = 0$), constraining the T1 vertebra and the inferior ends of muscle element and applying an appropriate external moment to the skull to achieve the desired position. The NM_{M50-Hill-E} model required a moment of 2.6 Nm and 0.8 Nm to achieve the desired 30° flexion and 30° axially rotated head position, respectively (Figures 81 and 82). The follower load representing the head and neck muscles was not considered in the head-neck model reported by Shateri and Cronin (2015). To be consistent with Shateri and Cronin (2015) methodology, the NM_{M50-Hill-E} model repositioned using the external BC did not include the follower load. The responses from the models repositioned in flexion and axial rotation, using the external BC- and muscle-based (from Phase #2a) approaches, were compared (Hadagali et al., 2024).

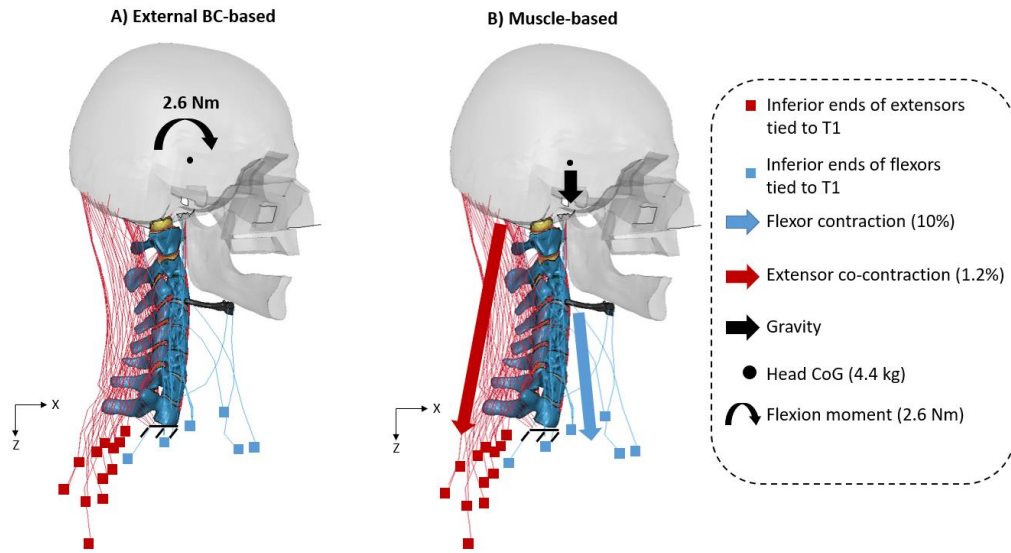


Figure 81: Repositioning the $NM_{M50-Hill-E}$ model in 30° flexion using two approaches. A) An external BC (moment) is applied to the head of the passive $NM_{M50-Hill-E}$ model, and B) as described in Phase #2a, flexors and extensors are activated at 0.1 and 0.012 activation levels, respectively, under gravity.

[Adapted from Hadagali et al. (2024)]

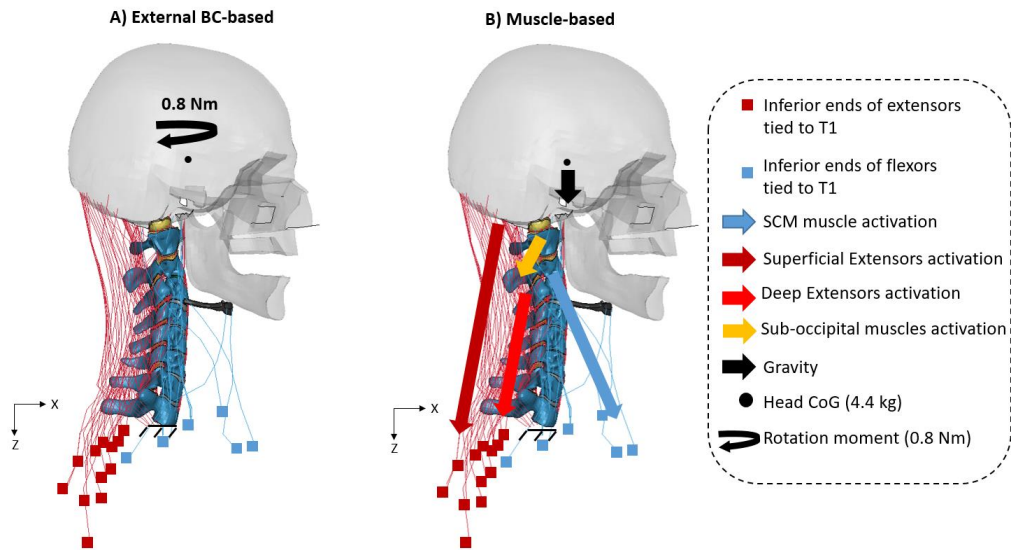


Figure 82: Repositioning the $NM_{M50-Hill-E}$ model in 30° axial rotation using two approaches. A) An external BC (moment) is applied to the head of the passive $NM_{M50-Hill-E}$ model, and B) as described in Phase #2a, different muscle groups are activated under gravity.

The response of the $NM_{M50-Hill-E}$ model repositioned using different approaches was assessed at the global and tissue-level starting from the global kinematics to strains in the AF collagen fibers. As one of the objectives of this research was to simulate non-neutral head-neck positions assumed by the live humans (including the RWA), the kinematic response of the model was assessed with the in vivo experimental data from the literature.

3.4.1 Global kinematics of the head-neck

An experimental study that measured different kinematic parameters while volunteers rotated their heads in 30° flexion while interacting with a hand-held device (Tapanya et al., 2021) was used to evaluate the response of the model repositioned using both methods (Figure 83). The experiments considered a point on the skin at the location of the C7 spinous process as a reference point to measure the kinematic parameters. The C7 reference point in the current study was obtained from the NM_{M50} model, which included detailed passive tissues (Barker and Cronin, 2021), and applied to the $NM_{M50-Hill-E}$ model for measurement purposes. The angle between the line connecting the C7 reference with the tragus and the horizontal line originating from the C7 reference was considered the craniovertebral (CV) angle. The horizontal distance between the vertical lines originating from the C7 reference and the tragus was measured to obtain the forward head distance (FHD). The gravitational moment arm (GMA) was measured as the horizontal distance between the vertical lines originating from the head CoG and the C7-T1 joint (Guan et al., 2015; Tapanya et al., 2021; Torkamani et al., 2023). The percent error between the experimental mean recorded at 30° head flexion and the model response was quantified for model assessment (Equation 3.1). The percentage change was calculated to assess if the kinematic response increased or decreased in the model repositioned using active muscle relative to the model repositioned using external BC (Equation 3.4).

$$\% \text{ Change} = \frac{\text{Active Muscle Response} - \text{External BC Response}}{\text{External BC Response}} * 100 \quad (\text{Equation 3.4})$$

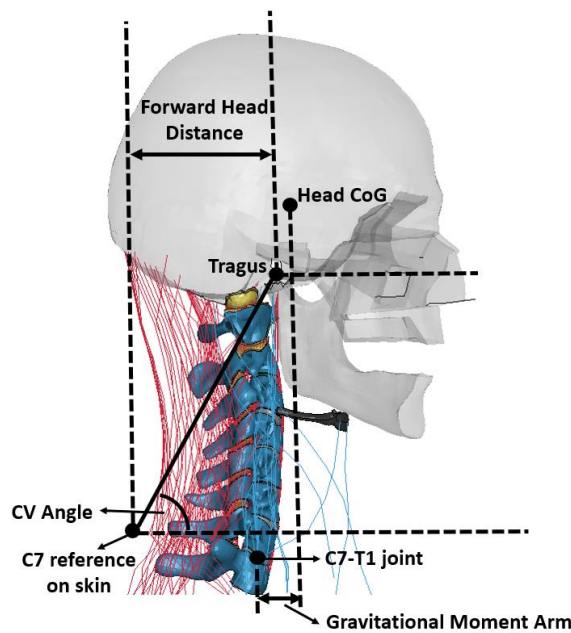


Figure 83: Illustration of the head and neck kinematic measurement methods in the $NM_{M50-HIII-E}$ model as described in the literature (Tapanya et al., 2021).

[Taken from Hadagali et al. (2024)]

An in vivo experimental study that measured the C0-C2 and C2-T1 axial rotations as the volunteers rotated their heads from neutral posture to a full axially rotated position (Guo et al., 2021) was used to assess the response of the model repositioned using both methods. The axial rotation response of C0-C2 and C2-T1 were extracted from the model repositioned in 30° head axial rotation using both the methods. The model response was assessed with the experimental mean reported for C0-C2 and C2-T1 axial rotation that corresponded to 30° head axial rotation. Similarly, the model response was assessed with the experimental mean reported for C2-T1 coupled lateral bending that corresponded to 30° head axial rotation. The percent error between the experimental mean and the model response was quantified for model assessment (Equation 3.1). The percentage change was calculated to assess if the kinematic response increased or decreased in the model repositioned using muscle-based method relative to the model repositioned using external BC-based method (Equation 3.4).

3.4.2 Intervertebral kinematics

The intervertebral rotations resulting from 30° head rotation in flexion from the two repositioning methods were assessed with the values predicted by the cervical spine predictor (CSP) tool (Reed and Jones, 2017) for the same amount of head rotation. The CSP tool was used due to a lack of experimental data on the intervertebral responses in flexion in any specific intermediate positions, such as 30° head rotation. The CSP tool predicted the vertebral rotations for C2 to C7 vertebrae relative to the T1 vertebra for the specified 30° head rotation in flexion, from which the intervertebral rotations were calculated and used for model assessment. The percent error between the mean rotation predicted by the CSP and the model response, based on equation 3.1, was quantified for model assessment. The percentage change was calculated to assess if the ROM response increased or decreased in the model repositioned using active muscle relative to the external BC condition, based on equation 3.2. The percentage change between the anterior translation of the intervertebral (C2–C3 to C7–T1) levels resulting from the two repositioning methods in flexion were also assessed.

There was no report of the intervertebral axial rotation within the ROM (such as 30° head rotation) in the experimental study by Guo et al. (2021) or any other study in the literature and hence, the assessment was limited to global kinematics. The CSP tool that was used to predict the intervertebral kinematic responses at specific intermediate positions was limited to flexion and extension and could not be used for axial rotation assessments.

3.4.3 Ligament distractions

To measure the ligament distractions, the length of the ligament in the initial neutral position was subtracted from the flexed position length (Figure 84). The ligament distraction responses were assessed using the experimental force-distraction response from isolated ligament specimens reported in the literature (Mattucci et al., 2012). Differences in the ligament distraction were assessed in the model repositioned using active muscle relative to the model repositioned using external BC.

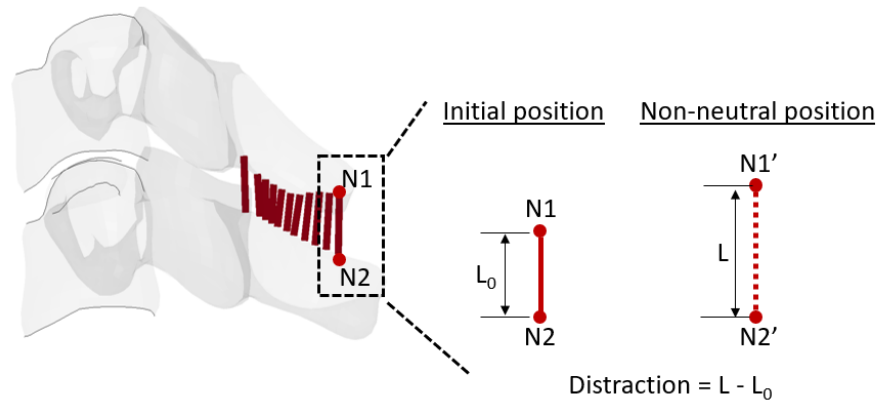


Figure 84: Illustrating the method to measure the ligament distractions in the $NM_{M50-Hill-E}$ model.

3.4.4 Muscle force

The section-plane that approximately sheered the mid-transverse section of the C7 vertebra, previously described in Phase #2a to verify the model equilibrium, was used to measure the flexor and extensor muscle force at the C7 level. Similar section-planes were created for C2 to C6 vertebrae to measure the muscle forces at the corresponding levels. The section-plane measured the muscle forces along the three primary axes from which the resultant force was calculated. The total muscle force (combining flexors and extensors) at each vertebral level in the repositioned models were compared with the experimental and numerical studies that replicated the in vivo muscles by the means of an externally applied compressive follower load. The follower load has been assumed to be uniform across the spinal column, with a majority of the experimental and numerical studies reporting the value of follower load to be between 50 N to 150 N (Barrey et al., 2015; X.-Y. Cai et al., 2020b; X. Cai et al., 2020; Palepu, 2013; Patwardhan et al., 2000; Wawrose et al., 2021; Zhang et al., 2023). The percentage change in the muscle force from the model repositioned using the external BC-based method to the muscle-based method was quantified.

3.4.5 IVD deformation

The deformation of the IVDs was measured in the anterior, middle and posterior aspects of the mid-sagittal section of the IVD tissue as described in the literature (Ito et al., 2005). The procedure comprised of measuring the horizontal and vertical displacements at the points A' (posterior), B' (middle) and C' (anterior) on the superior aspect of the IVD with respect to the corresponding points

A'', B'' and C'', respectively, on the inferior aspect of the IVD. To measure the deformation angle, the arctan of the ratio of horizontal displacement to the final disc height at the anterior, middle and posterior aspects was calculated (Figure 85). The IVD deformation in the literature has been reported for cadaveric cervical spine specimens (in vitro experiment) (Ito et al., 2005), and there is a lack of such data from in vivo experiments. Hence, the response from the repositioned models could not be directly assessed with in vivo data from the literature. However, the experimental data from the in vitro study (Ito et al., 2005) was used to verify if the IVD deformation response in the model was within the physiologic range. Differences in deformation from the model repositioned using the external BC method to the active muscle method were quantified. The IVD deformation was not assessed in the model repositioned in 30° axial rotation due to the limited anterior displacement of the LCS in this non-neutral position.

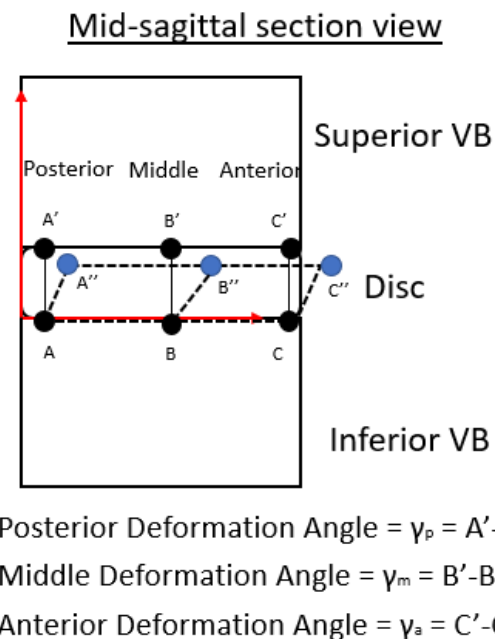


Figure 85: An illustration of the IVD global deformation measurement procedure as described in the literature (Ito et al. 2005).

[Taken from Hadagali et al. (2024)]

3.4.6 IVD force

The IVD forces (compressive and AP shear) when the head was rotated 30° in flexion were assessed at the C2-C3 to C7-T1 in both the repositioned models (Figure 86). Due to the lack of in vivo experimental IVD force data, the magnitude and the trends of the predicted compressive and shear force response across IVD levels were compared with the forces predicted by an existing MSK neck model (Barrett et al., 2020) that simulated in vivo head flexion. The percentage change in force from the model repositioned using the external BC method to the active muscle method was quantified.

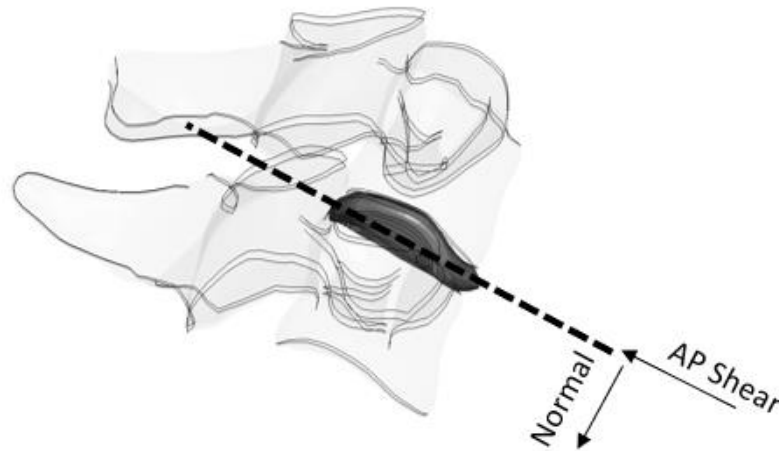


Figure 86: Illustrates the IVD force measurement using section plane in LS-Prepost when the $NM_{M50-Hill-E}$ model was repositioned in a non-neutral position. The compressive forces were measured in the direction normal to the section plane. During measurement, all other components except the IVDs were masked.

3.4.7 Collagen fiber strains in the AF

The strains were measured along the orientation of the collagen fibers in the AF (Figure 87). The results were compared with experiments that reported fiber failure strains along the fiber orientation on isolated fiber specimens in vitro (Holzapfel et al., 2005; Isaacs, 2012; Pezowicz, 2010). The percentage change in AF collagen fiber strain from the model repositioned using the external BC-based method to the muscle-based method was quantified.

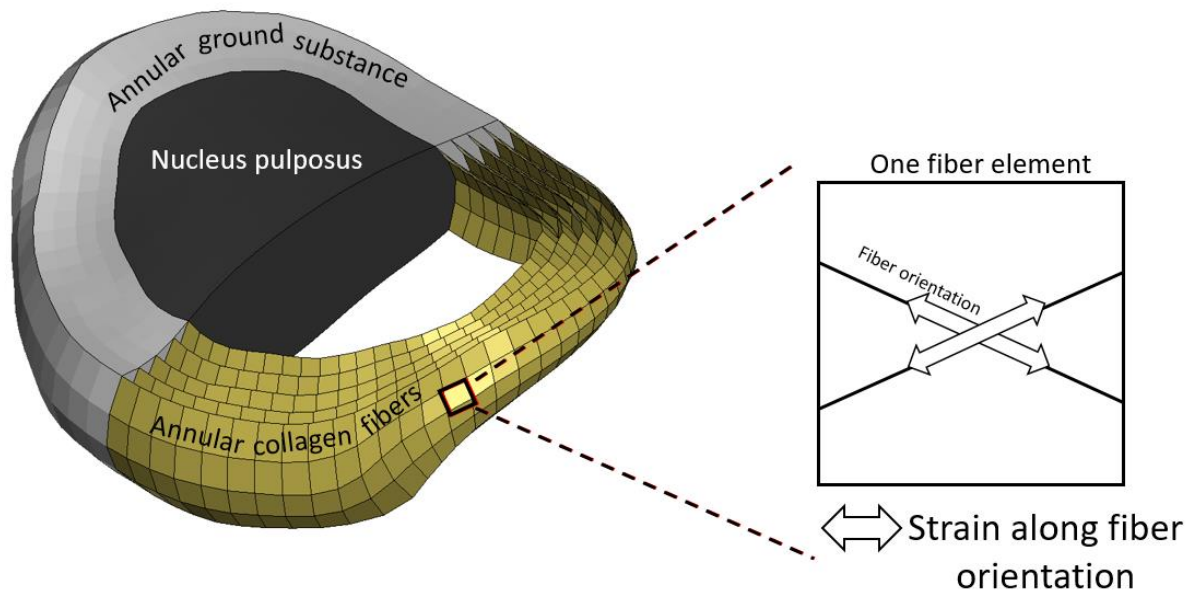


Figure 87: Illustration of the fiber orientation in the AF collagen fibers, along which the strains were measured and compared with the experimental data that reported strains along the fiber orientation on isolated fiber specimens.

[Adapted from Hadagali et al. (2024)]

3.5 Phase #3: Neck pain risk in rotary-wing aircrew (RWA)

3.5.1 Simulating the HSM relevant to RWA

The verified and validated $NM_{M50-Hill-E}$ model was used to assess the risk of neck pain in the RWA due to HSM and non-neutral head-neck positions. The HSM configurations included 1) *Head + Helmet (HH)* and 2) *Head + Helmet + NVG + CW (HHNC)*. The NVG property was inclusive of the BP. The mass and the inertial properties obtained from HGU/56P RWA helmet for the configurations above (HH and HHNC) were assigned along with the head properties (Bulger, 2019; Healey, 2019). The head and helmet masses were 4.4 kg and 1.3 kg, respectively. The NVG (inclusive of BP) and an external CW had a collective mass of 1.42 kg (Figure 88). The location of the CoG for the two HSM configurations relative to the CoG of the head was reported by Forde (Forde et al., 2011) (Figure 89). Simulating the HSM configurations included placing a node with mass and inertial properties tied to the rigid skull at the location reported by Forde et al. (2011) relative to the head CoG.

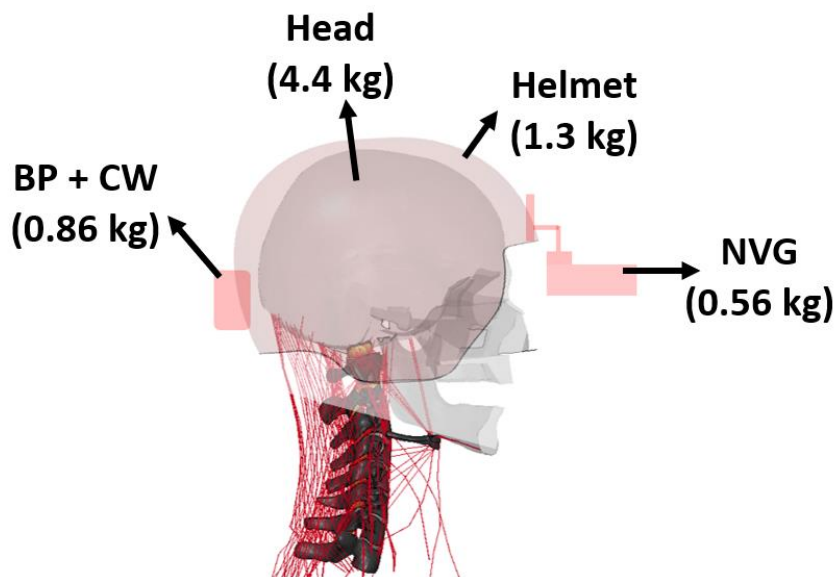


Figure 88: Illustrating the mass properties of the head and the HGU/56P RWA HSM that include the helmet, NVG, BP and CW.

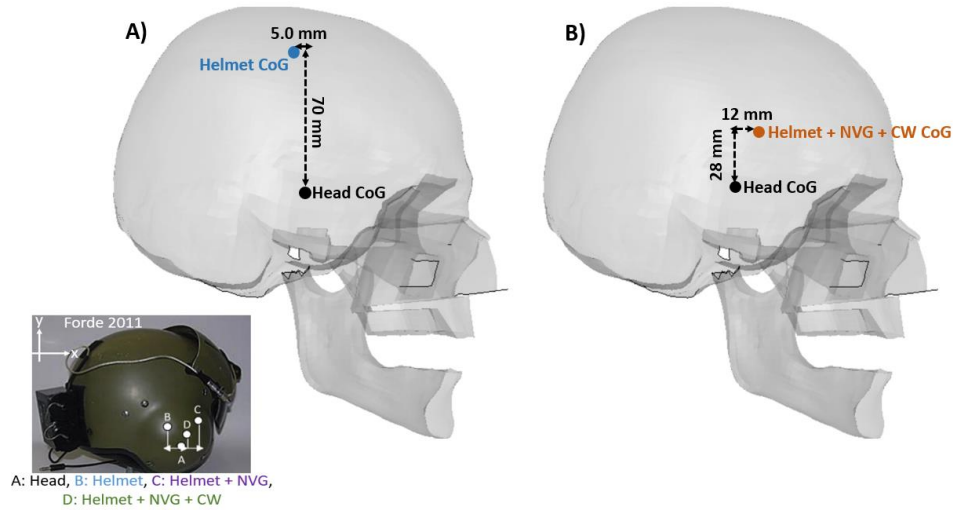


Figure 89: Illustrating the CoG locations for the helmet (A) and helmet with NVG (BP inclusive) and CW (B) relative to the CoG of the head as reported by Forde et al. (2011). The image of the RWA helmet in the inset is adapted from Forde et al. (2011).

3.5.2 Identifying the target non-neutral head-neck positions from the literature

The RWA performed multiple scanning tasks (12-22 tasks) that required repositioning the head-neck in various non-neutral positions (Tack et al., 2014). The non-neutral head-neck position during each scanning task was a combination of flexion/extension, axial rotation and lateral bending (around the three primary axes) (Forde et al., 2011; Tack et al., 2014). For example, during a night mission, in the AC-egress task that lasted 30.4 seconds, flying pilots on an average flexed 31.9° , extended 10.3° , rotated 19.5° to the left, rotated 12.5° to the right, laterally bent 9.8° to the left and right over the entire timeframe (Tack et al., 2014). Simulating non-neutral head-neck positions for each scanning task using the FE neck model was not a feasible option to focus on the effect of individual factors (i.e. HSM, head-neck deviation, etc.) on the neck pain owing to the dynamic changes in head-neck positions. In addition, simulating a lengthy physiologic task (lasting over 2 s) using a detailed FE model using a forward-dynamic approach could be computationally demanding. Hence, there was a requirement to identify a specific non-neutral position representative of the RWA scanning task to simulate using the FE neck model (NM_{M50-Hill-E}). The head-neck angles (around the three principal axes) for every non-neutral position assumed by the flying pilots, non-flying pilots and flight engineers (RWA sub-categories) were reported in the literature (Tack et al., 2014). A mean of the head-neck angle around the three principal

axes adapted by the flying pilots across all the tasks was calculated from the literature (Figure 90). The calculated mean of the head-neck angles was concurrent with the reported majority of time spent by the RWA in non-neutral positions (i.e. 10°-30° flexion, 0°-15° lateral bending and 10°-40° axial rotation) (Forde et al., 2011; Tack et al., 2014). Muscle-based repositioning method (Section 3.3.6) was used to simulate a flexion-only position (with and without the HSM) and a combined position (with the HSM) using the $NM_{M50-Hill-E}$ model.

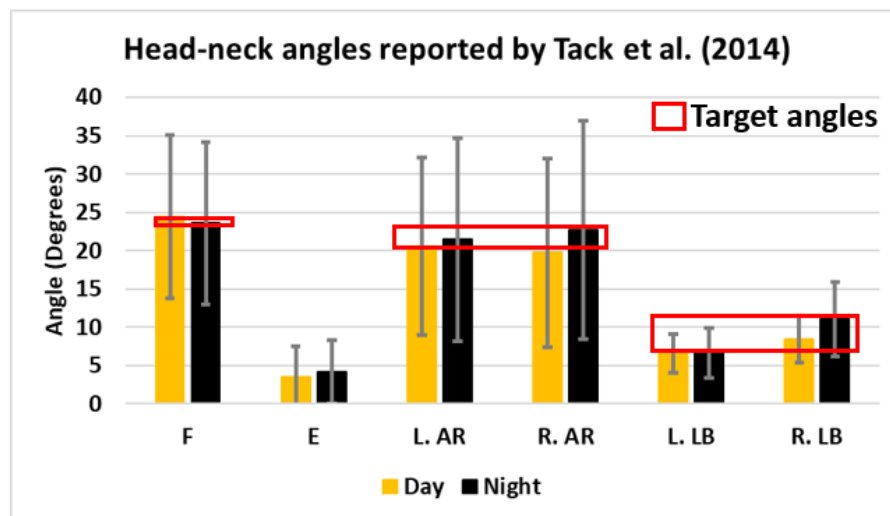


Figure 90: Reported head-neck angles in non-neutral positions adapted by the flying pilots (a sub-category of the RWA) that were investigated in this research. F: Flexion, E: Extension, AR: Axial rotation, LB: Lateral bending, L: Left and R: Right.

3.5.3 Methodology to measure the RWA head-neck angles

The method to measure the head-neck angle (θ) in the repositioned $NM_{M50-Hill-E}$ model in the sagittal and coronal planes for flexion (θ_f) and lateral bending (θ_{lb}), respectively, were consistent with the method reported in the literature (Tack et al., 2014). First, the vertical height of the head and neck from the base (T1) to the head CoG was measured in the neutral position. Next, the linear translations of the head CoG in the neck models were measured. The neutral vertical height and the translation of head CoG in vertical and horizontal directions after repositioning were used to calculate the head-neck angle. First, the difference between the neutral vertical height and the vertical translation value was calculated to get the final vertical height. Next, the horizontal translation value was divided by the final vertical height to get a ratio. The head-neck angle (θ_f and θ_{lb}) was then identified by calculating the arctan of

the ratio (Figure 91). The angular displacement of the head was used to measure the head axial rotation (θ_{ar}) in the $NM_{M50-Hill-E}$ model that simulated a combined position.

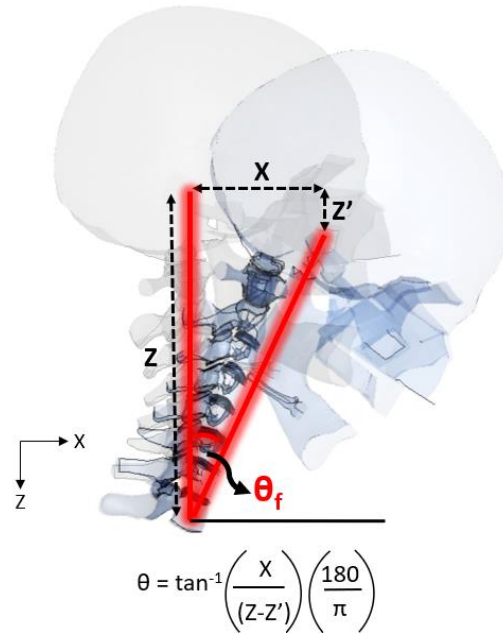


Figure 91: An illustration of the head-neck angle (θ_f) measurement in the sagittal plane (flexion), as described in the literature (Tack et al., 2014). This method of measurement was also applicable to measure the head-neck angle (θ_{lb}) in the coronal plane (lateral bending).

3.5.4 Simulating a flexion position with and without the HSM

The $NM_{M50-Hill-E}$ without the HSM (only head: 'H') and with the HSM (HH and HHNC) was repositioned in flexion (target $\theta_f=25^\circ$) using the muscle-based repositioning approach. A total of three flexion cases for different helmet configurations were simulated: 1) H_{25F} , 2) HH_{25F} , and 3) $HHNC_{25F}$ (Figure 92). The HH_{25F} case represented an RWA scanning task during the day mission when the NVG and CW were not mounted on the helmet. The $HHNC_{25F}$ case represented an RWA scanning task during the night mission. For the H_{25F} case, the model flexed at 24.2° at an activation level of 0.12 and 0.01 for the flexors and extensors, respectively. For the HH_{25F} case, the model flexed at 24.2° as well. The flexor activity was slightly reduced in comparison with the H_{25F} case, requiring an activation level of

0.1. The extensor muscles required an activation level of 0.043 to hold the head and neck with the helmet in the desired position. For the HHNC_{25F} case, the model flexed at 24.7°, with the flexors and extensors activated at 0.12 and 0.075, respectively. The NM_{M50-Hill-E} model with and without the HSM could achieve the head-neck flexion angle (θ) within 5% of the target angle 25° (i.e. 23.6° to 26.3°). The flexors to extensors activation ratio reduced from 12 in H_{25F} to 2.3 in HH_{25F} and 1.6 in HHNC_{25F} to compensate for the increasing HSM and increasing CoG distance relatively anterior to the spinal column.

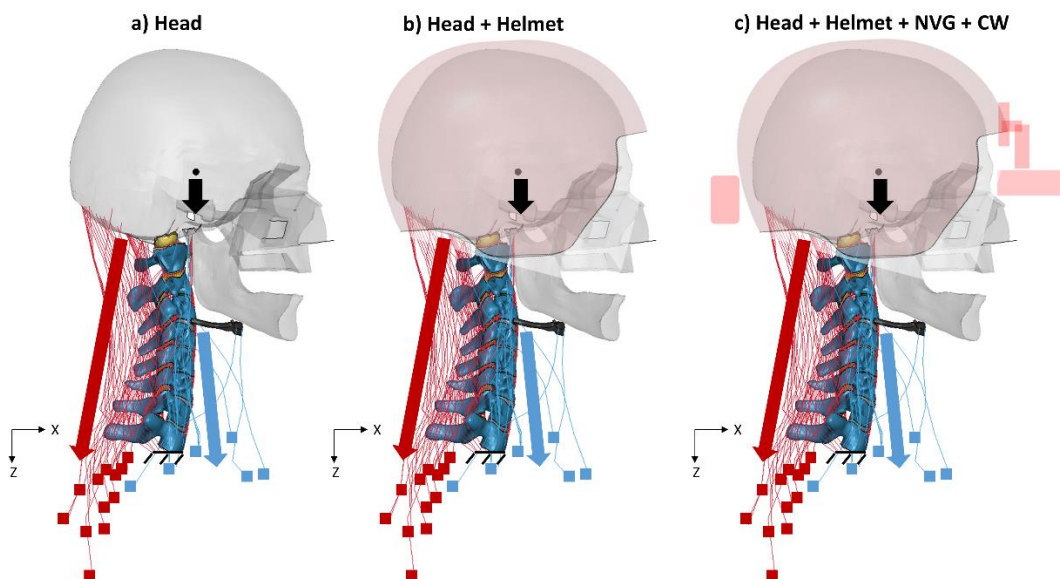


Figure 92: Illustration of the muscle-based methodology to reposition the validated NM_{M50 Hill-E} model without (a) and with the HSM (b and c) in 25°±5% head-neck flexion to assess the effect of HSM on the tissue-level response and associate the risk of neck pain in RWA.

3.5.5 Simulating a combined position with the HSM (HHNC configuration)

The model with the simulated HSM configuration (HHNC) was simulated for a combined position that included flexion (target $\theta_f=25^\circ$), lateral bend (target $\theta_{lb}=6^\circ$ to 10°) and axial rotation (target $\theta_{ar}=20^\circ$ to 25°) (HHNC_{25F|10LB|25AR}), mimicking the head-neck position adapted by the RWA. The target head-neck position investigated in this research was based on the calculated mean value from the literature for different RWA tasks (Tack et al., 2014) (Figure 90). The HHNC_{25F|10LB|25AR} case represented an increase in the magnitude of head-neck position relative to the HHNC_{25F} case due to the restricted FOV as a result of NVG in the RWA. The muscle activation strategy used in the NM_{M50-Hill-E} without HSM

to reposition the model in axial rotation (Phase #2a) was used as a reference to simulate the $HHNC_{25F|10LB|25AR}$ case. Multiple iterations were performed to identify a strategy to simulate the target head-neck position using the $NM_{M50-Hill-E}$ model.

Activation of the ipsilateral oblique capitis inferior and the rectus capitis major muscles enabled the axial rotation of the head, based on the findings from Phase #2a. Activation of the ipsilateral scalene and infrahyoid muscles along with a relatively lesser activation of the contralateral extensors, resulted in the oblique flexion of the head-neck with a coupled lateral bend. The co-contraction of the contralateral SCM, left oblique capitis inferior and rectus capitis major muscles prevented the head from axially rotating beyond the target 25° . The co-contraction of the ipsilateral extensor muscles prevented the head-neck from overly flexing beyond the target position (Figure 93). The head-neck with the simulated HSM (HHNC configuration) resulted in flexing 25° , laterally bending 8° and axially rotating 23.5° based on the identified activation levels.

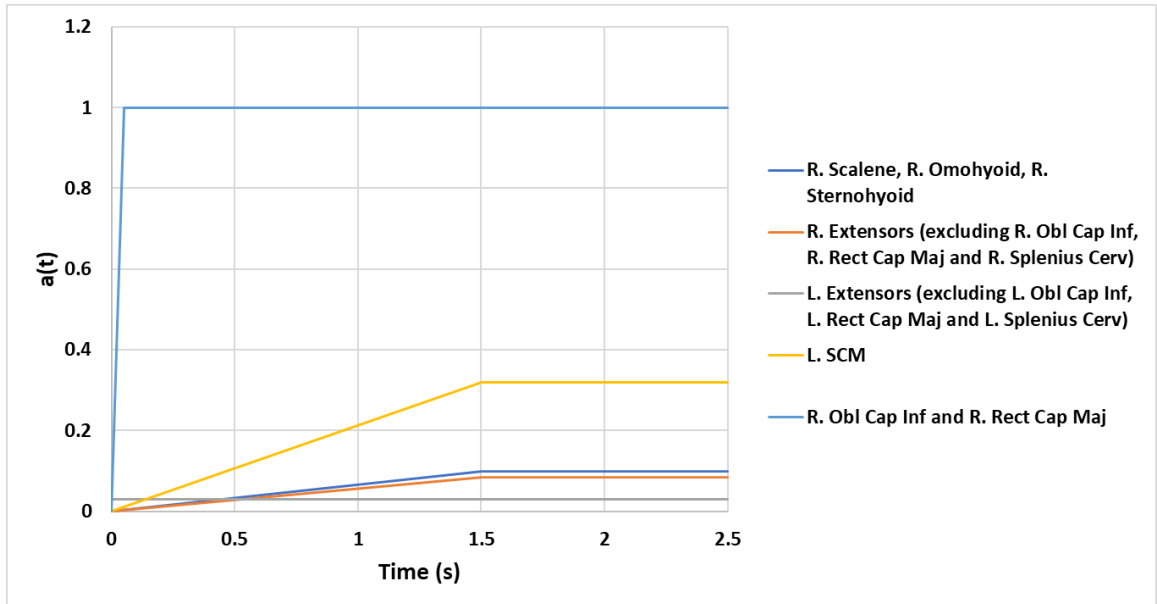


Figure 93: Muscle activation strategy describing the activation levels applied to different muscles to reposition the $NM_{M50-Hill-E}$ model with the helmet, NVG and CW in a combined flexion, lateral bending and axial rotation position to mimic the RWA task ($HHNC_{25F|10LB|25AR}$).

3.5.6 Neck pain assessments using tissue-level responses

The potential for neck pain was based on the predicted tissue response from the head-neck model, which was simulated for non-neutral positions with and without the HSM. The responses from the innervated tissues that were identified to be potential sources of neck pain were used as implications to assess the risk of neck pain in RWA. The innervated tissues that were investigated included the muscles, cervical spine ligaments, IVDs and vertebral endplates (Adams and Dolan, 2012; Bogduk, 2003; Byeon et al., 2013; Harrison et al., 2015; Healey, 2019; Jaumard et al., 2011; Panjabi, 2006; Peng and Bogduk, 2019; Rajasekaran et al., 2013; SJØGAARD et al., 1986). Vertebrae and spinal cord, although innervated and identified to be potential sources of neck pain, were not investigated as bony fractures and spinal cord injuries were less likely in the RWA (Aydoğ et al., 2004; Byeon et al., 2013). The H_{25F} case was considered a baseline to compare the tissue-level responses in the HH_{25F} and $HHNC_{25F}$ cases to assess the effect of HSM in 25° head-neck flexion. Similarly, the $HHNC_{25F}$ case was considered a baseline to compare the kinematic, kinetic and tissue-level responses in the $HHNC_{25F|10LB|25AR}$ case to assess the effect of non-neutral head-neck position magnitude with the inclusion of HSM ($HHNC$ configuration) on the risk of neck pain in RWA (Figure 94).

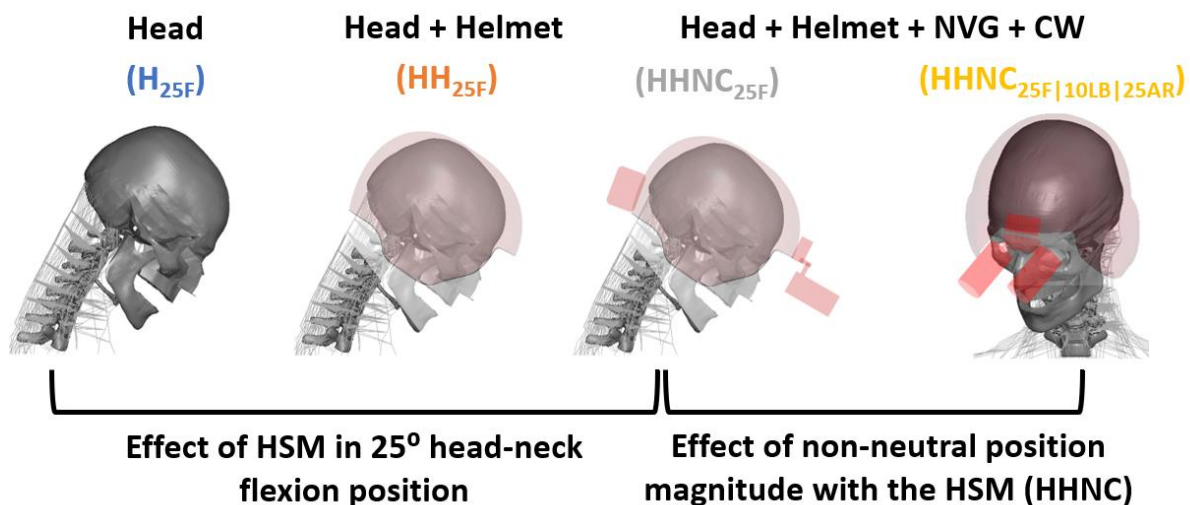


Figure 94: Pictorial representation of the four simulated cases relevant to the RWA and the comparisons made to understand the effect of added HSM and magnitude of head-neck positions on the risk of neck pain in the RWA.

The global head rotation, as well as intervertebral rotations, were compared between the H_{25F} , HH_{25F} and $HHNC_{25F}$ cases to ensure consistency toward understanding the interaction of HSM on the tissue-level response and also confirm if the responses were within the physiologic range. Similarly, the kinematic response between the $HHNC_{25F}$ and $HHNC_{25F|10LB|25AR}$ cases was also compared at the global and intervertebral levels to confirm if the responses were within the physiologic range. The simulated 4 cases were also verified for equilibrium using the FBD procedure described in Phase #2.

In the RWA, during missions, an increase in the muscular demand due to the added HSM and prolonged activity of the muscles has been associated with the risk of neck pain (Harrison et al., 2015; Healey, 2019; Healey et al., 2021; O’Conor et al., 2020). In the current study, increases in muscle forces were considered as indicators for increased muscular demand and, thereby, a potential risk of neck pain. Flexor and extensor muscle forces across C2 to C7 vertebrae were extracted as described in section 3.4.4. The forces exhibited by the muscles have not been reported to date from the experimental studies. However, the muscle forces reported in a few neck modelling studies in physiologic neutral neck positions were used for model assessment and comparison (Dibb et al., 2013). The percentage change in muscle force due to added HSM (HH_{25F} and $HHNC_{25F}$) relative to the H_{25F} case was quantified. Similarly, the percentage change in muscle force due to a deviated position ($HHNC_{25F|10LB|25AR}$ relative to $HHNC_{25F}$) was quantified.

In the RWA, the increase in mechanical load on the neck due to the usage of HSM in addition to non-neutral head-neck positions has been flagged as a risk factor for neck pain (Chafé and Farrell, 2016; Karakolis et al., 2015; Thuresson et al., 2005, 2003). In the current study, an increase in IVD forces was considered as an indicator of a potential risk of neck pain, as considered in existing neck and lower spine models (Barrett et al., 2022b, 2020; Mesfar and Moglo, 2012; Rossman et al., 2022). The compressive and shear forces in the C2-C3 to C7-T1 IVDs were extracted, and the percentage change in force due to added HSM (HH_{25F} and $HHNC_{25F}$) relative to the H_{25F} case was quantified. Similarly, the percentage change in IVD force due to a deviated position ($HHNC_{25F|10LB|25AR}$ relative to $HHNC_{25F}$) was quantified.

Epidemiological studies reported a higher incidence of ambulatory visits in the RWA population for cervical spine IVD degenerative disease requiring surgical intervention (Madison et al., 2023). Also, a magnetic resonance imaging (MRI) study reported incidences of IVD degeneration in 5 out of 10 RWA that were investigated (Landau et al., 2006). In the current study, an increase in the collagen fiber strains

in the AF was considered an indicator of the potential risk of tears and, eventually, the risk of degeneration in the IVDs. The strains were measured along the orientation of the collagen fibers, as described in Figure 87, and the percentage change due to HSM and non-neutral position magnitude was quantified.

Radiographic and MRI studies have reported a higher incidence of degenerative changes such as osteoarthritis and IVDs, respectively, in the cervical spine of the RWA population, which has been associated with the risk of neck pain (Aydoğ et al., 2004; Byeon et al., 2013; Landau et al., 2006). Based on existing FE neck models in the literature, the current study considered the increase in effective stresses in the vertebral endplates as an indicator of potential risk of endplate defects that can lead to degenerative changes in the spine (Adam et al., 2003; Jia et al., 2022; Li et al., 2022; Srinivasan et al., 2021). The effective stresses from the endplates were extracted from all four simulated cases, and the percentage change due to HSM and non-neutral position magnitude was quantified.

To date, no studies have reported the risk of RWA neck pain due to ligament injuries. Technical challenges associated with imaging the micro-damages in ligament tissues can be considered one of the reasons. But several studies have associated work-related disorders, including neck pain and low back pain, with injuries in ligaments (Panjabi, 2006; Solomonow, 2004). An increase in the ligament distraction response was considered an indicator of the potential risk of neck pain based on previous neck modelling studies that investigated whiplash-associated disorders (Cronin, 2014; Fice and Cronin, 2012; Shen, 2020). Ligament distraction was quantified by measuring the change in distance of origin and insertion points of the beam elements that represented the ligaments, as described in section 3.4.3 (Figure 84). In the model, each ligament had a displacement-based failure criterion implemented to predict ligament rupture during neck loading (Barker and Cronin, 2021; Mattucci et al., 2012; Shen, 2020). The force-displacement curves defined in the ligaments had distinct phases: toe region, linear region, traumatic/sub-failure region and post-traumatic/failure region. The threshold for the distinct phases of ligament response was based on experimental data from Mattucci et al. (2012) (Figure 95). These threshold values were used as metrics to quantify ligament distractions and relate them to the potential for neck pain in different head-neck positions that simulated the RWA scanning activities (Table D1 in Appendix D). The toe and the linear regions indicate that the ligament distraction is in the physiologic range. The traumatic/subfailure region is the phase where micro-damage to the ligament (at the fiber level) may occur, which cannot be observed macroscopically (Nordin and Frankel, 2001; Shen, 2020). The percentage change in ligament distraction in the HH_{25F} and $HHNC_{25F}$ cases relative

to the H_{25F} case was quantified. Similarly, the percentage change in ligament distraction in $HHNC_{25F|10LB|25AR}$ relative to $HHNC_{25F}$ was quantified.

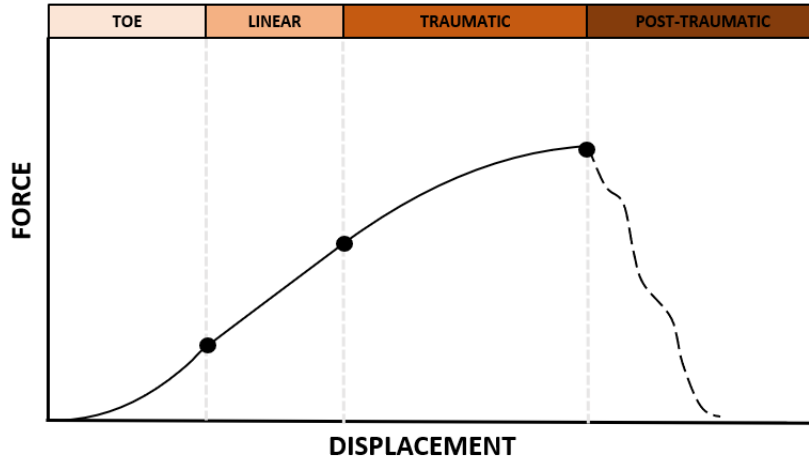


Figure 95: An exemplar Force vs. Displacement curve assigned to ligaments in the model is shown to illustrate the distinct phases in the mechanical response of ligament.

Chapter 4 Results

4.1 Phase #1: Enhancement, verification, and validation of the cervical spine model

4.1.1 Preliminary assessment of the UCS_{M50} model

The global (C0-C2) ROM response of the UCS_{M50} model extracted from the GHBMC M50-O v4.5 detailed FE neck model was verified to be similar to the model response reported by Lasswell et al. (2017) (Figures A1 and A2, Appendix A). A preliminary assessment of the UCS_{M50} model at the intervertebral levels identified that the C0-C1 and C1-C2 ROM in flexion at 1.5 Nm was not within the ± 1 SD of the experimental mean reported in the literature (Oda et al., 1992; Panjabi et al., 1991b) (Figures 96a and 96b). The percentage error in flexion ROM response of the UCS_{M50} model at 1.5 Nm was 49% in C0-C1 and 61% in C1-C2 relative to the experimental mean reported by Panjabi et al. (1991b). Similarly, the percentage error in flexion ROM response of the UCS_{M50} model at 1.5 Nm was 43% in C0-C1 and 54% in C1-C2 relative to the experimental mean reported by Oda et al. (1992).

A preliminary assessment of the UCS_{M50} model at the intervertebral levels identified that the C0-C1 ROM in extension at 1.5 Nm was outside the ± 1 SD of the experimental mean reported in the literature (Oda et al., 1992; Panjabi et al., 1991b) (Figure 96c). The C1-C2 ROM in extension at 1.5 Nm was within the ± 1 SD of the experimental mean reported by Panjabi et al. (1991b) and outside the ± 1 SD of the experimental mean reported by Oda et al. (1992) (Figure 96d). The percentage error in extension ROM response of the UCS_{M50} model at 1.5 Nm was 60% in C0-C1 and 32% in C1-C2 from the experimental mean reported by Panjabi et al. (1991b). Similarly, the percentage error in extension ROM response of the UCS_{M50} model at 1.5 Nm was 58% in C0-C1 and 90% in C1-C2 from the experimental mean reported by Oda et al. (1992).

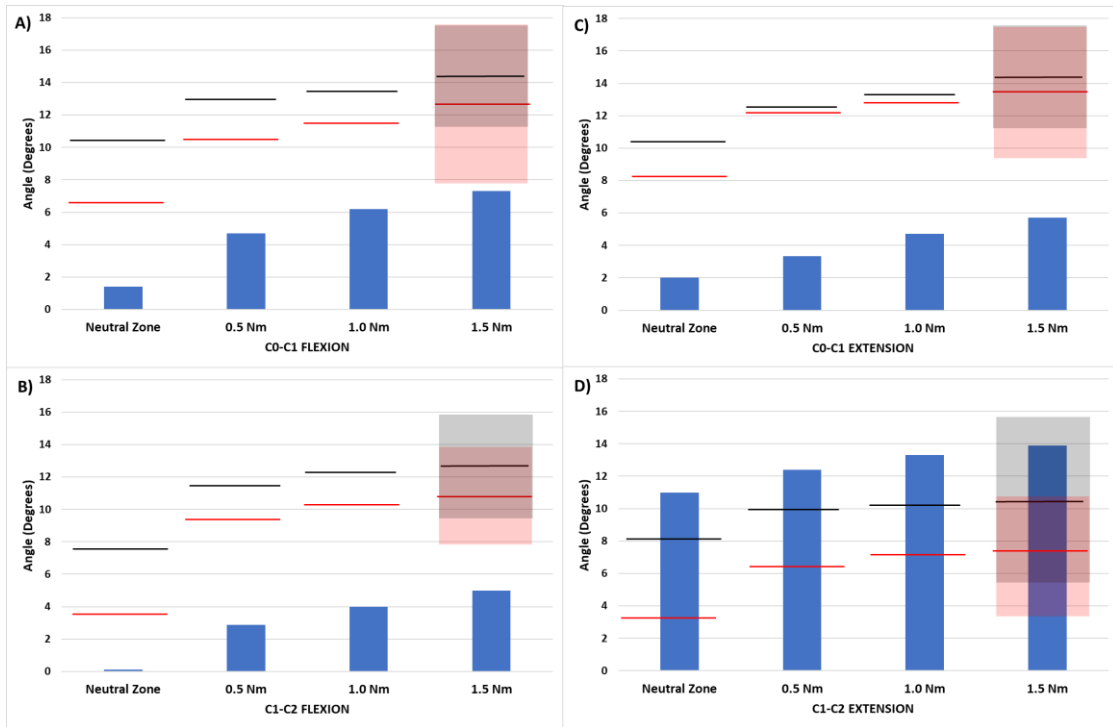


Figure 96: Response of the UCS_{M50} model (blue bars) compared with the experimental data (horizontal lines) during the preliminary assessment in flexion and extension. Horizontal black lines and the shaded grey region are experimental mean and ± 1 SD, respectively, from Panjabi et al. (1991b). The horizontal red lines and shaded red region are the experimental mean and ± 1 SD, respectively, from Oda et al. (1992).

Preliminary assessment of the UCS_{M50} model in axial rotation showed that the ROM of C0-C1 and C1-C2 at 1.5 Nm was within the ± 1 SD of the experimental mean reported for right and left axial rotation (Oda et al., 1992; Panjabi et al., 1991a) (Figure 97). The percentage error in axial rotation ROM response of the UCS_{M50} model at 1.5 Nm was 22% in C0-C1 and C1-C2 relative to the experimental mean reported by Panjabi et al. (1991a) for right axial rotation. The percentage error in axial rotation ROM response of the UCS_{M50} model at 1.5 Nm was 121% in C0-C1 and 29% in C1-C2 relative to the experimental mean reported by Panjabi et al. (1991a) for left axial rotation. The percentage error in axial rotation ROM response of the UCS_{M50} model at 1.5 Nm was 22% in C0-C1 and 25% in C1-C2 relative to the experimental mean reported by Oda et al. (1992) for right axial rotation. The percentage error in axial rotation ROM response of the UCS_{M50} model at 1.5 Nm was 9% in C0-C1 and 4% in C1-C2 relative to the experimental mean reported by Oda et al. (1992) for left axial rotation.

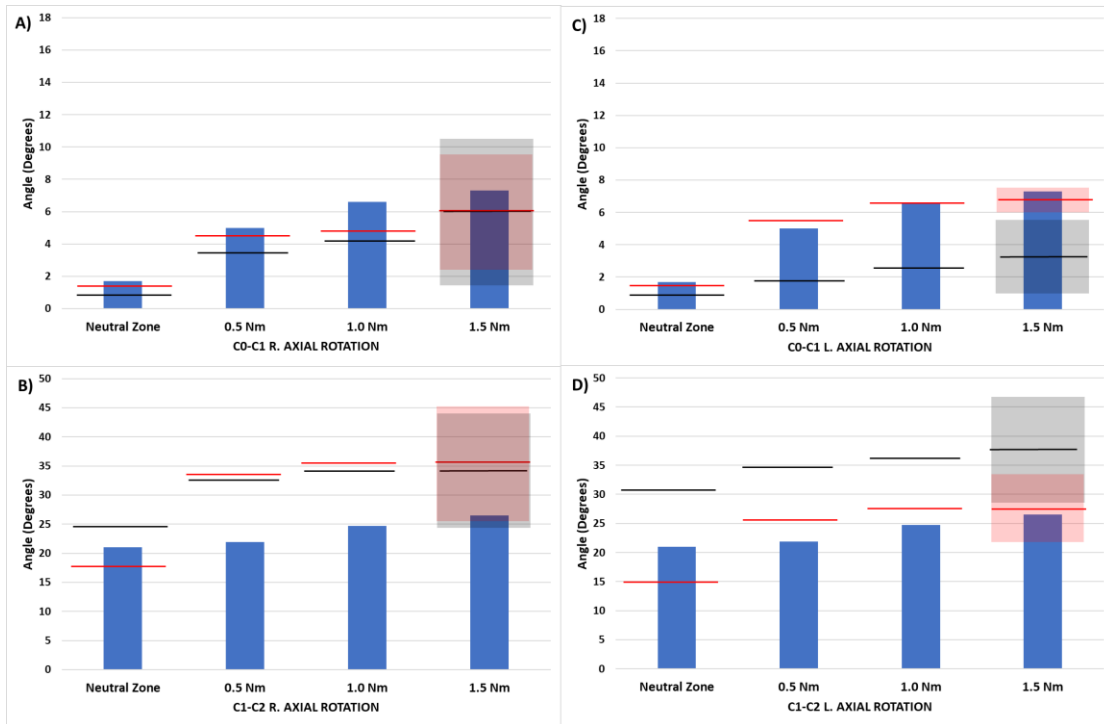


Figure 97: Response of the UCS_{M50} model (blue bars) compared with the experimental data (horizontal lines) during the preliminary assessment in axial rotation. Horizontal black lines and the shaded grey region are experimental mean and ± 1 SD, respectively, from Panjabi et al. (1991a). The horizontal red lines and shaded red region are the experimental mean and ± 1 SD, respectively from Oda et al. (1992).

From preliminary assessments, a visual examination of the UCS_{M50} model at the C0-C1 joint showed the occipital-condyles lifting up rather than rolling forward and sliding backward (in flexion) or vice versa (in extension), as reported in the literature (Bogduk and Mercer, 2000). The unphysical intervertebral motion response of the C0-C1 joint in the original model could be attributed, in part, to the faceted surfaces of the cartilage restricting motion. The intervertebral ROM response along with the unphysical motion of the C0-C1 joint indicate a need for improvement in biofidelity of the UCS_{M50} model, specifically in flexion and extension.

In addition to the ROM response, the preliminary DOE study on the UCS_{M50} model demonstrated a step-wise response (or abrupt jumps) in C0-C1 axial rotation between 0-1.5 Nm, owing to the contact challenges while the experimental data was smooth and continuous. Such intermittent responses were considered unphysical as it could potentially lead to overestimation of the contributions of some ligament laxity parameters in the sensitivity studies (Figure A3, Appendix A).

4.1.2 Anatomical enhancements to the UCS_{M50} model

Decreasing only the C1 cartilage thickness by 0.3 mm (UCS_{M50-Cartilage} model) increased the C0-C1 flexion by an average of 9.5° across 0-1.5 Nm (130% increase from the UCS_{M50} at 1.5 Nm). Similarly, there was an increase in C0-C1 extension by an average of 7.3° across 0-1.5 Nm (167% increase from the UCS_{M50} at 1.5 Nm). In C1-C2, there was an increase in flexion by an average of 2.5° across 0-1.5 Nm (82% increase from the UCS_{M50} at 1.5 Nm). In C1-C2, there was a decrease in extension by an average of 0.5° across 0-1.5 Nm (a negligible change from the UCS_{M50} at 1.5 Nm). In C1-C2 extension, the major change was observed in the neutral-zone (0 Nm) where the ROM reduced from 11° in UCS_{M50} to 8.6° in UCS_{M50-Cartilage} (a decrease of 22%) (Table A4 in Appendix A). Overall, decreasing the C1 cartilage thickness led to an increase in the C0-C1 flexion, C1-C2 flexion and C0-C1 extension ROM responses at 1.5 Nm to be within the ±1 SD of the experimental mean, thereby, improving the biofidelity of the model (Figure 98). A decrease in the C1 cartilage thickness also allowed the C0 cartilage to roll and slide over the C1 cartilage surface while reducing the intermittent rapid increases in the C0-C1 axial rotation, as observed in the literature (Figures A3 and A4, Appendix A).

Reorienting the alar ligaments to insert into the medial-lateral aspect of the occipital-condyle (Panjabi et al., 1991b) in the UCS_{M50-Cartilage} model had increased the C0-C1 extension by a mean of 3° (32% increase relative to UCS_{M50-Cartilage}) across 0-1.5 Nm. Alar ligament reorientation also increased the C1-C2 extension in the neutral zone by 3° (33% increase relative to UCS_{M50-Cartilage}) (Table A4, Appendix A). The effects of reorienting the alar ligaments were subtle in flexion (Figure 98).

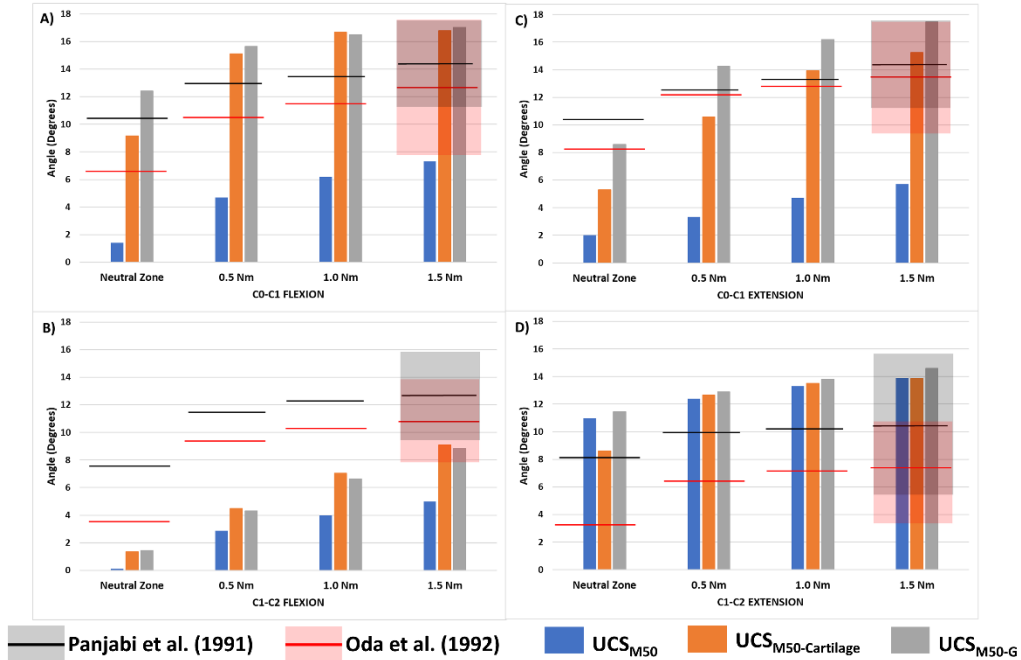


Figure 98: Effect of geometrical enhancements on the UCS model ROM in flexion and extension.

[Adapted from Hadagali and Cronin (2023)]

4.1.3 Ligament laxity identification in the UCS_{M50-G}

The sensitivity analysis identified ligaments (or combinations of ligaments) contributing 95% or more to the response: posterior atlanto-occipital membrane, posterior atlanto-axial membrane (PA-AM), anterior atlanto-occipital membrane, anterior atlanto-axial membrane, interspinous ligament (ISL), capsular ligament of C0-C1, capsular ligament of C1-C2 and alar ligament. In flexion loading, 98.1% of the C0-C1 motion was influenced by laxity in the posterior atlanto-occipital membrane, and 97.7% of the C1-C2 motion was influenced together by PA-AM (64.9%) and ISL (32.8%). In extension loading, 95.6% of the C0-C1 extension angle was influenced by laxity in the anterior atlanto-occipital membrane, while 97.6% of the C1-C2 motion was influenced by laxities in anterior atlanto-axial membrane (92.5%) and capsular ligament of C1-C2 (5.1%). Lastly, for axial rotation, laxities in capsular ligament of C0-C1 (90.3%), alar (2.6%), ISL (1.5%) and PA-AM (1.5%) together contributed to 95.9% of the C0-C1 motion. In C1-C2 axial rotation, laxities in the capsular ligament of C1-C2 and ISL laxities influenced 93.3% and 4.3% of the motion, respectively.

To optimize the laxities of the contributing ligaments for each level and mode of loading, a reduced range of laxity for each contributing ligament (an upper and a lower bound) were defined from the results of the DOE study (Table 9). The simultaneous optimization of all influential ligament laxities converged within four iterations when the metamodel accuracy had a root mean square error of less than 3%.

Table 9: Range of laxity for the highly contributing ligaments determined from DOE studies, and final ligament laxity values from the optimization study.

Contributing Ligaments	Reduced Laxity Range (mm)		Optimized Laxity (mm)
	Lower	Upper	
AA-OM	3.0	5.0	4.67
AA-AM	1.0	4.0	2.05
PA-OM	3.0	5.3	4.68
PA-AM	2.0	8.0	5.18
ISL	1.0	8.0	4.02
CL01	0.0	4.0	0.005
CL12	4.0	8.0	7.9
ALR	0.0	8.0	1.74

4.1.4 Verification and Validation of UCS_{M50-Opt} model

The intervertebral responses of the UCS_{M50-Opt} model in flexion, extension and axial rotation were verified with the target data (experimental mean) used for optimization (Panjabi et al., 1991b, 1991a). The percentage error between the target data and the UCS_{M50-Opt} model at 1.5 Nm was 5% for C0-C1 flexion, 13% for C1-C2 flexion, 4% for C0-C1 extension, 5% for C1-C2 extension, 3% for C0-C1 right axial rotation and 9% for C1-C2 right axial rotation (Figure 99).

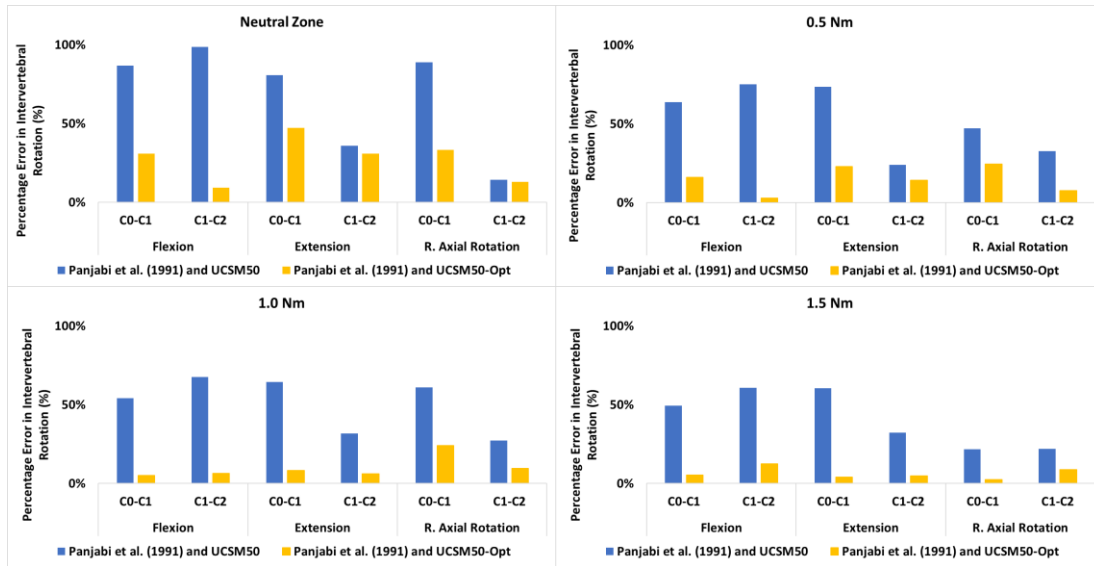


Figure 99: Verification of the optimized UCS_{M50-Opt} model with the target experimental data (Panjabi et al., 1991a, 1991b) used for optimization. Loading conditions for the models are shown in Figure 65.

A comparison of the model to independent experimental data (Oda et al., 1992) showed that the percentage error between the experimental mean and model response decreased with enhancements to the UCS model (Table A5, Appendix A). The percentage error between the experimental data from (Oda et al., 1992) and the UCS models (UCS_{M50} and UCS_{M50-Opt}) were calculated at the intervertebral levels for the three loading modes across the ROM. The mean percentage error across the intervertebral levels and loading modes decreased from 71% in UCS_{M50} to 38% in UCS_{M50-Opt} at the neutral-zone, 45% to 17% at 0.5 Nm, 42% to 16% at 1.0 Nm and 38% to 15% at 1.5 Nm (Figure 100).

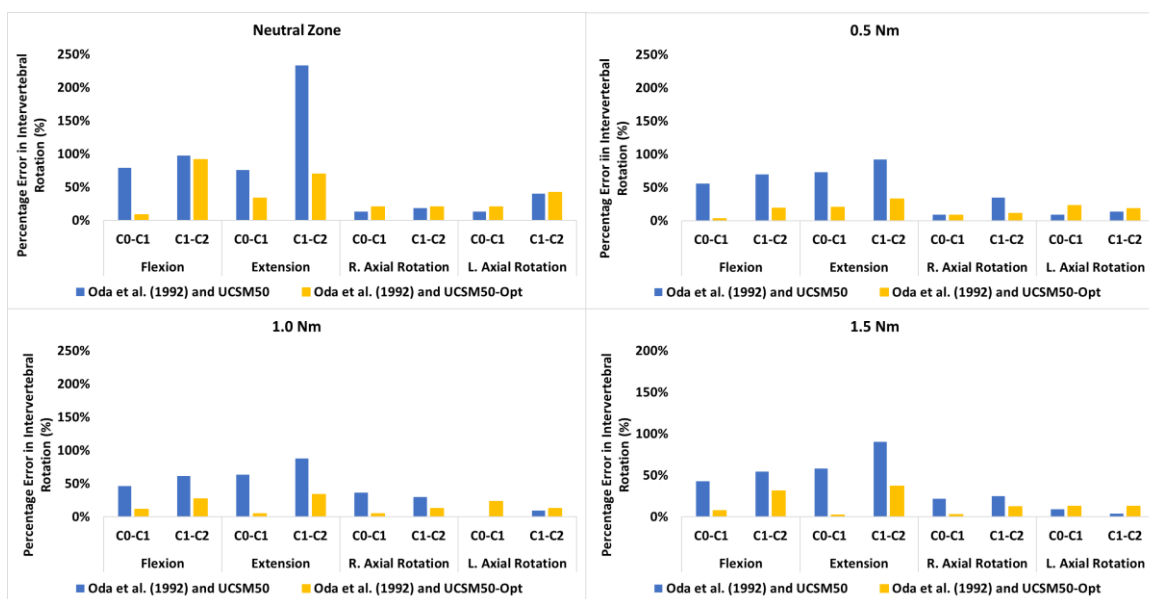


Figure 100: Validation of the optimized UCS_{M50-Opt} model with another experimental data (Oda et al., 1992). Loading conditions are shown in Figure 65.

4.1.5 Validation of the full ligamentous cervical spine model

First, the effect of facet cartilage enhancements on the LS model response was assessed by measuring the percentage change (increase or decrease) in response from LS_{M50-Opt} to LS_{M50-FC-Opt}. In flexion, the response was similar across C0-C1 to C6-C7 while differences were observed in extension and axial rotation loading modes with the enhancements to the facet cartilage. At 1.5 Nm flexion, there was an increase in C0-C1, C1-C2, C5-C6 and C6-C7 response by 3.1%, 2.1%, 10.0% and 0.4%, respectively, due to facet cartilage enhancement. At 1.5 Nm flexion, there was a negligible decrease in C2-C3, C3-C4 and C4-C5 response by 0.2%, 4.0% and 2.8%, respectively, due to facet cartilage enhancement (Table A6, Appendix A). At 1.5 Nm extension, there was an increase in the C0-C1 and C2-C3 response by 3.1% and 0.2%, respectively, due to facet cartilage enhancement. At 1.5 Nm extension, there was a decrease in C1-C2, C3-C4, C4-C5, C5-C6 and C6-C7 response by 19.0%, 25.8%, 53.4%, 43.4% and 9.0%, respectively, due to facet cartilage enhancement (Table A7, Appendix A). At 1.5 Nm axial rotation, there was a decrease in ROM response (between 18% to 48%) in all the intervertebral levels except C1-C2 where there was a subtle increase in response by 3% due to the enhanced facet cartilage (Table A8, Appendix A).

Next, the LS models (LS_{M50} , $LS_{M50-Opt}$ and $LS_{M50-FC-Opt}$) were validated with experimental data that reported the intervertebral kinematics of only the UCS. The mean percentage error between experiment data reported in Panjabi et al. (1991b) and Panjabi et al. (1991a) and the LS models at 0.5 Nm, across the loading modes and intervertebral levels improved from 54% in the LS_{M50} to 28% in the $LS_{M50-FC-Opt}$. Similarly, the percentage error improved from 55% to 21% at 1.0 Nm and 40% to 15% at 1.5 Nm (Figure 101). Assessment with (Oda et al., 1992) showed that the mean percentage error improved from 48% to 17% at 0.5 Nm, 41% to 16% at 1.0 Nm and 35% to 22% at 1.5 Nm (Figure 102).

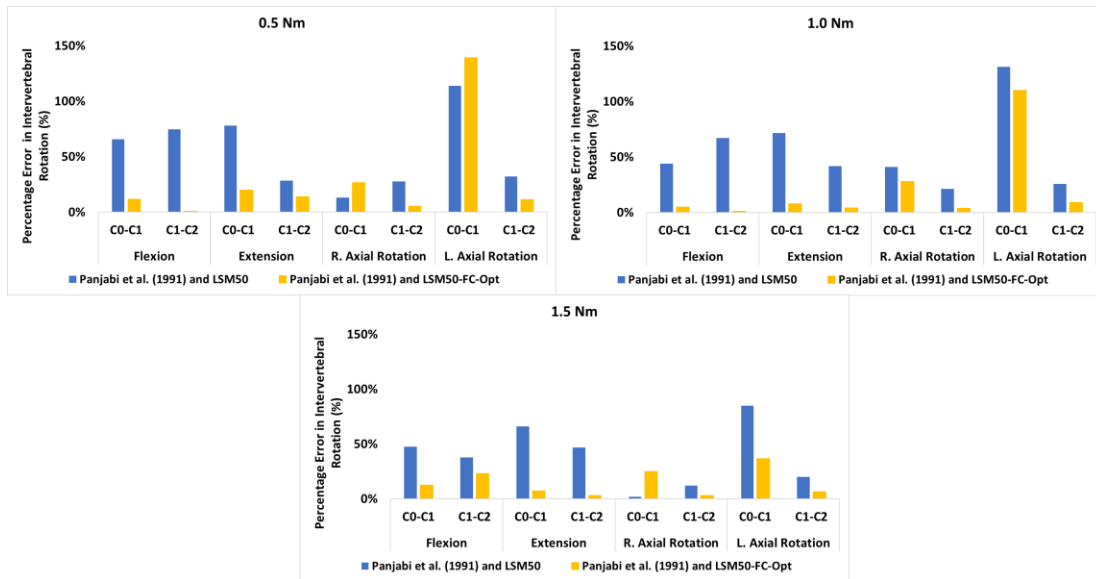


Figure 101: Comparison of the UCS_{M50} and $UCS_{M50-Opt}$ intervertebral rotations within the full ligamentous spine $LS_{M50-FC-Opt}$ model to experimental data reported by Panjabi et al. (1991a,b).

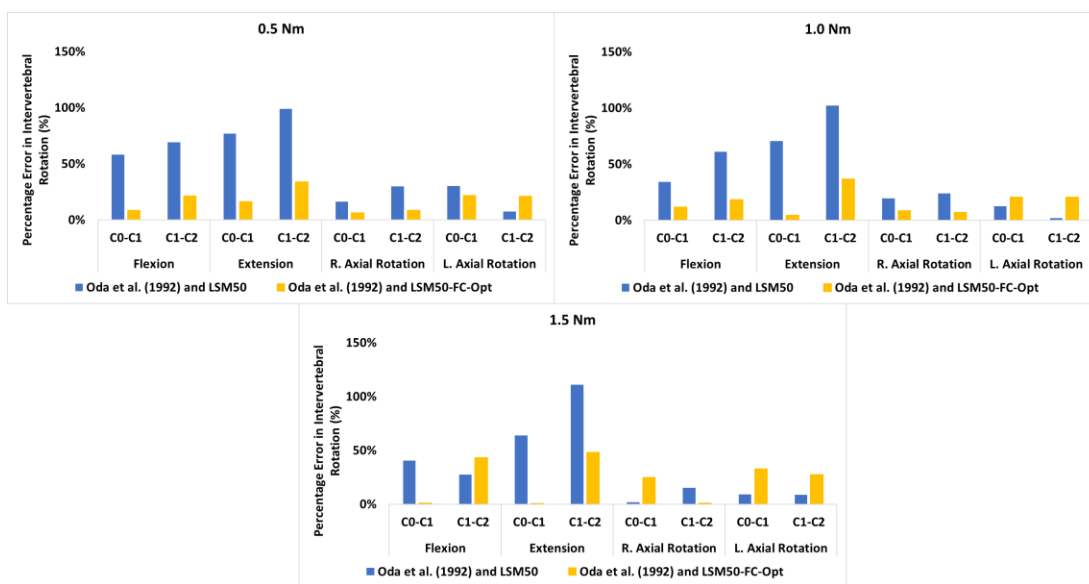


Figure 102: Comparison of the UCS_{M50} and UCS_{M50-Opt} intervertebral rotations within the full ligamentous spine LSM_{50-FC-Opt} model to experimental data reported by Oda et al. (1991).

Next, the LS models were validated with the experimental data that reported the intervertebral ROM of the full cervical spine (C0 to C7). Assessment with Ivancic (2013) showed improvement in the mean percentage error from 56% in LSM₅₀ to 47% in LSM_{50-FC-Opt} at 0.5 Nm, 73% in LSM₅₀ to 50% in LSM_{50-FC-Opt} at 1.0 Nm and 53% in LSM₅₀ to 49% in LSM_{50-FC-Opt} at 1.5 Nm. At 0.5 Nm, the mean percentage error between Ivancic (2013) and the models improved from 126% (LSM₅₀) to 75% (LSM_{50-FC-Opt}) in the UCS, while the error increased in the lower cervical spine (LCS) from 28% (LSM₅₀) to 36% (LSM_{50-FC-Opt}). At 1.0 Nm, the mean percentage error between Ivancic (2013) and the models improved from 97% (LSM₅₀) to 76% (LSM_{50-FC-Opt}) in the UCS, and from 63% (LSM₅₀) to 39% (LSM_{50-FC-Opt}) in the LCS. At 1.5 Nm, the mean percentage error between Ivancic (2013) and the models improved from 111% (LSM₅₀) to 97% (LSM_{50-FC-Opt}) in the UCS while no significant differences were observed in the LCS (Tables A9-A12, Appendix A). The response in the LCS levels in the LSM₅₀ and LSM_{50-Opt} had similar effects when assessed with Ivancic (2013) (Tables A9-A12, Appendix A).

Assessment with Panjabi et al. (1998) showed minimal increase in the mean percentage error from 26% in the LSM₅₀ to 30% in the LSM_{50-FC-Opt} at 1.0 Nm. At the UCS level, the mean percentage error between experimental data and models improved from 43% (LSM₅₀) to 35% (LSM_{50-FC-Opt}), while an increase in the mean percentage error was observed in the LCS levels from 19% (LSM₅₀) to 29%

(LS_{M50-FC-Opt}) (Figure 103). The response in the LCS levels in the LS_{M50} and LS_{M50-Opt} had similar effects when assessed with Panjabi et al. (1998) (Tables A9-A12, Appendix A).

Assessment with Panjabi et al. (2001) showed similarities in the mean percentage error with 32% in the LS_{M50} and 31% in the LS_{M50-FC-Opt} at 1.0 Nm. The mean percent error in the UCS level showed similar improvements (from 43% to 35%) when the model was assessed with Panjabi et al. (2001), as the experimental responses of the UCS reported in Panjabi et al. (1998) and Panjabi et al. (2001) were similar. At the LCS levels, the mean percentage error was 27% between Panjabi et al. (2001) and LS_{M50} and 29% between Panjabi et al. (2001) and LS_{M50-FC-Opt} (Figure 103). The response in the LCS levels in the LS_{M50} and LS_{M50-Opt} had similar effects when assessed with Panjabi et al. (2001) (Tables A9-A12, Appendix A).

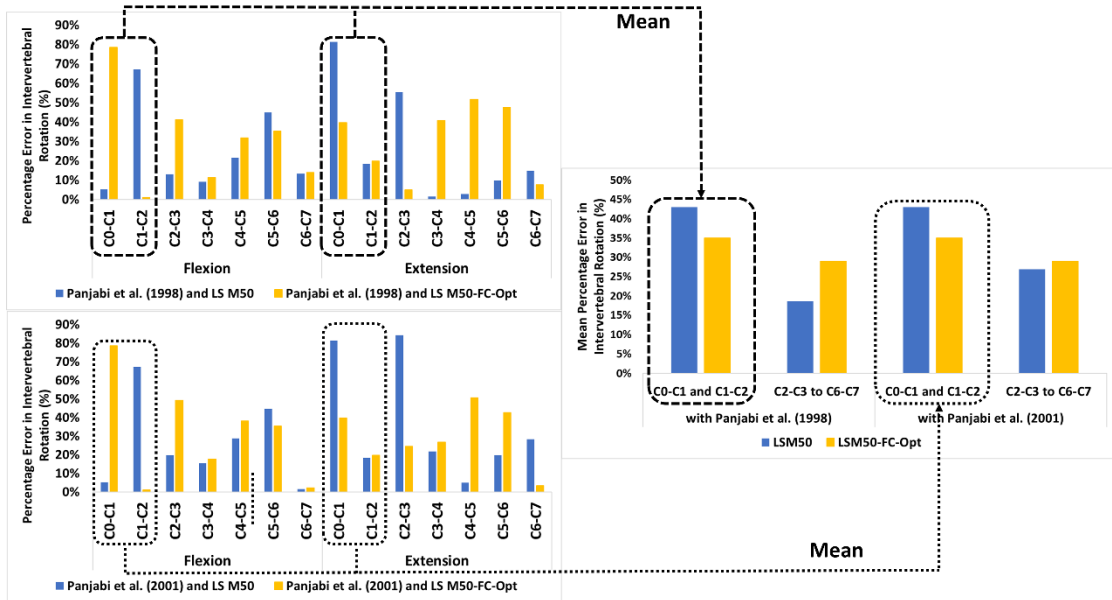


Figure 103: Left: Assessment of the UCS_{M50} in LS_{M50} and UCS_{M50-Opt} in LS_{M50-FC-Opt} for intervertebral rotations of the LS_{M50} and LS_{M50-FC-Opt} models. Models are assessed with experimental data reported by Panjabi et al. (1998) and Panjabi et al. (2001). Right: A single mean of the percentage error was calculated for UCS and LCS in flexion and extension.

The LS models were validated with experimental data that reported the intervertebral kinematics of LCS only that included experimental data from Camacho et al. (1997), Wheelton et al. (2006) and

Nightingale et al. (2007). Assessment with Camacho et al. (1997) showed increase in the mean percentage error in the $LS_{M50-FC-Opt}$ model compared to the LS_{M50} model. The mean percentage error increased from 25% in LS_{M50} to 42% in $LS_{M50-FC-Opt}$, 22% in LS_{M50} to 27% in $LS_{M50-FC-Opt}$ and 24% in LS_{M50} to 25% in $LS_{M50-FC-Opt}$ at 0.5 Nm, 1.0 Nm and 1.5 Nm, respectively. Similarly, assessment with Nightingale et al. (2007) also showed increase in the mean percentage error in the $LS_{M50-FC-Opt}$ model compared to the LS_{M50} model. At 0.5 Nm, the percent error in LS_{M50} and $LS_{M50-FC-Opt}$ were similar (38%). At 1.0 Nm and 1.5 Nm, there was an increase in the mean percentage error from 25% (LS_{M50}) to 37% ($LS_{M50-FC-Opt}$) and 22% (LS_{M50}) to 35% ($LS_{M50-FC-Opt}$), respectively. Assessment with Wheeldon et al. (2006) resulted in improvement in percentage error from 56% (LS_{M50}) to 34% ($LS_{M50-FC-Opt}$) at 0.5 Nm, 40% (LS_{M50}) to 31% ($LS_{M50-FC-Opt}$) at 1.0 Nm and 35% (LS_{M50}) to 29% ($LS_{M50-FC-Opt}$) at 1.5 Nm. The response in the LCS levels in the LS_{M50} and $LS_{M50-Opt}$ had similar effects when assessed with Camacho et al. (1997), Wheeldon et al. (2006) and Nightingale et al. (2007) (Tables A9-A12, Appendix A) (Hadagali and Cronin, 2023).

The effect of UCS enhancements on the improvement of full cervical spine models could be assessed by comparing the LS models responses with experiments that reported the intervertebral kinematics for only the UCS (Oda et al., 1992; Panjabi et al., 1991a, 1991b) and the full cervical spine (Ivancic, 2013; Panjabi et al., 2001b, 1998). The percentage error of LS_{M50} and $LS_{M50-FC-Opt}$ averaging across the loading modes, intervertebral levels, and incremental moments between the experimental data (Ivancic, 2013; Oda et al., 1992; Panjabi et al., 1991b, 1991a, 2001b, 1998) was 46% and 30%, respectively (Table A13, Appendix A).

A cumulative mean value for the experimental kinematic response for each level from C0-C1 to C6-C7 was calculated from the mean values reported in all the experimental studies (Camacho et al., 1997; Ivancic, 2013; Nightingale et al., 2007; Oda et al., 1992; Panjabi et al., 1991b, 1991a, 2001b, 1998; Wheeldon et al., 2006) for each loading mode separately in 0.5 Nm, 1.0 Nm, and 1.5 Nm applied moments (Tables A14-A17 in Appendix A). In flexion, the mean percentage error across C0-C1 to C6-C7 from 0.5 Nm to 1.5 Nm between the experimental cumulative mean and LS_{M50} was 34%. The mean percentage error across C0-C1 to C6-C7 and across 0.5 Nm to 1.5 Nm between the experimental cumulative mean and $LS_{M50-FC-Opt}$ reduced to 27% (Table A14 in Appendix A). Similarly, in extension, the mean percentage error across C0-C1 to C6-C7 from 0.5 Nm to 1.5 Nm between the experimental cumulative mean and models were 37% in LS_{M50} and 28% in $LS_{M50-FC-Opt}$ (Table A15 in Appendix A). In the right axial rotation, the mean percentage error across C0-C1 to C6-C7 from 0.5 Nm to 1.5 Nm

between the experimental cumulative mean and models were 54% in LS_{M50} and 25% in $LS_{M50-FC-Opt}$ (Table A16 in Appendix A). In the left axial rotation, the mean percentage error across C0-C1 to C6-C7 from 0.5 Nm to 1.5 Nm between the experimental cumulative mean and models were 52% in LS_{M50} and 27% in $LS_{M50-FC-Opt}$ (Table A17 in Appendix A).

The results in Tables A14-A17, in Appendix A, confirm that enhancements to the UCS model had only a modest influence on the LCS kinematic response while the enhancements to the facet cartilage influenced the LCS kinematic response in extension and axial rotation. The results also indicate that the enhancements to the LCS facet cartilage enhanced the LS model response in the axial rotation loading mode. The results on validation of the $LS_{M50-Opt}$ models has been reported in detail in the Appendix A and also in the recent publication (Hadagali and Cronin, 2023).

4.2 Phase #2a: Simulating non-neutral head-neck positions using muscle activation

4.2.1 Passive neck stiffness assessment of the NM_{M50} model

Under gravity, it was identified that the skin, adipose tissue and passive muscle components, previously validated for impact conditions (Barker and Cronin, 2020; Cronin et al., 2018), restricted the head from pitching forward in flexion. The notably less compliant response in the NM_{M50} model with relaxed muscles was also reported in the literature (Feller et al. 2016), concurring with the current findings. Removal of skin resulted in the head flexing 10° forward. Removing the skin and adipose tissue did not change the result indicating that skin had a major effect on the model response. Removal of all the three passive tissue components resulted in the model overly flexing ($\approx 70^\circ$) under the influence of gravity (Figure 104). The percentage error was 100% for the NM_{M50} model, 85% for the NM_{M50} model exclusive of skin (NM_{M50}|No SK) and 85% for the model exclusive of skin and adipose tissue (NM_{M50}|No SK and AT). With the exclusion of skin, adipose tissue and the passive muscles, the percentage error was 15%.

The contribution of the passive tissues in the stiffness of the NM_{M50} model was confirmed based on the assessments with McGill et al. (1994) experiment data that reported the moment vs rotation of the head in volunteers with relaxed neck muscles. The percentage error between the head rotation in the model and the experimental average for male subjects, at 5 Nm applied flexion moment, was calculated. The percentage error between the NM_{M50} model and the experimental mean was 86%. The NM_{M50} model without the skin resulted in a percentage error of 57%. Exclusion of the skin and adipose tissue in the NM_{M50} model improved the percentage error to 42%. Excluding the three components including skin, adipose tissue and the passive muscles from the NM_{M50} model resulted in the head rotation response beyond the experimental average with a percentage error of 26% (Figure 105).

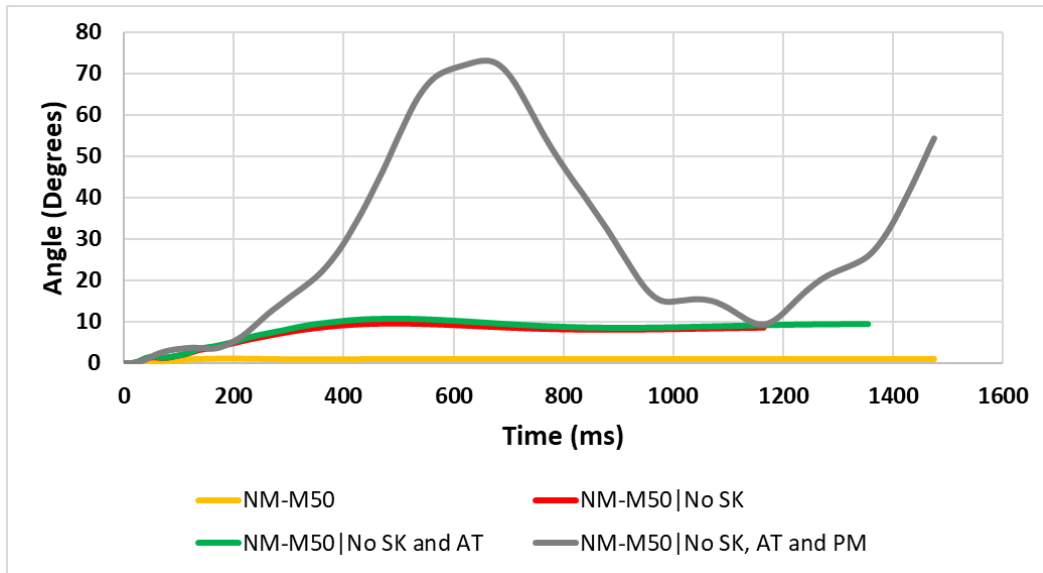


Figure 104: Preliminary assessments on the passive NM_{M50} model under gravitational loading indicated that the passive tissue components contributed to the stiff response.

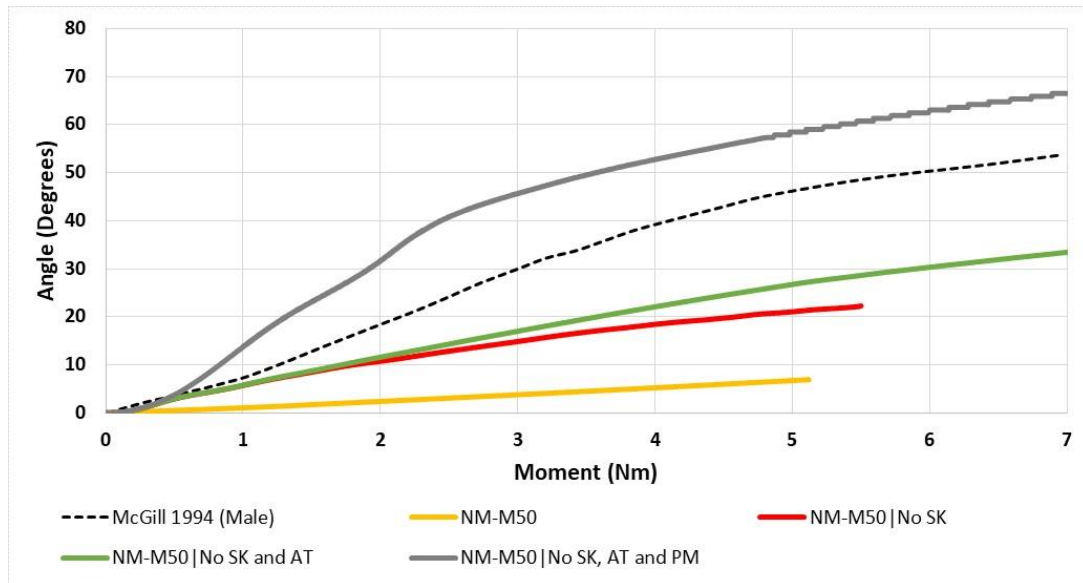


Figure 105: Preliminary assessments on the passive NM_{M50} model with the experimental data from McGill et al. (1994) also confirms the contribution of passive tissues to the stiff response.

4.2.2 Active neck stiffness assessment of the NM_{M50} model

Under gravity and fully activated contractor muscles (flexors), the head rotated 15° in flexion in the NM_{M50} model (Figure 106). The predicted compressive force was 800 N at the C5-C6 IVD, comparable to the force reported in the literature during a maximum voluntary contraction activity in flexion (Cheng et al., 2016). The compressive force predicted by the NM_{M50} model was approximately 4 times higher than the force predicted by an MSK head-neck model (Barrett et al., 2020) during a simulated physiologic 45° flexion (Hadagali et al., 2024). The resultant active and passive muscle forces combining flexors and extensors at the C5 level were 700 N and 36 N, respectively.

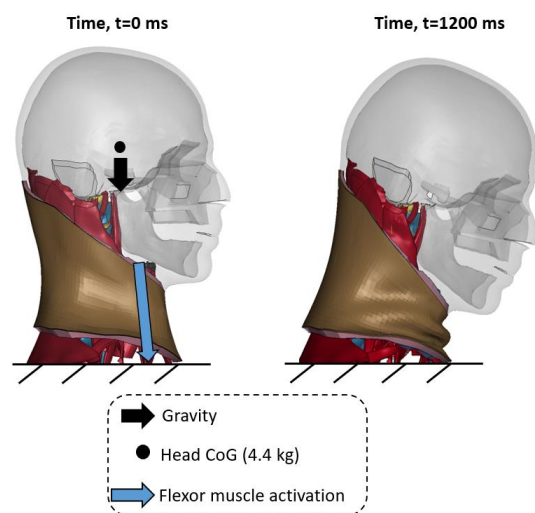


Figure 106: Response of the NM_{M50} model when the flexor muscles were fully activated under gravity.

[Taken from Hadagali et al. (2024)]

The skin and the adipose tissue in the anterior aspects of the neck buckled when the flexors were activated during the simulated forward flexion (Figure B1, Appendix B). Repositioning the model in flexion using active muscles resulted in a bucking response in the passive muscle component as well (Figure B2, Appendix B). There were uneven deformations in the 3D passive muscle elements in the regions where the nodes are shared with the 1D CE and support elements. The uneven deformations in the 3D passive muscles were causing an unrealistic stress response (Figure B3, Appendix B). From the literature, the head-neck positioning from a neutral to a non-neutral position took approximately 2

seconds, along with a static hold procedure that extended beyond 2 seconds (Barrett, 2016; Callaghan, 2014). The model took approximately 48 hours to simulate 2-second phenomena with the NM_{M50} model using LS-DYNA MPP 9.2, double-precision on 32 Intel Xeon E5-2683 2.1 GHz processors.

4.2.3 Passive neck stiffness assessment and improvement of the $NM_{M50-Hill}$ model

Under gravitational loading, the passive $NM_{M50-Hill}$ model flexed forward resulting in a 17° head rotation. With the application of a biofidelic passive muscle property (Persad et al., 2021) to the $NM_{M50-Hill}$ model ($NM_{M50-Hill-E}$), the head rotation increased to 33.5° degrees (Figure 107). The percentage error in the head rotation between the passive $NM_{M50-Hill}$ model and the average in vivo experimental data (Seacrist et al., 2012) was 84%. The percentage error in the head rotation between the passive $NM_{M50-Hill-E}$ model and the average in vivo experimental data from the literature improved to 46% with the biofidelic passive muscle property.

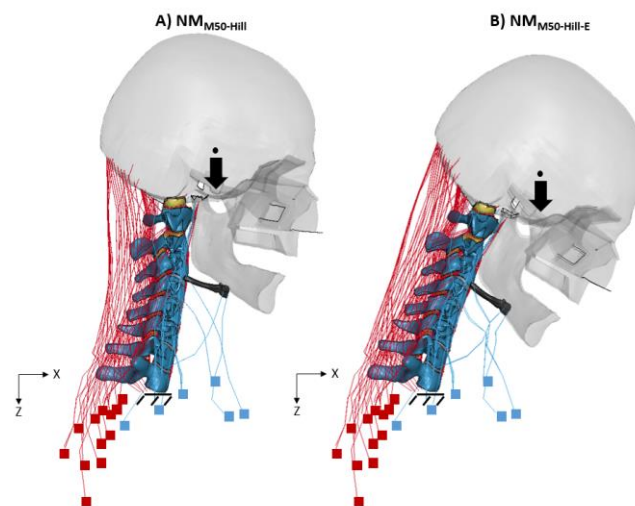


Figure 107: Comparing the response of the passive $NM_{M50-Hill}$ (A) and the passive $NM_{M50-Hill-E}$ (B) models under gravitational loading. The head in the $NM_{M50-Hill}$ and $NM_{M50-Hill-E}$ models with relaxed muscles rotated 17° and 33° , respectively.

The head rotation response in the passive $NM_{M50-Hill}$ model with the biofidelic passive muscle property ($NM_{M50-Hill-E}$) to an externally applied moment, based on an in vivo experimental set up (McGill et al., 1994), was assessed with the experimental average head rotation. In flexion and extension loading conditions, the percentage error between the head rotation in the model and the

experimental average for male subjects, at 5 Nm applied moment, was calculated. In flexion, the percentage error between the model and the experimental mean reduced from 47% ($NM_{M50-Hill}$) to 11% due to the biofidelic passive muscle property ($NM_{M50-Hill-E}$) (Figure 108a). In extension, the percentage error between the model and the experimental mean reduced from 44% ($NM_{M50-Hill}$) to 20% due to the biofidelic passive muscle property ($NM_{M50-Hill-E}$) (Hadagali et al., 2024) (Figure 108b).

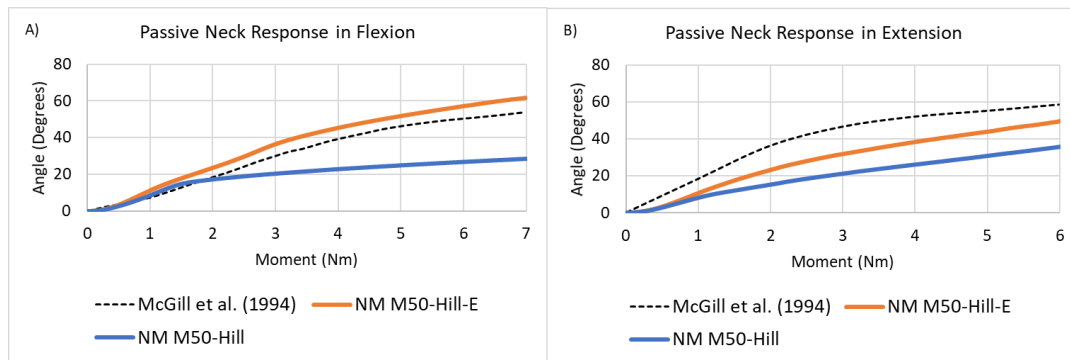


Figure 108: Comparing the head rotation in the $NM_{M50-Hill}$ and the $NM_{M50-Hill-E}$ models simulated for McGill et al. (1994) experiment on relaxed neck in flexion (A) and extension (B). The results indicate that the biofidelic passive muscle property improved the response of the model in physiologic conditions.

[Taken from Hadagali et al. (2024)]

4.2.4 Simulating head-neck flexion in the $NM_{M50-Hill-E}$ model using active muscles

From different iterations that were performed to identify an activation level for extensors, an activation level between 0.04 to 0.09 resulted in head extension, owing to the higher strength of the extensor muscles relative to the flexors. It was determined that the activation level of ≤ 0.03 for the extensors enabled flexion of the $NM_{M50-Hill-E}$ model, resulting in the head flexing $\approx 20^\circ$.

The muscle activation strategy, described in the Chapter 3, resulted in the $NM_{M50-Hill-E}$ model statically repositioned to the desired flexion position. In the vertical axis (Z axis), the summation of

muscle, head and neck forces (131.6 N) balanced with the reaction force experienced by the mid-transverse C7 vertebra (-131.6 N). Similarly, in the sagittal plane (X axis), the summation of muscle, head and neck forces (4.7 N) balanced with the reaction forced experienced by the mid-transverse C7 vertebra (-4.7 N) (Figure 109). The model predicted a reaction flexion moment of 1.5 Nm at the centroid of C7. The flexion moment (around Y axis) predicted by the model was within the acceptable physiologic value, in comparison with the experimental value of 15 Nm during maximum voluntary contraction in flexion (Cheng et al., 2016). The X, Y and Z axis forces in this section-plane balanced, confirming that the model was in equilibrium. The angular velocities of the head and C1-C7 vertebrae were 0 rad/ms, further ensuring equilibrium in the model.

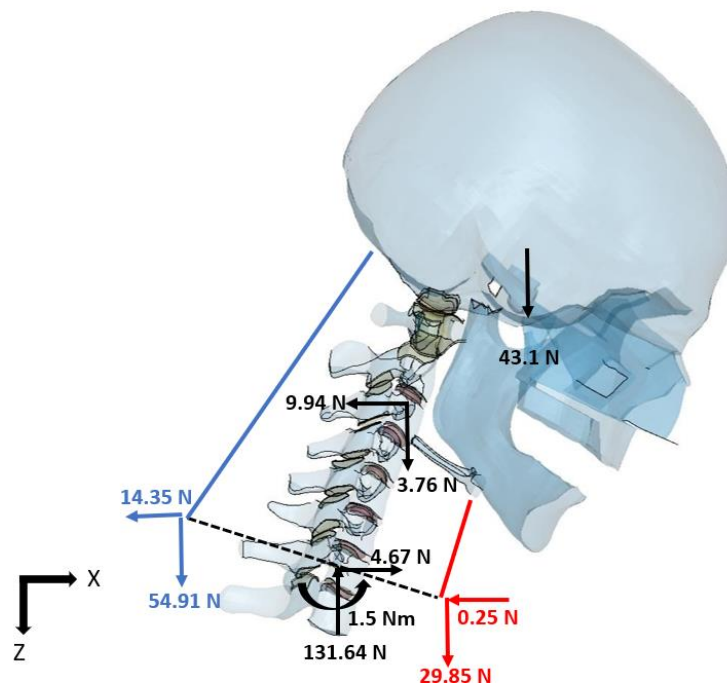


Figure 109: FBD of the $NM_{M50-HIII-E}$ model, demonstrating equilibrium in the 30° flexed position. FBD in the sagittal plane where the red and blue lines indicated flexor and extensor group of muscles, respectively.

4.2.5 Simulating head-neck axial rotation in the $NM_{M50-HIII-E}$ model using active muscles

The activation strategy, described in the ‘Methods’ section, applied to different group of muscles under gravity, resulted in the head rotating 30° in axial rotation. In the vertical axis (Z axis), the summation of muscle, head and neck forces (92.02 N) balanced with the reaction force experienced by the mid-

transverse C7 vertebra (-92.02 N). In the sagittal plane (X axis), the summation of muscle, head and neck forces (5.08 N) balanced with the reaction forced experienced by the mid-transverse C7 vertebra (-5.08 N). In the coronal plane (Y axis), the summation of muscle, head and neck forces (5.7 N) balanced with the reaction force experienced by the mid-transverse C7 vertebra (-5.7 N), confirming that the model was in equilibrium (Figure 110). The model predicted a reaction flexion moment of 1.3 Nm at the centroid of C7 due to the presence of gravity. The magnitude of the predicted moment was comparable with the reaction moment predicted by an existing MSK model for a similar head-neck position (Barrett et al., 2022a). The angular velocities of the head and C1-C7 vertebrae were 0 rad/ms, further ensuring equilibrium in the model.

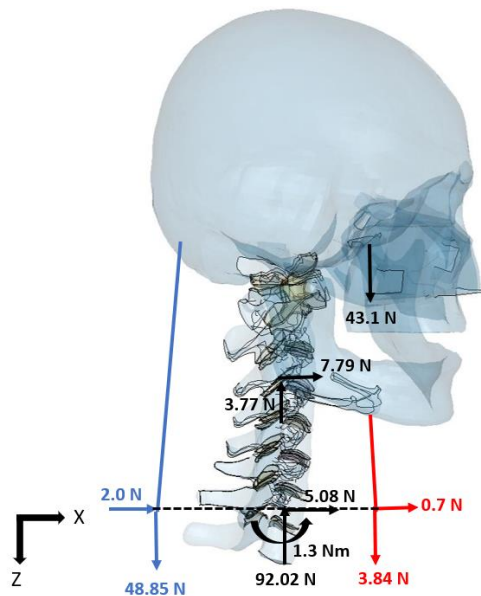


Figure 110: FBD of the $NM_{M50-Hill-E}$ model, demonstrating equilibrium in the 30° axially rotated position. FBD in the sagittal plane where the red and blue lines indicated flexor and extensor group of muscles, respectively.

4.3 Phase #2b: Quantifying the importance of active muscle repositioning using kinematic, kinetic and tissue-level responses

The external BC-based repositioning simulation was prescribed a run-time of 2.6 s, when the head rotation reached 30° flexion. In the muscle-based repositioning simulation, the head rotation reached 30° flexion at approximately 1.0 s run-time after which the model was allowed to stabilize by further continuing the simulation for 1.0 s. Both the simulations terminated normally within 15 hours of the computation time (12 hours and 15 hours for the BC- and muscle-based, respectively) using LS-DYNA MPP 9.2, double-precision on 32 Intel Xeon E5-2683 2.1 GHz processors. The results were extracted using a commercial FE post-processing software (LS-PrePost v4.6, LSTC, Livermore, CA). The differences between the external BC- and muscle-based repositioning approaches in flexion have been reported in a recent publication (Hadagali et al., 2024).

4.3.1 Comparing a conventional external BC- and muscle-based approaches of repositioning the NM_{M50-HIII-E} model in flexion

Both the BC and muscle-based repositioning methods produced similar CV angles, which were larger compared to the experiments, while the FHD and the GMA of the muscle-based repositioning was close to the experimental average compared to the BC method. The percent difference in the CV angle reduced from 36% (external BC) to 24% (active muscle). The percent difference in FHD between the model repositioned using both methods was similar (6% with external BC and 4% with active muscle). The percent difference in then GMA reduced from 12% to 2% with the active muscle method of repositioning (Table 10). Comparing the two repositioning methods, the CV angle was lower by 9%, while the FHD and GMA increased by 10% and 16%, respectively, for the active muscle method compared to the BC method.

Table 10: The experimental mean and the model response in flexion with the head rotated 30°. CV-Craniovertebral, FHD-Forward head distance, GMA-Gravitational moment arm.

Kinematic parameter	Experiment	Model		Percent Error		Percent Change (muscle relative to BC)
		Ex. BC-based	Muscle-based	Ex. BC-based	Muscle-based	
CV angle (degrees)	32.3±4.6	44	40	36%	24%	-9%
FHD (mm)	134.2±13.4	126.6	139.6	6%	4%	10%
GMA (mm)	91.4±10.5	80.4	92.9	12%	2%	16%

In general, the BC method had lower intervertebral rotations compared to the muscle-based method, with the largest difference for both methods at the C2-C3 level (Figure 111). At the intervertebral level, the mean percent difference in rotation across C2-C3 to C7-T1 in the model was 51% and 66% using the external BC and active muscle methods, respectively (Table 11).

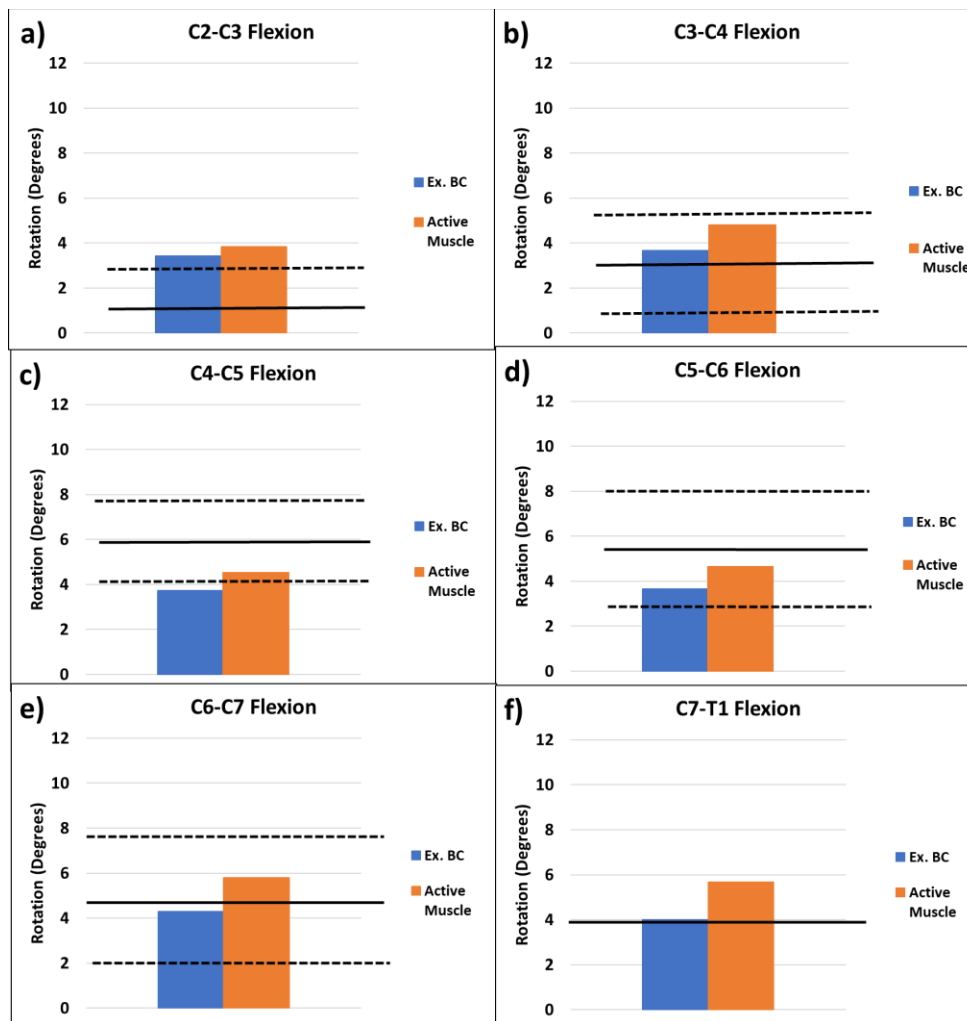


Figure 111: Intervertebral rotation response of the $NM_{M50-Hill-E}$ model repositioned using external BC (blue bars) and active muscle (orange bars) methods for 30° head flexion, compared with average (solid black) and ± 1 SD values (dashed black) from the CSP (Reed and Jones, 2017). The CSP did not report the SD for C7-T1.

[Taken from Hadagali et al. (2024)]

Table 11: The intervertebral rotation response (mean) predicted by the CSP (Reed and Jones, 2017) and the repositioned models in flexion with the head rotated 30°.

Level	CSP(°)	Ext BC (°)	Muscle (°)	% Difference wrt CSP		% Change
				Ext BC	Muscle	Ext BC- and Muscle-based
C2-C3	1.14	3.4	3.8	202%	237%	12%
C3-C4	3.12	3.7	4.8	18%	54%	31%
C4-C5	5.91	3.7	4.5	37%	23%	22%
C5-C6	5.43	3.7	4.6	32%	15%	27%
C6-C7	4.8	4.3	5.8	10%	21%	35%
C7-T1	3.84	4.0	5.7	4%	48%	42%
Mean				51%	66%	28%

The ligament distractions were generally higher for the muscle-based repositioning method compared to the BC method, corresponding to the higher average intervertebral rotation. The distraction in the anterior and posterior aspects of the ISL increased by a mean of 0.3 mm and 0.6 mm, respectively, across the C2-C3 to C7-T1 levels from external BC to active muscle method. In the anterior and posterior aspects of the CL, the mean distraction across C2-C3 to C7-T1 levels increased by 0.1 mm and 0.2 mm, respectively, due to the active muscle method of repositioning (Figure 112). The distraction in the LF across C2-C3 to C7-T1 increased by a mean of 0.3 mm due to the muscle-based repositioning method. The PLL experienced a similar response when the model was repositioned using both methods (Figures C1 to C3 in Appendix C). The mean difference in the distractions across C2-C3 to C7-T1, across each ligament in the posterior aspects of the vertebrae, increased by 0.2 mm with muscle-based repositioning (Figure 113). The distraction responses in all the ligaments were verified to be within the physiologic limits with the experimental data from Mattucci et al. (2012) (Figure C4 in Appendix C).

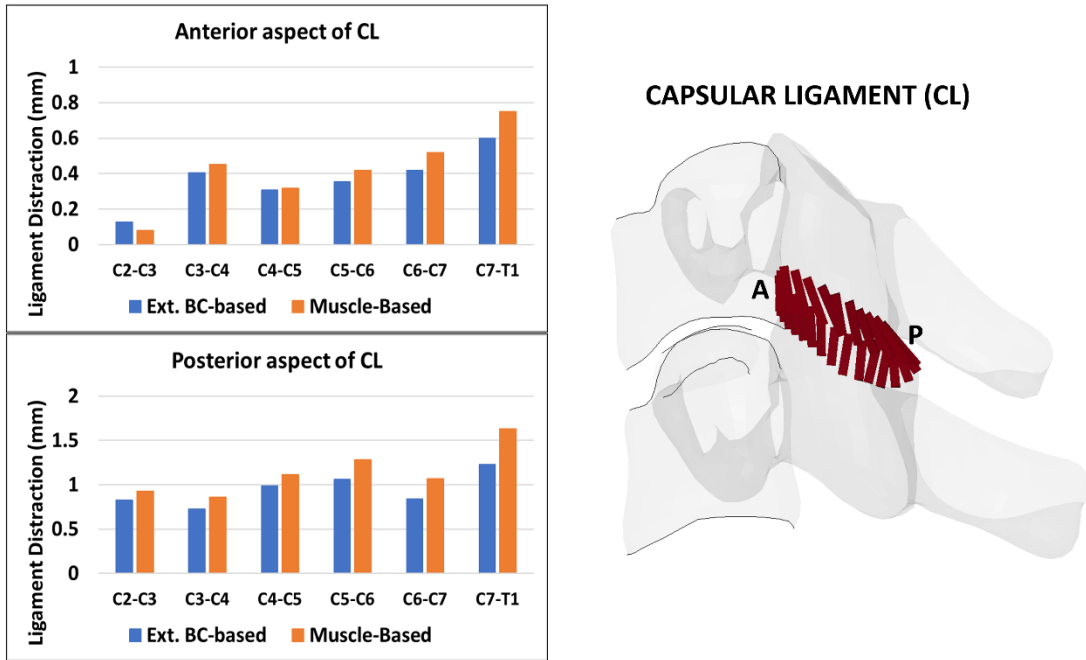


Figure 112: Capsular ligament (CL) distraction response for 30° head flexion. The distractions of the CL were measured in the anterior (A) and posterior (P) aspects of the ligaments.

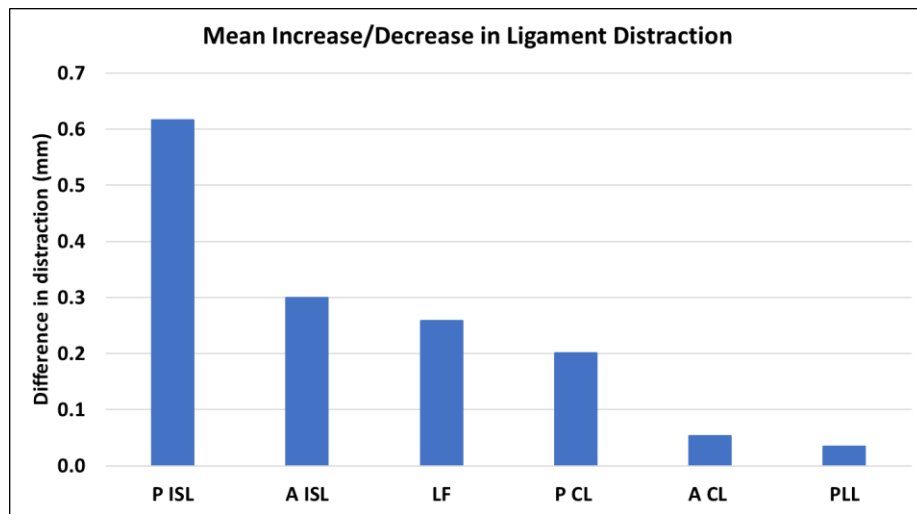


Figure 113: The mean difference in ligament distraction across C2-C3 to C7-T1 levels when the $NM_{M50-Hill-E}$ model was repositioned in 30° flexion using external BC- and muscle-based methods. The results show that the differences were highest in the ISL compared to other ligaments.

The mean muscle force across C2 to C7 increased from 38 N with the external BC method to 81 N with the muscle-based method (a mean increase by 115%). The muscle forces in the model repositioned using the muscle-based method gradually increased from 65 N in C2 to 87 N in C7 level, in contrast with the uniformly applied follower load across all the vertebral levels in the literature. The muscles forces were also within 50 N to 150 N in the model repositioned using muscle-based method, in agreement with the represented values in experimental and numerical studies (X.-Y. Cai et al., 2020b; Lee et al., 2011; Wawrose et al., 2021). The muscle force predicted by the $NM_{M50-Hill-E}$ model in muscle-based 30° flexion was approximately 10 times lesser than the muscle force in a fully tensed state (1000 N) as reported in existing head-neck models (Bruneau, 2019; Cheng et al., 2016; Dibb et al., 2013), thus confirming that the model response was within the physiologic range (Figure 114).

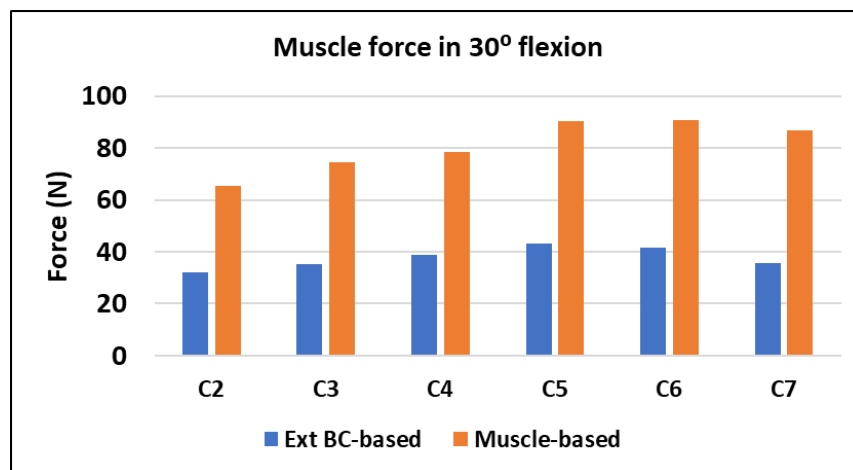


Figure 114: Muscle force at different vertebral levels when $NM_{M50-Hill-E}$ model was repositioned using different methods. The findings show that the muscles forces as a result of activation were not uniform through the length of the spinal column, in contrast with the existing assumptions from the literature.

[Taken from Hadagali et al. (2024)]

The IVD deformations were generally higher for the muscle-based repositioning, compared to the BC method (Figure 115). The C2-C3 IVD deformation in the anterior, middle and posterior aspects increased by a mean of 0.8° with the active muscle repositioning approach. Similarly, the deformations increased by a mean of 1.9° in C3-C4, 4.7° in C4-C5, 4.1° in C5-C6 and 4° in C6-C7 when the model was repositioned in 30° head flexion using the active muscle approach. The measured IVD deformation

angles for both repositioning methods were within the physiologic limits based on the comparison with experimental data (Ito et al., 2005).

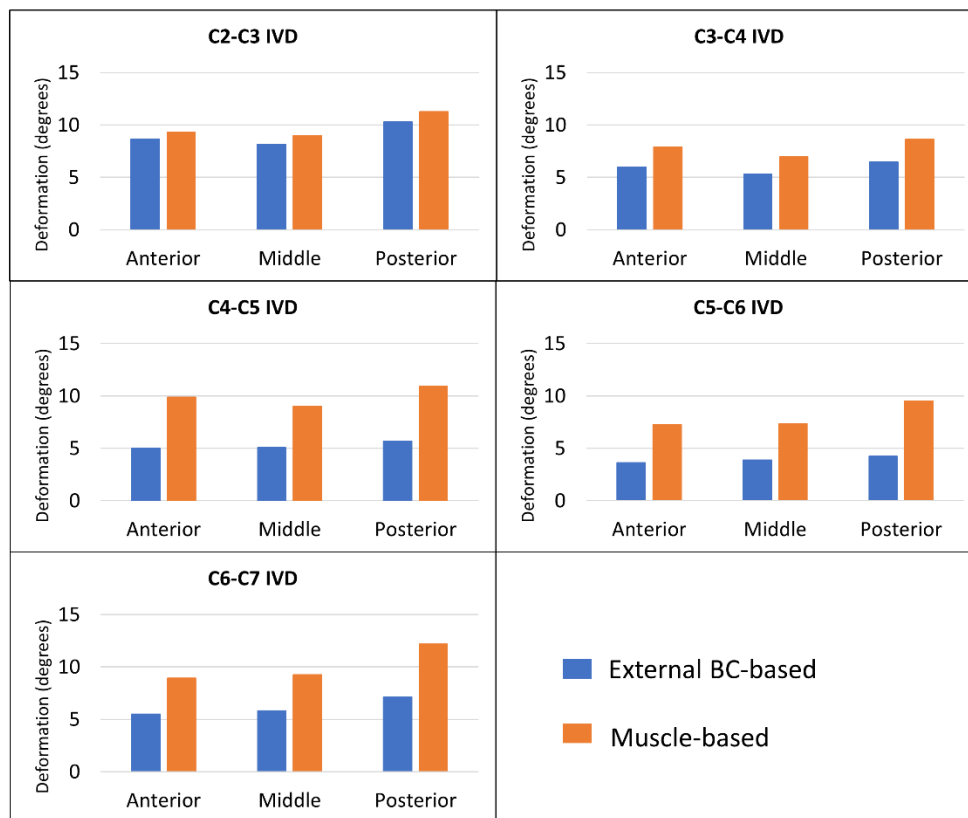


Figure 115: IVD global deformation angles in 30° head flexion simulated using external BC and muscle-based methods, compared to the experimental data reported for physiologic flexion (Ito et al., 2005).

[Taken from Hadagali et al. (2024)]

The muscle-based repositioning resulted in higher IVD compressive and shear forces, compared to the BC- based method. There was a mean increase in the compressive force by 232% across C2-C3 to C7-T1 with the muscle-based method (Figure 116a). The AP shear force averaged 4.7 N and 12.2 N across C2-C3 to C7-T1 when the model was repositioned using external BC- and muscle-based methods, respectively. With the muscle-based method, there was a mean increase in the AP shear force

by 165% across C2-C3 to C7-T1 (Figure 116b). The forces predicted by the model repositioned using active muscle were comparable with the forces predicted by the MSK neck model (Barrett et al., 2020).

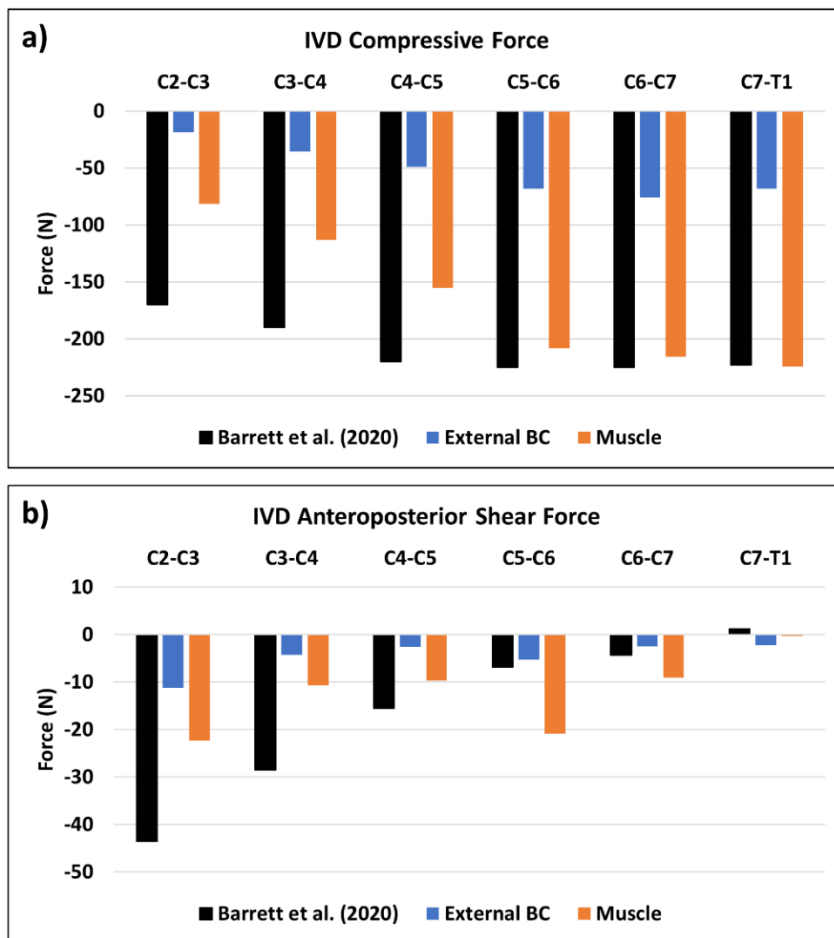


Figure 116: IVD compressive forces (a) and AP shear forces (b) in 30° head flexion simulated using an external BC- and muscle-based methods, compared to an MSK neck model (Barrett et al., 2020).

[Taken from Hadagali et al. (2024)]

Overall, there was a mean of 60% increase in the peak collagen fiber strains across all the levels when the model was repositioned using the muscle-based approach relative to the external BC approach (Figure 117). In the direction of the fibers, a maximum peak strain of 7.4% in the C6-C7 level and 12.5% in the C7-T1 level was observed in the external BC- and muscle-based methods, respectively. The peak strain in the fibers increased by 39% at the C2-C3 level, 40% at the C3-C4 level, 61% at the

C4-C5 level, 67% at the C5-C6 level, 57% at the C6-C7 level and 98% at the C7-T1 level when the model was flexed using muscle-based repositioning approach. The predicted strains along the fiber orientation were confirmed to be below the failure threshold reported in the literature (Holzapfel et al., 2005; Isaacs, 2012; Pezowicz, 2010) (Figures C9 to C14 in Appendix C).

Collagen fiber strains in the AF during flexion

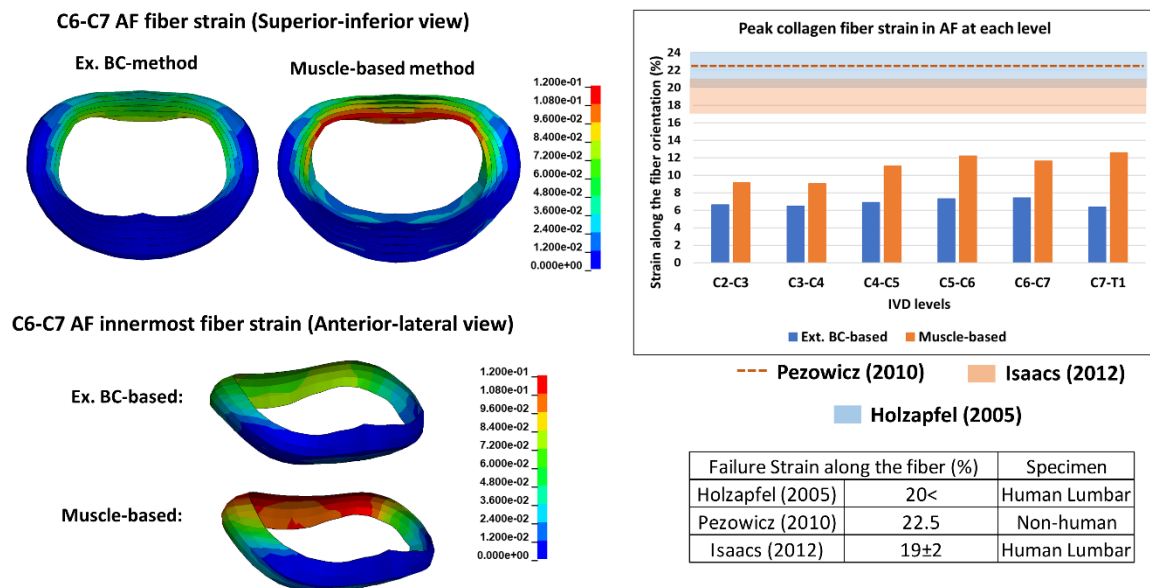


Figure 117: Collagen fiber strains along the fiber orientation in AF when 30° head flexion was simulated using external BC- and muscle-based methods.

[Taken from Hadagali et al. (2024)]

4.3.2 Comparing a conventional external BC- and muscle-based approaches of repositioning the NM_{M50-HIII-E} model in axial rotation

In general, the response of the model improved when active muscle was used to reposition the head in axial rotation (Figures 118 and 119). The percent error in the C0-C2 axial rotation response between the experimental mean and the model reduced from 27% to 15% with the muscle-based method. Also, the percent error in the C2-T1 axial rotation and C2-T1 coupled lateral bending responses reduced from 126% to 91% and 80% to 14%, respectively, with the muscle-based method (Table 12). The coupled lateral bending in the C2-T1, in the model repositioned using both the methods, was in the ipsilateral side (direction of head rotation), in agreement with the experimental data (Guo et al., 2021).

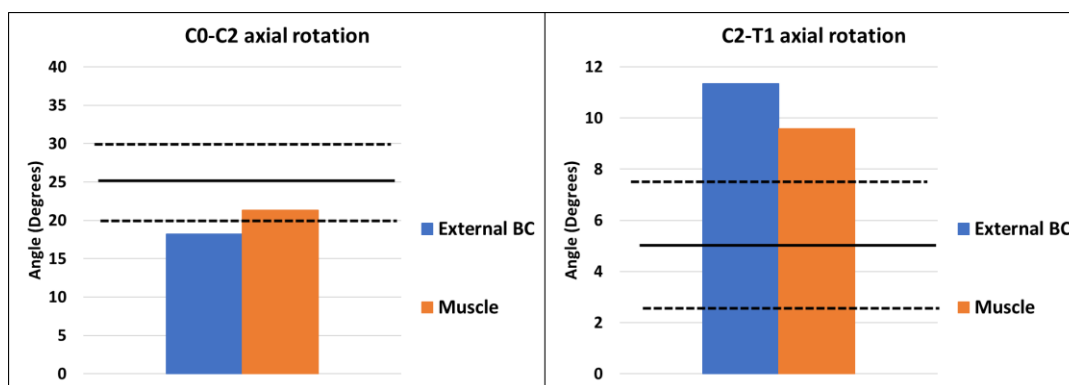


Figure 118: Axial rotation response of C0-C2 and C2-T1 in the model when the head was repositioned in 30° axial rotation using external BC (blue bar) and active muscle (orange bar) is compared with the experimental data (Guo et al., 2021). The experimental average (solid black) and ±1 SD values (dashed black) correspond to 30° head axial rotation.

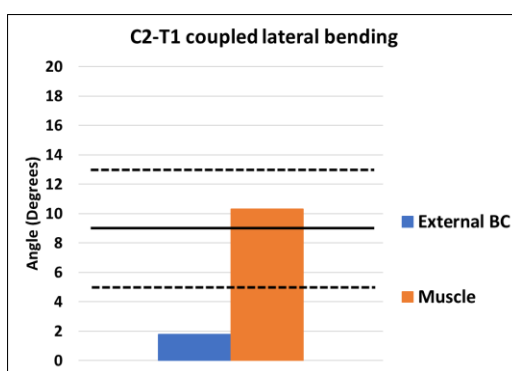


Figure 119: Coupled lateral bending response of C2-T1 in the model when the head was repositioned in 30° axial rotation using external BC (blue bar) and active muscle (orange bar) is compared with the experimental data (Guo et al., 2021). The experimental average (solid black) and ±1 SD values (dashed black) correspond to 30° head axial rotation.

Table 12: The experimental mean (Guo et al., 2021) and the model response in axial rotation with the head rotated 30°. AR-Axial rotation, CLB-Coupled lateral bending.

Level	Exp. Mean	Ex BC-based	Muscle-based	% Error		% Change
				Exp. & Ex. BC	Exp. & Muscle	Ex. BC and Muscle
C0-C2 AR	25	18.2	21.3	27%	15%	17%
C2-T1 AR	5	11.3	9.6	126%	91%	-15%
C2-T1 CLB	9	1.8	10.3	80%	14%	472%
Mean				78%	40%	158%

The ligament distractions were generally lower in axial rotation position compared to the flexion position. In the anterior and posterior aspects of the left CL (contralateral CL), the mean distraction across C2-C3 to C7-T1 levels increased by 0.3 mm and 0.4 mm, respectively, due to the muscle-based method of repositioning (Figure 120). In the anterior and posterior aspects of the right CL (ipsilateral CL), the mean distraction across C2-C3 to C7-T1 levels decreased by 0.8 mm and 0.4 mm, respectively, due to the muscle-based method of repositioning (Figure 120). The mean distraction in the posterior aspect of the ISL increased by 0.2 mm, across C2-C3 to C7-T1, with the muscle-based repositioning method. The PLL experienced a decrease in response by a mean of 0.2 mm, across C2-C3 to C7-T1, when the model was repositioned using both methods. The mean distraction in the anterior aspect of ISL and LF, across C2-C3 to C7-T1, remained similar (0 mm difference) with the muscle-based method (Figure C5-C7 in Appendix C). The mean difference in the distractions across C2-C3 to C7-T1 and across each ligament in the posterior aspects of the vertebrae, decreased by 0.1 mm with muscle-based repositioning (Figure 121). The distraction responses in all the ligaments were verified to be within the physiologic limits (Figure C8 in Appendix C).

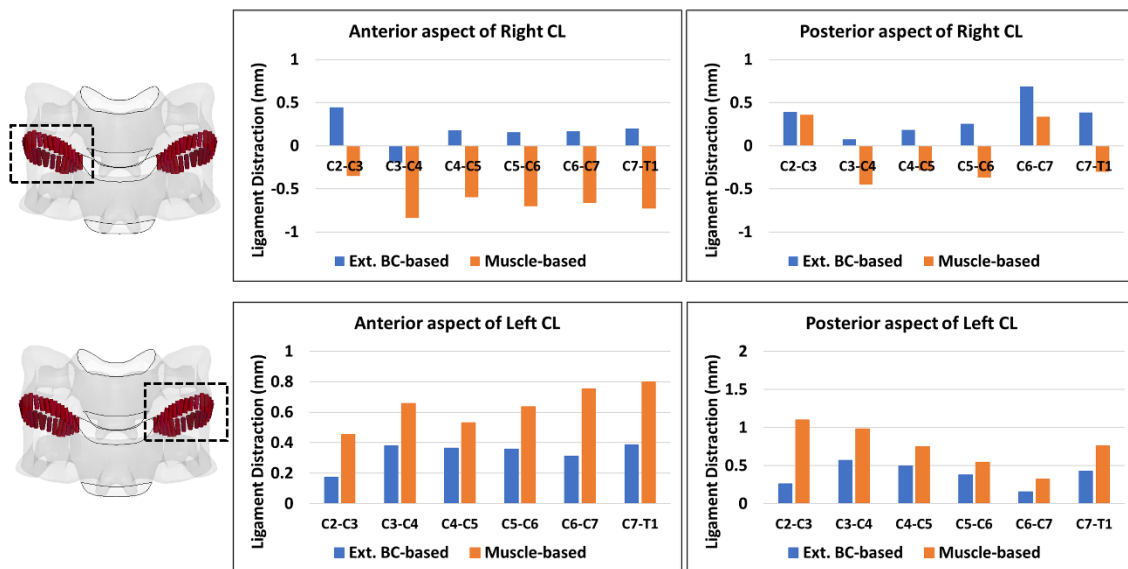


Figure 120: Capsular ligament distraction response in 30° head axial rotation simulated using different repositioning methods. The distractions in the CL were measured in the anterior and posterior aspects on the left (L) and right (R) sides of the spine.

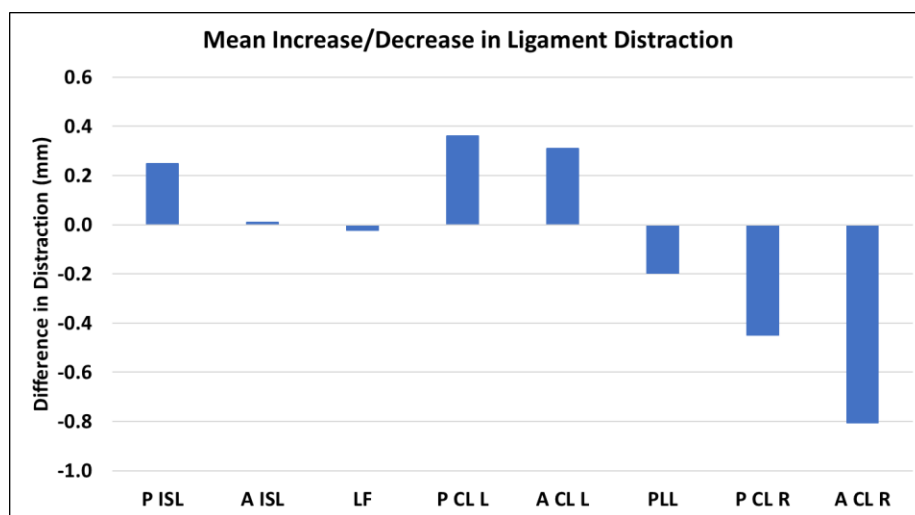


Figure 121: The mean difference in ligament distraction across C2-C3 to C7-T1 levels when the $NM_{M50-Hill-E}$ model was repositioned in 30° axial rotation using external BC- and muscle-based methods. The results show that the differences were highest in the ipsilateral CL compared to other ligaments.

The mean muscle force across C2 to C7 increased from 8 N with the external BC method to 65 N with the muscle-based method (a mean increase by 677%). The muscle forces in the model repositioned using the muscle-based method was relatively higher in C2 vertebral level (144 N) compared to the lower vertebral levels (40 N to 53 N). In the muscle-based repositioned model, the muscle forces were similar at the C4 to C7 vertebral levels with a mean of 52 N and within the representative values (50 N to 150 N) of follower load presented in the literature including experimental and numerical studies (X.-Y. Cai et al., 2020b; Lee et al., 2011). The muscle force predicted by the $NM_{M50-Hill-E}$ model in muscle-based 30° axial rotation was approximately 10 times lesser than the muscle force in a fully tensed state (1000 N <) as reported in existing head-neck models (Bruneau, 2019; Cheng et al., 2016; Dibb et al., 2013), thus confirming that the model response was within the physiologic range (Figure 122).

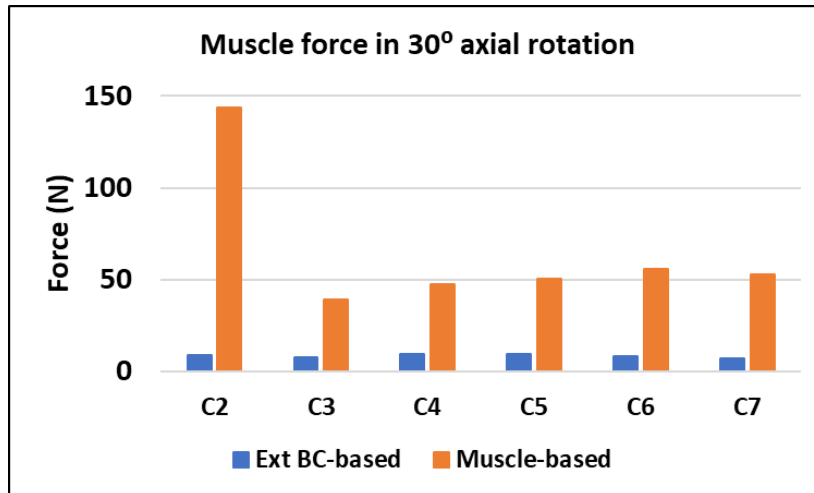


Figure 122: Muscle force at different vertebral levels when $NM_{M50-HH-E}$ model was repositioned using different methods. The findings show that the muscles forces as a result of activation were not uniform through the length of the spinal column, in contrast with the existing assumptions from the literature.

In the model repositioned using the external BC-based method, the compressive force in the IVDs was similar across all the levels ranging from 1.8 N in C6-C7 to 7.8 N in C3-C4 with a mean of 4.7 N at 30° head axial rotation. The muscle-based method of repositioning resulted in higher IVD compressive forces ranging from 67.2 N in C6-C7 to 90.1 N in C3-C4, with a mean of 77.2 N across all the levels (Figure 123a). The mean AP shear force across all the levels was 2.9 N and 2.7 N when the model was repositioned using external BC-based and muscle-based methods, respectively. In the model repositioned using the external BC-based method, the maximum AP shear force was observed in C7-T1 (4.5 N) while in the model repositioned using the muscle-based method, the maximum AP shear force was observed in C2-C3 (8.7 N) (Figure 123b). Across C2-C3 to C7-T1, the mean increase in compression and AP shear was 1990% and 5%, respectively, due to muscle-based repositioning.

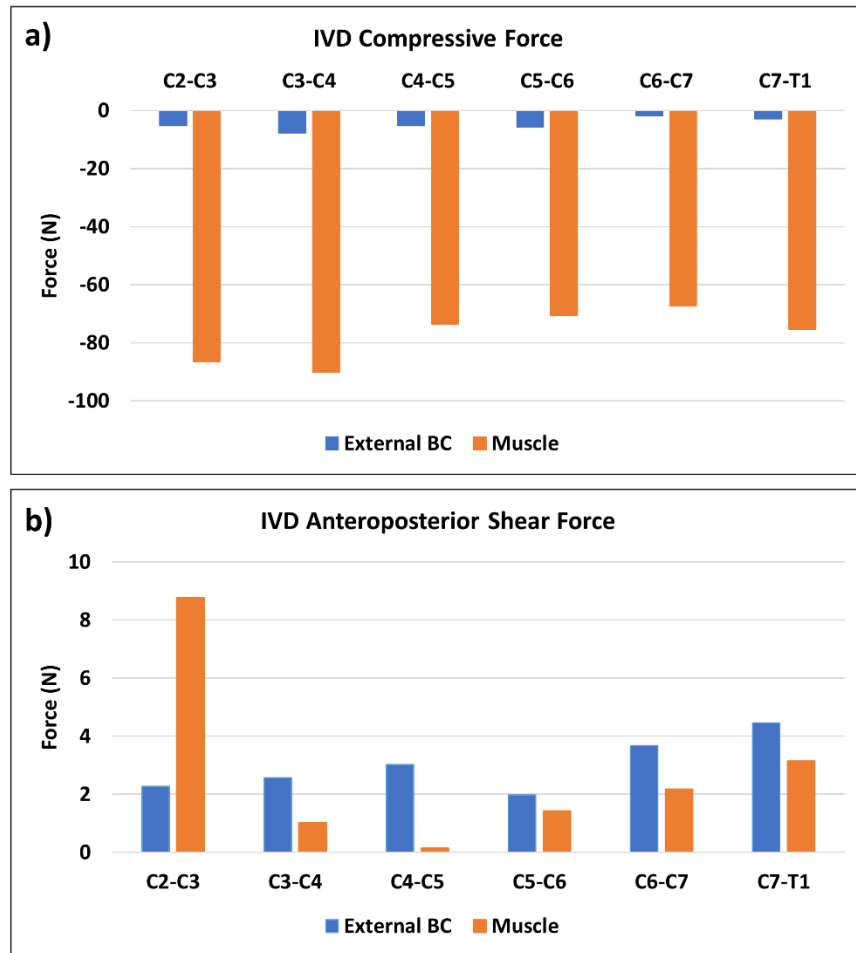


Figure 123: IVD compressive forces (a) and AP shear forces (b) in 30° head axial rotation simulated using an external BC- and muscle-based methods.

Similar to flexion, the current study demonstrated differences in the collagen fiber strains with different repositioning methods. In the direction of the fiber, a peak strain of 6.5% (C5-C6) and 9.1% (C2-C3) was observed in the model repositioned using external BC- and muscle-based methods, respectively. The peak strain in the AF fibers increased by 103% at the C2-C3 level, 49% at the C3-C4 level, 9% at the C4-C5 level, 11% at C5-C6 level, 41% at the C6-C7 level and 24% at the C7-T1 level when the head was axially rotated 30° using muscle-based repositioning approach. Overall, there was an average of 40% increase in the peak collagen fiber strains across all the levels when the model was repositioned using muscle-based method compared to the external BC-based method (Figure 124). The

predicted peak strains along the fiber direction were confirmed to be below the failure threshold reported in the literature (Holzapfel et al., 2005; Isaacs, 2012; Pezowicz, 2010) (Figures C15 to C20 in Appendix C).

Collagen fiber strains in the AF during axial rotation

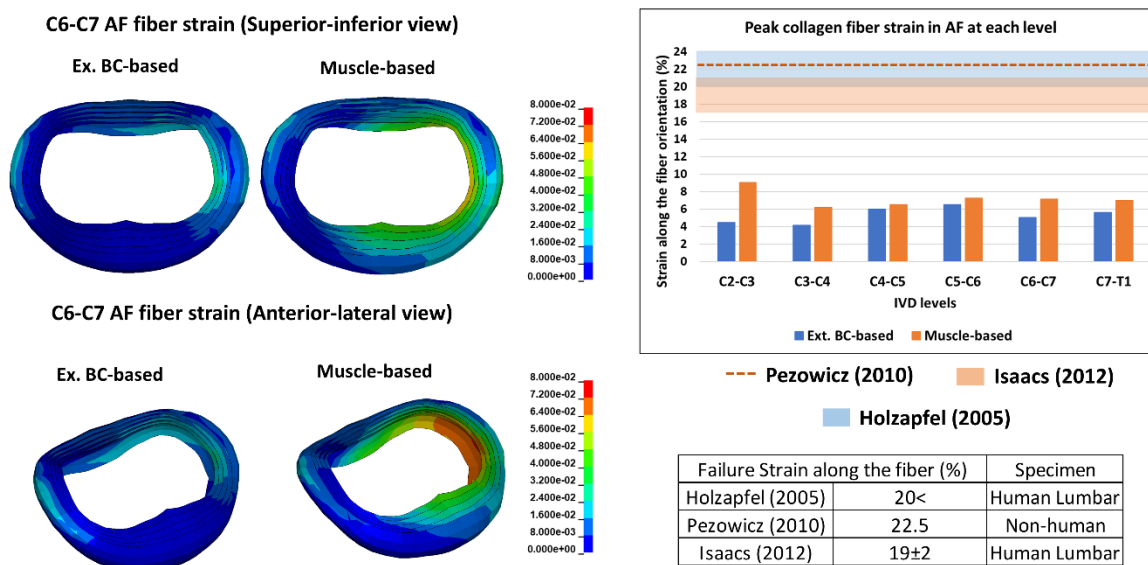


Figure 124: Collagen fiber strains along the fiber orientation in AF when 30° head axial rotation was simulated using external BC- and muscle-based methods.

4.4 Phase #3: Neck pain risk in rotary-wing aircrew (RWA)

4.4.1 Effect of HSM configuration in 25° head-neck flexion

The overall head rotation (C0-T1) when the model with and without the HSM was repositioned in a consistent head-neck flexion angle ($\theta=25^\circ\pm 5\%$) was 33° in the H_{25F} case, and 31° in the HH_{25F} and $HHNC_{25F}$ cases. The overall head rotation in flexion (in both the HSM cases) were comparable (6% decrease) to the overall head rotation in the H_{25F} case. The intervertebral kinematics of C2-T1 in the HH_{25F} case was comparable (3% mean increase) with the intervertebral kinematics of C2-T1 in the H_{25F} case. The intervertebral kinematics of C2-T1 in the $HHNC_{25F}$ case slightly increased by a mean of 8% compared to the intervertebral kinematics of C2-T1 in the H_{25F} case (Figure 125).

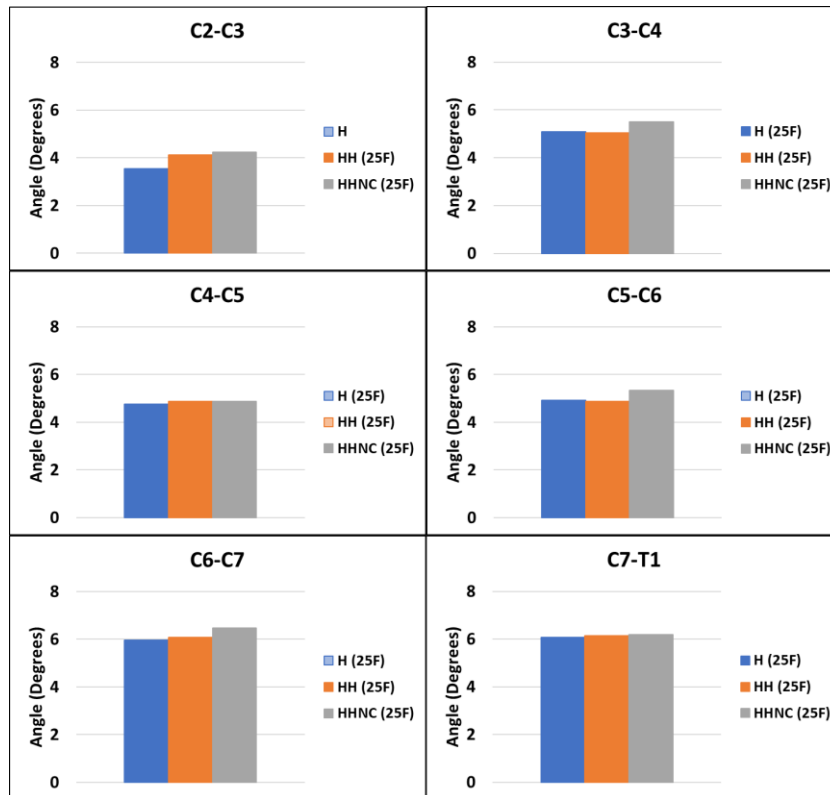


Figure 125: Intervertebral flexion response of the $NM_{M50-Hill-E}$ model with and without the HSM in 25° head-neck flexion. The assessment shows similarities in the intervertebral response in the C2-T1 levels ensuring consistency in the non-neutral head-neck position.

The models with HSM configurations were in equilibrium at 25° head-neck flexion based on the verification procedure described prior (Phase #2a). The reaction flexion moment at the centroid of C7 increased by 34% and 66% in the HH_{25F} and HHNC_{25F} cases, respectively, relative to the H_{25F} case. The vertical reaction force at the C7 vertebral section increased by 24% and 66% in the HH_{25F} and HHNC_{25F} cases, respectively, relative to the H_{25F} case (Figure 126).

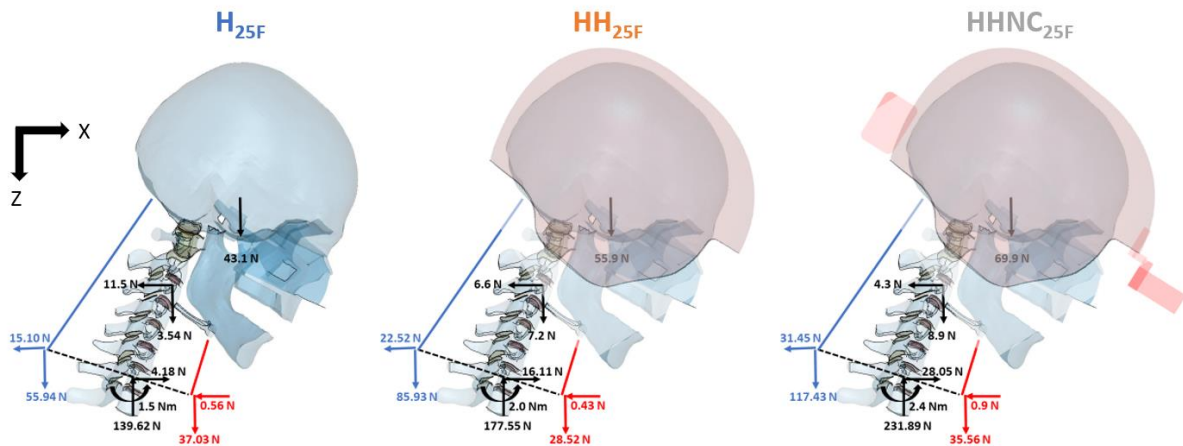


Figure 126: FBDs of the NM_{M50-HIII-E} model in 25° head-neck flexion with and without the HSM.

The overall muscle forces increased with the addition of HSM. Relative to H_{25F} case, there was a mean increase in muscle force by 29% in the HH_{25F} and 75% in the HHNC_{25F} cases, across C2 to C7 (Figure 127). The muscle forces increased from the cranial (C2) to the caudal (C7) region of the neck by 35%, 20% and 16% in H_{25F}, HH_{25F} and HHNC_{25F} cases, respectively. Specifically, the flexor muscle forces decreased by a mean of 22% and 4% in the HH_{25F} and HHNC_{25F} cases, respectively, relative to H_{25F} case, across C2 to C7 vertebral level. The extensor muscle forces increased by a mean of 60% and 122% in the HH_{25F} and HHNC_{25F} cases, respectively, relative to H_{25F} case, across C2 to C7 vertebral levels (Figure 128).

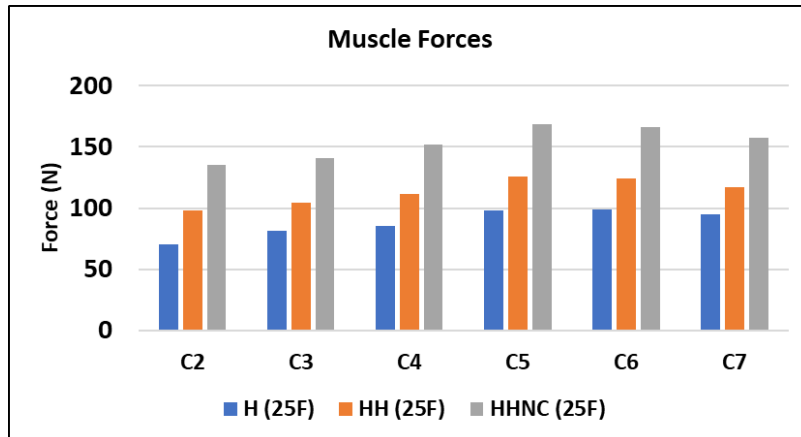


Figure 127: Summary of the overall muscle forces in H_{25F} , HH_{25F} and $HHNC_{25F}$ cases across C2 to C7 vertebral levels, indicating an increase in muscular demand with the addition of HSM.

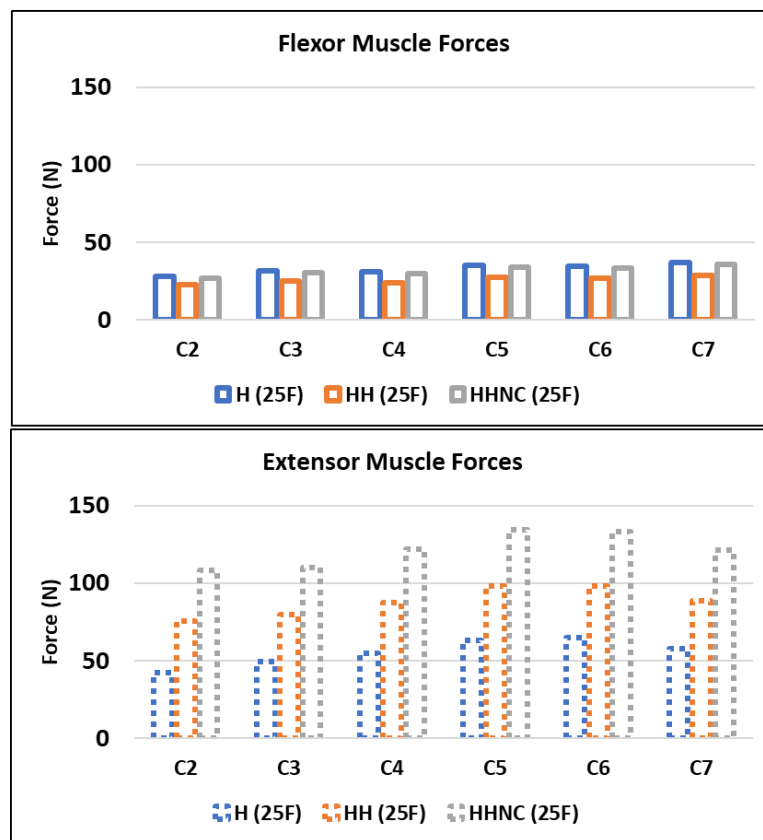


Figure 128: Summary of the flexor and extensor muscle forces in H_{25F} , HH_{25F} and $HHNC_{25F}$ cases across C2 to C7 vertebral levels, specifically indicating an increase in the extensor muscle demand with the addition of HSM.

The compression in the IVD ranged from 87 N at C2-C3 to 245 N at C7-T1 level in the H_{25F} case. In the HH_{25F} and $HHNC_{25F}$ cases, the compressive force ranged from 107 N and 139 N in C2-C3 to 279 N and 344 N in C7-T1, respectively (Figure 129a). The compressive forces experienced a maximum increase in C2-C3 with the inclusion of HSM by 22% and 60% in the HH_{25F} and $HHNC_{25F}$ cases, respectively, compared to the H_{25F} case (Figure 129b). Overall, there was a mean increase in IVD compression by 16% across C2-C3 to C7-T1 in the in the HH_{25F} case compared to the H_{25F} case. Similarly, there was a mean increase in the IVD compression by 47% across C2-C3 to C7-T1 in the in the $HHNC_{25F}$ case compared to the H_{25F} case.

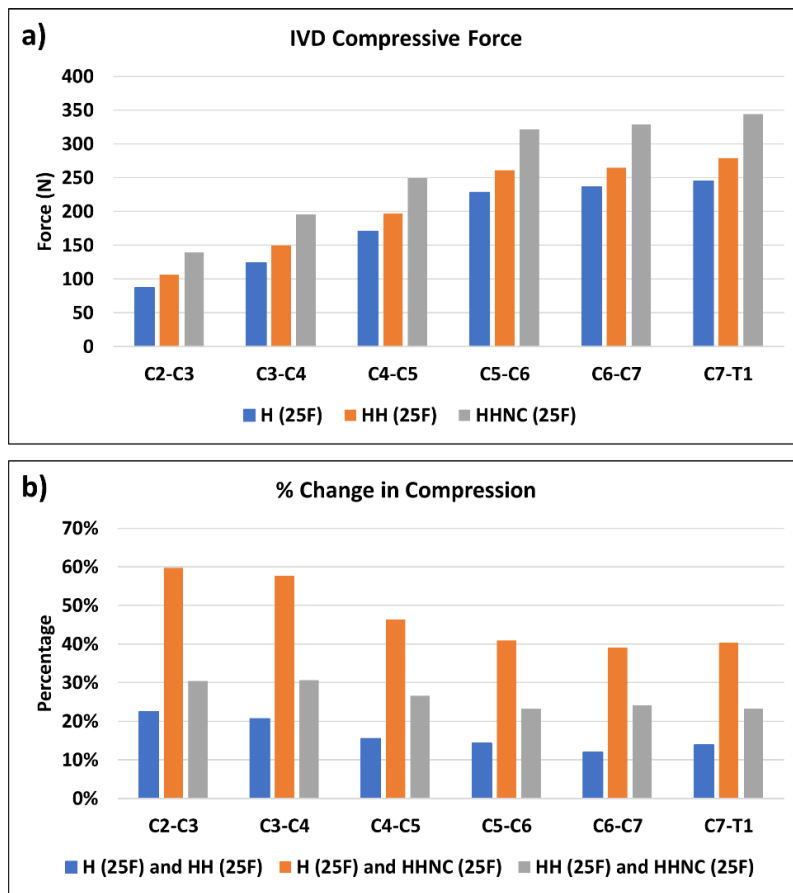


Figure 129: (a) Summary of the compressive forces in C2-C3 to C7-T1 IVDs in H_{25F} , HH_{25F} and $HHNC_{25F}$ cases. (b) Percent change showing increase in compression in C2-C3 to C7-T1 IVDs due to the added HSM.

The AP shear force ranged from 0.3 N in C7-T1 to 26 N in C2-C3 in the H_{25F} case, 0.8 N in C7-T1 to 29 N in C2-C3 in the HH_{25F} case and 1.2 N in C7-T1 to 35 N in C2-C3 in the $HHNC_{25F}$ case (Figure 130a). The IVDs experienced a mean increase in the AP shear force by 12% and 37% across C2-C3 to C6-C7 in the HH_{25F} and $HHNC_{25F}$ cases, respectively, relative to the H_{25F} case (Figure 130b). At the C6-C7 level, the AP shear force between the H_{25F} and HH_{25F} cases were similar. As the magnitude of the AP shear force in the C7-T1 level was low compared to other levels (≤ 1 N), a small increase in the force at this level led to a larger percent increase i.e. 170% increase in HH_{25F} and 307% increase in $HHNC_{25F}$, relative to H_{25F} .

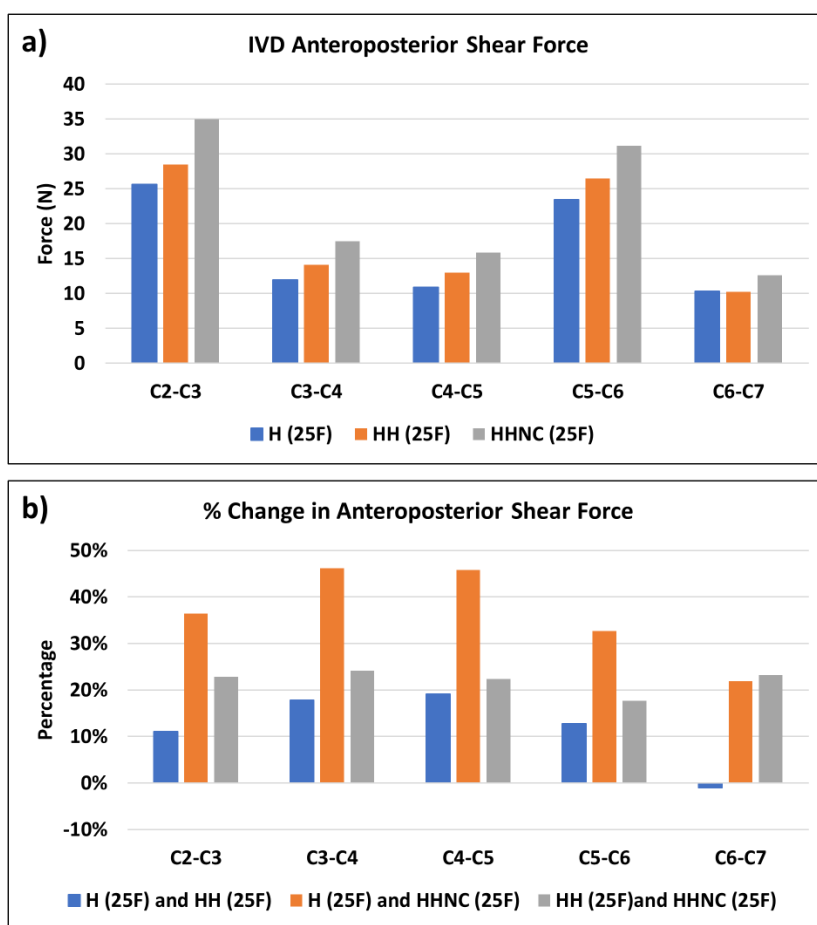


Figure 130: (a) Summary of the AP shear forces in C2-C3 to C6-C7 IVDs in H_{25F} , HH_{25F} and $HHNC_{25F}$. (b) Percent change showing increase in AP shear in C2-C3 to C6-C7 IVDs due to the added HSM.

The mean effective peak stress in the vertebral endplates across C2 to C7 vertebrae was 3.9 MPa in H_{25F} case, 4.6 Mpa in the HH_{25F} case and 5.8 Mpa in the HHNC_{25F} case. There was an increase in the peak stress in the HH_{25F} and HHNC_{25F} cases by a mean of 17% and 47%, respectively, across all the levels, relative to the H_{25F} case. The C2 inferior endplate experienced the highest peak stress relative to the other endplates in the HH_{25F} (7 Mpa) and HHNC_{25F} (11 Mpa) cases. The peak stress in the C2 inferior endplate and C3 superior endplate increased by 54% and 55%, respectively, in the HH_{25F} case relative to H_{25F} case. Similarly, the peak stress in the C2 inferior endplate and C3 superior endplate increased by 140% and 106%, respectively, in the HHNC_{25F} case relative to H_{25F} case. In all the endplates except C2 inferior and C3 superior, the increase in peak stress was $\leq 45\%$ in the HH_{25F} and HHNC_{25F} cases relative to the H_{25F} case (Figure 131). The peak stresses were observed in the bilateral aspects of the C2 inferior endplate in all the three cases simulated for 25° head-neck flexion with and without the HSM (Figure 132). The endplate effective stress contours for the remaining levels are furnished in Figures D1-D10 in Appendix D.

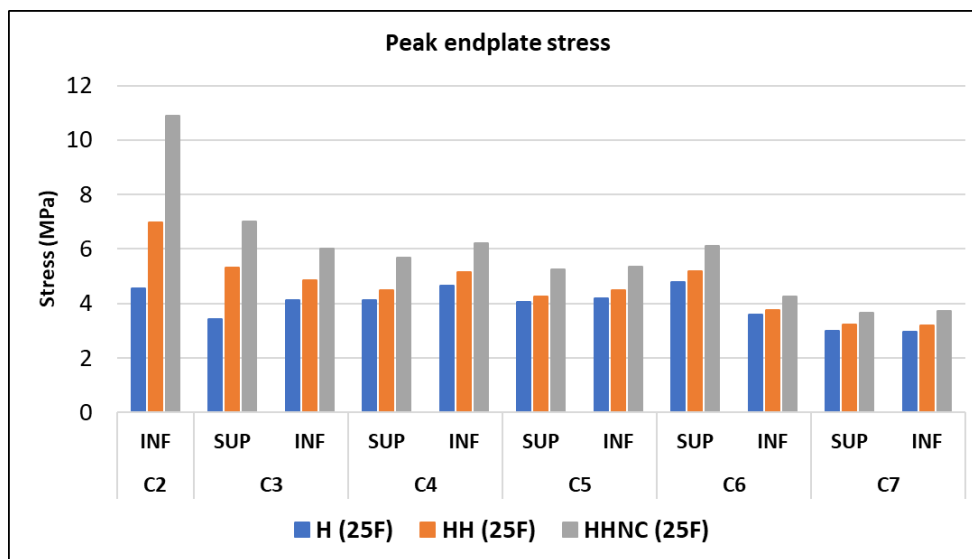


Figure 131: Peak endplate effective stresses across C2 to C7 vertebrae increased with the addition of HSM.

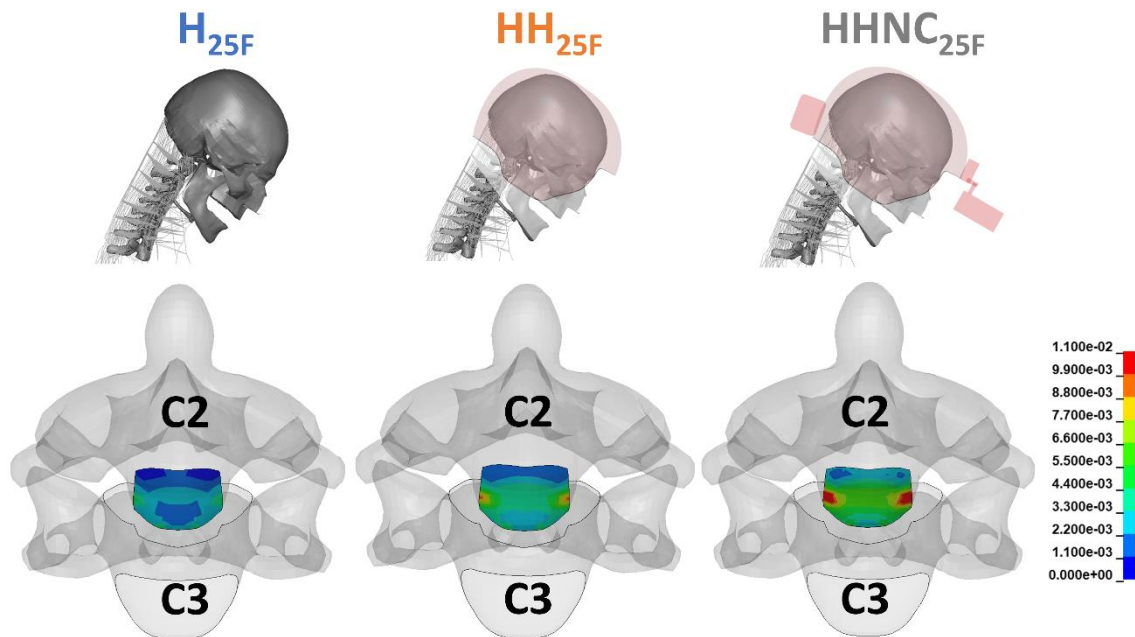


Figure 132: Effective stress contours in the C2 inferior endplate demonstrating an increase in stress as a result of added HSM.

In general, there was an increase in the peak fiber strains with the addition of HSM and a consistent head-neck position. With the addition of helmet (HH_{25F}), there was a mean increase in the fiber strains by 4% across C2-C3 to C7-T1 IVDs relative to the head without helmet (H_{25F}). With the addition of NVG and CW to the helmet (HHNC_{25F}), there was a mean increase in the fiber strains by 16% across C2-C3 to C7-T1 IVDs relative to H_{25F}. In the HH_{25F} case, the maximum increase in peak strain (7%) relative to H_{25F}, was identified in C2-C3 and C7-T1 IVDs. Similarly, in the HHNC_{25F} case, the maximum increase in peak strain (27%) relative to H_{25F} was identified in C7-T1 IVD (Figure 133). At the intervertebral levels, the highest fiber strains were observed in the C7-T1 IVD in all three cases (Figure 133). Within each IVD, peak strains were observed in the posterior aspects of the innermost layer of the collagen fibers (Figure 134). The collagen fiber strain contours for the remaining IVD levels are furnished in Figures D11-D15 in Appendix D.

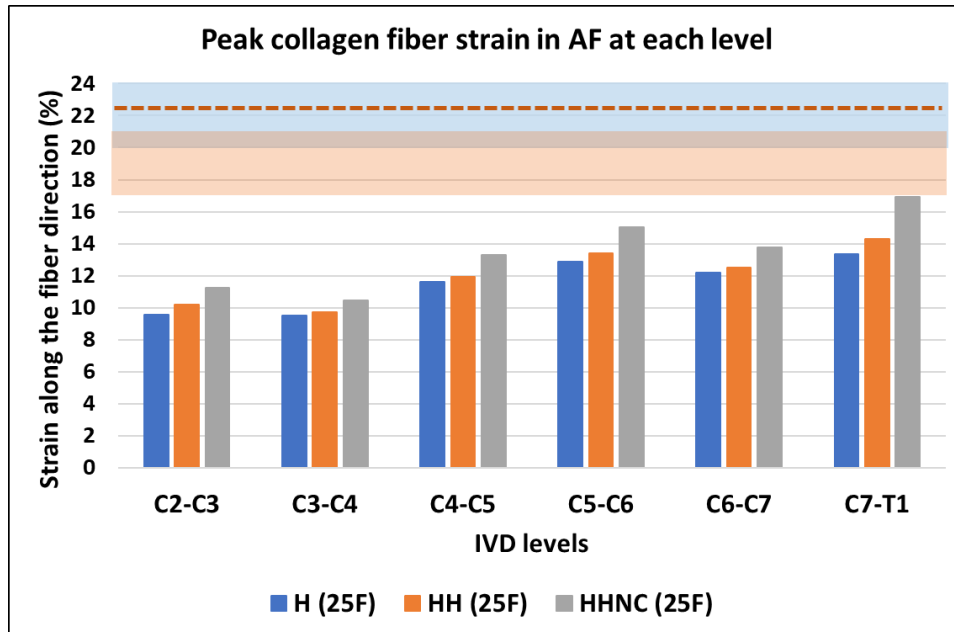


Figure 133: Collagen fiber peak strains along the fiber orientation in AF in 25° head-neck flexion with and without the HSM.

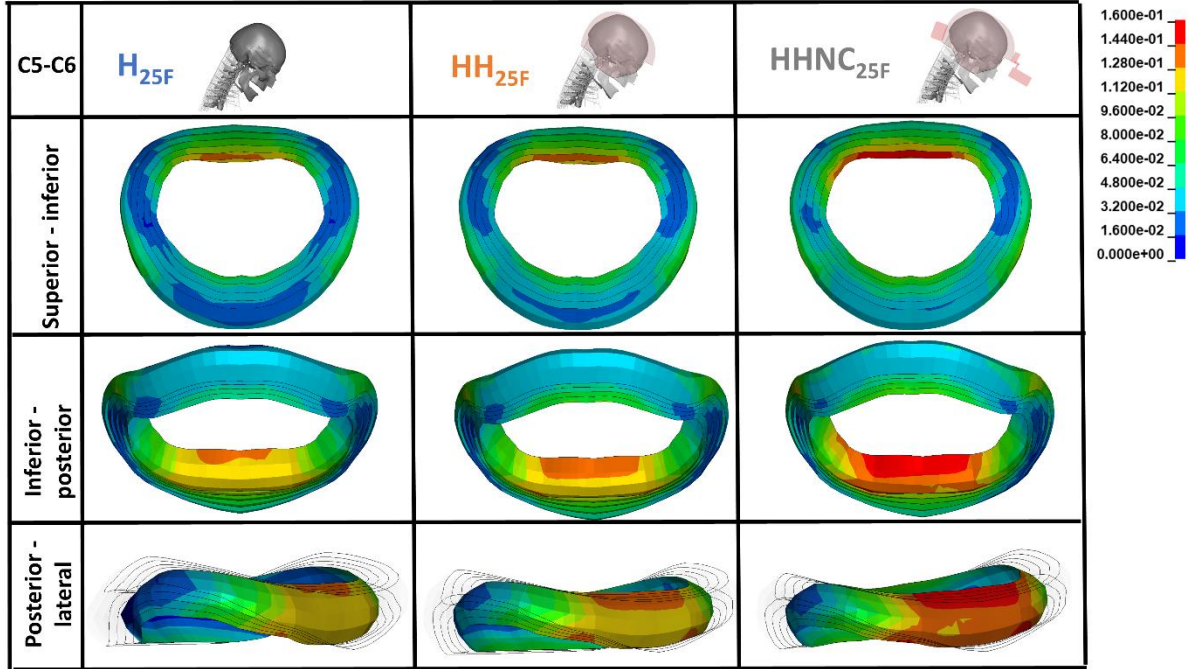


Figure 134: Illustrating the collagen fiber strain contours in the C5-C6 AF in 25° head-neck flexion with and without the HSM in different perspectives, namely superior-inferior, inferior-posterior and posterior-lateral. In the posterior-lateral view, the outer four layers of lamellae are made transparent for visual purposes.

Despite similarities in the peak fiber strains between the H_{25F} and HH_{25F} cases (4% increase), the area in the lamellae experiencing higher strains increased with the addition of a helmet. For example, in the innermost lamella of C4-C5 IVD, 8% of the area experienced a strain between 10%-15% in the H_{25F} case. With the addition of a helmet (HH_{25F}), 15% of the innermost layer of C4-C5 AF experienced a strain between 10% to 15%. Similarly, in the innermost lamella of C5-C6 IVD, 22% and 29% of the area experienced strains between 10%-15% in the H_{25F} and HH_{25F} cases, respectively (Figure 135).

The addition of NVG and CW to the helmet ($HHNC_{25F}$), along with a 16% increase in peak fiber strain relative to H_{25F} , also increased the area experiencing higher strains when compared to the H_{25F} case. The area in the innermost AF layer in the C2-C3 IVD that experienced strains between 10%-15% increased from 0% in H_{25F} to 11% in $HHNC_{25F}$. The area in the innermost AF layer in the C4-C5 IVD that experienced strains between 10%-15% increased from 8% in H_{25F} to 26% in $HHNC_{25F}$. The area in the innermost AF layer in the C5-C6 IVD that experienced strains between 10%-15% increased from 22% in H_{25F} to 36% in $HHNC_{25F}$ (Figure 135).

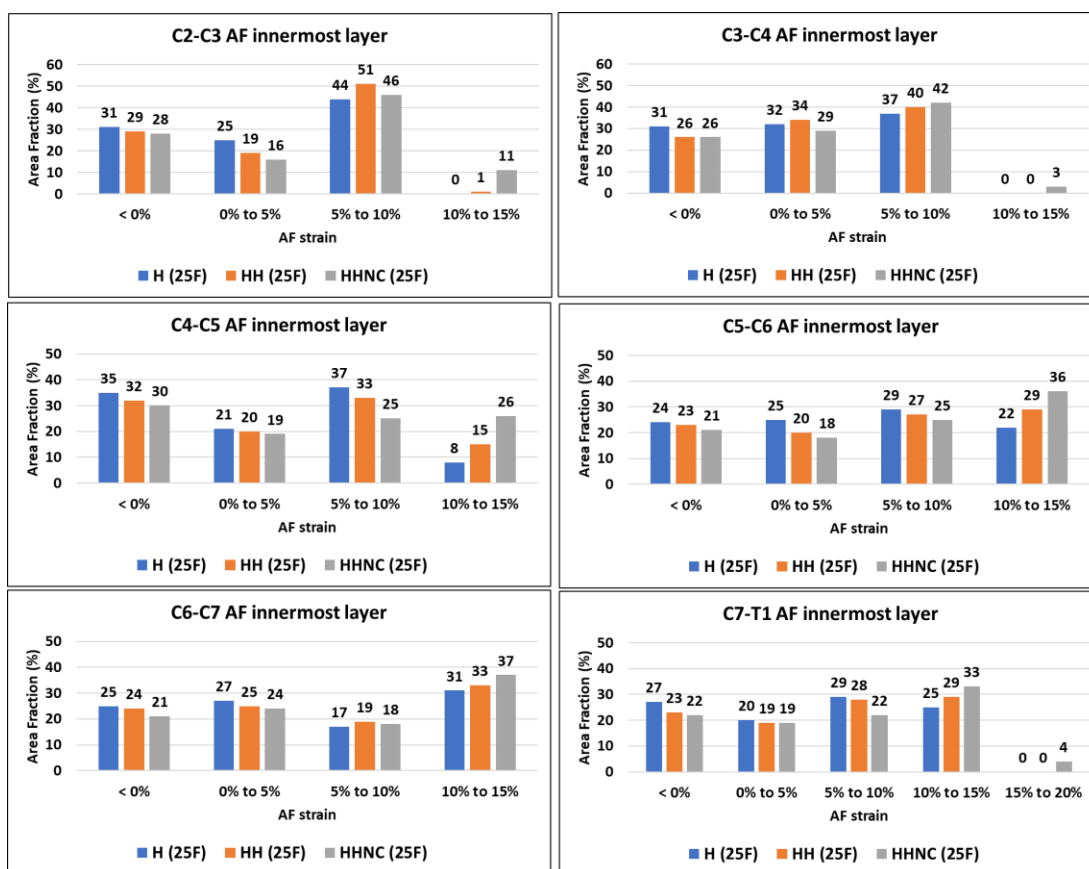


Figure 135: Quantifying the strain based on area fractions in the innermost collagen fiber layer of the AF that experienced relatively higher strains than the other layers. The results showed an increase in the area experiencing higher strains with the addition of HSM.

The ligament distractions were similar for the cases with and without the HSM, owing to similarities in the kinematics and intervertebral rotation. The mean difference in the distractions across C2-C3 to C7-T1, across each ligament in the posterior aspects of the vertebrae, decreased by 0.04 mm in the HH_{25F} case relative to the H_{25F} case. Similarly, the mean difference in the distractions across C2-C3 to C7-T1, across each ligament in the posterior aspects of the vertebrae, decreased by 0.03 mm in the HHNC_{25F} case relative to the H_{25F} case (Figure 136). The distractions in all the ligaments were in either toe or linear regions, indicating that the flexion position was within the physiologic limits based on Mattucci et al. (2012) (Figure 137).

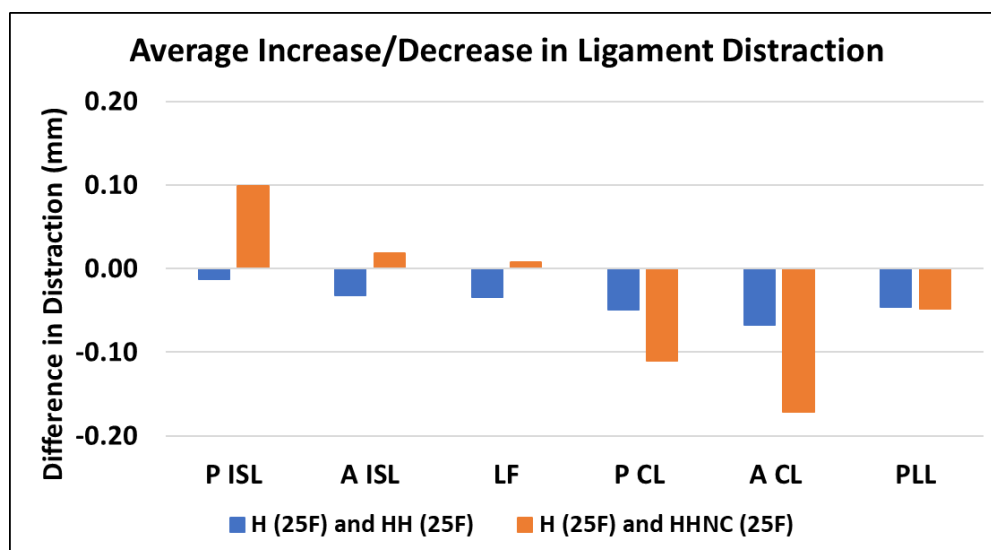


Figure 136: The mean difference in ligament distraction across C2-C3 to C7-T1 levels with and without the HSM in 25° head-neck flexion. The increase and decrease in distractions are in denoted in positive and negative, respectively. There were minor differences in the ligament distractions due to HSM.

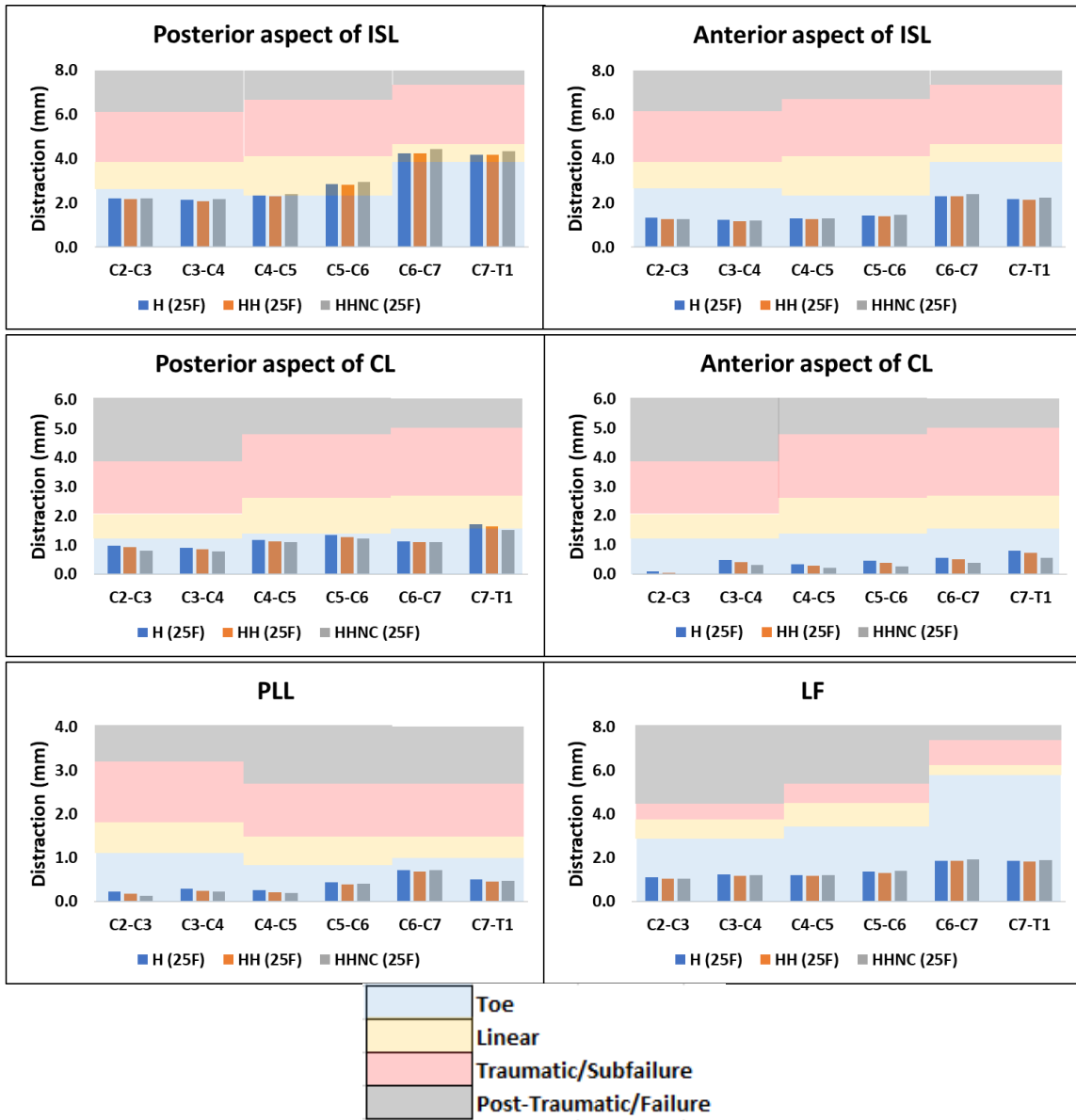


Figure 137: Ligament injury risk summary during the 25° head-neck flexion with and without the HSM. The results confirm that the ligaments elongated within the physiologic limits (toe and linear regions).

4.4.2 Effect of non-neutral head-neck position magnitude with the HSM (HHNC configuration)

The overall head rotation (C0-T1) in flexion when the model with the HSM was repositioned in the target flexion (HHNC_{25F}) and combined positions (HHNC_{25F|10LB|25AR}) was 33° and 28.5°, respectively. The axial rotation in the head caused an increase in the upper cervical spine extension (276% increase), thereby resulting in the decrease in overall head rotation by 4.5° in the combined position relative to flexion-only position. Despite similarities in the global head-neck flexion ($\theta=25^\circ$) in both the cases, the intervertebral flexion of C2-T1 between the two cases was not comparable owing to the coupled axial rotation and lateral bending in the HHNC_{25F|10LB|25AR} case. There was an increase in the intervertebral flexion in C2-C3 by 31%, C3-C4 by 13%, C4-C5 by 22%, C5-C6 by 4% and C7-T1 by 67% in the HHNC_{25F|10LB|25AR} case relative to HHNC_{25F} case. The intervertebral flexion reduced C6-C7 by 55% in the HHNC_{25F|10LB|25AR} case relative to HHNC_{25F} case (Figure 138).

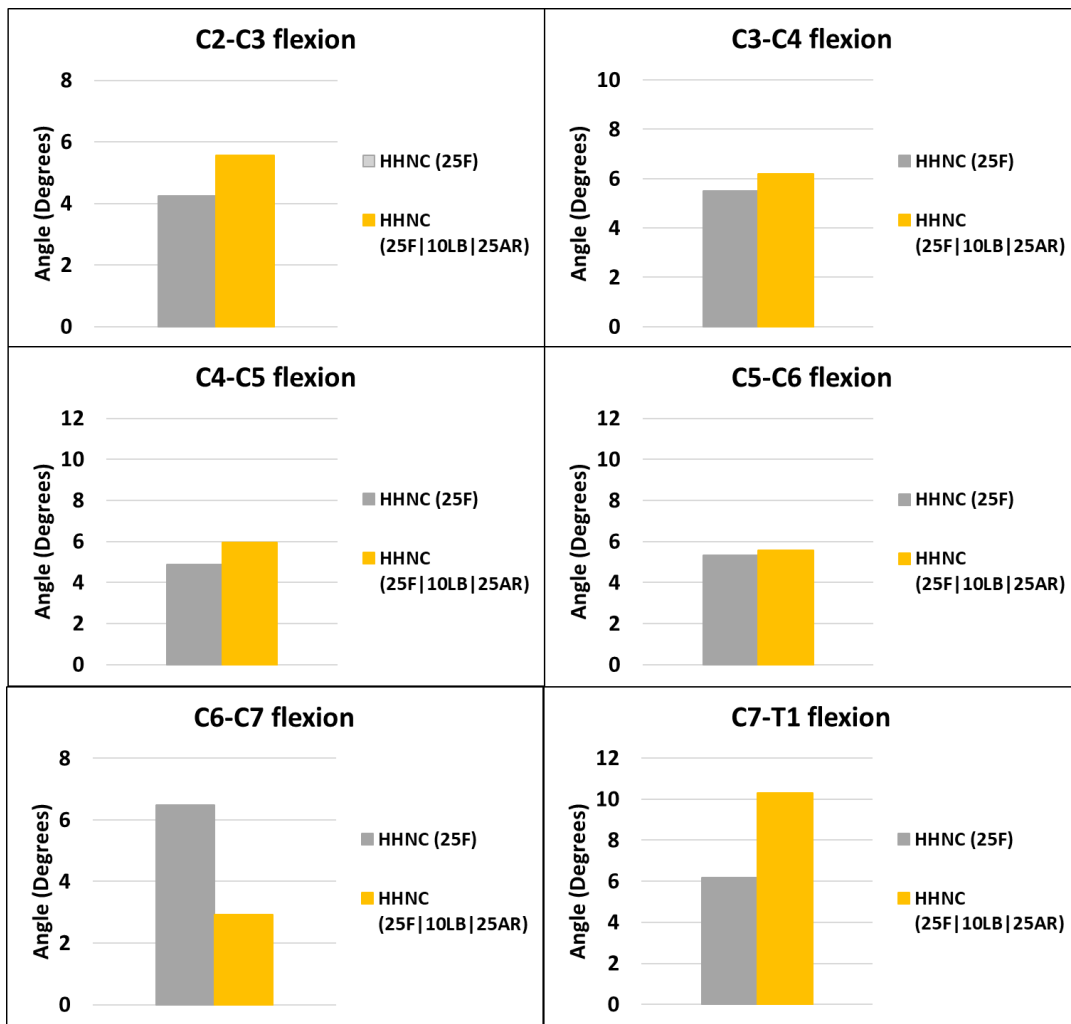


Figure 138: Intervertebral flexion response of the $NM_{M50-Hill-E}$ model inclusive of HSM in flexion ($HHNC_{25F}$) and a combined position ($HHNC_{25F|10LB|25AR}$). The assessment showed differences in the intervertebral response in the C6-T1 levels in the combined position relative to a flexion-only position.

The models repositioned in flexion-only and combined positions with the HSM were in equilibrium based on the verification procedure described prior (Phase #2). The reaction flexion moments at the centroid of C7 were identical in the $HHNC_{25F}$ (2.4 Nm) and $HHNC_{25F|10LB|25AR}$ cases (2.3 Nm). The vertical reaction force at the C7 vertebral section reduced by 12% in the $HHNC_{25F|10LB|25AR}$ relative to $HHNC_{25F}$ case (Figure 139).

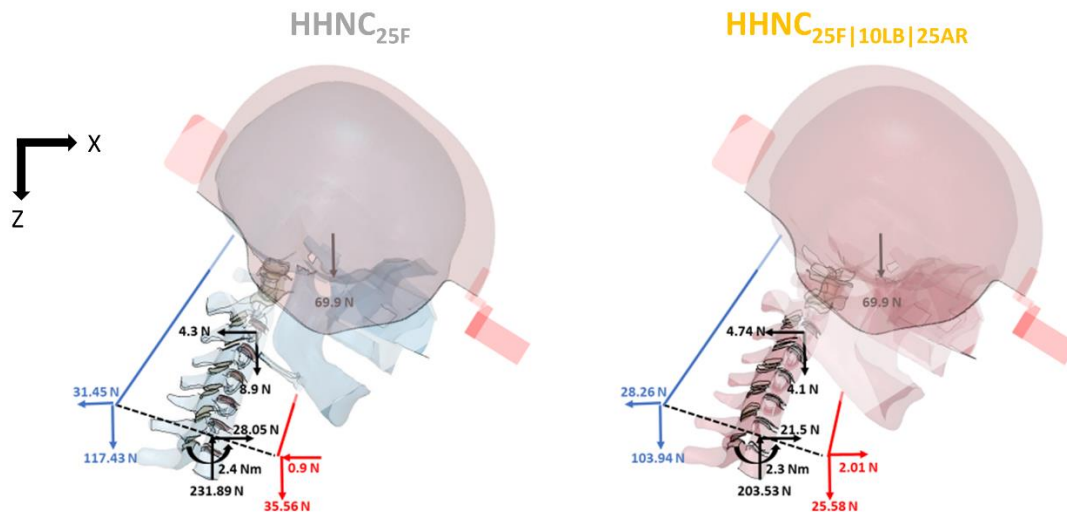


Figure 139: FBD of the $NM_{M50-Hill-E}$ model in head-neck flexion and combined positions with the HSM (HHNC).

The overall muscle forces decreased by 3% across C2 to C7 in a combined position compared to flexion-only position. The muscle forces increased only in the C2 level by 48% in the $HHNC_{25F|10LB|25AR}$ case relative to the $HHNC_{25F}$ case. In the rest of the levels, there was a mean decrease in the muscle force by 13% in the $HHNC_{25F|10LB|25AR}$ case relative to the $HHNC_{25F}$ case. In the $HHNC_{25F|10LB|25AR}$ case, the muscle force at C2 was higher compared to the other levels owing to the higher activation of oblique capitis inferior and rectus posterior major muscles (to axially rotate the head) (Figure 140). Specifically, the flexor muscle forces decreased by a mean of 21% in the $HHNC_{25F|10LB|25AR}$ case relative to $HHNC_{25F}$ case across C2 to C7 vertebral levels. The extensor muscle forces increased by 61% in the $HHNC_{25F|10LB|25AR}$ case relative to $HHNC_{25F}$ case at the C2 vertebral level. There was a decrease in extensor muscle force by 10% across C3 to C7 vertebral levels in the $HHNC_{25F|10LB|25AR}$ case relative to $HHNC_{25F}$ case (Figure 141).

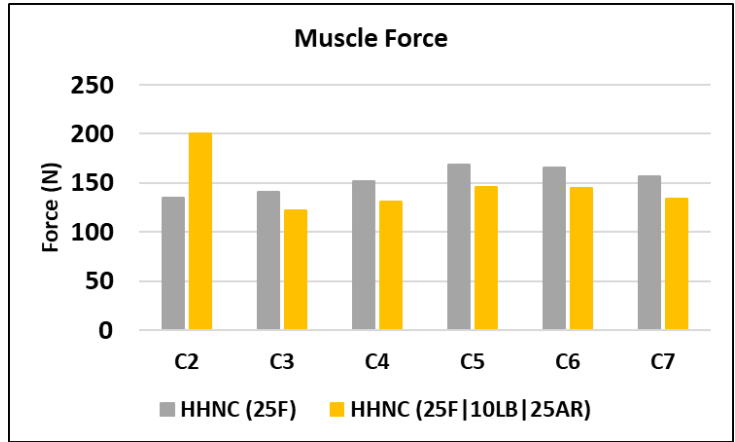


Figure 140: Summary of the overall muscle forces in HHNC_{25F} and HHNC_{25F|10LB|25AR} cases across C2 to C7 vertebral levels, indicating an increase in muscular demand in the C2 vertebral level due to axial rotation.

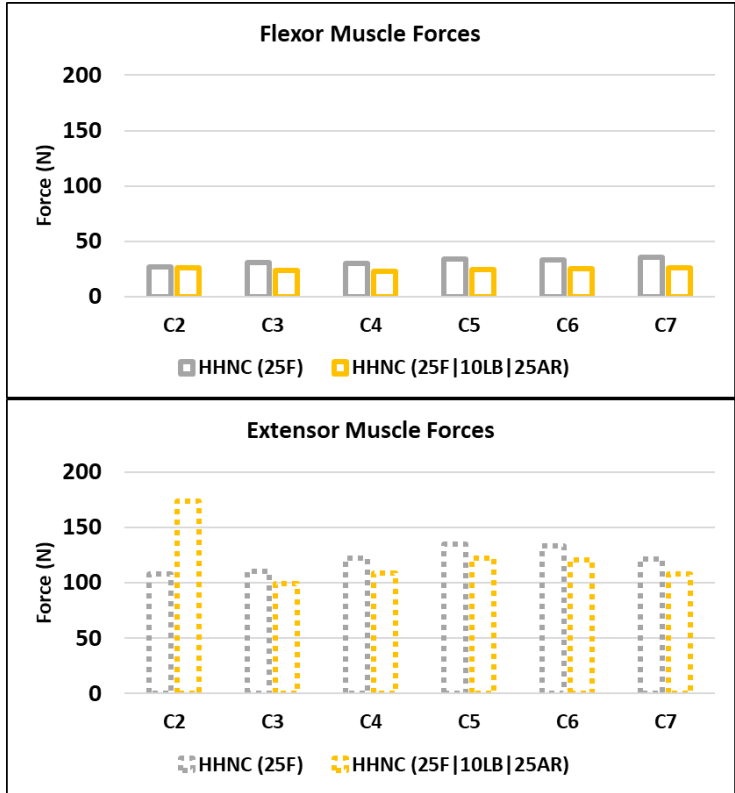


Figure 141: Summary of the flexor and extensor muscle forces in HHNC_{25F} and HHNC_{25F|10LB|25AR} cases across C2 to C7 vertebral levels, specifically indicating an increase in the extensor muscle demand at the C2 vertebral level due to axial rotation.

The compression in the IVD ranged from 202 N at C2-C3 to 352 N at C7-T1 level in the HHNC_{25F|10LB|25AR} case (Figure 142a). Overall, there was a mean increase in IVD compression by 14% across C2-C3 to C7-T1 in the in the HHNC_{25F|10LB|25AR} case compared to the HHNC_{25F} case. The compressive forces experienced a maximum increase in C2-C3 in the HHNC_{25F|10LB|25AR} case by 45% relative to the HHNC_{25F} case (Figure 142b). The C3-C4 and C4-C5 IVDs in the HHNC_{25F|10LB|25AR} case experienced an increase in compression by 22% and 7%, respectively, relative to HHNC_{25F} case. The increase in compression was minimal ($\leq 5\%$) in the C5-C6 to C7-T1 levels in the HHNC_{25F|10LB|25AR} case relative to the HHNC_{25F} case (Figure 142b).

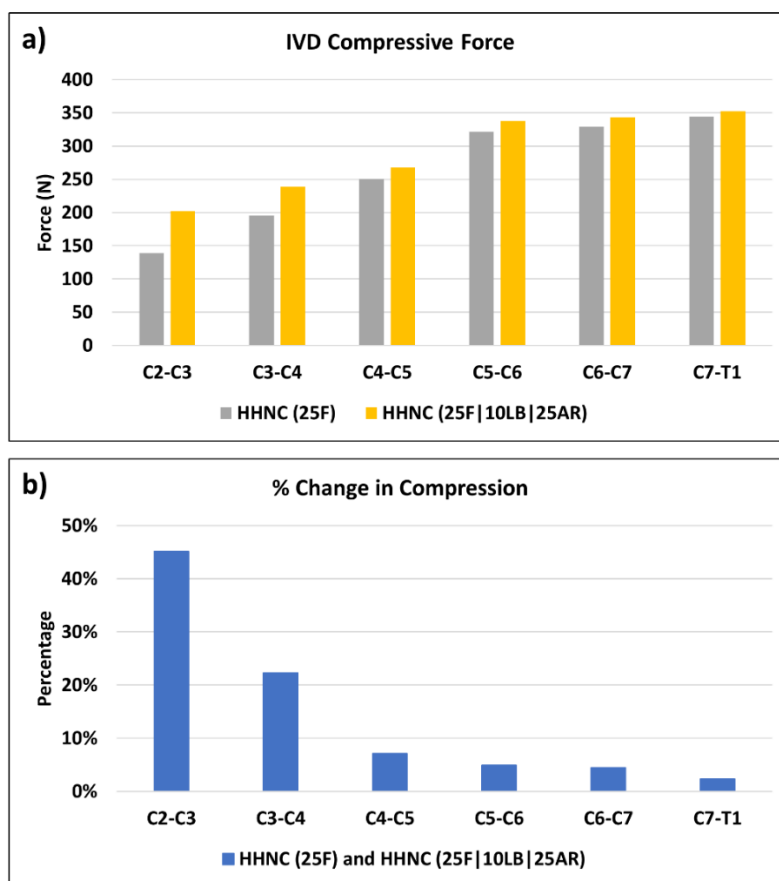


Figure 142: (a) Summary of the compressive forces in C2-C3 to C7-T1 IVDs in HHNC_{25F} and HHNC_{25F|10LB|25AR} cases, (b) Percent change showing an increase in compression in C2-C3 and C3-C4 IVDs due to axial rotation.

The AP shear force ranged from 0.7 N in C7-T1 to 56 N in C2-C3 in the HHNC_{25F|10LB|25AR} case (Figure 143a). The IVDs experienced a mean increase in the AP shear force by 20% across C2-C3 to C6-C7 in the HHNC_{25F|10LB|25AR} case, relative to HHNC_{25F} case (Figure 143b). As the AP shear force in the C7-T1 level, in both the cases, had lower magnitude (≤ 1 N), a small increase in the force at this level led to a larger percent change (45% decrease) in HHNC_{25F|10LB|25AR} relative to HHNC_{25F}. The increase in AP shear in the HHNC_{25F|10LB|25AR} relative to HHNC_{25F} case was highest at the C2-C3 level (60% increase). At C3-C4 and C6-C7 levels, there was a 30% and 16% increase in AP shear, respectively, in the HHNC_{25F|10LB|25AR} relative to HHNC_{25F} case. The AP shear in C4-C5 and C5-C6 were similar in both the cases (Figure 143b).

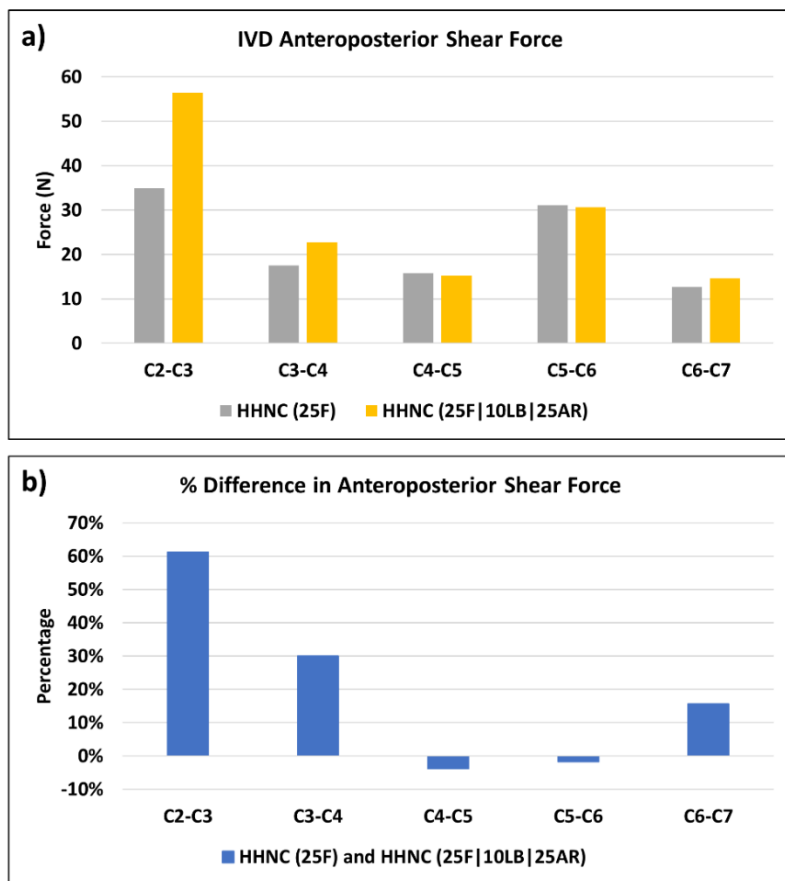


Figure 143: (a) Summary of the AP shear forces in C2-C3 to C6-C7 IVDs in HHNC_{25F} and HHNC_{25F|10LB|25AR} cases, (b) Percent change showing increase in AP shear in C2-C3, C3-C4 and C6-C7 IVDs due to axial rotation.

The mean effective peak stress in the vertebral endplates across C2 to C7 vertebrae was 5.8 MPa and 6.3 MPa in HHNC_{25F} and HHNC_{25F|10LB|25AR} cases, respectively. There was an increase in the peak stress in the HHNC_{25F|10LB|25AR} case by a mean of 9.7% across all the levels, relative to the HHNC_{25F} case. The C2 inferior endplate experienced the highest peak stress relative to the other endplates in the HHNC_{25F} (11 MPa) and HHNC_{25F|10LB|25AR} (10 MPa) cases. In the C2 inferior endplate, there was a 10% decrease in the peak stress in the HHNC_{25F|10LB|25AR} case compared to HHNC_{25F} case. In all the endplates except C2 inferior, the increase in peak stress was between 4% (C6 superior) to 27% (C4 superior) in the HHNC_{25F|10LB|25AR} case relative to the HHNC_{25F} case (Figure 144). The peak stresses were observed in the bilateral aspects of the C4 superior endplate in flexion and combined cases (Figure 145). The endplate effective stress contours for the remaining levels are furnished in Figures D16-D25 in Appendix D.

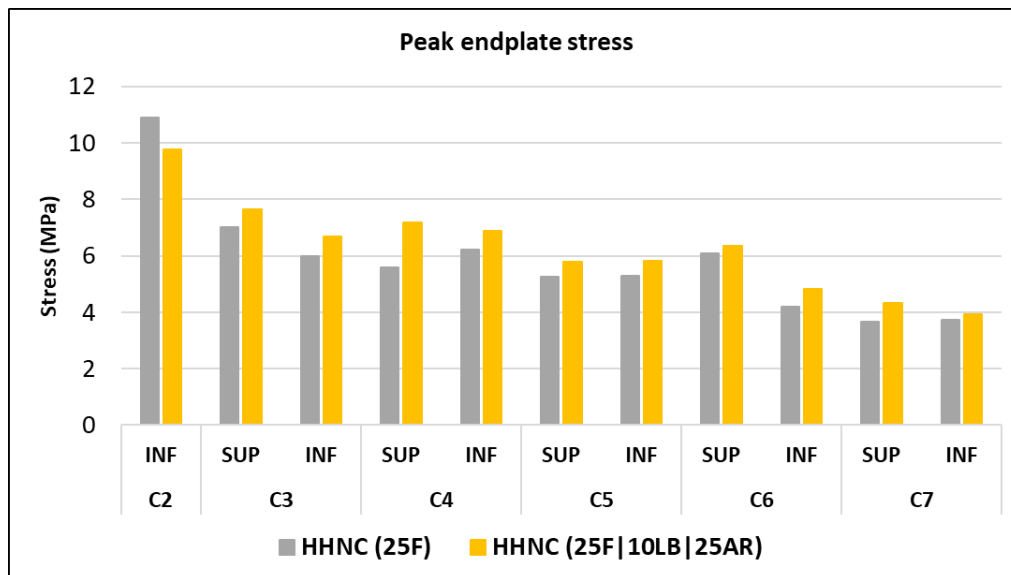


Figure 144: Peak endplate effective stresses across C2 to C7 vertebrae increased slightly when the head-neck deviated from a flexion-only to a combined position with the HSM (HHNC).

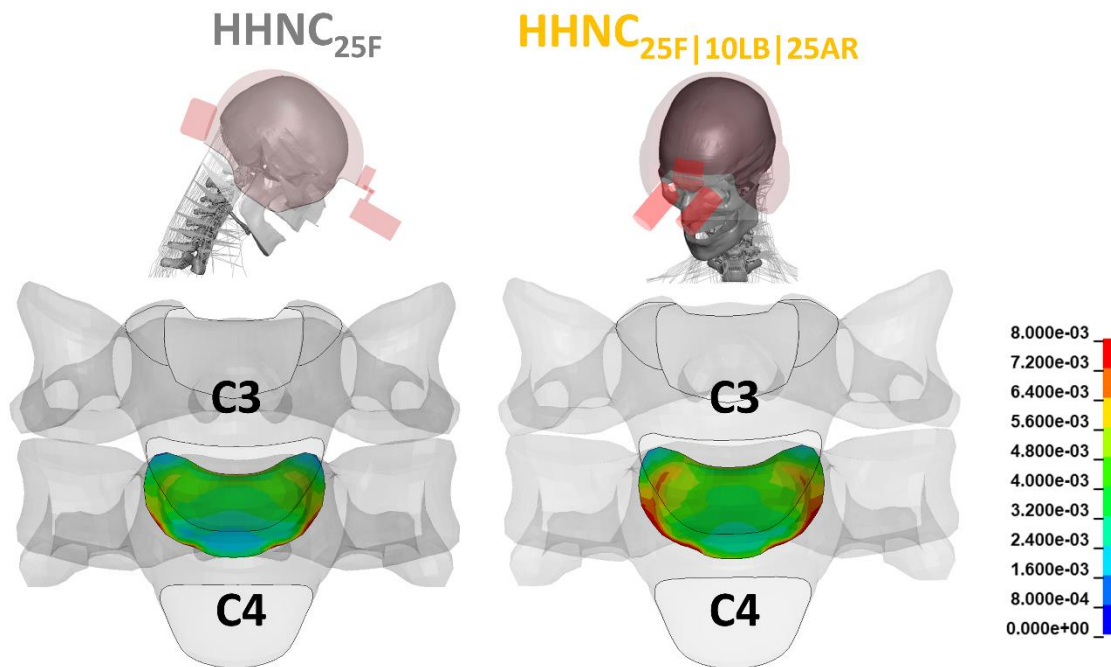


Figure 145: Effective stress contours in the C4 superior endplate demonstrating an increase in stress as a result of increase in magnitude of non-neutral position from a flexion-only to a combined position with the HSM (HHNC).

In general, there was a slight increase in the peak fiber strains with an increase in magnitude of head-neck position from flexion to combined. There was a mean % increase in the fiber strains by 9% across C2-C3 to C7-T1 IVDs from a flexion (HHNC_{25F}) to a combined position (HHNC_{25F10LB25AR}). There was an increase of 21% in the peak fiber strain in the C2-C3 IVD in the combined position compared to a flexed-only position. There was an increase in the peak fiber strains at the C3-C4 IVD by 17%, C4-C5 IVD by 5%, C5-C6 IVD by 8%, and C6-C7 IVD by 9% in the HHNC_{25F10LB25AR} case relative to HHNC_{25F} case. There was a slight decrease in the peak fiber strain by 3% in the C7-T1 IVD in the HHNC_{25F10LB25AR} case relative to HHNC_{25F} case (Figure 146). Compared to all the IVD levels, the peak fiber strain was highest in the C7-T1 IVD in both cases (HHNC_{25F} and HHNC_{25F10LB25AR}) (Figure 146). Within each IVD, peak strains were observed in the posterior aspects of the innermost layer of the collagen fibers (Figure 147). The collagen fiber strain contours for the remaining IVD levels are furnished in Figures D26-D30 in Appendix D.

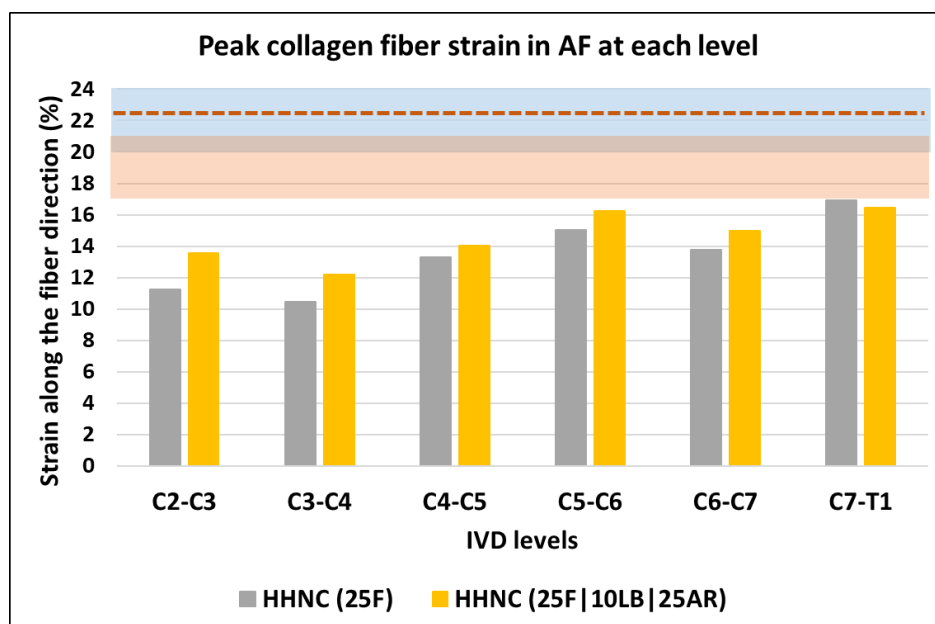


Figure 146: Collagen fiber peak strains along the fiber orientation in AF in head-neck flexion and combined positions with the HSM (HHNC).

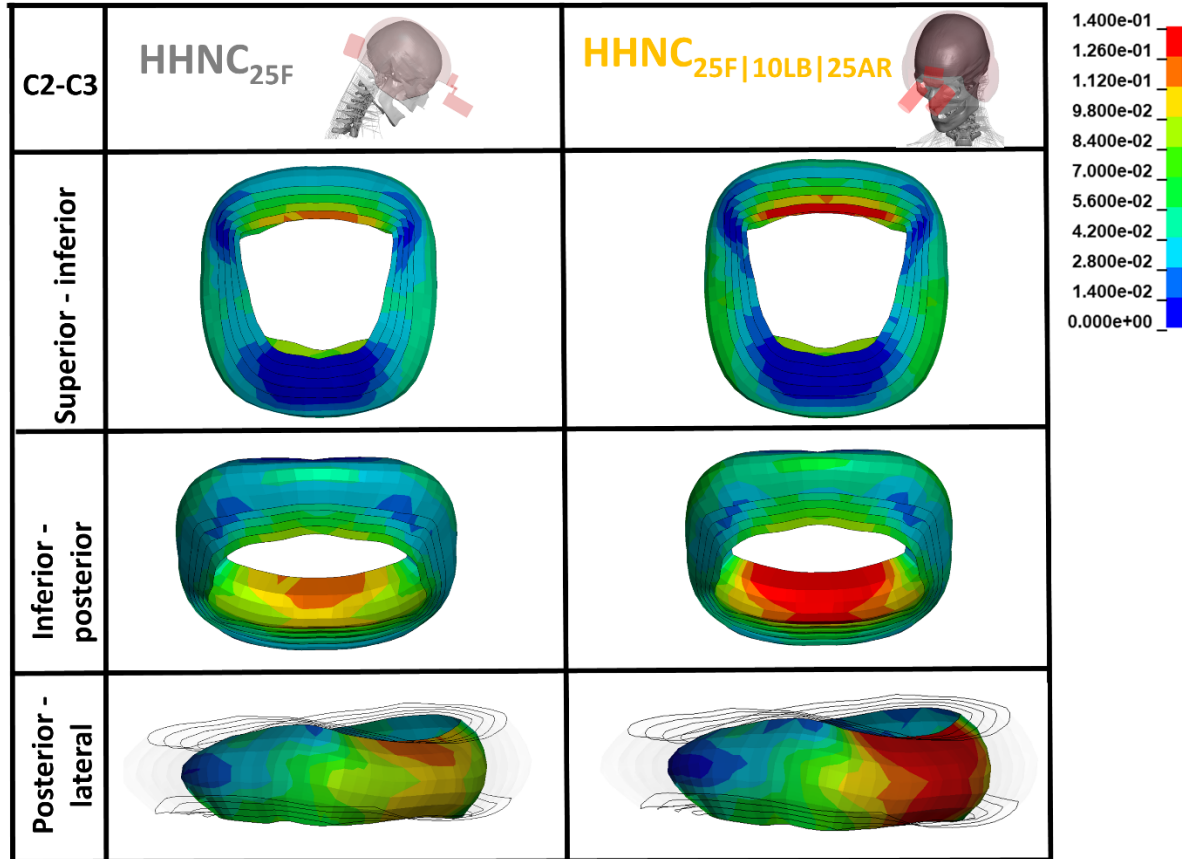


Figure 147: Illustrating the collagen fiber strain contours in the C2-C3 AF in head-neck flexion and combined positions with the HSM (HHNC) in different perspectives, namely superior-inferior, inferior-posterior and posterior-lateral. In the posterior-lateral view, the outer four layers of AF are made transparent for visual purposes to highlight the innermost layer.

In the innermost lamella of C2-C3 IVD, 11% of the area experienced strain between 10%-15% in the HHNC_{25F} case, while 23% of the area experienced strains between 10%-15% in the HHNC_{25F|10LB|25AR} case. Similarly, in the innermost lamella of C3-C4 IVD, 3% of the area experienced strain between 10%-15% in the HHNC_{25F} case. In comparison, 12% of the area experienced strains between 10%-15% in the HHNC_{25F|10LB|25AR} case. In the innermost fibers of C5-C6 AF, 0.4% of the area experienced strains between 15%-20% in the HHNC_{25F}, while 8% of the area experienced strains between 15%-20% in the HHNC_{25F|10LB|25AR} case (Figure 148).

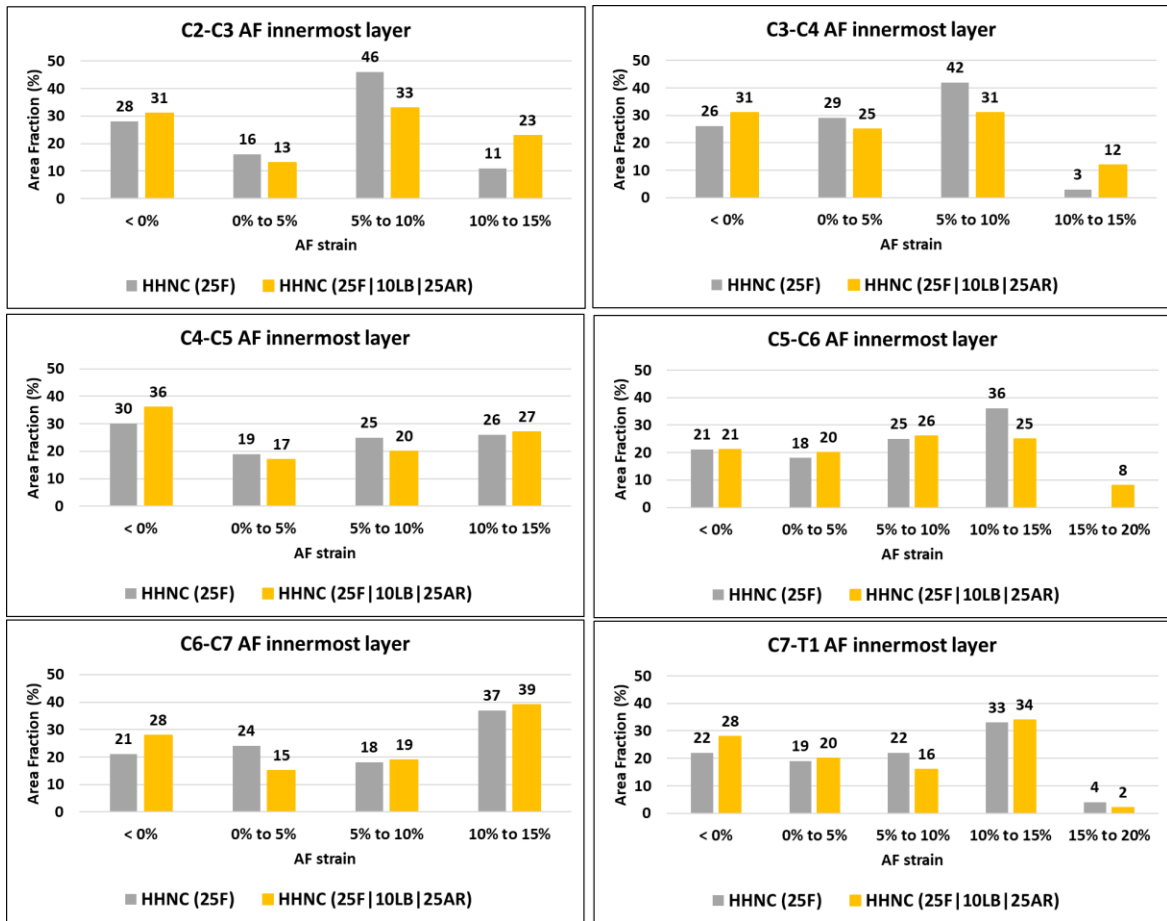


Figure 148: Quantifying the strains based on area fractions in the innermost collagen fiber layer of the AF that experienced relatively higher strains than the other layers. The results showed a modest increase in the area experiencing higher strains with the increase in magnitude of non-neutral position with the HSM (HHNC).

In general, the ligament distractions increased as a result of an increase in the magnitude of head-neck position from flexion to a combined position. The mean increases in the distractions across C2-C3 to C7-T1, across each ligament in the posterior aspects of the vertebrae, was 0.25 mm in the HHNC_{25F|10LB|25AR} case relative to the HHNC_{25F} case. The distractions in the ipsilateral side (right side) of the CL decreased by 0.08 mm and 0.31 mm in the anterior and posterior aspects, respectively. The distraction in the contralateral side (left side) of the CL increased by approximately 0.6 mm in the anterior and posterior aspects. The distractions in the posterior and anterior aspects of the ISL increased

by approximately 0.5 and 0.3 mm, respectively. Similarly, the PLL and LF distractions increased by approximately 0.1 and 0.3 mm, respectively (Figure 149). The distractions in all the ligaments were in either toe or linear regions, indicating that the flexion position was within the physiologic limits (Figure 150).

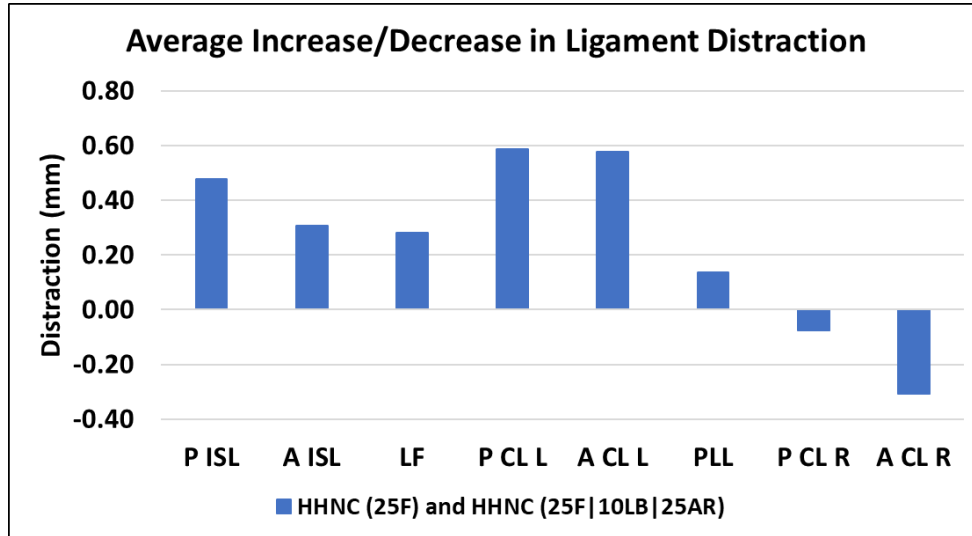


Figure 149: The mean difference in ligament distraction across C2-C3 to C7-T1 levels in head-neck flexion and combined positions with the HSM (HHNC). The increase and decrease in distractions are in denoted in positive and negative, respectively. The differences were higher in the contralateral CL.

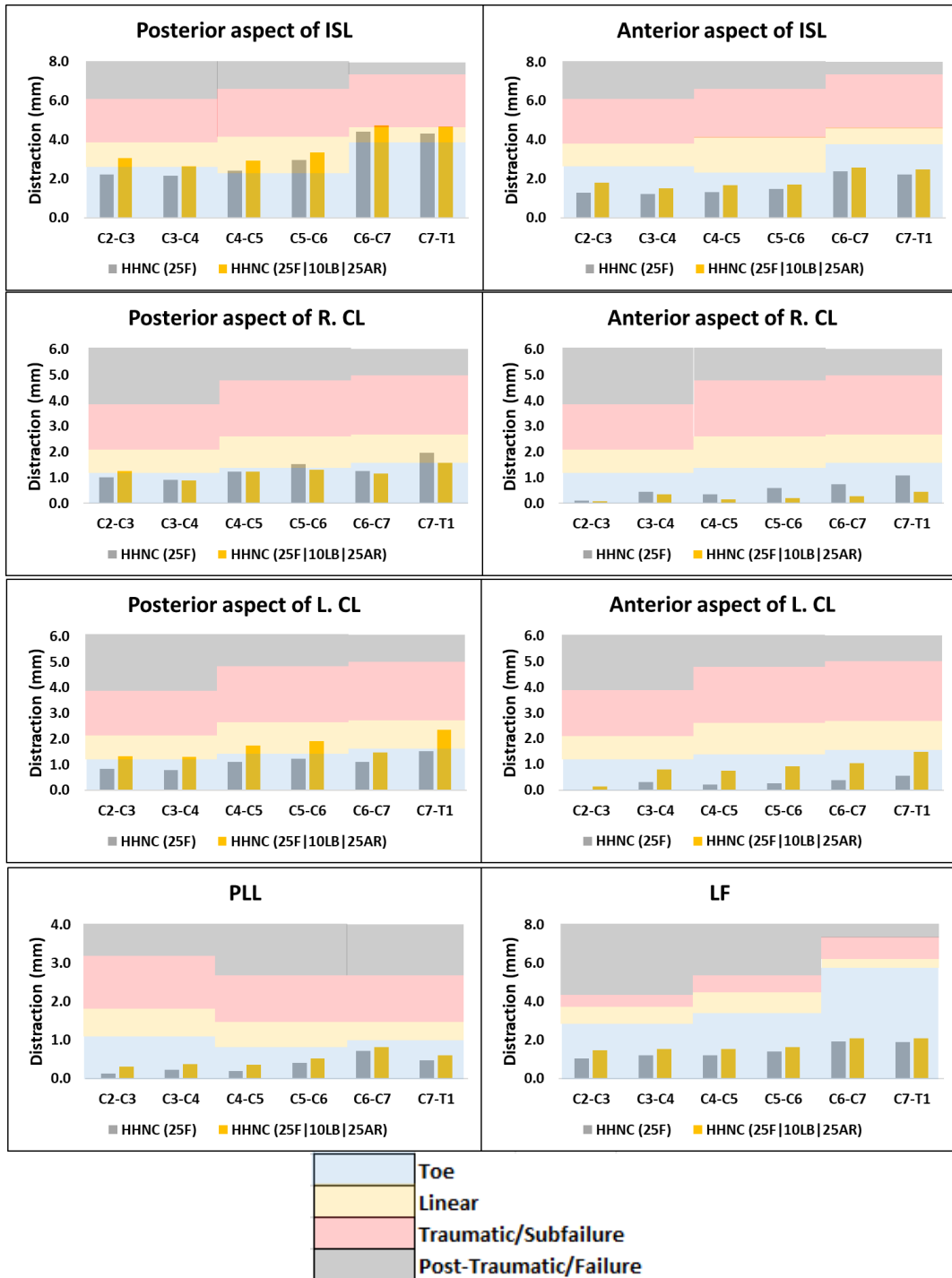


Figure 150: Ligament injury risk summary in head-neck flexion and combined positions with the HSM (HHNC). The results confirm that the ligaments elongated within the physiologic limits (toe and linear regions) with exception in the posterior ISL.

Chapter 5 Discussion

5.1 Phase #1: Enhancement, verification, and validation of the cervical spine model

This study enhanced and validated a detailed ligamentous cervical spine FE model across the ROM for the purpose of predicting intervertebral kinematics in simulations requiring a non-neutral initial spinal position. Owing to the non-linear nature of the UCS response in ROM, the current study considered UCS response at 0.5 Nm load increments rather than single point assessments presented in previous studies (Brolin and Halldin, 2004; Halldin et al., 2000; Herron et al., 2020; Liu et al., 2016; Mesfar and Moglo, 2013; Osth et al., 2016; Toosizadeh and Haghpanahi, 2011; Zhang et al., 2005), leading to an improved response in the UCS and an overall improvement in the whole LS response. While previous UCS model studies have focused on traumatic loading to the UCS, repositioning models and retaining stresses and strains following repositioning require an accurate response within the ROM. Although a model response at a single point in the ROM could agree with experimental data, this does not guarantee biofidelic response across the full range of loading from 0 Nm to 1.5 Nm. Thus, as demonstrated in Figures 100 and 101, the enhanced model from the present study improves the prediction of intervertebral motions within the full ROM, and it follows that tissue strain predictions may also improve within the full range of motion.

Within the present study, percentage errors were used for comparative purposes since they normalize the wide range of responses encountered at different vertebral levels. One limitation of this method is that the percent error in the neutral zone often appeared high but was related to small changes in moment corresponding to large changes in rotation. The very low slope in this region of the moment-rotation curve caused large differences in the percentage error values (Figures 100 and 101). For example, when the response of the models was assessed with (Oda et al., 1992), a difference of 8° in the neutral zone extension rotation between the original UCS model and experiment resulted in an error of 233%, which was reduced to 70% after model enhancements (Table A5, Appendix A). However, the context of calculating the percent error in this study was only to determine how close the model response was with respect to the experimental mean which could be estimated using Equation 3.1. Despite higher values, the calculated percent error still provided an estimate on the model response relative to experimental mean.

Experimental studies show that the UCS levels contributed to 50% of cervical spine motion in flexion (C0-C1: 25%, C1-C2: 25%), 46% of extension (C0-C1: 31% and C1-C2: 15%) and 73% of axial rotation (C0-C1: 8% and C1-C2: 65%) while the remaining contribution comes from C2-C7 (Ivancic, 2013; Panjabi et al., 2001b, 1998). Clearly, the data shows the dominance of UCS in the full cervical spine, where there are similar contributions from C0-C1 and C1-C2 in the sagittal plane and the greatest contribution of C1-C2 in the axial rotation. Hence, improving the biofidelity of the UCS model at the intervertebral level consequentially improved the biofidelity of the full cervical spine model. Improvements to the UCS had only a small effect on the LCS intervertebral rotations. However, while repositioning the neck model to a target non-neutral posture (e.g., flexion), a decreased rotation in the original UCS model would increase the rotation in the LCS to accommodate the head to the target posture. The increase in rotation in LCS can potentially overpredict the strains in the LCS tissues resulting from repositioning.

5.1.1 Benefits of the LHS-based DOE method

An LHS-based DOE was used for the ligament sensitivity study and found to be beneficial relative to traditional one-factor-at-a-time or full-factorial DOE to perform sensitivity analysis. The LHS-based DOE captured the interactions between variables, which was not possible using the one-factor-at-a-time method. When there were two or more ligaments that resisted the same motion, performing a sensitivity study by holding the laxity of one ligament constant while varying the other sequentially could underestimate the combined influence of the ligaments. For example, the PA-AM and the ISL connect the C1 with the C2 vertebrae posteriorly and combinedly provide resistance to C1-C2 in flexion (Bogduk and Mercer, 2000). Previous studies could have underestimated the influence of ISL in C1-C2 flexion while varying the laxities of PA-AM and ISL in a one-factor-at-a-time approach. For similar reasons, previous studies could have underestimated the influence of alar ligament laxity as alar ligaments can resist flexion, extension, and axial rotation of the UCS (Panjabi et al., 1991a). In contrast, a conventional full-factorial DOE method was computationally prohibitive since it would have resulted in 59,049 (3^{10}) simulations with an estimated run time of 590 weeks when considering ten variables and three conditions for each variable (one week to run 100 simulations on Intel Core i7-8700 3.7 GHz processor). Several studies have shown that LHS is an efficient method for performing sensitivity analysis with a limited number of simulations (Hadagali and Cronin, 2020; John et al., 2019a, 2018; Yang et al., 2005). In the current study, the sensitivity analysis was performed using 100 simulations

for flexion, 23 for extension and 68 for axial rotation, generated using LHS-based DOE in each loading mode.

5.1.2 Importance of intervertebral kinematics as the target response in the optimization process

Including laxity in the ligaments of the UCS has been shown to be necessary by previous studies (Cronin et al., 2012; Lasswell et al., 2017; Shateri and Cronin, 2015) to achieve the desired motions in the UCS. Previous studies optimized the laxity values with the whole UCS motion (C0-C2) as the target, while the present study optimized the laxity values with intervertebral (C0-C1 and C1-C2) motions as the target. The full UCS response in extension in the neutral zone was similar between UCS_{M50} (13°) and UCS_{M50-Opt} (11°); however, the optimization strategy used in the present study eliminated the likelihood of disproportionate intervertebral response at one of the two levels within the UCS model. For example, in UCS_{M50}, the neutral zone contribution of C0-C1 was 15% but was 50% in UCS_{M50-Opt}, in better agreement with the experimental data (Table 13). Such a disproportionate intervertebral response in UCS_{M50} could produce unphysical tissue-level strain responses in the UCS during neck model repositioning.

Table 13: Comparing the contribution levels of intervertebral UCS in extension in the UCS models with the experimental mean response. The results highlight the importance of assessing intervertebral response during UCS model validation to avoid disproportionate intervertebral rotations during non-neutral position simulations. NZ = Neutral Zone.

Panjabi et al. (1991)				
Extension		Experiment (%)	UCS _{M50} (%)	UCS _{M50-Opt} (%)
NZ	C0-C1	56	15	50
	C1-C2	44	85	50
0.5 Nm	C0-C1	56	21	53
	C1-C2	44	79	47
Oda et al. (1992)				
Extension		Experiment (%)	UCS _{M50} (%)	UCS _{M50-Opt} (%)
NZ	C0-C1	72	15	50
	C1-C2	28	85	50
0.5 Nm	C0-C1	65	21	53
	C1-C2	35	79	47

5.1.3 Verification of the computed ligament laxities with previous studies

The UCS laxity values determined in the current study (UCS_{M50-Opt}) were of a similar magnitude but differed from previous studies (Lasswell et al., 2017) (UCS_{M50}) owing to the focus on loading over the entire ROM and assessment at the intervertebral level (Table 14). The interactions of ligament laxities

and resulting intervertebral responses were complex in the UCS. Notably, the ISL (4.02 mm) and alar (1.74 mm) ligament laxities were not considered in previous studies but had an important effect on the C1-C2 flexion (Figure 151) and C0-C1 axial rotation (Figure 152), respectively. Geometrical enhancements to the UCS_{M50} and PA-AM laxity (3.3 mm) had minimal effect on the C1-C2 flexion, and the inclusion of ISL laxity along with an increase in PA-AM laxity (from 3.3 mm to 5.2 mm) helped improve the C1-C2 flexion response (Figure 151). The inclusion of alar ligament laxity did reduce the intermittent rapid increases in the C0-C1 axial rotation response (Figure 152). In general, the geometric enhancements increased the intervertebral motion (Figure 151), and the ligament laxity sought to optimize the UCS model for three modes of loading and a range of applied moments, improving the mean error between target experimental data (Panjabi et al., 1991b, 1991a) and UCS model response from 66% (UCS_{M50}) to 28% (UCS_{M50-Opt}) in the neutral zone and other regions (Figure 101).

Table 14: A comparison chart of laxity values (mm) in different UCS models indicating that the computed laxities vary when the model is validated at the full UCS level or intervertebral UCS levels.

UCS ligament	U. Waterloo Neck Model (Shateri and Cronin 2015)	Before GHBMC M50 v4.5 UCS (Cronin et al. 2012)	GHBMC M50 v4.5 UCS	
			UCS _{M50} (Laswell et al. 2017)	UCS _{M50-Opt} (Present)
AA-OM	5	0.9	5.8	4.67
AA-AM	1.4	1.4	3.3	2.05
PA-OM	2	0.9	5.8	4.68
PA-AM	2	1.4	3.3	5.18
ISL	3	Not considered	Not considered	4.02
CL01	Not considered	1.3	1.4	0.005
CL12	6	1.1	5.4	7.9
Alar	Not considered	Not considered	Not considered	1.74

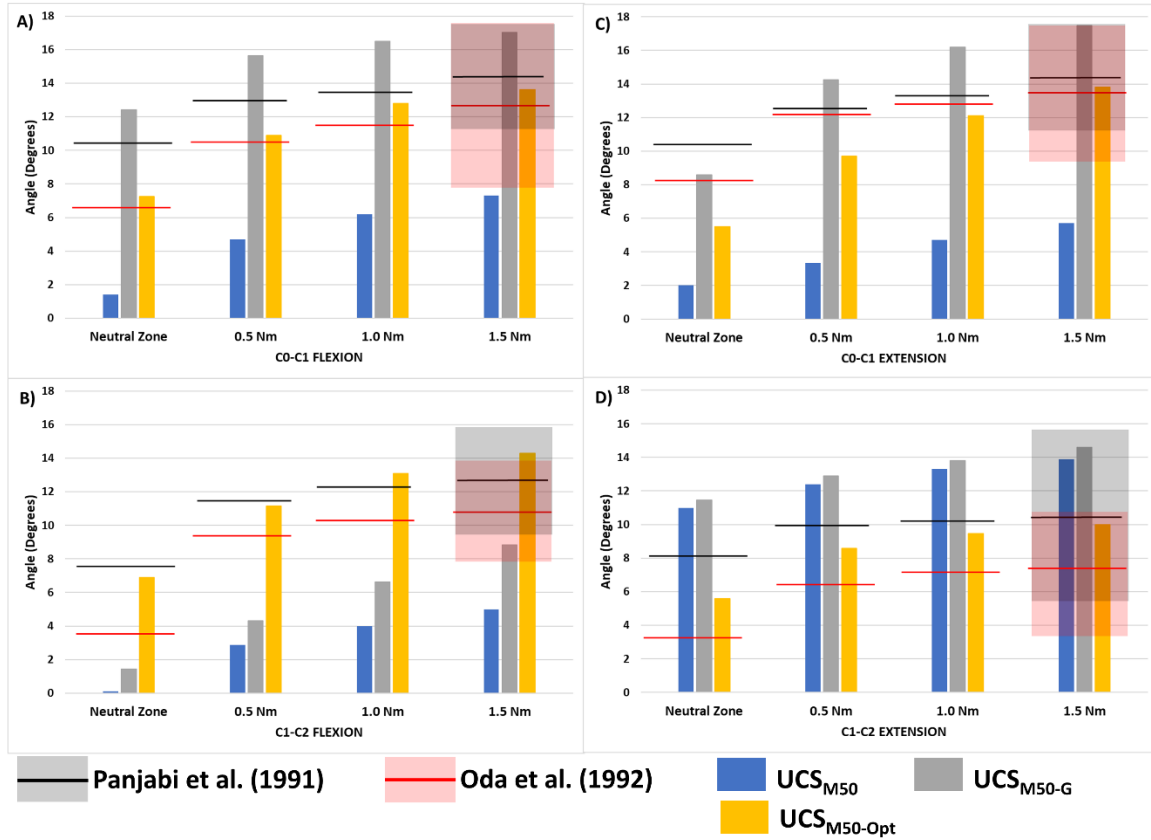


Figure 151: Intervertebral responses of the original (blue), geometrically enhanced (orange) and optimized (grey) UCS models verified with the target experimental mean response (black lines) from (Panjabi et al., 1991b) used for laxity optimization.

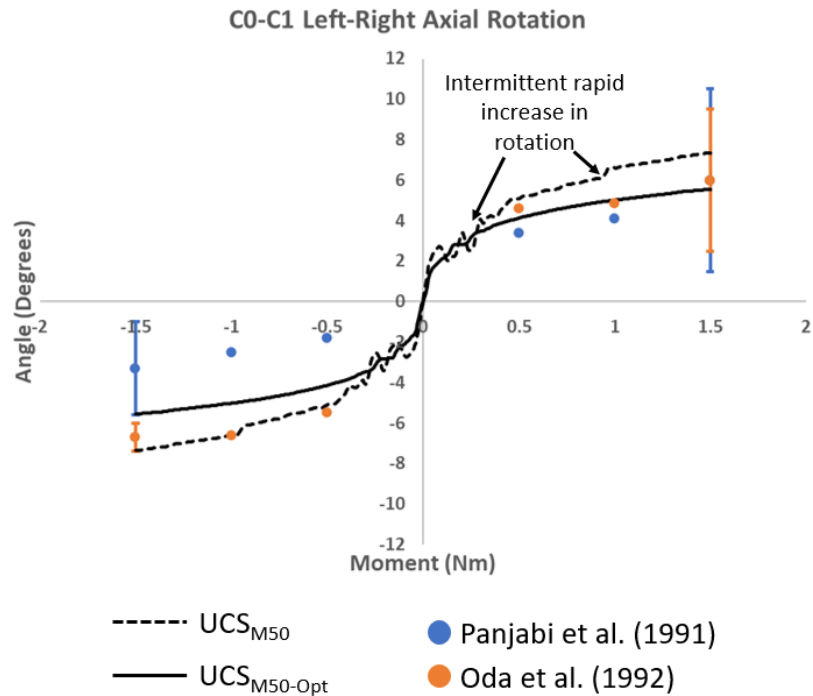


Figure 152: Demonstrating the effect of alar ligament laxity on the C0-C1 axial rotation response. The intermittent rapid increase in angular displacement in the UCS_{M50} and UCS_{M50-G} models were eliminated in the enhanced UCS_{M50-Opt} model owing to the inclusion of alar ligament laxity.

[Taken from Hadagali and Cronin (2023)]

5.1.4 Effect of facet-cartilage on the ROM response

Geometrical enhancements to the facet cartilage in the LCS resulted in the closure of the gap that was previously present in the LS_{M50} model (Corrales and Cronin, 2021b; Shen, 2020). Closure of the facet gap limited the ROM of the LCS motion segments in extension and axial rotation loading modes. The percentage error between the experimental data and the model response increased in extension and decreased in the axial rotation due to the biofidelic facet cartilage.

5.1.5 Summary of Phase #1

This study focused on evaluating the UCS model based on intervertebral kinematics rather than the whole UCS kinematics. The improvements in the UCS model led to improved response and reduced

the disproportionate intervertebral responses in previous models, which could lead to unrealistic tissue-level strain predictions in non-neutral positions. This study highlighted the importance of considering the intervertebral UCS kinematics during model evaluation to ensure accurate initial strains in non-neutral postures and thereby improve injury prediction capability in the model. The current study showed that subtle improvements to the UCS model geometry led to important improvements in the biofidelity of the model.

5.2 Phase #2a: Simulating non-neutral head-neck positions using muscle activation

5.2.1 Basis for simulating non-neutral head-neck positions using muscle activation

In vivo, the force acting on the head CoG (≈ 43 N in $NM_{M50-Hill-E}$), naturally located relatively anterior to the spinal column in a neutral position, induces flexion in the head-neck, which is countered by the muscle forces (co-contractors) to maintain an upright head position (Dibb et al., 2014; Seacrist et al., 2012). The force from the head, combined with the muscle forces, generates a reactive compressive force and moment in the spinal column (Figure 153). Similarly, the contractor and co-contractor muscles, along with force from the head, act accordingly to reposition the head and neck to a desired non-neutral position, generating a reactive compressive force and moment in the spinal column (Barrett et al., 2020; Butler, 1992; Cheng et al., 2008; Dibb et al., 2013; Mousavi-khatir et al., 2015; Straker et al., 2009). Depending on the inertial properties of the head and the location of the head CoG, the muscles contract or co-contract to maintain the head-neck in equilibrium in different positions. For instance, shifting the head CoG further anterior (as observed in a forward head posture condition) or increasing the mass (due to added helmet) could affect the activity in the extensor muscles in vivo to stabilize the head, thereby affecting the compressive force in the spine (Barrett et al., 2022b; Butler, 1992; Fiebert et al., 2021; Harrison et al., 2015; Kim, 2015). A couple of inferences can be made based on the described in vivo phenomena, as follows:

- 1) Muscle contractions in the neck serve two purposes: a) maintaining neutral and non-neutral head-neck positions and b) actuating the skeletal system to desired positions (Alizadeh et al., 2020b; Barrett, 2016; X.-Y. Cai et al., 2020b).
- 2) The properties (i.e. mass, moment of inertia, CoG) of the head and neck determine the in vivo muscle activities, which, in turn, determine the magnitude of the compressive force in the spinal column.

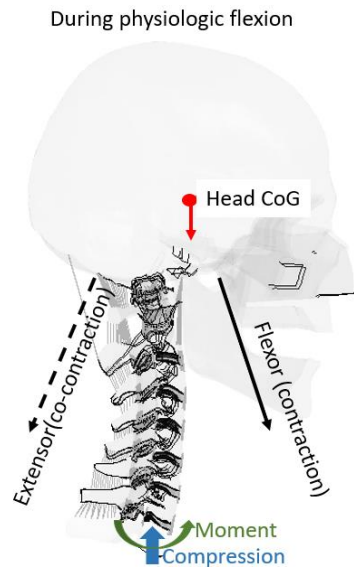


Figure 153: Illustration of reaction compressive force and moment in the spinal column due to activation and co-activation of muscles and head force during physiologic flexion in vivo.

5.2.2 Passive and active neck stiffness assessment of the NM_{M50} model

Assessment of the passive NM_{M50} model with the experimental data (McGill et al., 1994; Seacrist et al., 2012) showed that the material properties of the skin (SK), adipose tissue (AT) and the passive muscle (PM) components contributed to the stiff response. The material properties of the skin, adipose tissue and passive muscle components in the NM_{M50} model, although valid for impact conditions (Barker and Cronin, 2020; Cronin et al., 2018), were overly stiff in the physiologic conditions. The finding from this study is concurrent with the literature that reported the effect of skin, adipose tissue and passive muscle on the increased stiffness of the neck under applied gravity (Feller et al., 2016).

The presence of detailed SK, AT and PM components that existed in the original model (NM_{M50}) necessitated the need for activation levels that exceed the physiologic limits. From Equation 2.2 in background, the forces generated in the muscles depend on the activation levels. When higher activation levels are applied in the NM_{M50} model, the forces in the muscles increases. The increase in muscle forces influences the forces in the IVD, and thereby, stresses and strains in the spinal tissues. From Section 4.2.2, a fully activated flexors muscle group resulted in a relatively lower head rotation (15°) in NM_{M50} while existing MSK neck models predicted activation levels of 0-0.15 in a simulated

physiologic head rotation of 45° (Barrett et al., 2020). The full activation of flexors under gravity caused the active components of the muscles to generate a force of 700 N at the C5 level which led to IVD experiencing a compression of 800 N in C5-C6 for the simulated 15° flexion. The predicted active muscle force of 700 N was beyond the physiologic limits as studies have reported a muscle force between 50 N to 150 N in physiologic conditions (Barrey et al., 2015; X.-Y. Cai et al., 2020b; Patwardhan et al., 2000; Wawrose et al., 2021). The predicted IVD compression corresponding to 15° flexion can be considered higher because in a simulated 45° flexion, IVDs reportedly experienced a compression of <250 N (Barrett et al., 2020).

The buckling of the SK and AT components in the anterior aspects of the neck and formation of gaps between tissues, when NM_{M50} was repositioned, indicated that the interaction between the skin and adipose tissue with the internal structures was not well captured (Figure B1, Appendix B). The SK and AT buckling could be attributed to the BC in the model that included fully constraining nodes in the caudal ends of the skin and adipose tissue or lack of pre-tension in the tissues as observed in vivo. In reality, the skin and the adipose tissue of the neck and the torso is a continuous structure with no constraints, allowing unconstrained motion relative to the other internal structures. The buckling of the SK and AT components in the NM_{M50} model might also have contributed to restricted neck motion in flexion.

The buckling in the passive muscle component could be attributed to the lack of pre-tension as observed in vivo (Correia et al., 2023), which was considered non-biofidelic (Figure B2, Appendix B). During contraction, the muscles shorten in length, which could not be mimicked in the model with the representation of passive muscles using 3D elements and active muscles using 1D elements. In reality, the active and passive muscles co-exist as a single structure. Implementation of the muscles in the NM_{M50} model, where the active and passive components are separated, posed limitations. In addition, the NM_{M50} model comprised artificial support elements connecting vertebrae with the 1D CE to maintain the line of muscle action. As a result of the muscle implementation, the nodes common to the 1D CE and artificial support elements coincided with the nodes belonging to the 3D elements of the passive muscles, elaborately described in the background of this thesis (Barker and Cronin, 2021). When the muscles were activated, the shortening of the CE caused only the nodes connected to support elements, 1D CE and 3D passive muscle to displace, thereby resulting in an unrealistic deformation in the 3D elements of the passive muscles (Figure B3, Appendix B). The outcome from this study justified the need to include passive and active components within one element, as observed in Hill-type model.

Further in the research, one of the goals is to identify a strategy to activate the muscles to reposition the head-neck in flexion and combined positions to mimic RWA non-neutral positions. Simulating a flexion position could involve two groups of muscles (flexors and extensors). However, simulating a combined position involving flexion, lateral bending and axial rotation, as observed in RWA (Forde et al., 2011; Tack et al., 2014), could demand numerous assessments on multiple muscles that are involved in axial rotation and combined (flexion, lateral bend and axial rotation) physiologic motion. The computation time involved in assessing the effect of muscles on the physiologic motions using the NM_{M50} model could delay the process of identifying a muscle-activation strategy required to reposition the model, further justifying the need to simplify the model.

The assumption of limited effect of skin and adipose tissue properties in physiologic conditions was based on literature (Alizadeh et al., 2020b). From experimental studies, at strain levels corresponding to physiologic conditions, the tensile stress in the isolated subcutaneous adipose tissues was lower than 1 KPa (Alkhouli et al., 2013), relatively compliant in comparison to in vivo tensile behaviour of passive muscles at similar strain levels (Persad et al., 2021). The tensile stress in the skin, at strain levels corresponding to physiologic condition, in the direction perpendicular to the Langer lines/collagen fibers have shown to be negligible (Gąsior-Głogowska et al., 2013; Paul, 2017; Shergold et al., 2006). The skin and adipose tissues were excluded, considering their limited contribution to the structural response during a physiologic head-neck motion.

Despite a potential solution of revising the material properties of the skin, adipose tissue and passive muscle in the model, the hybrid muscle modelling strategy of 3D passive muscle embedded with the 1D CE and 1D support elements could still result in an uneven deformation in the 3D elements, leading to unrealistic tissue response. Replacing the 3D passive muscle elements with a passive elastic element (PEE) within the Hill-type model and parallel to the CE while retaining the skin and the adipose tissue components could also offer a feasible solution for unphysical element deformation, similar to existing models such as VIVA and THUMS (Kato et al., 2018; Putra et al., 2021). However, such a solution could result in a void between the adipose tissue and the ligamentous spine due to loss of muscle volume, thereby causing non-biofidelic interactions within the structures in the NM_{M50} .

5.2.3 Passive neck stiffness assessment of the $NM_{M50-Hill}$ model

The assessments on the passive $NM_{M50-Hill}$ model demonstrated that the passive muscle property used in the NM_{M50} model (Gierczycka et al., 2021) required enhancements to improve the biofidelity of the

model in physiologic conditions. The findings from the current study, not explored in the previous studies, suggest a requirement of compliant material properties for the passive muscles in the $NM_{M50-Hill}$ model to simulate physiologic conditions. Despite the improvement in head rotation under gravity after enhancements to passive muscle property in the $NM_{M50-Hill}$ model, there was a percentage error of 46% between the experimental average and the model response. Similarly, under externally applied extension moment, despite enhancements to the passive muscle property, there was a percentage error of 20%. The reasons for a relatively large percentage error could be attributed to different factors elaborated in the subsequent paragraph.

First, the model comprised only the first thoracic vertebra (T1), which was constrained in all the degrees of freedom. Studies have reported the contribution of the upper thoracic spine in the *in vivo* physiologic ROM of the cervical spine (Fiebert et al., 2021; Joshi et al., 2019; Krauss et al., 2008; Lau et al., 2010). One experimental study reported that 67%, 25% and 8% of the total head and neck flexion was contributed by the cervical spine, upper thoracic spine and lower thoracic spine, respectively (Tsang et al., 2013). Lack of appropriate BCs from the upper thoracic spine, thereby leading to a simplified BC (fully constrained T1 vertebra and neck muscle ends), could have limited the head-neck forward flexion under gravity. Second, the passive muscle property obtained from the experimental data was obtained from the gracilis muscles due to the lack of experimental data specific to neck muscles. The gracilis muscles are present in the lower extremities and act to flex and adduct the hip joint. They also play a role in flexion and internal rotation of the knee joint (Carr et al., 1995; McKee et al., 1990). The differences in the morphology and functionality of the gracilis muscles with respect to the neck muscles could also affect the mechanical properties, which have not been explored to date. Third, the 1D spring elements in the anterior aspects of the NM_{M50} model connecting the skull and the LCS to the hyoid bone, considered as simplified representations of suprahyoid muscles and pharyngeal tissues, are assigned a stiffness value. The properties of the 1D hyoid attachments, which were retained in the $NM_{M50-Hill-E}$ model, could also affect the physiologic motion of the cervical spine based on preliminary studies (not reported in this thesis).

5.2.4 Simulating non-neutral head-neck positions in the $NM_{M50-Hill-E}$ model using active muscles

Simplification of the model and implementing a biofidelic passive muscle property within the Hill-type muscles enabled implementation of biofidelic muscle activation levels required for physiologic

conditions. The muscle activation strategy used in this study to reposition the $NM_{M50-Hill-E}$ model was unique when compared to the strategies used in existing MSK neck models (Arshad et al., 2022; Barrett, 2016; Barrett et al., 2020), where the former followed a forward-dynamic approach while the latter an inverse-dynamic approach. In addition, due to the geometric variations between the MSK neck models and the $NM_{M50-Hill-E}$ model, the muscle activation strategy from the MSK neck models could not be directly applied to the $NM_{M50-Hill-E}$ model. However, the MSK neck models provided a quantitative reference to assess the identified activation levels to reposition the $NM_{M50-Hill-E}$ model. Co-contraction of the extensor muscles controlled the head and neck from overly flexing (owing to flexor contraction and anteriorly located head CoG relative to the spinal column) and maintained the desired non-neutral position. The extensor co-activation in the present study concurs with the *in vivo* experimental data from the literature that reported the recruitment of the extensor muscles during physiologic head and neck flexion (Barrett et al., 2020; Cheng et al., 2014, 2008; Namwongsa et al., 2019; Ning et al., 2015; Straker et al., 2009).

In the muscle-based flexion, the identified muscle activation level for flexors was based on the experimental studies that reported the muscle activities in the superficial flexor muscles, namely SCM and infrahyoid muscles, during physiologic activities (Callaghan, 2014; Cazzola et al., 2017; Cheng et al., 2016; Kim and Jeong, 2020; Mahmood et al., 2021; Newell et al., 2018). There was limited experimental data on the activity of deep neck flexors in the literature. Hence, the activation levels for these muscles identified for the SCM and infrahyoid muscles (0.1) were assumed for the deep neck flexors in this study. For similar reasons, a uniform activation level (0.012) was assumed for the extensor group of muscles.

5.2.5 Summary of Phase #2a

A methodology to simulate non-neutral head-neck positions in the FE head-neck model within the physiologic ROM using active musculature has been developed. Preliminary assessments from the current phase of this research provided insights into the response of the detailed GHBMC M50 head-neck model (NM_{M50}) to simulated physiologic conditions, which led to further modifications and enhancements to the passive tissues and passive muscle property ($NM_{M50-Hill-E}$). The current phase also highlighted the importance of biofidelic passive muscle property to simulate non-neutral head-neck positions using muscle activation, as observed *in vivo*. The novel repositioning method was initially

applied to simulate 30° physiologic flexion and axial rotation positions. The equilibrium of the head-neck model (NM_{M50-Hill-E}) in the non-neutral static position was verified using an FBD.

5.3 Phase #2b: Quantifying the importance of active muscle repositioning using kinematic, kinetic and tissue-level responses

The biofidelity of the predicted response in a computational model depends on the accuracy of the model geometry, material property and the loading conditions input into the model (Cronin et al., 2018). Phase #2b of this research aimed to quantify the effect of two repositioning methods (loading conditions) for 30° flexion and 30° axial rotation using kinematic, kinetic and tissue-level responses. The results in 30° flexion indicated that the repositioning method could result in gross kinematics (CV angle, FHD and GMA) similar to those reported in the literature but that tissue-level responses vary for the two methods. The results in 30° axial rotation indicated that the repositioning method could result in differences in gross kinematics as well as tissue-level responses. In general, results from this phase of research showed that a simplified neck model with biofidelic passive muscle property enabled input of physiologic activation levels to the muscles to achieve a desired kinematic outcome in flexion and axial rotation. The physiologic activation levels ensured that the muscle forces were within the physiologic limits. Physiologic muscle force outcome in the model resulted in the IVD forces and AF collagen fiber strains to be within the physiologic limits as well.

The presence of muscle attachments in the GHBMCM50-O could be considered unique compared to existing neck models where, the muscle curvature was maintained using ‘wrapping surface’ or ‘via-point’ methodology (Alizadeh et al., 2020b; Barrett, 2016) (Figure 63a). Similarly, the hyoid attachments in the GHBMCM50-O was unique compared to a majority of neck models where superior aspects of infrahyoid muscles are constrained to C2 or C3 vertebra (Cronin, 2014; John et al., 2019a; Mortensen et al., 2018; Shateri and Cronin, 2015) (Figure 63b). These attachment elements were implemented in the initial versions of the model and have been retained to date in the latest versions which are validated for multiple impact conditions (Barker and Cronin, 2022, 2020; Correia et al., 2020). The muscle attachment and hyoid attachment elements could be considered as simplified representations of the fascial tissues and pharyngeal tissues, respectively, which are complicated to be modeled. For this particular study, the presence of attachment elements could be considered suitable as the model predicted biofidelic responses at the global kinematic and tissue levels for physiologic conditions. The muscle attachments ensured that the relative distance between different muscles were maintained in non-neutral positions. Similarly, the hyoid attachments provided a boundary condition for the hyoid bone to which the infrahyoid muscles were attached. This boundary condition enabled the infrahyoid muscles to flex the head-neck forward, as reported in the literature (Siegmund et al., 2007).

The attachment of the supra-hyoid muscles to the skull provide structural support during voluntary flexion of the head when the infra-hyoid muscles are activated (Mortensen et al., 2018; Siegmund et al., 2007). However, the approach of using 1D elements to capture the behavior of the represented tissues resulted in an assignment of an arbitrary stiffness to the attachment elements. From a preliminary study, varying the stiffness of attachment elements, specifically the hyoid attachments, affected the kinematic outcome in the model. Hence, in this study, the stiffness values of the attachment elements as assigned in the NM_{M50} model was retained in the $NM_{M50-HIII-E}$ model, for consistency.

5.3.1 Comparing a conventional external BC- and muscle-based approaches of repositioning the $NM_{M50-HIII-E}$ model in flexion

Despite similarities in the head rotation in flexion, differences in the gross and intervertebral kinematics were noticed when the $NM_{M50-HIII-E}$ model was repositioned using external BC- and muscle-based methods. The SCM muscle originates near the mastoid process in the skull, behind the head CoG and inserts into the torso, thereby inducing flexion in the lower cervical spine while extending the head and the upper cervical spine (Head-C2) when activated (Mansoor and Rathore, 2018; Mortensen et al., 2018; Oi et al., 2004). In the current study, the SCM muscle activation and the upper neck extensor muscle co-activation reduced the Head-C2 flexion by 6.5° in the model repositioned using the active muscle compared to the model repositioned using external BC. As a result, there was a decrease in the CV angle by 4° and an increase in the FHD and GMA by 13 mm when the model was repositioned using the active muscles compared to the model repositioned using the external BC.

Although there is experimental data for in vivo full head-neck flexion (i.e. $\approx 60^\circ$) (Anderst et al., 2015; Ordway et al., 1999), there is limited data for intermediate flexion (i.e. 30°), thus the cervical spine predictor (CSP) tool was used. At the intervertebral level from C2-C3 to C7-T1, the difference in the kinematics between the two methods of repositioning was small, with the muscle-based repositioning having, on average, higher intervertebral rotations. The higher intervertebral rotations in the C2-C3 to C7-T1 in the model repositioned using the active muscle method were attributed to the SCM muscle activation. The SCM muscle activation causes the head-C2 to extend while flexing the C2-T1 (Mortensen et al., 2018; Oi et al., 2004). The limited flexion in the head-C2 caused the C2-T1 to flex more to achieve the target 30° global head-T1 flexion. The in vivo experimental data used by the CSP tool reported that C2-C3 rotated 4.5° in combined full flexion and extension, which was a small fraction (3.8%) of the C0-T1 full ROM (117°) (Reed and Jones, 2017; Snyder et al., 1975).

Experimental data (Snyder et al., 1975) attributed the lower C2-C3 ROM to the UCS extension during the initial part of flexion, where the chin thrusts forward and may or may not be overcome once the head starts to tilt down while approaching the maximum flexion (Reed and Jones, 2017; Snyder et al., 1975). The experimental data that was referred to and the method of fractions used by the CSP to predict the intervertebral kinematics for intermediate flexion positions affected the model assessments. Also, a lack of volumetric representation of the neck tissues (flesh, passive muscles, anterior tissues, etc.) could have caused a relatively higher flexion in the C2-C3 level. The intervertebral kinematics of the upper cervical spine were not included in the CSP, and hence, no assessments were made.

Owing to the increased intervertebral rotation for the muscle-based method, the ligament distractions were slightly higher. The increase in the IVD deformation in the model repositioned using the muscle-based method compared to the model repositioned using the external BC method was attributed to the increase in the anterior translation of the superior vertebra relative to the inferior vertebra due to the line of action of the muscle forces (Figure 154).

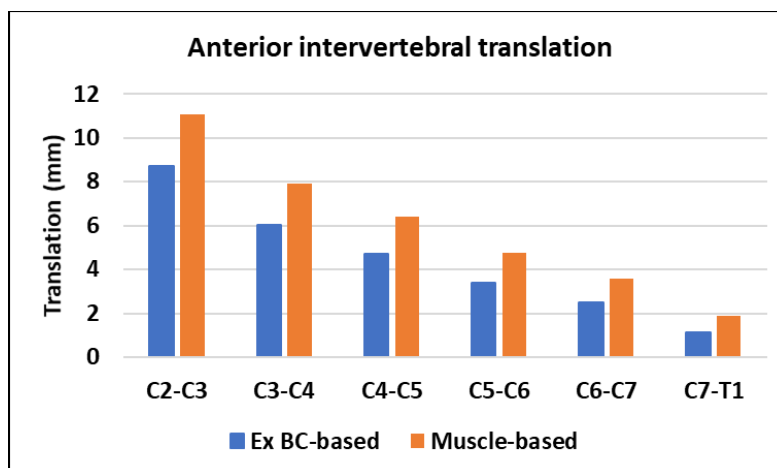


Figure 154: Anterior translations at the intervertebral levels when the $NM_{M50-Hill-E}$ model was repositioned using different methods in flexion. The increase in the anterior translation of the superior vertebra relative to the inferior vertebra in the model repositioned using the muscle-based method could be attributed to the differences in the line of muscle force.

The mean IVD compression of 53 N in the $NM_{M50-Hill-E}$ model repositioned in flexion using the external BC was attributed to the resistance provided by the passive muscle elements (PEE) of the

extensors that caused a reactive force in the spinal column. The increase in IVD forces in the spinal column (by a mean of 114 N) was primarily due to the muscle contractions that was required to keep the head and neck in balance under gravity, not considered in the model that was repositioned using the external BC repositioning method. The compressive forces in the model repositioned using both the methods increased cranially to caudally, as observed in the MSK neck model (Barrett et al., 2020). The magnitude of the predicted forces in the IVDs in the muscle-based repositioned model were also comparable with the MSK neck model predicted IVD forces (mean of 209 N) for a similar case of flexion. The mean AP IVD shear force across C2-C3 to C7-T1 in the MSK and FE neck model repositioned using a muscle-based method were similar, measuring 16.2 N and 12.2 N, respectively. The AP shear force decreased from C2-C3 to C4-C5 IVDs, followed by an increase in the C5-C6 IVD and a decrease in C6-C7 and C7-T1 IVDs in the FE neck model repositioned using both methods. The cause of the increase in the C5-C6 IVD AP shear force in the model repositioned using both methods was attributed to the SCM muscle orientation in the $NM_{M50-HIII}$ model. The moment arm of the SCM muscle was higher in the C5-C6 level compared to other superior levels and oriented in an AP direction. The SCM oriented in the superior-inferior direction at the levels below C5-C6 led to a decrease in the AP shear force in the C6-C7 and C7-T1 levels.

An increase in the collagen fiber strains in the AF when the model was repositioned using the active muscle method could be attributed to the increased IVD deformation and forces as a result of muscle activation. Higher fiber strains in the model repositioned using both methods were observed in the posterior aspects of the innermost concentric layers of the collagen fibers. Due to the lack of in vivo experimental data, it was not possible to assess the biofidelity of the AF collagen fiber strains and ligament distractions in the simulated 30° head flexion position. Also, due to the lack of in vitro experimental failure data on human cervical AF collagen fibers, the AF collagen fiber strains in the model were compared with the literature that reported failure data of AF collagen fibers from in vitro experiments on lumbar specimens (Holzapfel et al., 2005; Isaacs, 2012; Pezowicz, 2010).

5.3.2 Comparing a conventional external BC- and muscle-based approaches of repositioning the $NM_{M50-HIII-E}$ model in axial rotation

Despite a similarity in the overall axial rotation (30°) in the model repositioned using both methods, the results showed differences in the C0-C2 and C2-T1 responses. There was a minimal difference in the C0-C2 axial rotation response (3.1°, 17% change) between the model repositioned using the external

BC- and muscle-based methods. Similarly, the difference in the C2-T1 axial rotation (1.7°, 15% change) between the model repositioned using the external BC- and muscle-based method was minimal. With different repositioning methods, although the differences in C0-C2 and C2-T1 axial rotation were minimal, there was a major difference (by 427%) in the coupled lateral bending response in the C2-T1. The differences in the model kinematics owing to the muscle-based repositioning method could potentially affect the tissue-level responses, addressed in detail in subsequent paragraphs. The current study demonstrated that while assessing the head-neck kinematic in axial rotation, it was also important to assess the kinematics in the secondary axis of rotation (i.e. coupled motion) along with the primary axis of rotation (i.e. axial) (Lindenmann et al., 2022).

Similar to flexion, the increase in IVD forces in the spinal column in the model repositioned using the muscle-based compared to the IVD force in the model repositioned using external BC was attributed to the muscle contractions that held the head and neck in the position under gravitation force. The compressive forces in the model repositioned using active muscles decreased cranially to caudally owing to the higher muscle activation level in the upper cervical spine to rotate the head and C1 vertebra around the axial direction. The compressive forces predicted by the $NM_{M50-Hill-E}$ model in an axially rotated position were compared with the response from an existing MSK neck model that reported the compressive force in C5-C6 in 45° axial rotation to be 180 N (Barrett et al., 2022b). The forces in other IVDs were not reported in the MSK neck model. A difference of 110 N in C5-C6 compression between the model repositioned using the muscle-based method and the MSK neck model can be attributed to the differences in the degree of head rotation (30° in $NM_{M50-Hill-E}$ vs. 45° in the MSK neck model). However, additional experimental data is required to verify the response of the model in the given specific position. The mean AP IVD shear force across C2-C3 to C7-T1 in the $NM_{M50-Hill-E}$ model repositioned using the external BC- and muscle-based methods were similar (≈ 3 N) and comparable to the magnitude of AP shear force predicted by the MSK neck model at the C5-C6 level (Barrett et al., 2022b). Despite similarities in the mean AP IVD shear force in the $NM_{M50-Hill-E}$ model repositioned using both methods, there were differences in the force trends from C2-C3 to C7-T1. In the model repositioned using the muscle-based method, the higher AP shear force in C2-C3 was attributed to the higher muscle activity of ipsilateral oblique capitis inferior and rectus capitis major muscles to rotate the head and maintain the position of the head against the action of gravity.

An existing FE neck model that simulated in vivo axial rotation of the head-neck applied a follower load to the lower cervical spine prior to applying an external moment to the occiput (Palepu, 2013). In

contrast to the assumptions in the follower load methodology (uniform muscle force across the spinal levels), the model repositioned using active neck muscles demonstrated that the muscle forces varied across all the levels (Figure 114). An assumption of a uniform muscle force (follower load) across the spinal column, along with the application of an external BC to the skull, could affect the kinematic and IVD force response and, therefore, inaccurate estimation of the tissue-level response.

The $NM_{M50-HIII-E}$ model was repositioned in right axial rotation, and hence, the right CL (ipsilateral CL), in general, experienced lower distractions compared to the left CL (contralateral CL). Despite the decrease in C2-T1 axial rotation with the muscle-based method relative to the external BC-based method, there was an increase in the distraction on the contralateral CL owing to the increase in coupled lateral bending. The negative values in ipsilateral CL distraction indicated that the ipsilateral facet joints compressed when the model was repositioned using the muscle-based method.

An increase in the collagen fiber strains in the AF when the model was repositioned using the muscle-based method could be attributed to the increase in coupled lateral bending in C2-T1 and forces as a result of muscle activation. In the model repositioned using both methods, higher strains were observed in the posterior and posterior-contralateral aspects of the innermost concentric layers of the AF collagen fibers. Due to the lack of in vivo experimental data, it was not possible to assess the biofidelity of the fiber strains in the AF and ligament distractions in the simulated 30° head axial rotation position. The AF collagen fiber strains in the model were compared with the literature that reported failure data of AF collagen fibers from in vitro experiments on human lumbar and non-human IVD specimens for the same reasons mentioned in section 5.3.1 (Holzapfel et al., 2005; Isaacs, 2012; Pezowicz, 2010).

5.3.3 Demonstrating the importance of muscle-based repositioning method

An axial or a follower compressive load is optionally used as a simplified representation of head and neck muscle forces in addition to the external BC applied for repositioning the neck (X.-Y. Cai et al., 2020b; Cheng et al., 2023; Kwon et al., 2017; Lee et al., 2011; Manickam and Roy, 2021; Palepu, 2013; Rahman et al., 2023; Sun et al., 2022). Application of an axial compressive load, along with the external BC, would increase the IVD forces in the repositioned model. Repositioning the model in 30° head flexion using external BC with the axial load (43 N) (del Palomar et al., 2008) resulted in an increase in the IVD compressive force by a mean of 46 N across C2-C3 to C7-T1 relative to the model repositioned using external BC without the axial compression (Figure 155). When the model was repositioned in 30° head flexion using the muscle-based method, the IVD compressive forces increased

by a mean of 67 N relative to the IVD forces in the model repositioned using a combined external BC and axial load owing to the active muscle forces (Figure 155).

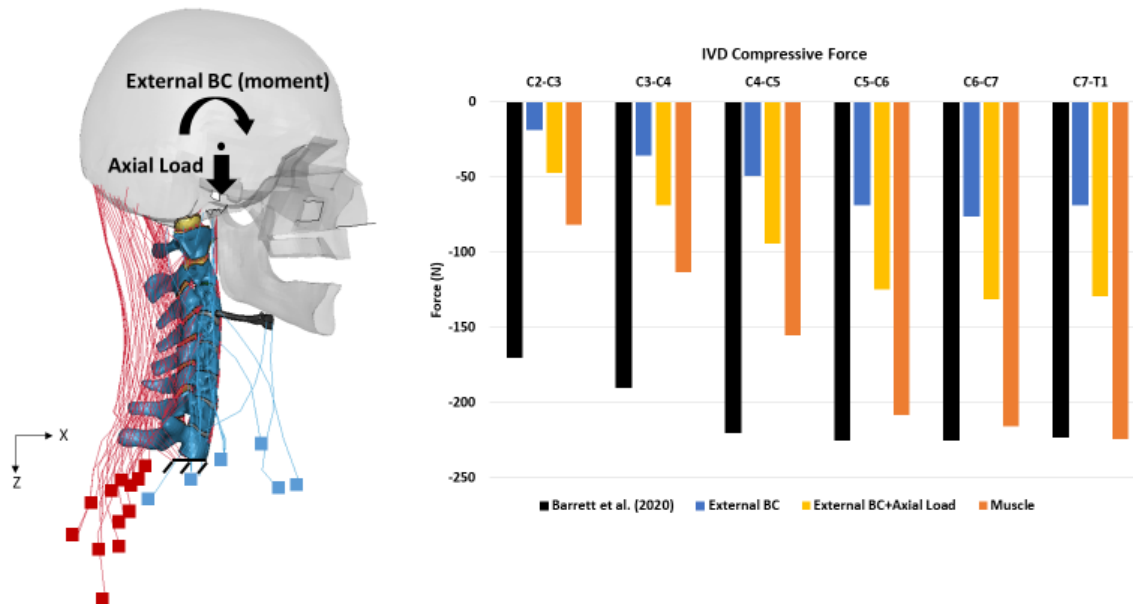


Figure 155: Illustrating the repositioning of the $NM_{M50-Hill-E}$ model in 30° flexion using an external BC (moment). An axial load of 43 N is also applied to simulate the weight of the head (Left side). The applied moment and axial load to the model were consistent with the literature (del Palomar et al., 2008). IVD compressive force comparison (Right side).

From Figure 155, in the model repositioned using the combined external BC and axial load, increasing the magnitude of the applied axial force to mimic the muscle force and thereby increasing the compressive force in the spinal column can seem logical. However, when the magnitude of the in vivo muscle force directly relies on the properties of the head and the type of non-neutral position (Section 5.2.1), pre-determining the muscle force can be challenging. Increasing the axial force by an arbitrary value may under- or over-estimate the force response in the repositioned model and can affect the tissue-level assessments. In muscle-based repositioning, depending on the mass, inertial and geometrical properties of the head, the extensors (co-contractors) activation was determined to hold the head in the desired non-neutral position, which resulted in a mean IVD compression of 166 N.

Application of a follower compressive load, which is a simplified representation of the complex in vivo musculature and uniform across all levels in the spine, would also increase the IVD forces in the model (Barrey et al., 2015; Patwardhan et al., 2000; Wawrose et al., 2021). However, the model repositioned using active neck muscles demonstrated that the muscle forces varied across all the levels (Figure 114). An assumption of a single uniform muscle force (follower load) across the spinal column could affect the force response in the IVD and, therefore, inaccurate estimation of the tissue-level response. In addition, an arbitrary assumption of a single follower load value between 50 N - 150 N can lead to either under- or over-estimation of the force response in the repositioned model and thereby, tissue-level assessments.

In a majority of the FE head-neck models in the literature, the complex in vivo musculature and weight of the head is simplified in the form of an axial or a follower compressive load in addition to applying an external BC (moment/displacement) to simulate non-neutral positions (X.-Y. Cai et al., 2020b; Cheng et al., 2023; Kwon et al., 2017; Lee et al., 2011; Liang et al., 2022; Manickam and Roy, 2021; Palepu, 2013; Rahman et al., 2023; Zhang et al., 2023). Application of such loads, where a single value between 50 N – 150 N is pre-determined and applied to the FE neck model, can be considered arbitrary as the pre-determined value is subjective. Also, the variation in the in vivo muscle forces with different non-neutral positions that can affect the spinal forces, as identified in this phase of research, cannot be reproduced using the axial- and follower-load methodology. As a result of a pre-determined, simplified head and muscle force, there could be an arbitrary increase in the compressive forces in the spinal column. However, the accuracy of the model response at the tissue-level due to arbitrary assumptions is ambiguous. This study quantitatively demonstrated that the assumption of an axial load as a replacement for head weight and complex neck muscles could have an arbitrary effect on the model response, which might not replicate the in vivo conditions accurately.

5.3.4 Importance of muscle-based repositioning method in the RWA context

From the background, one of the overarching scopes of this research is to provide accurate tissue-level assessments to enable better HSM designs for the RWA to overcome the issue of neck pain. From Section 5.2.1, the inertial and geometrical properties of the head and HSM determine the activity of the neck muscles accordingly to move and maintain the head and neck in static positions. In RWA, the increase in mass, moment of inertia, along with an anterior-shift of the head CoG (due to added HSM), induces the head and neck to flex more forward (Butler, 1992; Forde et al., 2011; Knight and Baber,

2004; Sovelius et al., 2008). To counter the increase in head-neck flexion and maintain the position, the demand in the extensor muscles increases, thereby increasing the spinal loads (Harrison et al., 2015). A simplified repositioning methodology can lead to an assumption of HSM as an arbitrary increase in compressive loading, which might not be able to capture the effect of HSM properties on the neck tissues or optimize helmet design to reduce the risk of pain.

For example, in an existing FE head-neck model from the literature, HSM and non-neutral head-neck positions were simulated using a two-step procedure (Mesfar and Moglo, 2012). The first step included applying an external BC to the head with a constrained T1 vertebra to simulate a non-neutral position. The second step included applying a compressive load to the head CoG in the non-neutral position (Mesfar and Moglo, 2012). The methodology reported by Mesfar and Moglo (2012) resulted in an obvious increase in IVD force with an increase in the applied compressive force to the head CoG, suggesting an increased risk of neck pain with the addition of HSM. The RWA HSM has flexible design configurations (with/without NVG, external/internal CW, up/down NVGs, etc.) depending on the time of the mission and the choice of the RWA personnel. Each design configuration of the HSM would have different CoG locations and inertial properties. When the effect of HSM is simplified by arbitrarily increasing the compressive load in the spinal column, it is challenging to assess the effect of different factors in the HSM design configurations on the neck tissues.

When RWA assumes a non-neutral head-neck position that combines rotation around all three primary axes, the muscle forces across the length of the spinal column can vary, as indicated in the phase #3 of this research. An over-simplification of the in vivo muscle forces using an axial load or a follower load might undermine the effect of upper cervical spine rotator muscles and their effect on the kinematic, kinetic and tissue-level response.

5.3.5 Summary of Phase #2b

Overall, the findings from the present phase underscore the importance of a biofidelic repositioning method to ensure that the predicted kinematic, kinetic and tissue-level responses in the repositioned FE neck model are accurate to enable better predictions of neck pain outcomes in the RWA due to HSM and non-neutral positions. A difference in the tissue-level strains and loads in the model repositioned using the muscle-based method could potentially lead to a more accurate estimate of neck pain risk in subsequent RWA scenarios (non-neutral positions combined with HSM configurations) when compared to the model repositioned using the external BC method.

5.4 Phase #3: Risk of neck pain in rotary-wing aircrew (RWA)

The objective of this study was to investigate the effect of HSM and magnitude of head-neck positions on the tissue-level response using a detailed FE head-neck model from which the risk of neck pain could be assessed. Generally, pain can be a result of disruption in the innervated tissues due to an external load which triggers the nociceptors (pain sensors) in the tissues. Tissues in the neck that are potential sources of neck pain include the peripheral aspects of IVDs, facet joints, muscles and ligaments (Section 2.4). These tissues are enriched with nociceptive bundles attributed to pain sensation (Bogduk, 2003, 1985; Feng et al., 2018; Fields et al., 2014; Ito and Creemers, 2013; Lotz et al., 2013; Mense, 2008; Peng and Bogduk, 2019; Sayson and Hargens, 2008).

Existing MB and MSK neck models have correlated the risk of neck pain using joint forces, joint moments and muscle activation levels. In MSK neck models, an increase in the joint forces due to added HSM in a non-neutral position was inferred to a potential risk of IVD herniation and, thereby, neck pain (Barrett et al., 2022a, 2020). Although joint forces in the MSK neck model informed the risk of neck pain in RWA, the risk of spine degenerative disorders and the potential for neck pain associated with such disorders, as observed in epidemiological studies, has not been assessed to date. Degenerative changes in the spinal column, specifically the presence of osteophytes and degenerated IVDs, have been associated with neck pain (Menkes and Lane, 2004; Peng and Bogduk, 2019; Tomaszewski et al., 2015; van der Kraan and van den Berg, 2007; Walocha, 2015). The assumption of hard tissues as rigid bodies and deformable tissues as 6-DOF joints in the MB (Fathollahi, 2012; Hetzler, 2021) and MSK neck models (Arshad et al., 2022; Barrett et al., 2022a) limited the previous studies from exploring the risk of spinal degenerations and associated neck pain.

From the tissue-level assessments in the current study, the findings were two-fold: 1) HSM influences the tissue response in muscles, IVDs and vertebral endplates, and 2) Magnitude of the head-neck position (flexion to a combined position) influences the tissue response in muscles, IVDs, vertebral endplates and ligaments. From this study, the kinetic and tissue-level response to an increase in the HSM (for e.g. inclusion of NVG and CW to helmet) along with increase in non-neutral head-neck position magnitude due to NVG explains why the prevalence of neck pain in RWA is high compared to the civilian population. Potential pathways to neck pain in the RWA identified from this study support the findings from the literature (Barrett et al., 2022a; Healey et al., 2021).

5.4.1 Muscle force response

An increase in extensor (co-contractor) muscle activity was attributed to the increased mass and a relative anterior-shift in CoG with the addition of HSM. The addition of HSM increased the flexion moment in the head-neck model, leading to an increase in the effort in extensor muscles to maintain the desired non-neutral position. The reduction in the flexors to extensors activation ratio as a result of HSM agrees with experimental and MSK neck model findings (Barrett et al., 2022b; Healey et al., 2021). In general, the experiments observed that the increase in muscle demand was influenced more due to non-neutral positions compared to added HSM (Healey, 2019; Thuresson et al., 2003). In the current study, added HSM resulted in a mean increase in the muscle activation level from 0.07 to 0.1 while increasing the magnitude of position from flexion to combined increased the mean activation level from 0.1 to 0.3 (Figure 93). The increase in activation levels due to HSM was relatively lesser compared to an increase due to increase in non-neutral position magnitude, in agreement with the experimental findings. A more detailed and a one-to-one comparison between the activation levels of individual muscles in the model with the response of corresponding muscle in humans could not be made as experimental data reported the muscle activity in selected superficial muscles. The muscle forces in the combined position were similar at all the vertebral levels except the C2 vertebra owing to the activation of the ipsilateral upper neck extensor to reposition the head with HSM in right axial rotation. The mean muscle force in 25° flexion with and without the HSM was $\leq 11\%$ of the mean muscle force (1350 N) reported in an MSK model that simulated a fully-tensed muscle in a neutral head-neck position (Dibb et al., 2013). The mean muscle force in the HHNC_{25F|10LB|25AR} case was also 11% of the mean force predicted by an MSK model in a fully-tensed neutral head-neck position (Dibb et al., 2013). Assessments on the muscle forces confirmed that the model response was within the physiologic limits and indicated that the pain could be a result of cumulative loading.

The increase in muscle force can have two-fold implications on the risk of neck pain in the RWA. First, the muscles can get injured based on the Cinderella hypothesis, where muscle contractions as low as 5% MVC for a prolonged period with little or no rest can cause overworking of the muscle fibers, impede blood supply, resulting in ischemic muscular pain and muscle fatigue in the muscles (Hägg, 2000; SJØGAARD et al., 1986). Few studies also postulated a risk of occlusion in the capillaries and arterioles within the muscles due to sustained periods of muscle contractions (Eriksen, 2004; Harrison et al., 2015). Second, an increase in muscle contractions can influence the risk of neck pain by increasing the reaction force in the spinal column, implying a potential for discogenic neck pain.

5.4.2 IVD force response

An increase in muscle activity due to the added HSM resulted in an increase in the compressive and shear forces in the IVDs. Similarly, with an increase in the magnitude of head-neck position from a pure flexion to a combined position, the increase in the C2-C3 and C3-C4 IVD compression was attributed to the increase in the upper neck extensor activation while repositioning the head in 25° axial rotation. The C5-C6 IVD compression in the HHNC_{25F} condition was 93 N more than in the H_{25F} case. A similar increase (102.3 N) was observed in the MSK neck model at the C5-C6 joint with the added helmet, NVG and CW (Barrett et al., 2022b). In the HHNC_{25F10LB|25AR} case, the compression in the C4-C5 to C7-T1 had a modest increase (<10%) relative to the HHNC_{25F} case owing to the similarities in the muscle forces and kinematics in the lower cervical spine. The similarities in the lower cervical spine kinematics between the HHNC_{25F} and HHNC_{25F10LB|25AR} cases were attributed to the major contribution from the upper cervical spine to reposition the head in axial rotation (Hadagali and Cronin, 2023; Panjabi et al., 1991a).

The mean IVD compression was less than 10% of the reported ultimate compressive tolerance (UCT) of the cervical spine (3900 N) in all the simulated cases. Similarly, the mean AP shear force was ≤5% of the reported failure tolerance (500 N) in all the simulated cases (Pintar et al., 1998; Shea et al., 1991). A lower force in the IVD compared to the failure tolerance levels implies a higher risk of neck pain due to cumulative loading rather than acute loading. The magnitude of the IVD forces from this study could also explain why RWA experience neck pain with more flight time (Adam, 2004).

Experimental studies have identified endplate failure in the FSUs when axial compressive loading was applied to the FSUs in a neutral position (Arun et al., 2017; BROWN et al., 1957; Desmoulin et al., 2020; Lundin et al., 1998; Rajasekaran et al., 2013; van Heeswijk et al., 2017; Wade et al., 2014; Yoganandan et al., 1988). While axial compressive loading has shown to cause damage to bony and endplate regions, experimental studies on FSUs have shown that complex loading, i.e. combined bending and axial compression, lead to herniation of the IVDs (Berg-Johansen et al., 2018; Desmoulin et al., 2020; Rade et al., 2018; Rajasekaran et al., 2013; van Heeswijk et al., 2017; Wade et al., 2014). From experimental studies, repeated exposure of the spinal column in combined compression (<30% of UCT) and flexion, as observed in the RWA, can increase the chances of IVD damage (Callaghan and McGill, 2001; Gooyers and Callaghan, 2015; Parkinson and Callaghan, 2009). One study on porcine FSU found that a compressive load of <10% of the UCT applied during cyclic flexion-extension resulted in structural changes in the IVDs, implicating a potential for IVD damage (Gooyers and

Callaghan, 2015). From this study, the IVD force response in a non-neutral head-neck position indicates a higher risk of damage in the IVDs in the RWA as their cervical spine is repeatedly exposed to a complex loading that combines compression and non-neutral positions while scanning the environment with the HSM.

Similarly, increasing shear forces have been attributed to the risk of IVD herniation (Barrett et al., 2020; Schmidt et al., 2013). In the current study, the increasing shear forces that were directed toward the posterior direction indicated a backward migration of the NP during flexion (Barrett et al., 2020). The increasing shear forces and the implication of backward migration of the NP further strengthen the postulated risk of damage to the IVDs in the RWA.

5.4.3 Collagen fiber strain response in the AF

From the literature, FSUs exposed to combined compression and bending (non-neutral position), as observed in the RWA head-neck positions, demonstrated a risk of annular fissures (Berg-Johansen et al., 2018; Desmoulin et al., 2020; Rade et al., 2018; Rajasekaran et al., 2013; van Heeswijk et al., 2017; Wade et al., 2014). Annular fissures can cause herniation and degeneration in IVDs (Adams and Dolan, 2012; Carragee et al., 2009; Rajasekaran et al., 2013; Tomaszewski et al., 2015). Assessing the tissue-level response in the collagen fibers was important to gain insight into the risk of annular fissures and the potential for herniations and IVD degeneration that could lead to neck pain in the RWA (Landau et al., 2006) (Figure 156).

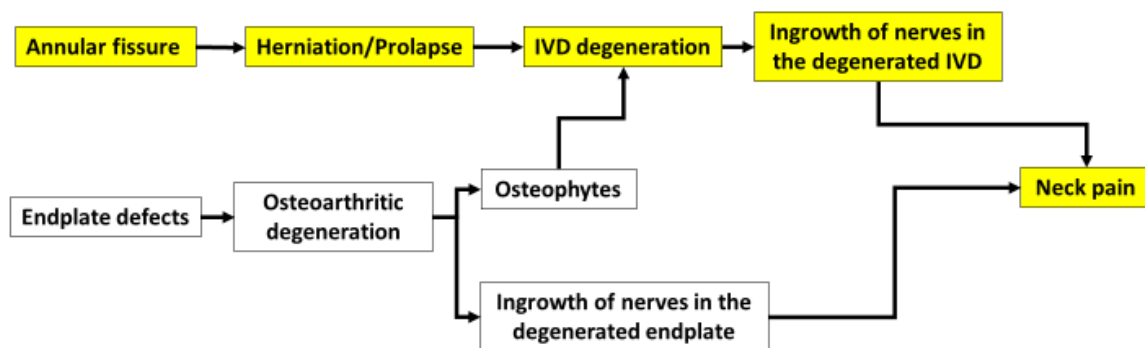


Figure 156: Illustrating the potential pathways to neck pain as reported in the literature. Annulus-driven IVD degeneration (Adams and Dolan, 2012; Carragee et al., 2009), a potential pathway to neck pain in the RWA, is highlighted in yellow.

In all the simulated cases, the tensile strains experienced in the collagen fibers were within the physiologic threshold reported in the literature on isolated fiber specimens (Holzapfel et al., 2005; Isaacs, 2012; Pezowicz, 2010). There was a lack of in vivo experimental or numerical data to compare the magnitude of the tensile strains in the collagen fibers specific to cervical IVDs as predicted in the current study. A mean increase in the strains by 27% in the HHNC_{25F|10LB|25AR} relative to the H_{25F} case indicated that a combination of HSM and non-neutral position increased the potential for annular fissure in RWA (HHNC_{25F|10LB|25AR}) compared to a civilian (H_{25F}). The responses were similar (4% increase) between the simulated H_{25F} and HH_{25F} (RWA day mission) cases, indicating a minimal effect of the helmet in 25° head-neck flexion on the potential for annular fissure. However, the inclusion of NVG and CW to the helmet (mimicking a night mission) in 25° flexion had a modest effect on the risk of annular fissure and a consequential annulus-driven IVD degeneration (12% mean increase from HH_{25F} to HHNC_{25F}). The modest increase in the collagen fiber strains with the addition of HSM in 25° head-neck flexion could be attributed to the similarities in the lower cervical spine (C2-T1) kinematics. A slight increase in magnitude of head-neck position with the HSM (HHNC) from 25° flexion to a combined position indicated a further risk of annular fissure and annulus-driven IVD degeneration (12% mean increase from HHNC_{25F} to HHNC_{25F|10LB|25AR}). The increase in fiber strain in the HHNC_{25F|10LB|25AR} relative to HHNC_{25F} by 21% and 17% in the C2-C3 and C3-C4 levels, respectively, were attributed to the increase in the coupled-lateral bending along with flexion of the C2-T1 in the combined position case.

In vitro studies on lumbar FSUs demonstrated that in combined compression and flexion positions (typically observed in RWA head-neck), posterior and posterolateral aspects of the IVDs are more susceptible to a herniation (Briar and Gregory, 2023; Callaghan and McGill, 2001; Tampier et al., 2007; van Heeswijk et al., 2017). The herniations are attributed to the tensile strain in the collagen fibers of the AF leading to annular fissures, which is one of the implications of IVD degeneration (Adams and Dolan, 2012; Iatridis et al., 2005). In all the simulated cases, the collagen fibers in the posterior and posterior-lateral aspects of the AF experienced higher tensile strains relative to the anterior region due to the flexion of the lower cervical spine.

In vitro experiments demonstrated microscopic rupture of collagen fibers (annular fissure) in the deep layers of posterior and posterior-lateral aspects of the IVDs, which worsened with an increasing number of cycles (Gooyers et al., 2015). The fissures are radial, i.e., they progress outward from the NP in the posterior or posterior-lateral direction with repeated exposure. Sometimes, the radial annular

fissures allow the migration of NP, which can reach the peripheral aspects of the IVD and expel (Adams and Dolan, 2012). In the model, the innermost concentric layer of the collagen fibers experienced peak strains, which decreased towards the outermost layers. The peak strains in the innermost layers were attributed to the fiber orientation, which was 45° with respect to the transverse plane compared to the relatively outer layers which were oriented $<45^\circ$ (Barker and Cronin, 2021). The results indicated a risk of annular fissure onset in the innermost layer of fibers, which might imply a potential for herniation and IVD degeneration with repeated exposure to HSM and non-neutral positions in the RWA. Although the time taken for a complete herniation is many years (Adams and Dolan, 2012), over-exertion by the RWA involving repetition in non-neutral head-neck positions with the HSM and increased flying hours can accelerate the process (Gooyers et al., 2015). Due to the lack of nociceptor nerve endings in the interior aspects of the healthy IVD, the annular fissures initiating from the innermost layers might not generate pain symptoms in the earlier stages. The collagen fibers are not innervated, but the progression of degeneration could increase the growth of nociceptive fiber bundles within the IVDs, and with repeated exposure, as observed in RWA, there could be an increased risk of neck pain (Adams and Dolan, 2012; García-Cosamalón et al., 2010; Peng and Bogduk, 2019; Tomaszewski et al., 2015).

An increase in the HSM and head-neck position magnitude from flexion to a combined position resulted in a larger area of the collagen fiber experiencing peak tensile strain. This result may indicate an increase in the magnitude of structural loss in the AF and the degenerated regions. Although there is sufficient evidence on the nociceptor ingrowth in degenerated IVDs and a risk of neck pain, there is a lack of data in the literature that correlates the magnitude of structural loss with an increase in the nociceptor ingrowth or intensity of neck pain.

5.4.4 Endplate stress response

Vertebral endplate defects can cause IVD degeneration as well as osteoarthritic degeneration (Adams and Dolan, 2012; Fields et al., 2018; Rade et al., 2018; Vergroesen et al., 2015). Assessing the tissue-level response in the vertebral endplate was important to gain insight into the risk of endplate defects and the potential for osteoarthritic (Aydoğ et al., 2004; Byeon et al., 2013) and IVD degeneration (Landau et al., 2006) that could lead to neck pain in the RWA (Figure 157).

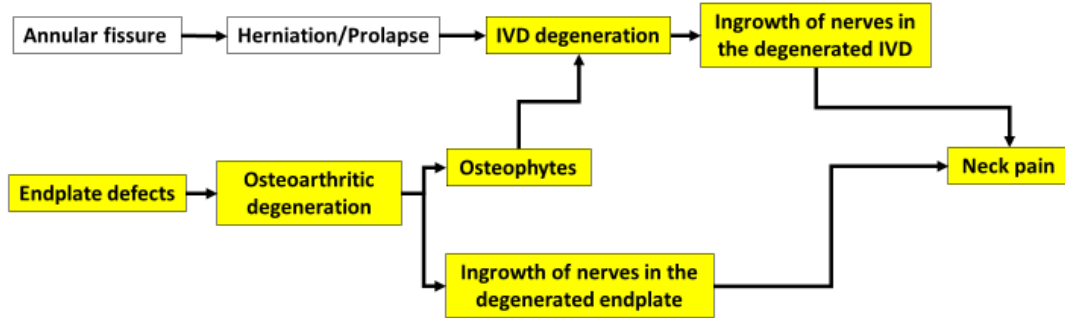


Figure 157: Illustrating the potential pathways to neck pain as reported in the literature. Endplate-driven IVD degeneration (Adams and Dolan, 2012), a potential pathway to neck pain in the RWA, is highlighted in yellow.

The effective stress experienced in the vertebral endplates varied between 2 MPa and 11 MPa in all the simulated cases. The C2-C3 inferior endplate experienced the highest stress relative to the other endplates. The magnitude of the peak effective stress in all the simulated cases was comparable with existing FE neck models (Srinivasan et al., 2021; Yoganandan et al., 1997). The stresses were higher in the endplates in the superior aspects of the cervical spine relative to the inferior aspects. The decrease in the stresses in the cranial-caudal direction was attributed to the increasing surface area of the endplates from C2 inferior (250 mm²) to C7 inferior (370 mm²). The inverse relationship between stress and area led to higher stresses in the C2 inferior endplates relative to the endplates in rest of the cervical spine. Also, peak effective stress was concentrated along the margins of the endplate in all the cases, in agreement with the findings from an existing cervical spine FE model (Srinivasan et al., 2021). The results indicated that the potential for endplate-related defects and a consequential endplate-driven spinal degeneration in RWA could be a result of HSM (a 46% increase from H_{25F} to HHNC_{25F}). The risk of endplate-related defects further increased when the magnitude of head-neck position increased from flexion to a combined position with a constant HSM (a 10% increase in peak stress from HHNC_{25F} to HHNC_{25F|10LB|25AR}).

Osteoarthritis is a joint disease, the etiology of which is multifactorial. Etiological factors include biomechanical instability in the form of increased mechanical stress, cartilage degradation, subchondral bone remodelling or muscle impairments (Egloff et al., 2012). Any existing biomechanical instability or trauma in the joint can lead to altered joint loading. The altered loading in the joint has been considered a key factor for the initiation and progression of osteoarthritis (Guilak, 2011; Martínez-Moreno et al., 2019). In the RWA, an increase in the effective endplate stresses with the added HSM

(as observed in this study), coupled with repeated exposures due to flying hours, can implicate a potential for endplate defects (not to be confused with failure) (Hee et al., 2011; Martin and Buckwalter, 2002), which can cause biomechanical instability. The biomechanical instability arising from the endplate defect can alter the loading in the spinal column, thereby increasing the risk of osteoarthritis onset (Martínez-Moreno et al., 2019). Repeated exposure of the spinal column to abnormal loadings can lead to the progression of osteoarthritis in the vertebral joints in the RWA neck, consistent with the radiological findings (Aydoğ et al., 2004; Byeon et al., 2013). An increase in the endplate stress and a potential for endplate defects can also implicate a risk of neck pain, as studies have reported that endplates with defects are highly innervated relative to endplates without defects (Feng et al., 2018).

Osteoarthritis is characterized by cartilage degradation and involves subchondral bone remodelling and osteophyte (osteo-cartilaginous outgrowths) formation at the articular surface, the pathophysiology of which is not fully understood to date. The formation of osteophytes can be triggered by various metabolic and mechanical factors (Junker et al., 2016; Roelofs et al., 2020; van der Kraan and van den Berg, 2007). Osteophytes have been identified as potential sources of pain in degenerated spinal structures (Menkes and Lane, 2004; Roelofs et al., 2020; van der Kraan and van den Berg, 2007). Osteophytes are usually formed outside the cortical bone, in the margins/edges of the vertebral endplate cartilage, in the anterior-lateral regions (Adams, 2009; Junker et al., 2016; Roelofs et al., 2020; van der Kraan and van den Berg, 2007; Wang MD et al., 2018). In the current study, the peak stresses in the endplates were observed in the margins of the endplates. The location of the peak endplate stresses identified in the current study was consistent with the location of osteophytes as reported in the literature, implicating a potential for osteophytic formation and a risk of neck pain in the RWA. The implications from this analysis pertaining to the risk of osteophytic formation are consistent with the epidemiological studies that reported osteophytes in the RWA (Aydoğ et al., 2004; Byeon et al., 2013).

Endplates are composed of a thin layer of hyaline cartilage and a layer of cortical bone. The hyaline cartilage is semi-permeable and allows diffusion of water and nutrients to and from the IVDs (Papadakis et al., 2011). Degenerative changes to the endplates as a result of osteoarthritis can hinder the supply of nutrients to the IVDs, causing the NP to dehydrate, initiating the process of IVD degeneration (Feng et al., 2018; Fields et al., 2018; Hee et al., 2011; Jackson et al., 2011; Lam et al., 2021; Ling et al., 2020; Lotz et al., 2013; Papadakis et al., 2011; Rutges et al., 2011; Vergroesen et al., 2015). As the IVD degenerates, the nociceptive fibers in the peripheral IVD regions start growing into the inner part of the AF and NP, increasing the chances of discogenic neck pain (García-Cosamalón et

al., 2010; Peng and DePalma, 2018; Tomaszewski et al., 2015). The results indicate a possibility of endplate-driven IVD degeneration and an associated risk of neck pain in the RWA, consistent with the MRI study that reported degenerated IVDs in RWA (Landau et al., 2006).

5.4.5 Ligament distraction response

With a changing HSM property and a constant non-neutral position, the results indicated that the HSM had less influence on the ligament distractions (<0.2 mm difference between H_{25F}, HH_{25F} and HHNC_{25F} cases). An increase in the magnitude of head-neck position from only flexion to a combined position increased the ligament distractions, specifically in the contralateral CL. The coupled lateral bending motion as a result of head axial rotation resulted in an increase in the distractions in contralateral CL. The results from this study indicate that the consequential reduction in the FOV in the RWA as a result of NVG usage can increase the risk of neck pain stemming from the ligaments.

The static or repetitive motion of the joints within the physiologic limits can result in creep, which is an indication of micro-damage in the collagen fibers of the ligament tissues. The micro-damage triggers an acute inflammatory response, which, when left noticed and undisturbed, heals over time (Frank et al., 1985; Leadbetter et al., 1991; Solomonow, 2004). However, acute inflammation, when left unnoticed or unrecovered, can develop into chronic inflammation, leading to permanent damage in the structural integrity and dysfunctionality of the ligaments (Leadbetter et al., 1991). In the current study, the ligament distractions in all the RWA cases were confined within the physiologic range (toe- and linear regions), indicating that the chances of a micro-damage or failure were unlikely during a single head-neck motion. Although ligament response suggests a low risk of injury to these tissues in these positions, there are chances that a persistent deviation (in flexion or combined motions) of the head-neck from the neutral position, with or without HSM, can induce micro-damage (sub-failure region). An increase in the ligament distraction response due to an increase in magnitude of head-neck position (due to NVG) for longer durations (and a lack of break) can accelerate the process of micro-damage in ligaments.

Repeatedly loading the ligaments or repeatedly distracting the ligaments at constant values over time is known to cause hysteresis, which is associated with creep, which causes laxity in the joints and joint instability (Solomonow, 2004). The spinal ligaments are embedded with mechanoreceptors that are connected to the neuromuscular control units, and any micro-damage or creep in the ligaments could also cause impaired muscle functions (Panjabi, 2006; Solomonow, 2004). Biomechanical instability in

the spinal column due to alterations in ligament properties can exacerbate the risk of degenerative disorders like osteoarthritis (Guilak, 2011; Jaumard et al., 2011; Martínez-Moreno et al., 2019; Solomonow, 2004). Results from this study indicate an increased risk of alterations in ligament properties and a cascade of joint disorders with an increase in the magnitude of head-neck non-neutral position due to the usage of NVG for a longer duration.

5.4.6 Tissue-level neck pain pathway

Epidemiological data indicated a risk of neck pain in the RWA due to degenerative changes in the cervical spine (Aydoğ et al., 2004; Byeon et al., 2013; Landau et al., 2006). However, to date, there is no explanation in the literature regarding the effect of HSM or magnitude of non-neutral positions on the possible pathways to degeneration and, eventually, neck pain. The results indicated that addition of HSM to bare head could lead to endplate-driven IVD degeneration, in agreement with X-ray studies that reported osteophytic changes in RWA (Aydoğ et al., 2004; Byeon et al., 2013). The results also indicated that an added HSM could lead to annulus-driven IVD degeneration, in agreement with the study that reported 3rd-grade IVD degeneration in 10 helicopter pilots (Landau et al., 2006). There is no epidemiological data that reports ligament as a source of neck pain in the RWA. However, the results from the current study indicated that ligaments can also be a potential pathway to neck pain, attributed to increase in magnitude of non-neutral positions which is one of the consequences of mounting NVG to the helmet (Figure 158).

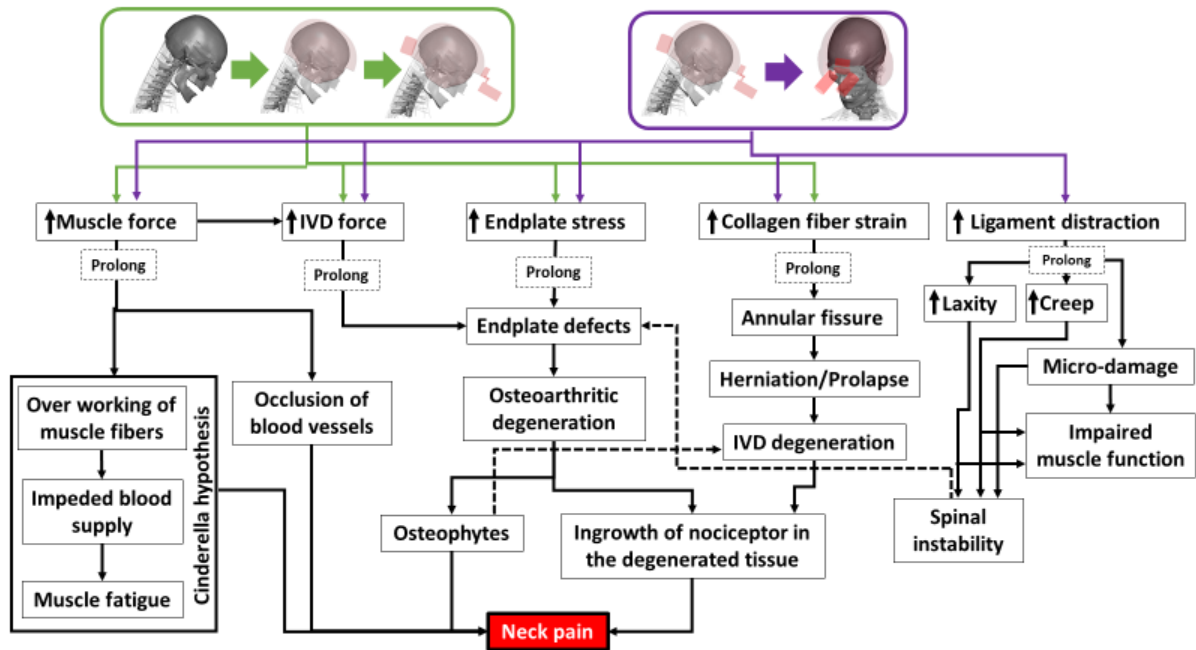


Figure 158: Flowchart illustrating the potential neck pain pathway at the tissue-level due to HSM and non-neutral position magnitudes in the RWA.

5.4.7 Cumulative trauma

An acute injury is a consequence of a single impactful event when the loads experienced by the tissues exceed the failure tolerance. A chronic injury is a consequence of multiple loading events when the loads experienced by the tissues within the physiologic limits over a period lead to a gradual loss in tolerance before injury occurs (Barrett, 2022) (Figure 159). An increase in the physiologic loads might accelerate the loss of tissue tolerance, thereby causing the tissues to be injured earlier, as observed in experimental studies (Gooyers et al., 2015; Parkinson and Callaghan, 2009). Cumulative mechanical trauma in the spine is influenced by various factors, including the magnitude of the applied load, frequency of repetition (rate of the cycle), duration of exposure and joint position. In the current study, only two factors, i.e. the magnitude of the applied load (HSM configurations) and joint position (flexion and combined) were considered. In all the RWA cases, the kinetic, kinematic and tissue-level responses were within the physiologic limits, indicating that neck pain in RWA can result from chronic injury sustained from cumulative trauma.

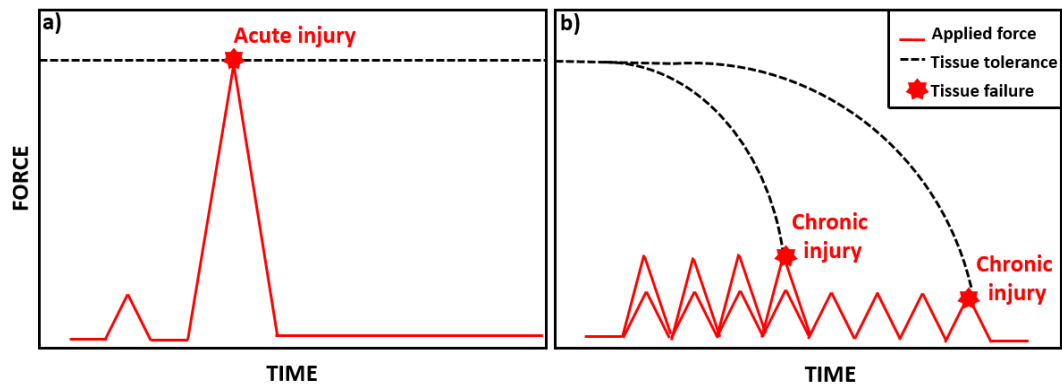


Figure 159: A) An illustration of an acute injury that is caused from a single loading event where the load exceeds the tolerance level of the tissue. B) An illustration of a chronic injury that is caused from reduced tissue tolerance due to multiple loading events within the physiological limits (Barrett, 2022).

From Parkinson and Callaghan (2009), the FSUs loaded at 10% UCT failed at 14400 ± 6859 cycles, while 30% UCT failed at 5031 ± 3944 cycles. An increase in the applied compression beyond 30% of the UCT resulted in IVD failure within less than 5,000 cycles in pre-flexed porcine FSU specimens (Gooyers and Callaghan, 2015). Similarly, in the current study, an increase in the IVD force by 100 N due to the added HSM indicated an accelerated reduction in tissue-level tolerance and the required number of cycles for a chronic injury onset. With the consideration of aircraft vibrations, it is likely that the tissue-level tolerance reduces at a much more exacerbated rate, further reducing the required number of cycles to chronic injury onset. Unlike the IVDs, for which a failure threshold for compressive forces values and the number of flexion cycles exist, there was no threshold for the number of cycles required to cause chronic injury in the ligaments or endplates.

5.4.8 Clinical relevance of the model outcome

From this study, the magnitude of predicted IVD compression and AF collagen fiber strains increased from C2-C3 to C7-T1 levels, for any given condition, indicating a higher risk of damages to the IVDs and a risk of annulus-driven IVD degeneration in the LCS. Overall, the outcome predicted by the model concurs with the clinical study that reported higher prevalence of disc degeneration in the LCS (Landau et al., 2006).

5.4.9 Other mechanisms that may lead to neck pain

Other than tissue-level biomechanical indicators such as stresses and strains, there could be physiological processes that might be initiated by other environmental factors (e.g. noise, temperature) and cause neck pain. For example, exposure to occupational cold has been shown to cause neck pain in Norwegian population (Stjernbrandt and Hoftun Farbu, 2022). However, the effect of such environmental factors on the pain-causing physiological processes has not been documented to date in the RWA. Moreover, it is not practical to experimentally capture the interactions of environmental factors with the physiological processes during a mission. Also, based on limitations in existing FE modeling capabilities, simulating the interaction of environmental factors (e.g. temperature) with physiological processes (e.g. dehydration) is not possible and can be considered beyond the scope of this research.

5.4.10 Summary of Phase #3

Overall, the present study provides insights into the interaction of HSM and non-neutral positions at the tissue-level, thereby taking a further step from inferring the risk of neck pain from joint forces and moments. The current study prioritized isolating potential neck pain pathways at the tissue-level to provide insight into the important factors that need to be considered when designing HSM to mitigate the risk of neck pain in RWA. From the current study, increase in HSM could potentially increase the risk of neck pain arising from muscles, IVDs and endplates, while increase in the magnitude of non-neutral positions could potentially increase the risk of neck pain arising from muscles, IVDs, endplates and ligaments. An increase in non-neutral head-neck position magnitude from a pure flexion to a combined (flexion, axial rotation and lateral bending) position can specifically affect the IVDs and muscles at the C2-C3 and C3-C4 levels and the contralateral CLs at all the levels. The tissue-level findings from this study on the risk of neck pain arising from cervical spinal degeneration agree with the recent clinical findings that report an increase in total IVD replacement cases in the RWA (Madison et al., 2023).

Chapter 6 Limitations and future work

6.1 Limitations

The repositioning simulations did not include the 3D passive muscle tissues, flesh and skin. The material properties of the skin, flesh and passive muscles were stiffer in quasi-static loading rates as the materials in the FE neck model were initially developed to simulate high-speed conditions (Gierczycka et al., 2021); therefore, they were replaced with more recent passive muscle tissue data. The muscle attachments (fascial tissues) and hyoid bone attachments (suprahyoid muscles and the pharyngeal tissues) in the FE neck model were represented as simplified springs due to geometrical complexity and scarcity of material properties and required further investigation. The hyoid bone attachments, despite the limitations, provided a BC for the skull and the hyoid bone that concurred with the anatomical constraints. The choice of 1D hill-type elements is another limitation of this research.

The muscles contract and generate forces in three dimensions. However, the force generated by the hill-type muscles is only in one dimension and may not completely replicate the *in vivo* physiologic motion (Randhawa and Wakeling, 2018; Roberts et al., 2019; Roberts and Azizi, 2011). Also, the PCSA varies across the length of the muscles, not accurately captured in the hill-type muscle, where the cross-section area is assumed to be constant throughout the muscle length. Future studies should look into enhancing the 3D passive muscle biofidelity to make it suitable for capturing physiologic motions. There are limited *in vivo* experimental data to verify intervertebral kinematics, IVD deformations, collagen fiber strain response and ligament distractions at different *in vivo* head-neck positions. In the present study, *in vitro* experimental data was used to assess the tissue-level response in the repositioned models.

The cause of neck pain is multifactorial, biomechanical factors being one of them. The current study limited the explorations to HSM and non-neutral positions. Although the amount of time spent by the RWA in non-neutral positions with the HSM is a key factor, due to the modelling capabilities, this factor could not be explored. The current study did not consider the effect of vibration. Cyclic loading from the aircraft vibration, along with the HSM and non-neutral positions, can further exacerbate the risk of neck pain in the RWA. The $NM_{M50-Hill-E}$ model was not developed to simulate fatigue, and it was not practical to simulate the reduction in tolerance in the tissues to exactly identify the number of cycles required for chronic injury.

The anatomy of the cervical IVD is known to be different than the lumbar or thoracic IVDs. The cervical IVDs have an uncovertebral cleft, and the orientation of the collagen fibers in the AF varies relative to the lumbar spine (Levangie and Norkin, 2005; Mercer and Bogduk, 1999). The AF in the cervical spine is crescent-shaped, which is thick in the anterior aspects and tapers in the lateral aspects, unlike concentric layers of collagen fibers in the lumbar IVDs (Mercer and Bogduk, 1999). In the current model (NM_{M50-Hill-E}) and in a majority of the existing FE head-neck models, the AF is assumed to be similar to the lumbar. Although the model prediction on the risk of neck pain jives with the clinical findings, biofidelic enhancements to the IVD geometry can further improve the model predicting capability.

6.2 Future work

The FE head-neck model investigated in the current study was based on a subject-specific male in the 50th-percentile stature with a relatively longer cervical spine. The effect of subjective variations such as spinal stature, spinal curvature or head inertial properties can have an effect on the muscle activation strategy. Differences in muscle activation strategy can affect the mechanical response from the kinematic to the tissue-level, which needs to be explored. Also, the current epidemiological data on the degenerative changes in RWA is inclusive of male pilots. However, from the literature, female pilots have demonstrated more vulnerability to neck injuries relative to male pilots. Future studies should investigate the risk of neck pain in female RWA.

In the current research, the potential solution to mitigate the risk of neck pain will be based on the investigations conducted on a healthy/non-degenerate cervical spine. However, in reality, there would be a progressive degeneration in tissues with prolonged use of the HSM, duration of flight hours and repeated non-neutral positions. A degenerated spine has been demonstrated to cause changes in the spinal motion, thereby exacerbating the risk of motion impairments, as demonstrated in numerous FE neck modelling studies (X.-Y. Cai et al., 2020b; Rahman et al., 2023). Future studies should investigate the interaction of HSM and non-neutral head-neck positions with the degenerated spinal components (e.g. reduction in IVD height, inclusion of osteophytes, etc.) on the risk of neck pain by assessing the tissue-level metrics. Such an assessment might be useful in assessing any potential modifications in the neck pain pathway due to the degenerated tissues. For example, an alteration in the kinematic of the head-neck due to osteoarthritic degeneration might alter the tissue-level response in the collagen fiber of the AF or ligament, thereby requiring a different solution to mitigate the risk of neck pain. Future

work should also consider simulating the RWA head-neck positions with the total IVD replacement to assess the risk of neck pain or implant failure (Madison et al., 2023).

Repetitive exposure to cyclic loading, such as aircraft vibration, can potentially lead to fatigue damage in the IVD and neck pain (Motiwale et al., 2018; Subramani et al., 2020). Future studies should consider assessing the risk of neck pain in the RWA due to cyclic loading from the aircraft vibrations, which could be an important factor in the onset of spinal degeneration in RWA (Healey et al., 2021). Mechanical damage models have been developed in previous studies to predict the risk of fatigue in IVDs due to cyclic loading (Motiwale et al., 2018; Subramani et al., 2020). Future studies can make use of such damage models to assess the risk of neck pain in the RWA due to vibrations. When exposed to vibration, the neck muscles would have to constantly work to maintain the head-neck position and the desired line of sight. Hence, a potential next step could be to introduce vibrations in simulations and enhance the muscle control system in the head-neck model to maintain the desired line of sight under cyclic loading.

Based on the findings from the current study, potential solutions that may be investigated in the future studies to reduce the risk of neck pain in RWA include:

- 1) Increasing the FOV in the NVG to decrease the magnitude of non-neutral positions.
- 2) Reducing the mass of HSM components such as helmet and NVG.
- 3) Designing the NVG with the CoG closer to the helmet, thereby reducing the need for a CW.


Chapter 7 Conclusions

The following conclusions can be drawn from this research work:

- The muscle-based method of repositioning the FE head-neck model captured the in vivo non-neutral positions within the physiologic ROM (in flexion and axial rotation) better than the conventional external BC-based method, based on kinematic assessments.
- The muscle-based and BC-based repositioning methodologies produced different spine kinetics and tissue-level response, demonstrating the need for a biofidelic method to simulate in vivo non-neutral head-neck positions. A biofidelic repositioning method can improve the response predicting capability of FE head-neck models at the tissue-level.
- An increase in the HSM from adding NVG and CW to the helmet, increased the muscle forces, IVD forces, endplate stresses and AF collagen fiber strains.
- Positioning the head-neck further away from a relatively neutral position, typically observed as a consequence of reduced FOV after mounting the NVG, increased the ligament distractions, muscle forces, IVD forces, endplate stresses and AF collagen fiber strains.
- Increased tissue-level responses from this study suggests a potential for neck pain response with HSM relative to no HSM.
- Increased tissue-level responses from this study suggests a potential for neck pain response when head-neck is positioned further away from a relatively neutral position.

Letters of copyright permission

CCC RightsLink PH ? 🔍



The biomechanical effects of S-type dynamic cage using Ti and PEEK for ACDF surgery on cervical spine varying loads
Author: Pechimuthu Susal Manickam, Sandipan Roy
Publication: The International Journal of Artificial Organs
Publisher: SAGE Publications
Date: 2021-10-01
Copyright © 2021, © SAGE Publications


Gratis Reuse

Permission is granted at no cost for use of content in a Master's Thesis and/or Doctoral Dissertation, subject to the following limitations. You may use a single excerpt or up to 3 figures tables. If you use more than those limits, or intend to distribute or sell your Master's Thesis/Doctoral Dissertation to the general public through print or website publication, please return to the previous page and select 'Republish in a Book/Journal' or 'Post on intranet/password-protected website' to complete your request.

[BACK](#) [CLOSE WINDOW](#)

© 2023 Copyright - All Rights Reserved | Copyright Clearance Center, Inc. | Privacy statement | Data Security and Privacy | For California Residents | Terms and Conditions
Comments? We would like to hear from you. E-mail us at customercare@copyright.com

CCC RightsLink PH ? 🔍



Fatigue damage prediction in the annulus of cervical spine intervertebral discs using finite element analysis
Author: Adhitya V. Subramani, Phillip E. Whitley, Harsha T. Garimella, et al
Publication: Computer Methods in Biomechanics & Biomedical Engineering
Publisher: Taylor & Francis
Date: Aug 17, 2020
Rights managed by Taylor & Francis


Thesis/Dissertation Reuse Request

Taylor & Francis is pleased to offer reuses of its content for a thesis or dissertation free of charge contingent on resubmission of permission request if work is published.

[BACK](#) [CLOSE](#)

© 2023 Copyright - All Rights Reserved | Copyright Clearance Center, Inc. | Privacy statement | Data Security and Privacy | For California Residents | Terms and Conditions
Comments? We would like to hear from you. E-mail us at customercare@copyright.com

CCC RightsLink PH ? 🔍



Cervical Spine Motion Requirements From Night Vision Goggles May Play a Greater Role in Chronic Neck Pain than Helmet Mass Properties
Author: Jeff M. Barrett, Laura A. Healey, Steven L. Fischer, Jack P. Callaghan
Publication: Human Factors: The Journal of the Human Factors and Ergonomics Society
Publisher: SAGE Publications
Date: 2022-04-26
Copyright © 2022, © SAGE Publications

Gratis Reuse

Permission is granted at no cost for use of content in a Master's Thesis and/or Doctoral Dissertation, subject to the following limitations. You may use a single excerpt or up to 3 figures tables. If you use more than those limits, or intend to distribute or sell your Master's Thesis/Doctoral Dissertation to the general public through print or website publication, please return to the previous page and select 'Republish in a Book/Journal' or 'Post on intranet/password-protected website' to complete your request.

[BACK](#) [CLOSE WINDOW](#)

© 2023 Copyright - All Rights Reserved | Copyright Clearance Center, Inc. | Privacy statement | Data Security and Privacy | For California Residents | Terms and Conditions
Comments? We would like to hear from you. E-mail us at customercare@copyright.com



Biomechanical analysis of customized cage conforming to the endplate morphology in anterior cervical discectomy fusion: A finite element analysis

Author: Bin Sun, Qing Han, Feng Xu, Sul, AoBo Zhang, Yang Liu, Peng Xia, JinCheng Wang, XiaoYu Yang
Publication: Heliyon
Publisher: Elsevier
Date: January 2023
 © 2023 Published by Elsevier Ltd.

Creative Commons Attribution-NonCommercial-No Derivatives License (CC BY NC ND)

This article is published under the terms of the Creative Commons Attribution-NonCommercial-No Derivatives License (CC BY NC ND). For non-commercial purposes you may copy and distribute the article, use portions or extracts from the article in other works, and text or data mine the article, provided you do not alter or modify the article without permission from Elsevier. You may also create adaptations of the article for your own personal use only, but not distribute these to others. You must give appropriate credit to the original work, together with a link to the formal publication through the relevant DOI, and a link to the Creative Commons user license above. If changes are permitted, you must indicate if any changes are made but not in any way that suggests the licensor endorses you or your use of the work.

Permission is not required for this non-commercial use. For commercial use please continue to request permission via RightsLink.

BACK

CLOSE WINDOW



Preliminary exploration of the biomechanical properties of three novel cervical porous fusion cages using a finite element study

Author: Zhi Xu et al
Publication: BMC Musculoskeletal Disorders
Publisher: Springer Nature
Date: Nov 10, 2023
 Copyright © 2023, The Author(s)

Creative Commons

This is an open access article distributed under the terms of the Creative Commons CC BY license, which permits unrestricted use, distribution, and reproduction in any medium, provided the original work is properly cited.

You are not required to obtain permission to reuse this article. CC0 applies for supplementary material related to this article and attribution is not required.

RightsLink Printable License	
12/09/23, 11:01 PM	12/09/23, 11:01 PM
<p>SPRINGER NATURE LICENSE TERMS AND CONDITIONS</p> <hr/> <p>Dec 09, 2023</p> <hr/> <p>This Agreement between University of Waterloo -- Prasannaiah Hadagali ("You") and Springer Nature ("Springer Nature") consists of your license details and the terms and conditions provided by Springer Nature and Copyright Clearance Center.</p>	
License Number	5685111465136
License date	Dec 09, 2023
Licensed Content Publisher	Springer Nature
Licensed Content Publication	Nature Reviews Rheumatology
Licensed Content Title	Cell-based strategies for IVD repair: clinical progress and translational obstacles
Licensed Content Author	Abbie L. A. Binch et al
Licensed Content Date	Feb 1, 2021
Type of Use	Thesis/Dissertation
Requestor type	academic/university or research institute
Format	print and electronic
Portion	figures/tables/illustrations
Number of figures/tables/illustrations	1
<p>https://s1100.copyright.com/AppDispatchServlet</p> <p>1/7</p>	

RightsLink Printable License	
12/09/23, 11:01 PM	12/09/23, 11:01 PM
Would you like a high resolution image with your order?	no
Will you be translating?	no
Circulation/distribution	1 - 29
Author of this Springer Nature content	no
Title of new work	Assessing the Tissue-Level Response and the Risk of Neck Pain in Rotary-Wing-Arcrow using a Finite Element Model of the Neck
Institution name	University of Waterloo
Expected presentation date	Mar 2024
Portions	Fig 1
Requestor Location	University of Waterloo [REDACTED] Attn: University of Waterloo
Total	0.00 CAD
Terms and Conditions	
<p>Springer Nature Customer Service Centre GmbH Terms and Conditions</p> <p>The following terms and conditions ("Terms and Conditions") together with the terms specified in your [RightsLink] constitute the License ("License") between you as Licensee and Springer Nature Customer Service Centre GmbH as Licensor. By clicking 'accept' and completing the transaction for your use of the material ("Licensed Material"), you confirm your acceptance of and obligation to be bound by these Terms and Conditions.</p> <p>1. Grant and Scope of License</p>	
<p>https://s1100.copyright.com/AppDispatchServlet</p> <p>2/7</p>	

12/023, 11:01 PM RightsLink Printable License

SPRINGER NATURE LICENSE TERMS AND CONDITIONS

Dec 09, 2023

This Agreement between University of Waterloo – Prusumah Hadagali ("You") and Springer Nature ("Springer Nature") consists of your license details and the terms and conditions provided by Springer Nature and Copyright Clearance Center.

License Number	5685111465136
License date	Dec 09, 2023
Licensed Content Publisher	Springer Nature
Licensed Content Publication	Nature Reviews Rheumatology
Licensed Content Title	Cell-based strategies for IVD repair: clinical progress and translational obstacles
Licensed Content Author	Abbie L. A. Binch et al
Licensed Content Date	Feb 1, 2021
Type of Use	Thesis/Dissertation
Requestor type	academic/university or research institute
Format	print and electronic
Portion	figures/tables/illustrations
Number of figures/tables/illustrations	1

https://s100.copyright.com/AppDispatchServlet 1/7

12/023, 11:01 PM RightsLink Printable License

Would you like a high resolution image with your order?	no
Will you be translating?	no
Circulation/distribution	1 - 29
Author of this Springer Nature content	no
Title of new work	Assessing the Tissue-Level Response and the Risk of Neck Pain in Rotary-Wing Aircraft using a Finite Element Model of the Neck
Institution name	University of Waterloo
Expected presentation date	Mar 2024
Portions	Fig 1
Requestor Location	University of Waterloo [Redacted]
Total	0.00 CAD
Terms and Conditions	

Springer Nature Customer Service GmbH Terms and Conditions

The following terms and conditions ("Terms and Conditions") together with the terms specified in your [RightsLink] constitute the License ("License") between you as Licensee and Springer Nature Customer Service Centre GmbH as Licensor. By clicking 'accept' and completing the transaction for your use of the material ("Licensed Material"), you confirm your acceptance of and obligation to be bound by these Terms and Conditions.

1. Grant and Scope of License

https://s100.copyright.com/AppDispatchServlet 2/7

12/9/23, 6:57 PM RightsLink Printable License

ELSEVIER LICENSE TERMS AND CONDITIONS

Dec 09, 2023

This Agreement between University of Waterloo -- Prasannaath Hadagali ("You") and Elsevier ("Elsevier") consists of your license details and the terms and conditions provided by Elsevier and Copyright Clearance Center.

License Number	5685020424097
License date	Dec 09, 2023
Licensed Content Publisher	Elsevier
Licensed Content Publication	Clinical Biomechanics
Licensed Content Title	Biomechanics of the cervical spine. I: Normal kinematics
Licensed Content Author	Nikolai Bogduk, Susan Mercer
Licensed Content Date	Nov 1, 2000
Licensed Content Volume	15
Licensed Content Issue	9
Licensed Content Pages	16
Start Page	633
End Page	648

<https://s100.copyright.com/AppDispatchServlet> 1/8

12/9/23, 6:57 PM RightsLink Printable License

Type of Use	reuse in a thesis/dissertation
Portion	figures/tables/illustrations
Number of figures/tables/illustrations	1
Format	both print and electronic
Are you the author of this Elsevier article?	No
Will you be translating?	No
Title of new work	Assessing the Tissue-Level Response and the Risk of Neck Pain in Rotary-Wing Aircrew using a Finite Element Model of the Neck
Institution name	University of Waterloo
Expected presentation date	Mar 2024
Portions	Fig. 3a
Requestor Location	University of Waterloo [Redacted]
Publisher Tax ID	GB-494-6272 12
Total	0.00 CAD
Terms and Conditions	INTRODUCTION

<https://s100.copyright.com/AppDispatchServlet> 2/8

12/09/23, 10:23 PM		RightClick Printable License
SPRINGER NATURE LICENSE TERMS AND CONDITIONS		
Dec 09, 2023		
<p>This Agreement between University of Waterloo -- Prasanna Hadagali ("You") and Springer Nature ("Springer Nature") consists of your license details and the terms and conditions provided by Springer Nature and Copyright Clearance Center.</p>		
License Number	5685101011307	
License date	Dec 09, 2023	
Licensed Content Publisher	Springer Nature	
Licensed Content Publication	Medical & Biological Engineering & Computing	
Licensed Content Title	The effect of follower load on the range of motion, facet joint force, and intradiscal pressure of the cervical spine: a finite element study	
Licensed Content Author	Xin-Yi Cai et al	
Licensed Content Date	May 28, 2020	
Type of Use	Thesis/Dissertation	
Requestor type	academic/university or research institute	
Format	print and electronic	
Portion	figures/tables/illustrations	
Number of figures/tables/illustrations	1	
		https://is100.copyright.com/AppDispatchServlet
		1/7

12/09/23, 10:23 PM		RightClick Printable License
Will you be translating?	no	
Circulation/distribution	1 - 29	
Author of this Springer Nature content	no	
Title of new work	Assessing the Tissue-Level Response and the Risk of Neck Pain in Rotary-Wing Aircraft using a Finite Element Model of the Neck	
Institution name	University of Waterloo	
Expected presentation date	Mar 2024	
Portions	Fig 1	
Requestor Location	University of Waterloo	
	Attn: University of Waterloo	
Total	0.00 CAD	
Terms and Conditions		
Springer Nature Customer Service Centre GmbH Terms and Conditions		
<p>The following terms and conditions ("Terms and Conditions") together with the terms specified in your [RightsLink] constitute the License ("License") between you as Licensee and Springer Nature Customer Service Centre GmbH as Licensor. By clicking "accept" and completing the transaction for your use of the material ("Licensed Material"), you confirm your acceptance of and obligation to be bound by these Terms and Conditions.</p>		
1. Grant and Scope of License		
<p>1.1. The Licensor grants you a personal, non-exclusive, non-transferable, non-sublicensable, revocable, world-wide License to reproduce, distribute, communicate to the public, make available, broadcast, electronically transmit or create derivative</p>		
		https://is100.copyright.com/AppDispatchServlet
		2/7

12/09/23, 7:22 PM RightsLink Printable License

WOLTERS KLUWER HEALTH, INC. LICENSE TERMS AND CONDITIONS

Dec 09, 2023

This Agreement between University of Waterloo -- Prasannaadh Hadagali ("You") and Wolters Kluwer Health, Inc. ("Wolters Kluwer Health, Inc.") consists of your license details and the terms and conditions provided by Wolters Kluwer Health, Inc. and Copyright Clearance Center.

License Number	5685030438104
License date	Dec 09, 2023
Licensed Content Publisher	Wolters Kluwer Health, Inc.
Licensed Content Publication	Neurosurgery
Licensed Content Title	Intervertebral Disk Degeneration and Repair
Licensed Content Author	James Dowdell, Mark Erwin, Theodore Choma, et al
Licensed Content Date	Feb 21, 2017
Licensed Content Volume	80
Licensed Content Issue	3S
Type of Use	Dissertation/Thesis
Requestor type	University/College
Sponsorship	No Sponsorship

<https://s100.copyright.com/AppDispatchServlet> 1/5

12/09/23, 7:22 PM RightsLink Printable License

Format	Print and electronic
Will this be posted online?	Yes, on a secure website
Portion	Figures/tables/illustrations
Number of figures/tables/illustrations	1
Author of this Wolters Kluwer article	No
Will you be translating?	No
Intend to modify/change the content	No
Title of new work	Assessing the Tissue-Level Response and the Risk of Neck Pain in Rotary-Wing Aircraft using a Finite Element Model of the Neck
Institution name	University of Waterloo
Expected presentation date	Mar 2024
Portions	Fig. 1
Requestor Location	University of Waterloo [REDACTED]
Publisher Tax ID	Attn: University of Waterloo 895524239 RT0001
Total	0.00 CAD

<https://s100.copyright.com/AppDispatchServlet> 2/5

12/9/23, 7:17 PM RightsLink Printable License

SPRINGER NATURE LICENSE TERMS AND CONDITIONS

Dec 09, 2023

This Agreement between University of Waterloo -- Prasannaah Hadagali ("You") and Springer Nature ("Springer Nature") consists of your license details and the terms and conditions provided by Springer Nature and Copyright Clearance Center.

License Number	5685030109196
License date	Dec 09, 2023
Licensed Content Publisher	Springer Nature
Licensed Content Publication	Annals of Biomedical Engineering
Licensed Content Title	Quantifying the Importance of Active Muscle Repositioning a Finite Element Neck Model in Flexion Using Kinematic, Kinetic, and Tissue-Level Responses
Licensed Content Author	Prasannaah Hadagali et al
Licensed Content Date	Nov 3, 2023
Type of Use	Thesis/Dissertation
Requestor type	academic/university or research institute
Format	print and electronic
Portion	full article/chapter
Will you be translating?	no

https://s100.copyright.com/AppDispatchServlet 1/6

12/9/23, 7:17 PM RightsLink Printable License

Circulation/distribution 1 - 29

Author of this Springer Nature content yes

Title of new work Assessing the Tissue-Level Response and the Risk of Neck Pain in Rotary-Wing Aircraft using a Finite Element Model of the Neck

Institution name University of Waterloo

Expected presentation date Mar 2024

Requestor Location University of Waterloo
[Redacted]
Attn: University of Waterloo

Total 0.00 CAD

Terms and Conditions

Springer Nature Customer Service Centre GmbH Terms and Conditions

The following terms and conditions ("Terms and Conditions") together with the terms specified in your [RightsLink] constitute the License ("License") between you as Licensee and Springer Nature Customer Service Centre GmbH as Licensor. By clicking 'accept' and completing the transaction for your use of the material ("Licensed Material"), you confirm your acceptance of and obligation to be bound by these Terms and Conditions.

1. Grant and Scope of License

1.1. The Licensor grants you a personal, non-exclusive, non-transferable, non-sublicensable, revocable, world-wide License to reproduce, distribute, communicate to the public, make available, broadcast, electronically transmit or create derivative works using the Licensed Material for the purpose(s) specified in your RightsLink License Details only. Licenses are granted for the specific use requested in the order and for no other use, subject to these Terms and Conditions. You acknowledge and agree that the rights granted to you under this License do not include the right to modify, edit, translate, include in collective works, or create derivative works of the Licensed Material in whole or in part unless expressly stated in your RightsLink

https://s100.copyright.com/AppDispatchServlet 2/6

12/29/23, 7:00 PM RightsLink Printable License

ELSEVIER LICENSE TERMS AND CONDITIONS

Dec 09, 2023

This Agreement between University of Waterloo -- Prasanna Hadagali ("You") and Elsevier ("Elsevier") consists of your license details and the terms and conditions provided by Elsevier and Copyright Clearance Center.

License Number	5685020575655
License date	Dec 09, 2023
Licensed Content Publisher	Elsevier
Licensed Content Publication	Clinical Biomechanics
Licensed Content Title	Differences in neck surface electromyography, kinematics and pain occurrence during physiological neck movements between neck pain and asymptomatic participants. A cross-sectional study
Licensed Content Author	Ion Lascauin-Aguirrebeña, Di J. Newham, Bernat Galarraga-Gallastegui, Duncan J. Critchley
Licensed Content Date	Aug 1, 2018
Licensed Content Volume	57
Licensed Content Issue	n/a
Licensed Content Pages	9
Start Page	1

<https://s100.copyright.com/AppDispatchServlet> 1/8

12/29/23, 7:00 PM RightsLink Printable License

End Page	9
Type of Use	reuse in a thesis/dissertation
Portion	figures/tables/illustrations
Number of figures/tables/illustrations	1
Format	both print and electronic
Are you the author of this Elsevier article?	No
Will you be translating?	No
Title of new work	Assessing the Tissue-Level Response and the Risk of Neck Pain in Rotary-Wing Aircrew using a Finite Element Model of the Neck
Institution name	University of Waterloo
Expected presentation date	Mar 2024
Portions	Fig 2
Requestor Location	University of Waterloo [REDACTED] Attn: University of Waterloo
Publisher Tax ID	GB 494 6272 12
Total	0.00 CAD
Terms and Conditions	https://s100.copyright.com/AppDispatchServlet

2/8

12/23, 7:27 PM		RightLink Printable License
Format	Print and electronic	
Will this be posted online?	Yes, on a secure website	
Portion	Figures/tables/illustrations	
Number of figures/tables/illustrations	1	
Author of this Wolters Kluwer article	No	
Will you be translating?	No	
Intend to modify/change the content	No	
Title of new work	Assessing the Tissue-Level Response and the Risk of Neck Pain in Rotary-Wing Aircraft using a Finite Element Model of the Neck	
Institution name	University of Waterloo	
Expected presentation date	Mar 2024	
Portions	Figure 1.	
Requestor Location	University of Waterloo [Redacted]	
Publisher Tax ID	895524239 RT0001 Attn: University of Waterloo	
Total	0.00 CAD	
		https://s100.copyright.com/AppDispatchServlet

12/23, 7:27 PM		RightLink Printable License
<p>WOLTERS KLUWER HEALTH, INC. LICENSE TERMS AND CONDITIONS</p> <p>Dec 09, 2023</p> <hr/> <p>This Agreement between University of Waterloo -- Prasanna Hadagali ("You") and Wolters Kluwer Health, Inc. ("Wolters Kluwer Health, Inc.") consists of your license details and the terms and conditions provided by Wolters Kluwer Health, Inc. and Copyright Clearance Center.</p>		
License Number	5685030706699	
License date	Dec 09, 2023	
Licensed Content Publisher	Wolters Kluwer Health, Inc.	
Licensed Content Publication	Spine	
Licensed Content Title	Comparison of Cervical Spine Biomechanics After Fixed- and Mobile-Core Artificial Disc Replacement: A Finite Element Analysis	
Licensed Content Author	Sang-Hun Lee, Yang-Jin Im, Ki-Tack Kim, et al	
Licensed Content Date	Apr 20, 2011	
Licensed Content Volume	36	
Licensed Content Issue	9	
Type of Use	Dissertation/Thesis	
Requestor type	University/College	
Sponsorship	No Sponsorship	
		https://s100.copyright.com/AppDispatchServlet

RightsLink Printable License	
12/9/23, 10:23 PM	
ELSEVIER LICENSE TERMS AND CONDITIONS	
Dec 09, 2023	
<p>This Agreement between University of Waterloo -- Prasanmath Hadagait ("You") and Elsevier ("Elsevier") consists of your license details and the terms and conditions provided by Elsevier and Copyright Clearance Center.</p>	
License Number	5685100663893
License date	Dec 09, 2023
Licensed Content Publisher	Elsevier
Licensed Content Publication	Clinical Biomechanics
Licensed Content Title	Effect of the transverse ligament rupture on the biomechanics of the cervical spine under a compressive loading
Licensed Content Author	Wissal Mesfar;Kodjo Moglo
Licensed Content Date	Oct 1, 2013
Licensed Content Volume	28
Licensed Content Issue	8
Licensed Content Pages	7
Start Page	846
End Page	852
https://s100.copyright.com/AppDispatchServlet	
1/8	

RightsLink Printable License	
12/9/23, 10:23 PM	
Type of Use	reuse in a thesis/dissertation
Portion	figures/tables/illustrations
Number of figures/tables/illustrations	1
Format	both print and electronic
Are you the author of this Elsevier article?	No
Will you be translating?	No
Title of new work	Assessing the Tissue-Level Response and the Risk of Neck Pain in Rotary-Wing Aircraft using a Finite Element Model of the Neck
Institution name	University of Waterloo
Expected presentation date	Mar 2024
Portions	figure 1b
Requestor Location	University of Waterloo [Redacted] Attn: University of Waterloo
Publisher Tax ID	GB 494 6272 12
Total	0.00 CAD
Terms and Conditions	INTRODUCTION
https://s100.copyright.com/AppDispatchServlet	
2/8	

12/29/23, 7:15 PM RightsLink Printable License

ELSEVIER LICENSE TERMS AND CONDITIONS

Dec 09, 2023

This Agreement between University of Waterloo -- Prasannaah Hadagali ("You") and Elsevier ("Elsevier") consists of your license details and the terms and conditions provided by Elsevier and Copyright Clearance Center.

License Number	5685021487116
License date	Dec 09, 2023
Licensed Content Publisher	Elsevier
Licensed Content Publication	Journal of Biomechanics
Licensed Content Title	Impact responses of the cervical spine: A computational study of the effects of muscle activity, torso constraint, and pre-flexion
Licensed Content Author	Roger W. Nightingale, Jake Sganga, Hattie Cutcliffe, Cameron R. 'Dale' Bass
Licensed Content Date	Feb 29, 2016
Licensed Content Volume	49
Licensed Content Issue	4
Licensed Content Pages	7
Start Page	558
End Page	564

<https://s100.copyright.com/AppDispatchServlet> 1/8

12/29/23, 7:15 PM RightsLink Printable License

Type of Use	reuse in a thesis/dissertation
Portion	figures/tables/illustrations
Number of figures/tables/illustrations	1
Format	both print and electronic
Are you the author of this Elsevier article?	No
Will you be translating?	No
Title of new work	Assessing the Tissue-Level Response and the Risk of Neck Pain in Rotary-Wing Aircrew using a Finite Element Model of the Neck
Institution name	University of Waterloo
Expected presentation date	Mar 2024
Portions	Fig. 2
Requestor Location	University of Waterloo [Redacted]
Publisher Tax ID	GB 494 6272 12
Total	0.00 CAD
Terms and Conditions	INTRODUCTION

<https://s100.copyright.com/AppDispatchServlet> 2/8

12/9/23, 10:31 PM		RightsLink Printable License
ELSEVIER LICENSE TERMS AND CONDITIONS		
Dec 09, 2023		
This Agreement between University of Waterloo -- Prassannaah Hadagali ("You") and Elsevier ("Elsevier") consists of your license details and the terms and conditions provided by Elsevier and Copyright Clearance Center.		
License Number	5685101142084	
License date	Dec 09, 2023	
Licensed Content Publisher	Elsevier	
Licensed Content Publication	Clinical Biomechanics	
Licensed Content Title	Passive cervical spine flexion: The effect of age and gender	
Licensed Content Author	Thomas Seacrist, Jami Saffioti, Sriram Balasubramanian, Jennifer Kaelowec, Robert Sterner, J. Felipe Garcia-España, Kristy B. Arbogast, Matthew R. Maltse	
Licensed Content Date	May 1, 2012	
Licensed Content Volume	27	
Licensed Content Issue	4	
Licensed Content Pages	8	
Start Page	326	
https://s100.copyright.com/AppDispatchServlet		
1/8		

12/9/23, 10:31 PM		RightsLink Printable License
End Page	333	
Type of Use	reuse in a thesis/dissertation	
Portion	figures/tables/illustrations	
Number of figures/tables/illustrations	1	
Format	both print and electronic	
Are you the author of this Elsevier article?	No	
Will you be translating?	No	
Title of new work	Assessing the Tissue-Level Response and the Risk of Neck Pain in Rotary-Wing Aircrew using a Finite Element Model of the Neck	
Institution name	University of Waterloo	
Expected presentation date	Mar 2024	
Portions	Fig 2	
Requestor Location	University of Waterloo [REDACTED] Attn: University of Waterloo	
Publisher Tax ID	GB 494 6272 12	
Total	0.00 CAD	
Terms and Conditions		
https://s100.copyright.com/AppDispatchServlet		
2/8		

12/29/23, 7:19 PM RightsLink Printable License

JOHN WILEY AND SONS LICENSE TERMS AND CONDITIONS

Dec 09, 2023

This Agreement between University of Waterloo -- Prasanmabh Hadagali ("You") and John Wiley and Sons ("John Wiley and Sons") consists of your license details and the terms and conditions provided by John Wiley and Sons and Copyright Clearance Center.

License Number	5685030211089
License date	Dec 09, 2023
Licensed Content Publisher	John Wiley and Sons
Licensed Content Publication	Journal of Orthopaedic Research
Licensed Content Title	Assessing the biofidelity of in vitro biomechanical testing of the human cervical spine
Licensed Content Author	Richard A. Wawrose, Forbes E. Howington, Clarissa M. LeVasseur, et al
Licensed Content Date	May 4, 2020
Licensed Content Volume	39
Licensed Content Issue	6
Licensed Content Pages	10
Type of use	Dissertation/Thesis

<https://s100.copyright.com/AppDispatchServlet> 1/6

12/29/23, 7:19 PM RightsLink Printable License

Requestor type	University/Academic
Format	Print and electronic
Portion	Figure/table
Number of figures/tables	1
Will you be translating?	No
Title of new work	Assessing the Tissue-Level Response and the Risk of Neck Pain in Rotary-Wing Aircrew using a Finite Element Model of the Neck
Institution name	University of Waterloo
Expected presentation date	Mar 2024
Portions	Fig. 1
Requestor Location	University of Waterloo [Redacted]
Publisher Tax ID	EU826007151
Total	0.00 CAD
Terms and Conditions	TERMS AND CONDITIONS

<https://s100.copyright.com/AppDispatchServlet> 2/6

RightsLink Printable License	
12/09/23, 10:26 PM	
ELSEVIER LICENSE TERMS AND CONDITIONS	
Dec 09, 2023	
<p>This Agreement between University of Waterloo -- Prasannaah Hadagali ("You") and Elsevier ("Elsevier") consists of your license details and the terms and conditions provided by Elsevier and Copyright Clearance Center.</p>	
License Number	5685100869697
License date	Dec 09, 2023
Licensed Content Publisher	Elsevier
Licensed Content Publication	The Spine Journal
Licensed Content Title	A new cervical artificial disc prosthesis based on physiological curvature of end plate: a finite element analysis
Licensed Content Author	Cheng, Cheng Yu, Peng Liu, Du-Geng Huang, Yong-Hong Jiang, Hang Feng, Ding-Jun Hao
Licensed Content Date	Nov 1, 2016
Licensed Content Volume	16
Licensed Content Issue	11
Licensed Content Pages	8
Start Page	1384
End Page	1391
https://s100.copyright.com/AppDispatchServlet	
1/8	

RightsLink Printable License	
12/09/23, 10:26 PM	
Type of Use	reuse in a thesis/dissertation
Portion	figures/tables/illustrations
Number of figures/tables/illustrations	1
Format	both print and electronic
Are you the author of this Elsevier article?	No
Will you be translating?	No
Title of new work	Assessing the Tissue-Level Response and the Risk of Neck Pain in Rotary-Wing Aircrew using a Finite Element Model of the Neck
Institution name	University of Waterloo
Expected presentation date	Mar 2024
Portions	Fig 2e
Requester Location	University of Waterloo [REDACTED] Attn: University of Waterloo
Publisher Tax ID	GB 494 0272 12
Total	0.00 CAD
Terms and Conditions	INTRODUCTION
https://s100.copyright.com/AppDispatchServlet	
2/8	

12/14/23, 10:12 AM Manage Account

Currency: CAD

Duration of Use: Up to 499
 Lifetime Unit Quantity: Assessing the risk of neck pain in the rotary-wing aircrew using a finite element model of the neck
 Duane Cronin

NEW WORK DETAILS

ADDITIONAL DETAILS

The Requesting Person / Organization to Appear on the License: Prasannaiah Hadgali

REQUESTED CONTENT DETAILS

Title, Description or Numeric Reference of the Portion(s)	Methods, Results, Discussion, Figures and Tables	Title of the Article / Chapter the Portion is From	Enhancing the Biomechanical Response of an Upper Cervical Spine Finite Element Model within the Physiologic Range of Motion and Its Effect On the Full Ligamentous Neck Model Response.
Hadgali, Prasannaiah; Cronin, Duane	146	Hadgali, Prasannaiah; Cronin, Duane	
Volume / Edition	1-11	Author of Portion(s)	Hadgali, Prasannaiah; Cronin, Duane
Page or Page Range of Portion	1-11	Issue, If Republishing an Article From a Serial	2023-01-01
		Publication Date of Portion	2023-01-01

American Society of Mechanical Engineers ASME Special Terms and Conditions

Permission is granted for the specific use of the ASME paper as stated herein and does not permit further use of the materials without proper authorization. As is customary, we request that you ensure proper acknowledgment of the exact sources of this material, the authors, and ASME as original publisher.

Total Items: 1 Subtotal: 0.00 CAD
Order Total: 0.00 CAD

Marketplace Permissions General Terms and Conditions

The following terms and conditions ("General Terms"), together with any applicable Publisher Terms and Conditions, govern User's use of Works pursuant to the Licenses granted by Copyright Clearance Center, Inc. ("CCC") on behalf of the applicable rightsholders of such Works through CCC's applicable Marketplace transactional licensing services (each, a "Service").

1) Definitions. For purposes of these General Terms, the following definitions apply:

- "License" is the licensed use the User obtains via the Marketplace platform in a particular licensing transaction, as set forth in the Order Confirmation.
- "Order Confirmation" is the confirmation CCC provides to the User at the conclusion of each Marketplace transaction. "Order Confirmation" terms are additional terms set forth on specific Order Confirmations not set forth in the General Terms that can include terms applicable to a particular CCC transactional licensing service and/or any rightsholder-specific terms.
- "Rightsholder(s)" are the holders of copyright rights in the Works for which a User obtains licenses via the Marketplace platform, which are displayed on specific Order Confirmations.
- "Terms" means the terms and conditions set forth in these General Terms and any additional Order Confirmation Terms collectively.
- "User" or "you" is the person or entity making the use granted under the relevant License. Where the person accepting the Terms on behalf of a User is a freelancer or other third party who the User authorized to accept the General Terms on the User's behalf, such person shall be deemed jointly a User for purposes of such Terms.
- "Works" are the copyright-protected works described in relevant Order Confirmations.

https://marketplace.copyright.com/ipc/ui/web/manage_account/orders/view-search/1427559

12/14/23, 10:12 AM Manage Account

Billing Status: Open

Payment Information

Prasannaiah Hadgali
 phadgali@waterloo.ca
 Payment method: Invoice

Customer Location:
 Mr. Prasannaiah Hadgali
 University of Waterloo

Order Details

1. Journal of biomechanical engineering

Article: Enhancing the Biomechanical Response of an Upper Cervical Spine Finite Element Model within the Physiologic Range of Motion and Its Effect On the Full Ligamentous Neck Model Response.

Order License ID	Type of Use	Publisher	Portion	0.00 CAD
1427559-1	Completed	AMERICAN SOCIETY OF MECHANICAL ENGINEERS	Chapter/article	0.00 CAD
0148-0731			Republish in a thesis/dissertation	

LICENSED CONTENT

Publication Title	Country	Rightsholder	United States of America
Journal of biomechanical engineering	United States of America	Mechanical Engineers ASME	
Enhancing the Biomechanical Response of an Upper Cervical Spine Finite Element Model within the Physiologic Range of Motion and Its Effect On the Full Ligamentous Neck Model Response.		Journal	
		Volume	146
		Issue	1

REQUEST DETAILS

Author/Editor	Author of requested content	Yes
AMERICAN SOCIETY OF MECHANICAL ENGINEERS.	Author of requested content	Yes
01/01/1977	Minor editing privileges?	No
English	Incidental Promotional Use?	No

Request Details

Chapter/article	Main product
1-11	Worldwide
11	Original language of publication
Print, Electronic	No
Author of requested content	Yes
Minor editing privileges?	No
Incidental Promotional Use?	No

https://marketplace.copyright.com/ipc/ui/web/manage_account/orders/view-search/1427559



Order Number: 1427561
Order Date: 14 Dec 2023

Payment Information

Billing Address:
Prasannaiah Hadagali
phadagali@waterloo.ca
Payment method: Invoice

Customer Location:
Mr. Prasannaiah Hadagali
University of Waterloo

Order Details

1. Journal of biomechanical engineering
Article: Spinal facet joint biomechanics and mechanotransduction in normal, injury and degenerative conditions.

Order License ID: 1427561-1
Order-detail status: Completed
ISSN: 1528-8951
Type of Use: Republish in a thesis/dissertation
Publisher: A S I M E INTERNATIONAL
Portion: Image/photo/illustration
Billing Status: Open

LICENSED CONTENT

Publication Title	Rightsholder
Journal of biomechanical engineering	American Society of Mechanical Engineers/ASME
Article Title: Spinal facet joint biomechanics and mechanotransduction in normal, injury and degenerative conditions.	e-journal
Start Page: 071010	7
Volume: 133	133
URL: http://ajph.sagepub.com/journalPermissions.nav/biomechanical	
Date: 01/01/1977	
Language: English	
Country: United States of America	

REQUEST DETAILS

Portion Type	Distribution
Number of Images / Photos / Illustrations: 1	Worldwide
Format (select all that apply): Print, Electronic Who will Republish the Content?: Academic Institution	Original language of publication
Duration of Use: Life of current edition	Copies for the Disabled? No
Lifetime Unit Quantity: Up to 499	Minor Editing Privileges? No
	Incidental Promotional Use? No
	Currency: CAD

Rights Requested

Main product

Institution Name: University of Waterloo
Expected Presentation Date: 2024-03-01

NEW WORK DETAILS

Title: Assessing the tissue-level response and the risk of neck pain in rotary-wing aircrew using a finite element model of the neck.

ADDITIONAL DETAILS

Instructor Name: Duane Cronin
The Requesting Person / Organization to Appear on the License: Prasannaiah Hadagali

REQUESTED CONTENT DETAILS

Title, Description or Numeric Reference of the Portion(s)	Title of the Article / Chapter the Portion Is From	Author of Portion(s)	Issue, If Republishing an Article From a Serial	Publication Date of Portion
Figure 1	Spinal facet joint biomechanics and mechanotransduction in normal, injury and degenerative conditions.	Jaurnard, Nicolas V; Welch, William C; Winkelstein, Beth	A	2011-07-01
Volume / Edition: 133				
Page or Page Range of Portion: 071010				

American Society of Mechanical Engineers ASME Special Terms and Conditions

Portions of the following ASME materials are included in this license. ONLY for the use of the materials without proper authorization. As is customary, we request that you ensure proper acknowledgment of the exact sources of this material, the authors, and ASME as original publisher.

Total Items: 1

Subtotal: 0.00 CAD
Order Total: 0.00 CAD

Marketplace Permissions General Terms and Conditions

The following terms and conditions ("General Terms"), together with any applicable Publisher Terms and Conditions, govern User's use of Works pursuant to the Licenses granted by Copyright Clearance Center, Inc. ("CCC") on behalf of the applicable Rightsholders of such Works through CCC's applicable Marketplace transactional licensing service (a "Service").

1) Definitions. For purposes of these General Terms, the following definitions apply:

"License" is the licensed use the User obtains via the Marketplace platform in a particular licensing transaction, as set forth in the Order Confirmation.

"Order Confirmation" is the confirmation CCC provides to the User at the conclusion of each Marketplace transaction. "Order Confirmation Terms" are additional terms set forth on specific Order Confirmations not set forth in the General Terms that can include terms applicable to a particular CCC transactional licensing service and/or any Rightsholder-specific terms.

"Rightsholder(s)" are the holder(s) of copyright rights in the Works for which a User obtains licenses via the Marketplace platform, which are displayed on specific Order Confirmations.

"Terms" means the terms and conditions set forth in these General Terms and any additional Order Confirmation Terms collectively.

"User" or "you" is the person or entity making the use granted under the relevant License. Where the person accepting the Terms on behalf of a User is a freelancer or other third party who the User authorized to accept the General Terms on the User's behalf, such person shall be deemed jointly a User for purposes of such Terms.

"Works(s)" are the copyright-protected works described in relevant Order Confirmations.

12/14/23, 10:23 AM RightsLink Printable License

ELSEVIER LICENSE TERMS AND CONDITIONS

Dec 14, 2023

This Agreement between University of Waterloo – Prasannah Hadagali ("You") and Elsevier ("Elsevier") consists of your license details and the terms and conditions provided by Elsevier and Copyright Clearance Center.

License Number 5687670892316

License date Dec 14, 2023

Licensed Content Publisher Elsevier

Licensed Content Publication International Journal of Industrial Ergonomics

Licensed Content Title Neck loads and posture exposure of helicopter pilots during simulated day and night flights

Licensed Content Author Kelsey A. Forde, Wayne J. Albert, Michael F. Harrison, J. Patrick Neary, James Croll, Jack P. Callaghan

Licensed Content Date Mar 1, 2011

Licensed Content Volume 41

Licensed Content Issue 2

Licensed Content Pages 8

Start Page 128

End Page 135

<https://s100.copyright.com/AppDispatchServlet> 1/8

12/14/23, 10:23 AM RightsLink Printable License

Type of Use reuse in a thesis/dissertation

Portion figures/tables/illustrations

Number of figures/tables/illustrations 1

Format both print and electronic

Are you the author of this Elsevier article? No

Will you be translating? No

Title of new work Assessing the Tissue-Level Response and the Risk of Neck Pain in Rotary-Wing Aircraft using a Finite Element Model of the Neck

Institution name University of Waterloo

Expected presentation date Mar 2024

Portions Fig 3

Requestor Location University of Waterloo
[Redacted]

Publisher Tax ID GB 494 6272 12

Total 0.00 CAD

Terms and Conditions

INTRODUCTION

<https://s100.copyright.com/AppDispatchServlet> 2/8

1/10/24, 1:37 PM RightsLink Printable License

Print and electronic

Will this be posted online? Yes, on a secure website

Portion Figures/tables/illustrations

Number of figures/tables/illustrations 1

Author of this Wolters Kluwer article No

Will you be translating? No

Intend to modify/change the content No

Title of new work Assessing the Tissue-Level Response and the Risk of Neck Pain in Rotary-Wing Aircrew using a Finite Element Model of the Neck

Institution name University of Waterloo

Expected presentation date Mar 2024

Portions Figure 1

Requestor Location University of Waterloo

Publisher Tax ID 895524239 RT0001

Total 0.00 CAD

<https://s100.copyright.com/AppDispatchServlet>

2/5

1/10/24, 1:37 PM RightsLink Printable License

WOLTERS KLUWER HEALTH, INC. LICENSE TERMS AND CONDITIONS

Jan 10, 2024

This Agreement between University of Waterloo -- Prasannah Indragali ("You") and Wolters Kluwer Health, Inc. ("Wolters Kluwer Health, Inc.") consists of your license details and the terms and conditions provided by Wolters Kluwer Health, Inc. and Copyright Clearance Center.

License Number 5705461097477

License date Jan 10, 2024

Licensed Content Publisher Wolters Kluwer Health, Inc.

Licensed Content Publication Spine

Licensed Content Title Load-Carrying Capacity of the Human Cervical Spine in Compression Is Increased Under a Follower Load

Licensed Content Author Avinash Patwardhan, Robert Havey, Alexander Ghanayem, et al

Licensed Content Date Jun 15, 2001

Licensed Content Volume 25

Licensed Content Issue 12

Type of Use Dissertation/Thesis

Requestor type University/College

Sponsorship No Sponsorship

<https://s100.copyright.com/AppDispatchServlet>

1/5

1/11/24, 2:02 AM		RightsLink Printable License
<p>ELSEVIER LICENSE TERMS AND CONDITIONS</p> <p>Jan 11, 2024</p> <hr/> <p>This Agreement between University of Waterloo – Prasannaiah Hadzaghi ("You") and Elsevier ("Elsevier") consists of your license details and the terms and conditions provided by Elsevier and Copyright Clearance Center.</p>		
License Number	5705760420490	
License date	Jan 11, 2024	
Licensed Content Publisher	Elsevier	
Licensed Content Publication	Journal of Biomechanics	
Licensed Content Title	An accurate finite element model of the cervical spine under quasi-static loading	
Licensed Content Author	A. Pérez del Palomar,B. Calvo,M. Doblare	
Licensed Content Date	Jan 1, 2008	
Licensed Content Volume	41	
Licensed Content Issue	3	
Licensed Content Pages	9	
Start Page	523	
End Page	531	
<p>https://s100.copyright.com/AppDispatchServlet 1/8</p>		
<p>1/11/24, 2:02 AM</p> <p>RightsLink Printable License</p>		
Type of Use	reuse in a thesis/dissertation	
Portion	figures/tables/illustrations	
Number of figures/tables/illustrations	1	
Format	both print and electronic	
Are you the author of this Elsevier article?	No	
Will you be translating?	No	
Title of new work	Assessing the Tissue-Level Response and the Risk of Neck Pain in Rotary-Wing Aircrew using a Finite Element Model of the Neck	
Institution name	University of Waterloo	
Expected presentation date	Mar 2024	
Portions	Fig 6	
Requestor Location	University of Waterloo [REDACTED] Alder-University of Waterloo	
Publisher Tax ID	GB-494-6272 12	
Total	0.00 CAD	
Terms and Conditions	INTRODUCTION	
<p>https://s100.copyright.com/AppDispatchServlet 2/8</p>		

RightsLink Printable License	
1/11/24, 2:08 AM	
<p>SPRINGER NATURE LICENSE TERMS AND CONDITIONS</p> <p>Jan 11, 2024</p> <hr/> <p>This Agreement between University of Waterloo -- Prasamaah Hadagali ("You") and Springer Nature ("Springer Nature") consists of your license details and the terms and conditions provided by Springer Nature and Copyright Clearance Center.</p>	
License Number	5705760805510
License date	Jan 11, 2024
Licensed Content Publisher	Springer Nature
Licensed Content Publication	Journal of Medical and Biological Engineering
Licensed Content Title	Parameter Study on How the Cervical Disc Degeneration Affects the Segmental Instantaneous Centre of Rotation
Licensed Content Author	Hong Zhang et al
Licensed Content Date	Feb 25, 2023
Type of Use	Thesis/Dissertation
Requestor type	academic/university or research institute
Format	print and electronic
Portion	figures/tables/illustrations
Number of figures/tables/illustrations	1
https://s100.copyright.com/AppDispatchServlet	
1/7	

RightsLink Printable License	
1/11/24, 2:08 AM	
Will you be translating?	no
Circulation/distribution	1 - 29
Author of this Springer Nature content	no
Title of new work	Assessing the Tissue-Level Response and the Risk of Neck Pain in Rotary-Wing Aircraft using a Finite Element Model of the Neck
Institution name	University of Waterloo
Expected presentation date	Mar 2024
Portions	Fig 1
Requestor Location	University of Waterloo [Redacted] Attn: University of Waterloo
Total	0.00 CAD
Terms and Conditions	
<p>Springer Nature Customer Service Centre GmbH Terms and Conditions</p> <p>The following terms and conditions ("Terms and Conditions") together with the terms specified in your [RightsLink] constitute the License ("License") between you as Licensee and Springer Nature Customer Service Centre GmbH as Licensor. By clicking 'accept' and completing the transaction for your use of the material ("Licensed Material"), you confirm your acceptance of and obligation to be bound by these Terms and Conditions.</p> <p>1. Grant and Scope of License</p> <p>1.1. The Licensor grants you a personal, non-exclusive, non-transferable, non-sublicensable, revocable, world-wide License to reproduce, distribute, communicate to the public, make available, broadcast, electronically transmit or create derivative</p>	
https://s100.copyright.com/AppDispatchServlet	
2/7	

Bibliography

- Adam, C., Pearcy, M., McCombe, P., 2003. Stress analysis of interbody fusion--finite element modelling of intervertebral implant and vertebral body. *Clin. Biomech. (Bristol, Avon)* 18, 265–272. [https://doi.org/10.1016/s0268-0033\(03\)00022-6](https://doi.org/10.1016/s0268-0033(03)00022-6)
- Adam, J., 2004. Results of NVG-induced neck strain questionnaire study in CH-146 Griffon aircrew. Toronto.
- Adams, M.A., 2009. Degenerative disc and vertebral disease – basic sciences. *Surg.* 27, 297–300. <https://doi.org/https://doi.org/10.1016/j.mpsur.2009.03.005>
- Adams, M.A., Dolan, P., 2012. Intervertebral disc degeneration: evidence for two distinct phenotypes. *J. Anat.* 221, 497–506. <https://doi.org/10.1111/j.1469-7580.2012.01551.x>
- Akçali, Ö., Satoglu, I.S., Çakiroğlu, M.A., 2020. Chapter 15 - Kinesiology of the cervical vertebral column, in: Angin, S., Şimşek, I.E.B.T.-C.K. of the H.B. (Eds.), . Academic Press, pp. 303–314. <https://doi.org/https://doi.org/10.1016/B978-0-12-812162-7.00015-1>
- Alizadeh, M., Aurand, A., Knapik, G.G., Dufour, J.S., Mendel, E., Bourekas, E., Marras, W.S., 2020a. An electromyography-assisted biomechanical cervical spine model: Model development and validation. *Clin. Biomech. (Bristol, Avon)* 80, 105169. <https://doi.org/10.1016/j.clinbiomech.2020.105169>
- Alizadeh, M., Knapik, G.G., Mageswaran, P., Mendel, E., Bourekas, E., Marras, W.S., 2020b. Biomechanical musculoskeletal models of the cervical spine: A systematic literature review. *Clin. Biomech.* 71, 115–124. <https://doi.org/10.1016/j.clinbiomech.2019.10.027>
- Alkhouli, N., Mansfield, J., Green, E., Bell, J., Knight, B., Liversedge, N., Tham, J.C., Welbourn, R., Shore, A.C., Kos, K., Winlove, C.P., 2013. The mechanical properties of human adipose tissues and their relationships to the structure and composition of the extracellular matrix. *Am. J. Physiol. Metab.* 305, E1427–E1435. <https://doi.org/10.1152/ajpendo.00111.2013>
- Anderst, W., Donaldson, W., Lee, J., Kang, J., 2016. Cervical Spine Disc Deformation During In Vivo Three-Dimensional Head Movements. *Ann. Biomed. Eng.* 44, 1598–1612. <https://doi.org/10.1007/s10439-015-1424-2>
- Anderst, W.J., Donaldson, W.F., Lee, J.Y., Kang, J.D., 2015. Three-dimensional intervertebral

- kinematics in the healthy young adult cervical spine during dynamic functional loading. *J. Biomech.* 48, 1286–1293. <https://doi.org/https://doi.org/10.1016/j.jbiomech.2015.02.049>
- Ang, B., Harms-Ringdahl, K., 2006. Neck pain and related disability in helicopter pilots: A survey of prevalence and risk factors. *Aviat. Space. Environ. Med.* 77, 713–719.
- Äng, B.O., 2008. Impaired neck motor function and pronounced pain-related fear in helicopter pilots with neck pain – A clinical approach. *J. Electromyogr. Kinesiol.* 18, 538–549. <https://doi.org/https://doi.org/10.1016/j.jelekin.2007.01.002>
- Aprill, C., Dwyer, A., Bogduk, N., 1990. Cervical zygapophyseal joint pain patterns. II: A clinical evaluation. *Spine (Phila. Pa. 1976)*. 15, 458–461. <https://doi.org/10.1097/00007632-199006000-00005>
- Ariëns, G.A., Bongers, P.M., Douwes, M., Miedema, M.C., Hoogendoorn, W.E., van der Wal, G., Bouter, L.M., van Mechelen, W., 2001. Are neck flexion, neck rotation, and sitting at work risk factors for neck pain? Results of a prospective cohort study. *Occup. Environ. Med.* 58, 200–207. <https://doi.org/10.1136/oem.58.3.200>
- Arndt, R., 1983. Working posture and musculoskeletal problems of video display terminal operators—review and reappraisal. *Am. Ind. Hyg. Assoc. J.* 44, 437–446. <https://doi.org/10.1080/15298668391405102>
- Arshad, R., Schmidt, H., El-Rich, M., Moglo, K., 2022. Sensitivity of the Cervical Disc Loads, Translations, Intradiscal Pressure, and Muscle Activity Due to Segmental Mass, Disc Stiffness, and Muscle Strength in an Upright Neutral Posture. *Front. Bioeng. Biotechnol.* 10. <https://doi.org/10.3389/fbioe.2022.751291>
- Artenian, D.J., Lipman, J.K., Scidmore, G.K., Brant-Zawadzki, M., 1989. Acute neck pain due to tendonitis of the longus colli: CT and MRI findings. *Neuroradiology* 31, 166–169. <https://doi.org/10.1007/BF00698847>
- Arun, M.W.J., Hadagali, P., Driesslein, K., Curry, W., Yoganandan, N., Pintar, F.A., 2017. Biomechanics of Lumbar Motion-Segments in Dynamic Compression. *Stapp Car Crash J.* 61, 1–25.
- Arun, M.W.J., Hadagali, P., Pintar, F., Yoganandan, N., 2018. Normalized frontal impact biofidelity kinematic corridors using post mortem human surrogates. *J. Mech. Behav. Biomed. Mater.* 79, 251

20–29. <https://doi.org/10.1016/j.jmbbm.2017.12.007>

Arun, M.W.J., Umale, S., Humm, J.R., Yoganandan, N., Hadagali, P., Pintar, F.A., 2016. Evaluation of kinematics and injuries to restrained occupants in far-side crashes using full-scale vehicle and human body models. *Traffic Inj. Prev.* 17, 116–123.

<https://doi.org/10.1080/15389588.2016.1197394>

Aydoğ, S.T., Türbedar, E., Demirel, A.H., Tetik, O., Akin, A., Doral, M.N., 2004. Cervical and lumbar spinal changes diagnosed in four-view radiographs of 732 military pilots. *Aviat. Space. Environ. Med.* 75, 154–157.

Barbe, M.F., Barr, A.E., 2006. Inflammation and the pathophysiology of work-related musculoskeletal disorders. *Brain. Behav. Immun.* 20, 423–429.

<https://doi.org/https://doi.org/10.1016/j.bbi.2006.03.001>

Barker, J., Cronin, D.S., 2022. Muscle Activation Affects Kinematic Response and Injury Risk in Non-Traditional Oblique Impact Scenarios Assessed with a Head and Neck Finite Element Model. *SAE Int. J. Transp. Saf.* 10, 135–162. <https://doi.org/https://doi.org/10.4271/09-10-02-0008>

Barker, J.B., Cronin, D., 2020. Multi-level Validation of a Male Neck Finite Element Model with Active Musculature. *J. Biomech. Eng.* <https://doi.org/10.1115/1.4047866>

Barker, J.B., Cronin, D.S., 2021. Multilevel Validation of a Male Neck Finite Element Model With Active Musculature. *J. Biomech. Eng.* 143. <https://doi.org/10.1115/1.4047866>

Barker, J.B., Cronin, D.S., Chandrashekar, N., 2014. High rotation rate behavior of cervical spine segments in flexion and extension. *J. Biomech. Eng.* 136, 121004.

<https://doi.org/10.1115/1.4028107>

Barker, J.B., Cronin, D.S., Nightingale, R.W., 2017. Lower Cervical Spine Motion Segment Computational Model Validation: Kinematic and Kinetic Response for Quasi-Static and Dynamic Loading. *J. Biomech. Eng.* 139. <https://doi.org/10.1115/1.4036464>

Barnamehei, H., Zhou, Y., Zhang, X., Vasavada, A., 2020. Cervical spine intervertebral kinematics estimated from inverse kinematics and compared to dynamic X-ray data. *Gait Posture* 81, 36–37. <https://doi.org/https://doi.org/10.1016/j.gaitpost.2020.07.041>

- Barr, A.E., Barbe, M.F., 2004. Inflammation reduces physiological tissue tolerance in the development of work-related musculoskeletal disorders. *J. Electromyogr. Kinesiol.* 14, 77–85. <https://doi.org/https://doi.org/10.1016/j.jelekin.2003.09.008>
- Barr, A.E., Barbe, M.F., 2002. Pathophysiological tissue changes associated with repetitive movement: a review of the evidence. *Phys. Ther.* 82, 173–187. <https://doi.org/10.1093/ptj/82.2.173>
- Barrett, J.M., 2022. A Biomechanical-Biochemical Hypothesis for the Role of Collagen in Injury. University of Waterloo.
- Barrett, J.M., 2016. An EMG-Driven Cervical Spine Model for the Investigation of Joint Kinetics: With Application to a Helicopter Pilot Population. University of Waterloo.
- Barrett, J.M., Healey, L.A., Fischer, S.L., Callaghan, J.P., 2022a. Cervical Spine Motion Requirements From Night Vision Goggles May Play a Greater Role in Chronic Neck Pain than Helmet Mass Properties. *Hum. Factors* 00187208221090689. <https://doi.org/10.1177/00187208221090689>
- Barrett, J.M., McKinnon, C., Callaghan, J.P., 2020. Cervical spine joint loading with neck flexion. *Ergonomics* 63, 101–108. <https://doi.org/10.1080/00140139.2019.1677944>
- Barrett, J.M., McKinnon, C.D., Dickerson, C.R., Callaghan, J.P., 2021. An Electromyographically Driven Cervical Spine Model in OpenSim. *J. Appl. Biomech.* 37, 481–493. <https://doi.org/10.1123/jab.2020-0384>
- Barrett, J.M., McKinnon, C.D., Dickerson, C.R., Laing, A.C., Callaghan, J.P., 2022b. Posture and Helmet Configuration Effects on Joint Reaction Loads in the Middle Cervical Spine. *Aerosp. Med. Hum. Perform.* 93, 458–466. <https://doi.org/10.3357/AMHP.5830.2022>
- Barrey, C., Rousseau, M.-A., Persohn, S., Campana, S., Perrin, G., Skalli, W., 2015. Relevance of using a compressive preload in the cervical spine: an experimental and numerical simulating investigation. *Eur. J. Orthop. Surg. Traumatol.* 25 Suppl 1, S155-65. <https://doi.org/10.1007/s00590-015-1625-2>
- Beauséjour, M.-H., Petit, Y., Hagen, J., Arnoux, P.-J., Thiong, J.-M. Mac, Wagnac, E., 2020. Contribution of injured posterior ligamentous complex and intervertebral disc on post-traumatic instability at the cervical spine. *Comput. Methods Biomech. Biomed. Engin.* 23, 832–843.

<https://doi.org/10.1080/10255842.2020.1767776>

- Beauséjour, M.-H., Wagnac, E., Arnoux, P.-J., Thiong, J.-M. Mac, Petit, Y., 2021. Numerical Investigation of Spinal Cord Injury After Flexion-Distractio n Injuries at the Cervical Spine. *J. Biomech. Eng.* 144. <https://doi.org/10.1115/1.4052003>
- Been, E., Shefi, S., Soudack, M., 2017. Cervical lordosis: the effect of age and gender. *Spine J.* 17, 880–888. <https://doi.org/10.1016/j.spinee.2017.02.007>
- Beier, G., Schuller, E., Schuck, M., Ewing, C., Becker, E., Thomas, D.J., 1980. Center of Gravity and Moments of Inertia of Human Heads, in: International Research Council on Biomechanics of Injury. Birmingham, UK, pp. 218–228.
- Berg-Johansen, B., Fields, A.J., Liebenberg, E.C., Li, A., Lotz, J.C., 2018. Structure-function relationships at the human spinal disc-vertebra interface. *J. Orthop. Res. Off. Publ. Orthop. Res. Soc.* 36, 192–201. <https://doi.org/10.1002/jor.23627>
- Beyer, B., Feipel, V., Dugailly, P.-M., 2020. Biomechanics of the upper cervical spine ligaments in axial rotation and flexion-extension: Considerations into the clinical framework. *J. craniovertebral junction spine* 11, 217–225. https://doi.org/10.4103/jcvjs.JCVJS_78_20
- Binch, A.L.A., Fitzgerald, J.C., Growney, E.A., Barry, F., 2021. Cell-based strategies for IVD repair: clinical progress and translational obstacles. *Nat. Rev. Rheumatol.* 17, 158–175. <https://doi.org/10.1038/s41584-020-00568-w>
- Bjur, D., Alfredson, H., Forsgren, S., 2005. The innervation pattern of the human Achilles tendon: studies of the normal and tendinosis tendon with markers for general and sensory innervation. *Cell Tissue Res.* 320, 201–206. <https://doi.org/10.1007/s00441-004-1014-3>
- Boakye-Yiadom, S., Cronin, D.S., 2018. On the importance of retaining stresses and strains in repositioning computational biomechanical models of the cervical spine. *Int. j. numer. method. biomed. eng.* 34. <https://doi.org/10.1002/cnm.2905>
- Boezaart, A.P., Smith, C.R., Chembrovich, S., Zasimovich, Y., Server, A., Morgan, G., Theron, A., Booyen, K., Reina, M.A., 2021. Visceral versus somatic pain: an educational review of anatomy and clinical implications. *Reg. Anesth. Pain Med.* 46, 629–636. <https://doi.org/10.1136/rapm-2020-102084>

- Bogduk, N., 2011. On cervical zygapophysial joint pain after whiplash. *Spine (Phila. Pa. 1976)*. 36, S194-9. <https://doi.org/10.1097/BRS.0b013e3182387f1d>
- Bogduk, N., 2003. The anatomy and pathophysiology of neck pain. *Phys. Med. Rehabil. Clin. N. Am.* 14, 455–472. [https://doi.org/https://doi.org/10.1016/S1047-9651\(03\)00041-X](https://doi.org/https://doi.org/10.1016/S1047-9651(03)00041-X)
- Bogduk, N., 1985. The Innervation of the Vertebral Column. *Aust. J. Physiother.* 31, 89–94. [https://doi.org/https://doi.org/10.1016/S0004-9514\(14\)60626-7](https://doi.org/https://doi.org/10.1016/S0004-9514(14)60626-7)
- Bogduk, N., Mercer, S., 2000. Biomechanics of the cervical spine. I: Normal kinematics. *Clin. Biomech. (Bristol, Avon)* 15, 633–648. [https://doi.org/10.1016/s0268-0033\(00\)00034-6](https://doi.org/10.1016/s0268-0033(00)00034-6)
- BOGDUK, N., WINDSOR, M., INGLIS, A., 1988. The Innervation of the Cervical Intervertebral Discs. *Spine (Phila. Pa. 1976)*. 13.
- Brault, J.R., Siegmund, G.P., Wheeler, J.B., 2000. Cervical muscle response during whiplash: evidence of a lengthening muscle contraction. *Clin. Biomech.* 15, 426–435. [https://doi.org/https://doi.org/10.1016/S0268-0033\(99\)00097-2](https://doi.org/https://doi.org/10.1016/S0268-0033(99)00097-2)
- Briar, K.J., Gregory, D.E., 2023. Combined flexion and compression negatively impact the mechanical integrity of the annulus fibrosus. *Eur. spine J. Off. Publ. Eur. Spine Soc. Eur. Spinal Deform. Soc. Eur. Sect. Cerv. Spine Res. Soc.* 32, 831–838. <https://doi.org/10.1007/s00586-022-07518-y>
- Bridger, R.S., Groom, M.R., Jones, H., Pethybridge, R.J., Pullinger, N., 2002. Task and Postural Factors are Related to Back Pain in Helicopter Pilots. *Aviat. Sp. Environ. Med.* 73, 805–811.
- Brolin, K., Halldin, P., 2004. Development of a finite element model of the upper cervical spine and a parameter study of ligament characteristics. *Spine (Phila. Pa. 1976)*. 29, 376–385. <https://doi.org/10.1097/01.brs.0000090820.99182.2d>
- Brolin, K., Halldin, P., Leijonhufvud, I., 2005. The effect of muscle activation on neck response. *Traffic Inj. Prev.* 6, 67–76. <https://doi.org/10.1080/15389580590903203>
- Brolin, K., Hedenstierna, S., Halldin, P., Bass, C., Alem, N., 2008. The importance of muscle tension on the outcome of impacts with a major vertical component. *Int. J. Crashworthiness* 13, 487–498. <https://doi.org/10.1080/13588260802215510>
- BROWN, T., HANSEN, R.J., YORRA, A.J., 1957. Some Mechanical Tests on the Lumbosacral

- Spine with Particular Reference to the Intervertebral Discs: A Preliminary Report. *JBJS* 39.
- Bruneau, D., 2019. Investigation of Head and Brain Response in Football Helmet Impacts using a Finite Element Model of the Head and Neck with Active Muscle. University of Waterloo.
- Bruneau, D., Cronin, D., 2019. Assessment of Head Kinematics for Bare Head and Helmeted Impacts Comparing an ATD and a Detailed Head and Neck Model with Active Musculature. *J. Biomech. Eng.* <https://doi.org/10.1115/1.4043667>
- Bulger, N., 2019. Medium Helmet with Installed NVG Inertias.
- Butler, B.P., 1992. Helmeted head and neck dynamics under whole-body vibration. University of Michigan.
- Byeon, J.H., Kim, J.W., Jeong, H.J., Sim, Y.J., Kim, D.K., Choi, J.K., Im, H.J., Kim, G.C., 2013. Degenerative changes of spine in helicopter pilots. *Ann. Rehabil. Med.* 37, 706–712. <https://doi.org/10.5535/arm.2013.37.5.706>
- Cai, X.-Y., Sang, D., Yuchi, C.-X., Cui, W., Zhang, C., Du, C.-F., Liu, B., 2020a. Using finite element analysis to determine effects of the motion loading method on facet joint forces after cervical disc degeneration. *Comput. Biol. Med.* 116, 103519. <https://doi.org/10.1016/j.compbimed.2019.103519>
- Cai, X.-Y., YuChi, C.-X., Du, C.-F., Mo, Z.-J., 2020b. The effect of follower load on the range of motion, facet joint force, and intradiscal pressure of the cervical spine: a finite element study. *Med. Biol. Eng. Comput.* 58, 1695–1705. <https://doi.org/10.1007/s11517-020-02189-7>
- Cai, X., Sun, M., Huang, Y., Liu, Z., Liu, C., Du, C., Yang, Q., 2020. Biomechanical Effect of L4–L5 Intervertebral Disc Degeneration on the Lower Lumbar Spine: A Finite Element Study. *Orthop. Surg.* 12, 917–930. <https://doi.org/https://doi.org/10.1111/os.12703>
- Callaghan, J.P., 2014. The Influence of Neck Posture and Helmet Configuration on Neck Muscle Demands. Waterloo, Ontario.
- Callaghan, J.P., McGill, S.M., 2001. Intervertebral disc herniation: studies on a porcine model exposed to highly repetitive flexion/extension motion with compressive force. *Clin. Biomech. (Bristol, Avon)* 16, 28–37. [https://doi.org/10.1016/s0268-0033\(00\)00063-2](https://doi.org/10.1016/s0268-0033(00)00063-2)
- Calvo, B., Ramírez, A., Alonso, A., Grasa, J., Soteras, F., Osta, R., Muñoz, M.J., 2010. Passive

- nonlinear elastic behaviour of skeletal muscle: Experimental results and model formulation. *J. Biomech.* 43, 318–325. <https://doi.org/https://doi.org/10.1016/j.jbiomech.2009.08.032>
- Camacho, D.L., Nightingale, R.W., Robinette, J.J., Vanguri, S.K., Coates, D.J., Myers, B.S., 1997. Experimental Flexibility Measurements for the Development of a Computational Head-Neck Model Validated for Near-Vertex Head Impact. *SAE Trans.* 106, 3989–4002.
- Carr, M.M., Manktelow, R.T., Zuker, R.M., 1995. Gracilis donor site morbidity. *Microsurgery* 16, 598–600. <https://doi.org/https://doi.org/10.1002/micr.1920160904>
- Carragee, E.J., Don, A.S., Hurwitz, E.L., Cuellar, J.M., Carrino, J.A., Herzog, R., 2009. 2009 ISSLS Prize Winner: Does discography cause accelerated progression of degeneration changes in the lumbar disc: a ten-year matched cohort study. *Spine (Phila. Pa. 1976)*. 34, 2338–2345. <https://doi.org/10.1097/BRS.0b013e3181ab5432>
- Cassidy, J.J., Hiltner, A., Baer, E., 1989. Hierarchical structure of the intervertebral disc. *Connect. Tissue Res.* 23, 75–88. <https://doi.org/10.3109/03008208909103905>
- Cazzola, D., Holsgrove, T.P., Preatoni, E., Gill, H.S., Trewartha, G., 2017. Cervical Spine Injuries: A Whole-Body Musculoskeletal Model for the Analysis of Spinal Loading. *PLoS One* 12, e0169329.
- Chafé, G., Farrell, P., 2016. Royal Canadian Air Force CH-146 Griffon aircrew 2014 spinal musculoskeletal trouble survey. Toronto.
- Chang, L., Wang, H., Guo, Y., Cai, Z., Zhan, H., 2022. Experimental and numerical analysis of biomechanical effects in cervical spine positioning rotation manipulation. *Int. j. numer. method. biomed. eng.* 38, e3651. <https://doi.org/https://doi.org/10.1002/cnm.3651>
- Cheng, C.-H., Cheng, H.-Y.K., Chen, C.P.-C., Lin, K.-H., Liu, W.-Y., Wang, S.-F., Hsu, W.-L., Chuang, Y.-F., 2014. Altered Co-contraction of Cervical Muscles in Young Adults with Chronic Neck Pain during Voluntary Neck Motions. *J. Phys. Ther. Sci.* 26, 587–590. <https://doi.org/10.1589/jpts.26.587>
- Cheng, C.-H., Chien, A., Hsu, W.-L., Chen, C.P.-C., Cheng, H.-Y.K., 2016. Investigation of the Differential Contributions of Superficial and Deep Muscles on Cervical Spinal Loads with Changing Head Postures. *PLoS One* 11, e0150608.

- Cheng, C.-H., Chiu, P.-Y., Chen, H.-B., Niu, C.-C., Nikkhoo, M., 2023. The influence of over-distraction on biomechanical response of cervical spine post anterior interbody fusion: a comprehensive finite element study. *Front. Bioeng. Biotechnol.* 11, 1217274.
<https://doi.org/10.3389/fbioe.2023.1217274>
- Cheng, C.-H., Lin, K.-H., Wang, J.-L., 2008. Co-contraction of cervical muscles during sagittal and coronal neck motions at different movement speeds. *Eur. J. Appl. Physiol.* 103, 647–654.
<https://doi.org/10.1007/s00421-008-0760-4>
- Christensen, S.W., Hirata, R.P., Graven-Nielsen, T., 2017. Altered pain sensitivity and axioscapular muscle activity in neck pain patients compared with healthy controls. *Eur. J. Pain* 21, 1763–1771. <https://doi.org/10.1002/ejp.1088>
- Christiansen, S., Cohen, S.P., 2018. Chronic Pain: Pathophysiology and Mechanisms BT - Essentials of Interventional Techniques in Managing Chronic Pain, in: Manchikanti, L., Kaye, A.D., Falco, F.J.E., Hirsch, J.A. (Eds.), . Springer International Publishing, Cham, pp. 15–25.
https://doi.org/10.1007/978-3-319-60361-2_2
- CLOWARD, R.B., 1960. The clinical significance of the sinu-vertebral nerve of the cervical spine in relation to the cervical disk syndrome. *J. Neurol. Neurosurg. Psychiatry* 23, 321–326.
<https://doi.org/10.1136/jnnp.23.4.321>
- Corrales, M.A., Cronin, D.S., 2021a. Sex, Age and Stature Affects Neck Biomechanical Responses in Frontal and Rear Impacts Assessed Using Finite Element Head and Neck Models. *Front. Bioeng. Biotechnol.* 9, 857. <https://doi.org/10.3389/fbioe.2021.681134>
- Corrales, M.A., Cronin, D.S., 2021b. Importance of the cervical capsular joint cartilage geometry on head and facet joint kinematics assessed in a Finite element neck model. *J. Biomech.* 123, 110528. <https://doi.org/https://doi.org/10.1016/j.jbiomech.2021.110528>
- Correia, M.A., Corrales, M.A., McLachlin, S.D., Cronin, D.S., 2023. Effect of muscle pre-tension and pre-impact neck posture on the kinematic response of the cervical spine in simulated low-speed rear impacts. *Int. j. numer. method. biomed. eng.* n/a, e3761.
<https://doi.org/https://doi.org/10.1002/cnm.3761>
- Correia, M.A., McLachlin, S.D., Cronin, D.S., 2021. Vestibulocollic and Cervicocollic Muscle Reflexes in a Finite Element Neck Model During Multidirectional Impacts. *Ann. Biomed. Eng.*

49, 1645–1656. <https://doi.org/10.1007/s10439-021-02783-2>

Correia, M.A., McLachlin, S.D., Cronin, D.S., 2020. Optimization of muscle activation schemes in a finite element neck model simulating volunteer frontal impact scenarios. *J. Biomech.* 104, 109754. <https://doi.org/10.1016/j.jbiomech.2020.109754>

Costigan, M., Scholz, J., Woolf, C.J., 2009. Neuropathic pain: a maladaptive response of the nervous system to damage. *Annu. Rev. Neurosci.* 32, 1–32. <https://doi.org/10.1146/annurev.neuro.051508.135531>

Cramer, G.D., 2014. Chapter 5 - The Cervical Region, in: Cramer, G.D., Darby Spinal Cord, and Ans (Third Edition), S.A.B.T.-C.A. of the S. (Eds.), . Mosby, Saint Louis, pp. 135–209. <https://doi.org/10.1016/B978-0-323-07954-9.00005-0>

Cronin, D.S., 2014. Finite element modeling of potential cervical spine pain sources in neutral position low speed rear impact. *J. Mech. Behav. Biomed. Mater.* 33, 55–66. <https://doi.org/10.1016/j.jmbbm.2013.01.006>

Cronin, D.S., Fice, J.B., Dewit, J.A., Moulton, J., 2012. Upper cervical spine kinematic response and injury prediction, in: 2012 IRCOBI Conference Proceedings - International Research Council on the Biomechanics of Injury. pp. 225–234.

Cronin, D.S., Singh, D., Gierczycka, D., Barker, J., Shen, D., 2018. Chapter 13 - Modeling the Neck for Impact Scenarios, in: Yang, K.-H.B.T.-B.F.E.M. as A. to I.B. (Ed.), . Academic Press, pp. 503–538. <https://doi.org/10.1016/B978-0-12-809831-8.00013-1>

Cross, S.A., 1994. Pathophysiology of Pain. *Mayo Clin. Proc.* 69, 375–383. [https://doi.org/10.1016/S0025-6196\(12\)62225-3](https://doi.org/10.1016/S0025-6196(12)62225-3)

Cusick, J.F., Yoganandan, N., 2002. Biomechanics of the cervical spine 4: major injuries. *Clin. Biomech. (Bristol, Avon)* 17, 1–20. [https://doi.org/10.1016/s0268-0033\(01\)00101-2](https://doi.org/10.1016/s0268-0033(01)00101-2)

Davis, J., Kaufman, K.R., Lieber, R.L., 2003. Correlation between active and passive isometric force and intramuscular pressure in the isolated rabbit tibialis anterior muscle. *J. Biomech.* 36, 505–512. [https://doi.org/10.1016/s0021-9290\(02\)00430-x](https://doi.org/10.1016/s0021-9290(02)00430-x)

de Bruijn, E., van der Helm, F.C.T., Happee, R., 2016. Analysis of isometric cervical strength with a nonlinear musculoskeletal model with 48 degrees of freedom. *Multibody Syst. Dyn.* 36, 339–

362. <https://doi.org/10.1007/s11044-015-9461-z>

De Loose, V., Van den Oord, M., Burnotte, F., Van Tiggelen, D., Stevens, V., Cagnie, B., Danneels, L., Witvrouw, E., 2009. Functional assessment of the cervical spine in F-16 pilots with and without neck pain. *Aviat. Space. Environ. Med.* 80, 477–481.
<https://doi.org/10.3357/asem.2408.2009>

del Palomar, A.P., Calvo, B., Doblare, M., 2008. An accurate finite element model of the cervical spine under quasi-static loading. *J. Biomech.* 41, 523–531.
<https://doi.org/https://doi.org/10.1016/j.jbiomech.2007.10.012>

Derouin, A.J., 2020. THE DEVELOPMENT AND VALIDATION OF A THREE-DIMENSIONAL VISUAL TARGET ACQUISITION SYSTEM TO ASSESS THE PERFORMANCE EFFECTS OF HEAD SUPPORTED MASS. Queen's Univesity.

Desmoulin, G.T., Pradhan, V., Milner, T.E., 2020. Mechanical Aspects of Intervertebral Disc Injury and Implications on Biomechanics. *Spine (Phila. Pa. 1976)*. 45.

DeWit, J.A., Cronin, D.S., 2012. Cervical spine segment finite element model for traumatic injury prediction. *J. Mech. Behav. Biomed. Mater.* 10, 138–150.
<https://doi.org/10.1016/j.jmbbm.2012.02.015>

Diao, H., Xin, H., Dong, J., He, X., Li, D., Jin, Z., 2017. Prediction of Cervical Spinal Joint Loading and Secondary Motion Using a Musculoskeletal Multibody Dynamics Model Via Force-Dependent Kinematics Approach. *Spine (Phila. Pa. 1976)*. 42.

Diao, H., Xin, H., Jin, Z., 2018. Prediction of in vivo lower cervical spinal loading using musculoskeletal multi-body dynamics model during the head flexion/extension, lateral bending and axial rotation. *Proc. Inst. Mech. Eng. Part H J. Eng. Med.* 232, 1071–1082.
<https://doi.org/10.1177/0954411918799630>

Dibb, A.T., Cox, C.A., Nightingale, R.W., Luck, J.F., Cutcliffe, H.C., Myers, B.S., Arbogast, K.B., Seacrist, T., Bass, C.R., 2013. Importance of muscle activations for biofidelic pediatric neck response in computational models. *Traffic Inj. Prev.* 14 Suppl, S116-27.
<https://doi.org/10.1080/15389588.2013.806795>

Dibb, A.T., Cutcliffe, H.C., Luck, J.F., Cox, C.A., Myers, B.S., Bass, C.R., Arbogast, K.B., Seacrist, T., Nightingale, R.W., 2014. Pediatric head and neck dynamics in frontal impact: analysis of
260

- important mechanical factors and proposed neck performance corridors for 6- and 10-year-old ATDs. *Traffic Inj. Prev.* 15, 386–394. <https://doi.org/10.1080/15389588.2013.824568>
- Dong, L., Winkelstein, B.A., 2010. Simulated whiplash modulates expression of the glutamatergic system in the spinal cord suggesting spinal plasticity is associated with painful dynamic cervical facet loading. *J. Neurotrauma* 27, 163–174. <https://doi.org/10.1089/neu.2009.0999>
- Dowdell, J., Erwin, M., Choma, T., Vaccaro, A., Iatridis, J., Cho, S.K., 2017. Intervertebral Disk Degeneration and Repair. *Neurosurgery* 80, S46–S54. <https://doi.org/10.1093/neuros/nyw078>
- Dureja, G., Iyer, R., Das, G., Ahdal, J., Narang, P., 2017. Evidence and consensus recommendations for the pharmacological management of pain in India. *J. Pain Res.* Volume 10, 709–736. <https://doi.org/10.2147/JPR.S128655>
- Dvorak, J., Panjabi, M., Novotny, J.E., Antinnes, J.A., 1991. In vivo flexion/extension of the normal cervical spine. *J. Orthop. Res.* 9, 828–834. <https://doi.org/10.1002/jor.1100090608>
- Dwyer, A., Aprill, C., Bogduk, N., 1990. Cervical zygapophyseal joint pain patterns. I: A study in normal volunteers. *Spine (Phila. Pa. 1976)*. 15, 453–457. <https://doi.org/10.1097/00007632-199006000-00004>
- Ebara, S., Iatridis, J.C., Setton, L.A., Foster, R.J., Mow, V.C., Weidenbaum, M., 1996. Tensile Properties of Nondegenerate Human Lumbar Anulus Fibrosus. *Spine (Phila. Pa. 1976)*. 21.
- Edgar, M.A., 2007. The nerve supply of the lumbar intervertebral disc. *J. Bone Joint Surg. Br.* 89-B.
- Egloff, C., Hügler, T., Valderrabano, V., 2012. Biomechanics and pathomechanisms of osteoarthritis. *Swiss Med. Wkly.* 142, w13583. <https://doi.org/10.4414/smw.2012.13583>
- Erbulut, D.U., Zafarparandeh, I., Lazoglu, I., Ozer, A.F., 2014. Application of an asymmetric finite element model of the C2-T1 cervical spine for evaluating the role of soft tissues in stability. *Med. Eng. Phys.* 36, 915–921. <https://doi.org/https://doi.org/10.1016/j.medengphy.2014.02.020>
- Eriksen, W., 2004. Linking work factors to neck myalgia: the nitric oxide/oxygen ratio hypothesis. *Med. Hypotheses* 62, 721–726. <https://doi.org/https://doi.org/10.1016/j.mehy.2003.12.015>
- Esrafilian, A., Stenroth, L., Mononen, M.E., Tanska, P., Avela, J., Korhonen, R.K., 2020. EMG-Assisted Muscle Force Driven Finite Element Model of the Knee Joint with Fibril-Reinforced Poroelastic Cartilages and Menisci. *Sci. Rep.* 10, 3026. <https://doi.org/10.1038/s41598-020->

- Faber, H., van Soest, A.J., Kistemaker, D.A., 2018. Inverse dynamics of mechanical multibody systems: An improved algorithm that ensures consistency between kinematics and external forces. *PLoS One* 13, e0204575.
- Falla, D., Bilenkij, G., Jull, G., 2004. Patients With Chronic Neck Pain Demonstrate Altered Patterns of Muscle Activation During Performance of a Functional Upper Limb Task. *Spine (Phila. Pa. 1976)*. 29.
- Farrell, P.S.E., Maceda, E., Niri, A., 2018. Correlating Helmet System Mass Properties with Pain Levels towards Helicopter Aircrew Neck-trouble Mitigating Solutions. *Proc. Hum. Factors Ergon. Soc. Annu. Meet.* 62, 67–70. <https://doi.org/10.1177/1541931218621015>
- Farrell, P.S.E., Shender, B.S., Goff, C.P., Baudou, J., Crowley, J., Davies, M., Day, S.E., Di Muzio, V., Dodson, W.W., Duvigneaud, N., Feberg, S., Fleischer, H., Jocelyn, K., Lopes, M., Van den Oord, M.H.A.H., Shivers, B.L., Sovelius, R., Slungaard, E., Smith, A., Smith, E., Werne, T., Wong, T., Beatty, H.W., 2020. NATO STO Technical Report (HFM-252): Aircrew Neck Pain Prevention and Management.
- Farrell, P.S.E., Tack, D.W., Nakaza, E.T., Bray-Miners, J., Farrell, C.M., 2014. Combined Task and Physical Demands Analyses towards a Comprehensive Human Work Model. *Proc. Hum. Factors Ergon. Soc. Annu. Meet.* 58, 939–943. <https://doi.org/10.1177/1541931214581197>
- Fathollahi, H., 2012. MULTI-BODY DYNAMIC ANALYSIS OF CERVICAL SPINE FOR HELICOPTER PILOTS. Ryerson University.
- Feller, L., Kleinbach, C., Fehr, J., Schmitt, S., 2016. Incorporating Muscle Activation Dynamics into the Global Human Body Model, in: *International Research Council on Biomechanics of Injury*. pp. 512–523.
- Feng, Z., Liu, Y., Yang, G., Battié, M.C., Wang, Y., 2018. Lumbar Vertebral Endplate Defects on Magnetic Resonance Images: Classification, Distribution Patterns, and Associations with Modic Changes and Disc Degeneration. *Spine (Phila. Pa. 1976)*. 43.
- Fice, J.B., Cronin, D.S., 2012. Investigation of whiplash injuries in the upper cervical spine using a detailed neck model. *J. Biomech.* 45, 1098–1102. <https://doi.org/10.1016/j.jbiomech.2012.01.016>

- Fice, J.B., Cronin, D.S., Panzer, M.B., 2011. Cervical spine model to predict capsular ligament response in rear impact. *Ann. Biomed. Eng.* 39, 2152–2162. <https://doi.org/10.1007/s10439-011-0315-4>
- Fiebert, I., Kistner, F., Gissendanner, C., DaSilva, C., 2021. Text neck: An adverse postural phenomenon. *Work* 69, 1261–1270. <https://doi.org/10.3233/WOR-213547>
- Fields, A.J., Ballatori, A., Liebenberg, E.C., Lotz, J.C., 2018. Contribution of the endplates to disc degeneration. *Curr. Mol. Biol. reports* 4, 151–160. <https://doi.org/10.1007/s40610-018-0105-y>
- Fields, A.J., Liebenberg, E.C., Lotz, J.C., 2014. Innervation of pathologies in the lumbar vertebral end plate and intervertebral disc. *Spine J.* 14, 513–521. <https://doi.org/10.1016/j.spinee.2013.06.075>
- Fischer, S., Stevenson, J., Reid, S., Hetzler, M., 2014. Spring-Based Helmet System Support Prototype to Address Aircrew Neck Strain. Kingston, Ontario.
- Forde, K.A., Albert, W.J., Harrison, M.F., Patrick Neary, J., Croll, J., Callaghan, J.P., 2011. Neck loads and posture exposure of helicopter pilots during simulated day and night flights. *Int. J. Ind. Ergon.* 41, 128–135. <https://doi.org/https://doi.org/10.1016/j.ergon.2011.01.001>
- Frank, C., Amiel, D., Woo, S.L.-Y., Akeson, W., 1985. Normal Ligament Properties and Ligament Healing. *Clin. Orthop. Relat. Res.* 196.
- Fraser, W.D., Crowley, J., Shender, B.S., Lee, V.M., 2015. Multinational survey of neck pain in rotor-wing aircrew.
- Frick, H., Kummer, B., R, P., 1990. Wolf-Heidegger's Atlas of Human Anatomy, 4th ed.
- Fujita, Y., Duncan, N.A., Lotz, J.C., 1997. Radial tensile properties of the lumbar annulus fibrosus are site and degeneration dependent. *J. Orthop. Res. Off. Publ. Orthop. Res. Soc.* 15, 814–819. <https://doi.org/10.1002/jor.1100150605>
- Fukui, S., Ohseto, K., Shiotani, M., Ohno, K., Karasawa, H., Naganuma, Y., Yuda, Y., 1996. Referred pain distribution of the cervical zygapophyseal joints and cervical dorsal rami. *Pain* 68, 79–83. [https://doi.org/https://doi.org/10.1016/S0304-3959\(96\)03173-9](https://doi.org/https://doi.org/10.1016/S0304-3959(96)03173-9)
- García-Cosamalón, J., del Valle, M.E., Calavia, M.G., García-Suárez, O., López-Muñiz, A., Otero, J., Vega, J.A., 2010. Intervertebral disc, sensory nerves and neurotrophins: who is who in discogenic pain? *J. Anat.* 217, 1–15. <https://doi.org/10.1111/j.1469-7580.2010.01227.x>

- Gąsior-Głogowska, M., Komorowska, M., Hanuza, J., Mączka, M., Zając, A., Ptak, M., Będziński, R., Kobielarz, M., Maksymowicz, K., Kuroпка, P., Szotek, S., 2013. FT-Raman spectroscopic study of human skin subjected to uniaxial stress. *J. Mech. Behav. Biomed. Mater.* 18, 240–252. <https://doi.org/https://doi.org/10.1016/j.jmbbm.2012.11.023>
- Gayzik, F.S., Moreno, D.P., Geer, C.P., Wuertz, S.D., Martin, R.S., Stitzel, J.D., 2011. Development of a full body CAD dataset for computational modeling: a multi-modality approach. *Ann. Biomed. Eng.* 39, 2568–2583. <https://doi.org/10.1007/s10439-011-0359-5>
- Gierczycka, D., Cronin, D., 2021. Importance of impact boundary conditions and pre-crash arm position for the prediction of thoracic response to pendulum, side sled, and near side vehicle impacts. *Comput. Methods Biomech. Biomed. Engin.* 24, 1531–1544. <https://doi.org/10.1080/10255842.2021.1900132>
- Gierczycka, D., Cronin, D.S., 2017. Occupant thorax response variations due to arm position and restraint systems in side impact crash scenarios. *Accid. Anal. Prev.* 106, 173–180. <https://doi.org/10.1016/j.aap.2017.05.017>
- Gierczycka, D., Rycman, A., Cronin, D., 2021. Importance of passive muscle, skin, and adipose tissue mechanical properties on head and neck response in rear impacts assessed with a finite element model. *Traffic Inj. Prev.* 22, 407–412. <https://doi.org/10.1080/15389588.2021.1918685>
- Gooyers, C.E., Callaghan, J.P., 2015. Exploring interactions between force, repetition and posture on intervertebral disc height loss and bulging in isolated porcine cervical functional spinal units from sub-acute-failure magnitudes of cyclic compressive loading. *J. Biomech.* 48, 3701–3708. <https://doi.org/https://doi.org/10.1016/j.jbiomech.2015.08.023>
- Gooyers, C.E., McMillan, E.M., Noguchi, M., Quadrilatero, J., Callaghan, J.P., 2015. Characterizing the combined effects of force, repetition and posture on injury pathways and micro-structural damage in isolated functional spinal units from sub-acute-failure magnitudes of cyclic compressive loading. *Clin. Biomech.* 30, 953–959. <https://doi.org/https://doi.org/10.1016/j.clinbiomech.2015.07.003>
- Gray, H., 1918. *Anatomy of the Human Body*. Lea & Febiger, Philadelphia.
- Gruber, H., Hanley, E., 2002. Observations on morphologic changes in the aging and degenerating human disc: Secondary collagen alterations. *BMC Musculoskelet. Disord.* 3, 9.

<https://doi.org/10.1186/1471-2474-3-9>

- Guan, X., Fan, G., Wu, X., Zeng, Y., Su, H., Gu, G., Zhou, Q., Gu, X., Zhang, H., He, S., 2015. Photographic measurement of head and cervical posture when viewing mobile phone: a pilot study. *Eur. spine J. Off. Publ. Eur. Spine Soc. Eur. Spinal Deform. Soc. Eur. Sect. Cerv. Spine Res. Soc.* 24, 2892–2898. <https://doi.org/10.1007/s00586-015-4143-3>
- Guilak, F., 2011. Biomechanical factors in osteoarthritis. *Best Pract. Res. Clin. Rheumatol.* 25, 815–823. <https://doi.org/10.1016/j.berh.2011.11.013>
- Guo, R., Zhou, C., Wang, C., Tsai, T.-Y., Yu, Y., Wang, W., Li, G., Cha, T., 2021. In vivo primary and coupled segmental motions of the healthy female head-neck complex during dynamic head axial rotation. *J. Biomech.* 123, 110513. <https://doi.org/https://doi.org/10.1016/j.jbiomech.2021.110513>
- Hadagali, P., 2014. Subject-specific finite element modeling of the adolescent thoracic spine for scoliosis research. Drexel University.
- Hadagali, P., Cronin, D.S., 2023. Enhancing the Biofidelity of an Upper Cervical Spine Finite Element Model Within the Physiologic Range of Motion and Its Effect on the Full Ligamentous Neck Model Response. *J. Biomech. Eng.* 145. <https://doi.org/10.1115/1.4055037>
- Hadagali, P., Cronin, D.S., 2020. Quantification of Upper Cervical Spine Motion Sensitivity to Ligament Laxity Using a Finite Element Human Body Model for Occupant Safety, in: *International Research Council on Biomechanics of Injury*. Berlin, Germany, pp. 229–230.
- Hadagali, P., Fischer, S.L., Callaghan, J.P., Cronin, D.S., 2024. Quantifying the Importance of Active Muscle Repositioning a Finite Element Neck Model in Flexion Using Kinematic, Kinetic, and Tissue-Level Responses. *Ann. Biomed. Eng.* 52, 510–525. <https://doi.org/10.1007/s10439-023-03396-7>
- Hadagali, P., Peters, J.R., Balasubramanian, S., 2018. Morphing the feature-based multi-blocks of normative/healthy vertebral geometries to scoliosis vertebral geometries: development of personalized finite element models. *Comput. Methods Biomech. Biomed. Engin.* 21, 297–324. <https://doi.org/10.1080/10255842.2018.1448391>
- Hägg, G.M., 2000. Human muscle fibre abnormalities related to occupational load. *Eur. J. Appl. Physiol.* 83, 159–165. <https://doi.org/10.1007/s004210000274>

- Halldin, P.H., Brolin, K., Kleiven, S., von Holst, H., Jakobsson, L., Palmertz, C., 2000. Investigation of Conditions that Affect Neck Compression- Flexion Injuries Using Numerical Techniques. *Stapp Car Crash J.* 44, 127–138.
- Hallquist, J.O., 2017. *LS-DYNA Keyword User's Manual*, Vol.2.
- Han, H., Gwon, S., Kim, M., Shin, G., 2018. Head tilt angle when using smartphone while walking. *Proc. Hum. Factors Ergon. Soc. Annu. Meet.* 62, 956–959.
<https://doi.org/10.1177/1541931218621220>
- Harniman, E., Carette, S., Kennedy, C., Beaton, D., 2004. Extracorporeal shock wave therapy for calcific and noncalcific tendonitis of the rotator cuff: a systematic review. *J. Hand Ther.* 17, 132–151. <https://doi.org/https://doi.org/10.1197/j.jht.2004.02.003>
- Harrison, M.F., Coffey, B., Albert, W.J., Fischer, S.L., 2015. Night Vision Goggle-Induced Neck Pain in Military Helicopter Aircrew: A Literature Review. *Aerosp. Med. Hum. Perform.* 86, 46–55.
- Harrison, M.F., Neary, J.P., Albert, W.J., Croll, J.C., 2011. Neck pain and muscle function in a population of CH-146 helicopter aircrew. *Aviat. Space. Environ. Med.* 82, 1125–1130.
<https://doi.org/10.3357/asem.2309.2011>
- Harrison, M.F., Neary, J.P., Albert, W.J., Kuruganti, U., Croll, J.C., Chancey, V.C., Bumgardner, B.A., 2009. Measuring neuromuscular fatigue in cervical spinal musculature of military helicopter aircrew. *Mil. Med.* 174, 1183–1189. <https://doi.org/10.7205/milmed-d-00-7409>
- Harrison, M.F., Neary, J.P., Albert, W.J., Veillette, D.W., McKenzie, N.P., Croll, J.C., 2007. Physiological Effects of Night Vision Goggle Counterweights on Neck Musculature of Military Helicopter Pilots. *Mil. Med.* 172, 864–870. <https://doi.org/10.7205/MILMED.172.8.864>
- Hayes, A.R., Vavalle, N.A., Moreno, D.P., Stitzel, J.D., Gayzik, F.S., 2014. Validation of simulated chestband data in frontal and lateral loading using a human body finite element model. *Traffic Inj. Prev.* 15, 181–186. <https://doi.org/10.1080/15389588.2013.799278>
- Healey, L.A., 2019. The effects of operationally relevant head supported mass on neck muscle activity during a rapid scanning task. University of Waterloo.
- Healey, L.A., Derouin, A.J., Callaghan, J.P., Cronin, D.S., Fischer, S.L., 2021. Night Vision Goggle

- and Counterweight Use Affect Neck Muscle Activity During Reciprocal Scanning. *Aerosp. Med. Hum. Perform.* 92, 172–181. <https://doi.org/10.3357/AMHP.5673.2021>
- Hedenstierna, S., Halldin, P., Brodin, K., 2008. Evaluation of a combination of continuum and truss finite elements in a model of passive and active muscle tissue. *Comput. Methods Biomech. Biomed. Engin.* 11, 627–639. <https://doi.org/10.1080/17474230802312516>
- Hee, H.T., Chuah, Y.J., Tan, B.H.M., Setiobudi, T., Wong, H.K., 2011. Vascularization and Morphological Changes of the Endplate After Axial Compression and Distraction of the Intervertebral Disc. *Spine (Phila. Pa. 1976)*. 36.
- Heller, J.G., Pedlow Jr., F.X., Gill, S.S., 2005. Anatomy of the Cervical Spine, in: *The Cervical Spine*. pp. 3–12.
- Herron, M.R., Park, J., Dailey, A.T., Brockmeyer, D.L., Ellis, B.J., 2020. Febio finite element models of the human cervical spine. *J. Biomech.* 113, 110077. <https://doi.org/https://doi.org/10.1016/j.jbiomech.2020.110077>
- Hetzler, M., 2021. DYNAMIC MODELLING FOR THE DESIGN OF HEAD-NECK LOAD CARRIAGE SYSTEMS. Queen’s University.
- Hill, R., 1979. Aspects of Invariance in Solid Mechanics, in: Yih, C.-S.B.T.-A. in A.M. (Ed.), . Elsevier, pp. 1–75. [https://doi.org/https://doi.org/10.1016/S0065-2156\(08\)70264-3](https://doi.org/https://doi.org/10.1016/S0065-2156(08)70264-3)
- Holzappel, G.A., Schulze-Bauer, C.A.J., Feigl, G., Regitnig, P., 2005. Single lamellar mechanics of the human lumbar anulus fibrosus. *Biomech. Model. Mechanobiol.* 3, 125–140. <https://doi.org/10.1007/s10237-004-0053-8>
- Iatridis, J.C., McClean, J.J., Ryan, D.A., 2005. Mechanical damage to the intervertebral disc annulus fibrosus subjected to tensile loading. *J. Biomech.* 38, 557–565. <https://doi.org/10.1016/j.jbiomech.2004.03.038>
- Iatridis, J.C., Setton, L.A., Foster, R.J., Rawlins, B.A., Weidenbaum, M., Mow, V.C., 1998. Degeneration affects the anisotropic and nonlinear behaviors of human anulus fibrosus in compression. *J. Biomech.* 31, 535–544. [https://doi.org/10.1016/s0021-9290\(98\)00046-3](https://doi.org/10.1016/s0021-9290(98)00046-3)
- Inami, S., Shiga, T., Tsujino, A., Yabuki, T., Okado, N., Ochiai, N., 2001. Immunohistochemical demonstration of nerve fibers in the synovial fold of the human cervical facet joint. *J. Orthop.*

Res. Off. Publ. Orthop. Res. Soc. 19, 593–596. [https://doi.org/10.1016/S0736-0266\(00\)00048-6](https://doi.org/10.1016/S0736-0266(00)00048-6)

Inoue, N., Espinoza Orías, A.A., 2011. Biomechanics of intervertebral disk degeneration. *Orthop. Clin. North Am.* 42, 487–vii. <https://doi.org/10.1016/j.ocl.2011.07.001>

Isaacs, J., 2012. *Micromechanics of the Annulus Fibrosus: Role of Biomolecules in Mechanical Function*. Drexel University.

Ito, K., Creemers, L., 2013. Mechanisms of Intervertebral Disk Degeneration/Injury and Pain: A Review. *Glob. Spine J.* 3, 145–151. <https://doi.org/10.1055/s-0033-1347300>

Ito, S., Ivancic, P.C., Pearson, A.M., Tominaga, Y., Gimenez, S.E., Rubin, W., Panjabi, M., 2005. Cervical intervertebral disc injury during simulated frontal impact. *Eur. Spine J.* 14, 356–365. <https://doi.org/10.1007/s00586-004-0783-4>

Ivancic, P.C., 2013. Effects of orthoses on three-dimensional load-displacement properties of the cervical spine. *Eur. spine J. Off. Publ. Eur. Spine Soc. Eur. Spinal Deform. Soc. Eur. Sect. Cerv. Spine Res. Soc.* 22, 169–177. <https://doi.org/10.1007/s00586-012-2552-0>

Jackson, A.R., Huang, C.-Y., Gu, W.Y., 2011. Effect of endplate calcification and mechanical deformation on the distribution of glucose in intervertebral disc: a 3D finite element study. *Comput. Methods Biomech. Biomed. Engin.* 14, 195–204. <https://doi.org/10.1080/10255842.2010.535815>

Janak, T., Lafon, Y., Petit, P., Beillas, P., 2018. Transformation Smoothing to use after Positioning of Finite Element Human Body Models, in: *International Research Council on Biomechanics of Injury*. pp. 18–33.

Jani, D., Chawla, A., Mukherjee, S., Goyal, R., Vusirikala, N., Jayaraman, S., 2012. Repositioning the knee joint in human body FE models using a graphics-based technique. *Traffic Inj. Prev.* 13, 640–649. <https://doi.org/10.1080/15389588.2012.664669>

Jaumard, N. V, Welch, W.C., Winkelstein, B.A., 2011. Spinal facet joint biomechanics and mechanotransduction in normal, injury and degenerative conditions. *J. Biomech. Eng.* 133, 71010. <https://doi.org/10.1115/1.4004493>

Jia, H., Xu, B., Qi, X., 2022. Biomechanical evaluation of percutaneous cement discoplasty by finite

element analysis. *BMC Musculoskelet. Disord.* 23, 594. <https://doi.org/10.1186/s12891-022-05508-1>

John, J., Klug, C., Kranjec, M., Svenning, E., Iraeus, J., 2022. Hello, world! VIVA+: A human body model lineup to evaluate sex-differences in crash protection. *Front. Bioeng. Biotechnol.* 10, 918904. <https://doi.org/10.3389/fbioe.2022.918904>

John, J.D., Saravana Kumar, G., Yoganandan, N., 2019a. Rear-Impact Neck Whiplash: Role of Head Inertial Properties and Spine Morphological Variations on Segmental Rotations. *J. Biomech. Eng.* 141. <https://doi.org/10.1115/1.4043666>

John, J.D., Saravana Kumar, G., Yoganandan, N., 2019b. Cervical spine morphology and ligament property variations: A finite element study of their influence on sagittal bending characteristics. *J. Biomech.* 85, 18–26. <https://doi.org/https://doi.org/10.1016/j.jbiomech.2018.12.044>

John, J.D., Yoganandan, N., Arun, M.W.J., Saravana Kumar, G., 2018. Influence of morphological variations on cervical spine segmental responses from inertial loading. *Traffic Inj. Prev.* 19, S29–S36. <https://doi.org/10.1080/15389588.2017.1403017>

Joshi, S., Balthillaya, G., Neelapala, Y.V.R., 2019. Thoracic Posture and Mobility in Mechanical Neck Pain Population: A Review of the Literature. *Asian Spine J.* 13, 849–860. <https://doi.org/10.31616/asj.2018.0302>

Junker, S., Krumbholz, G., Frommer, K.W., Rehart, S., Steinmeyer, J., Rickert, M., Schett, G., Müller-Ladner, U., Neumann, E., 2016. Differentiation of osteophyte types in osteoarthritis – proposal of a histological classification. *Jt. Bone Spine* 83, 63–67. <https://doi.org/https://doi.org/10.1016/j.jbspin.2015.04.008>

Juul-Kristensen, B., Clausen, B., Ris, I., Jensen, R.V., Steffensen, R.F., Chreiteh, S.S., Jørgensen, M.B., Sjøgaard, K., 2013. Increased neck muscle activity and impaired balance among females with whiplash-related chronic neck pain: a cross-sectional study. *J. Rehabil. Med.* 45, 376–384. <https://doi.org/10.2340/16501977-1120>

Kallakuri, S., Singh, A., Chen, C., Cavanaugh, J.M., 2004. Demonstration of substance P, calcitonin gene-related peptide, and protein gene product 9.5 containing nerve fibers in human cervical facet joint capsules. *Spine (Phila. Pa. 1976)*. 29, 1182–1186. <https://doi.org/10.1097/00007632-200406010-00005>

- Kamibayashi, L.K., Richmond, F.J., 1998. Morphometry of human neck muscles. *Spine (Phila. Pa. 1976)*. 23, 1314–1323. <https://doi.org/10.1097/00007632-199806150-00005>
- Kang, J., Chen, G., Zhai, X., He, X., 2019. In vivo three-dimensional kinematics of the cervical spine during maximal active head rotation. *PLoS One* 14, e0215357.
- Kapandji, I.A., 1974. *The Physiology of the Joints: The Trunk and the Vertebral Column*. Churchill Livingstone.
- Karakolis, T., Farrell, P., Fusina, G., 2015. Neck Overuse Injury in CH-146 Griffon Helicopter Aircrews. *Procedia Manuf.* 3, 4205–4212. <https://doi.org/https://doi.org/10.1016/j.promfg.2015.07.396>
- Kato, D., Nakahira, Y., Atsumi, N., Iwamoto, M., 2018. Development of Human-Body Model THUMS Version 6 containing Muscle Controllers and Application to Injury Analysis in Frontal Collision after Brake Deceleration, in: *International Research Council on Biomechanics of Injury*. pp. 207–223.
- Katz, W.A., Rothenberg, R., 2005. Section 3: The Nature of Pain: Pathophysiology. *JCR J. Clin. Rheumatol.* 11.
- Kh, N., Al-Hayali, N., Chiad, J., Nacy, S., Hussein, O., 2021. A Review of Passive and Quasi-Passive Lower Limb Exoskeletons for Gait Rehabilitation. *J. Mech. Eng. Res. Dev.* 44, 436–447.
- Kim, M.-S., 2015. Neck kinematics and sternocleidomastoid muscle activation during neck rotation in subjects with forward head posture. *J. Phys. Ther. Sci.* 27, 3425–3428. <https://doi.org/10.1589/jpts.27.3425>
- Kim, S., Jeong, W., 2020. Physiological and psychological neck load imposed by ballistic helmets during simulated military activities. *Fash. Text.* 7, 27. <https://doi.org/10.1186/s40691-020-00216-7>
- Kim, Y.-J., Park, J.-Y., Choi, K.-Y., Moon, B.-J., Lee, J.-K., 2017. Case reports about an overlooked cause of neck pain: calcific tendinitis of the longus colli: Case reports. *Medicine (Baltimore)*. 96, e8343. <https://doi.org/10.1097/MD.00000000000008343>
- Kleinbach, C., Martynenko, O., Promies, J., Haeufle, D.F.B., Fehr, J., Schmitt, S., 2017. Implementation and validation of the extended Hill-type muscle model with robust routing

capabilities in LS-DYNA for active human body models. *Biomed. Eng. Online* 16, 109.
<https://doi.org/10.1186/s12938-017-0399-7>

Knight, J.F., Baber, C., 2004. Neck Muscle Activity and Perceived Pain and Discomfort Due to Variations of Head Load and Posture. *Aviat. Sp. Environ. Med.* 75.

Kopperdahl, D.L., Keaveny, T.M., 1998. Yield strain behavior of trabecular bone. *J. Biomech.* 31, 601–608. [https://doi.org/10.1016/s0021-9290\(98\)00057-8](https://doi.org/10.1016/s0021-9290(98)00057-8)

Krauss, J., Creighton, D., Ely, J.D., Podlowska-Ely, J., 2008. The immediate effects of upper thoracic translatoric spinal manipulation on cervical pain and range of motion: a randomized clinical trial. *J. Man. Manip. Ther.* 16, 93–99. <https://doi.org/10.1179/106698108790818530>

Kwon, J.-W., Bang, S.H., Park, T.H., Lee, S.-J., Lee, H.-M., Lee, S.-B., Lee, B.H., Moon, S.-H., 2020. Biomechanical comparison of cervical discectomy/fusion model using allograft spacers between anterior and posterior fixation methods (lateral mass and pedicle screw). *Clin. Biomech. (Bristol, Avon)* 73, 226–233. <https://doi.org/10.1016/j.clinbiomech.2020.01.018>

Kwon, S.W., Kim, C.H., Chung, C.K., Park, T.H., Woo, S.H., Lee, S.-J., Yang, S.H., 2017. The Formation of Extragraft Bone Bridging after Anterior Cervical Discectomy and Fusion: A Finite Element Analysis. *J. Korean Neurosurg. Soc.* 60, 611–619.
<https://doi.org/10.3340/jkns.2017.0178>

Lam, W.M.R., Ren, X., Tan, K.C., Bhakoo, K.K., Kumarsing, R.A., Liu, L., Zhuo, W.H., Wong, H.K., Hey, H.W.D., 2021. The Impact of Static Distraction for Disc Regeneration in a Rabbit Model—A Longitudinal MRI Study BT - 17th International Conference on Biomedical Engineering, in: Lim, C.T., Leo, H.L., Yeow, R. (Eds.), . Springer International Publishing, Cham, pp. 101–107.

Landau, D.-A., Chapnick, L., Yoffe, N., Azaria, B., Goldstein, L., Atar, E., 2006. Cervical and lumbar MRI findings in aviators as a function of aircraft type. *Aviat. Space. Environ. Med.* 77, 1158–1161.

Lascurain-Aguirrebeña, I., Newham, D., Galarraga-Gallastegui, B., Critchley, D.J., 2018. Differences in neck surface electromyography, kinematics and pain occurrence during physiological neck movements between neck pain and asymptomatic participants. A cross-sectional study. *Clin. Biomech.* 57, 1–9.

- Lasswell, T.L., Cronin, D.S., Medley, J.B., Rasoulinejad, P., 2017. Incorporating ligament laxity in a finite element model for the upper cervical spine. *Spine J.* 17, 1755–1764.
<https://doi.org/10.1016/j.spinee.2017.06.040>
- Lau, K.T., Cheung, K.Y., Chan, kwok B., Chan, M.H., Lo, K.Y., Wing Chiu, T.T., 2010. Relationships between sagittal postures of thoracic and cervical spine, presence of neck pain, neck pain severity and disability. *Man. Ther.* 15, 457–462.
<https://doi.org/https://doi.org/10.1016/j.math.2010.03.009>
- Leadbetter, W.B., Buckwalter, J.A., Gordon, S.L., of Orthopaedic Surgeons, A.A., for Sports Medicine, A.O.S., 1991. *Sports-induced Inflammation: Clinical and Basic Science Concepts.* American Academy of Orthopaedic Surgeons.
- Lee, K.E., Davis, M.B., Mejilla, R.M., Winkelstein, B.A., 2004. In vivo cervical facet capsule distraction: mechanical implications for whiplash and neck pain. *Stapp Car Crash J.* 48, 373–395. <https://doi.org/10.4271/2004-22-0016>
- Lee, S.-H., Im, Y.-J., Kim, K.-T., Kim, Y.-H., Park, W.-M., Kim, K., 2011. Comparison of Cervical Spine Biomechanics After Fixed- and Mobile-Core Artificial Disc Replacement: A Finite Element Analysis. *Spine (Phila. Pa. 1976).* 36.
- Lee, S., Kang, H., Shin, G., 2015. Head flexion angle while using a smartphone. *Ergonomics* 58, 220–226. <https://doi.org/10.1080/00140139.2014.967311>
- Levangie, P.K., Norkin, C.C., 2005. *JOINT STRUCTURE & FUNCTION A COMPREHENSIVE ANALYSIS*, 4th ed. F.A. Davis Company.
- Li, F., Li, H., Lei, K., Zhang, B., Su, S., Hu, W., Cao, Y., Nie, J., 2021. A high-fidelity human cervical muscle finite element model for motion and injury studies. *Transp. Saf. Environ.* 3. <https://doi.org/10.1093/tse/tdab016>
- Li, S., Xu, B., Liu, Y., Zhang, J., Xu, G., Shao, P., Li, X., Hu, Y., Ma, X., 2022. Biomechanical Evaluation of Spinal Column after Percutaneous Cement Discoplasty: A Finite Element Analysis. *Orthop. Surg.* 14, 1853–1863. <https://doi.org/10.1111/os.13314>
- Li, T.-C., Liu, C.-J., Liu, S.-Y., Wang, X., Feng, J.-J., Wang, J.-T., Du, C.-F., 2023. Effect of muscle activation on dynamic responses of neck of pilot during emergency ejection: a finite element study. *Med. Biol. Eng. Comput.* <https://doi.org/10.1007/s11517-023-02817-y>

- LIANG, C., LI, H., TAO, Y., SHEN, C., LI, F., SHI, Z., HAN, B., CHEN, Q., 2013. New hypothesis of chronic back pain: low pH promotes nerve ingrowth into damaged intervertebral disks. *Acta Anaesthesiol. Scand.* 57, 271–277. <https://doi.org/https://doi.org/10.1111/j.1399-6576.2012.02670.x>
- Liang, W., Han, B., Hai, Y., Yang, J., Yin, P., 2022. Biomechanical Analysis of the Reasonable Cervical Range of Motion to Prevent Non-Fusion Segmental Degeneration After Single-Level ACDF. *Front. Bioeng. Biotechnol.* 10, 918032. <https://doi.org/10.3389/fbioe.2022.918032>
- Lin, D., He, Z., Weng, R., Zhu, Y., Lin, Z., Deng, Y., Yang, Y., Tan, J., Wang, M., Li, Y., Huang, G., Yu, G., Cai, D., Huang, X., Huang, W., 2023. Comparison of biomechanical parameters of two Chinese cervical spine rotation manipulations based on motion capture and finite element analysis . *Front. Bioeng. Biotechnol.* .
- Lindenmann, S., Tsagkaris, C., Farshad, M., Widmer, J., 2022. Kinematics of the Cervical Spine Under Healthy and Degenerative Conditions: A Systematic Review. *Ann. Biomed. Eng.* 50, 1705–1733. <https://doi.org/10.1007/s10439-022-03088-8>
- Ling, Z., Li, L., Chen, Y., Hu, H., Zhao, X., Wilson, J., Qi, Q., Liu, D., Wei, F., Chen, X., Lu, J., Zhou, Z., Zou, X., 2020. Changes of the end plate cartilage are associated with intervertebral disc degeneration: A quantitative magnetic resonance imaging study in rhesus monkeys and humans. *J. Orthop. Transl.* 24, 23–31. <https://doi.org/10.1016/j.jot.2020.04.004>
- Liu, B., Wu, B., Hoof, T. Van, Okito, J.-P.K., Liu, Z., Zeng, Z., 2015. Are the standard parameters of cervical spine alignment and range of motion related to age, sex, and cervical disc degeneration? *J. Neurosurg. Spine SPI* 23, 274–279. <https://doi.org/10.3171/2015.1.SPINE14489>
- Liu, H., Zhang, B., Lei, J., Cai, X., Li, Z., Wang, Z., 2016. Biomechanical Role of the C1 Lateral Mass Screws in Occipitoatlantoaxial Fixation: A Finite Element Analysis. *Spine (Phila. Pa. 1976)*. 41, E1312–E1318. <https://doi.org/10.1097/BRS.0000000000001637>
- Liu, J., Liu, H., Bu, W., Wang, Y., Xu, P., Wu, M., Fan, Y., 2023. Effects of different helmet-mounted devices on pilot’s neck injury under simulated ejection. *Comput. Methods Biomech. Biomed. Engin.* 26, 1510–1521. <https://doi.org/10.1080/10255842.2022.2124860>
- Liu, T., Khalaf, K., Adeeb, S., El-Rich, M., 2019. Effects of lumbo-pelvic rhythm on trunk muscle forces and disc loads during forward flexion: A combined musculoskeletal and finite element

- simulation study. *J. Biomech.* 82, 116–123. <https://doi.org/10.1016/j.jbiomech.2018.10.009>
- Liu, Y.K., Goel, V.K., Dejong, A., Njus, G., Nishiyama, K., Buckwalter, J., 1985. Torsional fatigue of the lumbar intervertebral joints. *Spine (Phila. Pa. 1976)*. 10, 894–900.
<https://doi.org/10.1097/00007632-198512000-00006>
- Lopez-Lopez, J.A., Vallejo, P., Rios-Tejada, F., Jimenez, R., Sierra, I., Garcia-Mora, L., 2001. Determination of lumbar muscular activity in helicopter pilots: a new approach. *Aviat. Space Environ. Med.* 72, 38–43.
- Lopik, D.W., Acar, M., 2007. Development of a multi-body computational model of human head and neck. *Proc. Inst. Mech. Eng. Part K J. Multi-body Dyn.* 221.
<https://doi.org/10.1243/14644193JMBD84>
- Lotz, J.C., Fields, A.J., Liebenberg, E.C., 2013. The role of the vertebral end plate in low back pain. *Glob. spine J.* 3, 153–164. <https://doi.org/10.1055/s-0033-1347298>
- Lu, Y., Chen, C., Kallakuri, S., Patwardhan, A., Cavanaugh, J.M., 2005a. Neurophysiological and biomechanical characterization of goat cervical facet joint capsules. *J. Orthop. Res. Off. Publ. Orthop. Res. Soc.* 23, 779–787. <https://doi.org/10.1016/j.orthres.2005.01.002>
- Lu, Y., Chen, C., Kallakuri, S., Patwardhan, A., Cavanaugh, J.M., 2005b. Neural response of cervical facet joint capsule to stretch: a study of whiplash pain mechanism. *Stapp Car Crash J.* 49, 49–65. <https://doi.org/10.4271/2005-22-0003>
- Lu, Y., Chen, C., Kallakuri, S., Patwardhan, A., Cavanaugh, J.M., 2005c. Development of an in vivo method to investigate biomechanical and neurophysiological properties of spine facet joint capsules. *Eur. spine J. Off. Publ. Eur. Spine Soc. Eur. Spinal Deform. Soc. Eur. Sect. Cerv. Spine Res. Soc.* 14, 565–572. <https://doi.org/10.1007/s00586-004-0835-9>
- Lundin, O., Ekström, L., Hellström, M., Holm, S., Swärd, L., 1998. Injuries in the Adolescent Porcine Spine Exposed to Mechanical Compression. *Spine (Phila. Pa. 1976)*. 23.
- Madison, A.M., Stewart, A., Robinette, A., Sous, S., Yoganandan, N., Chancey, V.C., 2023. Surgical Interventions for Cervical Intervertebral Disc Disease in U.S. Army Aviators: A Comprehensive Review and Identification of Knowledge Gaps.
- Maganaris, C.N., Baltzopoulos, V., Ball, D., Sargeant, A.J., 2001. In vivo specific tension of human

- skeletal muscle. *J. Appl. Physiol.* 90, 865–872. <https://doi.org/10.1152/jappl.2001.90.3.865>
- Mahmood, M.N., Tabasi, A., Kingma, I., Van Dieen, J., 2021. A Novel Passive Neck Orthosis for Patients with Degenerative Muscle Diseases: Development & Evaluation. *J. Electromyogr. Kinesiol.* 57, 102515. <https://doi.org/10.1016/j.jelekin.2021.102515>
- Manchikanti, L., Boswell, M. V, Singh, V., Pampati, V., Damron, K.S., Beyer, C.D., 2004. Prevalence of facet joint pain in chronic spinal pain of cervical, thoracic, and lumbar regions. *BMC Musculoskelet. Disord.* 5, 15. <https://doi.org/10.1186/1471-2474-5-15>
- Manickam, P.S., Ghosh, G., Shetty, G.M., Chowdhury, A.R., Roy, S., 2023. Biomechanical analysis of the novel S-type dynamic cage by implementation of teaching learning based optimization algorithm - An experimental and finite element study. *Med. Eng. Phys.* 112, 103955. <https://doi.org/https://doi.org/10.1016/j.medengphy.2023.103955>
- Manickam, P.S., Roy, S., 2021. The biomechanical effects of S-type dynamic cage using Ti and PEEK for ACDF surgery on cervical spine varying loads. *Int. J. Artif. Organs* 44, 748–755. <https://doi.org/10.1177/03913988211039525>
- Mansoor, S.N., Rathore, F.A., 2018. Accessory Clavicular Sternocleidomastoid Causing Torticollis in an Adult. *Prog. Rehabil. Med.* 3, 20180006. <https://doi.org/10.2490/prm.20180006>
- Martin, J.A., Buckwalter, J.A., 2002. Aging, articular cartilage chondrocyte senescence and osteoarthritis. *Biogerontology* 3, 257–264. <https://doi.org/10.1023/A:1020185404126>
- Martin, J.T., 2015. Nanofibrous disc-like angle ply structures for total disc replacement in a small animal model.
- Martínez-Moreno, D., Jiménez, G., Gálvez-Martín, P., Rus, G., Marchal, J.A., 2019. Cartilage biomechanics: A key factor for osteoarthritis regenerative medicine. *Biochim. Biophys. Acta - Mol. Basis Dis.* 1865, 1067–1075. <https://doi.org/https://doi.org/10.1016/j.bbadis.2019.03.011>
- Mathys, R., Ferguson, S.J., 2012. Simulation of the effects of different pilot helmets on neck loading during air combat. *J. Biomech.* 45, 2362–2367. <https://doi.org/10.1016/j.jbiomech.2012.07.014>
- Mattucci, S.F.E., Cronin, D.S., 2015. A method to characterize average cervical spine ligament response based on raw data sets for implementation into injury biomechanics models. *J. Mech. Behav. Biomed. Mater.* 41, 251–260. <https://doi.org/10.1016/j.jmbbm.2014.09.023>

- Mattucci, S.F.E., Moulton, J.A., Chandrashekar, N., Cronin, D.S., 2013. Strain rate dependent properties of human craniovertebral ligaments. *J. Mech. Behav. Biomed. Mater.* 23, 71–79. <https://doi.org/10.1016/j.jmbbm.2013.04.005>
- Mattucci, S.F.E., Moulton, J.A., Chandrashekar, N., Cronin, D.S., 2012. Strain rate dependent properties of younger human cervical spine ligaments. *J. Mech. Behav. Biomed. Mater.* 10, 216–226. <https://doi.org/https://doi.org/10.1016/j.jmbbm.2012.02.004>
- McGill, S.M., Jones, K., Bennett, G., Bishop, P.J., 1994. Passive stiffness of the human neck in flexion, extension, and lateral bending. *Clin. Biomech. (Bristol, Avon)* 9, 193–198. [https://doi.org/10.1016/0268-0033\(94\)90021-3](https://doi.org/10.1016/0268-0033(94)90021-3)
- McKee, N.H., Fish, J.S., Manktelow, R.T., McAvoy, G. V, Young, S., Zuker, R.M., 1990. Gracilis muscle anatomy as related to function of a free functioning muscle transplant. *Clin. Anat.* 3, 87–92. <https://doi.org/https://doi.org/10.1002/ca.980030202>
- McKinnon, C.D., Dickerson, C.R., Laing, A.C.T., Callaghan, J.P., 2016. Neck muscle activity during simulated in-flight static neck postures and helmet mounted equipment. *Occup. Ergon.* 13, 119–130. <https://doi.org/10.3233/OER-170245>
- Menkes, C.-J., Lane, N.E., 2004. Are osteophytes good or bad? *Osteoarthr. Cartil.* 12, 53–54. <https://doi.org/10.1016/j.joca.2003.09.003>
- Mense, S., 2008. Muscle pain: mechanisms and clinical significance. *Dtsch. Arztebl. Int.* 105, 214–219. <https://doi.org/10.3238/artzebl.2008.0214>
- Mercer, S., Bogduk, N., 1999. The ligaments and annulus fibrosus of human adult cervical intervertebral discs. *Spine (Phila. Pa. 1976)*. 24, 618–619. <https://doi.org/10.1097/00007632-199904010-00002>
- Mesfar, W., Moglo, K., 2013. Effect of the transverse ligament rupture on the biomechanics of the cervical spine under a compressive loading. *Clin. Biomech. (Bristol, Avon)* 28, 846–852. <https://doi.org/10.1016/j.clinbiomech.2013.07.016>
- Mesfar, W., Moglo, K., 2012. Biomechanics of the Cervical Spine Under Compressive Loading in Flexion and Extension: Muscles Net Moment Determination. <https://doi.org/10.1115/SBC2012-80946>

- Meyer, F., Bourdet, N., Deck, C., Willinger, R., Raul, J.S., 2004. Human Neck Finite Element Model Development and Validation against Original Experimental Data. *Stapp Car Crash J.* 48, 177–206.
- Millard, M., Uchida, T., Seth, A., Delp, S.L., 2013. Flexing computational muscle: modeling and simulation of musculotendon dynamics. *J. Biomech. Eng.* 135, 21005.
<https://doi.org/10.1115/1.4023390>
- Molinos, M., Almeida, C.R., Caldeira, J., Cunha, C., Gonçalves, R.M., Barbosa, M.A., 2015. Inflammation in intervertebral disc degeneration and regeneration. *J. R. Soc. Interface* 12, 20141191. <https://doi.org/10.1098/rsif.2014.1191>
- Moore, C.A.B., Barrett, J.M., Healey, L., Callaghan, J.P., Fischer, S.L., 2021. Predicting Cervical Spine Compression and Shear in Helicopter Helmeted Conditions Using Artificial Neural Networks. *IISE Trans. Occup. Ergon. Hum. Factors* 9, 154–166.
<https://doi.org/10.1080/24725838.2021.1938760>
- Morrow, D.A., Haut Donahue, T.L., Odegard, G.M., Kaufman, K.R., 2010. Transversely isotropic tensile material properties of skeletal muscle tissue. *J. Mech. Behav. Biomed. Mater.* 3, 124–129. <https://doi.org/https://doi.org/10.1016/j.jmbbm.2009.03.004>
- Mortensen, J.D., Vasavada, A.N., Merryweather, A.S., 2018. The inclusion of hyoid muscles improve moment generating capacity and dynamic simulations in musculoskeletal models of the head and neck. *PLoS One* 13, e0199912–e0199912. <https://doi.org/10.1371/journal.pone.0199912>
- Motiwale, S., Subramani, A., Kraft, R.H., Zhou, X., 2018. A non-linear multiaxial fatigue damage model for the cervical intervertebral disc annulus. *Adv. Mech. Eng.* 10, 1687814018779494. <https://doi.org/10.1177/1687814018779494>
- Mousavi-khatir, R., Talebian, S., Maroufi, N., Olyaie, G., 2015. Effect of static neck flexion in cervical flexion-relaxation phenomenon in healthy males and females. *J. Bodyw. Mov. Ther.* 20. <https://doi.org/10.1016/j.jbmt.2015.07.039>
- Mustafy, T., Moglo, K., Adeeb, S., El-Rich, M., 2016. Injury mechanisms of the ligamentous cervical C2–C3 Functional Spinal Unit to complex loading modes: Finite Element study. *J. Mech. Behav. Biomed. Mater.* 53, 384–396.
<https://doi.org/https://doi.org/10.1016/j.jmbbm.2015.08.042>

- Myers, B.S., Woolley, C.T., Slotter, T.L., Garrett, W.E., Best, T.M., 1998. The influence of strain rate on the passive and stimulated engineering stress--large strain behavior of the rabbit tibialis anterior muscle. *J. Biomech. Eng.* 120, 126–132. <https://doi.org/10.1115/1.2834292>
- Namwongsa, S., Puntumetakul, R., Neubert, M.S., Boucaut, R., 2019. Effect of neck flexion angles on neck muscle activity among smartphone users with and without neck pain. *Ergonomics* 62, 1524–1533. <https://doi.org/10.1080/00140139.2019.1661525>
- Naserkhaki, S., Jaremko, J.L., Adeeb, S., El-Rich, M., 2016. On the load-sharing along the ligamentous lumbosacral spine in flexed and extended postures: Finite element study. *J. Biomech.* 49, 974–982. <https://doi.org/https://doi.org/10.1016/j.jbiomech.2015.09.050>
- Nasim, M., Galvanetto, U., 2023. Muscle activity on head-first compression responses of a finite element neck model. *Forces Mech.* 10, 100163. <https://doi.org/https://doi.org/10.1016/j.finmec.2022.100163>
- Neary, P.J., Salmon, D.M., Harrison, M.F., Albert, W.J., 2010. NIGHT VISION GOGGLES-INDUCED NECK STRAIN AND MUSCLE FATIGUE CHARACTERISTICS OF GRIFFON HELICOPTER PERSONNEL. Regina, SK.
- Netto, K., Burnett, A., 2006. Neck muscle activation and head postures in common high performance aerial combat maneuvers. *Aviat. Space. Environ. Med.* 77, 1049–1055.
- Newell, R.S., Blouin, J.-S., Street, J., Cripton, P.A., Siegmund, G.P., 2018. The neutral posture of the cervical spine is not unique in human subjects. *J. Biomech.* 80, 53–62. <https://doi.org/10.1016/j.jbiomech.2018.08.012>
- Nie, X., Cheng, J.-I., Chen, W.W., Weerasooriya, T., 2010. Dynamic Tensile Response of Porcine Muscle. *J. Appl. Mech.* 78. <https://doi.org/10.1115/1.4002580>
- Nightingale, R.W., Carol Chancey, V., Ottaviano, D., Luck, J.F., Tran, L., Prange, M., Myers, B.S., 2007. Flexion and extension structural properties and strengths for male cervical spine segments. *J. Biomech.* 40, 535–542. <https://doi.org/10.1016/j.jbiomech.2006.02.015>
- Nightingale, R.W., Sganga, J., Cutcliffe, H., Bass, C.R. “Dale,” 2016. Impact responses of the cervical spine: A computational study of the effects of muscle activity, torso constraint, and pre-flexion. *J. Biomech.* 49, 558–564. <https://doi.org/10.1016/j.jbiomech.2016.01.006>

- Nightingale, R.W., Winkelstein, B.A., Knaub, K.E., Richardson, W.J., Luck, J.F., Myers, B.S., 2002. Comparative strengths and structural properties of the upper and lower cervical spine in flexion and extension. *J. Biomech.* 35, 725–732. [https://doi.org/10.1016/s0021-9290\(02\)00037-4](https://doi.org/10.1016/s0021-9290(02)00037-4)
- Nikita, E., 2017. Chapter 1 - The Human Skeleton, in: Nikita, E.B.T.-O. (Ed.), . Academic Press, pp. 1–75. <https://doi.org/https://doi.org/10.1016/B978-0-12-804021-8.00001-2>
- Nikkhoo, M., Cheng, C.-H., Wang, J.-L., Khoz, Z., El-Rich, M., Hebel, N., Khalaf, K., 2019. Development and validation of a geometrically personalized finite element model of the lower ligamentous cervical spine for clinical applications. *Comput. Biol. Med.* 109, 22–32. <https://doi.org/10.1016/j.combiomed.2019.04.010>
- Nikkhoo, M., Cheng, C.-H., Wang, J.-L., Niu, C.-C., Parnianpour, M., Khalaf, K., 2021. The Biomechanical Response of the Lower Cervical Spine Post Laminectomy: Geometrically-Parametric Patient-Specific Finite Element Analyses. *J. Med. Biol. Eng.* 41, 59–70. <https://doi.org/10.1007/s40846-020-00579-8>
- Nimbarte, A.D., Sivak-Callcott, J.A., Zreiqat, M., Chapman, M., 2013. Neck Postures and Cervical Spine Loading Among Microsurgeons Operating with Loupes and Headlamp. *IIE Trans. Occup. Ergon. Hum. Factors* 1, 215–223. <https://doi.org/10.1080/21577323.2013.840342>
- Ning, X., Huang, Y., Hu, B., Nimbarte, A.D., 2015. Neck kinematics and muscle activity during mobile device operations. *Int. J. Ind. Ergon.* 48, 10–15. <https://doi.org/https://doi.org/10.1016/j.ergon.2015.03.003>
- Nordin, M., Frankel, V.H., 2001. *Basic Biomechanics of the Musculoskeletal System*, 4th ed. Wolters Kluwer.
- O’Conor, D.K., Dalal, S., Ramachandran, V., Shivers, B., Shender, B.S., Jones, J.A., 2020. Crew-Friendly Countermeasures Against Musculoskeletal Injuries in Aviation and Spaceflight. *Front. Physiol.* 11, 837. <https://doi.org/10.3389/fphys.2020.00837>
- Oda, T., Panjabi, M., Crisco, J.J. 3rd, Bueff, H.U., Grob, D., Dvorak, J., 1992. Role of tectorial membrane in the stability of the upper cervical spine. *Clin. Biomech. (Bristol, Avon)* 7, 201–207. [https://doi.org/10.1016/S0268-0033\(92\)90002-L](https://doi.org/10.1016/S0268-0033(92)90002-L)
- Oi, N., Pandy, M.G., Myers, B.S., Nightingale, R.W., Chancey, V.C., 2004. Variation of neck muscle strength along the human cervical spine. *Stapp Car Crash J.* 48, 397–417.

- Omoigui, S., 2007. The biochemical origin of pain: the origin of all pain is inflammation and the inflammatory response. Part 2 of 3 - inflammatory profile of pain syndromes. *Med. Hypotheses* 69, 1169–1178. <https://doi.org/10.1016/j.mehy.2007.06.033>
- Ordway, N.R., Seymour, R.J., Donelson, R.G., Hojnowski, L.S., Edwards, W.T., 1999. Cervical Flexion, Extension, Protrusion, and Retraction: A Radiographic Segmental Analysis. *Spine (Phila. Pa. 1976)*. 24.
- Orsello, C.A., Phillips, A.S., Rice, G.M., 2013. Height and in-flight low back pain association among military helicopter pilots. *Aviat. Space. Environ. Med.* 84, 32–37. <https://doi.org/10.3357/ase.3425.2013>
- Osth, J., Brolin, K., Svensson, M.Y., Linder, A., 2016. A Female Ligamentous Cervical Spine Finite Element Model Validated for Physiological Loads. *J. Biomech. Eng.* 138, 61005. <https://doi.org/10.1115/1.4032966>
- Palepu, V., 2013. Biomechanical effects of initial occupant seated posture during rear end impact injury. University of Toledo.
- Panjabi, Dvorak, J., Crisco III, J.J., Oda, T., Wang, P., Grob, D., 1991a. Effects of Alar ligament transection on upper cervical spine rotation. *J. Orthop. Res.* 9, 584–593. <https://doi.org/10.1002/jor.1100090415>
- Panjabi, Dvorak, J., Crisco, J. 3rd, Oda, T., Hilibrand, A., Grob, D., 1991b. Flexion, extension, and lateral bending of the upper cervical spine in response to alar ligament transections. *J. Spinal Disord.* 4, 157–167. <https://doi.org/10.1097/00002517-199106000-00005>
- Panjabi, M., 2006. A hypothesis of chronic back pain: ligament subfailure injuries lead to muscle control dysfunction. *Eur. Spine J.* 15, 668–676. <https://doi.org/10.1007/s00586-005-0925-3>
- Panjabi, M., Chen, N.C., Shin, E.K., Wang, J.L., 2001a. The cortical shell architecture of human cervical vertebral bodies. *Spine (Phila. Pa. 1976)*. 26, 2478–2484. <https://doi.org/10.1097/00007632-200111150-00016>
- Panjabi, M., Crisco, J.J., Vasavada, A., Oda, T., Cholewicki, J., Nibu, K., Shin, E., 2001b. Mechanical properties of the human cervical spine as shown by three-dimensional load-displacement curves. *Spine (Phila. Pa. 1976)*. 26, 2692–2700. <https://doi.org/10.1097/00007632-200112150-00012>

- Panjabi, M., Nibu, K., Cholewicki, J., 1998. Whiplash injuries and the potential for mechanical instability. *Eur. Spine J.* 7, 484–492. <https://doi.org/10.1007/s005860050112>
- Panjabi, M., Pearson, A.M., Ito, S., Ivancic, P.C., Gimenez, S.E., Tominaga, Y., 2004. Cervical spine ligament injury during simulated frontal impact. *Spine (Phila. Pa. 1976)*. 29, 2395–2403. <https://doi.org/10.1097/01.brs.0000143173.92241.ab>
- Panzer, M.B., 2006. Numerical Modelling of the Human Cervical Spine in Frontal Impact. University of Waterloo.
- Panzer, M.B., Cronin, D.S., 2009. C4-C5 segment finite element model development, validation, and load-sharing investigation. *J. Biomech.* 42, 480–490. <https://doi.org/10.1016/j.jbiomech.2008.11.036>
- Panzer, M.B., Fice, J.B., Cronin, D.S., 2011. Cervical spine response in frontal crash. *Med. Eng. Phys.* 33, 1147–1159. <https://doi.org/10.1016/j.medengphy.2011.05.004>
- Papadakis, M., Sapkas, G., Papadopoulos, E.C., Katonis, P., 2011. Pathophysiology and biomechanics of the aging spine. *Open Orthop. J.* 5, 335–342. <https://doi.org/10.2174/1874325001105010335>
- Park, H., Park, J., Lin, S.-H., Boorady, L.M., 2014. Assessment of Firefighters' needs for personal protective equipment. *Fash. Text.* 1, 8. <https://doi.org/10.1186/s40691-014-0008-3>
- Parkinson, R.J., Callaghan, J.P., 2009. The role of dynamic flexion in spine injury is altered by increasing dynamic load magnitude. *Clin. Biomech. (Bristol, Avon)* 24, 148–154. <https://doi.org/10.1016/j.clinbiomech.2008.11.007>
- Patwardhan, A.G., Havey, R.M., Ghanayem, A.J., Diener, H., Meade, K.P., Dunlap, B., Hodges, S.D., 2000. Load-Carrying Capacity of the Human Cervical Spine in Compression Is Increased Under a Follower Load. *Spine (Phila. Pa. 1976)*. 25.
- Paul, S., 2017. Biodynamic Excisional Skin Tension (BEST) Lines: Revisiting Langer's Lines, Skin Biomechanics, Current Concepts in Cutaneous Surgery, and the (lack of) Science behind Skin Lines used for Surgical Excisions. *J. Dermatological Res.* 2, 77–87. <https://doi.org/10.17554/j.issn.2413-8223.2017.02.19>
- Pearson, A.M., Ivancic, P.C., Ito, S., Panjabi, M., 2004. Facet joint kinematics and injury mechanisms

during simulated whiplash. *Spine (Phila. Pa. 1976)*. 29, 390–397.

<https://doi.org/10.1097/01.brs.0000090836.50508.f7>

Peng, B., Bogduk, N., 2019. Cervical Discs as a Source of Neck Pain. An Analysis of the Evidence.

Pain Med. 20, 446–455. <https://doi.org/10.1093/pm/pny249>

Peng, B., DePalma, M.J., 2018. Cervical disc degeneration and neck pain. *J. Pain Res.* 11, 2853–

2857. <https://doi.org/10.2147/JPR.S180018>

Pengrong, O., Teng, lu, He, X., Gao, Z., Cai, X., Jin, Z., 2019. Biomechanical Comparison of

Integrated Fixation Cage Versus Anterior Cervical Plate and Cage in Anterior Cervical

Corpectomy and Fusion (ACCF): A Finite Element Analysis. *Med. Sci. Monit.* 25, 1489–1498.

<https://doi.org/10.12659/MSM.913630>

Persad, L.S., Binder-Markey, B.I., Shin, A.Y., Kaufman, K.R., Lieber, R.L., 2021. In vivo human

gracilis whole-muscle passive stress-sarcomere strain relationship. *J. Exp. Biol.* 224.

<https://doi.org/10.1242/jeb.242722>

Pezowicz, C., 2010. Analysis of selected mechanical properties of intervertebral disc annulus fibrosus

in macro and microscopic scale. *J. Theor. Appl. Mech.* 48.

Pintar, F.A., Yoganandan, N., Voo, L., 1998. Effect of Age and Loading Rate on Human Cervical

Spine Injury Threshold. *Spine (Phila. Pa. 1976)*. 23.

Plaga, J.A., Albery, C., Boehmer, M., Goodyear, C., Thomas, G., 2005. Design and Development of

Anthropometrically Correct Head Forms for Joint Strike Fighter Ejection Seat Testing.

Posch, M., Schranz, A., Lener, M., Senn, W., Äng, B.O., Burtscher, M., Ruedl, G., 2019. Prevalence

and potential risk factors of flight-related neck, shoulder and low back pain among helicopter

pilots and crewmembers: a questionnaire-based study. *BMC Musculoskelet. Disord.* 20, 44.

<https://doi.org/10.1186/s12891-019-2421-7>

Pousette, M., Martire, R., Linder, J., Kristoffersson, M., Äng, B., 2016. Neck Muscle Strain in Air

Force Pilots Wearing Night Vision Goggles. *Aerosp. Med. Hum. Perform.* 87, 928–932.

Pramudita, J.A., Kikuchi, S., Minato, I., Tanabe, Y., 2017. Effect of cervical spine alignment on neck

injury risk during rear-end impact – numerical study using neck finite element model. *Int. J.*

Crashworthiness 22, 453–466. <https://doi.org/10.1080/13588265.2017.1278638>

- Putra, I.P.A., Iraeus, J., Sato, F., Svensson, M.Y., Linder, A., Thomson, R., 2021. Optimization of Female Head–Neck Model with Active Reflexive Cervical Muscles in Low Severity Rear Impact Collisions. *Ann. Biomed. Eng.* 49, 115–128. <https://doi.org/10.1007/s10439-020-02512-1>
- Quinn, K.P., Bauman, J.A., Crosby, N.D., Winkelstein, B.A., 2010. Anomalous fiber realignment during tensile loading of the rat facet capsular ligament identifies mechanically induced damage and physiological dysfunction. *J. Biomech.* 43, 1870–1875. <https://doi.org/10.1016/j.jbiomech.2010.03.032>
- Quinn, K.P., Lee, K.E., Ahaghotu, C.C., Winkelstein, B.A., 2007. Structural changes in the cervical facet capsular ligament: potential contributions to pain following subfailure loading. *Stapp Car Crash J.* 51, 169–187. <https://doi.org/10.4271/2007-22-0008>
- Rade, M., Määttä, J.H., Freidin, M.B., Airaksinen, O., Karppinen, J., Williams, F.M.K., 2018. Vertebral Endplate Defect as Initiating Factor in Intervertebral Disc Degeneration: Strong Association Between Endplate Defect and Disc Degeneration in the General Population. *Spine (Phila. Pa. 1976)*. 43, 412–419. <https://doi.org/10.1097/BRS.0000000000002352>
- Rahman, W.U., Jiang, W., Zhao, F., Li, Z., Wang, G., Yang, G., 2023. Biomechanical effect of C5-C6 intervertebral disc degeneration on the human lower cervical spine (C3-C7): a finite element study. *Comput. Methods Biomech. Biomed. Engin.* 26, 820–834. <https://doi.org/10.1080/10255842.2022.2089026>
- Raj, P.P., 2008. Intervertebral Disc: Anatomy-Physiology-Pathophysiology-Treatment. *Pain Pract.* 8, 18–44. <https://doi.org/10.1111/j.1533-2500.2007.00171.x>
- Rajasekaran, S., Bajaj, N., Tubaki, V., Kanna, R.M., Shetty, A.P., 2013. ISSLS Prize Winner: The Anatomy of Failure in Lumbar Disc Herniation: An: In Vivo: , Multimodal, Prospective Study of 181 Subjects. *Spine (Phila. Pa. 1976)*. 38.
- Randhawa, A., Wakeling, J.M., 2018. Transverse anisotropy in the deformation of the muscle during dynamic contractions. *J. Exp. Biol.* 221. <https://doi.org/10.1242/jeb.175794>
- Rattanagraikanakorn, B., Schuurman, M., Gransden, D.I., Happee, R., De Wagter, C., Sharpanskykh, A., Blom, H.A.P., 2022. Modelling head injury due to unmanned aircraft systems collision: Crash dummy vs human body. *Int. J. Crashworthiness* 27, 400–413.

<https://doi.org/10.1080/13588265.2020.1807687>

Reed, M., Jones, M., 2017. A Parametric Model of Cervical Spine Geometry and Posture. *Ann Arbor*.

Richfield, D., 2014. Medical gallery of David Richfield. *Wiki J. Medicine* 1.

<https://doi.org/DOI:10.15347/wjm/2014.009>.

Rio, E., Moseley, L., Purdam, C., Samiric, T., Kidgell, D., Pearce, A.J., Jaberzadeh, S., Cook, J., 2014. The Pain of Tendinopathy: Physiological or Pathophysiological? *Sport. Med.* 44, 9–23.

<https://doi.org/10.1007/s40279-013-0096-z>

Roberts, T.J., Azizi, E., 2011. Flexible mechanisms: the diverse roles of biological springs in vertebrate movement. *J. Exp. Biol.* 214, 353–361. <https://doi.org/10.1242/jeb.038588>

Roberts, T.J., Eng, C.M., Sleboda, D.A., Holt, N.C., Brainerd, E.L., Stover, K.K., Marsh, R.L., Azizi, E., 2019. The Multi-Scale, Three-Dimensional Nature of Skeletal Muscle Contraction.

Physiology 34, 402–408. <https://doi.org/10.1152/physiol.00023.2019>

Roelofs, A.J., Kania, K., Rafipay, A.J., Sambale, M., Kuwahara, S.T., Collins, F.L., Smeeton, J., Serowoky, M.A., Rowley, L., Wang, H., Gronewold, R., Kapeni, C., Méndez-Ferrer, S., Little, C.B., Bateman, J.F., Pap, T., Mariani, F. V, Sherwood, J., Crump, J.G., De Bari, C., 2020. Identification of the skeletal progenitor cells forming osteophytes in osteoarthritis. *Ann. Rheum. Dis.* 79, 1625–1634. <https://doi.org/10.1136/annrheumdis-2020-218350>

Röhrle, O., Sprenger, M., Schmitt, S., 2017. A two-muscle, continuum-mechanical forward simulation of the upper limb. *Biomech. Model. Mechanobiol.* 16, 743–762.

<https://doi.org/10.1007/s10237-016-0850-x>

Rojas, C.A., Bertozzi, J.C., Martinez, C.R., Whitlow, J., 2007. Reassessment of the Craniocervical Junction: Normal Values on CT. *Am. J. Neuroradiol.* 28, 1819 LP – 1823.

<https://doi.org/10.3174/ajnr.A0660>

Roos, P.E., Vasavada, A., Zheng, L., Zhou, X., 2020. Neck musculoskeletal model generation through anthropometric scaling. *PLoS One* 15, e0219954.

Rossmann, S., Meyer, E., Rundell, S., 2022. Development of a finite element lumbar spine model to predict intervertebral disc herniation risk factors. *Comput. Methods Biomech. Biomed. Engin.*

25, 1–13. <https://doi.org/10.1080/10255842.2021.1922677>

- Rustenburg, C.M.E., Emanuel, K.S., Peeters, M., Lems, W.F., Vergroesen, P.-P.A., Smit, T.H., 2018. Osteoarthritis and intervertebral disc degeneration: Quite different, quite similar. *JOR SPINE* 1, e1033. <https://doi.org/https://doi.org/10.1002/jsp2.1033>
- Rutges, J.P.H.J., Jagt van der, O.P., Oner, F.C., Verbout, A.J., Castelein, R.J.M., Kummer, J.A., Weinans, H., Creemers, L.B., Dhert, W.J.A., 2011. Micro-CT quantification of subchondral endplate changes in intervertebral disc degeneration. *Osteoarthr. Cartil.* 19, 89–95. <https://doi.org/https://doi.org/10.1016/j.joca.2010.09.010>
- Safran, M.R., 1995. Elbow injuries in athletes. A review. *Clin. Orthop. Relat. Res.* 257–277.
- Salem, W., Lenders, C., Mathieu, J., Hermanus, N., Klein, P., 2013. In vivo three-dimensional kinematics of the cervical spine during maximal axial rotation. *Man. Ther.* 18, 339–344. <https://doi.org/https://doi.org/10.1016/j.math.2012.12.002>
- Salmon, D.M., Harrison, M.F., Patrick, N.J., 2011. Neck Pain in Military Helicopter Aircrew and the Role of Exercise Therapy. *Aviat. Sp. Environ. Med.* 82, 978–987.
- Sato, F., Nakajima, T., Ono, K., Svensson, M.Y., Kaneoka, K., 2015. Characteristics of Dynamic Cervical Vertebral Kinematics for Female and Male Volunteers in Low-speed Rear Impact, based on Quasi-static Neck Kinematics, in: *International Research Council on Biomechanics of Injury*. pp. 261–277.
- Sayson, J., Hargens, A., 2008. Pathophysiology of Low Back Pain during Exposure to Microgravity. *Aviat. Sp. Environ. Med.* 79.
- Schaible, H.-G., Richter, F., 2004. Pathophysiology of pain. *Langenbeck's Arch. Surg.* 389, 237–243. <https://doi.org/10.1007/s00423-004-0468-9>
- Schmidt, H., Bashkuev, M., Dreischarf, M., Rohlmann, A., Duda, G., Wilke, H.-J., Shirazi-Adl, A., 2013. Computational biomechanics of a lumbar motion segment in pure and combined shear loads. *J. Biomech.* 46, 2513–2521. <https://doi.org/https://doi.org/10.1016/j.jbiomech.2013.06.038>
- Schug, S.A., Daly, H.C.S., Stannard, K.J.D., 2011. Pathophysiology of Pain.
- Schwartz, D., Guleyupoglu, B., Koya, B., Stitzel, J.D., Gayzik, F.S., 2015. Development of a Computationally Efficient Full Human Body Finite Element Model. *Traffic Inj. Prev.* 16, S49–

S56. <https://doi.org/10.1080/15389588.2015.1021418>

- Seacrist, T., Saffioti, J., Balasubramanian, S., Kadlowec, J., Sterner, R., García-España, J.F., Arbogast, K.B., Maltese, M.R., 2012. Passive cervical spine flexion: The effect of age and gender. *Clin. Biomech.* 27, 326–333.
<https://doi.org/https://doi.org/10.1016/j.clinbiomech.2011.10.012>
- Senouci, M., FitzPatrick, D., Quinlan, J.F., Mullett, H., Coffey, L., McCormack, D., 2007. Quantification of the coupled motion that occurs with axial rotation and lateral bending of the head-neck complex: An experimental examination. *Proc. Inst. Mech. Eng. Part H J. Eng. Med.* 221, 913–919. <https://doi.org/10.1243/09544119JEIM265>
- Shah, A., 2014. Morphometric analysis of the cervical facets and the feasibility, safety, and effectiveness of Goel inter-facet spacer distraction technique. *J. craniovertebral junction spine* 5, 9–14. <https://doi.org/10.4103/0974-8237.135208>
- Sharma, S., Agarwal, A., 2008. Cervicalgia amongst helicopter pilots using helmet mounted devices. *Indian J. Aerosp. Med.* 52, 1–7.
- Shateri, H., 2012. Neck Response in Out of Position Rear Impact Scenarios. University of Waterloo.
- Shateri, H., Cronin, D.S., 2015. Out-of-Position Rear Impact Tissue-Level Investigation Using Detailed Finite Element Neck Model. *Traffic Inj. Prev.* 16, 698–708.
<https://doi.org/10.1080/15389588.2014.1003551>
- Shea, M., Edwards, W.T., White, A.A., Hayes, W.C., 1991. Variations of stiffness and strength along the human cervical spine. *J. Biomech.* 24, 95–107. [https://doi.org/10.1016/0021-9290\(91\)90354-p](https://doi.org/10.1016/0021-9290(91)90354-p)
- Shen, D., 2020. Investigation of Whiplash Associated Disorders using Finite Element Neck Models with Active Musculature in Frontal, Rear and Lateral Impact. University of Waterloo.
- Shen, Y.-W., Yang, Y., Liu, H., Qiu, Y., Li, M., Ma, L.-T., Gan, F.-J., 2022. Biomechanical Evaluation of Intervertebral Fusion Process After Anterior Cervical Discectomy and Fusion: A Finite Element Study. *Front. Bioeng. Biotechnol.* 10, 842382.
<https://doi.org/10.3389/fbioe.2022.842382>
- Shergold, O., Fleck, N., Radford, D., 2006. The uniaxial stress versus strain response of pig skin and

silicon rubber at low and high strain rates. *Int. J. Impact Eng.* 32, 1384–1402.

<https://doi.org/10.1016/j.ijimpeng.2004.11.010>

Shih, L., Patel, A., Diwan, S., 2019. Neck Pain BT - Academic Pain Medicine: A Practical Guide to Rotations, Fellowship, and Beyond, in: Khelemsky, Y., Malhotra, A., Gritsenko, K. (Eds.), . Springer International Publishing, Cham, pp. 219–225. https://doi.org/10.1007/978-3-030-18005-8_30

Siegmund, G.P., Blouin, J.-S., Brault, J.R., Hedenstierna, S., Inglis, J.T., 2007. Electromyography of superficial and deep neck muscles during isometric, voluntary, and reflex contractions. *J. Biomech. Eng.* 129, 66–77. <https://doi.org/10.1115/1.2401185>

Siegmund, G.P., Davis, M.B., Quinn, K.P., Hines, E., Myers, B.S., Ejima, S., Ono, K., Kamiji, K., Yasuki, T., Winkelstein, B.A., 2008. Head-turned postures increase the risk of cervical facet capsule injury during whiplash. *Spine (Phila. Pa. 1976)*. 33, 1643–1649. <https://doi.org/10.1097/BRS.0b013e31817b5bcf>

Siegmund, G.P., Myers, B.S., Davis, M.B., Bohnet, H.F., Winkelstein, B.A., 2001. Mechanical evidence of cervical facet capsule injury during whiplash: a cadaveric study using combined shear, compression, and extension loading. *Spine (Phila. Pa. 1976)*. 26, 2095–2101. <https://doi.org/10.1097/00007632-200110010-00010>

Siegmund, G.P., Winkelstein, B.A., Ivancic, P.C., Svensson, M.Y., Vasavada, A., 2009. The anatomy and biomechanics of acute and chronic whiplash injury. *Traffic Inj. Prev.* 10, 101–112. <https://doi.org/10.1080/15389580802593269>

Silva, A.J.C., Alves de Sousa, R.J., Fernandes, F.A.O., Ptak, M., Parente, M.P.L., 2022. Development of a Finite Element Model of the Cervical Spine and Validation of a Functional Spinal Unit. *Appl. Sci.* <https://doi.org/10.3390/app122111295>

SJØGAARD, G., KIENS, B., JØRGENSEN, K., SALTIN, B., 1986. Intramuscular pressure, EMG and blood flow during low-level prolonged static contraction in man. *Acta Physiol. Scand.* 128, 475–484. <https://doi.org/https://doi.org/10.1111/j.1748-1716.1986.tb08002.x>

Skaggs, D.L., Weidenbaum, M., Iatridis, J.C., Ratcliffe, A., Mow, V.C., 1994. Regional variation in tensile properties and biochemical composition of the human lumbar annulus fibrosus. *Spine (Phila. Pa. 1976)*. 19, 1310–1319. <https://doi.org/10.1097/00007632-199406000-00002>

- Snyder, R.G., Chaffin, D.B., Foust, D.R., 1975. Bioengineering study of basic physical measurements related to susceptibility to cervical hyperextension-hyperflexion injury. *Ann Arbor*.
- Solomonow, M., 2004. Ligaments: a source of work-related musculoskeletal disorders. *J. Electromyogr. Kinesiol.* 14, 49–60. <https://doi.org/https://doi.org/10.1016/j.jelekin.2003.09.011>
- Solomonow, M., Baratta, R. V, Zhou, B.-H., Burger, E., Zieske, A., Gedalia, A., 2003. Muscular dysfunction elicited by creep of lumbar viscoelastic tissue. *J. Electromyogr. Kinesiol.* 13, 381–396. [https://doi.org/https://doi.org/10.1016/S1050-6411\(03\)00045-2](https://doi.org/https://doi.org/10.1016/S1050-6411(03)00045-2)
- Solomonow, M., Zhou, B.H., Harris, M., Lu, Y., Baratta, R. V, 1998. The ligamento-muscular stabilizing system of the spine. *Spine (Phila. Pa. 1976).* 23, 2552–2562. <https://doi.org/10.1097/00007632-199812010-00010>
- Song, K.-S., Cho, J.H., Hong, J.-Y., Lee, J.H., Kang, H., Ham, D.-W., Ryu, H.-J., 2017. Neuropathic Pain Related with Spinal Disorders: A Systematic Review. *Asian Spine J.* 11, 661–674. <https://doi.org/10.4184/asj.2017.11.4.661>
- Sovellius, R., Oksa, J., Rintala, H., Huhtala, H., Siitonen, S., 2008. Neck Muscle Strain When Wearing Helmet and NVG During Acceleration on a Trampoline. *Aviat. Sp. Environ. Med.* 79.
- Srinivasan, S., Deepak, R., Yuvaraj, P., Davidson Jebaseelan, D., Yoganandan, N., Rajasekaran, S., 2021. Influence of Compressive Preloading on Range of Motion and Endplate Stresses in the Cervical Spine During Flexion/Extension, in: Lim, C.T., Leo, H.L., Yeow, R. (Eds.), 17th International Conference on Biomedical Engineering. Springer International Publishing, Cham, pp. 121–128.
- Standing, S., Borley, N.R., 2008. *Gray’s Anatomy: The Anatomical Basis of Clinical Practice*, ClinicalKey 2012. Churchill Livingstone/Elsevier.
- Steeds, C.E., 2009. The anatomy and physiology of pain. *Surg.* 27, 507–511. <https://doi.org/https://doi.org/10.1016/j.mpsur.2009.10.013>
- Steilen, D., Hauser, R., Woldin, B., Sawyer, S., 2014. Chronic neck pain: making the connection between capsular ligament laxity and cervical instability. *Open Orthop. J.* 8, 326–345. <https://doi.org/10.2174/1874325001408010326>
- Stemper, B.D., Yoganandan, N., Cusick, J.F., Pintar, F.A., 2006. Stabilizing effect of precontracted

neck musculature in whiplash. *Spine (Phila. Pa. 1976)*. 31, E733-8.

<https://doi.org/10.1097/01.brs.0000240210.23617.e7>

Stemper, B.D., Yoganandan, N., Pintar, F.A., 2004. Validation of a head-neck computer model for whiplash simulation. *Med. Biol. Eng. Comput.* 42, 333–338.

<https://doi.org/10.1007/BF02344708>

Stjernbrandt, A., Hoftun Farbu, E., 2022. Occupational cold exposure is associated with neck pain, low back pain, and lumbar radiculopathy. *Ergonomics* 65, 1276–1285.

<https://doi.org/10.1080/00140139.2022.2027030>

Storvik, S.G., Stemper, B.D., 2011. Axial head rotation increases facet joint capsular ligament strains in automotive rear impact. *Med. Biol. Eng. Comput.* 49, 153–161.

<https://doi.org/10.1007/s11517-010-0682-2>

Straker, L., Skoss, R., Burnett, A., Burgess-Limerick, R., 2009. Effect of visual display height on modelled upper and lower cervical gravitational moment, muscle capacity and relative strain. *Ergonomics* 52, 204–221. <https://doi.org/10.1080/00140130802331609>

Subramani, A. V, Whitley, P.E., Garimella, H.T., Kraft, R.H., 2020. Fatigue damage prediction in the annulus of cervical spine intervertebral discs using finite element analysis. *Comput. Methods Biomech. Biomed. Engin.* 23, 773–784. <https://doi.org/10.1080/10255842.2020.1764545>

Sun, B., Han, Q., Sui, F., Zhang, A., Liu, Y., Xia, P., Wang, J., Yang, X., 2023. Biomechanical analysis of customized cage conforming to the endplate morphology in anterior cervical discectomy fusion: A finite element analysis. *Heliyon* 9, e12923.

<https://doi.org/https://doi.org/10.1016/j.heliyon.2023.e12923>

Sun, Z., Lu, T., Li, J., Liu, J., Hu, Y., Mi, C., 2022. A finite element study on the effects of follower load on the continuous biomechanical responses of subaxial cervical spine. *Comput. Biol. Med.* 145, 105475. <https://doi.org/https://doi.org/10.1016/j.compbimed.2022.105475>

<https://doi.org/https://doi.org/10.1016/j.compbimed.2022.105475>

Swartz, E.E., Floyd, R.T., Cendoma, M., 2005. Cervical spine functional anatomy and the biomechanics of injury due to compressive loading. *J. Athl. Train.* 40, 155–161.

Tack, D., Bray-Miners, J., Nakaza, E.T., Osborne, A., Mangan, B., 2014. Griffon Helicopter Neck Strain Project: Part 1: Mission Function Task Analysis and Physical Demands Analysis Report. Part 2: Physical Demands Analysis Library.

- Takatori, R., Tokunaga, D., Inoue, N., Hase, H., Harada, T., Suzuki, H., H, I., Nishimua, T., An, H.S., Kubo, T., 2008. In vivo segmental motion of the cervical spine in rheumatoid arthritis patients with atlantoaxial subluxation. *Clinical Exp. Rheumatol.* 26.
- Tampier, C., Drake, J.D.M., Callaghan, J.P., McGill, S.M., 2007. Progressive disc herniation: an investigation of the mechanism using radiologic, histochemical, and microscopic dissection techniques on a porcine model. *Spine (Phila. Pa. 1976)*. 32, 2869–2874.
<https://doi.org/10.1097/BRS.0b013e31815b64f5>
- Tapanya, W., Puntumetakul, R., Swangnetr Neubert, M., Boucaut, R., 2021. Influence of neck flexion angle on gravitational moment and neck muscle activity when using a smartphone while standing. *Ergonomics* 64, 900–911. <https://doi.org/10.1080/00140139.2021.1873423>
- Thomae, M.K., Porteous, J.E., Brock, J.R., Allen, G.D., Heller, R.F., 1998. Back pain in Australian military helicopter pilots: a preliminary study. *Aviat. Space. Environ. Med.* 69, 468–473.
- Thuresson, M., Ang, B., Linder, J., Harms-Ringdahl, K., 2003. Neck muscle activity in helicopter pilots: effect of position and helmet-mounted equipment. *Aviat. Space. Environ. Med.* 74, 527–532.
- Thuresson, M., Äng, B., Linder, J., Harms-Ringdahl, K., 2005. Mechanical load and EMG activity in the neck induced by different head-worn equipment and neck postures. *Int. J. Ind. Ergon.* 35, 13–18. <https://doi.org/https://doi.org/10.1016/j.ergon.2004.06.008>
- Tierney, G.J., Simms, C.K., 2017. The effects of tackle height on inertial loading of the head and neck in Rugby Union: A multibody model analysis. *Brain Inj.* 31, 1925–1931.
<https://doi.org/10.1080/02699052.2017.1385853>
- Tomaszewski, K.A., Saganiak, T., Walocha, J., 2015. The biology behind the human intervertebral disc and its endplates. *Folia Morphol. (Warsz)*. 74.
- Tominaga, Y., Ndu, A.B., Coe, M.P., Valenson, A.J., Ivancic, P., IuM, S., Rubin, W., Panjabi, M., 2006. Neck ligament strength is decreased following whiplash trauma. *BMC Musculoskelet. Disord.* 7, 103.
- Tongprapai, W., Rattanapan, N., Torudom, Y., Sukjamsri, C., 2021. Development of a Ligamentous Finite Element Model of the Human Cervical Spine, in: 2021 IEEE National Biomedical Engineering Conference (NBEC). pp. 122–126.

<https://doi.org/10.1109/NBEC53282.2021.9618719>

- Toosizadeh, N., Haghpanahi, M., 2011. Generating a finite element model of the cervical spine: Estimating muscle forces and internal loads. *Sci. Iran.* 18, 1237–1245.
<https://doi.org/https://doi.org/10.1016/j.scient.2011.10.002>
- Torkamani, M.H., Mokhtarinia, H.R., Vahedi, M., Gabel, C.P., 2023. Relationships between cervical sagittal posture, muscle endurance, joint position sense, range of motion and level of smartphone addiction. *BMC Musculoskelet. Disord.* 24, 61. <https://doi.org/10.1186/s12891-023-06168-5>
- Treede, R.-D., Rief, W., Barke, A., Aziz, Q., Bennett, M.I., Benoliel, R., Cohen, M., Evers, S., Finnerup, N.B., First, M.B., Giamberardino, M.A., Kaasa, S., Kosek, E., Lavand'homme, P., Nicholas, M., Perrot, S., Scholz, J., Schug, S., Smith, B.H., Svensson, P., Vlaeyen, J.W.S., Wang, S.-J., 2015. A classification of chronic pain for ICD-11. *Pain* 156, 1003–1007.
<https://doi.org/10.1097/j.pain.000000000000160>
- Tsang, S.M.H., Szeto, G.P.Y., Lee, R.Y.W., 2013. Normal kinematics of the neck: the interplay between the cervical and thoracic spines. *Man. Ther.* 18, 431–437.
<https://doi.org/10.1016/j.math.2013.03.002>
- Ulrich, J.A., Liebenberg, E.C., Thuillier, D.U., Lotz, J.C., 2007. ISSLS Prize Winner: Repeated Disc Injury Causes Persistent Inflammation. *Spine (Phila. Pa. 1976)*. 32.
- Van den Oord, M.H.A.H., Frings-Dresen, M.H.W., Sluiter, J.K., 2012. Optimal helmet use and adjustments with respect to neck load: The experience of military helicopter aircrew. *Int. J. Ind. Ergon.* 42, 73–79. <https://doi.org/https://doi.org/10.1016/j.ergon.2011.09.001>
- van der Kraan, P.M., van den Berg, W.B., 2007. Osteophytes: relevance and biology. *Osteoarthr. Cartil.* 15, 237–244. <https://doi.org/https://doi.org/10.1016/j.joca.2006.11.006>
- Van Ee, C.A., Nightingale, R.W., Camacho, D.L., Chancey, V.C., Knaub, K.E., Sun, E.A., Myers, B.S., 2000. Tensile properties of the human muscular and ligamentous cervical spine. *Stapp Car Crash J.* 44, 85–102. <https://doi.org/10.4271/2000-01-SC07>
- van Heeswijk, V.M., Thambyah, A., Robertson, P.A., Broom, N.D., 2017. Posterolateral Disc Prolapse in Flexion Initiated by Lateral Inner Annular Failure: An Investigation of the Herniation Pathway. *Spine (Phila. Pa. 1976)*. 42.

- van Lopik, D.W., Acar, M., 2007. Dynamic verification of a multi-body computational model of human head and neck for frontal, lateral, and rear impacts. *Proc. Inst. Mech. Eng. Part K J. Multi-body Dyn.* 221, 199–217. <https://doi.org/10.1243/14644193JMBD89>
- Varghese, V., Baisden, J., Yoganandan, N., 2022. Normalization technique to build patient specific muscle model in finite element head neck spine. *Med. Eng. Phys.* 107, 103857. <https://doi.org/https://doi.org/10.1016/j.medengphy.2022.103857>
- Vasavada, A.N., Brault, J.R., Siegmund, G.P., 2007. Musculotendon and fascicle strains in anterior and posterior neck muscles during whiplash injury. *Spine (Phila. Pa. 1976)*. 32, 756–765. <https://doi.org/10.1097/01.brs.0000259058.00460.69>
- Vasavada, A.N., Peterson, B.W., Delp, S.L., 2002. Three-dimensional spatial tuning of neck muscle activation in humans. *Exp. Brain Res.* 147, 437–448. <https://doi.org/10.1007/s00221-002-1275-6>
- Vavalle, N.A., Davis, M.L., Stitzel, J.D., Gayzik, F.S., 2015. Quantitative Validation of a Human Body Finite Element Model Using Rigid Body Impacts. *Ann. Biomed. Eng.* 43, 2163–2174. <https://doi.org/10.1007/s10439-015-1286-7>
- Vavalle, N.A., Schoell, S.L., Weaver, A.A., Stitzel, J.D., Gayzik, F.S., 2014. Application of Radial Basis Function Methods in the Development of a 95th Percentile Male Seated FEA Model. *Stapp Car Crash J.* 58, 361–384. <https://doi.org/10.4271/2014-22-0013>
- Vergroesen, P.-P.A., Kingma, I., Emanuel, K.S., Hoogendoorn, R.J.W., Welting, T.J., van Royen, B.J., van Dieën, J.H., Smit, T.H., 2015. Mechanics and biology in intervertebral disc degeneration: a vicious circle. *Osteoarthr. Cartil.* 23, 1057–1070. <https://doi.org/https://doi.org/10.1016/j.joca.2015.03.028>
- Von Forell, G.A., Stephens, T.K., Samartzis, D., Bowden, A.E., 2015. Low Back Pain: A Biomechanical Rationale Based on “Patterns” of Disc Degeneration. *Spine (Phila. Pa. 1976)*. 40, 1165–1172. <https://doi.org/10.1097/BRS.0000000000000982>
- Wade, K.R., Robertson, P.A., Thambyah, A., Broom, N.D., 2014. How healthy discs herniate: a biomechanical and microstructural study investigating the combined effects of compression rate and flexion. *Spine (Phila. Pa. 1976)*. 39, 1018–1028. <https://doi.org/10.1097/BRS.0000000000000262>

- Walker, L.B., Harris, E.H., Pontius, U.R., 1973. Mass, Volume, Center of Mass and Mass Moment of Inertia of Head and Neck of Human Body, in: Stapp Car Crash Conference. pp. 525–537.
- Walocha, K.A.T.A.U.-K.S.A.U.-T.G.A.U.-J.A., 2015. The biology behind the human intervertebral disc and its endplates. *Biol. behind Hum. intervertebral disc its endplates*.
<https://doi.org/10.5603/FM.2015.0026>
- Wang, H., Wang, K., Deng, Z., Li, X., Qin, Y.-X., Zhan, H., Niu, W., 2019. Effects of facet joint degeneration on stress alterations in cervical spine C5–C6: A finite element analysis. *Math. Biosci. Eng.* 16, 7447–7457. <https://doi.org/10.3934/mbe.2019373>
- Wang, K., Wang, H., Deng, Z., Li, Z., Zhan, H., Niu, W., 2017. Cervical traction therapy with and without neck support: A finite element analysis. *Musculoskelet. Sci. Pract.* 28, 1–9.
<https://doi.org/https://doi.org/10.1016/j.msksp.2017.01.005>
- Wang MD, K., Jiang PhD, C., Wang PhD, L., Wang MD, H., Niu PhD, W., 2018. The biomechanical influence of anterior vertebral body osteophytes on the lumbar spine: A finite element study. *Spine J.* 18, 2288–2296. <https://doi.org/https://doi.org/10.1016/j.spinee.2018.07.001>
- Wang, S., Park, J., Wang, Y., 2021. Cross-cultural comparison of firefighters' perception of mobility and occupational injury risks associated with personal protective equipment. *Int. J. Occup. Saf. Ergon.* 27, 664–672. <https://doi.org/10.1080/10803548.2019.1607027>
- Wang, Y.-J., Shi, Q., Lu, W.W., Cheung, K.C.M., Darowish, M., Li, T.-F., Dong, Y.-F., Zhou, C.-J., Zhou, Q., Hu, Z.-J., Liu, M., Bian, Q., Li, C.-G., Luk, K.D.K., Leong, J.C.Y., 2006. Cervical intervertebral disc degeneration induced by unbalanced dynamic and static forces: a novel in vivo rat model. *Spine (Phila. Pa. 1976)*. 31, 1532–1538.
<https://doi.org/10.1097/01.brs.0000222019.84095.23>
- Ward, S.R., Winters, T.M., O'Connor, S.M., Lieber, R.L., 2020. Non-linear Scaling of Passive Mechanical Properties in Fibers, Bundles, Fascicles and Whole Rabbit Muscles. *Front. Physiol.* 11. <https://doi.org/10.3389/fphys.2020.00211>
- Warm, J., Matthews, G., Chiu, C.-Y., Werchan, P., Deaton, J., 2006. +Gz Acceleration Loss of Consciousness: Time Course of Performance Deficits With Repeated Experience. *Hum. Factors* 48, 109–120. <https://doi.org/10.1518/001872006776412144>

- Wawrose, R.A., Howington, F.E., LeVasseur, C.M., Smith, C.N., Couch, B.K., Shaw, J.D., Donaldson, W.F., Lee, J.Y., Patterson, C.G., Anderst, W.J., Bell, K.M., 2021. Assessing the biofidelity of in vitro biomechanical testing of the human cervical spine. *J. Orthop. Res. Off. Publ. Orthop. Res. Soc.* 39, 1217–1226. <https://doi.org/10.1002/jor.24702>
- Wheeldon, J.A., Pintar, F.A., Knowles, S., Yoganandan, N., 2006. Experimental flexion/extension data corridors for validation of finite element models of the young, normal cervical spine. *J. Biomech.* 39, 375–380. <https://doi.org/10.1016/j.jbiomech.2004.11.014>
- White, N.A., Danelson, K.A., Gayzik, F.S., Hsu, W., Powers, A., Stitzel, J.D., 2016. Effects of cervical arthroplasty on neck response during a simulated rotary-wing aircraft impact. *Int. J. Crashworthiness* 21, 323–337. <https://doi.org/10.1080/13588265.2016.1178365>
- White, N.A., Danelson, K.A., Gayzik, F.S., Stitzel, J.D., 2014. Head and neck response of a finite element anthropomorphic test device and human body model during a simulated rotary-wing aircraft impact. *J. Biomech. Eng.* 136, 1110011–1110018. <https://doi.org/10.1115/1.4028133>
- Winkelstein, B.A., Nightingale, R.W., Richardson, W.J., Myers, B.S., 2000. The cervical facet capsule and its role in whiplash injury: a biomechanical investigation. *Spine (Phila. Pa. 1976)*. 25, 1238–1246. <https://doi.org/10.1097/00007632-200005150-00007>
- Winters, J.M., 1995. How detailed should muscle models be to understand multi-joint movement coordination? *Hum. Mov. Sci.* 14, 401–442. [https://doi.org/https://doi.org/10.1016/0167-9457\(95\)00023-6](https://doi.org/https://doi.org/10.1016/0167-9457(95)00023-6)
- Winters, J.M., Stark, L., 1988. Estimated mechanical properties of synergistic muscles involved in movements of a variety of human joints. *J. Biomech.* 21, 1027–1041. [https://doi.org/https://doi.org/10.1016/0021-9290\(88\)90249-7](https://doi.org/https://doi.org/10.1016/0021-9290(88)90249-7)
- Winters, J.M., Stark, L., 1985. Analysis of Fundamental Human Movement Patterns Through the Use of In-Depth Antagonistic Muscle Models. *IEEE Trans. Biomed. Eng. BME-32*, 826–839. <https://doi.org/10.1109/TBME.1985.325498>
- Woo, S.L.-Y., Buckwalter, J.A., 1988. Injury and repair of the musculoskeletal soft tissues. Savannah, Georgia, June 18–20, 1987. *J. Orthop. Res.* 6, 907–931. <https://doi.org/10.1002/jor.1100060615>
- Wu, H., Liu, W., Mi, L., Liu, Q., 2023. Acute neck tendonitis with dyspnea: A case report. *World J. Clin. cases.* <https://doi.org/10.12998/wjcc.v11.i18.4419>

- Wu, S.-K., Kuo, L.-C., Lan, H.-C.H., Tsai, S.-W., Su, F.-C., 2010. Segmental Percentage Contributions of Cervical Spine During Different Motion Ranges of Flexion and Extension. *Clin. Spine Surg.* 23.
- Xu, Z., Li, Y., Huang, W., Wang, Z., Xu, X., Tian, S., 2023. Preliminary exploration of the biomechanical properties of three novel cervical porous fusion cages using a finite element study. *BMC Musculoskelet. Disord.* 24, 876. <https://doi.org/10.1186/s12891-023-06999-2>
- Yamada, H., 1977. *Strength of Biological Materials.*
- Yang, K.H., Hu, J., White, N.A., King, A.I., Chou, C.C., Prasad, P., 2006. Development of numerical models for injury biomechanics research: a review of 50 years of publications in the Stapp Car Crash Conference. *Stapp Car Crash J.* 50, 429–490. <https://doi.org/10.4271/2006-22-0017>
- Yang, K.H., Kish, V.L., 1988. Compressibility measurement of human intervertebral nucleus pulposus. *J. Biomech.* 21, 865.
- Yang, R.J., Wang, N., Tho, C.H., Bobineau, J.P., Wang, B.P., 2005. Metamodeling Development for Vehicle Frontal Impact Simulation. *J. Mech. Des.* 127, 1014–1020. <https://doi.org/10.1115/1.1906264>
- Ye, L., Chen, C., Liu, Y., Li, Z., Lu, G., 2022. Effect of cervical spine motion on displacement of posterolateral annulus fibrosus in cervical spondylotic radiculopathy with contained posterolateral disc herniation: a three-dimensional finite element analysis. *J. Orthop. Surg. Res.* 17, 548. <https://doi.org/10.1186/s13018-022-03450-5>
- Yoganandan, N., Halliday, A., Dickman, C., Benzel, E., 2005. *Practical Anatomy and Fundamental Biomechanics.* pp. 109–135. <https://doi.org/10.1016/B978-0-443-06616-0.50012-2>
- Yoganandan, N., Kumaresan, S., Pintar, F.A., 2001. Biomechanics of the cervical spine Part 2. Cervical spine soft tissue responses and biomechanical modeling. *Clin. Biomech. (Bristol, Avon)* 16, 1–27. [https://doi.org/10.1016/s0268-0033\(00\)00074-7](https://doi.org/10.1016/s0268-0033(00)00074-7)
- Yoganandan, N., Kumaresan, S., Voo, L., Pintar, F.A., 1997. Finite element model of the human lower cervical spine: parametric analysis of the C4-C6 unit. *J. Biomech. Eng.* 119, 87–92. <https://doi.org/10.1115/1.2796070>
- Yoganandan, N., Maiman, D.J., Pintar, F., Ray, G., Myklebust, J.B., Sances, A.J., Larson, S.J., 1988.

Microtrauma in the Lumbar Spine: A Cause of Low Back Pain. *Neurosurgery* 23.

Yow, B.G., Piscoya, A.S., Wagner, S.C., 2020. Cervical Spine Anatomy BT - Handbook of Spine Technology, in: Cheng, B. (Ed.), . Springer International Publishing, Cham, pp. 1–19.

https://doi.org/10.1007/978-3-319-33037-2_2-1

Yu, C.-C., Liu, P., Huang, D.-G., Jiang, Y.-H., Feng, H., Hao, D.-J., 2016. A new cervical artificial disc prosthesis based on physiological curvature of end plate: a finite element analysis. *Spine J.* 16, 1384–1391. <https://doi.org/10.1016/j.spinee.2016.06.019>

Zhang, H., Sang, D., Zhang, B., Ren, Y.-N., Wang, X., Feng, J.-J., Du, C.-F., Liu, B., Zhu, R., 2023. Parameter Study on How the Cervical Disc Degeneration Affects the Segmental Instantaneous Centre of Rotation. *J. Med. Biol. Eng.* 43, 163–175. <https://doi.org/10.1007/s40846-023-00779-y>

Zhang, Q.H., Teo, E.C., Ng, H.W., 2005. Development and validation of a CO-C7 FE complex for biomechanical study. *J. Biomech. Eng.* 127, 729–735. <https://doi.org/10.1115/1.1992527>

Zheng, L., Jahn, J., Vasavada, A.N., 2012. Sagittal plane kinematics of the adult hyoid bone. *J. Biomech.* 45, 531–536. <https://doi.org/10.1016/j.jbiomech.2011.11.040>

Zhou, X., Chen, X., Roos, P.E., Whitley, P., 2019. Effects of Head Supported Mass on Predicted Neck Musculoskeletal Loadings During Walking and Running.

<https://doi.org/10.1115/DETC2019-97389>

Appendices

Appendix A

Supplementary materials for Phase #1

Table A1: Design-space generated by LHS-based DOE for flexion

Simulation case	Variables for Flexion									
	Apic_lax	CL01_lax	CL12_lax	ISL12_lax	LCrx_lax	PA12_lax	PO12_lax	Tect_lax	Tran_lax	UCrx_lax
1	0	0	0	0	0	0	0	0	0	0
2	3.04023	5.49902	1.7561	1.57868	2.41751	0.390612	5.12119	2.00698	6.84701	5.17756
3	6.34957	4.05491	7.05208	0.039662	6.42	5.80899	7.64726	2.13457	6.40537	7.2664
4	5.62143	0.635808	7.6113	3.53327	0.886382	3.54519	3.32121	1.28339	6.33803	6.85486
5	5.94012	2.07656	5.98087	7.81638	2.76949	4.38684	4.51368	5.43163	0.003988	4.96829
6	6.96015	2.57506	1.66078	7.63211	7.35509	4.00334	1.36259	6.86667	2.3222	4.92647
7	2.20745	6.37287	4.54398	1.33789	5.57317	5.93506	4.07271	0.565969	4.78817	5.89657
8	7.44915	6.00139	4.22935	5.93594	1.39326	3.265	1.88949	6.26214	1.36422	1.97107
9	5.16206	2.01879	3.56072	7.16231	5.85469	0.558771	6.28956	5.7169	5.78484	3.24907
10	2.15405	7.12909	5.30978	6.6189	6.8367	1.43764	2.26141	6.15709	0.518635	0.997794
11	0.245529	0.02847	5.72517	7.3586	3.02014	7.95432	7.49117	5.06549	7.73209	4.48153
12	7.29611	6.52532	4.17022	1.05336	3.67709	3.43795	1.4624	3.3114	1.98106	7.65349
13	4.53497	0.138525	0.41737	2.87223	1.2219	1.66	7.92754	0.938413	0.122597	3.17943
14	2.07473	7.57491	1.03154	3.72472	4.7381	1.29528	0.068537	5.81194	0.381014	1.35201
15	5.43166	4.76316	2.12462	7.22412	5.08608	3.60579	4.88074	7.51317	4.17727	2.07901
16	1.49223	5.09348	4.80746	7.97917	3.10095	1.0917	5.79166	4.99328	7.00829	1.53354
17	1.13093	1.36282	6.86901	0.428833	1.5538	4.77059	7.00907	2.52664	4.48299	7.57365
18	3.20595	6.90087	4.02324	5.98767	4.10822	6.81708	1.747	6.44672	5.44316	6.89327
19	1.74735	6.73228	1.86227	0.612327	0.945224	1.73269	1.82473	3.17153	6.78611	7.97576
20	0.358675	1.19427	0.575744	1.83026	2.15675	3.67699	6.15034	6.09722	5.63304	3.10633
21	6.39055	6.19629	0.89135	6.95713	2.93972	0.289999	5.64962	0.545199	4.01058	5.68356
22	5.55091	7.83598	5.4544	2.42072	7.80543	0.036756	6.08616	1.18678	0.660441	0.907262
23	7.37493	1.86418	3.23106	4.30931	4.14965	6.23517	6.65221	3.33885	2.9665	2.58374
24	1.40722	2.92774	0.675201	0.82215	6.73764	6.49177	0.085051	1.05708	4.22947	4.04994
25	5.20519	3.1806	7.53922	5.86326	0.479781	2.81917	4.12597	1.37186	3.06143	5.56789
26	5.0358	1.43898	5.96148	0.524316	1.15528	0.56702	1.18438	7.65916	0.185284	2.36102
27	5.33852	2.29657	2.43235	1.88102	3.53903	6.67681	0.950707	7.11749	7.38392	7.44536
28	4.20519	1.78046	2.01713	0.087027	5.11909	1.52885	3.22968	0.695676	7.66025	0.738617
29	7.169	3.13252	5.86811	4.52744	0.180414	7.47617	2.41589	7.77754	0.406648	2.16521
30	6.84181	6.11022	6.82807	2.52017	5.25451	2.36184	3.03098	1.61345	2.64195	0.498144
31	2.58178	3.30862	5.75308	2.91655	3.90339	7.02311	6.02319	4.19238	3.58457	6.30301
32	6.29666	0.199535	0.258979	7.54942	2.71767	0.84369	5.56141	4.85374	1.80796	1.05607
33	0.207693	4.84267	3.25509	0.804803	3.56944	2.18916	3.73909	2.85834	3.2714	4.29184
34	3.67755	2.40178	0.524287	7.34944	5.38986	1.97035	3.83501	7.84447	7.13454	6.39978
35	0.029391	5.7566	2.96323	0.28435	2.21295	6.31482	4.7985	0.37054	0.303443	3.97738
36	7.72144	3.45455	2.205	2.27451	0.550704	1.9006	2.94602	3.07829	1.44618	0.104904
37	4.38649	2.61539	4.67708	4.78707	0.758122	4.25703	3.4632	5.58918	2.41392	2.85179
38	3.39167	4.89764	6.4469	5.35215	7.1079	0.700387	5.04499	3.74662	2.42466	0.877857
39	4.85808	5.23504	7.00117	4.07864	4.91857	7.52009	0.744366	7.25802	5.21147	3.91884
40	3.99605	0.938631	2.82259	4.42151	5.79458	7.63432	4.39149	4.5246	5.50994	3.61648
41	7.64335	5.37374	4.76358	6.26875	1.4747	5.8665	0.677199	2.64422	4.86925	1.80949
42	5.80728	0.557951	6.315	4.91046	6.11004	0.954641	6.56817	2.94351	5.84455	2.81952
43	3.24009	6.7042	1.39131	6.88157	3.82192	3.39237	1.06578	0.983442	5.40598	7.07807
44	7.5473	3.97576	4.30048	6.79475	7.47854	4.94342	7.83508	4.08661	4.41214	0.430729
45	2.81382	1.06051	0.176427	7.90699	7.19777	2.07628	6.4974	2.38552	6.56956	1.56047
46	6.53974	4.21584	1.82501	3.91324	4.62234	7.05029	5.46468	1.88286	3.81732	6.10152
47	1.63591	0.391203	3.36998	6.47738	5.98552	2.49106	1.02505	5.19039	3.48507	2.31968
48	1.8859	1.28065	2.82903	0.679965	0.278714	3.03991	5.22138	6.31964	3.7929	4.40336
49	6.65201	2.89744	5.07468	3.45862	7.35093	5.03568	4.73852	1.6427	3.21979	4.59427
50	4.5236	4.63397	4.44134	0.199555	5.42617	6.18835	0.517156	7.36181	4.69881	2.66461

Table A1 (Continued): Design-space generated by LHS-based DOE for flexion

Simulation case	Variables for Flexion									
	Apic_lax	CL01_lax	CL12_lax	ISL12_lax	LCrx_lax	PA12_lax	PO12_lax	Tect_lax	Tran_lax	UCrx_lax
51	7.0826	0.6495	1.5959	6.77297	2.83902	2.53821	7.91025	6.66164	1.03574	3.76599
52	6.70783	1.48779	7.93732	6.37277	4.03119	2.71703	0.628762	2.49993	2.82178	4.26543
53	2.61565	4.46254	7.22509	6.45016	4.22123	2.89996	7.0626	7.52779	6.0771	0.631425
54	7.85171	0.740403	6.2919	1.2469	1.123	6.13397	2.02801	4.55792	1.5138	7.72195
55	0.643147	7.48037	2.0371	2.43716	2.04914	3.74783	3.97861	3.54414	5.14245	5.04979
56	4.63511	6.60445	3.05722	3.14429	4.48932	1.18373	7.56894	3.83391	7.53472	5.48519
57	4.12283	5.71306	7.79889	0.394562	3.17773	1.54321	0.290603	4.6365	7.04564	1.65687
58	3.47285	5.26583	7.38814	1.0081	2.65711	4.68039	7.67916	0.741703	3.9534	3.51694
59	5.32673	3.90618	0.045691	0.941056	1.85462	6.92497	3.56504	5.87648	1.58182	2.67979
60	0.564717	4.59593	7.84813	5.62351	4.40423	3.87251	6.44653	3.67341	6.28658	3.86985
61	1.94831	0.849157	2.51014	3.23903	0.1405	0.48184	4.29284	2.99001	7.89246	5.97488
62	2.27379	1.58134	3.75641	3.22279	6.6017	7.77247	7.23482	7.92215	0.602561	1.26915
63	6.02208	6.43151	2.39816	4.74597	5.95629	7.75012	4.58293	6.50792	4.65338	3.35192
64	0.940207	2.21847	5.40398	7.51004	3.36809	1.23911	0.476105	4.75922	2.83104	6.01569
65	3.92766	3.67847	6.62505	4.5056	5.58641	3.09724	6.76476	4.35919	7.78542	3.70534
66	3.80248	5.97448	0.148721	6.19165	2.26734	5.37881	1.37446	6.71831	1.09462	7.80532
67	6.14901	3.48862	7.50078	1.46746	6.98043	0.783554	2.33209	6.61368	5.314	3.00443
68	1.18409	2.42833	6.54399	5.01089	6.49838	7.35838	0.820025	5.92275	1.2597	7.15273
69	3.13842	7.97419	3.67777	3.02682	6.63687	7.89817	5.87688	5.14551	2.72195	0.687912
70	0.780023	7.63249	1.36596	5.19663	3.29283	4.34989	2.75684	7.70135	3.68658	6.73053
71	0.107075	5.6224	1.19181	1.62778	3.41316	2.29988	3.91142	6.90318	7.49731	2.45001
72	1.79062	4.12271	4.98712	2.59632	1.37309	3.1623	5.70937	2.25704	3.08501	4.79325
73	3.54571	3.80237	7.28379	2.73972	6.87677	4.69625	4.63836	1.43189	7.31941	0.254621
74	0.82496	2.7455	5.13019	2.21355	6.16507	0.129325	5.92518	3.93274	1.73106	6.58868
75	3.59343	6.96666	5.644	4.65746	1.93063	4.52269	6.7903	6.9738	5.08069	1.75504
76	1.3134	2.99085	2.28209	7.69767	6.31534	2.1662	1.95891	5.55742	0.942918	7.91291
77	3.7961	7.42985	3.84488	1.41495	4.97128	5.58872	4.93107	2.06461	7.23401	4.63211
78	6.5679	2.13118	1.46129	3.66861	7.85929	1.85787	3.67545	7.09841	0.816744	5.75164
79	7.7592	7.85676	3.13415	5.53563	1.73653	5.70344	5.33899	0.093725	6.49352	4.69776
80	5.70235	1.62747	7.70918	7.08112	1.95826	6.43726	0.402701	4.26462	6.7002	7.27351
81	4.31852	4.40109	7.1409	1.98297	4.3425	5.32947	4.25627	5.27231	2.51771	6.17107
82	2.82938	3.75673	6.76797	1.19464	0.586443	4.52873	0.237239	5.37688	0.793923	0.02032
83	2.40633	0.323139	6.16947	4.2489	1.04282	0.240168	7.36042	1.50372	6.87241	5.14989
84	4.10014	4.34697	3.44133	3.87103	0.003718	3.9226	2.52696	2.73757	2.17285	7.41861
85	2.91694	3.58298	5.22266	3.62643	7.59431	5.43839	5.30599	0.85487	5.96441	6.63237
86	6.13468	3.37212	4.11123	4.17775	2.51425	7.30781	3.1499	3.98676	1.16955	4.17155
87	7.25991	7.04726	6.13933	4.01536	7.18347	4.05018	2.62389	0.246207	4.60309	6.36685
88	0.654711	5.46436	6.66492	1.75203	6.27652	2.62942	6.33576	4.84575	1.91539	1.40568
89	0.455295	1.72987	0.785623	5.33003	5.23239	6.58103	1.54265	4.43637	5.69961	2.96573
90	6.93675	0.98318	3.48942	4.94227	7.99166	5.12235	3.26656	2.75013	1.64927	2.24769
91	7.98618	7.2904	4.92456	5.15526	2.48329	4.85709	2.11467	2.29621	6.00538	5.35597
92	4.7108	4.98622	1.11087	6.70646	5.73692	5.19164	3.47795	0.180451	3.35435	5.63514
93	4.98494	5.05832	3.95778	2.79426	3.75348	4.19582	2.42897	3.44042	2.26044	1.88574
94	1.25914	0.416117	4.48123	2.12733	7.61817	7.19512	6.91407	1.73799	4.29141	0.403475
95	1.57371	5.89838	2.71157	5.45116	0.351396	1.02506	2.7049	0.031963	7.98148	6.50239
96	2.7202	2.74882	0.334937	5.80668	1.62472	6.71325	2.86705	0.482483	3.40528	1.15092
97	0.982732	6.26551	2.58719	6.13753	7.68877	2.98021	7.11998	1.84264	4.06326	0.236953
98	5.83963	6.83267	1.2196	3.35019	4.812	7.1821	1.28475	7.33146	6.17753	3.44767
99	2.44013	7.20697	0.884075	5.73363	4.60142	5.99903	1.65639	6.01882	2.04907	5.25812
100	4.80654	7.7164	5.51863	2.03061	0.7261	5.56819	7.32172	3.60757	4.94554	7.01337

Table A2: Design-space generated by LHS-based DOE for extension

Simulation case	Variables for Extension			
	AA12_lax	AO12_lax	CL01_lax	CL12_lax
1	0	0	0	0
2	4.49754	4.14054	1.14957	0.524259
3	6.49819	3.13167	7.70785	0.01425
4	0.555962	0.933976	2.3934	4.51428
5	0.90181	5.94891	0.237378	6.06999
6	3.03178	5.05549	5.21382	2.28951
7	4.00735	1.93605	7.55576	5.11424
8	5.73751	0.442382	6.06355	5.53339
9	7.44495	7.67247	0.958203	1.94889
10	3.87206	7.52641	6.95934	2.95226
11	1.29747	3.8607	4.59037	5.06118
12	2.48585	0.165873	2.05568	7.22367
13	7.26495	1.14008	4.78508	4.32017
14	5.43897	2.59988	3.44229	7.36923
15	2.15476	7.23722	6.6608	3.75199
16	6.86185	1.46138	5.49468	2.72032
17	5.03004	3.35357	0.439592	0.830112
18	0.295334	6.70438	4.08888	6.75149
19	7.92697	5.61816	3.05977	3.52315
20	1.59738	5.33884	1.81647	1.44712
21	2.57129	6.40475	2.63756	1.49825
22	3.30441	4.70682	6.42048	7.82144
23	5.86922	2.40641	3.80898	6.38734

Table A3: Design-space generated by LHS-based DOE for axial rotation

Simulation cases	Variables for Axial Rotation							
	AA12_lax	AIAT_lax	Alar_lax	CL01_lax	CL12_lax	ISL12_lax	PA12_lax	Tect_lax
1	0	0	0	0	0	0	0	0
2	4.49364	3.90154	7.93247	4.07461	3.11397	0.343538	7.32232	7.9888
3	2.70648	4.98212	6.85995	5.2797	3.9919	5.84469	1.72118	3.54394
4	0.135548	2.6805	4.2976	3.71879	4.10992	7.17848	5.8137	3.16545
5	5.27299	3.06859	2.08519	5.67787	3.66233	1.15816	4.02354	6.7532
6	1.02889	1.10433	4.02377	3.48457	0.964908	4.51591	0.029381	6.9685
7	3.26665	2.25571	5.4883	1.76807	2.14363	5.85823	0.895245	3.77581
8	1.86425	6.26566	7.64872	1.6223	0.570036	7.68857	7.85618	0.179805
9	7.63577	1.28431	1.13308	0.495963	4.70197	5.65951	2.31202	0.823267
10	3.1296	6.60317	4.61062	2.64775	5.66883	7.9441	3.0387	5.40689
11	0.396912	7.49244	2.73768	4.98492	4.86293	2.05851	6.82183	4.02514
12	7.00374	7.57358	7.36484	6.36324	5.16491	5.44823	5.36728	4.73746
13	6.69975	1.98674	5.87611	7.23053	6.95923	6.26237	4.92278	0.510779
14	3.00548	3.63126	1.20052	4.7481	7.38231	7.76314	5.19278	5.00051
15	4.65533	6.95976	2.94978	0.647724	7.73595	6.77519	2.4985	7.05546
16	2.23255	5.90136	3.31745	3.84059	6.1443	1.99778	3.3358	2.29894
17	1.60596	2.05649	5.52978	6.76743	7.88738	3.64869	4.43237	7.6926
18	4.77122	2.38242	1.01744	0.122467	2.88322	2.28783	2.63236	4.20357
19	2.62326	4.33591	5.67812	7.60238	6.52935	6.14018	3.93659	1.16425
20	0.551359	3.55986	3.10828	2.04388	0.407328	1.35256	1.12571	7.42133
21	6.40281	4.08953	3.36295	4.22157	5.49915	3.75609	0.767055	1.26873
22	1.12077	7.77737	6.63517	3.15978	5.90901	3.16459	5.47958	0.395269
23	7.37652	4.0455	4.41006	7.04674	1.66283	4.9929	6.34195	1.66259
24	2.13759	3.2594	5.34091	5.81871	1.46057	6.35925	7.90112	1.93058
25	7.68582	6.33065	7.19133	5.24224	6.00145	0.76732	5.6547	0.106035
26	7.42646	0.200336	3.6563	6.23393	6.76963	1.26331	7.20887	7.52529
27	7.97863	0.017486	4.99872	2.52323	2.27032	7.45599	0.53938	5.59478
28	6.23814	0.750863	6.98394	6.48202	1.91683	7.32601	2.14554	0.958391
29	7.08265	2.84733	2.17599	5.9756	2.38942	4.76524	7.49239	3.38947
30	5.57052	6.16196	6.77487	1.4551	7.77151	0.704961	3.74708	2.25689
31	3.77407	3.43487	0.281788	6.9329	0.756196	3.5651	5.89674	5.61555
32	1.30672	0.56164	2.62019	7.85494	7.58321	6.80995	0.468881	2.56073
33	0.24105	1.77863	6.56052	4.5302	5.76736	1.6426	0.698978	4.61362
34	5.49198	0.390449	3.52239	0.382982	0.213597	4.40155	1.64039	6.26391
35	0.067873	6.5039	6.35448	2.94979	1.406	5.56819	0.318312	4.8416
36	1.51425	6.77207	2.4293	5.02598	4.90705	2.66368	1.41165	3.31225
37	6.46674	4.65259	7.53257	2.33043	3.25381	1.51836	6.7191	2.73304
38	4.97347	4.52319	3.88982	7.39457	0.639913	4.24785	4.8059	2.92686
39	7.18068	4.24851	5.22398	0.056329	0.347051	6.96203	2.2482	5.04748
40	5.90022	7.89288	1.81146	1.99965	0.883522	0.488771	7.08946	6.91607
41	3.97911	0.950709	0.564775	0.803635	6.61994	1.01173	3.44059	1.47218
42	5.21016	4.73941	5.99521	1.12998	6.90778	0.918212	7.67019	3.02668
43	4.7883	2.46926	5.77889	4.54095	3.85019	2.24083	4.28622	4.37936
44	2.28051	7.74668	0.210736	4.86531	3.79826	1.86699	6.19901	0.898504
45	4.12778	7.07941	5.08536	6.59592	1.24266	5.02507	1.2283	4.16631
46	4.18369	5.19419	0.686567	6.81795	3.54357	3.03978	5.02757	7.2242
47	2.39525	0.684799	2.00522	3.44363	7.09653	4.13393	3.14609	4.45871
48	2.82426	3.74884	7.43336	1.89419	1.68746	7.15928	5.52041	5.27144
49	6.02583	7.35737	6.23119	5.92053	2.23589	0.405854	2.89345	2.75876
50	6.60752	5.52006	4.7378	5.582	0.114727	6.66854	6.55304	5.80717

Table A3 (Continued): Design-space generated by LHS-based DOE for axial rotation

Simulation cases	Variables for Axial Rotation							
	AA12_lax	AIAT_lax	Alar_lax	CL01_lax	CL12_lax	ISL12_lax	PA12_lax	Tect_lax
51	0.614887	3.11835	1.35391	4.38473	4.26891	5.15336	5.97712	6.37286
52	4.35088	4.84638	6.11611	7.99813	2.71888	0.095568	4.33392	1.89401
53	3.86432	0.30682	4.84008	3.99857	6.391	7.56498	1.84444	2.03566
54	3.61975	1.48013	1.67385	2.22983	5.44381	6.082	6.2962	3.64538
55	0.862367	5.77849	2.37308	3.03237	1.82989	4.05396	1.02146	7.8021
56	6.88654	1.85937	1.57367	5.3831	6.26342	2.38923	6.64252	1.35325
57	6.14623	5.09369	0.876347	2.42112	1.11067	4.55614	6.97063	3.9337
58	5.03987	5.48729	7.76793	7.40409	3.09049	3.29445	0.195096	6.09049
59	7.8403	2.98252	1.45672	3.60655	7.42462	3.45716	7.6036	7.33205
60	0.789504	5.68883	4.44982	2.83186	5.0472	2.60255	2.83447	6.45069
61	2.94575	6.04404	0.736911	0.323771	4.64007	0.205871	3.4934	2.42746
62	3.35868	1.00696	0.001399	1.03239	3.35398	1.67487	2.55493	5.93556
63	1.96263	1.38223	7.16063	7.74126	4.36506	5.26501	1.9535	6.00593
64	1.42121	2.56085	2.8189	6.20441	7.20954	3.83253	4.65576	5.19925
65	5.76159	6.8848	3.05632	1.34658	5.26943	2.8608	3.69976	0.323416
66	5.68141	1.62293	3.70751	0.880498	2.57116	2.89348	1.5172	6.63051
67	3.55232	5.3174	4.08811	1.21969	4.51697	4.89462	4.68556	1.78712
68	1.71457	7.20997	0.47094	3.29139	2.78264	6.53465	4.16776	0.641556

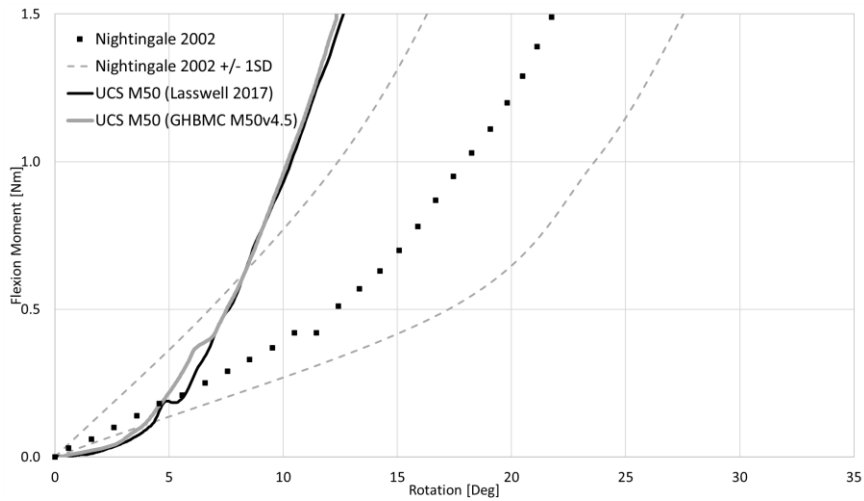


Figure A1: Initial verification of the extracted UCS_{M50} model from GHBMCM50 v4.5 with the UCS_{M50} model reported by Lasswell et al. (2017) showed similarities in the global (C0-C2) ROM in flexion.

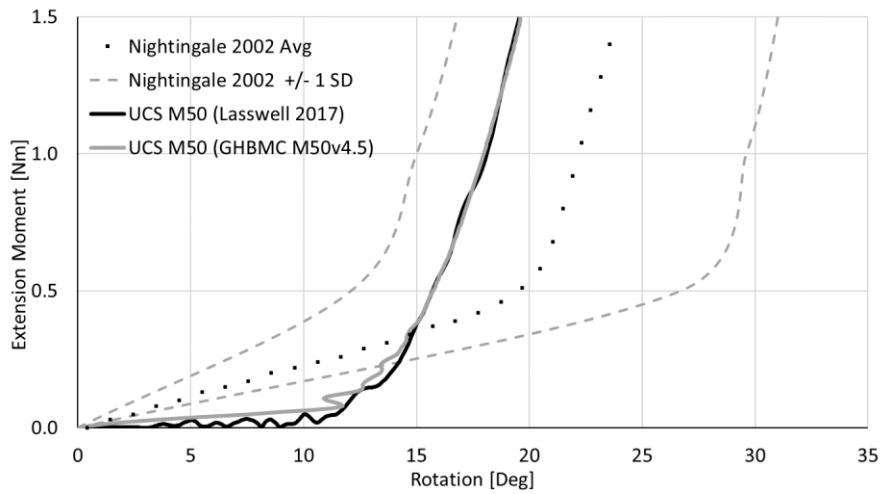


Figure A2: Initial verification of the extracted UCS_{M50} model from GHBMCM50 v4.5 with the UCS_{M50} model reported by Lasswell et al. (2017) showed similarities in the global (C0-C2) ROM in extension.

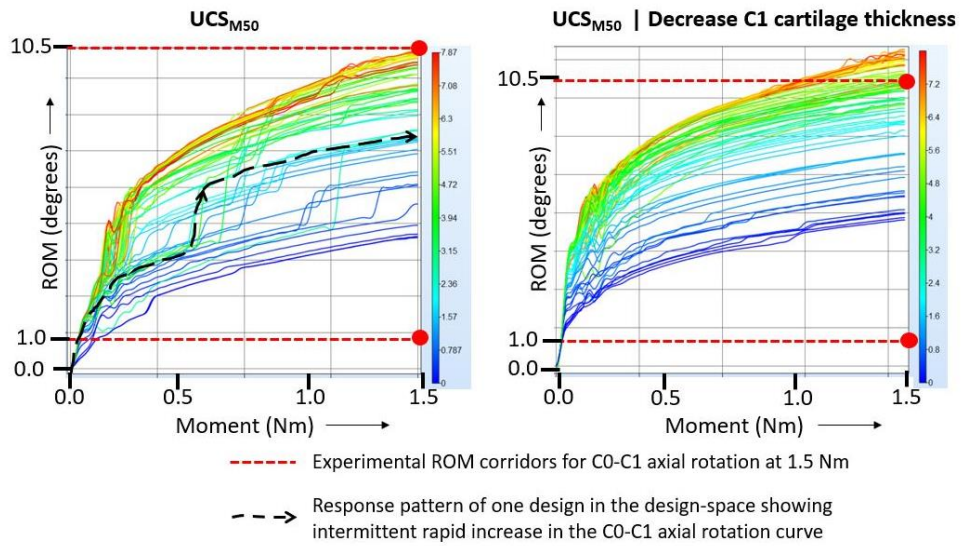


Figure A3: Moment-rotation plots for the original UCS_{M50} model, demonstrating abrupt jumps in rotation (left) and the UCS_{M50}-Cartilage (right) demonstrating a relatively continuous rotation response.

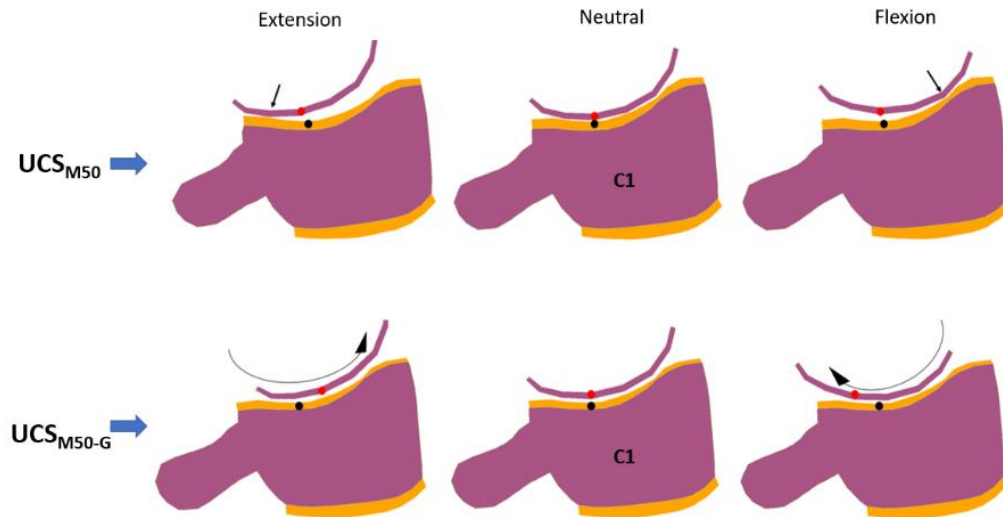


Figure A4: Illustration of the relative motion of C0 over C1 in the UCS_{M50} and UCS_{M50-G} models, demonstrating the effect of geometrical enhancements in the model. The straight arrow in UCS_{M50} flexion and extension identifies the region where the elements in the C1 facets limit relative motion.

Table A4: Model assessment with geometrical enhancements

	Loading Mode	Level	Experiment		Model (degree)			Percentage Difference		Percentage Change			Percentage Error (Exp. Mean and Model)	
			Mean (degree)	UCS _{M59}	UCS _{M59-Carilage}	UCS _{M59-Carilage} / UCS _{M59-C}	UC _{M59} and UCS _{M59-Carilage}	UC _{M59-Carilage} and UCS _{M59-C}	UCS _{M59} and UCS _{M59-Carilage}	UCS _{M59-Carilage} and UCS _{M59-C}	Exp. and UCS _{M59-Carilage}	Exp. and UCS _{M59-C}		
Neutral Zone	Flexion	C0-C1	10.5	1.4	9.2	12.4	147%	30%	554%	35%	13%	18%		
		C1-C2	7.6	0.1	1.4	1.4	173%	5%	1260%	5%	82%	81%		
	Extension	C0-C1	10.4	2.0	5.3	8.6	90%	47%	165%	62%	49%	17%		
		C1-C2	8.1	11.0	8.6	11.5	24%	28%	-22%	33%	6%	41%		
0.5 Nm	Flexion	C0-C1	13.0	4.7	15.1	15.6	105%	3%	222%	3%	16%	20%		
		C1-C2	11.5	2.9	4.5	4.3	44%	4%	57%	-4%	61%	62%		
	Extension	C0-C1	12.6	3.3	10.6	14.3	105%	30%	219%	35%	16%	13%		
		C1-C2	10.0	12.4	12.7	12.9	2%	2%	2%	2%	27%	29%		
1.0 Nm	Flexion	C0-C1	13.5	6.2	16.7	16.5	92%	1%	169%	-1%	23%	22%		
		C1-C2	12.3	4.0	7.0	6.6	55%	6%	76%	-6%	43%	46%		
	Extension	C0-C1	13.2	4.7	13.9	16.2	99%	15%	196%	16%	5%	23%		
		C1-C2	10.1	13.3	13.5	13.8	2%	2%	2%	2%	34%	37%		
1.5 Nm	Flexion	C0-C1	14.4	7.3	16.8	17.0	79%	1%	130%	1%	17%	18%		
		C1-C2	12.7	5.0	9.1	8.8	58%	3%	82%	-3%	28%	31%		
	Extension	C0-C1	14.4	5.7	15.2	17.5	91%	14%	167%	15%	6%	21%		
		C1-C2	10.5	13.9	13.9	14.6	0%	5%	0%	5%	32%	39%		
Average	C0-C1 Flexion	C0-C1	12.9	4.9	14.4	15.4	106%	9%	269%	10%	17%	20%		
		C1-C2	12.9	4.9	14.4	15.4	106%	9%	269%	10%	17%	20%		
	C1-C2 Flexion	C0-C1	12.7	3.9	11.3	14.1	96%	26%	187%	32%	19%	19%		
		C1-C2	11.0	3.0	5.5	5.3	82%	4%	369%	-2%	54%	55%		
C1-C2 Extension	C0-C1	9.7	12.7	12.2	13.2	7%	9%	-5%	11%	25%	36%			
	C1-C2	9.7	12.7	12.2	13.2	7%	9%	-5%	11%	25%	36%			

Table A5: Verifying the UCS_{M50-Opt} with the target experimental mean response set during optimization. Validating the UCS_{M50-Opt} intervertebral responses with another independent data set from Oda et al. (1992)

		Range of Motion (degrees)					Percentage error between Model Response and Experimental Mean				
		Experimental Mean		GHBMc M50 UCS v4.5			UCS M50 and Experimental Mean		UCS M50-Opt and Experimental Mean		
		Target	Oda et al. (1992)	UCS M50	GHBMc M50	UCS M50-Opt	Target	Oda et al. (1992)	Target	Oda et al. (1992)	Oda et al. (1992)
Flexion	NZ	CO-C1	10.5	6.7	1.4	7.3	87%	79%	31%	8%	
		CI-C2	7.6	3.6	0.1	6.9	99%	97%	9%	92%	
	0.5 Nm	CO-C1	13	10.6	4.70	10.90	64%	56%	16%	3%	
		CI-C2	11.5	9.4	2.86	11.16	75%	70%	3%	19%	
	1.0 Nm	CO-C1	13.5	11.5	6.20	12.80	54%	46%	5%	11%	
		CI-C2	12.3	10.3	4.00	13.08	67%	61%	6%	27%	
Extension	1.5 Nm	CO-C1	14.4	12.7	7.30	13.62	49%	43%	5%	7%	
		CI-C2	12.7	10.9	5.00	14.30	61%	54%	13%	31%	
	NZ	CO-C1	10.4	8.3	2.00	5.50	81%	76%	47%	34%	
		CI-C2	8.1	3.3	11.00	5.60	36%	233%	31%	70%	
	0.5 Nm	CO-C1	12.6	12.1	3.32	9.70	74%	73%	23%	20%	
		CI-C2	10	6.45	12.40	8.57	24%	92%	14%	33%	
R-Axial Rotation	1.0 Nm	CO-C1	13.2	12.75	4.70	12.12	64%	63%	8%	5%	
		CI-C2	10.1	7.09	13.30	9.47	32%	88%	6%	34%	
	1.5 Nm	CO-C1	14.4	13.5	5.70	13.80	60%	58%	4%	2%	
		CI-C2	10.5	7.3	13.90	10.00	32%	90%	5%	37%	
	NZ	CO-C1	0.9	1.5	1.70	1.20	89%	13%	33%	20%	
		CI-C2	24.5	17.7	21.00	21.30	14%	19%	13%	20%	
L-Axial Rotation	0.5 Nm	CO-C1	3.4	4.6	5.00	4.23	47%	9%	24%	8%	
		CI-C2	32.5	33.6	21.90	30.00	33%	35%	8%	11%	
	1.0 Nm	CO-C1	4.1	4.85	6.60	5.09	61%	36%	24%	5%	
		CI-C2	34	35.2	24.70	30.70	27%	30%	10%	13%	
	1.5 Nm	CO-C1	6	6	7.30	5.85	22%	22%	3%	3%	
		CI-C2	34	35.3	26.50	31.00	22%	25%	9%	12%	
L-Axial Rotation	NZ	CO-C1	0.9	1.5	1.70	1.20	89%	13%	33%	20%	
		CI-C2	30.4	15	21.00	21.30	31%	40%	30%	42%	
	0.5 Nm	CO-C1	1.8	5.5	5.00	4.23	178%	9%	135%	23%	
		CI-C2	34.6	25.4	21.90	30.00	37%	14%	13%	18%	
	1.0 Nm	CO-C1	2.5	6.6	6.60	5.09	164%	0%	104%	23%	
		CI-C2	36	27.2	24.70	30.70	31%	9%	15%	13%	
1.5 Nm	CO-C1	3.3	6.7	7.30	5.85	121%	9%	77%	13%		
	CI-C2	37.4	27.5	26.50	31.00	29%	4%	17%	13%		

Table A6: Percentage change in ROM values in the LS models with after enhancements to the UCS and facet cartilage in flexion

Flexion	Levels	LS models			% Change	
		LS _{M50}	LS _{M50-Opt}	LS _{M50-FC-Opt}	LS _{M50} and LS _{M50-Opt}	LS _{M50-Opt} and LS _{M50-FC-Opt}
0.5 Nm	C0-C1	4.45	11.42	11.50	157%	1%
	C1-C2	2.91	11.39	11.42	292%	0%
	C2-C3	2.82	2.81	2.86	0%	2%
	C3-C4	2.68	2.72	2.70	1%	-1%
	C4-C5	2.48	2.47	2.46	0%	0%
	C5-C6	2.19	2.18	2.26	-1%	4%
	C6-C7	2.53	2.54	2.51	1%	-1%
1.0 Nm	C0-C1	7.57	12.35	12.85	63%	4%
	C1-C2	4.04	11.97	12.18	196%	2%
	C2-C3	4.19	5.42	5.23	29%	-4%
	C3-C4	3.64	3.50	3.55	-4%	1%
	C4-C5	3.77	3.58	3.28	-5%	-8%
	C5-C6	3.04	3.19	3.55	5%	11%
	C6-C7	3.65	3.64	3.62	0%	-1%
1.5 Nm	C0-C1	7.57	12.22	12.60	61%	3%
	C1-C2	7.92	15.30	15.63	93%	2%
	C2-C3	4.29	5.70	5.69	33%	0%
	C3-C4	3.64	3.69	3.55	2%	-4%
	C4-C5	5.76	5.41	5.26	-6%	-3%
	C5-C6	3.04	3.30	3.63	9%	10%
	C6-C7	4.65	4.67	4.69	0%	0%

Table A7: Percentage change in ROM values in the LS models with after enhancements to the UCS and facet cartilage in extension

Extension	Levels	LS models			% Change	
		LS _{M50}	LS _{M50-Opt}	LS _{M50-FC-Opt}	LS _{M50} and LS _{M50-Opt}	LS _{M50-Opt} and LS _{M50-FC-Opt}
0.5 Nm	C0-C1	2.78	9.92	10.13	256%	2%
	C1-C2	12.83	8.81	8.62	-31%	-2%
	C2-C3	4.28	4.28	2.44	0%	-43%
	C3-C4	3.52	3.63	1.33	3%	-63%
	C4-C5	4.03	3.94	1.58	-2%	-60%
	C5-C6	4.25	4.28	1.61	1%	-62%
	C6-C7	3.50	3.49	2.48	0%	-29%
1.0 Nm	C0-C1	3.77	11.81	12.20	214%	3%
	C1-C2	14.32	10.31	9.70	-28%	-6%
	C2-C3	4.97	4.99	3.36	0%	-33%
	C3-C4	4.14	4.18	2.49	1%	-40%
	C4-C5	5.04	4.78	2.37	-5%	-50%
	C5-C6	5.27	5.31	2.52	1%	-53%
	C6-C7	4.36	4.39	3.51	1%	-20%
1.5 Nm	C0-C1	4.88	13.00	13.40	167%	3%
	C1-C2	15.39	13.36	10.82	-13%	-19%
	C2-C3	5.19	3.96	3.96	-24%	0%
	C3-C4	4.71	4.55	3.37	-3%	-26%
	C4-C5	5.85	6.58	3.07	12%	-53%
	C5-C6	5.99	5.54	3.14	-7%	-43%
	C6-C7	5.08	5.16	4.70	2%	-9%

Table A8: Percentage change in ROM values in the LS models with after enhancements to the UCS and facet cartilage in axial rotation

Axial Rotation	Levels	LS models			% Change	
		LS _{M50}	LS _{M50-Opt}	LS _{M50-FC-Opt}	LS _{M50} and LS _{M50-Opt}	LS _{M50-Opt} and LS _{M50-FC-Opt}
0.5 Nm	C0-C1	3.85	4.41	4.30	15%	-2%
	C1-C2	23.53	30.70	30.77	30%	0%
	C2-C3	3.38	3.37	1.44	0%	-57%
	C3-C4	3.18	3.20	1.92	1%	-40%
	C4-C5	3.16	3.16	2.23	0%	-29%
	C5-C6	3.07	3.07	2.16	0%	-30%
	C6-C7	2.72	2.71	1.67	0%	-38%
1.0 Nm	C0-C1	5.78	6.78	5.25	17%	-23%
	C1-C2	26.76	33.50	32.78	25%	-2%
	C2-C3	4.01	4.08	1.95	2%	-52%
	C3-C4	4.07	4.10	2.98	1%	-27%
	C4-C5	4.29	4.27	3.39	0%	-21%
	C5-C6	4.34	4.37	3.21	1%	-27%
	C6-C7	3.61	3.66	2.59	2%	-29%
1.5 Nm	C0-C1	6.11	8.72	4.51	43%	-48%
	C1-C2	29.92	34.11	35.00	14%	3%
	C2-C3	4.39	4.45	2.39	1%	-46%
	C3-C4	4.55	4.66	3.66	2%	-21%
	C4-C5	5.28	5.28	4.33	0%	-18%
	C5-C6	5.11	5.16	3.99	1%	-23%
	C6-C7	4.24	4.30	3.21	1%	-25%

Table A9: Comparing the ROMs from LS models with experimental data. Grey regions indicate lack of data.

		Range of Motion (degrees)											
		Experimental Average							GHBMC M50 Full Cervical Spine				
		Panjabi 1991	Oda 1992	Camacho 1997	Panjabi 1998	Panjabi 2001	Wheeldon 2006	Nightingale 2007	Ivancic 2013	LS M50	LS M50-Opt	LS M50-FC-Opt	
Flexion	0.5 Nm	C0-C1	13	10.6					8.7	4.5	11.4	11.5	
		C1-C2	11.5	9.4					7.7	2.9	11.4	11.4	
		C2-C3			3.71			4.37		2.6	2.8	2.8	2.9
		C3-C4			4.17			5.08	4.88	3.6	2.7	2.7	2.7
		C4-C5			4.3			4.53	4.04	3.7	2.5	2.5	2.5
		C5-C6			4.05			5.18	6.94	3.6	2.2	2.2	2.3
		C6-C7			3.78			4.04	2.52	3.1	2.5	2.5	2.5
	1.0 Nm	C0-C1	13.5	11.5		7.2	7.2			9.2	7.6	12.3	12.9
		C1-C2	12.3	10.3		12.3	12.3			7.9	4.0	12.0	12.2
		C2-C3			5.02	3.7	3.5	6.57		2.7	4.2	5.4	5.2
		C3-C4			5.05	4	4.3	6.7	7.1	3.9	3.6	3.5	3.5
		C4-C5			5.79	4.8	5.3	6.24	5.53	3.9	3.8	3.6	3.3
		C5-C6			5.15	5.5	5.5	7.37	9.13	3.9	3.0	3.2	3.6
		C6-C7			3.78	4.2	3.7	6.15	3.74	3.2	3.6	3.6	3.6
	1.5 Nm	C0-C1	14.4	12.7						9.7	7.6	12.2	12.6
		C1-C2	12.7	10.9						8.7	7.9	15.3	15.6
		C2-C3			5.82			8.04		3.1	4.3	5.7	5.7
		C3-C4			5.58			7.7	8.61	4.4	3.6	3.7	3.5
		C4-C5			6.74			7.31	6.51	4	5.8	5.4	5.3
		C5-C6			5.84			8.78	10.53	4.1	3.0	3.3	3.6
		C6-C7			4.44			7.59	4.6	3.4	4.6	4.7	4.7
Extension	0.5 Nm	C0-C1	12.6	12.1					7.6	2.8	9.9	10.13	
		C1-C2	10	6.45					3	12.8	8.8	8.62	
		C2-C3			4.82			2.72		3	4.3	4.3	2.44
		C3-C4			3.78			2.06	2.88	2.8	3.5	3.6	1.33
		C4-C5			3.2			1.84	2.97	3	4.0	3.9	1.58
		C5-C6			3.87			2.39	2.98	5.3	4.2	4.3	1.61
		C6-C7			3.02			3.23	2.33	4.9	3.5	3.5	2.48
	1.0 Nm	C0-C1	13.2	12.75		20.2	20.2			8.5	3.8	11.8	12.2
		C1-C2	10.1	7.09		12.1	12.1			2.5	14.3	10.3	9.7
		C2-C3			5.5	3.2	2.7	3.79		2	5.0	5.0	3.4
		C3-C4			4.42	4.2	3.4	3.17	4.5	3.1	4.1	4.2	2.5
		C4-C5			3.58	4.9	4.8	3.04	4.54	4.3	5.0	4.8	2.4
		C5-C6			4.58	4.8	4.4	3.46	4.73	5	5.3	5.3	2.5
		C6-C7			3.53	3.8	3.4	4.4	3.65	4.8	4.4	4.4	3.5
	1.5 Nm	C0-C1	14.4	13.5						8.9	4.9	13.0	13.4
		C1-C2	10.5	7.3						3.3	15.4	13.4	10.8
		C2-C3			5.88			4.47		3.3	5.2	4.0	4.0
		C3-C4			4.77			3.94	5.72	3.6	4.7	4.5	3.4
		C4-C5			3.88			3.94	5.66	4.2	5.9	6.6	3.1
		C5-C6			5.02			4.15	6.01	5.8	6.0	5.5	3.1
		C6-C7			3.83			5.12	4.62	5.4	5.1	5.2	4.7
Axial Rotation	0.5 Nm	C0-C1	3.4	4.6						3.8	4.4	4.3	
		C1-C2	32.5	33.6						23.5	30.7	30.8	
		C2-C3									3.4	3.4	1.4
		C3-C4									3.2	3.2	1.9
		C4-C5									3.2	3.2	2.2
		C5-C6									3.1	3.1	2.2
		C6-C7									2.7	2.7	1.7
	1.0 Nm	C0-C1	4.1	4.85						3.08	5.8	6.8	5.3
		C1-C2	34	35.2						23.4	26.8	33.5	32.8
		C2-C3								2.1	4.0	4.1	2.0
		C3-C4								2.7	4.1	4.1	3.0
		C4-C5								2.5	4.3	4.3	3.4
		C5-C6								2.4	4.3	4.4	3.2
		C6-C7								1.2	3.6	3.7	2.6
	1.5 Nm	C0-C1	6	6							6.1	8.7	4.5
		C1-C2	34	35.3						29.9	34.1	35.0	35.0
		C2-C3									4.4	4.4	2.4
		C3-C4									4.5	4.7	3.7
		C4-C5									5.3	5.3	4.3
		C5-C6									5.1	5.2	4.0
		C6-C7									4.2	4.3	3.2
Axial Rotation	0.5 Nm	C0-C1	1.8	5.5						3.8	4.4	4.3	
		C1-C2	34.6	25.4						23.5	30.7	30.8	
		C2-C3									3.4	3.4	1.4
		C3-C4									3.2	3.2	1.9
		C4-C5									3.2	3.2	2.2
		C5-C6									3.1	3.1	2.2
		C6-C7									2.7	2.7	1.7
	1.0 Nm	C0-C1	2.5	6.6						3.3	5.8	6.8	5.3
		C1-C2	36	27.2						28.5	26.8	33.5	32.8
		C2-C3								2.7	4.0	4.1	2.0
		C3-C4								2.6	4.1	4.1	3.0
		C4-C5								2.5	4.3	4.3	3.4
		C5-C6								2.4	4.3	4.4	3.2
		C6-C7								1.2	3.6	3.7	2.6
	1.5 Nm	C0-C1	3.3	6.7							6.1	8.7	4.5
		C1-C2	37.4	27.5						29.9	34.1	35.0	35.0
		C2-C3									4.4	4.4	2.4
		C3-C4									4.5	4.7	3.7
		C4-C5									5.3	5.3	4.3
		C5-C6									5.1	5.2	4.0
		C6-C7									4.2	4.3	3.2

Table A10: Assessing the LS_{M50} model with experimental data. Grey regions indicate lack of data

		Percentage Error between Model Response and Experimental Mean								
		LS M50 and Experimental Mean								
		Panjabi 1991	Oda 1992	Camacho 1997	Panjabi 1998	Panjabi 2001	Wheeldon 2006	Nightingale 2007	Ivancic 2013	
Flexion	0.5 Nm	C0-C1	66%	58%					49%	
		C1-C2	75%	69%					62%	
		C2-C3			24%			35%		9%
		C3-C4			36%			47%	45%	25%
		C4-C5			42%			45%	39%	33%
		C5-C6			46%			58%	68%	39%
		C6-C7			33%			37%	0%	18%
	1.0 Nm	C0-C1	44%	34%		5%	5%			18%
		C1-C2	67%	61%		67%	67%			49%
		C2-C3			17%	13%	20%	36%		55%
		C3-C4			28%	9%	15%	46%	49%	7%
		C4-C5			35%	21%	29%	40%	32%	3%
		C5-C6			41%	45%	45%	59%	67%	22%
		C6-C7			4%	13%	1%	41%	3%	14%
	1.5 Nm	C0-C1	47%	40%						22%
		C1-C2	38%	27%						9%
		C2-C3			26%			47%		39%
		C3-C4			35%			53%	58%	17%
		C4-C5			15%			21%	11%	44%
		C5-C6			48%			65%	71%	26%
		C6-C7			5%			39%	1%	37%
Extension	0.5 Nm	C0-C1	78%	77%					63%	
		C1-C2	28%	99%					328%	
		C2-C3			11%			57%		43%
		C3-C4			7%			71%	22%	26%
		C4-C5			26%			119%	36%	34%
		C5-C6			10%			78%	42%	20%
		C6-C7			16%			8%	50%	29%
	1.0 Nm	C0-C1	71%	70%		81%	81%			56%
		C1-C2	42%	102%		18%	18%			473%
		C2-C3			10%	55%	84%	31%		149%
		C3-C4			6%	1%	22%	31%	8%	34%
		C4-C5			41%	3%	5%	66%	11%	17%
		C5-C6			15%	10%	20%	52%	11%	5%
		C6-C7			24%	15%	28%	1%	20%	9%
	1.5 Nm	C0-C1	66%	64%						45%
		C1-C2	47%	111%						366%
		C2-C3			12%			16%		57%
		C3-C4			1%			19%	18%	31%
		C4-C5			51%			49%	3%	39%
		C5-C6			19%			44%	0%	3%
		C6-C7			33%			1%	10%	6%
R.Axial Rotation	0.5 Nm	C0-C1	13%	16%						
		C1-C2	28%	30%						
		C2-C3								
		C3-C4								
		C4-C5								
		C5-C6								
		C6-C7								
	1.0 Nm	C0-C1	41%	19%						88%
		C1-C2	21%	24%						14%
		C2-C3								91%
		C3-C4								51%
		C4-C5								71%
		C5-C6								81%
		C6-C7								201%
	1.5 Nm	C0-C1	2%	2%						
		C1-C2	12%	15%						
		C2-C3								
		C3-C4								
		C4-C5								
		C5-C6								
		C6-C7								
L.Axial Rotation	0.5 Nm	C0-C1	114%	30%						
		C1-C2	32%	7%						
		C2-C3								
		C3-C4								
		C4-C5								
		C5-C6								
		C6-C7								
	1.0 Nm	C0-C1	131%	12%						75%
		C1-C2	26%	2%						6%
		C2-C3								49%
		C3-C4								57%
		C4-C5								71%
		C5-C6								81%
		C6-C7								201%
	1.5 Nm	C0-C1	85%	9%						
		C1-C2	20%	9%						
		C2-C3								
		C3-C4								
		C4-C5								
		C5-C6								
		C6-C7								

Table A11: Assessing the LSM_{50-Opt} model with experimental data. Grey regions indicate lack of data

		Percentage Error between Model Response and Experimental Mean								
		LS M50-Opt and Experimental Mean								
		Panjabi 1991	Oda 1992	Camacho 1997	Panjabi 1998	Panjabi 2001	Wheeldon 2006	Nightingale 2007	Ivancic 2013	
Flexion	0.5 Nm	C0-C1	12%	8%					31%	
		C1-C2	1%	21%					48%	
		C2-C3			24%			36%		8%
		C3-C4			35%			47%	44%	25%
		C4-C5			43%			45%	39%	33%
		C5-C6			46%			58%	69%	40%
		C6-C7			33%			37%	1%	18%
	1.0 Nm	C0-C1	9%	7%		71%	71%			34%
		C1-C2	3%	16%		3%	3%			52%
		C2-C3			8%	46%	55%	17%		101%
		C3-C4			31%	12%	19%	48%	51%	10%
		C4-C5			38%	25%	33%	43%	35%	8%
		C5-C6			38%	42%	42%	57%	65%	18%
		C6-C7			4%	13%	2%	41%	3%	14%
	1.5 Nm	C0-C1	15%	4%						26%
		C1-C2	21%	40%						76%
		C2-C3			2%			29%		84%
		C3-C4			34%			52%	57%	16%
		C4-C5			20%			26%	17%	35%
		C5-C6			44%			62%	69%	20%
		C6-C7			5%			38%	2%	37%
Extension	0.5 Nm	C0-C1	21%	18%					31%	
		C1-C2	12%	37%					194%	
		C2-C3			11%			57%		43%
		C3-C4			4%			76%	26%	30%
		C4-C5			23%			114%	33%	31%
		C5-C6			11%			79%	44%	19%
		C6-C7			16%			8%	50%	29%
	1.0 Nm	C0-C1	11%	7%		42%	42%			39%
		C1-C2	2%	45%		15%	15%			312%
		C2-C3			9%	56%	85%	32%		149%
		C3-C4			5%	0%	23%	32%	7%	35%
		C4-C5			34%	2%	0%	57%	5%	11%
		C5-C6			16%	11%	21%	53%	12%	6%
		C6-C7			24%	15%	29%	0%	20%	9%
	1.5 Nm	C0-C1	10%	4%						46%
		C1-C2	27%	83%						305%
		C2-C3			33%			11%		20%
		C3-C4			5%			15%	21%	26%
		C4-C5			70%			67%	16%	57%
		C5-C6			10%			34%	8%	4%
		C6-C7			35%			1%	12%	4%
R.Axial Rotation	0.5 Nm	C0-C1	30%	4%						
		C1-C2	6%	9%						
		C2-C3								
		C3-C4								
		C4-C5								
		C5-C6								
		C6-C7								
	1.0 Nm	C0-C1	65%	40%						120%
		C1-C2	1%	5%						43%
		C2-C3								94%
		C3-C4								52%
		C4-C5								71%
		C5-C6								82%
		C6-C7								205%
	1.5 Nm	C0-C1	45%	45%						
		C1-C2	0%	3%						
		C2-C3								
		C3-C4								
		C4-C5								
		C5-C6								
		C6-C7								
L.Axial Rotation	0.5 Nm	C0-C1	145%	20%						
		C1-C2	11%	21%						
		C2-C3								
		C3-C4								
		C4-C5								
		C5-C6								
		C6-C7								
	1.0 Nm	C0-C1	171%	3%						105%
		C1-C2	7%	23%						18%
		C2-C3								51%
		C3-C4								58%
		C4-C5								71%
		C5-C6								82%
		C6-C7								205%
	1.5 Nm	C0-C1	164%	30%						
		C1-C2	9%	24%						
		C2-C3								
		C3-C4								
		C4-C5								
		C5-C6								
		C6-C7								

Table A12: Assessing the LS_{M50-FC-Opt} model with experimental data. Grey regions indicate lack of data

		Percentage Error between Model Response and Experimental Mean									
		LS _{M50-FC-Opt} and Experimental Mean									
		Panjabi 1991	Oda 1992	Camacho 1997	Panjabi 1998	Panjabi 2001	Wheeldon 2006	Nightingale 2007	Ivanic 2013		
Flexion	0.5 Nm	C0-C1	12%	8%						32%	
		C1-C2	1%	22%						46%	
		C2-C3			23%			34%		10%	
		C3-C4			35%			47%	45%	25%	
		C4-C5			43%			46%	39%	33%	
		C5-C6			44%			56%	67%	37%	
		C6-C7			34%			38%	0%	19%	
	1.0 Nm	C0-C1	5%	12%		78%	78%			40%	
		C1-C2	1%	18%		1%	1%			54%	
		C2-C3			4%	41%	49%	20%		94%	
		C3-C4			30%	11%	18%	47%	50%	9%	
		C4-C5			43%	32%	38%	47%	41%	16%	
		C5-C6			31%	35%	35%	52%	61%	9%	
		C6-C7			4%	14%	2%	41%	3%	13%	
	1.5 Nm	C0-C1	13%	1%						30%	
		C1-C2	23%	43%						80%	
		C2-C3			2%			29%		84%	
		C3-C4			36%			54%	59%	19%	
		C4-C5			22%			28%	19%	31%	
		C5-C6			38%			59%	66%	11%	
		C6-C7			6%			38%	2%	38%	
	Extension	0.5 Nm	C0-C1	20%	16%						33%
			C1-C2	14%	34%						187%
			C2-C3			49%			10%		19%
C3-C4					65%			35%	54%	52%	
C4-C5					51%			14%	47%	47%	
C5-C6					58%			33%	46%	70%	
C6-C7					18%			23%	6%	49%	
1.0 Nm		C0-C1	8%	4%		40%	40%			43%	
		C1-C2	4%	37%		20%	20%			288%	
		C2-C3			39%	5%	25%	11%		68%	
		C3-C4			44%	41%	27%	21%	45%	20%	
		C4-C5			34%	52%	51%	22%	48%	45%	
		C5-C6			45%	47%	43%	27%	47%	50%	
		C6-C7			0%	8%	3%	20%	4%	27%	
1.5 Nm		C0-C1	7%	1%						51%	
		C1-C2	3%	48%						228%	
		C2-C3			33%			11%		20%	
		C3-C4			29%			14%	41%	6%	
		C4-C5			21%			22%	46%	27%	
		C5-C6			37%			24%	48%	46%	
		C6-C7			23%			8%	2%	13%	
R.Axial Rotation	0.5 Nm	C0-C1	27%	6%							
		C1-C2	5%	8%							
		C2-C3									
		C3-C4									
		C4-C5									
		C5-C6									
		C6-C7									
	1.0 Nm	C0-C1	28%	8%						70%	
		C1-C2	4%	7%						40%	
		C2-C3								7%	
		C3-C4								10%	
		C4-C5								35%	
		C5-C6								34%	
		C6-C7								116%	
	1.5 Nm	C0-C1	25%	25%							
		C1-C2	3%	1%							
		C2-C3									
		C3-C4									
		C4-C5									
		C5-C6									
		C6-C7									
L.Axial Rotation	0.5 Nm	C0-C1	139%	22%							
		C1-C2	11%	21%							
		C2-C3									
		C3-C4									
		C4-C5									
		C5-C6									
		C6-C7									
	1.0 Nm	C0-C1	110%	20%						59%	
		C1-C2	9%	21%						15%	
		C2-C3								28%	
		C3-C4								14%	
		C4-C5								35%	
		C5-C6								34%	
		C6-C7								116%	
	1.5 Nm	C0-C1	37%	33%							
		C1-C2	6%	27%							
		C2-C3									
		C3-C4									
		C4-C5									
		C5-C6									
		C6-C7									

Table A13: Assessing the improvement in biofidelity of LS model with enhanced UCS model

Mean % Error across loading modes and intervertebral levels				
Moment	Experiment	LS _{M50}	LS _{M50-Opt}	LS _{M50-FC-Opt}
0.5 Nm	Panjabi et al. (1991a,b)	54%	30%	28%
	Oda et al. (1992)	48%	17%	17%
	Ivancic (2013)	56%	41%	47%
1.0 Nm	Panjabi et al. (1991a,b)	55%	34%	21%
	Oda et al. (1992)	41%	18%	16%
	Panjabi et al. (1998)	26%	25%	30%
	Panjabi et al. (2001)	32%	31%	31%
	Ivancic (2013)	73%	73%	50%
1.5 Nm	Panjabi et al. (1991a,b)	40%	36%	15%
	Oda et al. (1992)	35%	29%	22%
	Ivancic (2013)	53%	54%	49%
Average		46%	35%	30%

Table A14: Assessment of LS model response with Cumulative Mean Experimental data in flexion

Assessment of intervertebral C0-C7 in Flexion						% Error		
		Cumulative Mean	LS _{M50}	LS _{M50-Opt}	LS _{M50-FC-Opt}	LS _{M50}	LS _{M50-Opt}	LS _{M50-FC-Opt}
0.5 Nm	C0-C1	10.8	4.5	11.4	11.5	58%	6%	6%
	C1-C2	9.5	2.9	11.4	11.4	69%	20%	20%
	C2-C3	3.56	2.82	2.81	2.9	21%	21%	20%
	C3-C4	4.43	2.68	2.72	2.7	39%	39%	39%
	C4-C5	4.14	2.48	2.47	2.5	40%	40%	41%
	C5-C6	4.94	2.19	2.18	2.3	56%	56%	54%
	C6-C7	3.36	2.53	2.54	2.5	25%	24%	25%
1.0 Nm	C0-C1	9.7	7.6	12.3	12.9	22%	27%	32%
	C1-C2	11	4	12	12.2	64%	9%	11%
	C2-C3	4.3	4.19	5.42	5.2	3%	26%	22%
	C3-C4	5.2	3.64	3.50	3.5	30%	32%	31%
	C4-C5	5.3	3.77	3.58	3.3	28%	32%	38%
	C5-C6	6.0	3.04	3.19	3.6	49%	47%	41%
	C6-C7	4.1	3.65	3.64	3.6	12%	12%	12%
1.5 Nm	C0-C1	12.3	7.6	12.2	12.6	38%	1%	2%
	C1-C2	10.8	7.9	15.3	15.6	27%	42%	45%
	C2-C3	5.65	4.29	5.70	5.7	24%	1%	1%
	C3-C4	6.57	3.64	3.69	3.5	45%	44%	46%
	C4-C5	6.14	5.76	5.41	5.3	6%	12%	14%
	C5-C6	7.3	3.04	3.30	3.6	58%	55%	50%
	C6-C7	5	4.65	4.67	4.7	7%	7%	6%
Mean % Error from C0-C1 to C6-C7 across 0.5 Nm to 1.5 Nm						34%	26%	27%

Table A15: Assessment of LS model response with Cumulative Mean Experimental data in extension

Assessment of intervertebral C0-C7 in Extension						% Error		
		Cumulative Mean	LS _{M50}	LS _{M50-Opt}	LS _{M50-FC-Opt}	LS _{M50}	LS _{M50-Opt}	LS _{M50-FC-Opt}
0.5 Nm	C0-C1	10.8	2.8	9.9	10.1	74%	8%	6%
	C1-C2	6.5	12.8	8.8	8.6	97%	35%	33%
	C2-C3	3.5	4.28	4.28	2.4	22%	22%	30%
	C3-C4	2.8	3.52	3.63	1.3	26%	30%	52%
	C4-C5	2.75	4.03	3.94	1.6	47%	43%	43%
	C5-C6	3.63	4.25	4.28	1.6	17%	18%	56%
	C6-C7	3.37	3.50	3.49	2.5	4%	4%	26%
1.0 Nm	C0-C1	15	3.8	11.8	12.2	75%	21%	19%
	C1-C2	8.8	14.3	10.3	9.7	63%	17%	10%
	C2-C3	3.4	4.97	4.99	3.4	45%	45%	2%
	C3-C4	3.8	4.14	4.18	2.5	9%	10%	34%
	C4-C5	4.2	5.04	4.78	2.4	20%	14%	43%
	C5-C6	4.5	5.27	5.31	2.5	17%	18%	44%
	C6-C7	3.9	4.36	4.39	3.5	11%	12%	11%
1.5 Nm	C0-C1	12.3	4.9	13	13.4	60%	6%	9%
	C1-C2	7	15.4	13.4	10.8	120%	91%	55%
	C2-C3	4.5	5.19	3.96	4.0	15%	12%	12%
	C3-C4	4.5	4.71	4.55	3.4	5%	1%	25%
	C4-C5	4.42	5.85	6.58	3.1	32%	49%	31%
	C5-C6	5.24	5.99	5.54	3.1	14%	6%	40%
	C6-C7	4.74	5.08	5.16	4.7	7%	9%	1%
Mean % Error from C0-C1 to C6-C7 across 0.5 Nm to 1.5 Nm						37%	22%	28%

Table A16: Assessment of LS model response with Cumulative Mean Experimental data in right axial rotation

Assessment of intervertebral C0-C7 in R. Axial Rotation						% Error		
		Cumulative Mean	LS _{M50}	LS _{M50-Opt}	LS _{M50-FC-Opt}	LS _{M50}	LS _{M50-Opt}	LS _{M50-FC-Opt}
0.5 Nm	C0-C1	4	3.85	4.4	4.3	4%	10%	8%
	C1-C2	33.05	23.53	30.7	30.8	29%	7%	7%
	C2-C3							
	C3-C4							
	C4-C5							
	C5-C6							
	C6-C7							
1.0 Nm	C0-C1	4.01	5.8	6.8	5.3	45%	70%	31%
	C1-C2	30.86	26.8	33.5	32.8	13%	9%	6%
	C2-C3	2.1	4	4.1	2.0	90%	95%	7%
	C3-C4	2.7	4.1	4.1	3.0	52%	52%	10%
	C4-C5	2.5	4.3	4.3	3.4	72%	72%	35%
	C5-C6	2.4	4.3	4.4	3.2	79%	83%	34%
	C6-C7	1.2	3.6	3.7	2.6	200%	208%	116%
1.5 Nm	C0-C1	6	6.1	8.7	4.5	2%	45%	25%
	C1-C2	34.65	29.9	34.1	35.0	14%	2%	1%
	C2-C3							
	C3-C4							
	C4-C5							
	C5-C6							
	C6-C7							
Mean % Error from C0-C1 to C6-C7 across 0.5 Nm to 1.5 Nm						54%	59%	25%

Table A17: Assessment of LS model response with Cumulative Mean Experimental data in left axial rotation

Assessment of intervertebral C0-C7 in L. Axial Rotation						% Error		
		Cumulative Mean	LS _{M50}	LS _{M50-Opt}	LS _{M50-FC-Opt}	LS _{M50}	LS _{M50-Opt}	LS _{M50-FC-Opt}
0.5 Nm	C0-C1	3.65	3.85	4.41	4.3	5%	21%	18%
	C1-C2	30	23.53	30.7	30.8	22%	2%	3%
	C2-C3							
	C3-C4							
	C4-C5							
	C5-C6							
	C6-C7							
1.0 Nm	C0-C1	4.13	5.8	6.8	5.3	40%	65%	27%
	C1-C2	30.56	26.8	33.5	32.8	12%	10%	7%
	C2-C3	2.7	4	4.1	2.0	48%	52%	28%
	C3-C4	2.6	4.1	4.1	3.0	58%	58%	14%
	C4-C5	2.5	4.3	4.3	3.4	72%	72%	35%
	C5-C6	2.4	4.3	4.4	3.2	79%	83%	34%
	C6-C7	1.2	3.6	3.7	2.6	200%	208%	116%
1.5 Nm	C0-C1	5	6.1	8.7	4.5	22%	74%	10%
	C1-C2	32.45	29.9	34.1	35.0	8%	5%	8%
	C2-C3							
	C3-C4							
	C4-C5							
	C5-C6							
	C6-C7							
Mean % Error from C0-C1 to C6-C7 across 0.5 Nm to 1.5 Nm						52%	59%	27%

Appendix B

Supplementary materials for Phase #2a

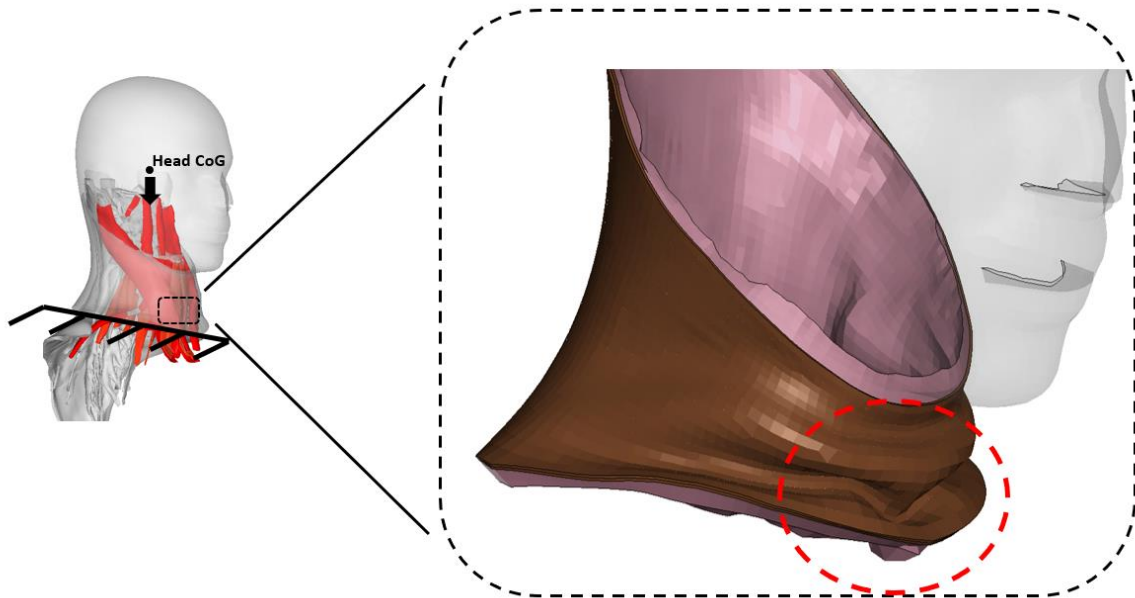


Figure B1: Illustration of the buckling in the skin and adipose tissue components (highlighted in the red-dotted circle) in the NM_{M50} model during the simulated forward flexion. Fully activating the flexors under gravity resulted in the head rotating 15° in flexion. The head is made transparent while other components are masked for illustrative purposes.

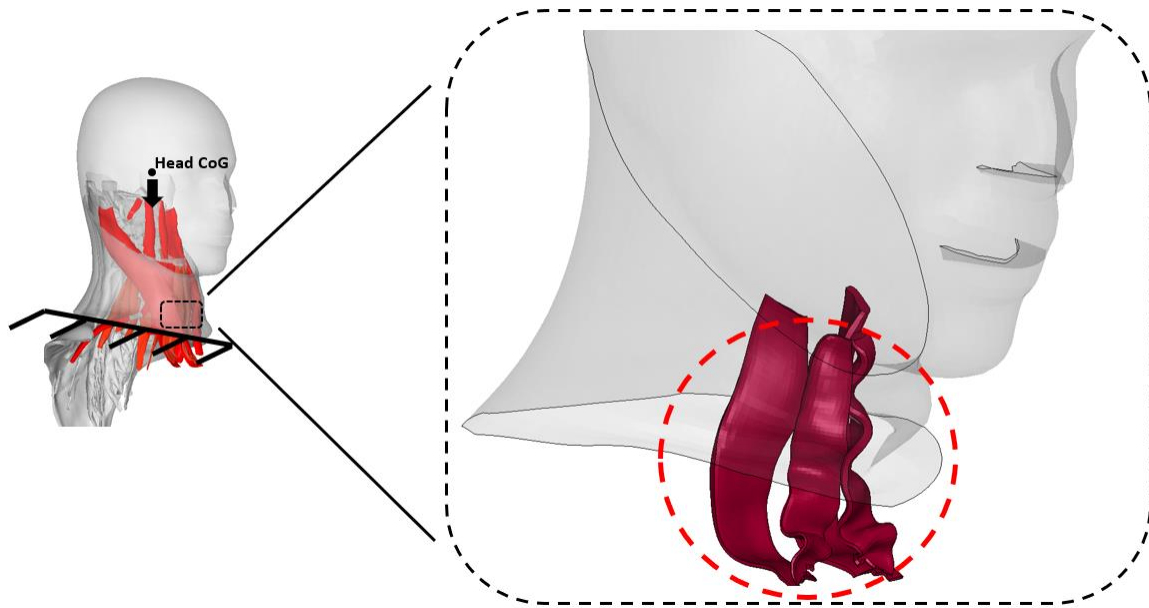


Figure B2: Illustration of the buckling in the 3D elements of the passive sternohyoid muscle (highlighted in the red-dotted circle) in the NM_{M50} model during the simulated forward flexion. The head rotated 15° in flexion when the flexors were fully activated under gravity. Buckling of the passive muscle component was observed in the anterior aspects of the neck. The neck skin and the head are made transparent while other components are masked for illustrative purposes.

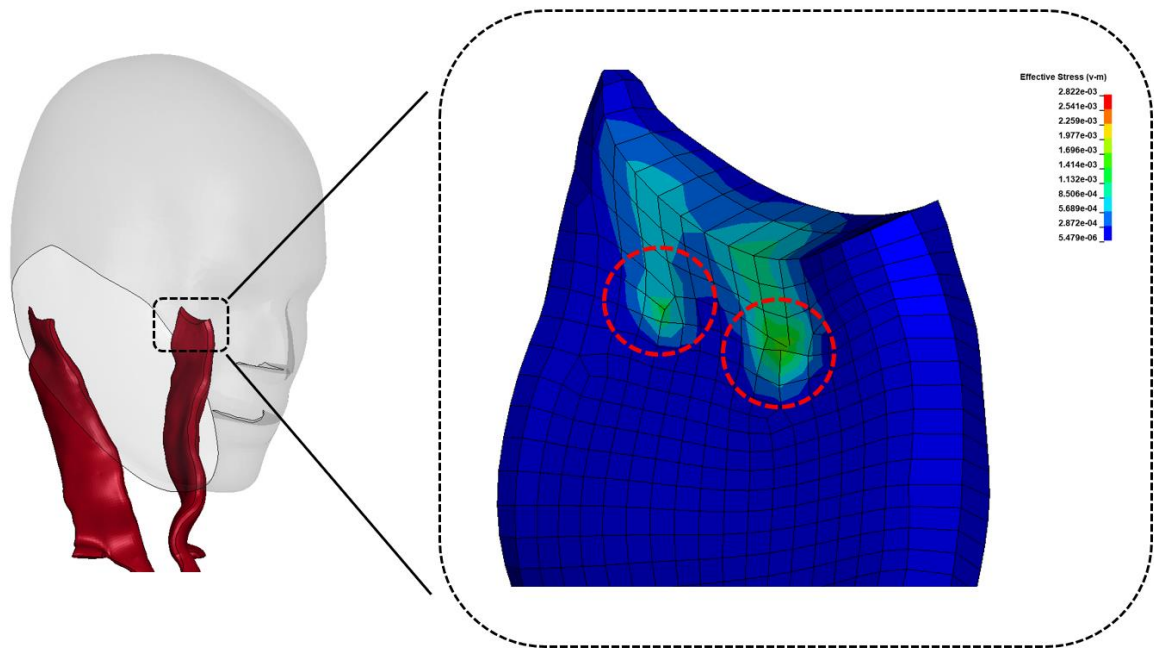


Figure B3: Illustration of the unphysical deformation in the 3D elements of the Sternocleidomastoid passive muscle (highlighted in the red-dotted circle) in the NM_{M50} model when the flexors were activated. The unphysical element deformation resulted in an uneven distribution of stress in the passive muscle tissue. All the other components are masked for illustrative purposes.

[Taken from Hadagali et al. (2024)]

Appendix C

Supplementary materials for Phase #2b

Ligament distraction response in 30° head flexion:

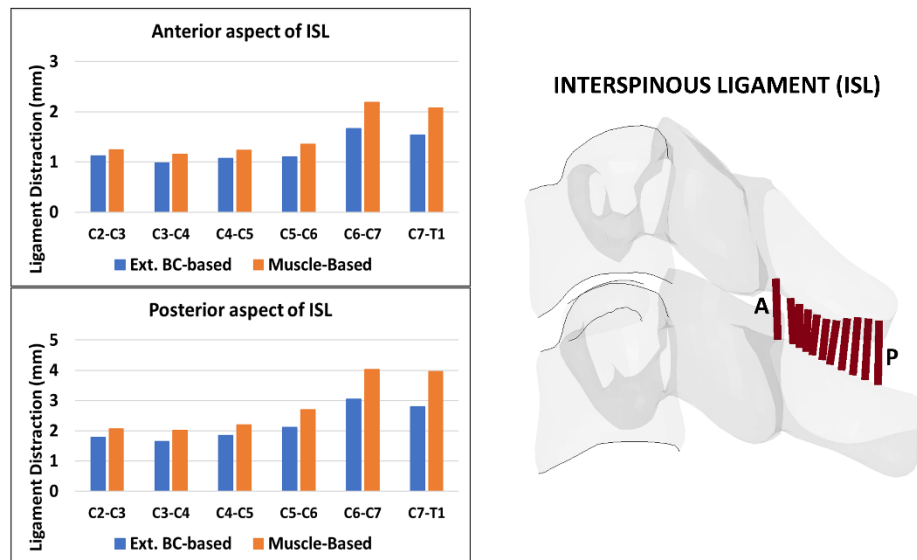


Figure C1: Interspinous ligament (ISL) distraction response for 30° head flexion. The distractions of the ISL were measured in the anterior (A) and posterior (P) aspects of the ligaments.

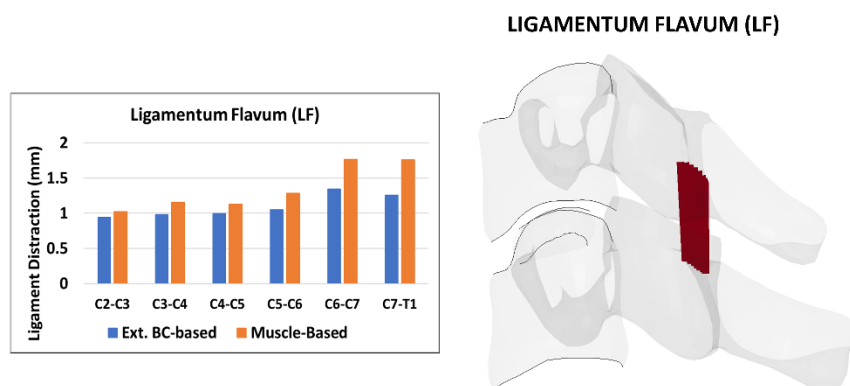


Figure C2: Ligamentum flavum (LF) distraction response for 30° head flexion.

POSTERIOR LONGITUDINAL LIGAMENT (PLL)

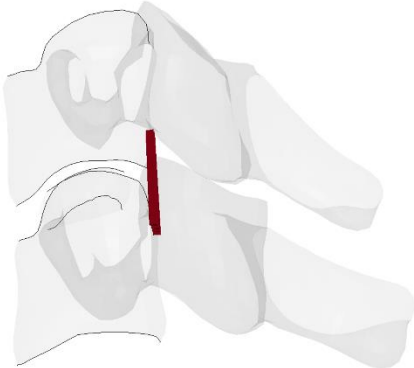
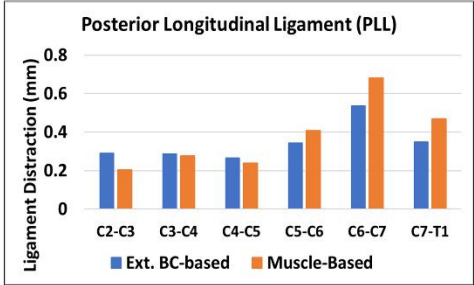


Figure C3: Posterior longitudinal ligament (PLL) distraction response for 30° head flexion.

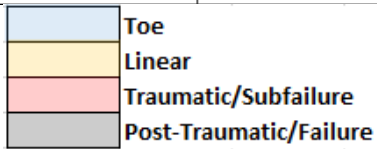
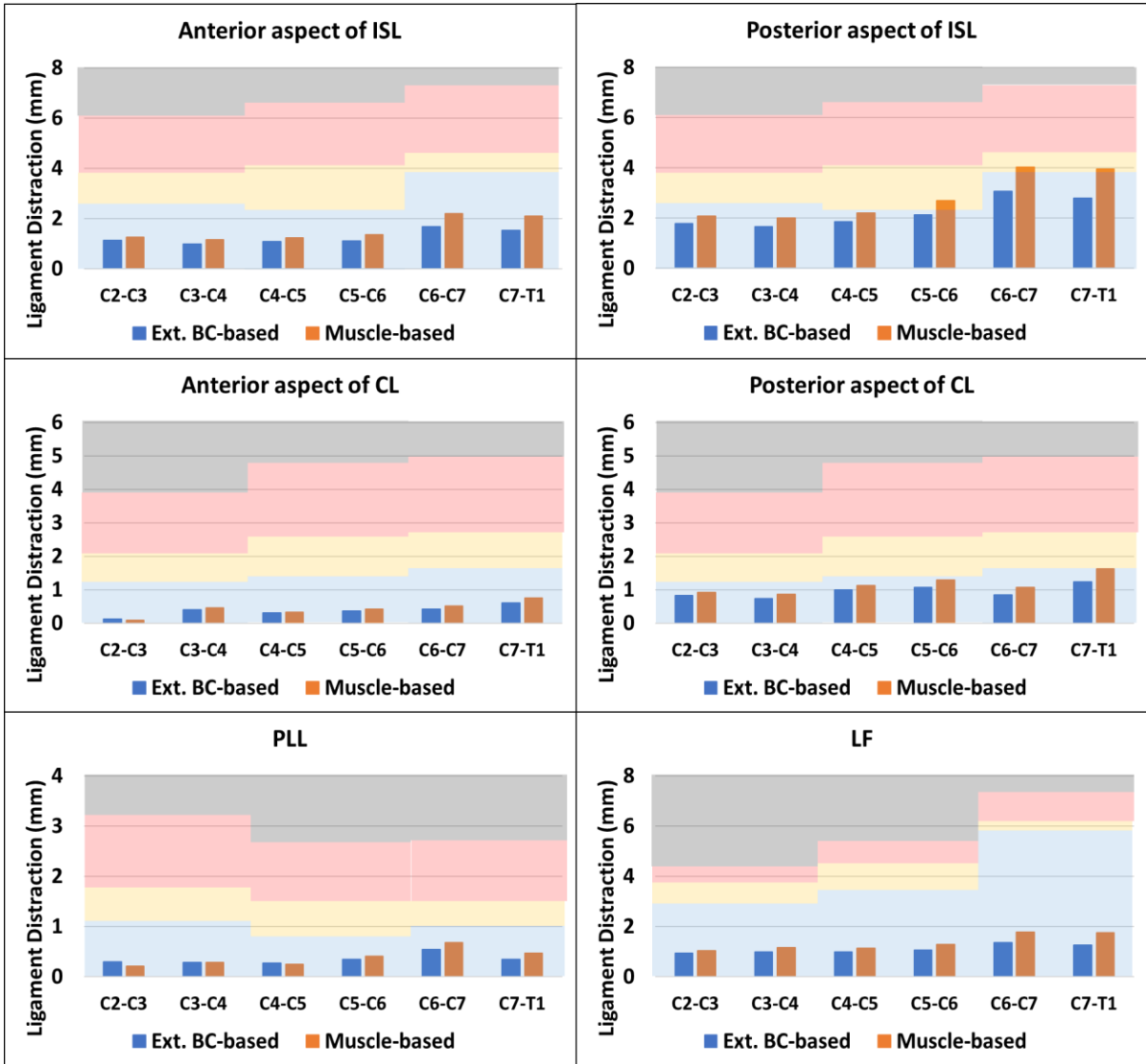


Figure C4: Assessment of the ligament response in 30° head flexion indicating that the distraction was within the physiologic limits based on experimental data (Mattucci et al. 2012).

Ligament distraction response in 30° head axial rotation:

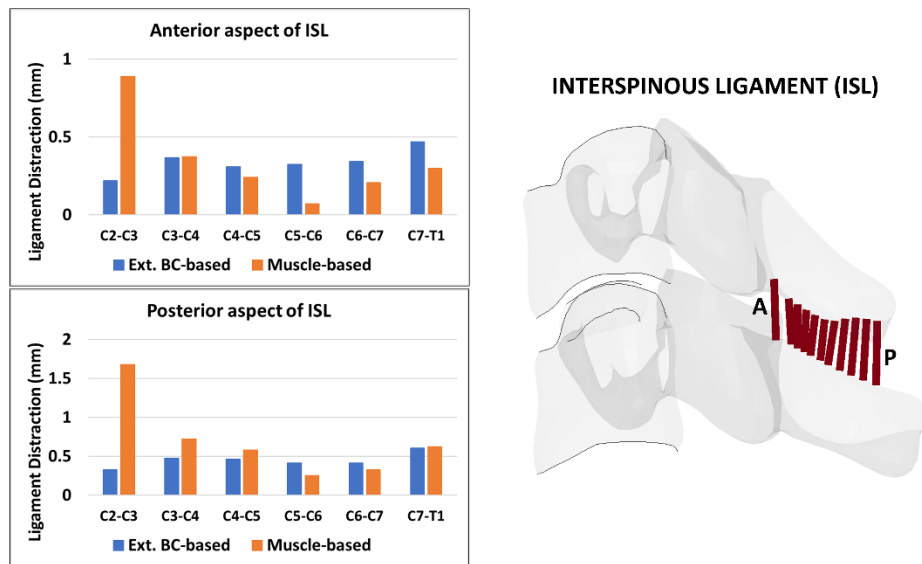


Figure C5: Interspinous ligament (ISL) distraction response for 30° head axial rotation. The distractions of the ISL were measured in the anterior (A) and posterior (P) aspects of the ligaments.

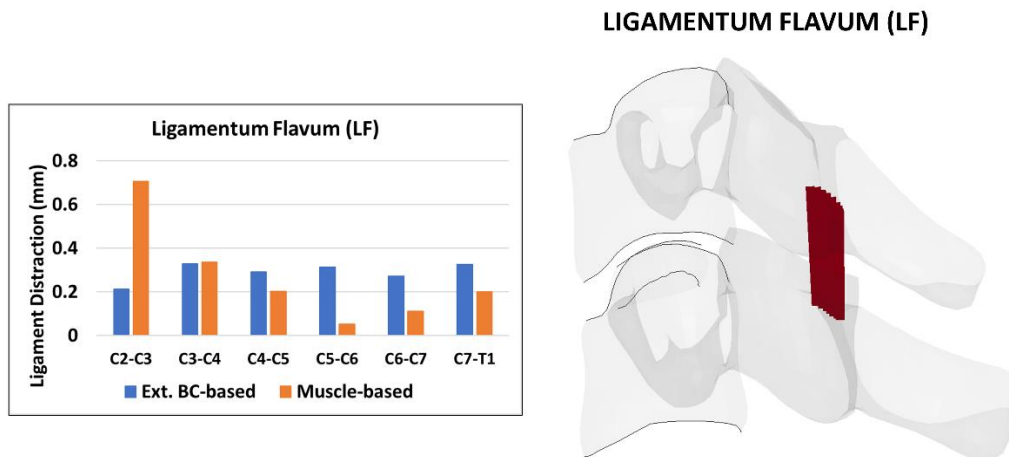


Figure C6: Ligamentum flavum (LF) distraction response for 30° head axial rotation.

POSTERIOR LONGITUDINAL LIGAMENT (PLL)

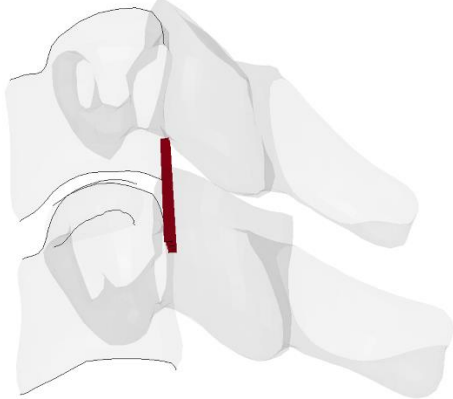
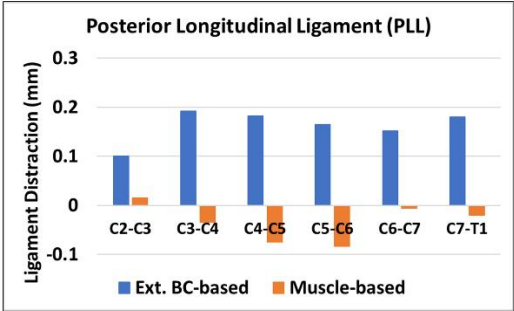


Figure C7: Posterior longitudinal ligament (PLL) distraction response for 30° head axial rotation.

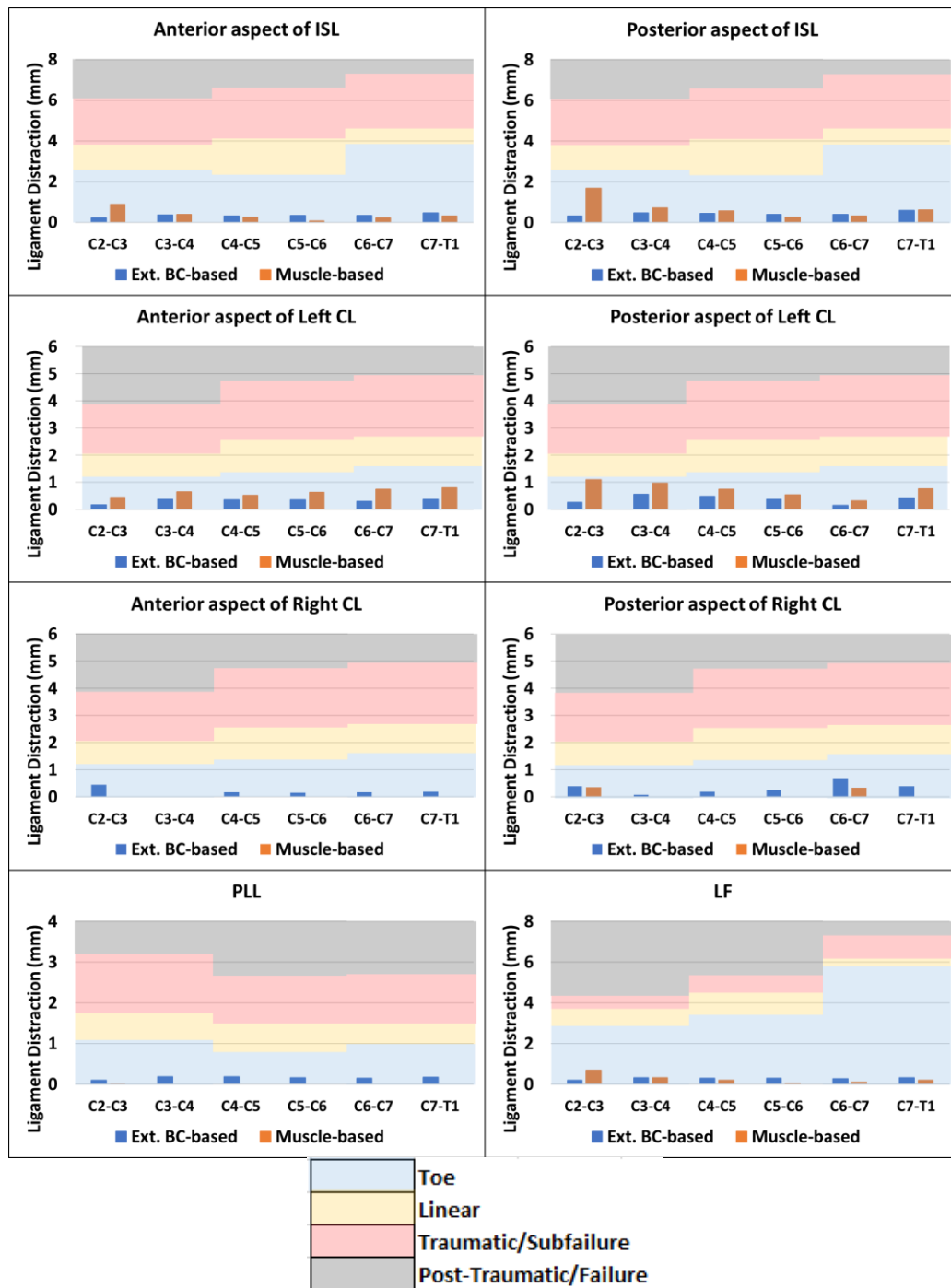


Figure C8: Assessment of the ligament response in 30° head axial rotation indicating that the distraction was within the physiologic limits based on experimental data (Mattucci et al. 2012). Few ligaments in CL and PLL that shortened (negative value) are not visible in the figure.

AF fiber strain response in 30° head flexion:

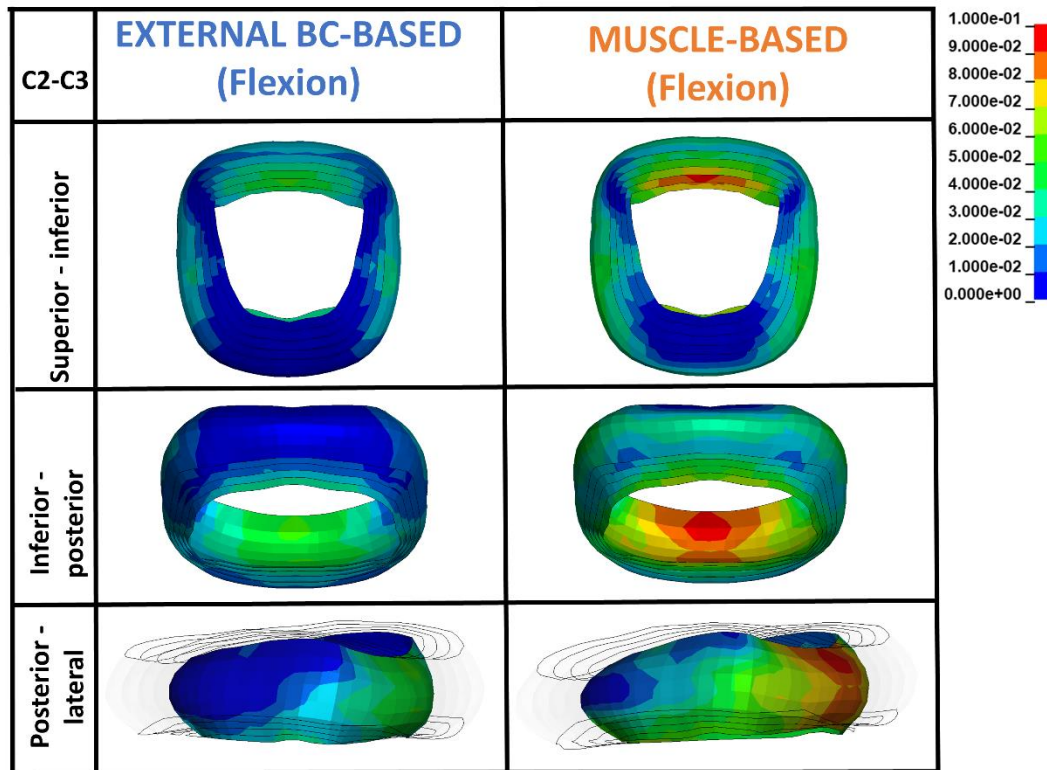


Figure C9: Illustrating the strain response contours in the C2-C3 AF collagen fibers in 30° head flexion in different perspectives , namely superior-inferior, inferior-posterior and posterior-lateral. In the posterior-lateral view, the outer four layers of lamellae are made transparent for visual purposes.

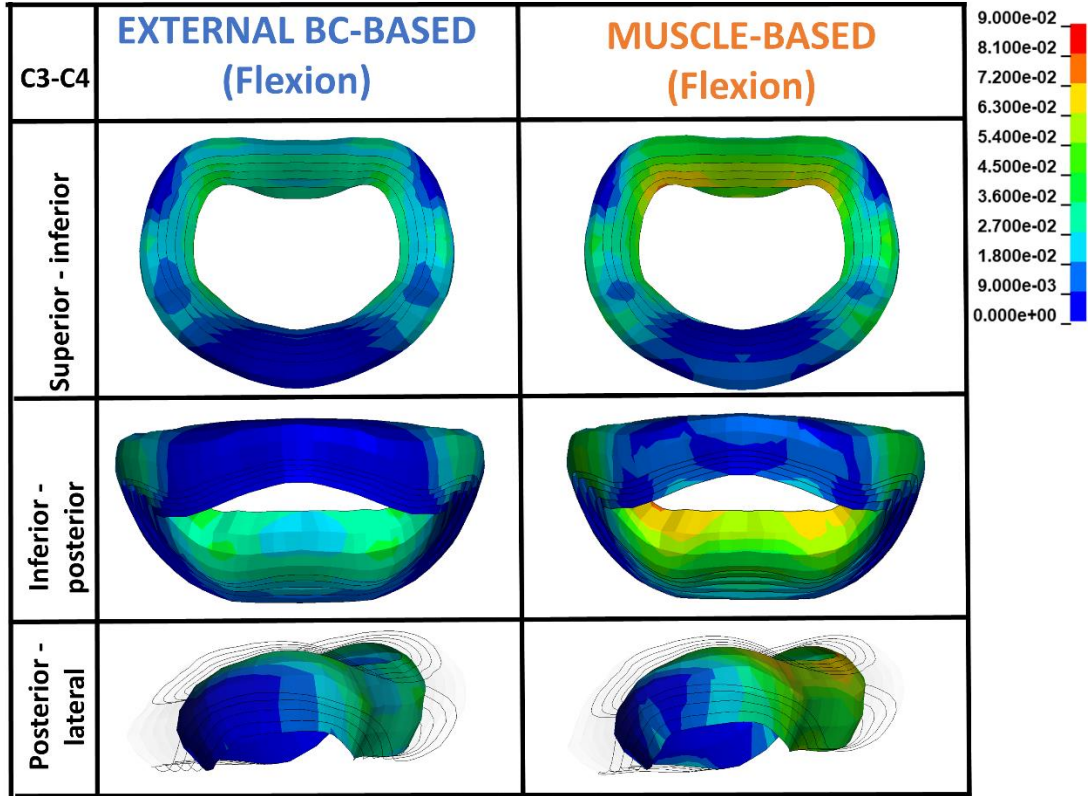


Figure C10: Illustrating the strain response contours in the C3-C4 AF collagen fibers in 30° head flexion in different perspectives, namely superior-inferior, inferior-posterior and posterior-lateral. In the posterior-lateral view, the outer four layers of lamellae are made transparent for visual purposes.

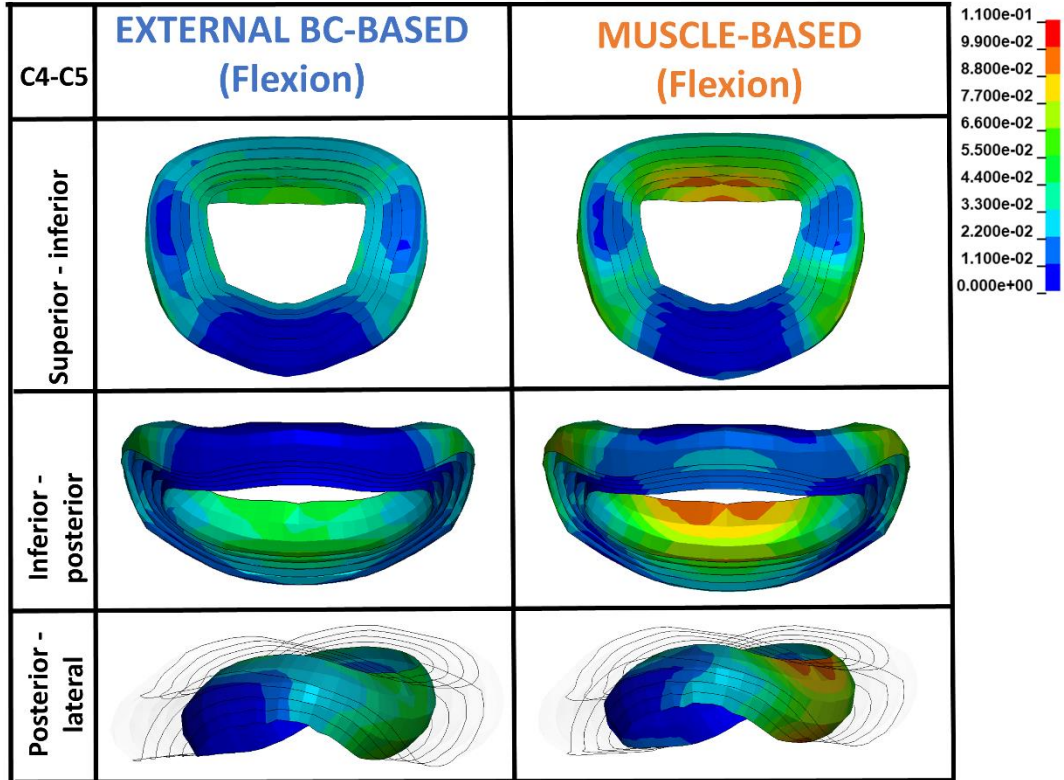


Figure C11: Illustrating the strain response contours in the C4-C5 AF collagen fibers in 30° head flexion in different perspectives, namely superior-inferior, inferior-posterior and posterior-lateral. In the posterior-lateral view, the outer four layers of lamellae are made transparent for visual purposes.

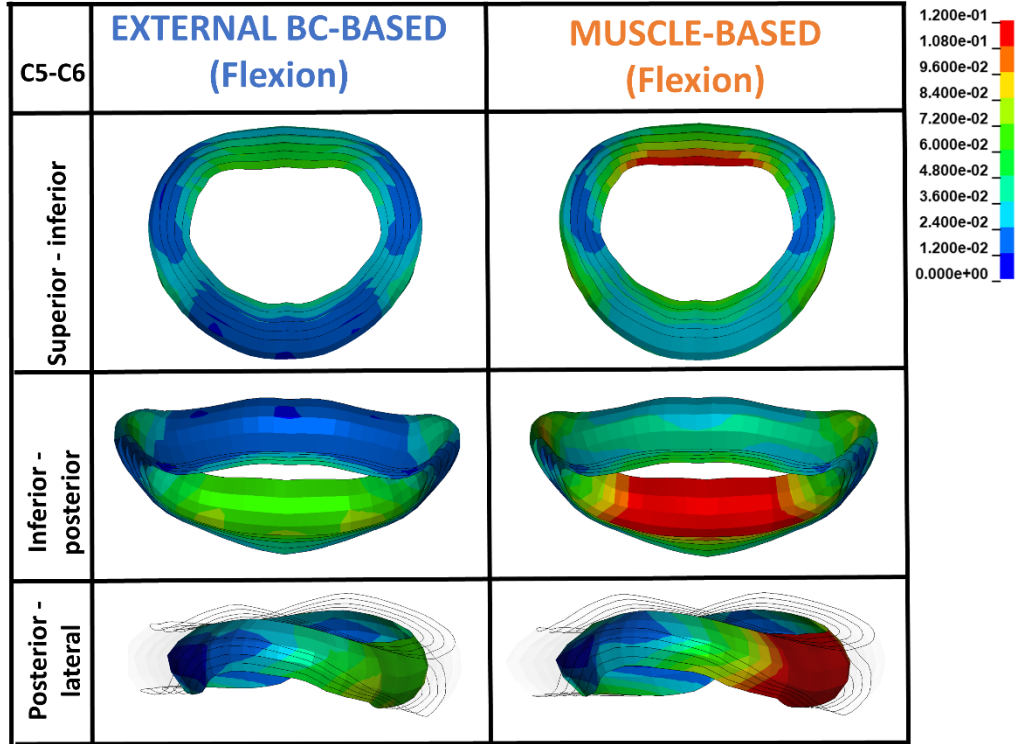


Figure C12: Illustrating the strain response contours in the C5-C6 AF collagen fibers in 30° head flexion in different perspectives , namely superior-inferior, inferior-posterior and posterior-lateral. In the posterior-lateral view, the outer four layers of lamellae are made transparent for visual purposes.

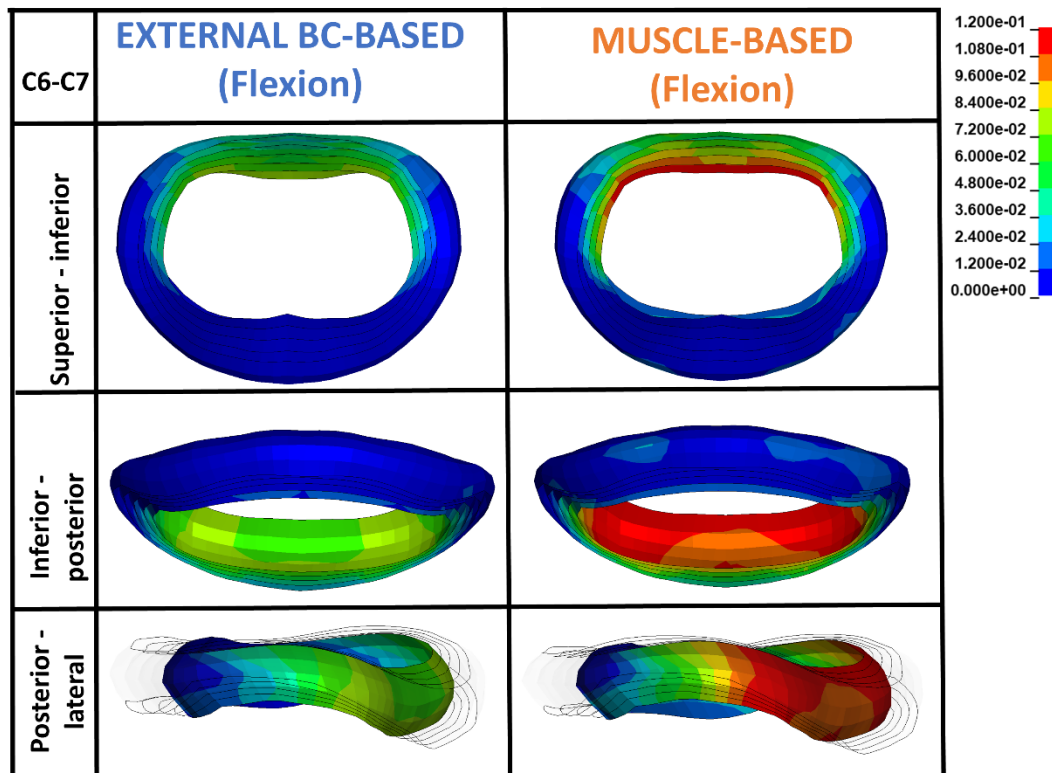


Figure C13: Illustrating the strain response contours in the C6-C7 AF collagen fibers in 30° head flexion in different perspectives , namely superior-inferior, inferior-posterior and posterior-lateral. In the posterior-lateral view, the outer four layers of lamellae are made transparent for visual purposes.

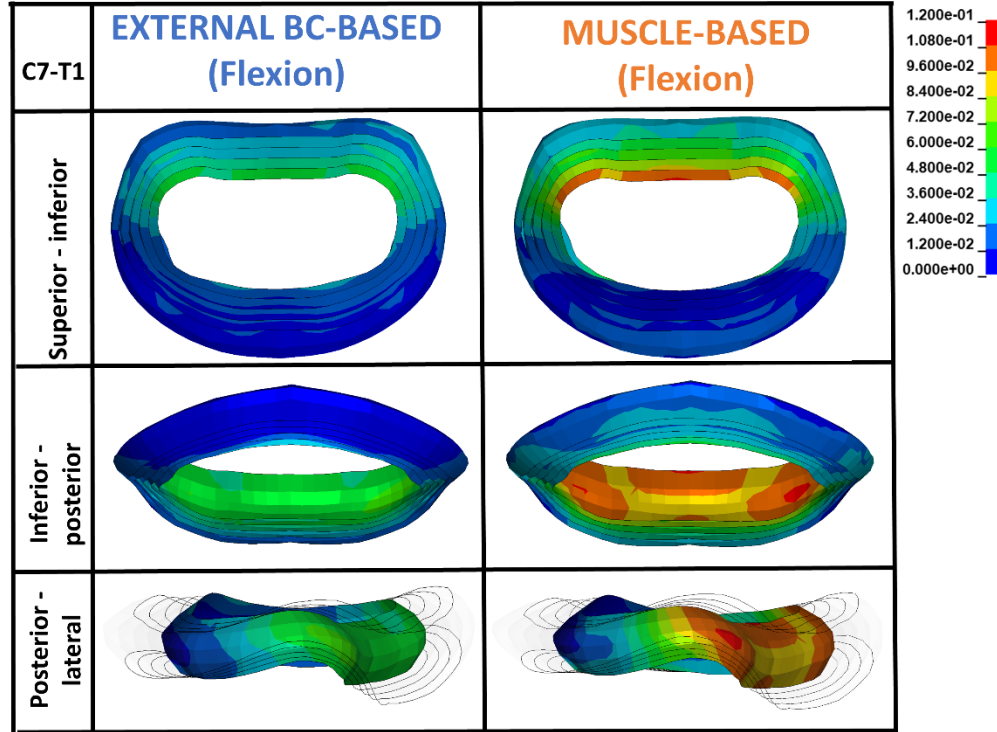


Figure C14: Illustrating the strain response contours in the C7-T1 AF collagen fibers in 30° head flexion in different perspectives , namely superior-inferior, inferior-posterior and posterior-lateral. In the posterior-lateral view, the outer four layers of lamellae are made transparent for visual purposes.

AF collagen fiber strain response in 30° head axial rotation:

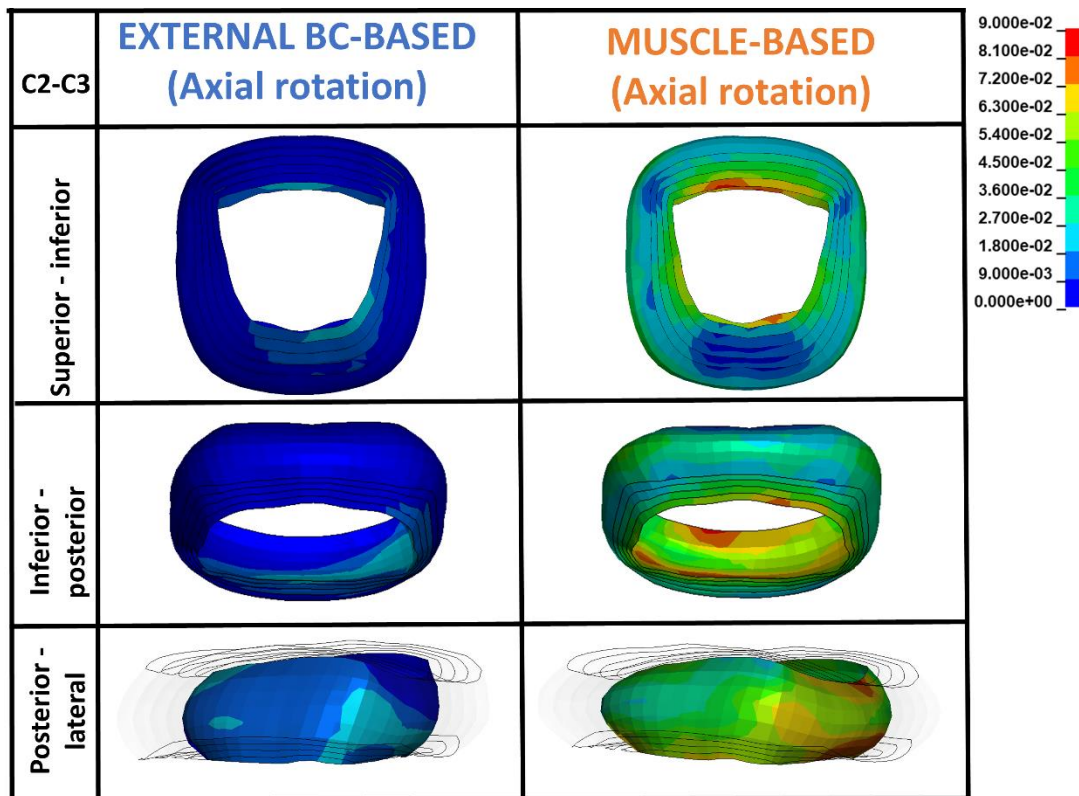


Figure C15: Illustrating the strain response contours in the C2-C3 AF collagen fibers in 30° head axial rotation in different perspectives, namely superior-inferior, inferior-posterior and posterior-lateral. In the posterior-lateral view, the outer four layers of lamellae are made transparent for visual purposes.

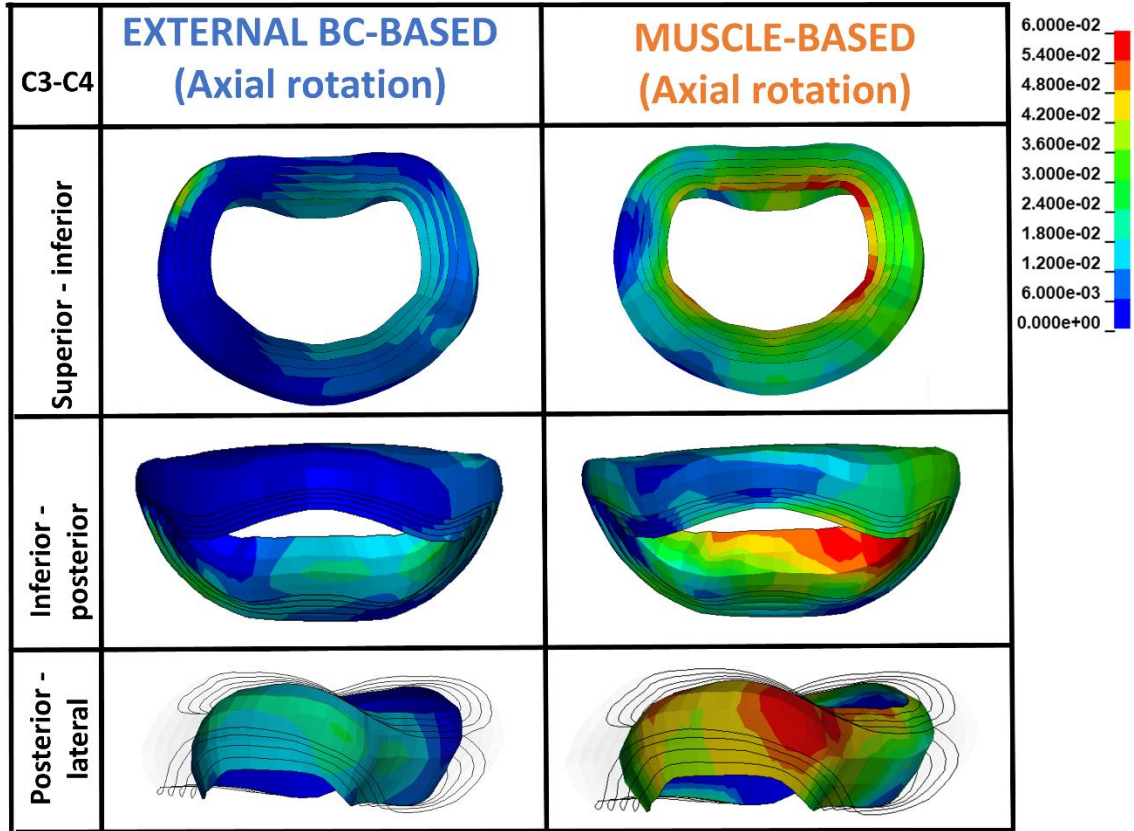


Figure C16: Illustrating the strain response contours in the C3-C4 AF collagen fibers in 30° head axial rotation in different perspectives, namely superior-inferior, inferior-posterior and posterior-lateral. In the posterior-lateral view, the outer four layers of lamellae are made transparent for visual purposes.

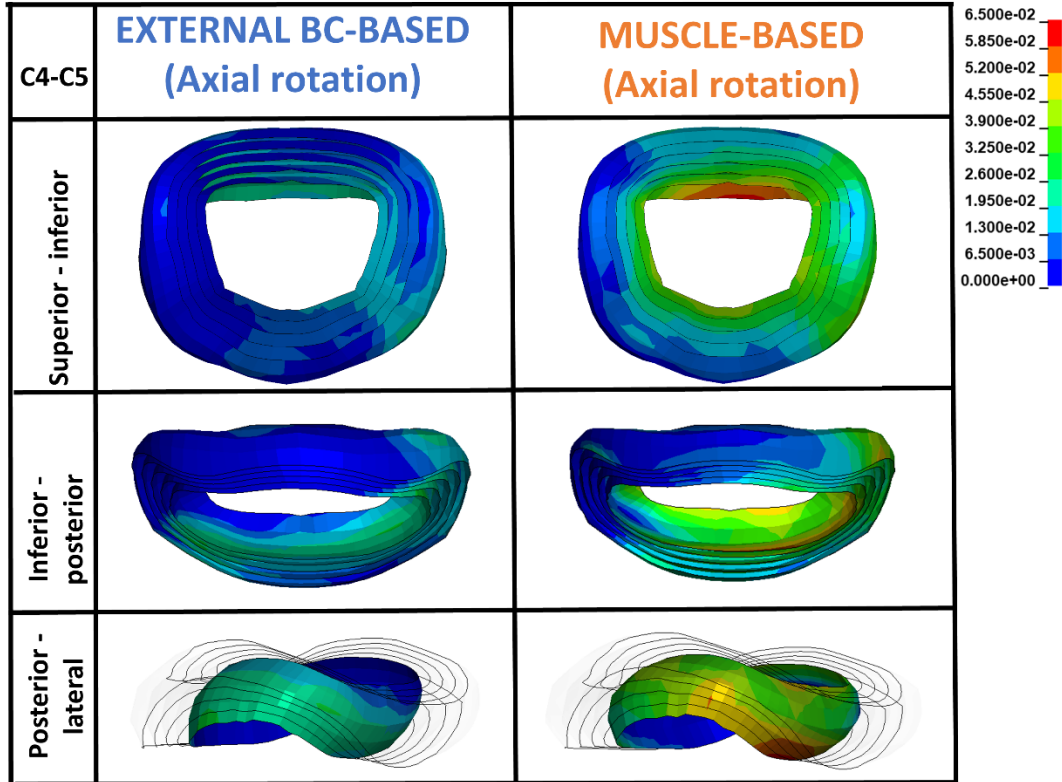


Figure C17: Illustrating the strain response contours in the C4-C5 AF collagen fibers in 30° head axial rotation in different perspectives, namely superior-inferior, inferior-posterior and posterior-lateral. In the posterior-lateral view, the outer four layers of lamellae are made transparent for visual purposes.

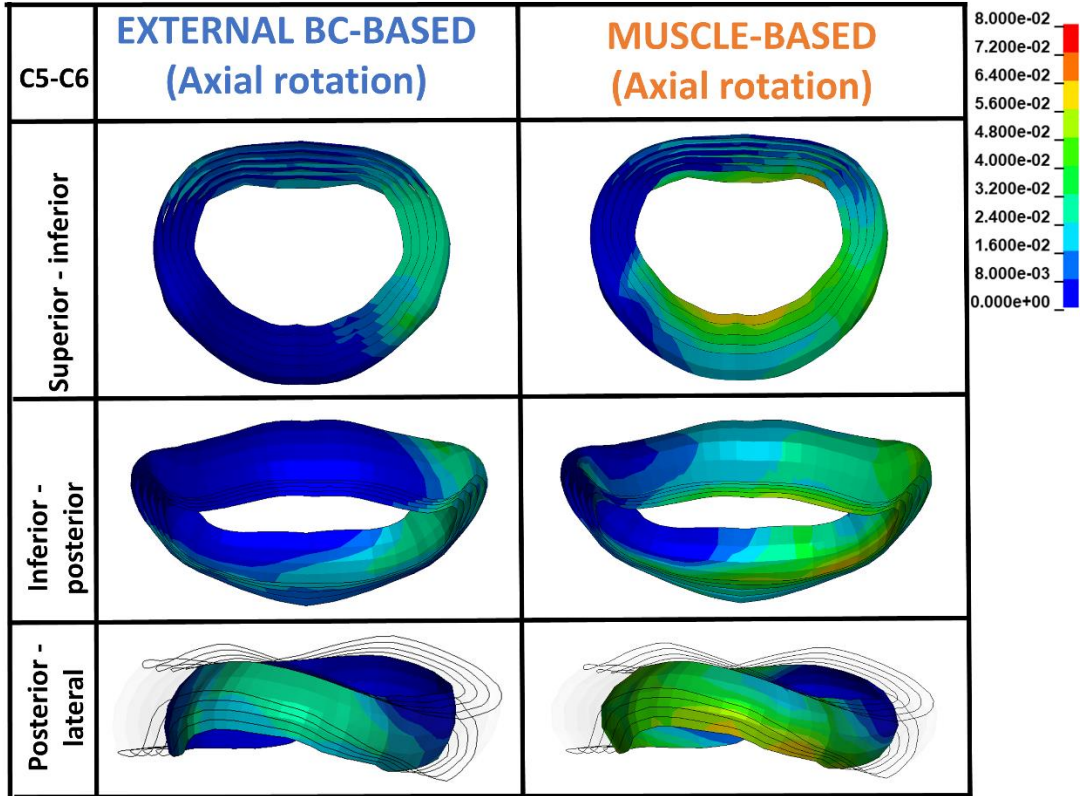


Figure C18: Illustrating the strain response contours in the C5-C6 AF collagen fibers in 30° head axial rotation in different perspectives, namely superior-inferior, inferior-posterior and posterior-lateral. In the posterior-lateral view, the outer four layers of lamellae are made transparent for visual purposes.

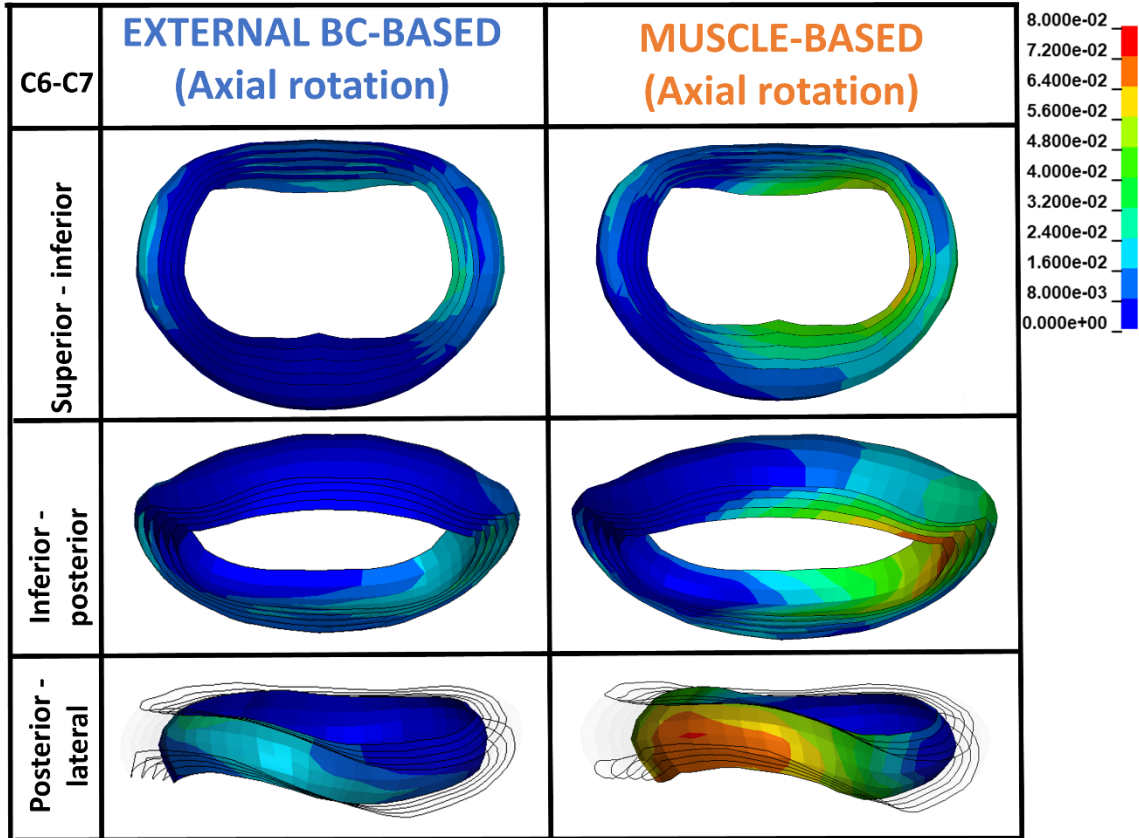


Figure C19: Illustrating the strain response contours in the C6-C7 AF collagen fibers in 30° head axial rotation in different perspectives, namely superior-inferior, inferior-posterior and posterior-lateral. In the posterior-lateral view, the outer four layers of lamellae are made transparent for visual purposes.

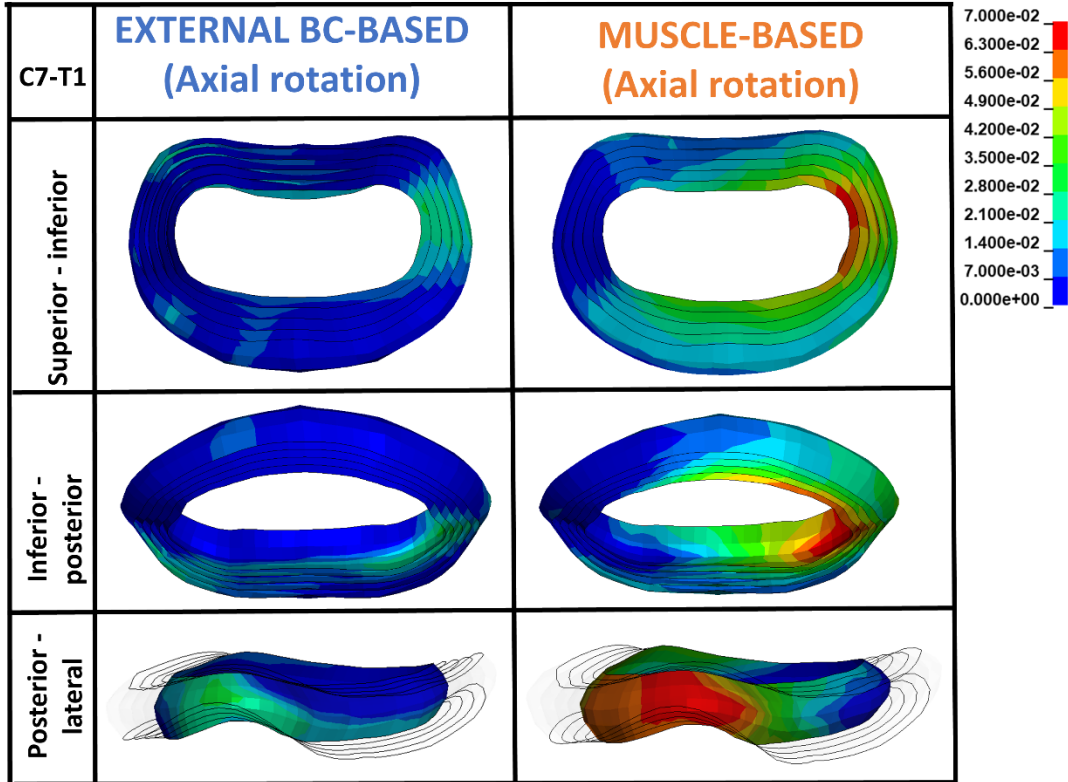


Figure C20: Illustrating the strain response contours in the C7-T1 AF collagen fibers in 30° head axial rotation in different perspectives, namely superior-inferior, inferior-posterior and posterior-lateral. In the posterior-lateral view, the outer four layers of lamellae are made transparent for visual purposes.

Appendix D

Supplementary materials for Phase #3

Table D1: Length of different regions in cervical spine ligament mechanical behavior as modeled in the GHBMC M50-O FE head-neck model based on experimental data (Barker and Cronin, 2021)

Ligament	Distance (mm)	C2-C3	C3-C4	C4-C5	C5-C6	C6-C7	C7-T1
ALL	Toe region	0 - 1.5	0 - 1.5	0 - 1.4	0 - 1.4	0 - 1.8	0 - 1.8
	Linear region	1.5 - 2.7	1.5 - 2.7	1.4 - 2.4	1.4 - 2.4	1.8 - 3.0	1.8 - 3.0
	Subfailure region	2.7 - 3.9	2.7 - 3.9	2.4 - 3.4	2.4 - 3.4	3.0 - 4.4	3.0 - 4.4
	Failure region	3.9<	3.9<	3.4<	3.4<	4.4<	4.4<
PLL	Toe region	0 - 1.1	0 - 1.1	0 - 0.8	0 - 0.8	0 - 1.0	0 - 1.0
	Linear region	1.1 - 1.8	1.1 - 1.8	0.8 - 1.5	0.8 - 1.5	1.0 - 1.5	1.0 - 1.5
	Subfailure region	1.8 - 3.2	1.8 - 3.2	1.5 - 2.7	1.5 - 2.7	1.5 - 2.7	1.5 - 2.7
	Failure region	3.2<	3.2<	2.7<	2.7<	2.7<	2.7<
CL	Toe region	0 - 1.2	0 - 1.2	0 - 1.4	0 - 1.4	0 - 1.6	0 - 1.6
	Linear region	1.2 - 2.1	1.2 - 2.1	1.4 - 2.6	1.4 - 2.6	1.6 - 2.7	1.6 - 2.7
	Subfailure region	2.1 - 3.9	2.1 - 3.9	2.6 - 4.8	2.6 - 4.8	2.7 - 5.0	2.7 - 5.0
	Failure region	3.9<	3.9<	4.8<	4.8<	5.0<	5.0<
LF	Toe region	0 - 2.9	0 - 2.9	0 - 3.4	0 - 3.4	0 - 5.8	0 - 5.8
	Linear region	2.9 - 3.7	2.9 - 3.7	3.4 - 4.5	3.4 - 4.5	5.8 - 6.2	5.8 - 6.2
	Subfailure region	3.7 - 4.4	3.7 - 4.4	4.5 - 5.4	4.5 - 5.4	6.2 - 7.3	6.2 - 7.3
	Failure region	4.4<	4.4<	5.4<	5.4<	7.3<	7.3<
ISL	Toe region	0 - 2.6	0 - 2.6	0 - 2.3	0 - 2.3	0 - 3.8	0 - 3.8
	Linear region	2.6 - 3.8	2.6 - 3.8	2.3 - 4.1	2.3 - 4.1	3.8 - 4.6	3.8 - 4.6
	Subfailure region	3.8 - 6.1	3.8 - 6.1	4.1 - 6.6	4.1 - 6.6	4.6 - 7.3	4.6 - 7.3
	Failure region	6.1<	6.1<	6.6<	6.6<	7.3<	7.3<

Effect of HSM configuration in 25° head-neck flexion:

Endplate effective stress response:

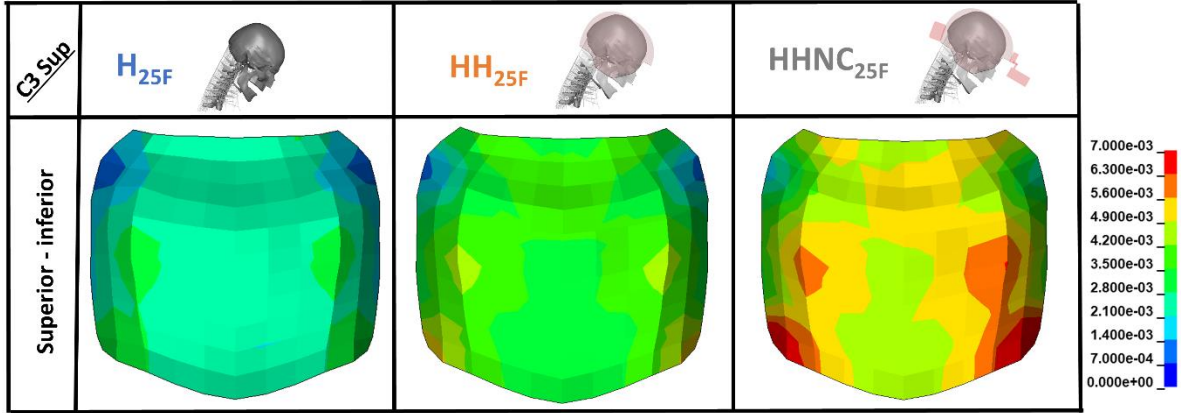


Figure D1: Illustrating the effective stress contours in the C3 superior endplate in 25° head-neck flexion with and without the HSM (superior-inferior perspective).

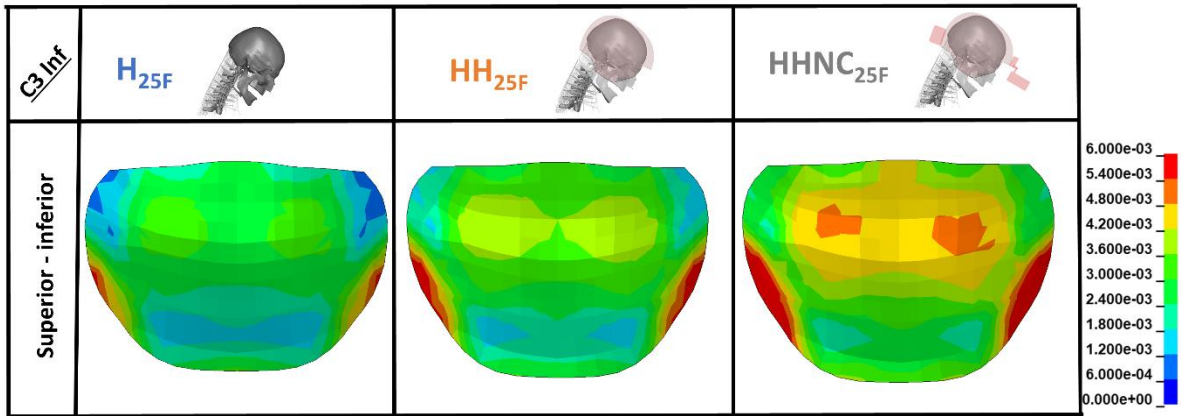


Figure D2: Illustrating the effective stress contours in the C3 inferior endplate in 25° head-neck flexion with and without the HSM (superior-inferior perspective).

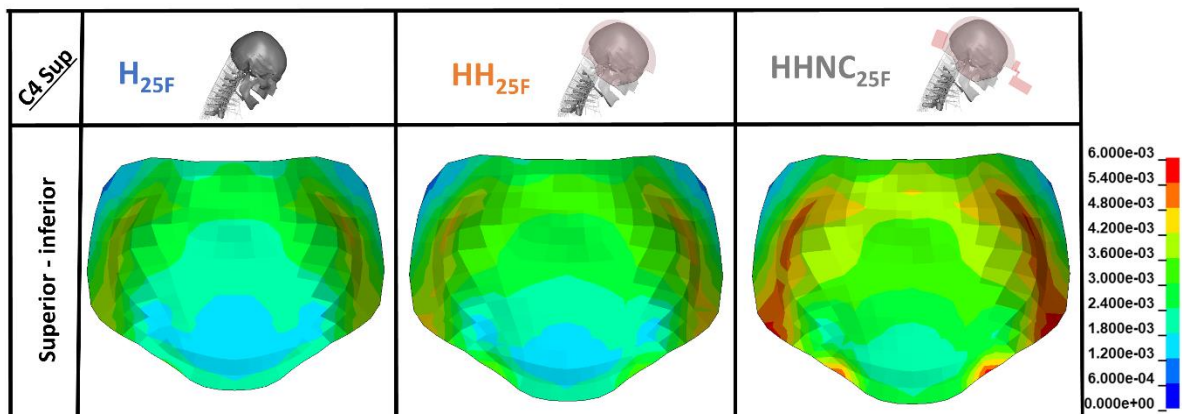


Figure D3: Illustrating the effective stress contours in the C4 superior endplate in 25° head-neck flexion with and without the HSM (superior-inferior perspective).

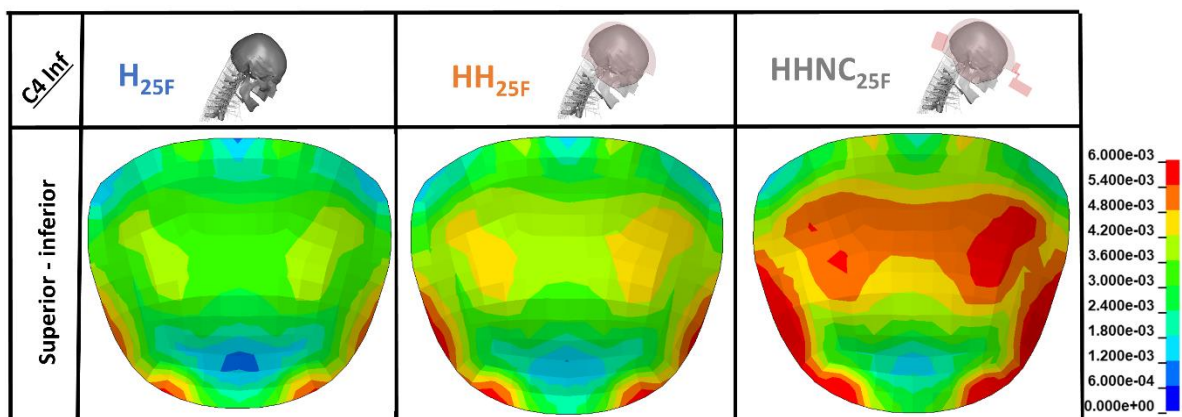


Figure D4: Illustrating the effective stress contours in the C4 inferior endplate in 25° head-neck flexion with and without the HSM (superior-inferior perspective).

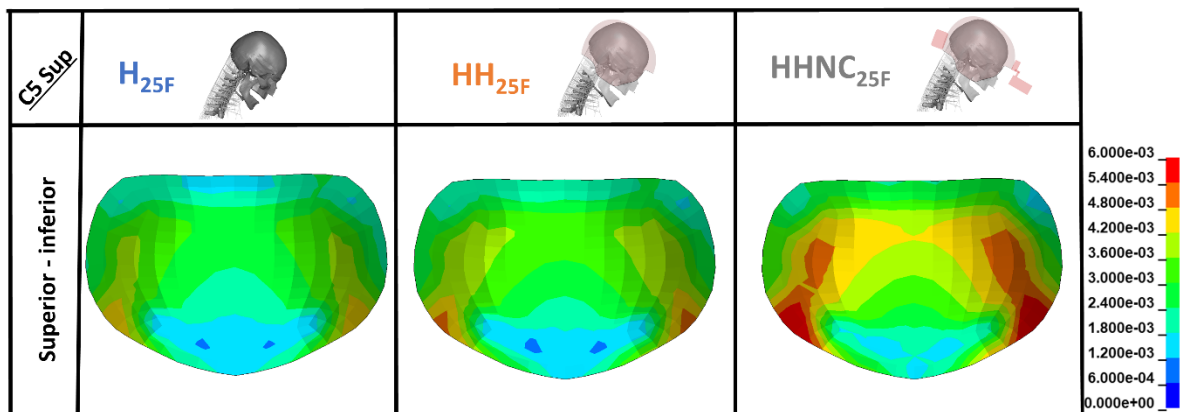


Figure D5: Illustrating the effective stress contours in the C5 superior endplate in 25° head-neck flexion with and without the HSM (superior-inferior perspective).

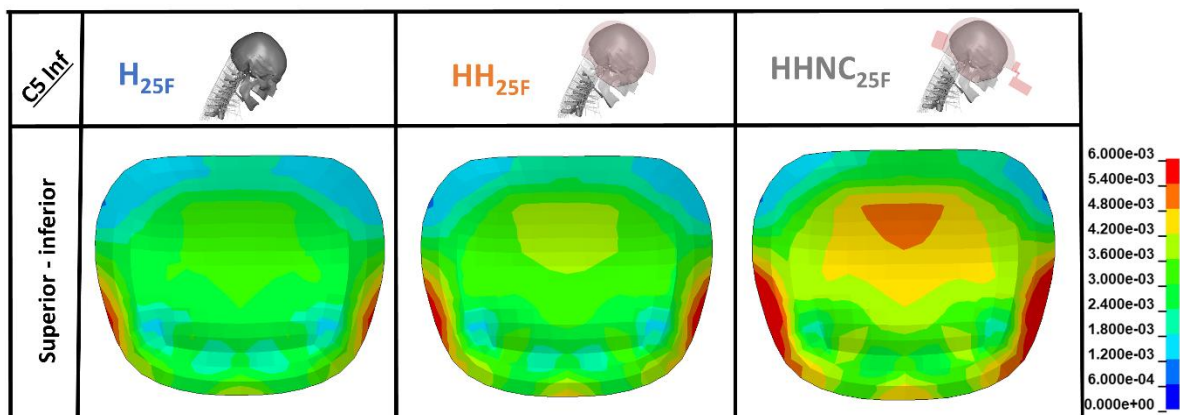


Figure D6: Illustrating the effective stress contours in the C5 inferior endplate in 25° head-neck flexion with and without the HSM (superior-inferior perspective).

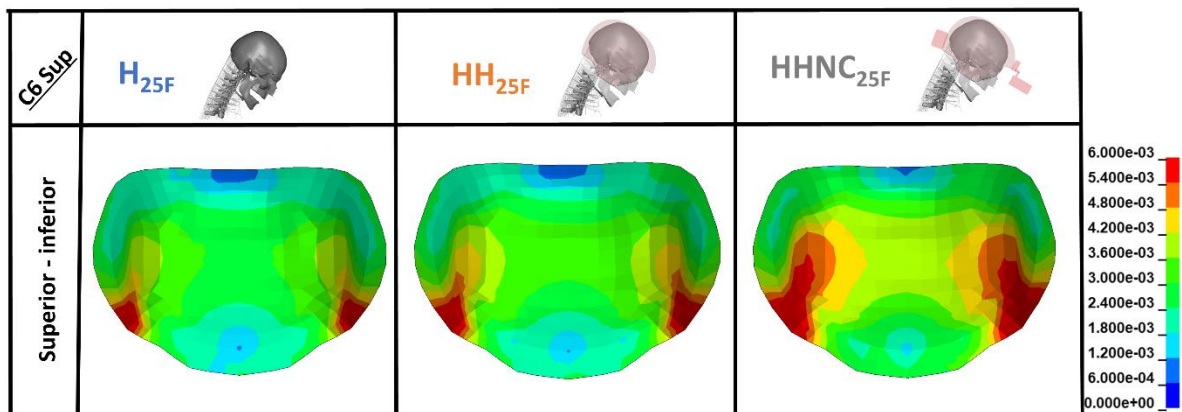


Figure D7: Illustrating the effective stress contours in the C6 superior endplate in 25° head-neck flexion with and without the HSM (superior-inferior perspective).

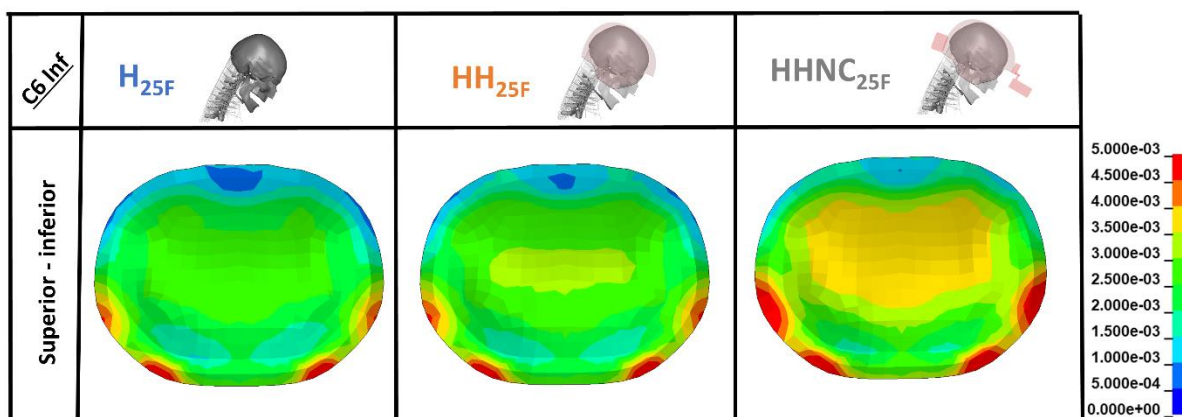


Figure D8: Illustrating the effective stress contours in the C6 inferior endplate in 25° head-neck flexion with and without the HSM (superior-inferior perspective).

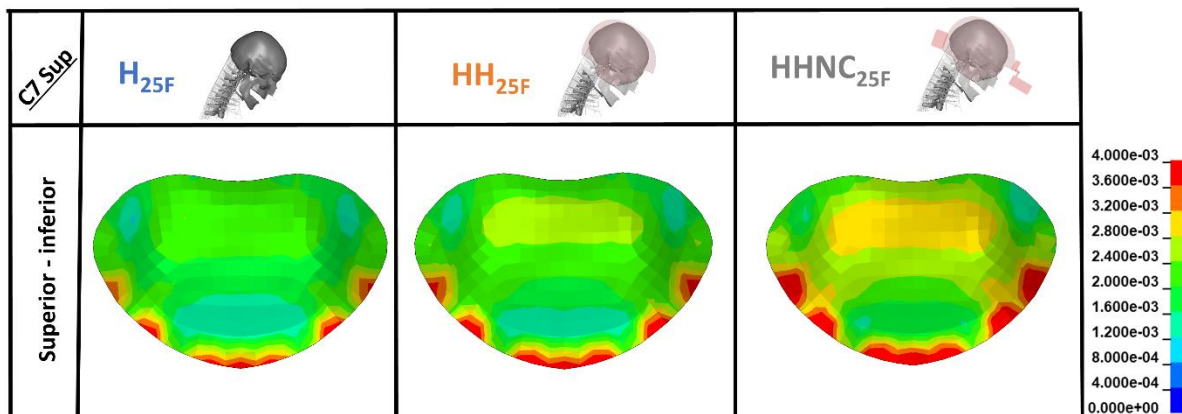


Figure D9: Illustrating the effective stress contours in the C7 superior endplate in 25° head-neck flexion with and without the HSM (superior-inferior perspective).

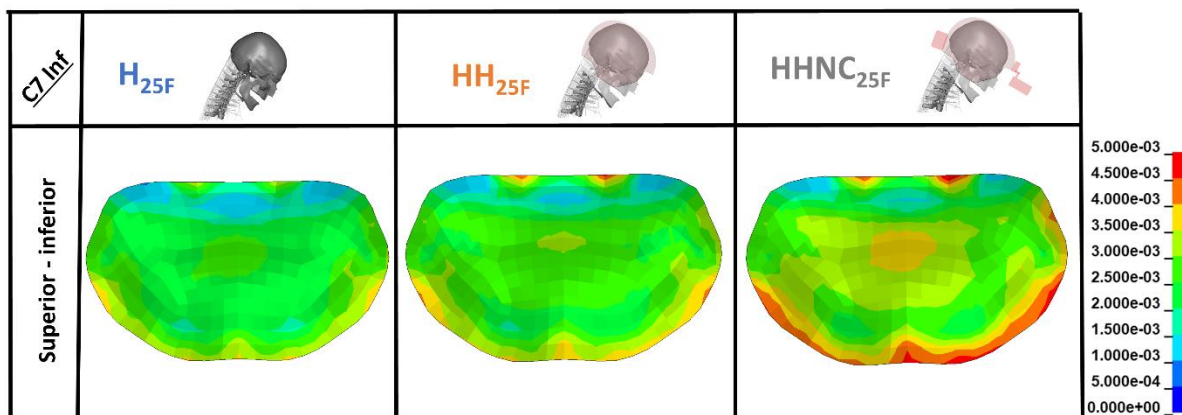


Figure D10: Illustrating the effective stress contours in the C7 inferior endplate in 25° head-neck flexion with and without the HSM (superior-inferior perspective).

AF collagen fiber strain response:

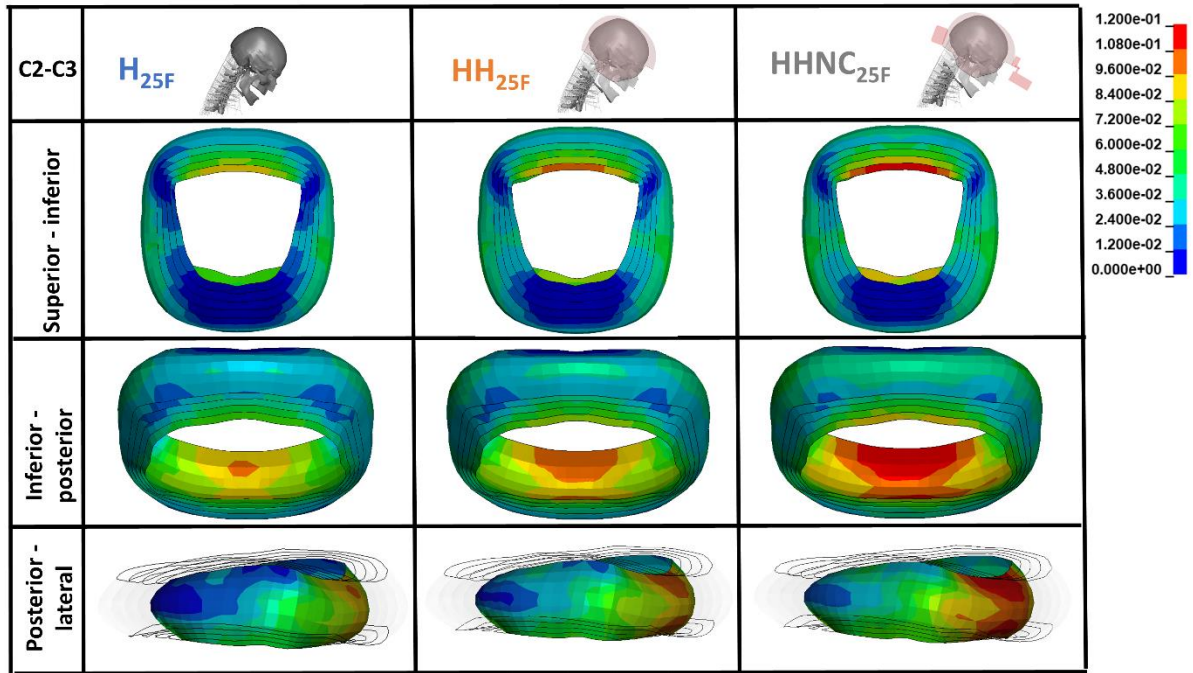


Figure D11: Illustrating the collagen fiber strain contours in the C2-C3 AF in 25° head-neck flexion with and without the HSM in different perspectives, namely superior-inferior, inferior-posterior and posterior-lateral. In the posterior-lateral view, the outer four layers of lamellae are made transparent for visual purposes.

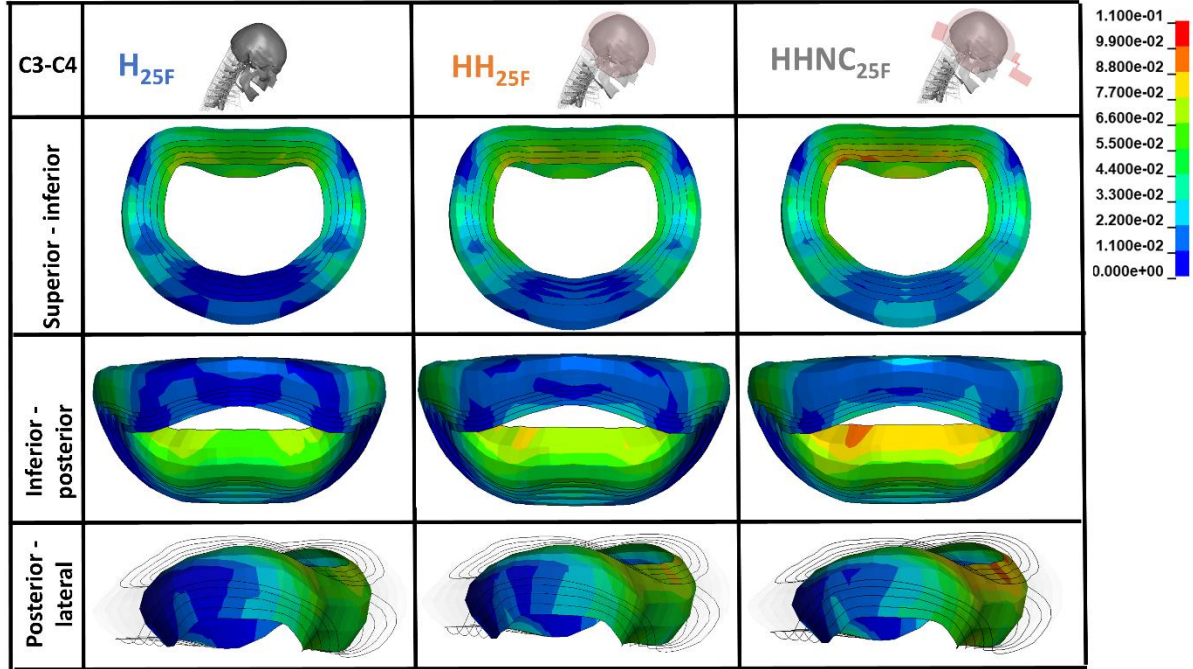


Figure D12: Illustrating the collagen fiber strain contours in the C3-C4 AF in 25° head-neck flexion with and without the HSM in different perspectives, namely superior-inferior, inferior-posterior and posterior-lateral. In the posterior-lateral view, the outer four layers of lamellae are made transparent for visual purposes.

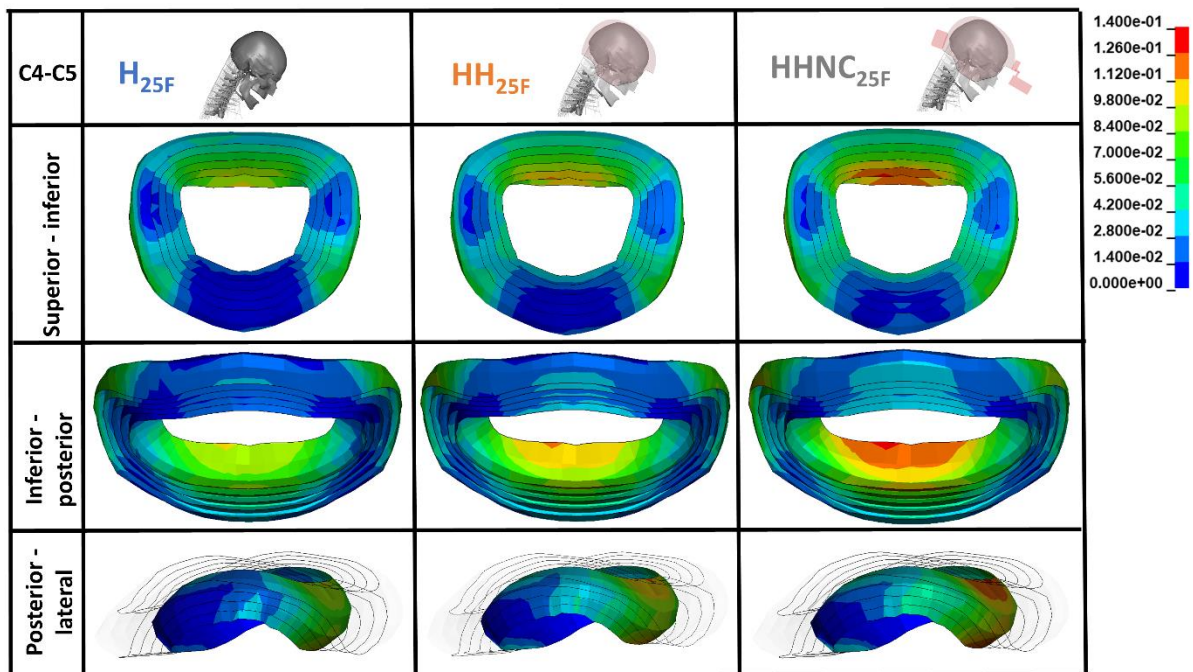


Figure D13: Illustrating the collagen fiber strain contours in the C4-C5 AF in 25° head-neck flexion with and without the HSM in different perspectives, namely superior-inferior, inferior-posterior and posterior-lateral. In the posterior-lateral view, the outer four layers of lamellae are made transparent for visual purposes.

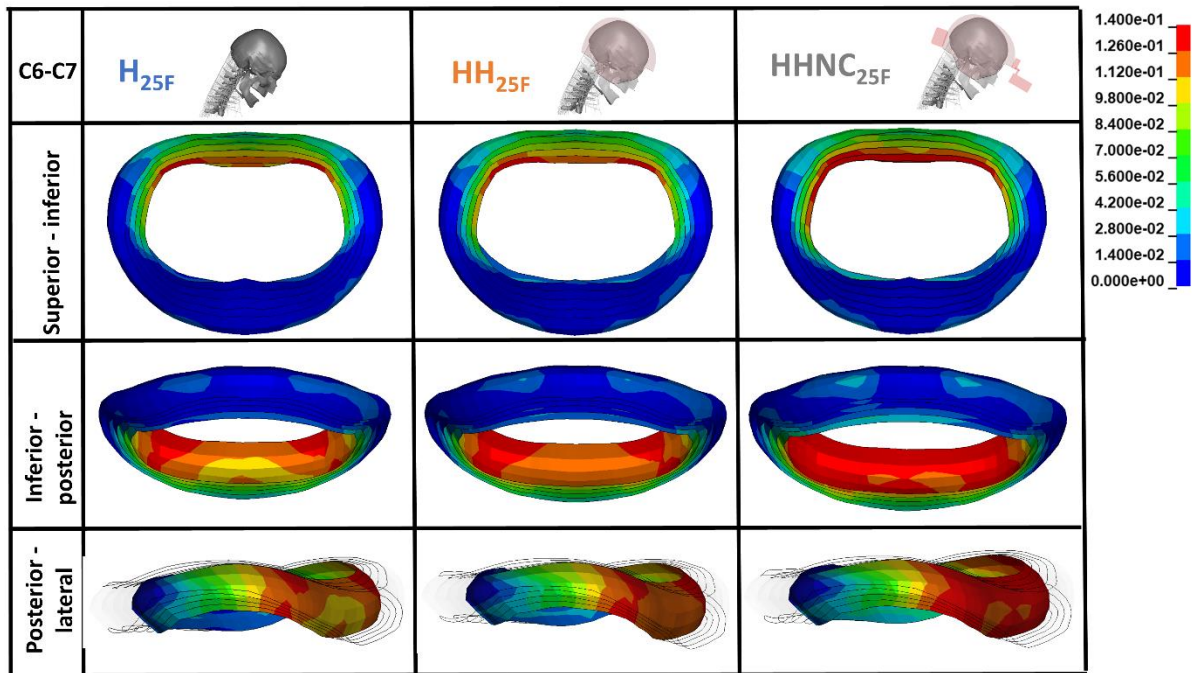


Figure D14: Illustrating the collagen fiber strain contours in the C6-C7 AF in 25° head-neck flexion with and without the HSM in different perspectives, namely superior-inferior, inferior-posterior and posterior-lateral. In the posterior-lateral view, the outer four layers of lamellae are made transparent for visual purposes.

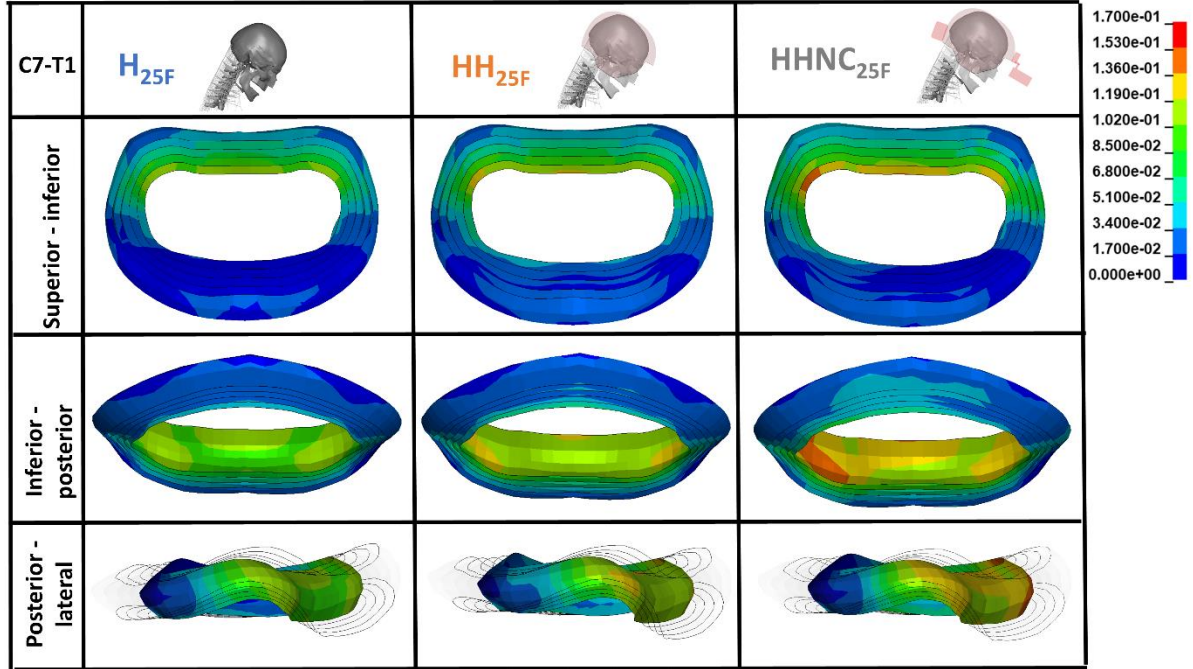


Figure D15: Illustrating the collagen fiber strain contours in the C7-T1 AF in 25° head-neck flexion with and without the HSM in different perspectives, namely superior-inferior, inferior-posterior and posterior-lateral. In the posterior-lateral view, the outer four layers of lamellae are made transparent for visual purposes.

Effect of non-neutral head-neck position magnitude with the HHNC HSM configuration:

Endplate effective stress response:

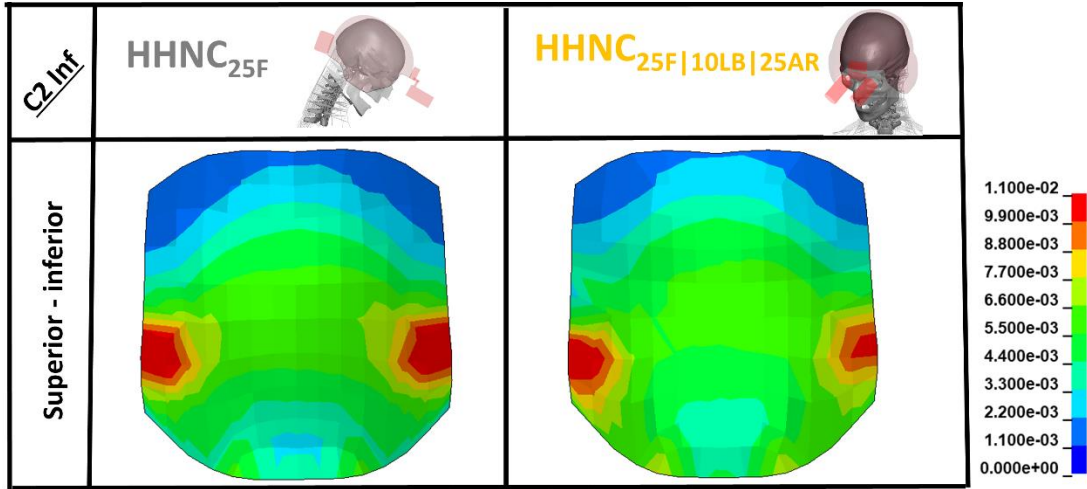


Figure D16: Illustrating the effective stress contours in the C2 inferior endplate in head-neck flexion and combined positions with the HSM (HHNC) (superior-inferior perspective).

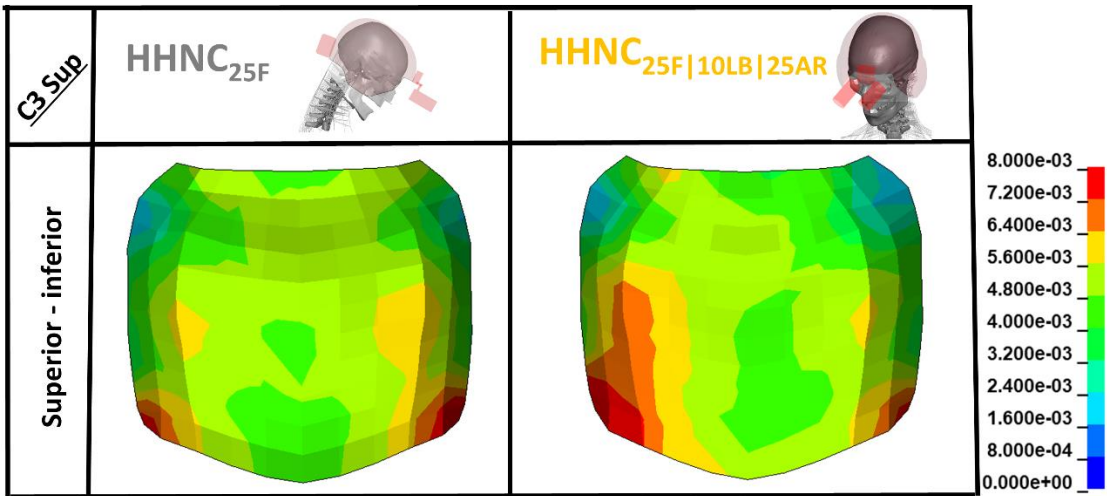


Figure D17: Illustrating the effective stress contours in the C3 superior endplate in head-neck flexion and combined positions with the HSM (HHNC) (superior-inferior perspective).

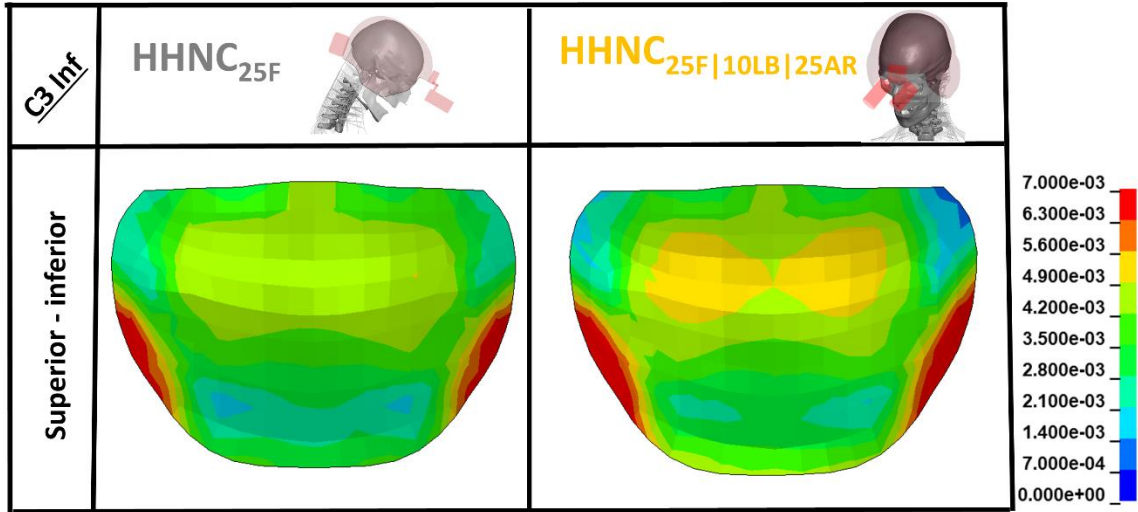


Figure D18: Illustrating the effective stress contours in the C3 inferior endplate in head-neck flexion and combined positions with the HSM (HHNC) (superior-inferior perspective).

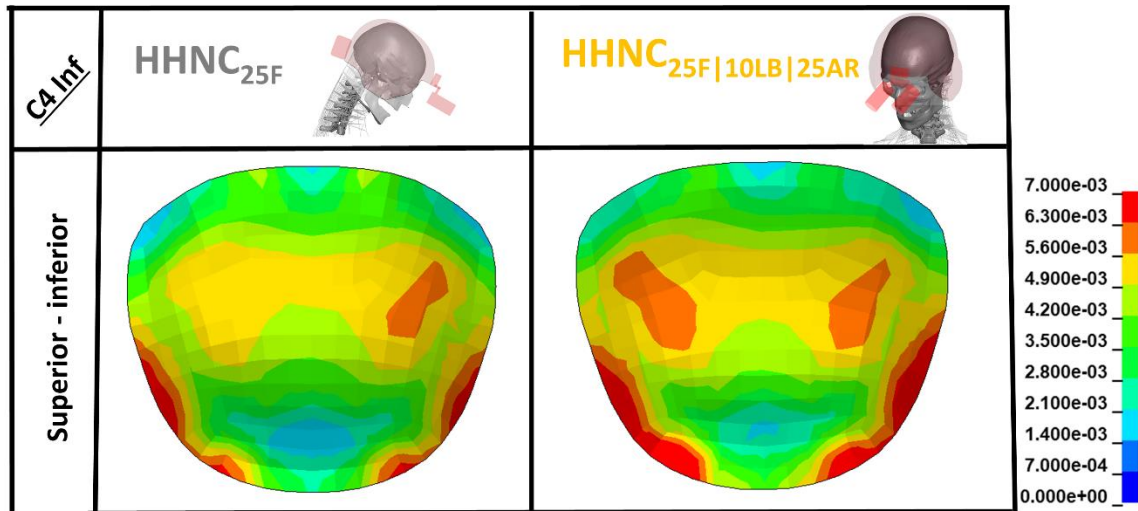


Figure D19: Illustrating the effective stress contours in the C4 inferior endplate in head-neck flexion and combined positions with the HSM (HHNC) (superior-inferior perspective).

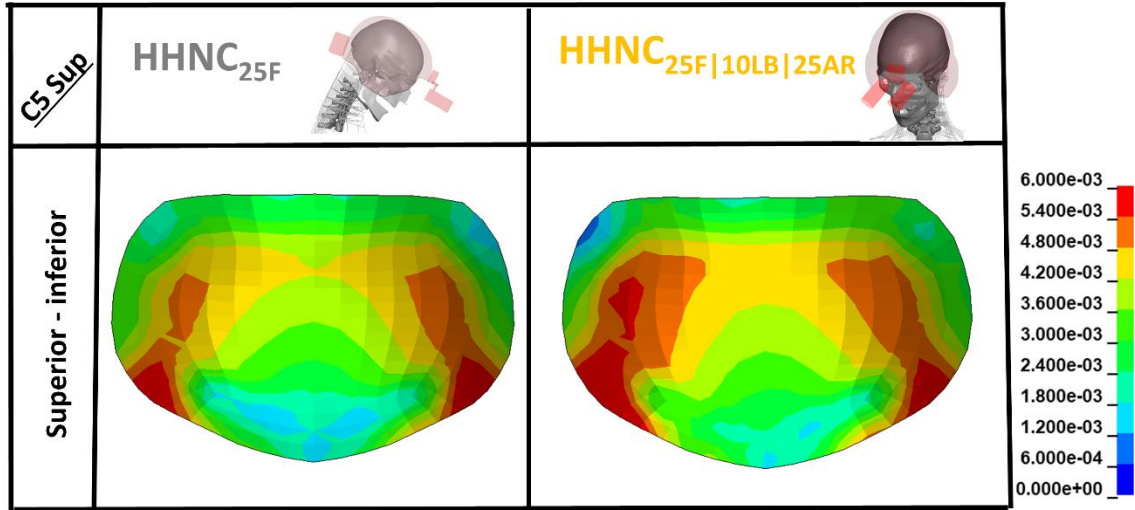


Figure D20: Illustrating the effective stress contours in the C5 superior endplate in head-neck flexion and combined positions with the HSM (HHNC) (superior-inferior perspective).

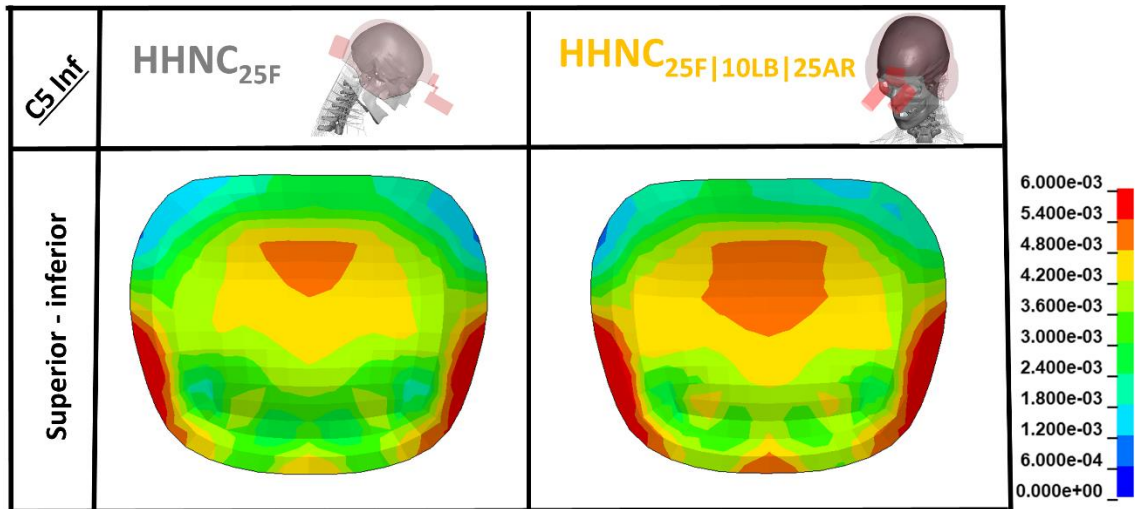


Figure D21: Illustrating the effective stress contours in the C5 inferior endplate in head-neck flexion and combined positions with the HSM (HHNC) (superior-inferior perspective).

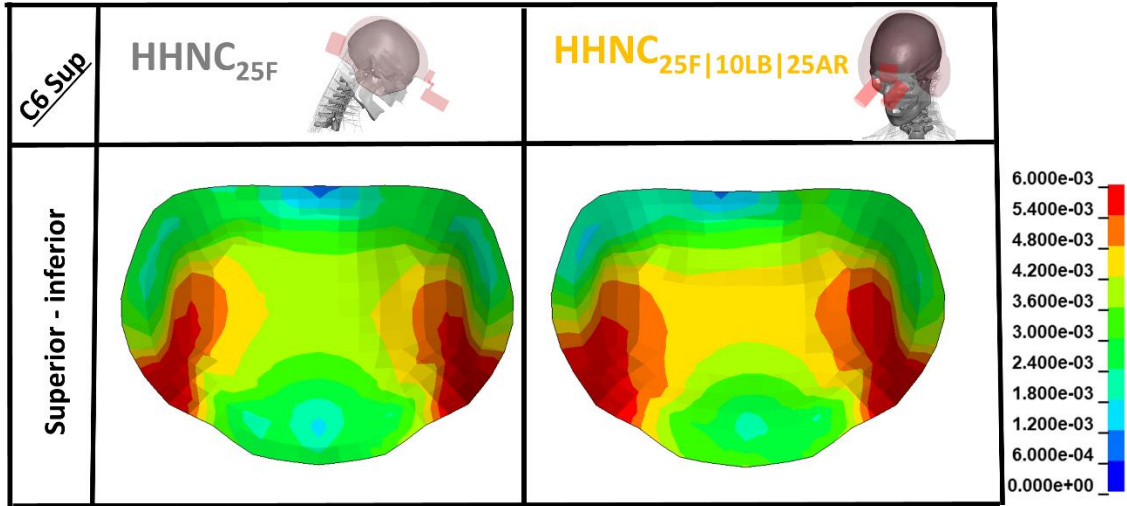


Figure D22: Illustrating the effective stress contours in the C6 superior endplate in head-neck flexion and combined positions with the HSM (HHNC) (superior-inferior perspective).

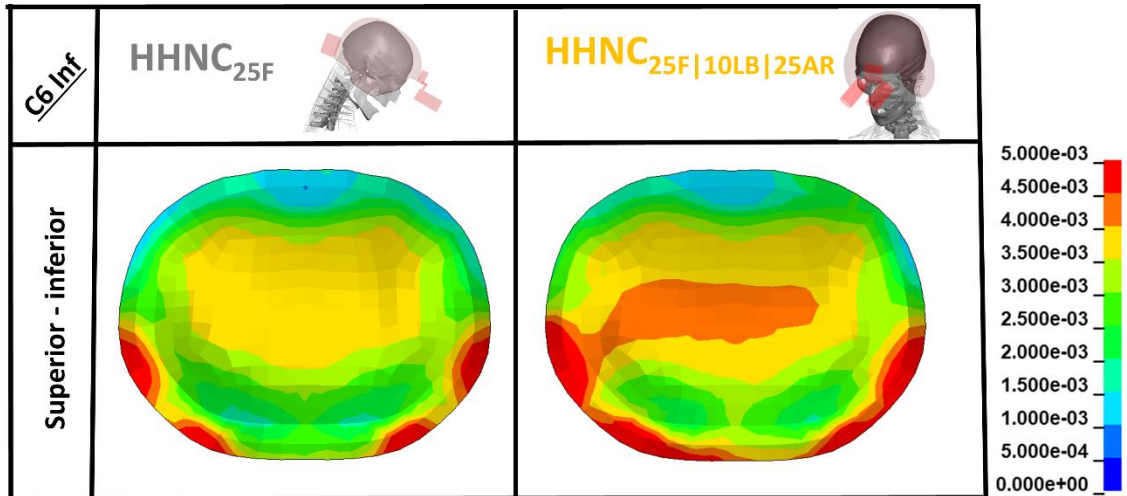


Figure D23: Illustrating the effective stress contours in the C6 inferior endplate in head-neck flexion and combined positions with the HSM (HHNC) (superior-inferior perspective).

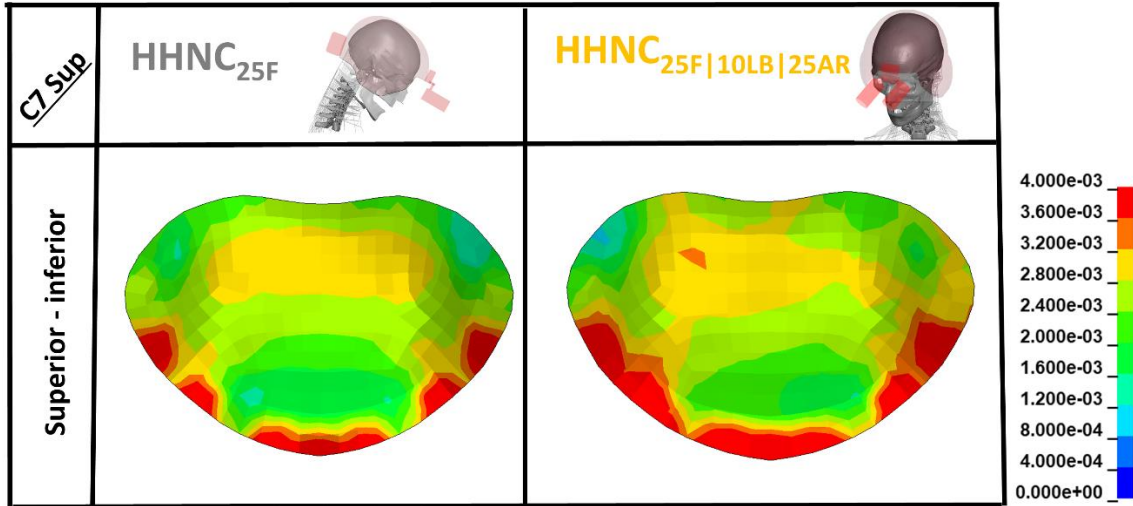


Figure D24: Illustrating the effective stress contours in the C7 superior endplate in head-neck flexion and combined positions with the HSM (HHNC) (superior-inferior perspective).

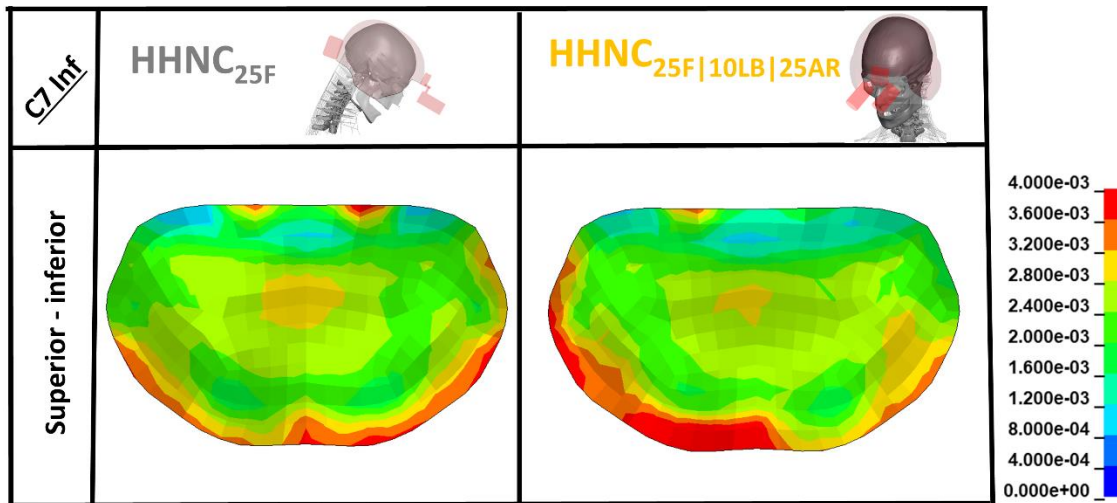


Figure D25: Illustrating the effective stress contours in the C7 inferior endplate in head-neck flexion and combined positions with the HSM (HHNC) (superior-inferior perspective).

AF collagen fiber strain response:

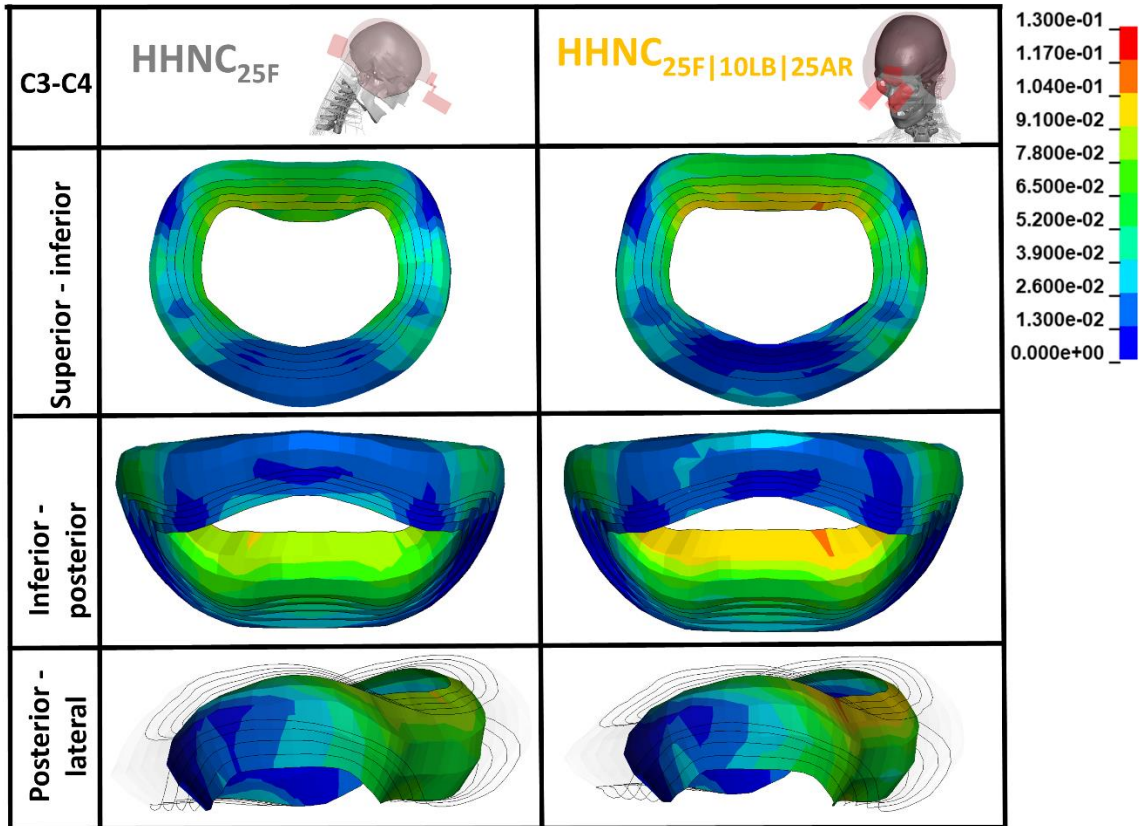


Figure D26: Illustrating the collagen fiber strain contours in the C3-C4 AF in head-neck flexion and combined positions with the HSM (HHNC) in different perspectives, namely superior-inferior, inferior-posterior and posterior-lateral. In the posterior-lateral view, the outer four layers of AF are made transparent for visual purposes to highlight the innermost layer.

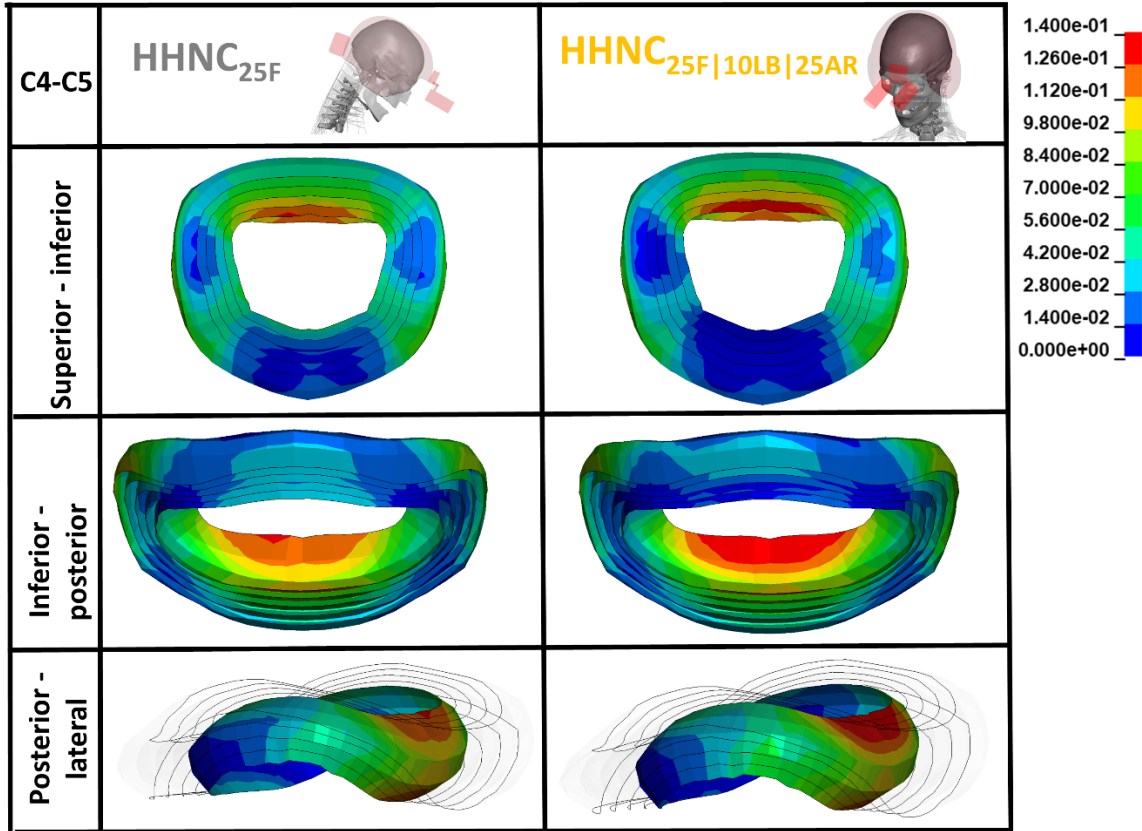


Figure D27: Illustrating the collagen fiber strain contours in the C4-C5 AF in head-neck flexion and combined positions with the HSM (HHNC) in different perspectives, namely superior-inferior, inferior-posterior and posterior-lateral. In the posterior-lateral view, the outer four layers of AF are made transparent for visual purposes to highlight the innermost layer.

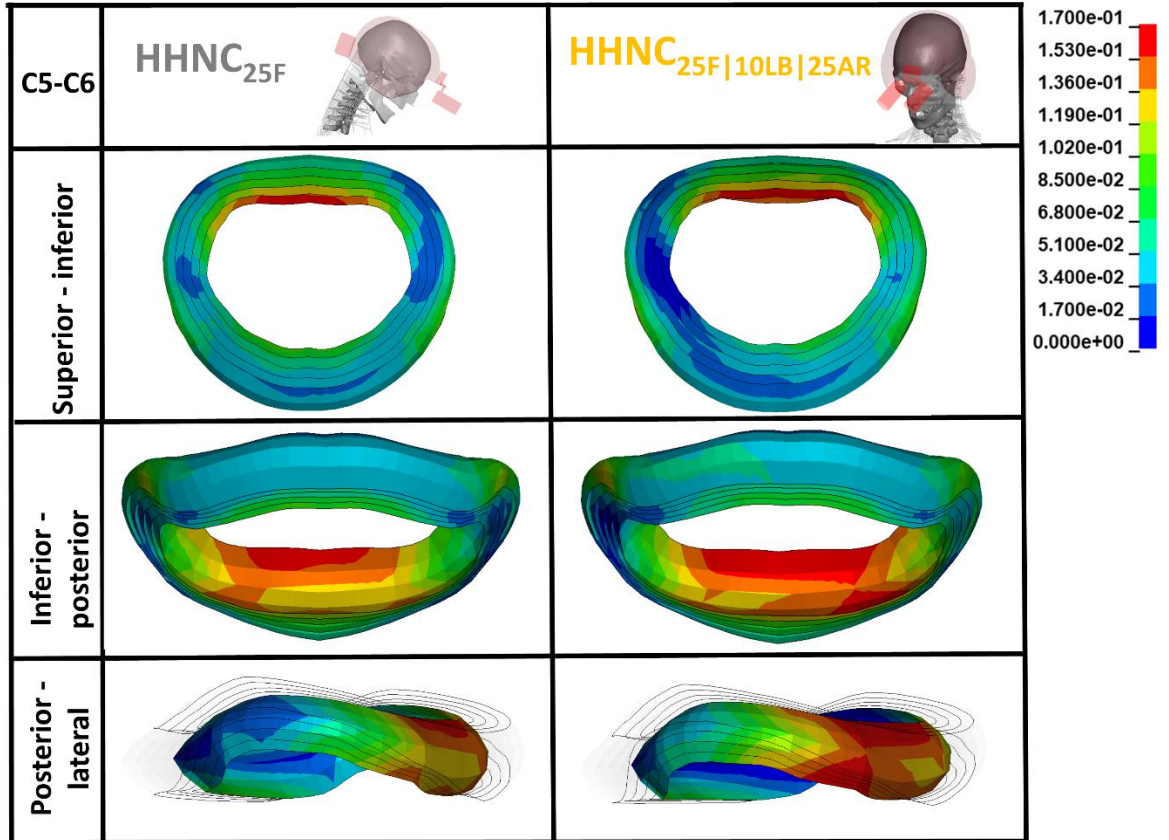


Figure D28: Illustrating the collagen fiber strain contours in the C5-C6 AF in head-neck flexion and combined positions with the HSM (HHNC) in different perspectives, namely superior-inferior, inferior-posterior and posterior-lateral. In the posterior-lateral view, the outer four layers of AF are made transparent for visual purposes to highlight the innermost layer.

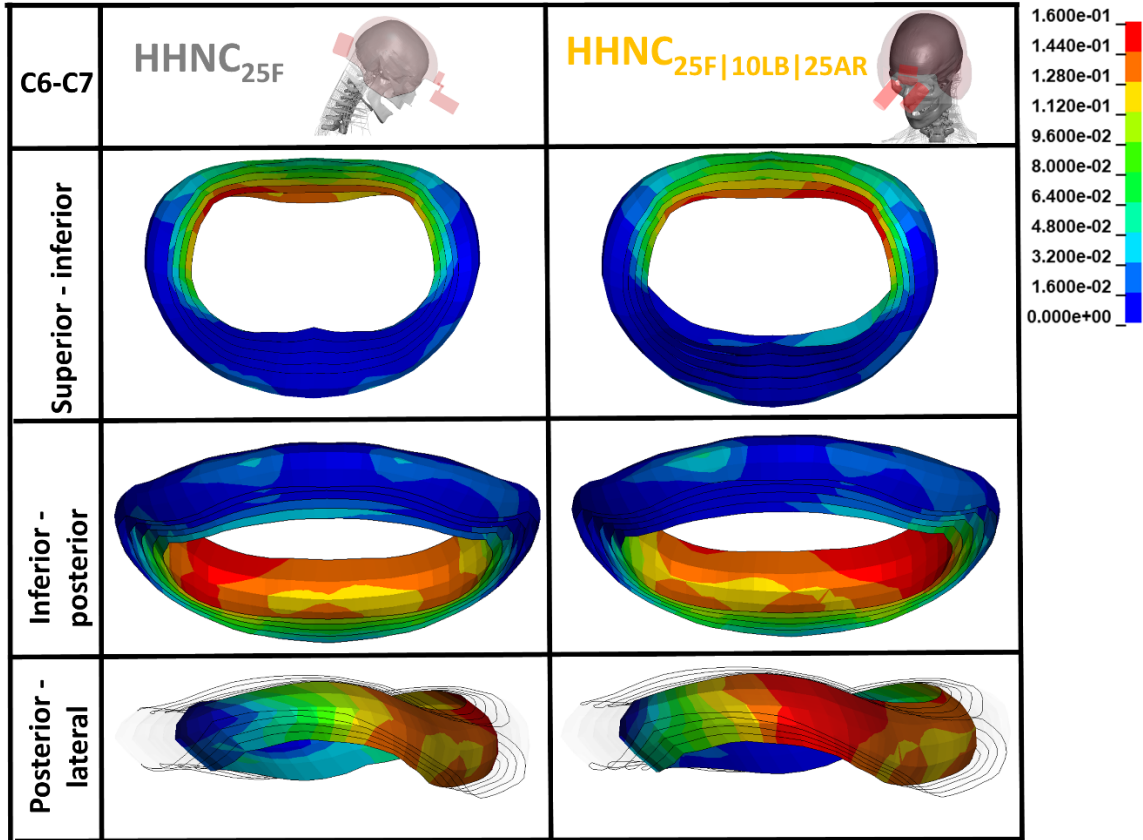


Figure D29: Illustrating the collagen fiber strain contours in the C6-C7 AF in head-neck flexion and combined positions with the HSM (HHNC) in different perspectives, namely superior-inferior, inferior-posterior and posterior-lateral. In the posterior-lateral view, the outer four layers of AF are made transparent for visual purposes to highlight the innermost layer.

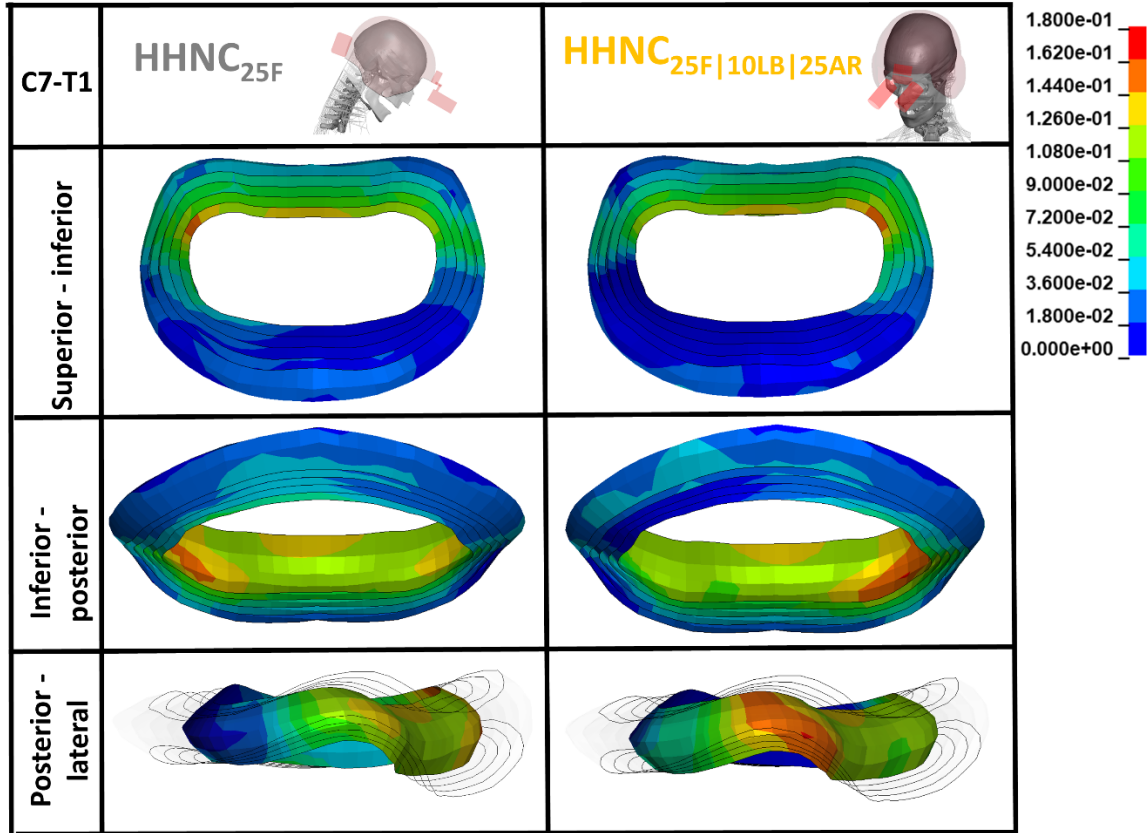


Figure D30: Illustrating the collagen fiber strain contours in the C7-T1 AF in head-neck flexion and combined positions with the HSM (HHNC) in different perspectives, namely superior-inferior, inferior-posterior and posterior-lateral. In the posterior-lateral view, the outer four layers of AF are made transparent for visual purposes to highlight the innermost layer.